UNIVERSIDAD COMPLUTENSE DE MADRID

FACULTAD DE CIENCIAS QUÍMICAS
DEPARTAMENTO DE QUÍMICA FÍSICA I

TESIS DOCTORAL

Exceptional properties of [n]CPPs: why molecular morphology and size matter?

Las excepcionales propiedades de los [n]CPPs: ¿por qué importa tanto el tamaño y la estructura molecular?

MEMORIA PARA OPTAR AL GRADO DE DOCTORA

PRESENTADA POR

Miriam Peña Álvarez

DIRECTORES

Mercedes Taravillo Corralo
Juan Casado Cordón
Valentín García Baonza

Madrid, 2017

Exceptional Properties of [n]CPPs: Why Molecular Morphology and Size Matter?

Las Excepcionales Propiedades de los [n]CPPs: ¿Por qué Importa Tanto el Tamaño y la Estructura Molecular?

Miriam Peña Álvarez

Universidad Complutense Madrid
Facultad de Ciencias Químicas
Departamento de Química Física I

Madrid 2016

Universidad Complutense de Madrid
Facultad de Ciencias Químicas
Departamento de Química Física I

Exceptional Properties of [n]CPPs: Why Molecular Morphology and Size Matter?

Las excepcionales propiedades de los [n]CPPs: ¿por qué importa tanto el tamaño y la estructura molecular?

Memoria para optar al grado de Doctor presentada por

Miriam Peña Álvarez

Bajo la dirección de

Mercedes Taravillo Corralo, Universidad Complutense de Madrid

Juan Casado Cordón, Universidad de Málaga

Valentín García Baonza, Universidad Complutense de Madrid

Madrid 2016

A mi madre y a mi padre

sin los cuales no hubiera sido posible

Tesis Doctoral

Exceptional Properties of [n]CPPs: Why Molecular Morphology and Size Matter?

"Las excepcionales propiedades de los [n]CPPs: ¿por qué importa tanto el tamaño y la estructura molecular?"

Directores:

Mercedes Taravillo Corralo
Profesora Titular de Universidad
Departamento de Química Física I, Facultad de Ciencias Químicas
Universidad Complutense de Madrid

Juan Casado Cordón
Profesor Titular de Universidad
Departamento de Ciencias, Campus de Teatinos
Universidad de Málaga

Valentín García Baonza
Catedrático de Universidad
Departamento de Química Física I, Facultad de Ciencias Químicas
Universidad Complutense de Madrid

Autora:

Miriam Peña Álvarez
Universidad Complutense de Madrid
Facultad de Ciencias Químicas
Departamento de Química Física I

Madrid, 2016

Agradecimientos

Muchas son las personas con quienes he tenido la suerte de coincidir a lo largo de estos años de formación predoctoral y muchísimo es, lo que me han enseñado y aportado, no sólo a nivel científico, sino, sobre todo, a nivel personal. A todas ellas quiero expresarles mi más sincero agradecimiento, este viaje habría sido imposible sin vuestra inestimable ayuda.

En primer lugar quisiera agradecer al Ministerio de Educación, Cultura y Deporte la concesión de una beca predoctoral FPU que ha hecho posible el desarrollo de mi trabajo; y al Departamento de Química Física I por el uso de varios de sus medios durante estos años.

A nivel personal quiero dar las gracias a mis directores de tesis: Dña. Mercedes Taravillo, D. Juan Casado Cordón y D. Valentín García Baonza por su gran dedicación durante estos años. Gracias a los tres, porque cada uno constituyen piezas esenciales en mi formación. En especial, quiero agradecer a Merecedes, darme la oportunidad de formar parte de este equipo. Le doy las gracias por todo lo que me ha enseñado, por su disponibilidad, consejos, dedicación, apoyo, ayuda incondicional, y todas las facilidades que me ha ofrecido. He de hacer una mención especial a Juan, al que quiero dar las gracias por el entusiasmo contagioso puesto en todas las investigaciones, trabajos y discusiones, y por sus ganas de enseñar que hacen que todo esfuerzo merezca la pena. Le estoy muy agradecida por adoptarme como estudiante aun cuando no lo era, por su disponibilidad, su dedicación, su incondicional apoyo, por sus buenos consejos, por ayudarme tanto. Por último, y no por ello menos importante, le quiero agradecer a Valen que me acogiese en su maravilloso equipo. Gracias por sus conversaciones, discusiones y consejos, y gracias por ponerme tantas oportunidades delante y dejarme participar en todas ellas.

Gracias a D. J. Teodomiro López Navarrete, que en todo momento me acogió, facilitándome la utilización de todos los equipos de los Servicios Centrales de Apoyo a la Investigación de la Universidad de Málaga, y más allá le agradezco su ayuda y apoyo cuando lo he necesitado.

Por otro lado, tengo que agradecer especialmente "con honores" a Dña. M. Carmen Ruíz Delgado, dado que lo que hoy sé de cálculos se lo debo a ella. Agradecerle su ayuda, paciencia, apoyo y dedicación, siempre con una sonrisa.

Durante mi doctorado he tenido la suerte de realizar dos estancias por las que quiero agradecer dicha oportunidad a la Comunidad Europea y al Ministerio de Educación, Cultura y Deporte estas grandes oportunidades.

My first stay was in Prague, in the electrochemical materials department of the J. Heyrovsky Institute of Physical Chemistry of the Academy of Sciences of the Czech Republic. This stay is responsible for my European Ph. D diploma. I would like to thank Dr. Otakar Frank for his help and support and for including me in his Czech Science Foundation project Nr. 14-15357S, through which the financial support for my experiments in Prague was provided. Por último, agradecer a la Dra. Elena del Corro el haberme ofrecido esta oportunidad y regalarme su entrega, esfuerzo y entusiasmo.

My second stay was in the Science Department of Georgetown University, in Washington DC under Prof. Miklos Kerstez supervision. I would like to infinitely thank him for all his support, the energy he put in his teaching and his willingness to share professional and scientific knowledge. I would like to thank as well all the members of his group with who I had the chance to share not only the working space but also unforgettable moments. Thanks, Meagan, Pierre, Troy, and more specially thank you Lili.

Por cuestiones técnicas me he visto envuelta en un ir y venir a Málaga; maratones de experimentos que no podrían haber sido más satisfactorios. De esta satisfacción son responsables todos los miembros del grupo de Espectroscopia Molecular De Materiales para la Electrónica Orgánica. Gracias a todos y todas por acogerme tan bien, Belén, Cristina, Estefanía, Rafa, Rocío y

Víctor, infinitamente gracias. Y por último, gracias al equipo de "*workaholic*" Zafra y Paula; su ayuda, su amabilidad y el haberme enseñado simplemente que "¡la vida es así!". Hago mención doble de agradecimiento a Paula, por todos los momentos compartidos, y ante todo, por su amistad.

Llega el turno de agradecer a los que más cerca me quedan, el equipo de Madrid del grupo de altas presiones. Gracias a este equipazo que para todo vale por tantísimos momentos de risas, estrés, cafés, comidas, que regalan al día a día el gusto de trabajar: Adri, Alba, Álvaro, Bérengère, Edu, Irene, a la que la aceptamos como nuestra, Javi, Laura, Lucky, Merche, Óscar y Víctor. En este grupo también incluyo a Isa, a la que le agradezco de una manera más particular su compañía, su apoyo y su amistad. Y como no gracias a Ángel y Ele, mis primeros compañeros de despacho y de vida científica en el grupo; les debo muchísimo, tanto en lo profesional como en lo personal. A Ángel le agradezco su disponibilidad y ayuda incondicional, sus ganas de enseñar, enfrentándose a mis preguntas, y su constante respuesta "vamos a mirarlo". A Ele le debo el haber podido trabajar con una celda entre otras muchas cosas. Le agradezco su ayuda cuando más lo he necesitado y enseñarme que cuando las cosas se hacen con gusto e ilusión, siempre salen.

No puedo olvidar mi agradecimiento al "*MALTA team*", por todas las reuniones y congresos, que indudablemente han formado una parte fundamental de mi formación. Agradecer su profesionalidad, entusiasmo y el que muestren su lado más humano que hace que el grupo de alta presión sea único.

Me gustaría ahora agradecer de una manera especial a la profesora del departamento de Química Inorgánica de la UCM Dña. Mercedes Cano. A ella y al profesor D. José Vicente que en tercero de carrera me inyectaron esa dosis de inquietud y ganas de trabajar en un laboratorio, básicos para hacer la tesis.

Echando la vista un poco más atrás en el tiempo, en mi paso por la Universidad Complutense de Madrid he conocido a muchísima gente que sin duda alguna me han enseñado muchísimo y de todos ellos me llevo un poquito. Entre este mar de gente conocí a lo que ahora forman parte de mis mayores apoyos: gracias Leti, Andrea, Cástor, Iñigo, Paula y San. Gracias por formar tan buen equipo, estando formado por personas tan diferentes, las piezas encajan perfectamente. Alegría, diversión, coraje, valentía y entusiasmo os definen, *thank you*. Gracias por la vida que desprendéis, por tantos buenos momentos y nuestras gymkanas entre clase y labo. Inolvidable.

Dentro de este grupo debo destacar la presencia de mi compañera de aventuras, San, o futura Doctora Alexandra Rodríguez Rivero, a la que tanto debo. Una amiga de las que siempre están ahí, tanto en los buenos como en los malos momentos. Gracias por crecer conmigo.

En mis decisiones para llegar hasta aquí ha influido la futura Doctora Paula Ruiz Castillo. Entre las muchas cosas recuerdo la emoción en cada duda resuelta, cada problema entendido y cada "Mir inténtalo", le doy las gracias por cada una de los pasos que hemos disfrutado juntas.

También, quiero mencionar a Paula Rubi, Jorge, Juanjo, os agradezco el simplemente estar siempre disponibles con una sonrisa, broma o palabra, dispuesta al entendimiento. Gracias.

Gracias a mi gente de Fuensa y en especial al Grupo 11 por tantos y tantos buenos momentos de dispersión y risas. Gracias también a Eva, Ana, Lidi y Jesús, por sencillamente ser el mejor grupo. Gracias en especial a Lidi, por todo su apoyo, consejos y buenos momentos, gracias por ser mi compañera de fatiga bibliotecaria, gracias por siempre estar ahí.

Por último y más importante agradecer a toda mi familia su apoyo incondicional, gracias a mis tíos, primos y cuñadas favoritas, Marta, Bea e Isa. Especialmente agradecer a mis hermanos, José Carlos, Javier y Mario, su ejemplo, su afán de superación, hábitos y costumbres, sus palabras y "hechos", su apoyo, ayuda y disponibilidad. Así mismo, siendo yo la mezcla de mis tres hermanos, todo lo que somos se lo debemos a mis padres, Máximo y Teresa, mis mayores ídolos y ejemplo de ilusión por aprender y conocer. A mis padres les doy las gracias por ser mi apoyo y sustento, por darme mi espacio de confort y tranquilidad, facilitando y allanándome el camino. Finalmente, agradecer a Rien su incesante ayuda, disponibilidad y energía, sin importar el lugar, el día, ni la hora, porque querer es poder, *dank je wel*.

Index

List of Most used Abbreviations

[n]CPP: cyclic paraphenylene with *n* phenyl units.

[n]LPP: linear paraphenylene with *n* phenyl units.

PPP: poly-paraphenylene.

CNTs: carbon nanotubes

SWCNTs: single walled carbon nanotubes.

DWCNTs: double walled carbon nanotubes.

MWCNTs: multi walled carbon nanotubes.

DFT: density functional theory.

B3LYP: calculation at the spin restricted hybrid functional with three parameters of Becke and Lee-Yang-Parr.

UB3LYP: DFT calculation at the spin unrestricted hybrid functional with three parameters of Becke and Lee-Yang-Parr.

6-31G(d,p): Split valence double zeta basis sets 6 Gaussian functions are used to describe the core orbitals. The valence electrons are represented by three Gaussians: the contracted part by two Gaussians and the diffuse part by one Gaussian. It includes polarization functions corresponding to *p* orbitals for hydrogen and *d* orbitals for the first and second row elements.

TDDFT: time-dependent density functional theory.

UV-vis: ultraviolet-visible.

SAC: sapphire anvil cell.

PT: pressure transition.

PTL: pressure torsional limit.

FWHM: full width half maximum.

HOMO: highest occupied molecular orbital.

LUMO: lowest unoccupied molecular orbital.

RFM: radial flexural mode.

RBM: radial breathing mode.

p-RBM: pseudo-radial breathing mode.

BLA: bond length alternation.

ECC model: effective conjugation coordinate model.

NICS: nucleus-independent chemical shifts.

Chapter 1

Framework

Cycloparaphenylenes ([n]CPPs from now on), were firstly synthesized in 2008, and promptly joined the fascinating world of carbon nano-materials in their own right. Since then, the number of studies concerning their size-dependent optical, electronic, and morphological properties is steadily growing. These cyclic molecular systems are formed by phenyl units connected each other in their para-position, a configuration that resembles an ultra-short armchair single-wall carbon nanotube (SWCNT). The number of π electrons which form the cycle increases with increasing the number of phenyl units but, in contrast to what occurs in their linear analogues ([n]LPPs), the energy gap in [n]CPPs is lower for the smaller cycles. Consequently, among the major interests is to understand how the energy gap changes with the size of [n]CPPs. Additionally, their cyclic electron-rich cavity provides [n]CPPs with the ability to host and to stabilize either electron-rich or electron-poor guests. Such hosting capability broadens their potential applications, since the resulting supramolecular structures would share interesting properties of both the host and the guest.

The development of new [n]CPP-based nanostructures relies on the control of the electronic gap governed by the magnitude of their electronic π–conjugation. In this Ph. D. Thesis we put forward a systematic study on the electronic properties of [n]CPPs, providing a thorough link between [n]CPPs with both SWCNTs and [n]LPPs. Curvature, strain and electronic π–conjugation are the main characteristics of [n]CPPs that we will systematically study to examine their unexplored properties, and eventually their potential applications.

In addition, we shall use [n]CPPs as models to realize the concept of radial cyclic electronic π–conjugation, which has been only theoretically considered so far. Within the cyclic π–conjugation terminology, we will analyze the required morphological parameters and to which extent they modulate the molecular properties. The understanding of this novel and interesting concept can provide us with the basic tools for synthesizing tailored molecular materials with the desired properties.

Let us emphasize that we shall take advantage of the success of Raman spectroscopy for characterizing carbon-based materials. Raman spectroscopy is also among the most suitable tools to probe the electronic properties of such materials due to the high susceptibility of the π-electrons polarizability. In this Ph. D. Thesis we present a systematic study of a series of [n]CPPs considering all the geometrical parameters that might be involved in their vibrational modes. We shall examine the influence of size on the Raman spectra of [n]CPPs, together with the effect of oxidation and mechanical compression, since these two effects might also induce drastic changes on their molecular structures. Finally, we will explore the hosting capabilities of [n]CPPs as well as their mechanical properties relative to those of SWCNTs.

In summary, the title of this Ph. D. Thesis reflects our aim to explain the effect that the cyclic morphology may cause on the molecular properties and the electronic π–conjugation of [n]CPPs, addressing the point at which extent these properties might be modulated by strain, size, shape, or a combination of them.

1.1. Introduction

Since the discovery of benzene as the first cyclic conjugated system,[1] major efforts have been made to understand the structural and electronic properties resulting from its in-plane p_z infinite conjugation.[2,3] Soon after the discovery of the properties of benzene, more complex molecules, formed by a series of several conjugated units took the scientific attention (e.g.; Polyacetylene (PA)[4]). These systems are known as polyconjugated species, in which the extended conjugation of the p_z orbitals provides distinct chemical and physical properties. In other important conjugated π-systems, denominated polyaromatic molecules, the π orbitals are located in the same plane and parallel to each other.[5]

Polyaromatic systems can be divided into two classes based on the extent of the delocalization. The first class consists of a linear chain of aromatic units linked to each other by single or quasi single C-C bonds, as in linear paraphenylenes,[6,7] [n]LPPs, where *n* is the number of phenyl units, or as in parathiophenes[8] (see Figure 1a and 1b, respectively). Under certain geometrical conditions, two p_z orbitals from neighboring units that face each other, can overlap and generate interring delocalization extending the aromatic conjugation. The second class of polyaromatic systems consists of polycondensed aromatic rings, ranging from small to very large polycyclic aromatic hydrocarbons (PAHs), such as phenanthrene, and tetracene (see Figure 1c and 1d). PAHs are substantially rigid over sizeable distances so there are no barriers to delocalization through the conjugated structural plane. The two–dimensional "polymer" of these systems is graphene.[9,10] Hence, the properties of the PAHs small units can be used to explain certain behaviors of larger solids, with the added advantages of high solubility and their controlled synthesis.

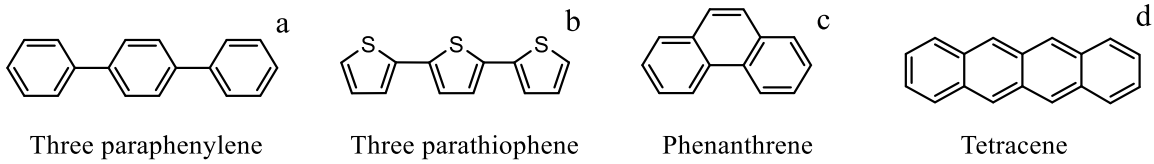

Figure 1. a) three paraphenylene, b) three parathiophene, c) phenanthrene, d) tetracene.

The properties of the polyaromatics molecules conjugated along the *xy* plane have been well studied. However, the potential effects caused by p_z orbitals orientational change towards a radial cyclic p_z configuration still remain unexplored. Theoretical cyclic systems with radially oriented π orbitals such as [n]cyclophenacenes (Figure 2a),[11] and [n]cyclacenes (Figure 2b)[12] have been largely investigated.[13] Unfortunately, to our knowledge the synthesis of those cyclic structures has not been achieved yet.[14] In line with the PAHs definition, [n]cyclophenacenes and [n]cyclacenes have been

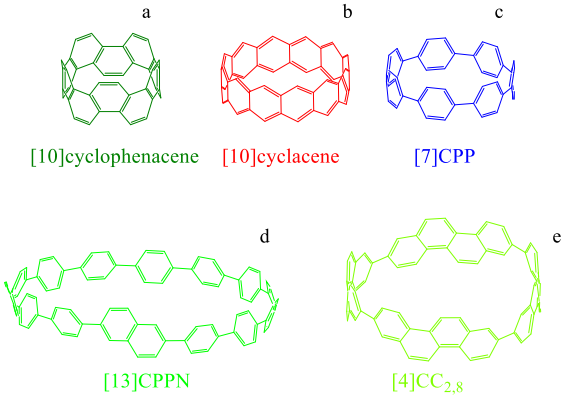

Figure 2. a) [10]cyclophenacene, b)[10]cyclacene, c) [7]Cyclo-paraphenylene ([7]CPP), d) cyclo [13]paraphenylene-2,6-paphthylene ([13]CPPN), e) [4]cyclo-2,8-chrysenylene ([4]$CC_{2,8}$).

proposed as templates for the bottom-up synthesis of armchair and zigzag Single Walled Carbon Nanotubes (SWCNTs) (see Figure 3 with the definitions of the different classes of nanotubes).[15,16] In recent years, cyclo[n]paraphenylenes ([n]CPPs, with *n* = number of phenyl rings), see Figure 2c, have been suggested as models to explore the above mentioned effect of the radial cyclic p_z configuration.[14,17,18] [n]CPPs offer the great advantage of being synthetically available.[19] Remarkably, one of the most interesting features of the [n]CPPs is that they are thought to be the shortest cylindrical version of (n,n) armchair SWCNTs (see Figure 3b).[14,20-24] In this regard, the bottom-up synthesis of armchair SWCNTs using [n]CPPs as templates has been persecuted.[15,25-27]

[n]CPPs are conjugated pure hydrocarbons with a cyclic disposition of 1,4-substituted benzenes. As shown in Figure 4, the [n]CPP's p_z orbitals are oriented towards the center of the macrocycle. Moreover, [n]CPPs have been successfully prepared over a wide array of diameters[24,28-34] ranging from 0.669 nm in [5]CPP[28] to 2.4 nm in [18]CPP.[19] Therefore, the role of the radial p_z orientation can be experimentally studied as a function of *n*, up to the oligomeric limit for the largest [n]CPPs. Many efforts have been done to improve the synthetic route to [n]CPPs and to other radial conjugated derivatives,[35] such as cyclo [13]paraphenylene-2,6-paphthylene ([13]CPPN),[36] or the [4]cyclo-2,8-chrysenylene ([4]$CC_{2,8}$),[37] (Figure 2d and 2e, respectively). Likewise, [13]CPPN and [4]$CC_{2,8}$ could be considered templates of chiral SWCNTs, the (15,14) and the (12,8)SWCNT, respectively.[36,37]

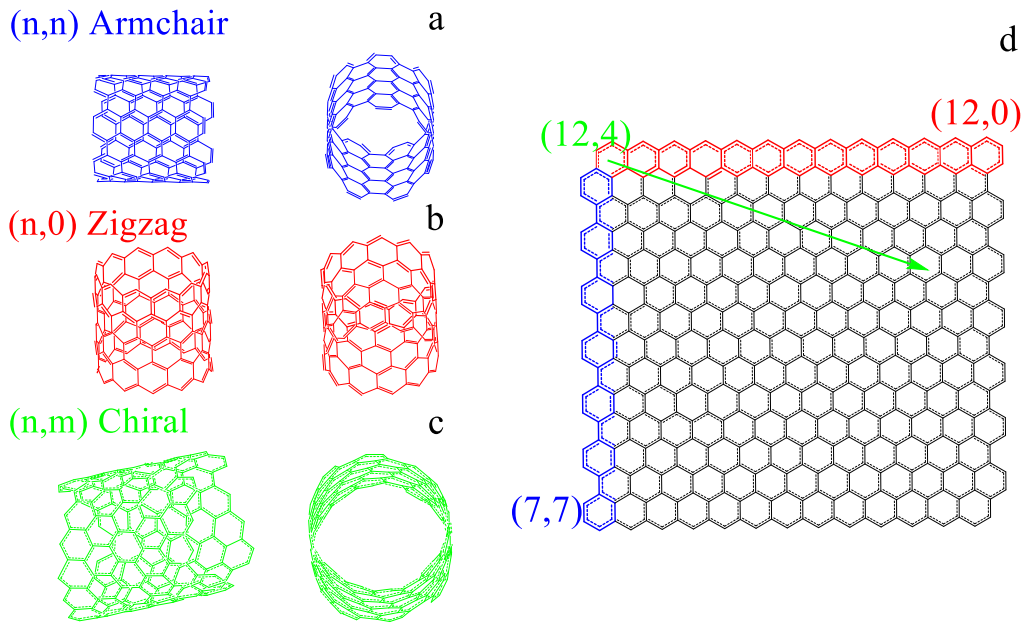

Figure 3. Different types of SWCNTs based on the (n,m) chiral parameters: a) n = m, armchair; b) m = 0, zigzag; c) m ≠ 0 and ≠ n, chiral. d) Graphene sheet, where colored regions are used to mark the rolling directions to form the corresponding SWCNTs. Blue is used for armchair, red is used for zigzag and green for chiral SWCNTs.

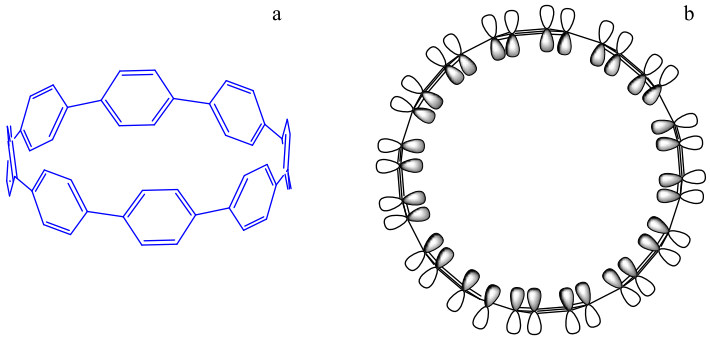

Figure 4. a) [8]Cycloparaphenylene ([8]CPP). b) Schematic representation of the radial π system of [8]CPP in its D_{8h} conformation.

Many potential applications resulting from their cyclic polyaromaticity have been ascribed to [n]CPPs.[35,38] For instance, they can function as light harvesting devices when forming the so-called "Russian dolls": [n]CPPs of the appropriate size occupying the inner cavity of larger [n]CPPs;[39] or as funnels to purify fullerenes, endo or empty, of determined diameters from raw carbonaceous materials.[40,41] In the following we briefly describe some of the most interesting issues of their structure, and the implications in their properties.

- Large [n]CPPs have features close to those of long [n]LPPs. However, large [n]CPPs are more energetic systems than long [n]LPPs. Such energy difference is due to the remnant energy required to deform planar phenyl units towards cyclisation of the [n]CPPs. This consequential energy involved in phenyl deformation and cyclic closure is referred as strain.[42] Phenyl deformation required to form the smaller cycles is larger the smaller the [n]CPPs are; thus, strain energy exponentially increases with the decreasing *n*, being about 114 kcal mol^{-1} for [5]CPP.[28,42-45] Strikingly, these highly energetic systems are stable, which is presumably due to the steadiness that radial cyclic π–conjugation provides.

- Additionally, it has also been suggested that changes from a benzoid to a quinonoid configuration are possible.[19,28] Quinonoidization would be the result of a redistribution of the π electron density from the aromatic phenyl units: aromaticity would be disturbed to form local double bonds between C_{ipso}-C_{ipso} on one side and C_{ortho}-C_{ortho} on the other.

- As shown in Figure 5b, in [n]CPPs the HOMO-LUMO energy gap shrinks with a decreasing *n*. Such an effect has been related with several factors, with the main one being the bending of the structure.[44,45] This is the opposite trend to that depicted by their linear analogues. As seen in Figure 5a, in [n]LPPs the energy gap decreases with the increasing number of phenyl units which form the oligomer. Such an energy gap decrease is due to the lengthening on the in-plane π–conjugation with additional phenyl units.[46]

- On the other hand, the emission maxima in the fluorescence spectra red-shift with a decreasing *n*. This red-shift is in agreement with the quantum efficiency diminution and with longer fluorescence lifetimes for smaller *n*.[45-49] These counterintuitive properties have been ascribed to the growing strain in the smaller [n]CPPs.[45] Thus, [n]CPPs are appropriate for organic electronic applications.

- [n]CPPs, as [n]LPPs do, depict torsional angles between neighboring phenyl units.[28-34,44] Thus, in principle the p_z orbitals from neighboring units do not overlap. As result, conjugation between neighboring phenyl units is not entirely favored. However, in [n]CPPs these torsions

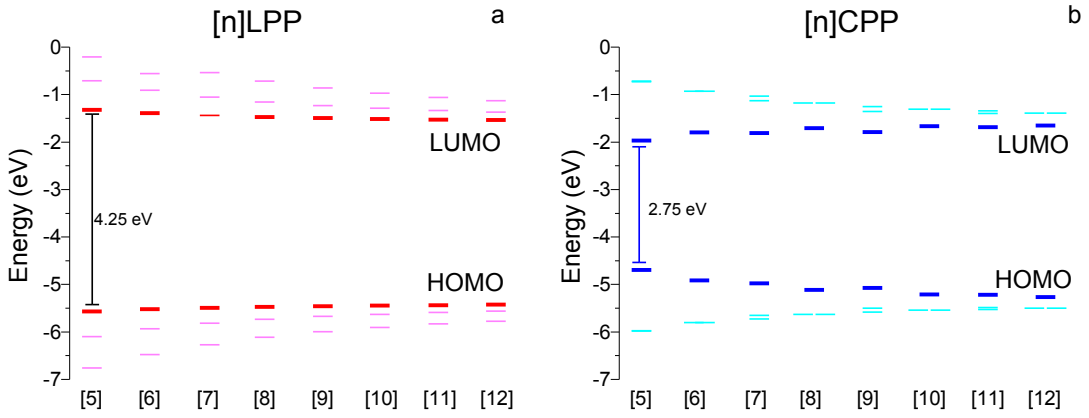

Figure 5. Schematic representation of the frontier molecular orbitals and their energies for the different oligophenylenes molecules: a)[n]LPPs; b) [n]CPPs. Red and dark blue correspond to the frontier orbitals HOMO and LUMO, and pink and light blue to HOMO-1, HOMO-2, LUMO+1 and LUMO+2, for [n]LPPs and [n]CPPs, respectively.[8,43,44,45]

diminish with a decreasing *n*.[50] Subsequently, smaller [n]CPPs could be better approaches for the radial cyclic conjugation concept and also as armchair SWCNTs models.

- Finally, [n]CPPs cyclic shape offers an electron-rich cavity formed by π orbitals. This cavity is able to host other π systems.[38,51] Hence, in analogy with SWCNTs, the resulting supramolecular structures would be stabilized by convex-concave π-π interactions.[52-54]

It must be noted that even though [n]CPPs are suggested as models for radial cyclic π–conjugation, this concept has not been experimentally approached yet. Therefore, a determinant factor of this work will be the extent of the π delocalization or localization along the cyclic systems, considering size and configurational effects.

Raman spectroscopy is controlled by the change in polarizability along the molecular vibrational modes. Then, the π delocalization of conjugated systems drastically outlines their Raman spectra.[55,56] Hence, the Raman spectral analysis of [n]CPPs can provide valuable information about the radial cyclic π–configuration.

Moreover, comparisons between the [n]CPPs spectra with those of their linear analogues,[57,58] and those of SWCNTs will be of great support to better understand their Raman spectra and, therefore, radial cyclic π–configuration effects. In contrast to other π conjugated polyaromatic systems, the [n]LPPs Raman spectra are not highly *n* dependent.[8] Conversely, Raman spectra of SWCNTs are highly diameter and chirality dependent. Unfortunately, commercial CNTs samples are not pure, being formed by tubes of several diameters and chiralities among other carbonaceous materials. Therefore, their Raman signal it is rather complex and there is still certain unambiguity in the assignment of their main vibrational modes.[59-61]

Presumably, when radial cyclic conjugation is present, as it is expected in [n]CPPs, the Raman spectra of [n]CPPs and [n]LPPs should be different. Distinctions should be present not only because of their different symmetries, linear and cyclic, but also because of their dissimilar π configurations, modulating the polarizabilities and so their Raman spectra. Distinctions might be even more noticeable and revealing when analyzing their responses to external perturbations. For instance, when [n]LPPs are oxidized, it is known that charged domains appear with different configurational character in each domain.[62-64] Also, when [n]LPPs are subjected to high pressures, there have been observed conformational changes in which their torsional angles decrease, being then the in-plane π conjugation enhanced. In this regard, the radial cyclic π–configuration of [n]CPPs should modulate their response to those perturbations differently. On the other hand, it is known that CNTs respond to high pressure by deformations along their cross sectional tubular shape. Ovallization pressure of the CNTs has been related with their diameter.[65] However, nothing is known about how [n]CPPs would behave against such kind of mechanical stress. It should be expected that [n]CPPs would respond differently or similarly to [n]LPPs or CNTs, providing fundamental information about their physical–chemical properties.

As we see below, between the main goals of this thesis are to prove the radial cyclic conjugation concept, and the existence or nonexistence of the exotic quinonoid configuration. To do so, geometrical and electronic perturbations will be induced in [n]CPPs using Raman spectroscopy as diagnostic tool. Thus, we will take advantage of the great versatility of Raman spectroscopy, since it can be coupled to many perturbative techniques. For instance, high pressure, not only induces the formation of non-reachable phases at room conditions, but it also allows exploring some mechanical parameters and the deformability of the system.

With the support of calculations based on the density functional theory (DFT) methodologies, this work intends to conduct a deep analysis of the electronic and structural effects which configure the [n]CPPs Raman spectra. We will combine the analysis of the experimental Raman frequencies and intensities with DFT computations to provide a consistent interpretation of the Raman spectra. Also and, more importantly, we will attempt to establish relevant structure-property trends. Our high

pressure results will be also complemented by DFT calculations, exploiting the advantage of computational studies able to approach unrealistic conformers at room conditions.

Among the [n]CPPs properties aim of study are: phenylene conjugation pattern, how curvature and cyclic closure modulates it, oxidized electronic structures (under cationic or dicationic state), their elasticity against deformation, their high or low temperature response, configurational changes and the role of charge transfer in the formation of supramolecular structures.

To be capable to evaluate how [n]CPPs would respond to any alteration by Raman spectroscopy, first we had to understand their Raman spectra without any perturbation. Thus, an extensive preliminary work had to be done to assign the most important Raman features of the [n]CPPs; and an exhaustive analysis of the implications of symmetry and cycle dimension in these features was done from several perspectives. We will present a systematic study of the structural and electronic properties of the [n]CPPs in comparison with those of their linear analogues, [n]LPPs, and, in some cases, with those of SWCNTs.

To end this introduction should be mentioned that when this thesis was started (beginning 2012), there were no reports about Raman characterization of these molecular systems, and up to today there are only three publications on this regard.[50,66,67] Thus, one of the first questions to solve was how we should approach this problem, either as cyclic analogs of the [n]LPPs or as analogs of the SWCNTs. As discussed along the thesis, we have alternatively used both approaches when each one was suitable.

To facilitate the reader's understanding of all the points to which we will refer, in the next sections of this chapter we provide a summary of the state of the art and main known issues of the [n]CPPs. Related topics about CNTs and [n]LPPs will be also briefly reviewed to support a more complete interpretation.

1.2. Aromatic Molecules π Radially Configured

In this section we will describe some issues about cyclic aromatic molecules, with particular emphasis on those related with this work.

Interestingly, many other structures with the p_z radial configuration had been suggested before the first synthesis of [n]CPPs succeed. However, such structures have caused a minor impact compared to that generated by the [n]CPPs. Their expected large conjugational properties have attracted the interest of the scientists since a long time ago. In fact the first unsuccessful efforts date back to 1934, by Parekh and Guha.[68] They tried to synthesize the smallest member of the cycloparapheneylenes series, with only two phenyl members [2]CPP, and they also raised the possibility of synthesizing [3]CPP (see Figure 6a and 6b); but, they were not able to succeed in their attempt of reaching such strained structures.[68]

In chronological terms, it can be considered that the synthesis and characterization of rigid aromatic macrocycles started from 1957, when Eglinton and Galbraith, described the synthesis of the cyclic dimer of 1,2-diethynylbenzene,[69,70] schematized in Figure 6c.

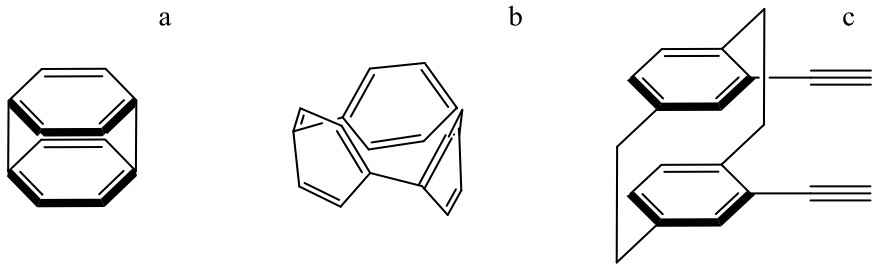

Figure 6. Molecular structures of a) [2]CPP and b) [3]CPP. c) Scheme of a cyclic dimer of 1,2-diethynylbenzene.

In 1996 other important cyclic π structures were successfully synthesized by Herges et al.[71] These molecules were called "picotubes" given their resemblance (see Figure 7a) with a (4,4)CNT. They consist of four anthracene units arranged in a tube-like configuration, with a diameter of about 0.54 nm.[71] However, to our knowledge that beautiful strategy has not yet been extended to synthesize picotubes of larger diameters. This tetramer was referred to depict large delocalization between its equatorial phenyl units, Figure 7a. Unfortunately, when analyzing its crystal structure, it was found that under its equilibrium configuration the double bonds between neighboring units were localized,[72] Figure 7b, so no π delocalization along the cycle was possible.

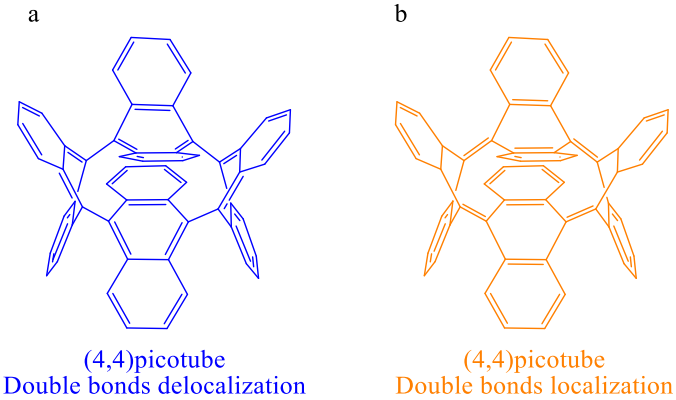

Figure 7. Side view of a (4,4) picotube. a) Benzoid configuration; b) quinonoid configuration. Atomic positions were taken from ref. [71,72].

None of these structures, cyclic dimer of 1,2-diethynylbenzene and picotubes, have been received with such successful welcoming as the [n]CPPs.[18] After their first synthesis was achieved, in 2008 by Bertozzi et al.,[19] the scientific interest relied on them exponentially increased. In that first successful approach [9]-, [12]- and [18]CPP were obtained.[19] These paved the way for the preparation of [n]CPPs of almost all sizes, being now available from [5]- up to [18]CPP, as shown in Figure 8. The smaller [n]CPPs of the series came slower in time, [8]CPP in 2010,[30] [7]CPP in 2011,[31] [6]CPP in 2012[29] and [5]CPP in 2014.[28]

There has been a competition for finding the better synthetic route between the protagonist synthetic groups of Itami,[34] Yamago[31,33] and Jasti.[19-24] Interestingly, this resulted in three different strategies. The approaches of Jasti[19] and Itami[34] have two steps, firstly, cyclisation of a non-aromatic precursor and then a final aromatization step responsible for inserting the strain into the system as

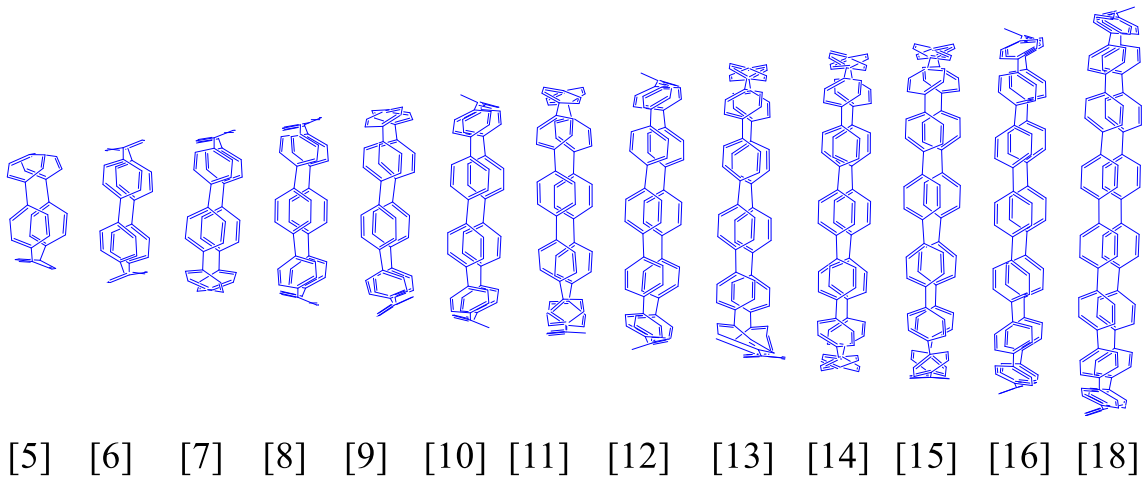

Figure 8. Side view of the molecular structures of all the [n]CPPs synthesized so far.

well; Yamago's approach[31] also involves two steps but in this case there is no aromatization step, the first step gave rise a cyclic aromatic non-strained intermediate and the second step is responsible for incorporating the strain. Additionally, many refinements and improvements have come to optimize the conditions towards multigram scale[24,73] with [5]-, [9]-, [12]- and [15]CPP already commercially available. As mentioned in the previous section, using [n]CPPs and their derivatives, synthetics have struggled to achieve the controlled bottom-up synthesis of CNTs with specific diameter and chirality.[36,37,52,74-77] Right after the first synthesis of [n]CPPs was achieved followed theoretical and experimental works in which their striking properties saw the light.[42,44,45,78]

In the area of carbon-based π materials, radially π conjugated systems have been in the spotlight because of their unique structures and unprecedented photo-physical properties. They are characterized by both infinite π conjugation and shape persistent cyclic structures which can be used to control the direction of conjugation. Not much is known about how this conjugation works in the sense that it is related to phenyl bending or pyramidalization required to deform planar phenyl units towards cyclisation of the [n]CPPs, as shown in Figure 9. In this sense we wonder if there is a limit from which it becomes dominant overcoming the energy involved in the phenyl bending destabilization.

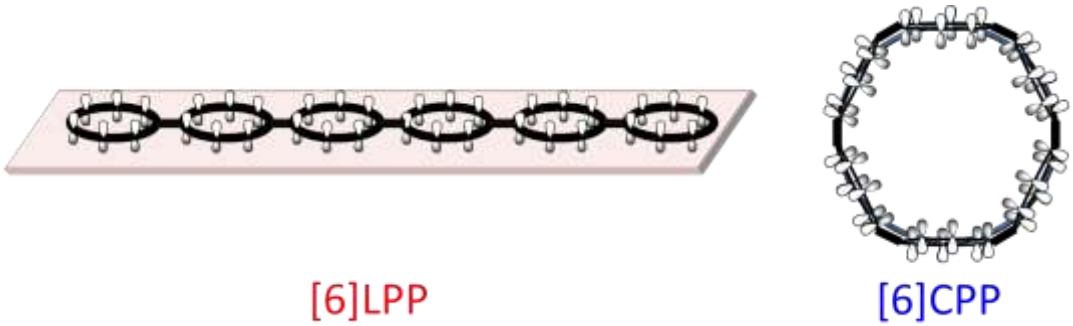

Figure 9. Scheme representing the p_z orbital distribution in non-twisted configurations of: a) [6]LPP; b) [6]CPP.

To finish this section, we should mention other important cyclic π systems: the thiophene-based molecules, as those shown in Figure 10. Recently, such molecules have been also proposed as candidates to address the radial cyclic conjugation topic. This would broaden the possibilities to obtain organic materials with whichever desired properties. Within these thiophene-based molecules, oligothiophenes are suggested as models for:

- Perpendicular linear π–conjugation.[79,80]
- Quasi radial conjugation, as that exhibited by compounds where are formed by alternated phenyl and thiophene units (CPTs)[81] (see Figure 10c).

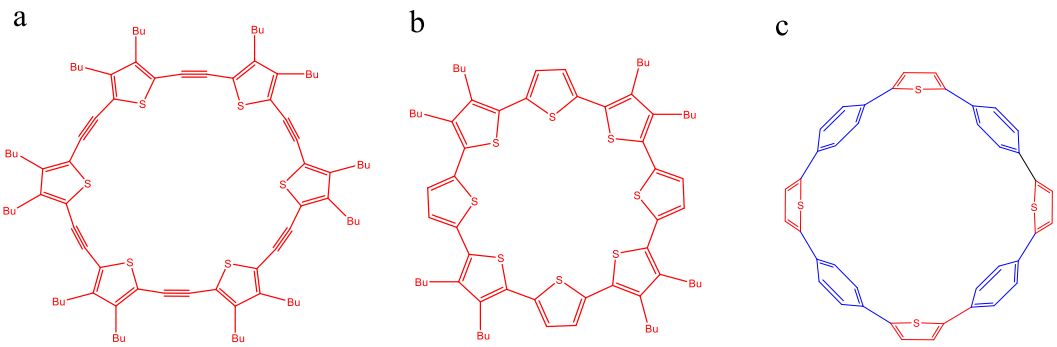

Figure 10. Chemical structure of: a) Cyclic parathienylene-Acetylene; b) Cyclo[10]thiophene; c) Cyclo-[4]-1,4-phenylene-2',5'-thienylene ([4]CPT).

Thiophene-based π systems are the ones which occupy a broader applications spectrum because of their synthetic availability, stability in various redox states, and widespread adjustable electronic properties.[82,83] In general, it has been reported that, linear and planar π conjugated thio-based systems including thiophenes, show an increase in HOMO energy level and a decrease of LUMO energy level with the increasing number of thiophene units.[19,28-34,73,74] In CPTs the LUMOs follow the general tendency to decrease in energy with the increase of phenyl–thiophene units, while HOMOs remain almost unaltered, so the energy gap decreases with the increasing *n*, as in the other thio-based materials.

In the next section the main characteristics of the [n]CPPs are briefly outlined.

1.3. Size Dependent Structural Properties of [n]CPPs

1.3.1. Strain and Bending

From a fundamental point of view, strain is produced in closing para-phenylenes into a ring, typically by an angle distortion at the C_{ipso} atoms. This strain might be taken at the expense of aromatic character of the individual phenyl rings. Ring strain energy (RSE), is then defined as the energy needed to distort bonds and bond angles to close a ring structure,[84] as plotted in Figure 11 for the simpler example going from [5]LPP to [5]CPP.

Strain energy of [n]CPPs was earlier estimated by Bachrach et al.[42] and by Segawa et al.[44] from DFT calculations of the optimized energy minimum structures. The methodologies used to estimate the strain are based on the homodesmotic reactions (see Figure 12a).[85] In a homodesmotic reaction the reactants and products contain equal number of carbon and hydrogen atoms in the same state of hybridization. This matching of hybridization and groups gives more accurate estimates of the intrinsic strain energy in rings and the cyclic delocalization. Quantifying these effects depends critically on the scheme for partitioning the total molecular energy, as well as the choice of the reference compounds. A reference system must contain unstrained components of the test molecule in the absence of the ring.

In Figure 12b, the [n]CPPs strain energy as a function of *n* is represented. It is observed how cyclic strain exponentially increases with the decrease of the number of benzenes. Of this series, the shortest members accumulate an impressive cyclic strain energy (~114 kcal mol^{-1} for [5]CPP), as the 360° curvature is shared only by five rings in such a way that the phenyl rings partially lose their planar configuration, as it is schematized in Figures 13a and 13b.[28] Strain must be taken at the expense of aromaticity of individual phenyl units, i. e., as a result of the folding of the benzene units to enable the closing of the cycles. Nonetheless, the largest synthesized analogue, [18]CPP, still possesses a significant strain energy (~32 kcal mol^{-1}), compared to its linear configuration which would have no strain.

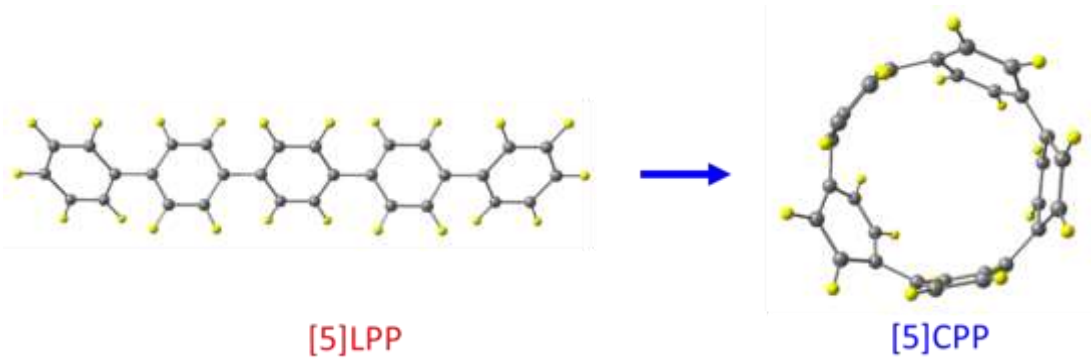

Figure 11. Scheme of the optimized structures of the molecules of [5]LPP and [5]CPP.

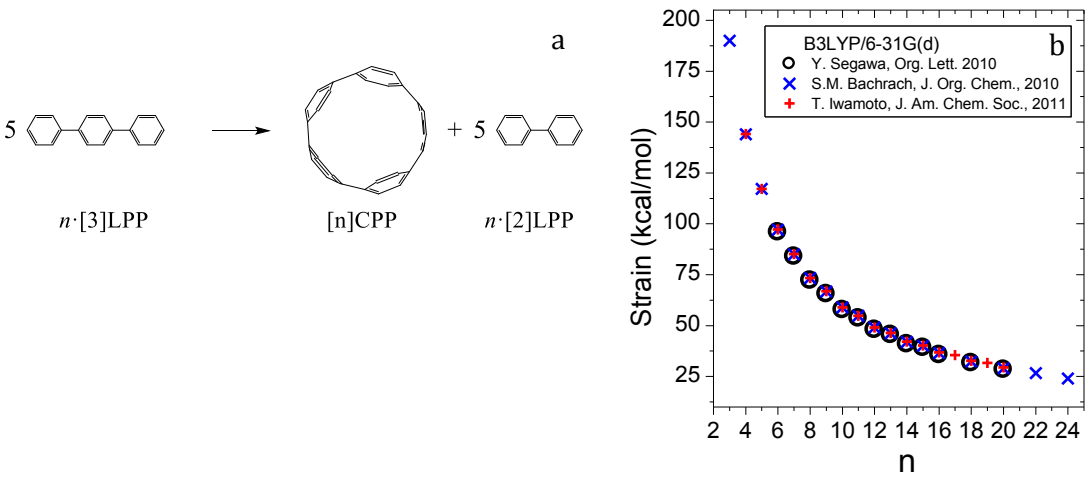

Figure 12. a) Hypothetical homodesmotic reaction for the calculation of strain energies of the [*n*]CPPs. b) Strain energy for the [n]CPPs as a function of *n*. Data taken from refs. [42-45].

The closure of the LPP to form its corresponding CPP analogue would involve the bending of the C_{ortho}-C_{ipso}-C_{ortho} angle, as depicted in Figures 13a and 13b. Furthermore, when these C-C bonds are taken out of the benzene planarity, carbon atoms tend to pyramidalize. The pyramidalization or bending, defined by the α angle plotted in Figure 13, causes the exohedral lobes of the π orbitals to be larger than their endohedral counterparts.[86,87] Thus, strain is mostly caused by the phenyl bending, that is larger as smaller *n* is, reaching the experimental limit in [5]CPP, where a bending of about 20° has been described. Such bending angle is closer to the angle formed in the sp^2 hybridization of a pure double C-C bond, ~30°, as shown for ethene in Figure 13c. This is the reason [n]CPPs have been broadly hypothesized to depict quinonoid character, when [n]CPPs are forced in some extent to loss their aromatic character within the planar phenyl unit.

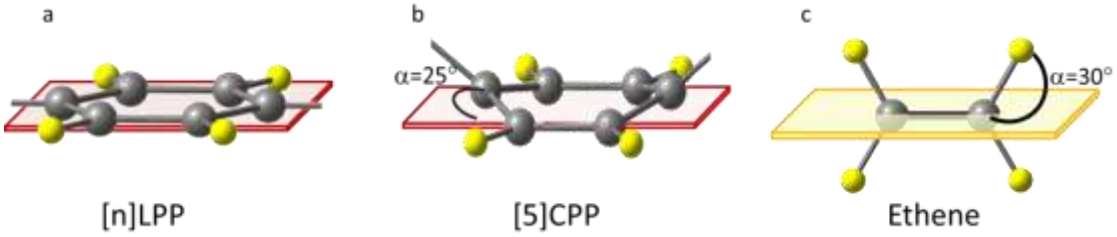

Figure 13. Side view for an out-of-plane distortion of: a) a phenyl unit in [n]LPPs, each unit remains planar; b) a phenyl unit in [5]CPP with a distortion about 25°; c) Ethene, α is the angle between an H atom and the plane which only contains the C atoms.

1.3.2. Torsional Angles between Neighboring Phenyl Units

As above mentioned, [n]LPPs, with zero-strain, in their lowest energy conformation depict torsions between neighboring phenyl units to minimize ortho hydrogen-hydrogen steric interaction. This conformation for [6]LPP is plotted in Figure 14a. Interring torsional angles predicted by molecular simulations are approximately 45°-50° for biphenyl and terphenyl, 30°-40° for hexaphenyl, and 27° in single isolated poly para-phenylene (PPP) chains.[88-91]

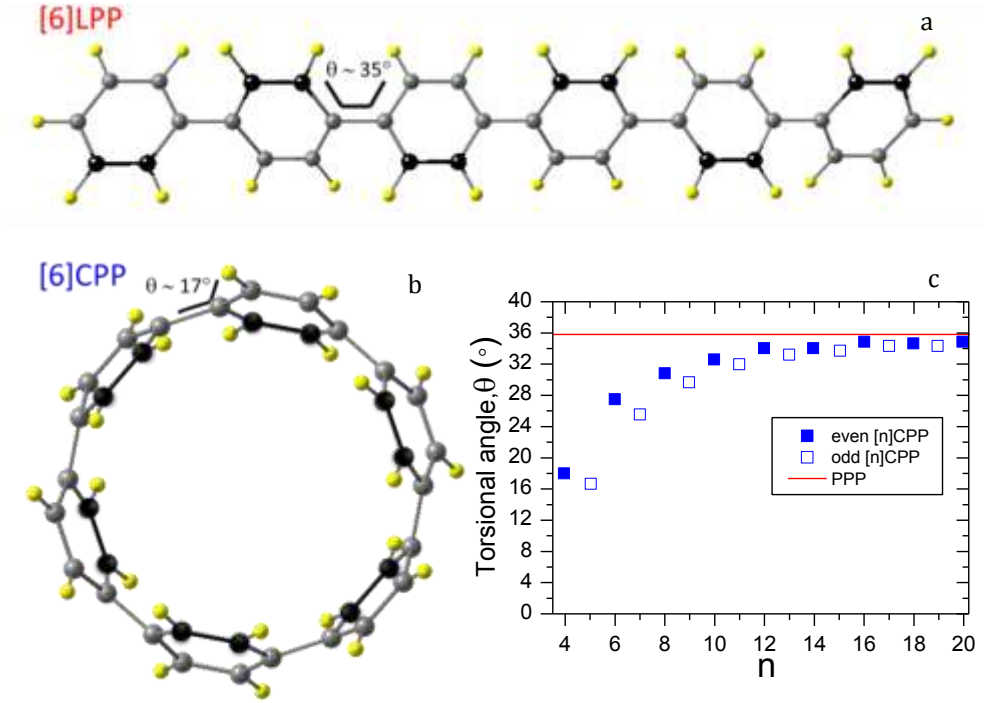

Figure 14. a) Optimized geometry of [6]LPP. b) Optimized geometry of [6]CPP. c) Average torsional angle as a function of *n* for [n]CPPs. When *n* is even, the angle is constant across the whole cycle; when *n* is odd, the angle varies, therefore the open blue squares indicate the average value of θ. The red line at 35.8° indicates the torsional angle of a long poly-paraphenylene (PPP) molecule and is an approximation of the torsional angle for [n]CPP when n $\rightarrow\infty$. Data taken from ref. [50].

For [n]CPPs, their lowest-energy conformations have been computed also exhibiting torsional angles.[19,28-34,44] Thus, [n]CPPs with even *n* have $D_{(n/2)d}$ symmetry at these conformations, with phenyl units alternately canted; while [n]CPPs with odd *n* have a 3-benzene helical unit, and the other benzene units alternate with varying dihedral angles, thus rendering them asymmetrical molecules with C_1 symmetry.[50]

In [n]LPPs torsional angles are not affected by *n a lot*. In contrast, [n]CPPs depict an important dependence resulting from the cyclic strain. Moreover, an even-odd effect has been predicted as well. Figure 14c shows the average torsional angles for the molecules of [n]CPPs. Data have been calculated by DFT methodologies at the B3LYP/6-31G(d) level by Chen et al. for isolated molecules.[50] It is observed that while in the larger [n]CPPs phenyl units can rotate almost freely, as in [n]LPPs,[92,93,94] in the smaller [n]CPPs, with larger strain, those rotations are hindered, thus their torsional angles are lower.[50]

As described above, [n]CPP molecules have been proposed as templates in the synthesis of armchair SWCNTs. In any possible nanotube formation, the torsions are an important geometrical parameter which must be taken into account, also seeking counteract the H…H repulsions which generate the torsion for the [n]CPP self-assembly. So, modulation and minimization of the torsion toward zero would maximize the tubular configuration where probably the self-assembly would be more favored. In this regard, it has been observed the planarization of the [n]LPPs when are submitted to high pressures, about 1 GPa.[95] We wonder if this mild conditions would be enough to promote the formation of the more symmetrical conformation of the [n]CPPs, with symmetry D_{nh}, to then possess a ribbon-like structure, which one might associate with SWCNTs.

1.3.3. Benzoid-Quinonoid Forms. Aromaticity and Conjugation Length Evaluation

As depicted in Figure 15, in compounds such as benzene the p_z orbitals are perpendicular to the ring plane, while in compounds such as the [n]CPPs, the inner lobes of the p_z orbitals all point toward the axis of the cylinder.[13] The latter is the so-called radial cyclic π-conjugation and it exists in the belt-like conjugated systems. Thus, in normal aromatics, the sp^2-hybridized ring atoms retain their preferential trigonal planar configuration, whereas radial-cyclic-conjugated-systems exhibit pyramidalized sp^2 centers, with a partial sp^3 character. As seen before, in rings with small diameters, pyramidalization causes a considerable amount of strain, justifying why these systems are less common than normal aromatics. This new class of conjugation has attracted scientists since long time ago, but it was with the fullerene discovery[96] when it took off. As evident, SWCNTs are also characterized by radially oriented π orbitals.

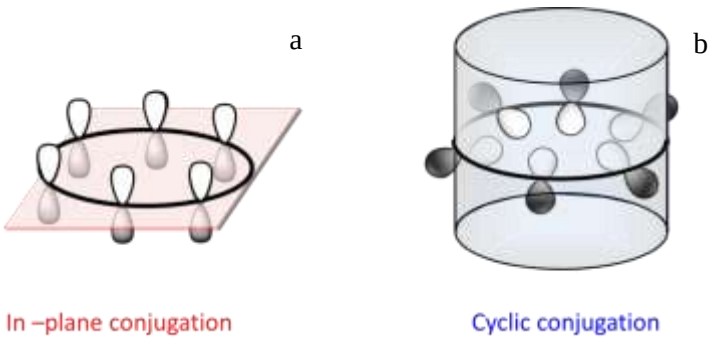

Figure 15. Representation of the topologies of electron π-conjugated systems. a) "Standard" double side Hückel aromaticity, where the p orbitals are all perpendicular to the ring plane, such as in benzene. b) Radial cyclic conjugation, where the inner lobes of the p_z orbitals all point toward the axis of the cylinder.

As already mentioned above, a distortion of the aromaticity has been suggested for the [n]CPPs. Thus, their quinonoid conformations have been studied. It is obvious that the smallest [n]CPP with the largest strain is where a quinonoid structure could be stable, since such conformation would lower that strain.[19] In Figure 16 the two conformations are plotted for [5]CPP. When the phenyl units keep their aromatic character the conformation is that referred as benzoid (see Figure 16a). On the other hand, when the bending is larger and the conjugation within each phenyl is attenuated by the formation of localized double bonds between the C_{ipso}-C_{ipso} and C_{ortho}-C_{ortho} bonds, we have the quinonoid conformer (see Figure 16b). However, it has been demonstrated that the most stable conformation of [5]CPP is the benzoid one.[28] By x-ray diffraction crystallography, the following bond lengths have been found for [5]CPP: C_{ipso}-C_{ipso} = 1.49 Å, C_{ipso}-C_{ortho} = 1.40 Å and C_{ortho}-C_{ortho} = 1.38 Å.[28]

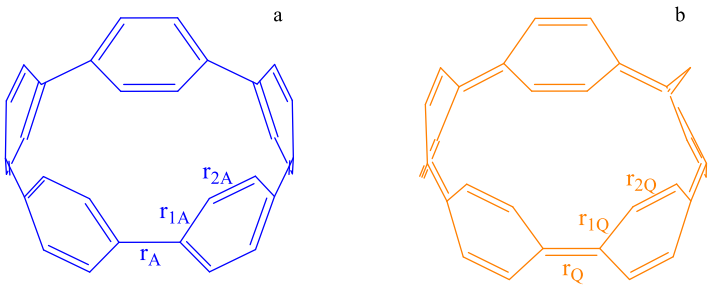

Figure 16. Scheme of the molecule of [5]CPP under two conformations: a) Benzoid conformation, BLA > 0. b) Hypothetical quinonoid conformation, BLA < 0.

Even the smallest of the series, [5]CPP, depicts an aromatic character, against any intuitive prediction.[19,28-34] Thus, the stabilization provided by the aromatic phenyls overcomes their large strain, and aromatic configurations are preferred even though those bending angles are closer to those of quinonoid configurations, with localized double bonds. In this work we will put much attention to this striking characteristics, unique for the [n]CPPs. We will intend to find possible strategies to induce the formation of such quinonoid configuration with large cyclic conjugations.

In addition, other stabilizing factor must exis,t which compensate the extra energy and makes the highly strained [5]CPP stable. As shown in Figure 16, the smallest [n]CPP, depicts small torsions where their π orbitals are almost parallel radially oriented inwards the cavity of cycle. Previously, it has been suggested to be the shortest inner unit of the fullerenes C_{60} and C_{70}, as shown in Figure 17. Thereby π orbitals of neighboring benzenes might be easily interacting as non-limited aromatic conjugation, providing the system with that stabilizing driving force. Then, it is asked which of the conformers, [5]CPP benzoid or [5]CPP quinonoid, would be the analogues to the above mentioned fullerene central units. Whichever it is, it should imply no hindering for the π total delocalization.[28]

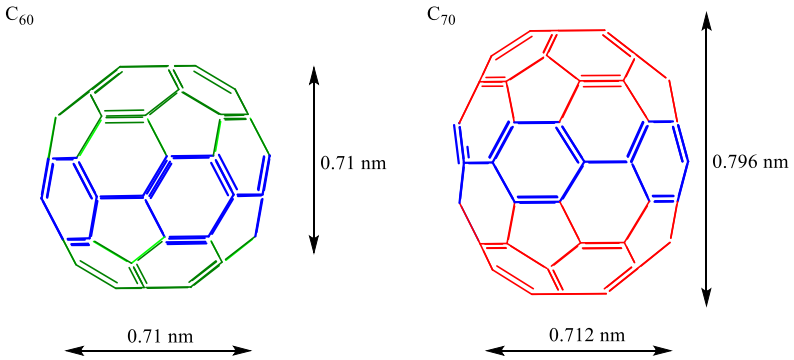

Figure 17. Scheme of the molecular structures of the fullerenes C_{60} and C_{70}, in green and red, respectively. The [5]CPP equatorial belt has been marked in blue.

Next, we briefly outlined the most common tools used to give a quantitative measurement of the aromatic character: the parameters so-called BLA and NICS and the Raman spectroscopy.

1.3.3.1. Bond Length Alternation

The most common and legitimate parameter used to define the loss of conjugation through quinonoidization is the bond length alternation, so-called BLA. This parameter has a value equal to 0 for a totally conjugated system, as benzene, with all C-C bonds equivalent. For [n]CPPs the definition of the BLA would be as follows:

$$BLA = r + r_2 - 2r_1 \quad (1)$$

(see distances defined in Figure 16) where r is the C-C interring distance C_{ipso}-C_{ipso}, r_1 is the C_{ipso}-C_{ortho} distance and r_2 is the distance C_{ortho}-C_{ortho}. Thus, any aromatic [n]CPP would depict positive close to 0 BLA, while their quinonoid tautomers would show negative values.

To our knowledge, synthetic organic chemists have accomplished the synthesis of the [5]CPP, but nothing is known about [4]CPP from an experimental point of view. [4]CPP is theoretically predicted to still depict benzenoid character.[42] Comparing [4]CPP with the 9,9',10,10'-Tetradehydrodianthracene, (2,2)picotube,[97] with a BLA about -0.22 Å,[72] the latter is synthetically approachable because of its lowering strain with the formation of a quinonoid structure.

1.3.3.2. Nucleus-Independent Chemical Shifts

Even though the BLA parameter is most commonly used to discern between aromatic or non-aromatic character, the so-called Nucleus-Independent Chemical Shifts (NICS), can be also used as an

aromaticity criteria.[98] In aromatics there is a strong ring current induced by an external magnetic field perpendicular to the ring plane. The magnetic field induced by the ring current is opposed to the external field inside the ring and parallel to it, as shown in Figure 18a for benzene. This gives rise to an upfield NMR shift of protons in the ring and a downfield shift of the "outer" protons. NICS is defined as the negative value of the absolute magnetic shielding computed at a ring center. Significant negative values imply aromaticity (diatropic ring current) and positive values correspond to antiaromaticity (paratropic ring current).

For example, from DFT calculations at the B3LYP/6-311+G(d,p) level, a NICS value of benzene at the center of its D_{6h} plane, $NICS_{benzene}(0)$, is found equal to -8.03 ppm.[98] When the diatropic rings are placed 1 Å above benzene center, as shown in Figure 18a, $NICS_{benzene}(1)$, is equal to -10.2 ppm. NICS linearly decreases when calculated to further distances than 1 Å from benzene center.[98]

Previous studies have carried out calculations of this quantity for [n]CPPs and [n]LPPs analogues, with *n* ranging from 5 to 18.[78] Wong found that, at the PBE0/6-31G(d,p) level of theory, NICS(1) of the [n]LPPs remained constant regardless *n* around -10.2 ppm (with a NICS(1) value for benzene equal to -11.5 ppm).[78] Furthermore, NICS(1) of the [n]CPPs were always less negative (i.e., less aromatic) than their linear counterparts, being -8.14 ppm for [5]CPP and -10.11 ppm for [18]CPP. Such variation was considered as a loss of aromatic character in the small [n]CPPs due to phenyl bending and so certain quinonoidal character was acquired.

However, what Wong did not explore was any possible current generation within the [n]CPPs cavity, as illustrated in Figure 18b. The better π overlap within the more quinonoid units would induce a cyclic conjugation which, would as well lead to certain π confinement within the cavity. Thus there should be remnant current induced by a magnetic field within the cavity. We will consider this unexplored possibility which definitely would have fundamental consequences in the conceptual radial cyclic π–configuration definition. Therefore along this thesis this will be an important point to be addressed.

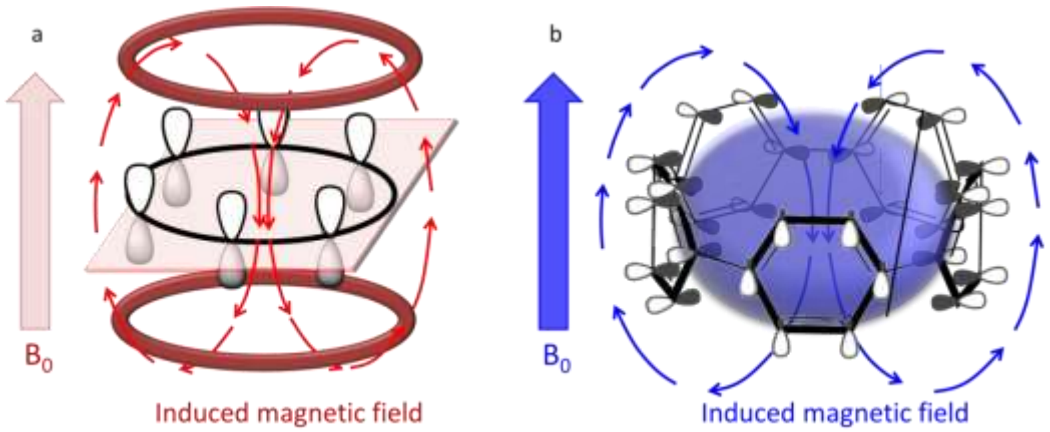

Figure 18. Ring current induced by an external magnetic field perpendicular to the ring plane. The magnetic field induced by the ring current is opposed to the external field inside the ring and parallel to it: a) Benzene, b) [6]CPP, where the ring current on each phenyl unit happen to converge in the center of the cavity.

1.3.3.3. Raman Spectroscopy and π Electron Delocalization

In order to define the π electron delocalization in [n]CPPs, Raman spectroscopy is also a very adequate tool. The electronic cloud related with the π electrons is highly polarizable, so changes in the Raman features are directly related with how such electron cloud is distributed.[55,56] Several theories have appeared relating the Raman features with the electron delocalization length of conjugated molecules, such as, linear paraphenylenes and other conjugated materials.[6,7,8] As above mentioned, [n]CPPs are the first experimental examples in which cyclization in a radial conjugated

system is inserted. Thus not much is known about how phenyl cyclization affects the π electronic delocalization, as well as the Raman spectra. We wonder if the mentioned theories applied to the linear conjugated molecules could be useful in their cyclic analogues.

These theories have gone through different interpretations and derivation along the times. Going from conjugation length model (CL), based on Albrecht´s theory;[57,99] to the "amplitude mode" (AM) by Horovitz.[100] Such theories have been mainly applied to polyacetylene describing a large electron-phonon coupling as an empirical term when atoms move along the dimerization coordinate.

The last of the theories referring to conjugation in polyconjugated systems is the so-called Effective Conjugation Coordinate (ECC) model. This was built on classical molecular dynamics concepts from the idea that in polyconjugated systems there exists a particular vibrational coordinate strongly coupled with π electrons, referred as the я mode and related to the parameter BLA. In [n]LPPs the G_{A1g} mode has been the considered one to contribute mostly to the я mode, referring in many cases as the BLA mode.[58,101]

As mentioned, one of the pillars of this thesis is the Raman characterization of the [n]CPPs. When this thesis was started, at the beginning of 2012, nothing was published on this topic. During its development three different articles were published.[50,66,67] These researchers considered the [n]CPPs as analogs to carbon nanotubes, sometimes doing forced assignments in search of that analogy. Also certain assignments were done and referred the frequency shift to depend on *n*. However, their main weakness entails a lack of quantification or structural relationships. Because of the potential applicability of [n]CPPs we consider that a mayor effort should be done to get as much information as possible from Raman spectroscopy, which has become one of the goals of this work.

1.4. [n]CPPs and SWCNTs

Considering the possibilities that CNTs and graphene offer because of their high conductivity[102,103] and strength,[104] one can think that the applications given to them are too little. The reasons are mainly based on the polydispersity of those materials, with different sizes, chiralities and contaminants. As result, tedious preparation and purification steps are required in order to be able to apply those materials at large scale. Moreover, CNTs and graphene exhibit low solubility in water and in common organic solvents, which makes them very arduous to work with. In this sense, chemists seek for novel carbon-based materials of interest in different scientific and technological fields, with similar properties to those of graphene and CNTs. In this regard, as already commented, one of the major potentials of [n]CPPs was in the idea of using them as molecular templates for the controlled bottom-up synthesis of carbon nanotubes.[15,25,26] After several efforts in 2013 that attempt succeeded,[27] as is summarized in Figure 19. However, the diameter of the tubes and yield was not as good as expected,[27] so further work is expected in this field.

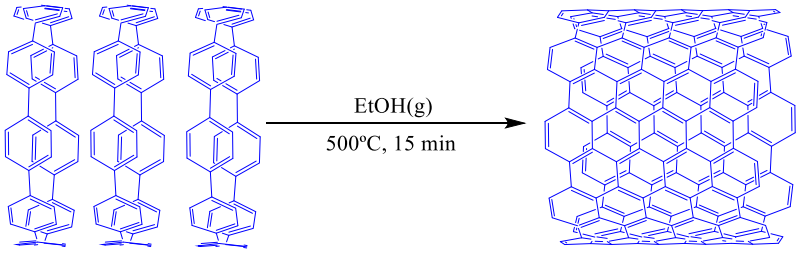

Figure 19. "Growth-from-template" strategy for the bottom-up synthesis of structurally uniform SWCNTs by using [12]- or [9]CPP. Conditions: a solution of CPP (10 μL of a 0.5 mM solution in toluene or 1,2-dichloroethane) was spin-coated at 4000 rpm on a C-plane sapphire substrate plate (pretreated by ultrasonication in acetone and methanol, followed by ozone cleaning). The reaction plate, placed in the chamber, was heated at 500 ºC for 15 minutes with a flow of ethanol gas.

Even if [n]CPPs are thought of as SWCNTs templates, nothing is known about their similarities and differences other than their close tubular shape. We wonder if [n]CPPs molecular systems will in fact behave analogously to SWCNTs, with similar strength and flexibility along their cross sectional direction.

On the other hand, as already mentioned, one of the most important characteristics of CNTs, is their capability to form π-π interactions. It is known that CNTs offer a great capability to act as host systems, being able to keep into their cavity any system which possibly fits. Through convex-concave π interactions the peapods of fullerenes are highly stable, and so these have been largely approached because the combined properties fullerene-CNT. However, due to the diameter inhomogeneity of CNTs, this application has not yet been completely exploited. Nonetheless, because the controlled size of the [n]CPPs these could act as selective hosts or guests of different diameters.

Interestingly, the [n]CPPs hosting ability seems to be one of their largest potentials. In 2011 this function was demonstrated in solution by the encapsulation of C_{60} by [10]CPP, preferred over other bigger and smaller [n]CPP molecules.[105] Diameters of [10]CPP (1.38 nm) and C_{60} (0.71 nm) are precisely the most appropriate. [10]CPP rearranges along its perimeter to depict a less canted configuration able to better hold the C_{60} unit, with a perfect π-π overlapping denoted by the distance between each other, 0.334 nm, as shown in Figures 20a and 21a.[24] This distance is identical to the interplanar van der Waals distance between graphite sheets, thus suggesting the importance of this particular intermolecular force in the formation of the complex. These results indicate that [n]CPPs can serve as excellent models to gain understanding of the convex–concave π–π interactions. Binding constants for the complex were obtained in different solvents: log K_a was equal to 6.4 in toluene and to 3.8 in 1,2-dichlorobenzene.

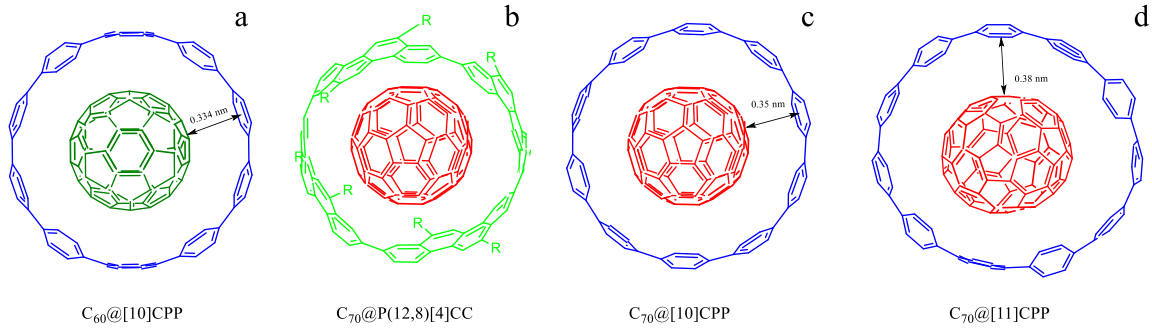

Figure 20. Top view of the host-guest complexes; a) C_{60}@[10]CPP; b) C_{70}@[4]CC((P)-(12,8)-[4]cyclo-2,8-chrysenylene, with R=hexyl); c) C_{70}@[10]CPP, lying orientation; d) C_{70}@[11]CPP, standing orientation.

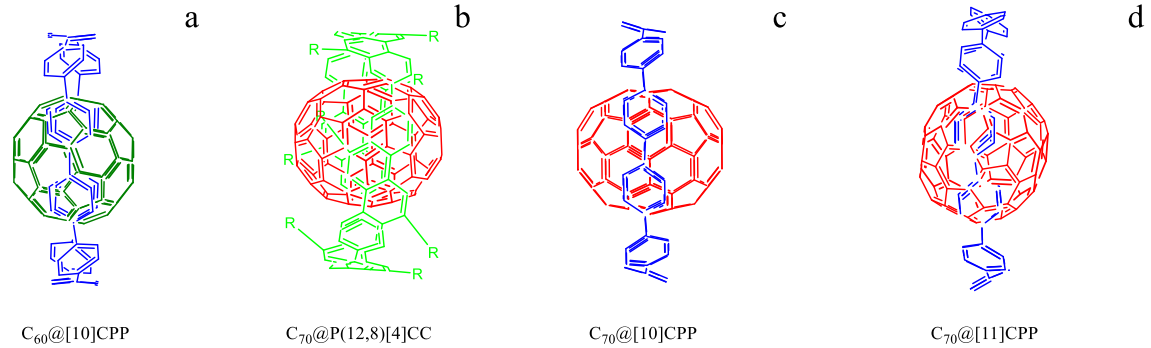

Figure 21. Side view of the host-guest complexes; a) C_{60}@[10]CPP; b) C_{70}@[4]CC, (P)-(12,8)-[4]cyclo-2,8-chrysenylene, with R=hexyl; c) C_{70}@[10]CPP, lying orientation; d) C_{70}@[11]CPP, standing orientation.

Other [n]CPPs derivatives, as the above mentioned [4]cyclo-2,8-chrysenylene ([4]$CC_{2,8}$), have been suggested for the encapsulation of fullerenes,[40] as shown in Figures 20b and 21b with (P)-(12,8)-[4]cyclo-2,8-chrysenylene, with R=hexyl. These seem to be more appropriate for filtering applications since they have a much higher binding constant with fullerene C_{60}: log K_a was equal to 9.6 in 1,2-dichlorobenzene.[41] Moreover and very importantly, in such complexes, the C_{60} molecule is held while it can freely rotate in the cavity. Subsequently, it was found that an even larger binding constant was reached with C_{70} as guest molecule. The binding constant of C_{70} in 1,2-dichlorobenzene was log K_a equal to 9.7.[41] This value could be attributed to the oval shape of C_{70}.[41]

Encapsulation of C_{70} by [n]CPPs has also been explored.[51] It has been found than the C_{70}@[n]CPP complexes have higher binding constants than with C_{60}, but still lower than when using C_{70}@(P)(12,8)- [4]CC. The most favored [n]CPPs to host C_{70}, because dimensional reasons, are [10]- and [11]CPP. Binding constants in toluene (values within brackets are in 1,2-dichlorobenzene) were obtained: log K_a was equal to 4.9 (3.9) for C_{70}@[10]CPP and to 5.2 (3.8) for C_{70}@[11]CPP.[51]

On the other hand, one of the most interesting properties of the C_{70}@[n]CPP complexes is that they have the ability of selectivity accommodate the fullerene in different orientations, lying or standing, depending on size of [n]CPP, as shown in Figures 20c,d and 21c,d. C_{70} has an ellipsoidal shape with long (0.796 nm) and short axes (0.712 nm).[106] As experimentally observed and owing to [10]CPP diameter (1.38 nm), the C_{70} adopts a lying configuration (it long axis is perpendicular to the [10]CPP radial plane) to reach the optimal π interacting distance. Instead, with a diameter for [11]CPP of 1.52 nm, C_{70} aligns its long axis parallel to the [11]CPP radial plane, with a standing configuration.[51]

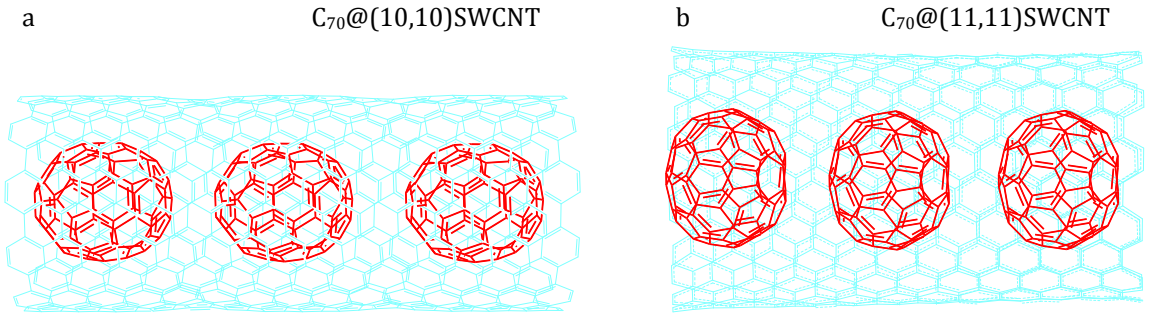

Figure 22. Structures of a) C_{70}@(10,10)SWCNT peapod in lying orientation, b) C_{70}@(11,11)SWCNT peapod in standing orientation.

Even though C_{60} and C_{70} can be hosted by CNTs of the right diameter as well, [n]CPPs complexes have the advantage of differentiation and selectivity. For instance, C_{70} can be hosted by SWCNTs in lying or standing orientations, as shown in Figures 22a and 22b. However, due to the non-selective diameter sample usually these contain mixture of both. Therefore it was not possible to experimentally conduct a proper assignment of their spectral fingerprints. Any experimental distinction done so far has been conducted by electronic optical microscopy. Thus, the [n]CPPs molecular approach could be used to develop a diagnostic, which would allow the rapid identification between the different guest orientations and the better or worst host-guest interaction.

It is also interesting to note that Fomine et al. in 2012 suggested that [n]CPPs of the adequate size could encapsulate each other, forming the so-called "Russian dolls".[39] These authors predicted by DFT calculations the principal electronic properties of several complexes. In Figure 23 we show two of the suggested complexes, formed with two types of [n]CPPs (Figure 23a) and with three [n]CPPs (Figure 23b). These complexes could be considered as the shortest examples of double and triple walled CNTs, respectively. From simple geometrical considerations, they thought that the most stable complex is formed when the distance between two concentric [n]CPPs should be ($2\pi\Delta r$).[39] With Δr =

3.5 Å, this distance is 22 Å, which corresponds to five phenyl units. This means that these authors suggested that the successful formation of these complexes between [n]CPPs requires that they differ by five repeating units. In Figure 23a is shown the complex predicted by the encapsulation of [4]CPP (diameter = 0.555 nm) by [9]CPP (diameter = 1.222 nm), and in Figure 23b the triple Russian doll predicted by the interactions between [4]-, [9]- and [14]CPP (diameter = 1.9 nm).

One of the most important characteristic expected from the Russian dolls complexes comes from their optical properties. Fomine et al. obtained that they behave as optically independent units, at least in the case of the $S_0 \rightarrow S_1$ transition, and they predicted that electron excitation is limited to only one cycle. As the $S_0 \rightarrow S_1$ excitation energy increases from the small [n]CPPs to the bigger ones and the macrocycles are optically independent, it could be performed a system useful for light harvesting or as an antenna. So, after the outer macrocycle of the complex absorbs light, excitons are generated that migrate through the inner rings of the molecular complex, carrying the energy obtained from the light. The excitons move to the smallest (central) ring in order to emit light. Because the energy of the light is captured and then transferred by excitons, the CPP Russian doll complex may act as an artificial molecular antenna. The advantage that these systems would offer against other conventional dendrimeric molecular antennas is that Russian doll complexes should be formed by self-assembly.

To our knowledge, such complexes have not been synthesized yet. In this work we will attempt to achieve their formation by subjecting a state-solid mixture of them to high pressures. We choose the [6]CPP and [12]CPP with diameters about 1.63 and 0.83 nm, respectively.[43] Then, the remaining distance between the two centered units would be the appropriate for the formation of van der Waals interactions, as shown in Figure 23c.

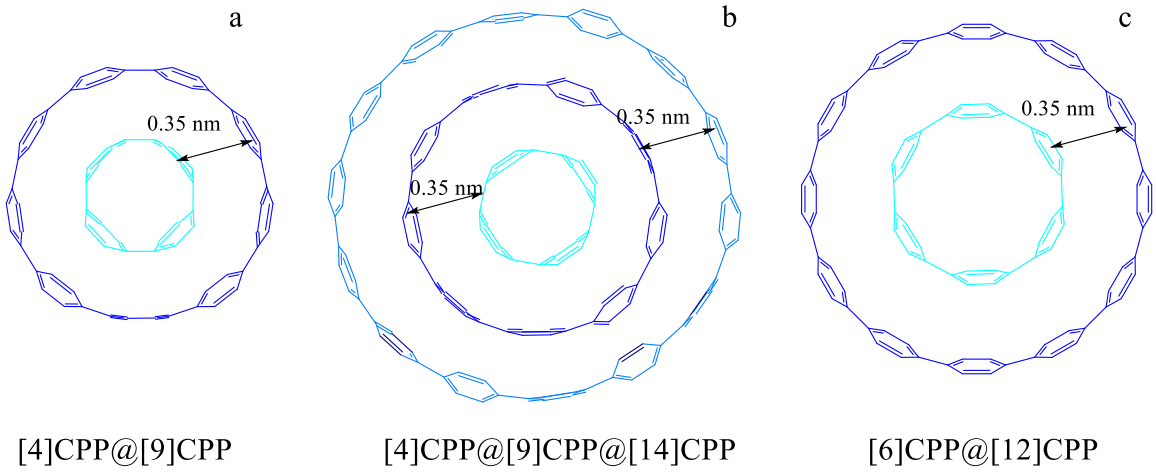

Figure 23. Top view of the [n]CPPs host-guest complexes: a) [4]CPP@[9]CPP; b) [4]CPP@[9]CPP@[14]CPP; c) [6]CPP@[12]CPP.

On the other hand, the growing importance of CNTs and graphene in nanoscience and nanotechnology is based on their exceptional electronic, mechanical and chemical properties. For instance, it has been reported that graphene is one of the strongest materials with a Young modulus of about 1 TPa,[104] being very close that registered for CNTs.[107] However along their diameter they deform against external forces in a rate which increases with the increasing diameter. Thus, such characteristic could be beneficious or a drawback depending on the kind of applicability desired.

It is known that pressure-dependent Raman experiments provide key information about the bond anharmonicity and the mechanical strength of CNTs.[108] As their selective diameter synthesis and diameter purification are still not sufficiently available, there are few high-pressure experimental works which study their properties while taking their size into consideration.[109] Then, the study of high pressure behavior of the CPPs could be helpful to give answers to some of the CNTs open

questions. In this sense, nothing is known about how [n]CPPs are affected by the mechanical deformation.

Note that high pressure allows us to explore not only the state of certain systems under extreme conditions, but to access to properties of such systems by analyzing their response to those conditions. In our interest of exploring possible mechanical, chemical and spectroscopic analogies between [n]CPPs and SWCNTs, we will here study [n]CPPs in an oligomeric approach to SWCNTs. Furthermore, the study of the [n]CPPs might provide relevant insights about the exclusive properties imparted by their unique *belt*-shape structure and relate them to the properties of SWCNTs.

Finally, it is known that high pressure increases the molecular reactivity, being able to promote the formation of systems with new properties not reachable otherwise under room conditions. For instance, carbon monoxide at pressures between 3 and 4 GPa becomes a high energy density material.[110] Hence, the reactivity of [n]CPPs under extreme conditions and the subsequent formation of novel materials could be explored with our studies.

1.5. Questions to Solve

The aim of this thesis is not just a tedious spectroscopic description to reach a mere vibrational assignment. We hope to show that the vibrational spectra of these materials are unique probes for understanding their structural properties at the molecular level, together with the interpretation of many phenomena. Raman spectroscopy of the [n]CPPs will be the tool which, combined with other techniques, such as high pressure, temperature or chemical oxidation, reveals the importance of such a radial cyclic configuration. We intend to find the more reasonable answers to the following open questions:

- Will the [n]CPPs be molecular models of armchair SWCNTs? If this assumption is right, their properties could then be extrapolated for the understanding of the one dimensional systems. Or, on the contrary, will there be a new system which can be englobed between those exhibiting disturbed aromatic conjugation?
- Could the [n]CPPs be used for the interpretation of the radial cyclic π–conjugation therefore replacing the [n]cyclacenes?
- Are the quinonoid configurations with local double bond localization real? Could these be reformulated from the expected shortening of the C_{ortho}-C_{ortho} bond?

1.6. Objectives

We will use Raman spectroscopy to study the vibrational properties of [n]CPPs, from [5]CPP to [12]CPP, and to conduct a proper assignment of the main spectral contributions. This strategy will allow us to study structural and electronic characteristics of these systems, as well as their benzoid-quinonoid character. On the other hand, [n]CPPs can be used as SWCNTs molecular models to better understand their diameter and chiral dependent properties, and to characterize certain Raman bands related with the structural conditions of the tubes. We will combine the information on the experimental Raman frequencies and intensities with the density functional theory (DFT) computations to provide a consistent interpretation of the [n]CPPs Raman spectra. Thus, this work will aim:

- To discuss the common features shown by the Raman spectra of poly-conjugated molecules which can be ascribed to π electron delocalization. This description will be accompanied by models developed in order to account for such spectroscopic peculiarities.
- To synthesis cationic and dicationic species of [n]CPPs and to *in-situ* characterize them by Raman spectroscopy and UV-Vis-near IR.

- To study the cations and dications of the [n]CPPs to reveal the electronic charge configuration and the properties of those charged cycles.
- To analyze high and low temperature configurational changes. [6]-, [8]- and [12]-CPP will be studied by Raman spectroscopy at different temperatures.
- To follow the [n]CPPs response to high pressure, analyzing their deformability and reactivity under pressure. High pressure experiments up to 12 GPa will be conducted and followed by Raman spectroscopy in [n]CPPs.
- To provide new insights on the plastic and conformational properties of these nanohoop-shaped systems.
- To investigate their flexural rigidity, comparing their behavior with that exhibited by CNTs.
- To explore the formation of π-π concave-convex interactions between [n]CPPs and fullerenes, several studies will be carried out:

  -Several solid state mixtures of [n]CPPs of different sizes and C_{60} will be compressed and followed by Raman spectroscopy.

  -A series of four 1:1 host-guest supramolecular complexes of [n]CPPs and C_{70} will be analyzed by Raman spectroscopy in solid state and complemented with the analysis of their spectroscopic responses under mechanical and thermal stresses.

1.7. Organization of This Work

This dissertation has been organized in several chapters: 1. Introduction; 2. Methodology; 3.-7. Results; 8. Discussion; 9. Conclusion.

After the introduction presented here, in chapter two we will describe the followed methodologies, both experimental and computational. Regarding the experimental data, we will also explain how the data were processed and which parameters have been the most important to analyze. Furthermore, we will describe the different Raman spectrometers used along this work. In that chapter we will also do a brief description of the most relevant Raman bands of the carbon systems which will be used as references: SWCNTs, LPPs, C_{60} and C_{70}. This chapter finalizes with a brief report of the main calculation methodologies carried out and the points needed to understand the obtained results.

Chapters three to seven collect the main results of this work. Chapters 3-6 is the main text of the publications and the supplementary information of each one has been included in the appendixes (1-4):

- **Chapter 3:** *From Linear to Cyclic Oligoparaphenylenes: Electronic and Molecular Changes Traced in the Vibrational Raman Spectra and Reformulation of the Bond Length Alternation Pattern Section.* In this chapter we conduct a thorough comparison between the Raman spectra of linear and cyclic paraphenylenes. We have accounted for any structural and electronic similitude and difference which definitely will configure their vibrational properties.
- **Chapter 4:** *Properties of Sizeable [n]Cycloparaphenylenes as Molecular Models of Single-Wall Carbon Nanotubes Elucidated by Raman Spectroscopy: Structural and Electron-Transfer Responses under Mechanical Stress*. Here we do a comparison between the Raman spectra of [n]CPPs and SWCNTs at room conditions. We also evaluate the [n]CPP elastic behavior against deformation. Moreover, we compare the [n]CPP capability to form host-guess complexes with fullerene C_{60}, as that of SWCNTs.
- **Chapter 5:** *Chameleon-like Behaviour of Cyclo[n]paraphenylenes in Complexes with C_{70}. On their Impressive Electronic and Structural Adaptability as Probed by Raman Spectroscopy.* In this

chapter we analyze the [n]CPP conformational capability to anisotropically host C_{70}. We demonstrate the [n]CPP flexibility in terms of ovallization and torsions of their neighboring phenyl units to be able to accommodate to the C_{70}.

- **Chapter 6:** *The Raman Fingerprint of Cyclic Conjugation: The case of the Stabilization of Cations and Dications in Cycloparaphenylenes* This chapter describes the synthesis of cationic and dicationic [n]CPPs, which was experimentally characterized by UV-Vis-near IR and near-resonant Raman spectroscopies. The analysis was supported by DFT theoretical calculations of the spectra, electronic configurations and structural parameters.

- **Chapter 7:** *High Pressure Response of [n]CPPs: Mechanical Modulation of the Cross Section.* In this chapter a preliminary section about the high pressure response of SWCNTs and [n]LPPs is provided. Then, an exhaustive study about the Raman spectra at high pressure of [n]CPPs will be conducted. We focus on any possible electronic and structural piece of information provided by induced changes in the [n]CPPs Raman spectra.

In chapter 8 we discuss the main points outlined in the objectives section of this introductive chapter and we summarize the main conclusions of this work, so the main open questions are globally addressed. Finally, in chapter 9 we will close this thesis with the main conclusion reached from this work.

1.8. Publications

Part of the work presented in this thesis has already been published in international journals. Currently, other related manuscripts are being processed. Manuscripts published or submitted to the date are:

- **From Linear to Cyclic Oligoparaphenylenes: Electronic and Molecular Changes Traced in the Vibrational Raman Spectra and Reformulation of the Bond Length Alternation Pattern Section**.
  M. Peña Alvarez, L. Qiu, M. Taravillo, V. G. Baonza, M. C. Ruiz Delgado, S. Yamago, R. Jasti, J. T. López Navarrete, J. Casado, M. Kertesz.
  Phys. Chem. Chem. Phys DOI:10.1039/C5CP05500H (2015).

- **Properties of Sizeable [n]Cycloparaphenylenes as Molecular Models of Single-Wall Carbon Nanotubes Elucidated by Raman Spectroscopy: Structural and Electron-Transfer Responses under Mechanical Stress.**
  M. Peña-Alvarez, P. M. Burrezo, M. Kertesz, T. Iwamoto, S. Yamago, J. Xia, R. Jasti, J. T. López Navarrete, M. Taravillo, V. G. Baonza, J. Casado.
  Angew. Chem. Int. Ed. **53**, 7033-7037 (2014).

- **Chameleon-like Behaviour of Cyclo[n]paraphenylenes in Complexes with C_{70}. On their Impressive Electronic and Structural Adaptability as Probed by Raman Spectroscopy.**
  M. Peña Alvarez, P. Mayorga Burrezo, T. Iwamoto, L. Qiu, M. Kertesz, M. Taravillo, V. G. Baonza, J. T. López Navarrete, S. Yamago, J. Casado.
  Faraday Discussions **173,** 157-171 (2014).

- **The Raman Fingerprint of Cyclic Conjugation: The case of the Stabilization of Cations and Dications in Cycloparaphenylenes**

Additionally several related works have been published:

- **Probing the Stress Effect on the Electronic Structure of Graphite by Resonant Raman Spectroscopy**.
  M. Peña-Alvarez, E. del Corro, V. G. Baonza, M. Taravillo.
  Journal of Physical Chemistry C **118**, 25132–25140 (2014).

- **Decorating Graphene Oxide/Nanogold with Dextran-based Polymer Brushes for the Construction of Ultrasensitive Electrochemical Enzyme Biosensors.**
  A. Boujakhrout, A. Sánchez, P. Díez, S. Jiménez-Falcao, P. Martínez-Ruiz, M. Peña-Álvarez, J. M. Pingarrón, R. Villalonga.
  Journal of Materials Chemistry B **3**, 3518–3524 (2015).

- **Single Layer Molybdenum Disulphide under Direct Compression: Low-Pressure Band-Gap Engineering**.
  M. Peña-Alvarez, E. del Corro, A. Morales-García, L. Kavan, M. Kalbac, O. Frank.
  Nano Letters **15**, 3139–3146 (2015).

1.9. References

1 A. Kekulé, *Liebigs Ann.* **137**, 129–196 (1866).

2 G. Herzberg, *Infrared and Raman spectra of polyatomic molecules*, Van Nostrand, Princeton (1954).

3 C. R. Bailey, C. K. Ingold, H. G. Poole, C. L. Wilson, *J. Chem. Soc*. 222–235 (1946).

4 G. Natta, G. Mazzanti, P. Corradini, *Rendi. Accad. Naz. Lincei. Classe Sci. Fis. Mat. Nat*. **25**, 3 (1958).

5 M. Kertesz, C. H. Choi, S. Yang, *Chem. Rev*. **105**, 3448–3481 (2005).

6 L. Cuff, M. Kertesz, *Macromol*. **27**, 762–770 (1994).

7 G. Zerbi, B. Chierichetti, O. Inganas, *J. Chem. Phys*. **94**, 4637–4645 (1991).

8 V. Hernandez, C. Castiglioni, M. Del Zoppo, G. Zerbi, *Phys. Rev. B* **50**, 9815–9823 (1994).

9 C. Castiglioni, E. Di. Donato, M. Tommasini, F. Negri, G. Zerbi, *Synth. Met.* **139**, 885–888 (2003).

10 M. Tommasini, E. di Donato, C. Castiglioni, G. Zerbi, N. Severin, T. Böhme, J. P. Rabe, XVII International Winter School / Euroconference on Electronic Properties of Novel Materials-AIP Conf. Proc. Kirchberg, Tirol (Austria), American Institute of Physics, 6-13 March, **723**, 334 (2004).

11 Y. Matsuo, K. Tahara, M. Sawamura, E. Nakamura, *J. Am. Chem. Soc*. **126**, 8725–8734 (2004).

12 H. S. Choi, K. S. Kim, *Angew. Chem. Int. Ed*. **38**, 2256–2258 (1999).

13 R. Herges, *Chem. Rev.* **106**, 4820–4842 (2006).

14 E. S. Hirst, F. Wang, R. Jasti, *Org. Lett.* **13**, 6220–6223 (2011).

15 B. D. Steinberg, T. L. Scott, *Angew. Chem. Int. Ed*. **48**, 5400–5402 (2009).

16 P. R. Ashton, G. R. Brown, N. S. Isaacs, D. Giuffrida, F. H. Kohnke, J. P. Mathias, A. M. Z. Slawin, D. R. Smith, J. F. Stoddart, D. J. Williams, *J. Am. Chem. Soc.* **114**, 6330–6353 (1992).

17 P. Li, T. J. Sisto, E. R. Darzi, R. Jasti, *Org. Lett.* **16**, 182–185 (2014).

18 K. Tahara, Y. Tobe, *Chem. Rev*. **106**, 5274–5290 (2006).

19 R. Jasti, J. Bhattacharjee, J. B. Neaton, C. R. Bertozzi, *J. Am. Chen. Soc*. **130**, 17646–7647 (2008).

20 T. J. Sisto, M. R. Golder, E. S. Hirst, R. Jasti, *J. Am. Chem. Soc*. **133**, 15800–15802 (2011).

21 T. J. Sisto, R. Jasti, *Synlett* **23**, 483–489 (2012).

22 E. S. Hirst, R. Jasti, *J. Org. Chem*. **77**, 10473–10478 (2012).

23 R. Jasti, C. R. Bertozzi, *Chem. Phys. Lett*. **494**, 1–7 (2010).

24 J. Xia, J. W. Bacon, R. Jasti, *Chem. Sci*. **3**, 3018–3021 (2012).

25 H. B. Li, A. J. Page, S. Irle, K. Morokuma, *Chem. Phys. Chem.* **13**, 1479–1485 (2012).

26 H. B. Li, A. J. Page, S. Irle, K. Morokuma, *J. Am. Chem. Soc*. **134**, 15887–15896 (2012).

27 H. Omachi, T. Nakayama, E. Takahashi, Y. Segawa, K. Itami, *Nature Chem*. **5**, 572–576 (2013).

28 P. J. Evans, E. R. Darzi, R. Jasti, *Nature Chem.* **6**, 404–408 (2014).

29 J. Xia, R. Jasti, *Angew. Chem. Int. Ed.* **51**, 2474–2476 (2012).

30 F. Sibbel, K. Matsui, Y. Segawa, A. Studer, K. Itami, *Chem. Commun.* **50**, 954–956 (2014).

31 S. Yamago, Y. Watanabe, T. Iwamoto, *Angew. Chem. Int. Ed.* **49**, 757–759 (2010).

32 Y. Segawa, P. Šenel, S. Matsuura, H. Omachi, K. Itami, *Chem. Lett*. **40**, 423–425 (2011).

33 E. Kayahara, Y. Sakamoto, T. Suzuki, S. Yamago, *Org. Lett*. **14**, 3284–3287 (2012).

34 Y. Segawa, S. Miyamoto, H. Omachi, S. Matsuura, P. Senel, T. Sasamori, N. Tokitoh, K. Itami, *Angew. Chem. Int. Ed.* **50**, 3244–3248 (2011).

35 S. E. Lewis, *Chem. Soc. Rev.* **44**, 2221–2304 (2015).

36 H. Omachi, Y. Segawa, K. Itami, *Org. Lett*. **13**, 2480–2483 (2011).

37 S. Hitosugi, W. Nakanishi, T. Yamasaki, H. Isobe, *Nat. Commun*. **2**, 492 (2011).

38 E. R. Darzi, R. Jasti, *Chem. Soc. Rev.* **44**, 6401–6410 (2015).

39 S. Fomine, M. G. Zolotukhin, P. Guadarrama, *J. Mol. Model.* **18**, 4025–4032 (2012).

40 H. Isobe, S. Hitosugi, T. Yamasaki, R. Iizuka, *Chem. Sci*. **4**, 1293–1297 (2013).

41 S. Hitosugi, R. Iizuka, T. Yamasaki, R. Zhang, Y. Murata, H. Isobe, *Org. Lett*. **15**, 3199–3201 (2013).

42 S. M. Bachrach, D. Stück, *J. Org. Chem*. **75**, 6595–6604 (2010).

43 T. Iwamoto, Y. Watanabe, Y. Sakamoto, T. Suzuki, S. Yamago, *J. Am. Chem. Soc.* **133**, 8354–8361 (2011).

44 Y. Segawa, H. Omachi, K. Itami, *Org. Lett.* **12**, 2262–2265 (2010).

45 Y. Segawa, A. Fukazawa, S. Matsuura, H. Omachi, S. Yamaguchi, S. Irle, K. Itami, *Org. Biomol. Chem*. **10**, 5979–5984 (2012).

46 N. I. Nizhegorodov, S. W. Downey, M. B. Danailov, *Spectrochim. Acta A* **56**, 783–795 (2000).

47 M. Fujitsuka, D. W. Cho, T. Iwamoto, S. Yamago, T. Majima, *Phys. Chem. Chem. Phys*. **14**, 14585–14588 (2012).

48 T. Nishihara, Y. Segawa, K. Itami, Y. Kanemitsu, *J. Phys. Chem. Lett.* **3**, 3125–3128 (2012).

49 C. Camacho, T. A. Niehaus, K. Itami, S. Irle, *Chem. Sci*. **4**, 187–195 (2013).

50 H. Chen, M. R. Golder, F. Wang, R. Jasti, A. K. Swan, *Carbon* **67**, 203–213 (2014).

51 T. Iwamoto, Y. Watanabe, H. Takaya, T. Haino, N. Yasuda, S. Yamago, *Chem. – Eur. J*. **19**, 14061–14068 (2013).

52 T. J. Sisto, X. Tian, R. Jasti, *J. Org. Chem*. **77**, 5857–5860 (2012).

53 B. Anis, F. Börrnert, M. H. Rümmeli, C. A. Kuntscher, *J. Phys. Chem. C* **117**, 21995–22001 (2013).

54 B. W. Smith, M. Monthioux, D. E. Luzzi, *Nature* **396**, 323–324 (1998).

55 M. Gussoni, C. Castiglioni, and G. Zerbi, *Spectroscopy of Advanced Materials*, edited by R. J. H. Clark, R. E. Hester ,Wiley, New York, Vol. 11, p. 251(1991).

56 E. Ehrenfreund, Z. Vardeny, O. Brafman, B. Horovitz, *Phys. Rev. B* **36**, 1535–1553 (1987).

57 H. Kuzmany, A. Imhoff, D. B. Fitchen, A. Sarhangi, *Phys. Rev. B* **26**, 7109–7112 (1982).

58 C. Castiglioni, M. Gussoni, G. Zerbi, *Synth. Met*. **29**, E1–E6 (1989).

59 H. Kataura, Y. Kumazawa, Y. Maniwa, I. Umezu, S. Suzuki, Y. Ohtsuka, Y. Achiba, *Synth. Met.* **103**, 2555–2558 (1999).

60 R. B. Weisman, S. M. Bachilo, *Nano Lett*. **3**, 1235–1238 (2003).

61 E. H. Hároz, J. G. Duque, X. Tu, M. Zheng, A. R. Hight Walker, R. H. Haige, S. K. Doorn, J. Kono, *Nanoscale* **5**, 1411–1439 (2013).

62 M. Banerjee, R. Shukla, R. Rathore, *J. Am. Chem. Soc*. **131**, 1780–1786 (2009).

63 E. Zojer, J. Cornil, G. Leising, J. L. Brédas, *Phys. Rev. B* **59**, 7957–7967 (1999).

64 L. Cuff, C. Cui, M. Kertesz, *J. Am. Chem. Soc*. **116**, 9269–9274 (1994).

65 J. A. Elliott, J. K. W. Sandler, A. H. Windle, R. J. Young, M. S. P. Shaffer, *Phys. Rev. Lett*. **92**, 095501–4 (2004).

66 M. Fujitsuka, T. Iwamoto, E. Kayahara, S. Yamago, T. Majima, *Chem. Phys. Chem*. **14**, 1570–1572 (2013).

67 H. Chen, M. R. Golder, F. Wang, S. K. Doorn, R. Jasti, S. Tretiak, A. K. Swan, *J. Phys. Chem. C* **119**, 2879–2887 (2015).

68 V. C. Parekh, P. C. Guha, *J. Indian Chem. Soc.* **11**, 95–100 (1934).

69 F. Eglinton, A. R. Galbraith, *Proc. Chem. Soc*. 350–351 (1957).

70 F. Sondheimer, *Acc. Chem. Res*. **5**, 81–91 (1972).

71 S. Kammermeier, P. G. Jones, R. Herges, *Angew. Chem. Int. Ed.* **35**, 2669–2671 (1996).

72 M. Machón, R. Reich, J. Maultzsch, H. Okudera, A. Simon, R. Herges, C. Thomsen, *Phys. Rev. B* **72**, 155402 (2005).

73 H. Omachi, S. Matsuura, Y. Segawa, K. Itami, *Angew. Chem. Int. Ed*. **49**, 10202–10205 (2010).

74 A. Yagi, Y. Segawa, K. Itami, *J. Am. Chem. Soc*. **134**, 2962–2965 (2012).

75 J. Xia, M. R. Golder, M. E. Foster, B. M. Wong, R. Jasti, *J. Am. Chem. Soc*. **134**, 19709–19715 (2012).

76 S. Yamago, E. Kayahara, T. Iwamoto, *Chem. Rec*. **14**, 84–100 (2014).

77 T. Iwamoto, E. Kayahara, N. Yasuda, T. Suzuki, S. Yamago, *Angew. Chem. Int. Ed.* **53**, 6430–6434 (2014).

78 B. M. Wong, *J. Phys. Chem. C* **113**, 21921–21927 (2009).

79 K. Nakao, M. Nishimura, T. Tamachi, Y. Kuwatani, H. Miyasaka, T. Nishinaga, M. Iyoda, *J. Am. Chem. Soc*. **128**, 16740–16747 (2006).

80 J. Krömer, I. Rios-Carreras, G. Fuhrmann, C. Mush, M. Wunderlin. T. Debaerdemaeker, E. Mena-Osteritz, P Bäerle, *Angew. Chem. Int. Ed*. **39**, 3481–3486 (2000).

81 H. Ito, Y. Mitamura, Y. Segawa, K. Itami, *Angew. Chem. Int. Ed*. **54**, 159–163 (2015).

82 R. Chance, D. S. Boudreaux, J. L. Bredas, R. Silbey, in *Handbook of Conducting Polymers*, Edited by T. J. Skotheim, M. Dekker, New York, Vol. 2, p. 825 (1986).

83 L. Elsenbaumer, L. W. Shacklett, in *Handbook of Conducting Polymers*, , Edited by T. J. Skotheim, M. Dekker, New York, Vol. 2, p. 216 (1986).

84 A. Greenberg, J. F. Liebman, *Strained Ring Molecules*, Academic, New York (1978).

85 P. George, M. Trachtman, C. W. Bock, A. M. Brett, *J. C. S. Perkin Trans.* **2**, 1222–1227 (1976).

86 A. Hirsch, O. Vostrowsky, *Top. Curr. Chem.* **245**, 193–237 (2005).

87 Z. Chen, W. Thiel, A. Hirsch, *Chem. Phys. Chem.* **4**, 93–97 (2003).

88 O. Bastiansen, *Acta Chem. Scand*. **3**, 408–414 (1949).

89 S. Tsuzuki, K. Tanabe, *J. Phys. Chem*. **95**, 139–144 (1991).

90 K. N. Baker, A. V. Fratini, T. Resch, H. C. Knachel, W. W. Adams, E. P. Socci, B. L. Farmer, *Polymer* **34**, 1571–1587 (1993).

91 C. Ambrosch-Draxl, J. A. Majewski, P. Vogl, G. Leising, *Phys. Rev. B* **51**, 9668–9676 (1995).

92 A. P. Rice, F. S. Tham, E. L. Chronister, *J. Chem. Cryst.* **43**, 14–25 (2013).

93 Y. Delugeard, J. Desuche, J. L. Baudour, *Acta Cryst.* **B32**, 702–705 (1976).

94 J. L. Baudour, *Acta Cryst.* **B47** 935–949 (1991).

95 S. Guha, W. Graupner, R. Resel, M. Chandrasekhar, H. R. Chandrasekhar, R. Glaser, G. Leising, *Phys. Rev. Lett*. **82**, 3625–3628 (1999).

96 H. W. Kroto, J. R. Heath, S. C. O'Brien, R. F. Curl, R. E. Smalley, *Nature* **318**, 162–163 (1985).

97 R. L. Viavattene, F. D. Greene, L. D. Cheung, R. Majeste, L. M. Trefonas, *J. Am. Chem. Soc.* **96**, 4342–4343 (1974).

98 Z. Chen, C. S. Wannere, C. Corminboeuf, R. Putcha, P. V. R. Schleyer, *Chem. Rev.* **105**, 3842–3888 (2005).

99 G. P. Brivio, E. Mulazzi, *Chem. Phys. Lett.***95**, 555–560 (1983).

100 B. Horovitz, *Solid State Commun.* **41**, 729–734 (1982).

101 S. Krichene, J. P. Buisson, S. Lefrant, *Synth. Met*. **17**, 589–594 (1987).

102 B. Bhushan, D. Luo, S. R. Schricker, W. Sigmund, S. Zauscher, *Handbook of Nanomaterials Properties*, Springer-Verlag, Berlin (2014).

103 P. M. Ajayan, M. Terrones, A. de la Guardia, V. Huc, N. Grobert, B. Q.Wei, H. Lezec, G. Ramanath, T. W. Ebbesen, *Science* **296**, 705–707 (2002).

104 C. Lee, X. Wei, J. W. Kysar, J. Hone, *Science* **321**, 385–388 (2008).

105 T. Iwamoto, Y. Watanabe, T. Sadahiro, T. Haino, S. Yamago, *Angew. Chem. Int. Ed.* **50**, 8342–8344 (2011).

106 A. V. Nikolaev, T. J. S. Dennis, K. Prassides, A. K. Soper, *Chem. Phys. Lett*. **223**, 143–148 (1994).

107 M. Meo, M. Rossi, *Comp. Sci. Tech*. **66**, 1597–1605 (2006).

108 E. T. Thostenson, Z. Ren, T. W. Chou, *Comp. Sci. Tech*. **13**, 1899–1912 (2001).

109 A. J. Ghandour, I. F. Crowe, J. E. Proctor Y. W. Sun, M.P. Halsall, I. Hernandez, A. Sapelkin, D. J. Dunstan, *Phys. Rev. B* **87**, 085416 (2013).

110 M. J. Lipp, W. J. Evans, B. J. Baer, C. S. Yoo, *Nature Mat*. **4**, 211–215 (2005).

Chapter 2

Methodology

The backbone of this thesis is constituted by the Raman analysis of [n]CPPs to extract structural and electronic information. Raman spectroscopy can be used to study to almost any sample form and conditions. Raman spectroscopy is a very complete diagnostic tool since it allows property and compositional gradients to be probed. In our work, we combine Raman spectroscopy with several techniques which will disturb the system in a controlled way. Some of those perturbations will be: high pressure modulation, extreme temperature, laser excitation and chemical oxidation. Moreover, calculations based on the density functional theory (DFT) are conducted to provide theoretical support for the bands assignment and experimental interpretation.

2.1. Introduction

In this chapter the experimental procedure followed in each kind of experiments will be detailed. Because of the importance of Raman spectroscopy in the study of conjugated structures firstly the fundamentals behind it will be outlined. Then we will explain the spectral treatment required to obtain the essential information, followed by the Raman spectrophotometerss used in this thesis. Along this work we will refer to the Raman spectra of linear para-phenilenes and carbon nanotubes, so next we do is to provide the reader with some basics about Raman spectroscopy of these systems. Moreover, we will work with fullerenes C_{60} and C_{70}, so here we give a brief explanation about the origin of the bands that we will follow.

Once the diagnostic tool is described, here we will revise the perturbation tools used to modulate the systems. The principles behind the high pressure generation will be outlined. To that aim a sapphire anvil cell (SAC) is used without medium transmitting media, placing the sample into a partially drilled gold gasket and using diamond chips as pressure sensor. We use of a SAC instead of a DAC (diamond anvil cell) to avoid undesired fluorescence observed on commercial diamond anvils, which would hinder the Raman experiment registration. The reason to use no pressure transmitting media is that this could interfere with the sample and it could be hosted into the [n]CPPs' cavities. We consider that the constituting [n]CPPs molecules act as transmitting media themselves.

Temperature experiments are carried out with two goals: to compare our results with those given in the literature obtained at 100 K,; and to explore the [n]CPPs conformational properties by combination of high temperature with laser excitation,

Oxidation experiments are carried out to explore the properties of the neutral systems and their capabilities to pursuit configurational changes, providing information about π delocalization. Experimental conditions are detailed in this chapter. When dealing with conjugated systems it is important to explore their electronic properties by means of UV-Vis spectroscopy, since this will inform us about the band gap trends. Therefore, we combine Raman spectroscopy with UV-Vis-NIR of the neutral and cationic species

Finally, in this thesis we conduct computational studies to support our experimental analysis. These calculations have all been carried out using the Gaussian 09 package[1] and have been based on the density functional theory (DFT) at the B3LYP/6-31G(d,p) level. We have explored the potential energy surface of [n]CPPs over geometrical optimizations, conformational analysis, electron density distribution, charge distribution, Raman frequency and intensity calculations, electronic spectra predictions and nuclear independent shifts calculations. In section 2.6 we postulate some basics about the fundamentals behind the DFT, basis sets and the different concepts treated along this work.

2.2. Raman Spectroscopy

2.2.1. Fundamentals

A molecular system, and by extrapolation a polymer, is defined by their atomic configurations, interatomic distances, oxidation state, etc. which are projected on the way that the elements of the system are able to vibrate. Every molecule, at all temperatures even absolute zero is continually executing vibrational motions. During vibrations, inter atomic distances and bond angles change periodically without producing any net translation of the center of mass. In molecular polyatomic molecules, each nucleus performs their own oscillation, all the vibration motions may seem randomly but in fact a proper analysis reveals that they are basic and simple depicting symmetrical characters. The superposition of the vibratory motion is known as normal vibrations or normal modes. There are many vibrational normal modes for each molecular symmetry, having each their own frequency. These are represented by normal modes wave functions, where all the wave functions of normal modes in their ground states, ψ_0 are bases for the totally symmetric representation of the point group of the molecule.

When a laser beam goes through the sample and interacts with it, most of this light goes through without any perturbation. Nevertheless, approximately ~10^{-5} of the light beam is scattered because of its interaction with rotational, vibrational and electronic levels. The analysis of that scattered light is the base of Raman spectroscopy. Specifically, Raman scattering is explained as the system polarizability changed induced by the interaction with an electromagnetic field, with the resultant electric dipole moment induction *P:*

$$P = \alpha E \tag{1}$$

where E is the external electric field and α is the polarizability. This is the resultant of a charge distribution into the system, as electronic cloud, deformed by the external electric field. The external electric field are vectors consisting of three components in the *x*, *y* and *z* directions. Polarizability is a tensor with six independent coordinates, α_{xx}, α_{yy}, α_{zz}, α_{xy}, α_{xz}, α_{yz}. A normal mode to be active needs that any of its integrals indicated in equation 2 to be different to zero.

$$\langle \psi_i | \alpha_{uv} | \psi_0 \rangle \tag{2}$$

Where ψ_0 and ψ_i are the fundamental and the vibrational excited state wave functions respectively; *u* is *x*, *y* or *z* and *v* is equals to *x, y* or *z*. Because ψ_0 belongs to the totally symmetric representation, the polarizability term and ψ_i must belong to the same representation in order to that mode to be active.[2]

Normal vibrational modes are defined independently to each other as *Lj*. A normal mode displacement can be decomposed into modes expressed in internal coordinates, $\overrightarrow{B_k}$. As internal coordinates several variants can be considered such as increments of bond length and bond angles. These must be chosen to represent bond stretching and angle bendings or torsions, so it extraordinarily simplifies the view when coming from cartesians coordinates.

$$\overrightarrow{L_j} = \sum_{k>1} c_{j,k} \overrightarrow{B_k} \tag{3}$$

where $c_{j,k}$ is the coefficient of the B_1 component of the j^{th} normal mode Thus, these normal modes contain substantial information about the system, since each vibration is defined by the atomic movements involved. Polarizability can be expressed as function their normal coordinates of a vibrational mode (*j*):

$$\alpha_j = \alpha_j^0 + \sum_k \left(\frac{\partial \alpha_j}{\partial L_j} \right)_0 L_j + \text{higher terms} \tag{4}$$

α_j^0 is the polarizability at the equilibrium position and $\left(\frac{\partial \alpha_a}{\partial L_j}\right)_0 L_j$ refers to how polarizability changes in such specific vibrational mode with respect to the internal coordinates, evaluated at the equilibrium position.[3]

$$P = \underbrace{\alpha_0 E_0 \cos(2\pi \nu_{laser} t)}_{\text{Rayleigh line}} + \underbrace{\frac{1}{2}\left(\frac{\partial \alpha}{\partial L_j}\right)_0 L_j \cos(2\pi(\nu_{laser} + \nu_j)t)}_{\text{Anti - Stokes}} + \underbrace{\frac{1}{2}\left(\frac{\partial \alpha}{\partial L_j}\right)_0 L_j \cos(2\pi(\nu_{laser} - \nu_j)t)}_{\text{Stokes}} \quad (5)$$

where E_0 and ν_{laser} are the external electric field and the frequency of the laser respectively. If the displacements involved in that vibration, *j*, do not induced any polarizability change, thus that vibration won't be Raman active. Raman scattering occurs thus when a molecular vibration can change the polarizability. The change is described by the polarizability derivative,

$$\left(\frac{\partial \alpha}{\partial L_j}\right) \neq 0 \quad (6)$$

being the selection rule for a Raman – active vibration that a change in polarizability is required during the vibration.

Because of the larger populations in the fundamental vibrational state, rather than in the excited one, the Stokes lines are stronger than the anti-Stoles ones under normal conditions. Since both give the same information, it is customary to measure only the Stokes side of the spectrum

Resonance Raman (RR) scattering occurs when the exciting laser energy is chosen in a way that its energy intercepts the main fold of an electronic excited state. Excitation of these continua produces RR spectra that show extremely strong enhancement of the Raman bands originated in this particular electronic transition. The term "near-resonance" is used when the exciting line is close in energy to the electronic excite state.

2.2.2. Experimental Observables

It is commonly known that when vibrational spectra are taken as a source of information on the structure and properties of any kind of condensed phase molecule, three main experiment observables are routinely recorded: frequencies, intensities and band shapes.

i) Vibrational Frequencies or Peak Frequencies

Vibrational frequencies or peak frequencies ν_j, are directly related with the force constant involved with that vibration and with the atomic mass of the atoms involved. This from a very simplistic but visual way can be defined for a diatomic molecule as:

$$\omega_m = \frac{1}{2\pi c}\sqrt{K/\mu} \quad (7)$$

where *K* is the force constant and μ is the reduced mass of that diatomic molecule. This is considered from a harmonic approximation. These restoring forces would linear with the displacements, which is accepted since the vibrational amplitudes are small for fundamental one quantum transitions. Anharmonicity plays an important and non-negligible role for higher vibrational quantum levels. Frequencies are determined mainly by molecular geometry, atomic masses, kinetic coupling, and intra-and inter-molecular vibrational potentials. When looking at π conjugated molecular systems, as are the case of the [n]CPPs, the π delocalization may shift vibrational frequencies from the traditional group frequencies.

ii) Integrated Intensities

Intensities in Raman are modulated by the electronic distribution and by its fluctuations when the molecular geometry is periodically distorted by a given normal mode of vibration. In Raman spectroscopy the electric field of the exciting beam induces into the system a polarization that is described by the polarizability tensor and its changes during normal modes.

As intensity we refer to the area under the peak, or sometimes relative intensities between integrated bands or peak heights. The Stokes Raman intensities integrate over the frequency domain is directly related with the bond polarizability derivatives:[4]

$$I_j \propto \left(\nu_{laser} + \nu_j\right)^4 \left(\frac{\partial \alpha}{\partial L_j}\right) \partial L_j \tag{8}$$

where ν_{laser} is the frequency of the laser, ν_{laser} is the vibrational amplitude of the involved mode,j, *Lj* are the cartesian coordinates involved in the mode, and α is polarizability. Delocalized π orbitals depict high mobility and large polarizability, so the transition moments which determine Raman intensities are modulated by the extent of delocalization of the π electrons along the molecular skeleton.

The Effective Conjugation Coordinate model, ECC model,[5,6] postulates that: due to the high polarizability of the π electronic cloud in π conjugated systems the vibrational modes with A_{1g} symmetry will be enhanced. Then the A_{1g} modes would be the ones carrying most of the spectral intensity of the active Raman bands, even if other active modes belonging to different point groups might be active as well.

iii) Band Shapes

Band shapes may provide information on molecular motions of the whole molecule (librations), on inter- or intra-molecular energy transfer (which determines the lifetimes of the vibrational levels), on the distribution of molecular geometries in a given flexible molecular system, and on a possible molecular heterogeneity of the sample. In this thesis band shapes will be neglected and we will always consider Lorentzian peak profiles. We will refer to Lorentzian band shapes associated with single vibrational modes, Figure 1 (equation 9) and to band profiles resulting from a superposition of many modes, Figure 2 and equation 10.

$$I = I_0 + \frac{2Area}{\pi} \frac{FWHM}{4\left(\omega - \omega_c\right)^2} + \omega^2 \tag{9}$$

$$I = I_0 + \frac{2Area_1}{\pi} \frac{FWHM_1}{4\left(\omega - \omega_{c1}\right)^2} + \omega^2 + \frac{2Area_2}{\pi} \frac{FWHM_2}{4\left(\omega - \omega_{c2}\right)^2} + \omega^2 \tag{10}$$

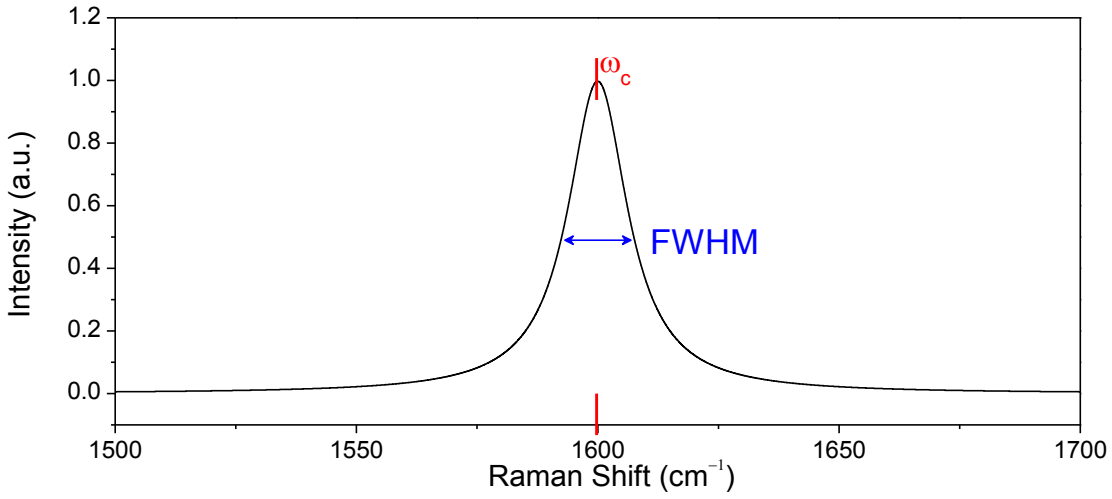

Figure 1. Single peak profile for a Lorentzian profile according to equation 9.

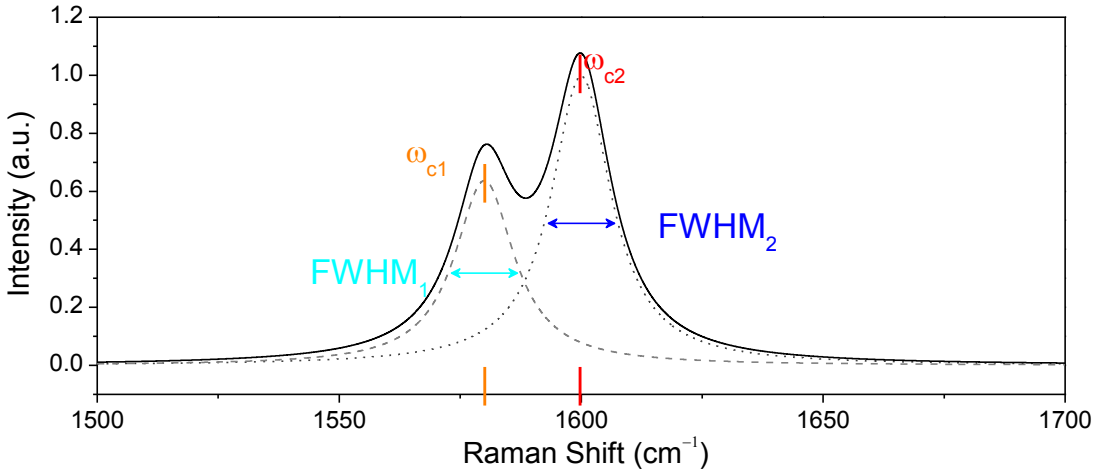

Figure 2. Combination band of a double peak Lorentzian profile according to equation 10.

2.2.3. Spectral Treatment and Analysis

In this thesis many peaks of interest are close to each other, so to be able to conduct an accurate assignment of the bands center we combined the second derivative spectral methodology [7] with the Lorentzian peak fitting. We obtain the bands center from the second derivative analysis, and we used them for the fitting of the peaks. As an example in Figure 3 we show a peak formed by two contributions, clearly distinguishable in the second derivate. Then we would use their Raman shift at the second derivate minima as starting parameters in the fitting to two contributions.

Along this work experimental intensities are quoted as their heights when fitted with Lorentzian profiles with FWHM ranging between 6 and 15 cm^{-1}, depending on the band, but constant for each band regardless of *n* for all the room conditions experiments. For experiments at high pressure, high-low temperature, oxidation, or laser excitation, their FWHMs are adapted as it was required.

When dealing with organic materials whose absorption bands occupy certain ranges of the UV-VIS one advantage is that resonant conditions can be reached and so more enhanced intensities. However there is a very important drawback which is the resultant fluorescence which in several cases my overlap with the vibrational spectrum. There are different origins from fluorescence background hindering the peaks visibility. For instance, in specific measurements, such us high pressure experiments, fluorescence could be coming from the anvils due to variable amounts of impurities present in synthetic sapphires Such florescence can be reduced by changing the excitation line, as far as possible from the absorption band, and also by the closure of the grid before the monochromator light entrance, but in most of the cases there is always some remaining background which hinders the assigment of the vibrational peaks. In those cases we proceed with a cleaning methodology based on the background fitting to them most adequate profile and thus we subtracted that background, as pictured in Figure 4.

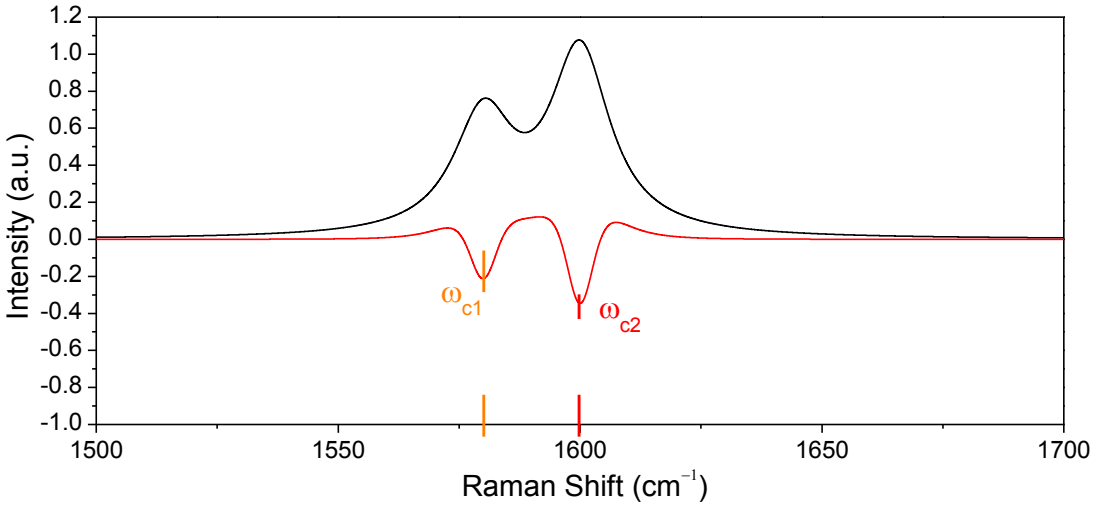

Figure 3. Second derivative of the Raman spectra of double Lorentzian peak shown, in red and black respectively.

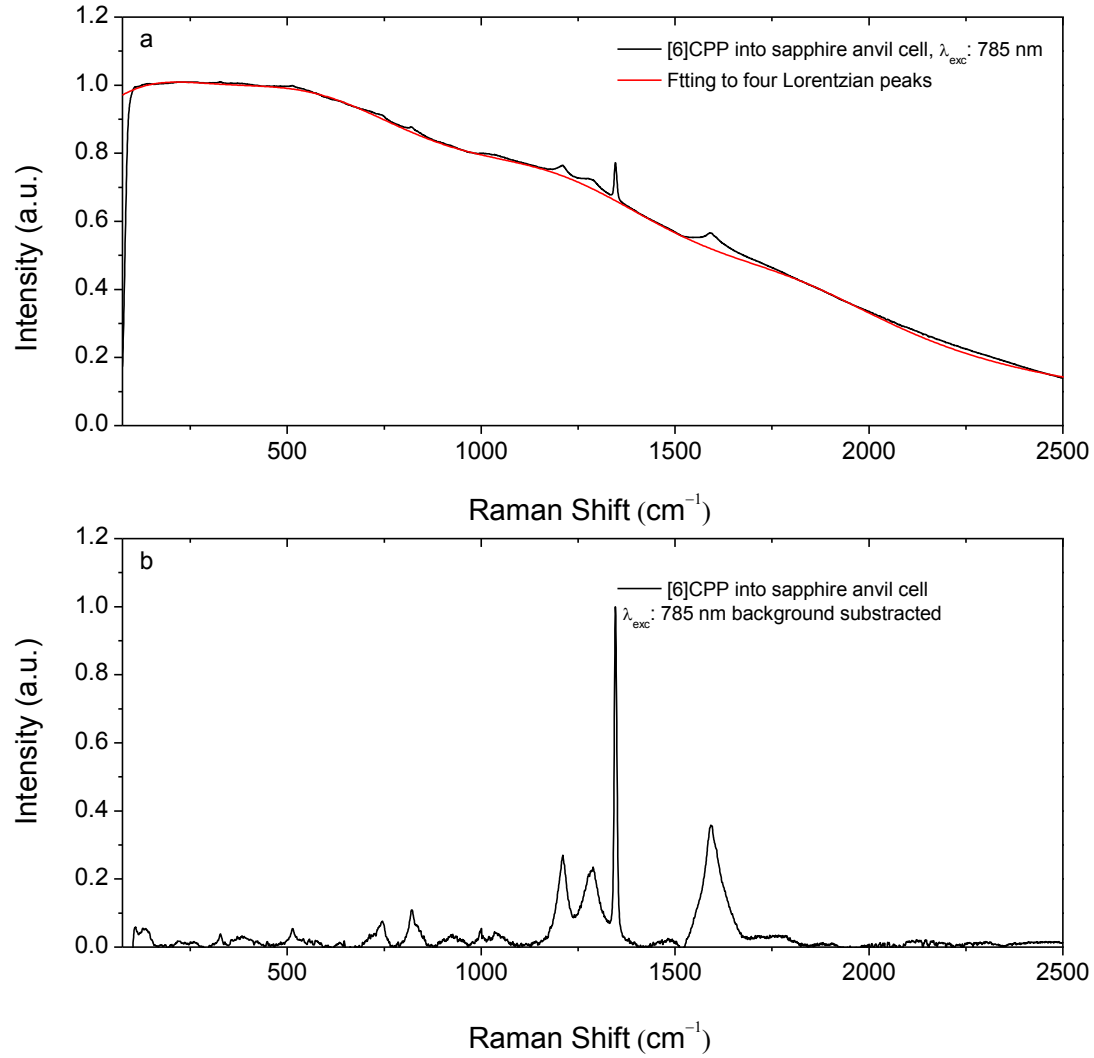

Figure 4 a) Raman spectrum of [6]CPP into the SAC, normalized to the most intense region, background has been fitted to four Lorentzian peaks. b) Background-corrected Raman spectrum of compressed [6]CPP normalized to the most intense peak.

2.2.4. Raman Spectrophotometers

In this thesis several Raman spectrophotometers have been used. In general the preferences of election have been guided by the excitation lines possibilities, combined with the best possible resolution.

RENISHAW Microscope

This device is part of the central services for research support from Malaga University.[8] Raman measurements at room conditions of the different [n]CPPs were conducted with this Invia Reflex Raman RENISHAW microscope. Measurements were conducted with the 785 nm as excitation wavelength using a monochromator with 3000 grooves/mm with a spectral resolution of 0.5-1 cm^{-1}.

Senterra Dispersive Raman Spectrophotometers from Bruker

This device is part of the central services for research support from Malaga University. [9] It combines a dispersive Raman spectrophotometers with a confocal microscope in a single device. Spectrophotometers is located on a platform of a confocal optical microscope and it has a class I protection from laser radiation. Detection is done through a high-sensitive CCD detector (charge couple device) with a Peltier-cooling to −70°C (thermoelectrically cooled). It counts with two diffraction gratings: 400 grooves/mm and 1200 grooves/mm. In our case we used only the high resolution one, 1200 grooves /mm, which provides a standard spectral resolution of 3 cm^{-1}. The Raman spectral range goes from 80 cm^{-1} to 4500 cm^{-1}, regardless the used excitation line. It counts with two inserted solid state lasers of 532 nm with maximum power of 20 mW and 785 nm with maxim power of 100 mW; and with another external laser of 633 nm with maximum power of 10 mW. It counts with fiber-optic sensor for recording the spectra of samples in an external sample compartment, so samples in solution can be easily measured. There is one sensor for each wavelength. This is useful to do spectral-chemistry, so the oxidation reduction processes can be followed in situ by UV-Vis and Raman as well with the same tray.

The calibration wavelength is continuous throughout the process of the spectral registration. The method used calibrates the system automatically with unmatched wavelength precision and accuracy using a Neon light as reference.

Raman scattering radiation is collected in back–scattering configuration spatial resolution of 0.5 μm, and spot size of about 3 μm. The confocal optics with hybrid iris is controlled by computer. Aperture: combined slotted aperture for high luminosity and round aperture for confocal measurements. The confocal resolution is about 2 μm. It has attached a color CCD camera to visualize the viewpoint, with a resolution 1.3 megapixel. It also counts with a trinocular head for optical lenses with different degrees which enable us to couple this device with other heating/cooling and high pressure devices:- 20x (working distance: 1.3 mm); and 50x (working distance: 0.38 mm).

This device has been used for most of the high pressure and high/low temperature experiments, as well as to conduct resonant Raman measurements oin oxidized species.

FT-Raman Ram II

This device is part of the central services for research support from Malaga Universiity.[9] It is supplied with a Germanium detector which works at the liquid nitrogen temperature, so it counts with an external cooling camera which needs of nitrogen filling. It works with backscattering. Laser excitation line is 1064 nm Nd:YAG. Laser power can range between 10 and 200 mW. Spectral resolution ranges between 1 and 4 cm^{-1}. It does not count with any coupled microscope so this technique could not be used when sample alignment was required, in other words, high pressure experiments cannot be conducted through this device.

This device was used mainly during spectral-chemistry experiments, to reach resonant conditions with the product.

Spectra-Physics Solid State Laser Operating at 532 nm Coupled to a Micro-Raman Spectrophotometers with an ISA HR460 Monochromator

This spectrophotometers is part of the Raman devices of the University Complutense of Madrid. It is equipped with two holographic diffraction gratings of 600 and 2400 grooves/mm, being the later the one used in this work. The HR460 monochromator with a liquid nitrogen-cooled CCD detector (ISA CCD3000, 1024 x 256 pixels) is used to record the spectra. The laser light is focused on to the sample by using a small lens of 18 mm focal length) located in front of the sample. The typical diameter of the laser spots at the sample is about 25 μm. The Raman signal is collected in near backscattering geometry using a 10x Mitutoyo long working distance objective coupled to a 10x Navitar zoom system and focused on to the slit the monochromator. Spatial filtering is performed through the optical path, which allows us to optimize the signal from the sample and to reduce fluorescence. Raman measurements were performed using an air-cooled argon ion laser, and Spectra-Physics solid state laser, operating at 488.0 and 532.0 nm respectively. The optical system is always calibrated with a standard neon discharge lamp. This spectrophotometers was used to conduct preliminary runs on the [n]CPPs and [n]LPPs with pressure as external perturbing variable.

Confocal Raman Spectrophotometers (Voyage, BWTek)

This spectrophotometers is part of the Raman equipment's of the University Complutense of Madrid. Confocal Raman spectrophotometers (Voyage, BWtek) one uses a 532 nm line of a solid state laser for excitation. The laser beam is focused through a microscope (Olympus BX5), with a ×10 long-working distance objective and the scattered light was analyzed on an air-cooled CCD (Hamamatsu S10141-1107S, 2048(h) × 122(v) pixels). The spectral resolution is 4–5cm^{-1}.

We used this device to conduct Raman measurements as a function of laser excitation time. The manual control of the laser allows us to excite the sample during continuous time even if Raman measurements are not being conducted. Moreover, this device shows another advantage against the ISA HR460 monochromator device, as it will be shown we do experiments as a function of time and temperature. Since the dusty sample needs to be horizontal to be hold in our heating device, the use of this spectrophotometers was convenient.

LabRAM HR Spectrophotometers

The Horiba Jobin-Yvon spectrophotometers from the The Nanocarbon Group at the Heyrovsky Institute of Physical Chemistry, ASCR Prague.[10] The grating with 1800 grooves/mm was used. For the sample excitation we used an Ar/Kr laser (488.0 nm). A 50× objective was used, providing a laser spot of about 1 μm in diameter. This spectrophotometers is provided with Notch filters which allowed us to measure from 50 cm^{-1}. The laser power on the sample was kept below 1 mW to avoid sample damage. This device was use for high pressure measurements on single walled carbon nanotubes. The 488 nm excitation line was use to reach resonant conditions with the sample.

Election of the Excitation Lines for our Experiments

As mentioned at the beginning of this section this thesis is based on the study of the cycle paraphenylene, molecular systems whose absorption maximum is between 300- 350 nm (as seen in the introduction chapter). This is why to avoid interactions with the absorption tail. we tried to go as far as possible of the tail, so the main excitation line used was 785 nm. We use excitation lasers with higher energies in specific experiments: to search for conformational transitions; and to look for convenient resonant conditions of charges species.

In this thesis we have also worked with fullerene samples, which require the use of a low energetic laser excitation. As known, fullerene polymerizes while is being excited, so those experiments have also been conducted with the 785 nm line. In each chapter the excitation line used for each kind of test, as well as the specific experimental conditions will be indicated.

2.3. Raman Spectroscopy at Room Conditions of Samples

Vibrational spectroscopy has played a key role in the study of the most relevant groups of linear poly-aromatics, in two dimensional conjugated systems as in graphene and graphite, or in carbon nanotubes and fullerenes. All these systems have in common that they are formed by conjugated sp^2 carbon. In the case of the linear poly-aromatics, such conjugation might be interrupted by torsions between the oligomeric units; while the other here mentioned are substantially rigid and there are not barriers to delocalization.

The backbone of this thesis is based on the vibrational spectroscopic study of [n]cycle para-phenylenes, being one of the mayor goals to define its π electronic character and extension of delocalization. When this thesis started not much was known about the Raman spectra of these molecular systems. During the develop of this thesis three studies have been published about the main Raman features of [n]CPPs.

As already commented in the introduction, there are several factors which relate linear para-phenylenes with cycle para-phenylenes, and carbon nanotubes with [n]CPPs. Therefore we consider that a section in which we explain the main Raman features of the [n]LPPs and SWCNTs is required to have in mind along the description and discussions done in the next sections of this thesis.

Moreover, we will also conduct experiments where [n]CPPs will act as hosts for fullerenes C_{60} and C_{70}. Raman spectroscopy will be used as diagnostic tool. Here we discretely show a brief summary of the most important fundamentals of these fullerene Raman spectroscopy, because interactions with their hosts could induce certain modulations on their Raman shifts.

2.3.1. Linear Paraphenylenes

The ECC postulate that the A_{1g} bands of a π conjugated molecular system show selective intensity enhancement and frequency dispersion with conjugation length.[11-16] The enhanced intensity and Raman shifts of the marked bands have been ascribed to the fact that π electrons experience different degrees of confinement within the structural units, thus affecting the electron delocalization along the chain.

Much attention has been focused on poly-para-phenylene (PPP) because it is an organic conducting polymer.[17-19] The basic physical phenomenon which gives rise to the peculiar electrical and optical properties of poly-conjugated molecules is the delocalization of n electrons along the chain backbone, which increases with the increasing number of phenyl units, lowering the energy gap.

Within these terms, the Raman spectrum of pristine poly-para-phenylene and the infrared spectra have be interpreted.[15] The Raman spectrum of oligo-phenylenes has been described by several authors and is mainly characterized by three intense modes of A_g symmetry. Figure 5 and Table 1 show the [6]LPP Raman spectrum with the eigenvectors of the main vibrational modes.

- C–C interring stretching motion that is coupled to a C–H bending motion, at ~1220 cm^{-1}.
- A_{1g} mode, assigned to the phenyl ring breathing mode coupled to the C-C intra-ring stretching mode, near 1280 cm^{-1}.
- C–C stretching mode near 1600 cm^{-1}. We will refer to it as GA_{1g} mode to show uniformity in our nomenclature, in analogy to graphite C-C stretching mode.[20-26]

In π conjugated systems the Raman shift of the GA_{1g} band have been related with the π delocalization degree, showing a smooth Raman downshift with the lengthening of the delocalization. However the dispersion shown by the GA_{1g} Raman shift in [n]LPPs very smooth, not being possible to then stablish any connection with the conjugational length,[27] and it is its intensity which is mostly affected by the π conjugation lengthening.

It turns out that the [n]LPPs IR spectra are not affected by conformational changes, but fortunately their Raman spectra are strongly conformational dependent. The intensity ratio $IA_{1g}1280/IA_{1g}1220$ is used as indicator of the extension of the conjugated,[21,24] and has subsequently been used to monitor the quality of synthetic routes PPP.[6,28] This decreases with the decreasing torsion between neighboring benzene rings, so with the increasing coplanarity of the p_z orbitals belonging to different phenyl units, so in this extent, the π delocalization is favored.

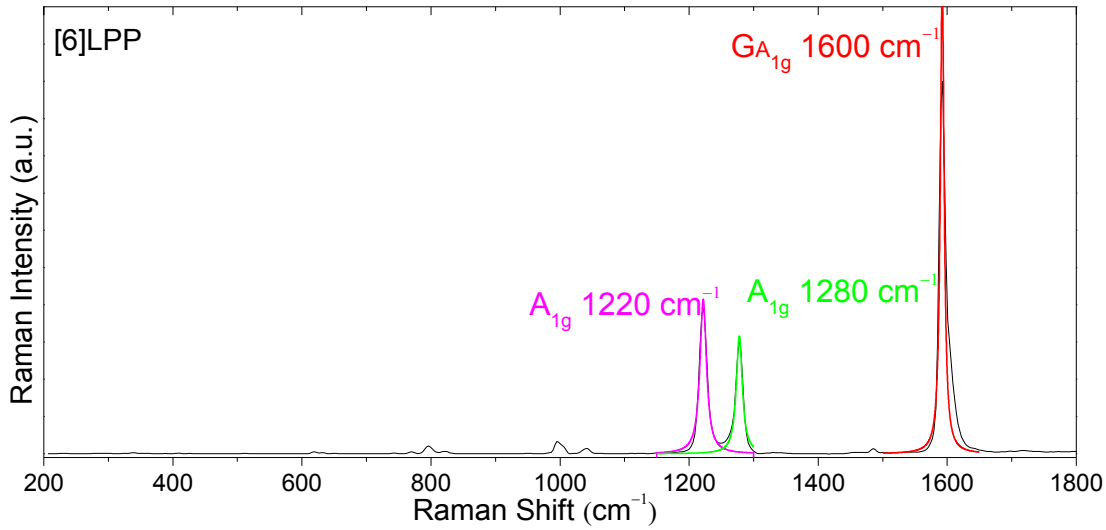

Figure 5. Raman spectrum (black lines) of [6]CPPs in the 200 -1800 cm^{-1} region. The band deconvolutions are shown in color

Table 1. Vibrational eigenvectors associated with the A_{1g} bands of the Raman spectrum of [6]LPP, obtained from calculations at the B3LYP/6-31G(d,p) level.

~1220 cm^{-1} C–H bending motion + C–C interring stretching	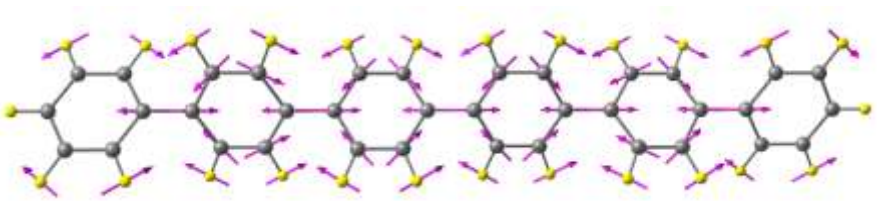
~1280 cm^{-1} Phenyl breathing mode + C-C intra-ring stretching mode	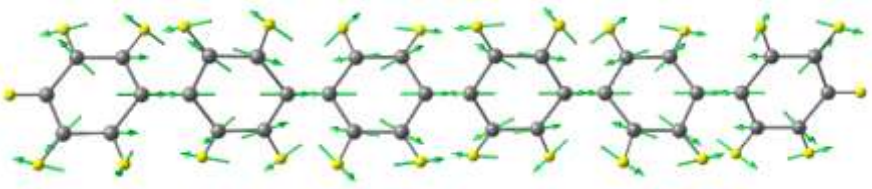
~1600 cm^{-1} C-C stretching mode	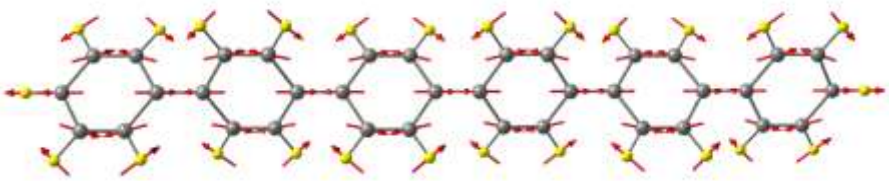

2.3.2. Single Walled Carbon Nanotubes

SWCNT diameter and chirality are related with the direction taken a graphene sheet to form the tube. To describe this direction the chiral parameters are used as n,m:

- when *n* and m are equal to each other, armchair CNTs result,
- when *n* and m are different and different to zero, we have chiral nanotubes,
- when m is equal to zero, then we have zigzag SWCNTs.

equation 11 relates the chiral parameters with the corresponding tube diameter[29]

$$d = \frac{a_0}{\pi}\sqrt{n^2 + nm + m^2} \tag{11}$$

a_0 is proportional to the C-C distance and equals to 2.494 Å.

It is well known that Raman spectroscopy is a good tool to selectively study SWCNTs of different diameters. This is due to the fact that SWCNTs of different diametes have different allowed optical transitions, as explained and studied by Kataura et al. .[33-35] We choose the 488 nm line as excitation line for the measurements of the SWCNTs of 0.7 nm to 1.1 nm diameter, in accordance with the resonant optical transitions.

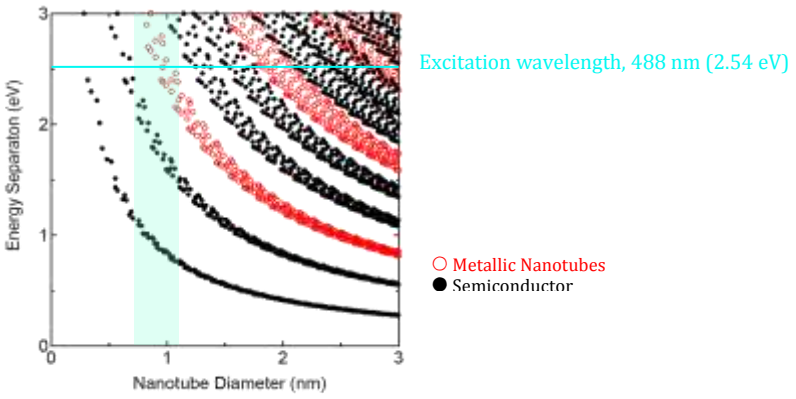

Figure 6. Kataura's diagram: SWCNTs transition energies as diameter function.[37] The vertical light blue bar indicates the diameter range of our experimental sample, 0.7-1.1 nm. The horizontal cyan line indicates the chosen excitation energy for our experiments. As seen the 488 nm line is resonant with metallic SWCNTs of the selected diameters.

Raman spectroscopy is a widely used tool for the characterization of carbon based materials, in particular in SWCNTs. In principle the Radial Breathing Modes (RBMs) and the G modes are those whose evolution has been mainly related with their structural, electronic and mechanical properties.[38,39,40] Therefore in this work RBMs and G modes will be the bands whose behavior will be mainly explored.

In Figure 7 we show the first order Raman spectrum of SWCNTs with diameters ranging from 0.7-1.1 nm, enriched with chiral (7, 6) SWCNTs. The RBMs, with A_{1g} symmetry, appear in the Raman spectral region between 100 and 300 cm^{-1}. RBMs are consequence of collective vibration of the carbon atoms in the radial direction of the tube, as shown in Table 2.[52] These are resonant bands mainly visible only for those diameters and chiralities in resonance with the excitation energy.[41]

The RBMs shift is directly related with the CNT diameter and even though many approximations and improvements have been done to obtain a most accurate relationship, the simplest and most used is this given in equation 12.[49,42]

$$\omega_{RBM}\left(cm^{-1}\right) = \frac{227}{d(nm)} \tag{12}$$

The G bands are the most intense Raman bands in the SWCNTs Raman spectra, being centred between 1530 and 1600 cm^{-1}. This is a first order vibrational mode,[43] which set their origin on the in plane C-C stretching band of graphene (G band). It splits in two when the graphene sheet rolls up to form the nanotube because of the generation of preferential vibrational directions along the tube and across the tube diameter. Due to the symmetry breaking, the Raman G band consist of three modes [A_{1g}, E_{1g}, and E_{2g}] and six modes [two A_1 modes, two E_1 modes, and two E_2 modes] for achiral (armchair or zigzag tubes) and chiral tubes, respectively.[44,45,46] Because the normal mixture of chirality and diameters on the studied SWCNTs, usually these modes are observed as two most intense peaks, G^+ and G^-. According to the vibrational displacement patterns, these G^- and G^+ modes correspond to either transversal (TO) or longitudinal (LO) modes, respectively in the semiconductor CNTs, meaning that the nuclear displacements can be either orthogonal (TO, A_{1g}) or parallel (LO, E_{1g}) relative to the nanotube axis direction, see Table 2. In armchair SWCNTs these G^- and G^+ modes correspond to the axial (LO, E_{1g}) and circumferential (TO, A_{1g}) modes respectively, which is only result of the Kohn anomalies due to their metallicity.[47,48] In Figure 7 we see that because we have chiral tubes enriched on (7,6) chirality the spectrum in the G region can be fitted to 6 contributions

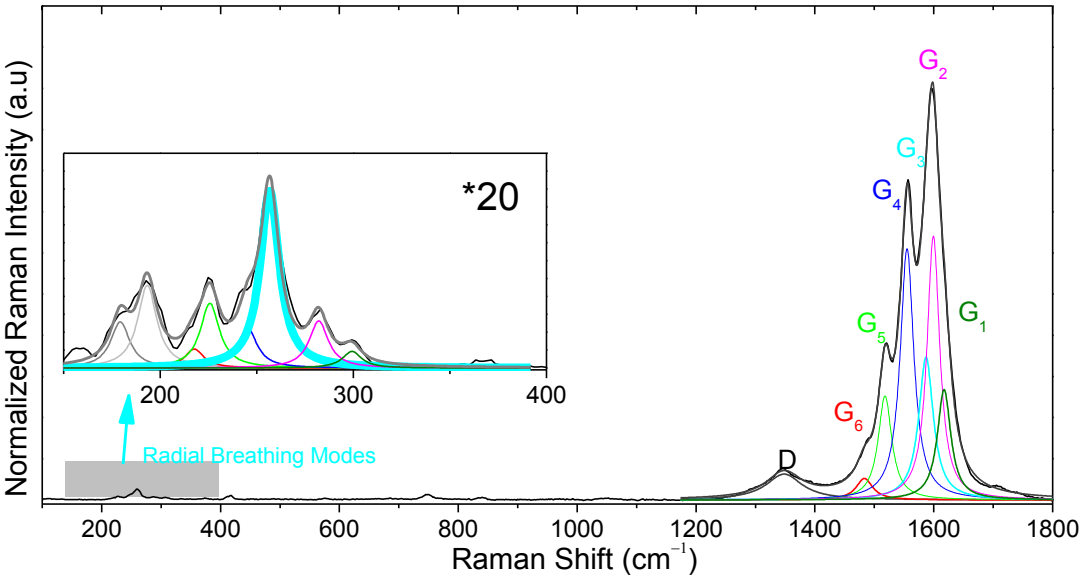

Figure 7. Resonant Raman spectra of SWCNTs with diameters between 0.7 and 1.1 nm, enriched with (7,6)SWCMT. Laser excitation energy: 2.54 eV. Colored lines correspond to the deconvolution of the RBMs, in the insert zoomed low frequency region, and G band contributions in the 1600 cm^{-1} region.

Table 2. Vibrational eigenvectors associated with the RBM, GLO and G circumferential and G longitudinal bands of the Raman spectrum of (6,6)SWCNT, obtained from calculations at the AM1/ STO-3G semi-empirical level.

Radial breathing mode	G band ,C- C stretching circumferential mode	G band ,C- C stretching transversal mode
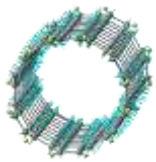	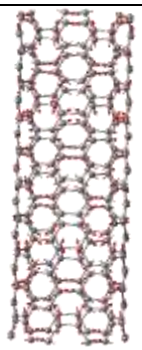	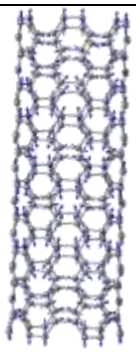

2.3.3. Fullerene C_{60}

Fullerene C_{60}, discovered by Kroto,[56] is a highly symmetric molecule which belongs to the I_h point group. Solid C_{60} is one of the most abundant fullerenes. Its ability to act as electron donor and acceptor, up to six electrons, makes it very attractive for possible optical and electronic applications.[57] Raman spectroscopy is a very convenient tool to judge possible symmetry break from any electronic inter molecular interactions. Also Raman spectroscopy is continently usable to judge if when combined or joint to other molecular systems it is going to act as donor or acceptor and which kind of interaction might be occurring.[58]

In Figure 8 we have the Raman spectrum of C_{60} in solid state measured at 785 nm. Because of its high symmetry there are not many active vibrational bands. In Figure 8 we have marked the most interesting ones, accompanied by their corresponding vibrational eigen vectors:

- Cage squashing mode around 271 cm^{-1}, H_g symmetry
- Radial breathing mode around 496 cm^{-1}
- Tangential C-C stretching mode, also referred as pentagonal pitching, around 1468 cm^{-1}.[59]

Splittings of the cage squashing mode, are useful to judge any symmetry distortion. The Raman shift of the pentagonal pitching mode is high sensitive to C_{60} would interact, pentagons are the most reactive paths in C_{60}. So upshift or downshift observed in this band can be interpreted in a manner that C_{60} is acting as acceptor and donor, respectively.

It is important to mention that even though Raman spectroscopy in this regard is very useful, some care must be taken when using it to deal with molecule because it has been demonstrated that high energetic excitation laser induce the C_{60} polymerization.[60] So all the experiments in this thesis in which C_{60} is involved have been conducted with the 785 nm excitation line.

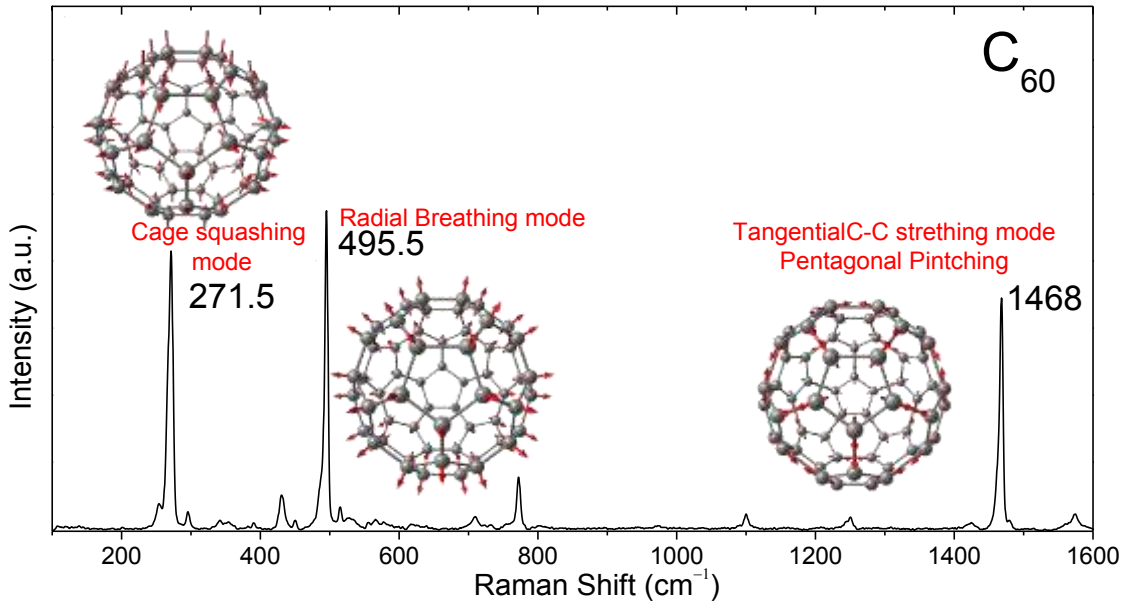

Figure 8. Raman spectrum of fullerene C_{60} at room conditions, measured with 785 nm as excitation wavelength. Inserted eigen vectors correspond to the vibrational modes of the marked bands, calculated for the optimized geometry at the B3LYP/6-31G(d,p) level.

2.3.4. Fullerene C_{70}

C_{70} is ellipsoidal, so two different axis cross the molecule, the size of the C_{70} long axis is 0.796 nm and of the short axis is 0.712 nm, approximately that of C_{60}.[61] C_{70} could be considered as a C_{60} molecule in whose equatorial diameter a belt of [5]CPP is inserted, this reduces the symmetry of C_{60}, I_h, to D_{5h}, increasing the number of individual Raman peaks. Interestingly this equatorial belt depicts different C-C distances than those in C_{60}.[62] Remarkably, C_{70} could be considered the shortest (5,5) armchair carbon nanotube.[63] As C_{60}, C_{70} can act as electron donor an acceptor.

C_{70} and C_{60} have the ability to form supramolecular structures acting as guest, occupying the cavity of other bigger molecules, or as host, hosting other molecules in their inner space. In this sense, fullerenes can arrange with carbon nanotubes forming the so called peapods. In this regard C_{70} can arrange in different configurations, lying on its long axis over the tube walls or standing on its short axis.[64]

Even though the Raman spectrum of this molecule becomes more complex, there are several key bands which can be followed for diagnostic incomplexation or intramolecular linkages. In Figure 9 we present the Raman spectrum of solid C_{70} measured with the 785 nm excitation wavelength. This excitation line is conveniently chosen because C_{70} can also polymerize with high energetic excitation lines.[60] The main Raman bands of C_{70} are:

- 1564 cm^{-1} which is due to a tangential C-C stretching mode or G-like mode;
- 456 cm^{-1} which is the radial breathing mode with has slightly more vibrational amplitudes along the long axial direction of the ellipsoid.
- 256 cm^{-1} which also corresponds to a sort of breathing radial-like mode (squashing mode) featured by main vibrational amplitudes in the atoms placed in the equatorial segment of C_{70}.[65-67]

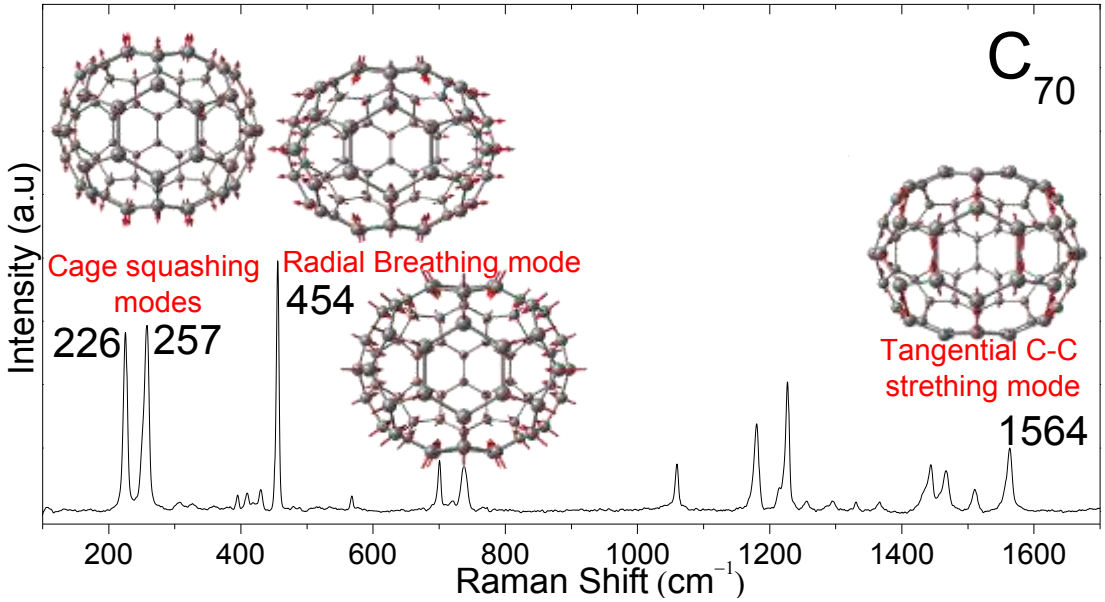

Figure 9. Raman spectrum of fullerene C_{70} at room conditions, measured with 785 nm as excitation wavelength. Inserted eigen vectors correspond to the vibrational modes of the marked bands, calculated for the optimized geometry at the B3LYP/6-31G(d,p) level.

2.4. Extreme Conditions Generation

In this work we have used different techniques to perturb the molecular system. The analysis of the molecular [n]CPPs response to those perturbation will provide us with information about their π electronic skeleton, delocalization, configurational, and also mechanical properties. With these aims three different methodologies have been used. The two first consist on moving along the potential well as a function of distance, using high pressure, shortening distances, and high temperature, to lengthening distances. The third one consist on chemically oxidize the [n]CPPs. In this section the used high pressure, and temperature techniques and the methodology followed during oxidation processes will be described.

2.4.1. High Pressure Experiments

In the high pressure spectroscopy field the fundamental requirement is that the high pressure device must be transparent to the radiation used as characterization tool. So that the most common devices are the diamond anvil cells which used confronted diamonds with tiny culets on their joining surface. The principle behind this technique is that pressure is equals to force over area, so small areas, within the μm magnitude order, can generate pressure in the 10 GPa order of magnitude. Bear in mind that atmospheric pressure is about 10^5Pa, so these pressures are about 10^4 orders above those. Diamond anvil cells, DAC, field is quickly developing in the last times because through these kind of experiments very valuable information can be obtained. In this thesis the anvil cell used is one designed in our group, Figure 10a.

Even though diamond is the hardest material, allow to reach extremely high pressure, for Raman spectroscopy characterization it presents the drawback of its broad first order Raman band, C-C stretching around 1330 cm^{-1}. When dealing with carbonaceous materials, more importantly with graphite like materials as nanotubes are, this can be an important shortcoming because this is a very intense band which covers the D band. In molecular systems as [n]CPPs this can overlap with important bands as it will be shown later on. Moreover, commercial diamonds normally depict undesired fluorescence which can totally hinder successful Raman spectral registration when dealing with molecules whose Raman scattering might be not intense enough to overcome this fluorescence, as shown in Figure 11a.

Therefore in this thesis sapphire anvils are used as alternative anvils. Sapphire Raman bands appear in the low frequency range and are well characterized, Figure 11b. These are not too intense and can be conveniently avoided with good confocal microscopy. We use commercial anvils of Al_2O_3 transparent corundum, bought from Roditi company.[68] The ones used for this thesis were bought with conical shape and polished tips of about 350 μm. Because a perfect alignment between sapphire tips is required, further polishing of the culets has been done before proceeding with the cell preparation. This step is done through a polishing machine, Graves Mark IV. This allows us to prepare couple of anvils with the exact the same culet zero angled. Moreover this also allows us to reutilize the anvils if the culet scratches during high pressure experiments.

a

b

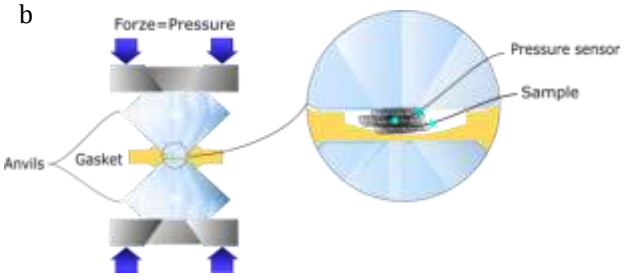

Figure 10. a) Picture of the cell design and build up by our research group. b) Scheme of the sapphire anvil cell setup used along this thesis.

As shown in Figure 10b, usually a metallic gasket is placed between the anvils so the sample is be hold between the culets. Generally a transmitting media is used to guarantee hydrostatic conditions in the gasket hole. Transmitting medium can be inner gases, or mixtures ethanol/ethanol/water. Since [n]CPPs are able to host molecules in their inner cavities., we decided to use no transmitting medium to avoid uncontrolled secondary perturbations. So, in this work the sample will be place directly in the gasket hole. Additionally, as shown in Figure 10b, we do not use a totally drilled gasket, but partial to avoid the sample to escape out of the gasket when it becomes fatty during compression. We chose the most inert metal as gasket, gold.

To be able to follow the different pressuring steps there are two possibilities, either measure the change of sample volumen, impossible with this pressure set up; or to use a calibrated equation of state for certain spectroscopic characteristic. Normally rubi chips are placed together with the sample, and the shift of its fluorescence bands is used as pressure sensor. However, this implies that either the Raman monochromator can be manually moved towards the rubi fluorescence region, 690 nm, or coupled to a fluorescence spectrophotometer. Because most of the high pressure Raman experiments for this thesis are conducted by the Senterra spectrophotometers unable to manually move the grating, we use diamond chips, as pressure sensor. The Raman shift of diamond with pressure is very well calibrated, equation 13 and Figure 12a.[69] This present the advantage versus the use of a diamond anvil that the peaks are local and not as intense as those coming from an anvil, allowing to reach of the whole Raman spectral range without covering it, as shown in Figure 12b.

$$p(GPa) = 0.356\ \left(\omega(cm^{-1}) - 1332.3\right) \tag{13}$$

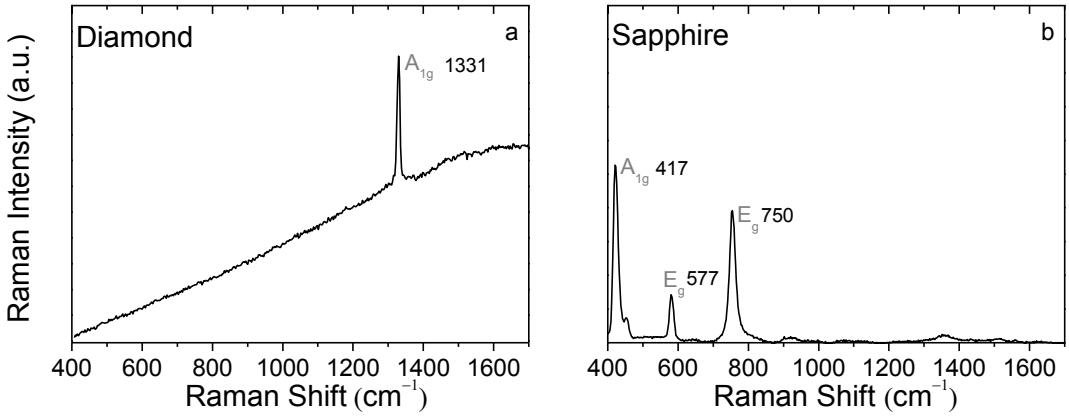

Figure 11. a) Raman spectrum a commercial diamond anvil normalized to the C-C stretching diamond band. b) Raman spectrum of a sapphire anvil measured with the 785 nm excitation line.

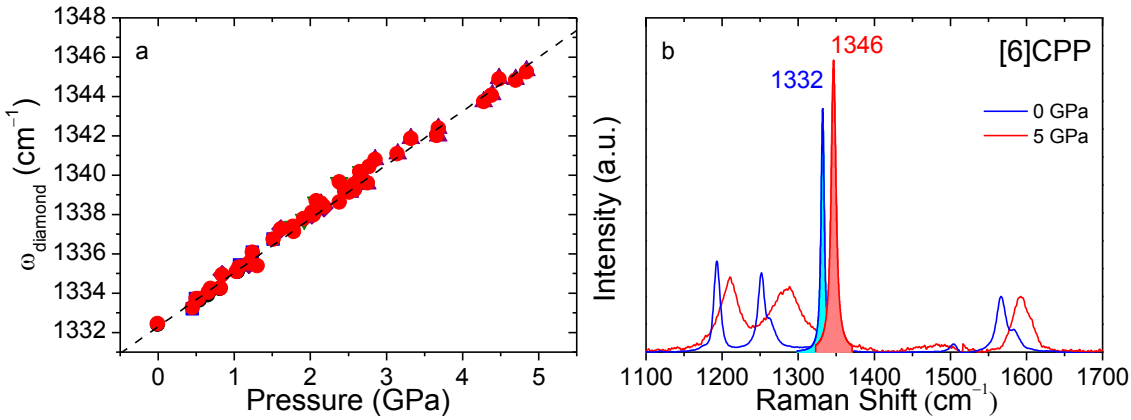

Figure 12. a) Calibration of the diamond Raman shift as a function of pressure, taken from Ref.[70]. b) Raman spectra of [6]CPP into a SAC at two different pressures, colored areas correspond to the diamond peak used as pressure sensor.

2.4.2. Temperature Dependent Experiments

Linkam TS1500 *with a T95* system controller was coupled to the Confocal Raman spectrophotometers (Voyage, BWTEK) to conduct temperature experiments coupled to laser excitation (532 nm). This device can heat within a temperature range from ambient up to 773 K, allowing us to observe and characterize samples through its quartz lid window. The high temperature stage system is equipped with a Pt/Rh thermocouple in direct contact with the ceramic heating element to detect and control the sample temperature. During the experiments, the temperature is stabilized within ± 0.1 degrees. This device was used for laser excitation time and temperature dependent experiments, chapters 4 and 5.

Linkam FTIR600 system coupled to confocal Senterra micro Raman to conduct Raman experiments with the 785 nm. This heating device allows to measure within 190 K and 870 K approximately. The sample must be placed between two sapphire plates of 0.5 mm thickness. This device was used to measure Raman dependent evolution of [6] and [8]CPP avoiding any laser induced perturbation, chapter 3.

2.4.3. Oxidation Conditions

The formation of charged species, cations and dications in this work, is done by a controlled addition of a stoichiometric amount of the oxidant agent over the neutral sample. The main factors to have into account in order to have a successful process are the choice of the solvent and of the oxidant agent. The solvent needs to guarantee the stability of the charged specie and the solubility of the neutral, charged and oxidant agents. The solvent used in this work is dichloromethane, DCM. Chemical oxidations have been conducted using Triethyloxonium hexachloroantimoniate ($Et_3O^+SbCl_6^-$) as oxidant agent. All the reactions were done in DCM solution of [n]CPP, 10^{-4} M, by stepwise addition of the oxidant agent to the spectrophotometric cell with the solution of the initial sample using micro-syringes. UV-Vis-NIR spectra were register after the addition of a oxidant drop to control the oxidation process.

This technique is also used to characterize the oxidized species combined with resonant or near resonant Raman spectroscopy.

2.5. Electronic Spectroscopy

. Electronic spectroscopy studies the electronic transitions between different electronic states, which generally should be in the UV-Vis spectral region. This electronic transition involves a change into the electronic distribution which can be accompanied by a change into the dipolar moment.

Each electronic state can be pictured as a potential energy surface (PES), related with the electronic configurations formed by the linear combination of molecular orbitals. Thus there should be as many PES as electronic state. In the meanwhile, each PES is filled by vibrational and rotational states. Electronic transitions in atoms provide thin linear spectral lines, however in molecules broad absorption or emission bands are usually observed. In molecules, the electronic transitions occur from the ground state, electronic, vibrational and rotational most populated (Boltzamn distribution). Then the interaction with an electromagnetic field induces the molecular vertical electron transition (Frank Condon's rule). As a consequence of such vertical electronic transition, also transitions to excited vibrational and rotational levels within such excited electronic state, area induced. Therefore, different transitions with different energies and close to each other are possible justifying the broadening of the absorption peaks.

Group theory and molecular symmetry can be used as supplementary tool for the interpretation of any electronic spectrum. When light with certain wavelength hits a molecule, the electric field of the light interacts with the molecular dipolar moment and so the molecular Hamiltonian is perturbed.

This induces a mixt or transition between the fundamental molecule's wave function (ψ_i) with other wave functions from excited estates (ψ_i). In general those transitions are given by:

$$M_{0i} = \langle \psi_i | \hat{\mu} | \psi_0 \rangle = \int \psi_i \hat{\mu} \psi_0 d\tau \tag{14}$$

where μ corresponds to the electric dipole momentum operator. The difference in the charge distribution between two states corresponds to an electric dipole. Such a transition can therefore couple with electromagnetic radiation by interaction with the oscillating electric vector and therefore transfer energy to, or from, the electric field. The electric dipole operator has the form:

$$\hat{\mu} = e\left(x\vec{i} + y\vec{j} + z\vec{k}\right) \tag{15}$$

where e is the charge and $\left(x\vec{i} + y\vec{j} + z\vec{k}\right)$ are the vectorial coordinates. When expression 15, is inserted in equation 14 the obtained result can be expressed as three separate equations because of the orthogonality of the cartesian coordinates:

$$\begin{aligned} M_{0i}^{x} &= e\langle \psi_i | x | \psi_0 \rangle \\ M_{0i}^{y} &= e\langle \psi_i | y | \psi_0 \rangle \\ M_{0i}^{z} &= e\langle \psi_i | z | \psi_0 \rangle \end{aligned} \tag{16}$$

These equations mean that the transition from the 0th stat to the ith state may acquire its intensity by interacting with an electric vector oscillating in the *x*, the *y* or the *z* direction. If only one of these integrals is nonzero the transition will be active and if tis nonzero in only one direction it will be active and polarized in that direction, if it is active in two perpendicular directions it will be plane polarized. This information may be obtained very simply from a knowledge of the irreducible representation to with the wave functions ψ_I and ψ_i belong.

$$\begin{aligned} \Gamma &= \Gamma(\psi_i) \times \Gamma(x) \times \Gamma(\psi_0) \\ \Gamma &= \Gamma(\psi_i) \times \Gamma(y) \times \Gamma(\psi_0) \\ \Gamma &= \Gamma(\psi_i) \times \Gamma(z) \times \Gamma(\psi_0) \end{aligned} \tag{17}$$

Thus when any of these irreducible representations contain the total symmetric one, the transition will be active. Then the problem of deciding whether a certain transition is electric dipole allowed, and what the polarization is reduced to decide which, if any, of the three integrals are nonzero.

We Take as example the even [n]CPPs with $D_{(n/2)d}$ symmetry, more specifically [10]CPP belonging to the D_{5d} punctual group, whose HOMO orbitals have a_{2g} symmetry and LUMO a_{1g}. In this symmetry group light, *x,y,z* electromagnetic filed coordinates, would interart within thet, E_{1u} and A_{2u} symmetry. For the transition to be allowed the product between excited state, light and ground estate needs to be non-zero. This can be extrapolated to symmetry terms where the mentioned product should in total collect the total symmetrical product, $M_{0i}^{x,yz} = e\langle \Psi_f | x, y, z | \Psi_0 \rangle = A_{1g} \neq 0$.

For [10]CPP HOMO-LUMO electronic transition, their product with light is E_{1u} and A_{1u}, so this transition is not symmetry allowed, as shown in Figure 13a. However, the [10]CPP LUMO+1 orbital belongs to the e_{1u} point group, as shown in Figure 13b, the transition HOMO-LUMO+1 will be allowed in the *x* and *y* directions, so the absorption bands observed would mainly come from this polarized transition.

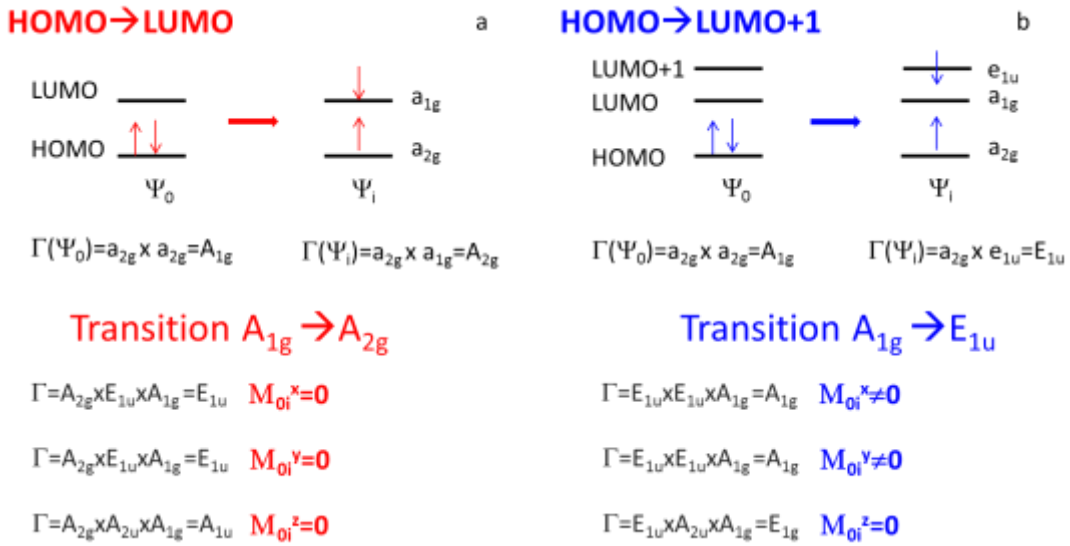

Figure 13. a) Electronic states involved in the HOMO – LUMO transition and irreducible representations of the light induced transition. b) Electronic states involved in the HOMO – LUMO+1 transition and irreducible representations of the light induced transition.

2.5.1. Devices

Depending on the spectral ranged required two different spectrophotometers were used:

- **UV-Vis Spectrophotometer Angilet** (190-1100 nm). It is a multi-diode spectrophotometer formed by 910 elements, one per nm. Its spectral resolution of up to 1.0 nm.

- **UV-Vis-NIR Spectrophotometer Cary 5000** (175-3300 nm). out-of-plane double Littrow monochromator design minimizes photometric noise and stray light, using a PbSmart NIR detector for extended photometric range, providing spectral resolution up to 0.01 nm.

2.6. Quantum Mechanics Calculations

In this thesis quantum calculations are used to support the vibrational assignments of the [n]CPPs and also to study possible effects of distorted configurations by Raman spectroscopy. Our calculations for these π conjugated molecules are conducted uniquely by density functional theory (DFT) methodologies. As already anticipated we are going to look for good agreements between experimental and computed vibrational predictions. In this regard, B3LYP level has been demonstrated to provide excellent results on vibrations. Moreover, as basis set we need to compromise to obtain as good results as possible in a reasonable computational time. [n]CPPs are uniquely formed by a conjugated carbon skeleton and hydrogens, so it is necessary to account for the polarizability of such conjugated skeleton. We do an initial seek for that compromise finding that the basis set double zeta 6-31G(d,p) provides good results. Such basis set includes d polarization on the carbon atoms and p polarization on the hydrogen atoms. It is necessary to count with the right molecular structure to be able to obtain good predictions, so that, a good geometry optimization towards the global minimum is required.

In this section the basic concepts about the computational techniques used in this work are summarized. We are going to briefly explain the theoretical concepts behind any computational study starting from the basics of Hartree Fock moving up to the DFT B3LYP hybrid method The need of extended basis sets will be also explained. We will point out the different parameters which taken into account to get not erroneous results, such as geometry optimization, unrestricted calculation, atomic charges; and how the frequency and vertical transition energy calculations are done.

2.6.1. Introduction

The solution to any quantum chemical problem starts with finding the solution to the Schrödinger equation time independent (Ψ).

$$\hat{H}\Psi = E\Psi \tag{18}$$

being E the total energy of the system, $\hat{H}$ the Hamiltonian which contains the electronic terms of movement, repulsion and attraction with the nucleus:

$$\hat{H} = -\frac{\hbar}{2m_e}\sum_{i}^{electrons}\nabla_i^2 - \frac{\hbar}{2}\sum_{A}^{nuclei}\frac{1}{M_A}\nabla_A^2 - \frac{e^2}{4\pi\varepsilon_0}\sum_{i}^{electrons}\sum_{i}^{nuclei}\frac{Z_A}{r_{iA}} + \frac{e^2}{4\pi\varepsilon_0}\sum_{i}^{electrons}\sum_{j>}^{electrons}\frac{1}{r_{ij}} + \frac{e^2}{4\pi\varepsilon_0}\sum_{A}^{nuclei}\sum_{B>}^{nuclei}\frac{Z_A Z_B}{R_{AB}} \tag{19}$$

where Z_A is the nuclear charge, M_A is the mass of the nucleus A, m_e is the mass of the electron, R_{AB} is the distance between nuclei A and B, r_{ij} is the distance between electrons i and j, r_{iA} is the distance between the electron and nucleus A, ε_0 is the permittivity of free space, and $\hbar$ is the Planck constant divided by 2π. The Schrödinger equation can be solved exactly only for atoms or molecules containing one electron. For this reason, numerical methods have been developed to calculate approximate wave functions trying to solve the Schrödinger equation for poly-electronic and polyatomic structures from different approaches.

The first approximation is that called Born Oppenheimer approach. It is based on the fact that nuclear mass is much higher than that of the electrons, the former would move much slower. So, it could be considered that nucleus is going to interact with an electronic cloud, while electrons interact with a static nucleus. This leads to a nuclear kinetic energy term which is zero, and a nuclear-nuclear Coulombic energy term which is constant.[71]

2.6.2. Ab Initio Calculations. Hartree-Fock[72,73]

Hartree-Fock approximation is based on the assumption that electrons move independently of each other. This considers that individual electrons are confined to functions called spin orbitals, χ_i. Each of the N electrons feels the presence of an average field made up of all the other (N-1) electrons. To ensure that the total (many-electron) wave function Ψ is antisymmetric upon interchange of electron coordinates (Pauli´s principle), it is written in the form of a single Slater determinant:[74]

$$\Psi = \frac{1}{\sqrt{n!}}\begin{vmatrix} \chi_1(1) & \chi_2(1)... & \chi_n(1) \\ \chi_1(2) & \chi_2(2)... & \chi_n(2) \\ ... & ... & ... \\ \chi_1(n) & \chi_2(n)... & \chi_n(n) \end{vmatrix} \tag{20}$$

The Hartree-Fock (HF) method is a prescription for finding the single Slater determinant that gives the lowest energy for the ground-state in the absence of electron correlation. The main goal of HF methodology is to find the best approximation for the best set of mono-electronics functions, χ_i in the Slater determinant. When dealing with a molecular system these functions correspond to molecular orbitals, and in the atomic case with atomic orbitals.

The most significant drawback of HF theory is that it fails to adequately represent electron correlation. Electrons are assumed to be moving in an average potential of the other electrons and so the instantaneous position of an electron is not influenced by the presence of a neighboring electron. But, in fact, the motions of electrons are correlated and they tend to "avoid" each other more than HF theory would suggest giving rise to a lower energy. The correlation energy is defined as the difference between the Hartree-Fock energy and the exact energy:[75]

$$E_{corr} = E_{correlation} = E_{exact} - E_{HF} \tag{21}$$

By extending the mode to include electron correlation in a more realistic manner, and by judicious choice of a basis set, more accurate calculations can be made. Such as: configuration interaction,[76] perturbational method or Møller-Pesset[77] and Coupled Cluster methods.[78]

2.6.2.1. Self-Consistent Field

HF is based in the variational principle for which the best functions will be those which give the lowest total electronic energy. To do so the Self Consistent Field (SCF) is used, which suggests a first a poly-electronic function as starting point, then the energy of the ground state is calculated, a parameter on the function is changed, the energy is recalculated and it keeps iterating until energy variations are low enough, reaching a limit to consider that the system is consistent. In a SCF calculation the wave function is gradually refined until self-consistency is achieved.[71,79,80]

2.6.3. Semi-Empirical Calculations

Instead of calculating all matrix elements, other methods are used with empirical parameters and other approximations.[81] Often many integrals are approximated as zero (the terms used often are 'neglected' integrals, such as in the NDO methods: neglect of differential overlap methods). These are, however, compensated by parametrizations such that the final computed numbers are forced to be reasonable.

2.6.4. DFT Methodology

Density functional theory is based on the possibility of working with some physical observable to determine energy and other molecular properties instead of working with its wave function, which has rather odd units of probability density to the one-half power. The energy Hamiltonian operator depends only on the positions and atomic numbers of the nuclei and the total number of electrons, *N*. The dependence on *N* immediately suggests that a useful physical observable would be the electron density ρ, since integrated over all space it gives *N*.

In the language of DFT, electrons interact with one another and with an "external potential". Hohenberg-Kohn theorem establishes that a dependence of the energy on the ground state density is sufficient to show that this density determines the Hamiltonian operator.[82] Integration of the density gives the number of the electrons, so all that remains to define the operator is determination of the external potential, i.e. the charges and positions of the nuclei.

2.6.4.1. Kohn-Sham Self-Consistent Field Methodology[83]

Kohn and Sham realized that things would be considerably simpler if only the Hamiltonian operator were one for a non-interacting system of electrons. Such Hamiltonian can be expressed as a sum of one-electron operators. The Kohn-Sham functions are the ϕ_i orbitals which allow the electron density estimation by summing all the occupied n-orbitals.[83]

$$\rho(r) = \sum_{i=1}^{n} |\varphi_i(r)|^2 \tag{22}$$

The Kohn-Sham equations are very similar to the HF equations. The former are obtained applying the variational principle to the electronic energy $E(\rho)$. The KS orbitals are estimated directly from the KS equations and at the same time from the electron density. The procedure to solve the KS equations is an iterative method repeated until convergence is reached.[84] The resolution of the KS equations provides a orbitals set, KS orbitals, from which the electronic density can be built up. A fictitious non interacting electronic system is considered, its density is taken as the starting point for the real electron density with interacting electrons. Since the density determines the position and atomic numbers of the nuclei, these quantities are necessarily identical in the non-interacting and in the real system. The energy functional is divided into specific components to facilitate the analysis:

$$E[\rho(r)] = T_{ni}[\rho(r)] + V_{ne}[\rho(r)] + V_{ee}[\rho(r)] + \Delta T[\rho(r)] + \Delta V_{ee}[\rho(r)] \tag{23}$$

where the terms refer respectively to: T_{ni}, the kinetic energy of the non-interacting electrons; V_{ne}, the nuclear-electron interaction; V_{ee}, the classical electron-electron repulsion; ΔT, the correction to the kinetic energy deriving from the interacting nature of the electrons; and ΔV_{ee}, all non-classical corrections to the electron-electron repulsion energy. The "difficult" terms are ΔT and ΔV_{ee}, which have been lumped together in a term, E_{xc}, typically referred to as the exchange–correlation energy. This includes the effects of quantum mechanical exchange and correlation, and also the correction for the classical self–interaction energy and for the difference in kinetic energy between the fictitious non–interacting system and the real one. The functional dependence of E_{xc} on the electron density is expressed as an interaction between the electron density and an "energy density" ε_{xc}:[71,75]

$$E_{xc}[\rho(r)] = \int \rho(r)\varepsilon_{xc}[\rho(r)]dr \tag{24}$$

DFT contains no approximations: it is exact. All we need to know is Exc as a function of [ρ(r)]. Considerably research effort has gone into finding functions of the density that may be expected to reasonably approximate Exc. The key contrast between HF and DFT is that in HF approximations are done to solve the wave function but equations are exact, and electron motions are uncorrelated so it does not include dispersion interactions. However, DFT is an exact theory based on the total electron density, but the relevant equations must be solved approximately because a key operator has unknown form. In DFT terms kinetic E, electron nuclear attraction, electron-electron repulsion, are approximated in the exchange-correlation term, which gives rise to hundreds of exchange-correlation approximations.

2.6.4.2. Local Density Approximation

The term local density approximation (LDA) was originally used to indicate any density functional theory where the value of ε_{xc} at some position r could be computed exclusively from the value of ρ at that position, i.e., the "local" value of ρ.[75] In principle, then, the only requirement on ρ is that it should be single-valued at every position, and it can otherwise be wildly ill-behaved. In practice, the only functionals conforming to this definition that have seen much application are those that derive from analysis of the uniform electron gas (where the density is the same at every position).

2.6.4.3. Density Gradient and Kinetic Energy Density Corrections

In a molecular system, the electron density is typically rather far from spatially uniform, so there is good reason to believe that the LDA approach will have limitations. One obvious way to improve the correlation functional is to make it depend not only on the local value of the density, but on the extent to which the density is locally changing, i.e., the gradient of the density. The first derivative of a function at a single position is a local property, so the term for functionals that depend on both the density and the gradient of density is "gradient–corrected". Including a gradient correction defines the "generalized gradient approximation" (GGA).[71,75,79,80]

$$\varepsilon_{xc}^{GGA}[\rho(r)] = \varepsilon_{xc}^{LDA}[\rho(r)] - \Delta\varepsilon_{xc}\left[\frac{|\nabla\rho(r)|}{\rho(r)^{4/3}}\right] \tag{25}$$

In the literature several GGA exchange functionals have been developed:

- *B*, Becke functional,[85] adopts a mathematical form that has a correct asymptotic behavior at long range for the energy density; it incorporates a single empirical parameter whose value was optimized by fitting to the exactly known exchange energies of the six noble gas atoms.
- *LYP* (from Lee, Yang and Parr[86]). It does not correct the LDA expression but instead computes the correlation energy in *toto*. It contains four empirical parameters fit to the helium atom. Of all the correlation functions this is the only one that provides an exact cancellation of the self–interaction error in one-electron systems.
- *BLYP* combines Becke2s GGA exchange with the GGA correlation function of LYP.

2.6.4.4. Meta-GGA Functionals

The GGA density functionals depend on the ground-state electron probability density and its firsts derivatives. One way to improve on GGA functionals is to go to functionals that also depend on the second derivatives.[71,75,79,80]

2.6.4.5. Hybrid Functionals

Hybrid exchange–correlation functionals include some Hartree-Fock exchange energy and GGA or meta-GGA functionals.[87] A hybrid exchange-correlation functional is usually constructed as a linear combination of the Hartree–Fock exact exchange functional and any number of exchange and correlation explicit density functionals. The parameters determining the weight of each individual functional are typically specified by fitting the functional's predictions to experimental data or accurately calculated thermochemical data, although in the case of the "adiabatic connection functionals" the weights can be set *a priori*.[88] Becke was the first to do this, developing the three parameter functional expression for B3PW91.[89] Subsequently, this functional was modified to use LYP instead of PW91. Because LYP is designed to compute the full correlation energy, parameterization emphasized thermochemistry and does not include dispersion interactions, atomization energies, ionization potentials, proton affinities, and total atomic energies.[90] B3LYP model is defined by

$$E_{xc}^{B3LYP} = (1-a)E_x^{LSDA} + aE_x^{HF} + b\Delta E_x^B + (1-c)E_c^{LSDA} + cE_c^{LYP} \quad (26)$$

This has exactly the same *a*, *b*, *c* parameters, 0.2, 0.72 and 0.81 respectively, as in B3PW91, resulting in

$$E_{xc}^{B3LYP} = 0.8E_x^{LSDA} + 0.2E_x^{HF} + 0.72\Delta E_x^B + 0.19E_c^{LSDA} + 0.81\Delta E_c^{LYP} \quad (27)$$

B3LYP contains the Lee Yang Parr functional, including the local and non-local terms, and the hybrid exchange functional with combination or the exact exchange functionals HF with the Becke.

2.6.5. Basis Sets[91]

Direct solution of the Hartree-Fock equations is not a practical proposition for molecules and so it is necessary to adopt an alternative approach. The most popular strategy is to write each spin orbital as linear combination of single electron orbitals, where one-electron orbitals ϕ_v are commonly called basis function:

$$\psi_i = \sum_{v=1}^{K} c_{vi}\phi_v \quad (28)$$

Basis functions are labeled with Greek letters. *K* basis functions should provide a total of *K* molecular orbitals, although not all of these will necessarily be occupied by electrons. A set of coefficients that gives the lowest energy wave function is required, and some scheme for changing the coefficients to derive the wave function. For a given basis set and functional form of the wave function (i.e a Slater determinant) the best set of coefficients is that for which the energy is a minimum, as it is obtained from equation 29:

$$\frac{\partial E}{\partial c_{vi}} = 0 \quad (29)$$

2.6.5.1. Gaussian Type of Orbitals

The basis sets most commonly used in quantum mechanical calculations are composed of atomic functions. An obvious choice would be the Slater type of orbitals for many electron atoms, but these are not amenable to implementation in molecular orbital calculations because of the difficulty of some of their integrals, particularly when the atomic orbitals are centered on different nuclei. However, when involving one or two centers these are approachable. It is common in *ab initio*

calculations to replace the Slater orbital's by functions based upon Gaussians, for which *ab initio* calculations use basis functions comprising integral powers of *x*, *y* and *z*:

$$x^a y^b z^c \exp\left(-\alpha r^2\right) \tag{30}$$

α determines the radial extent (or "spread" of a Gaussian function); a function with large value of α does not spread very far whereas a small value of α gives a large spread. The order of these Gaussian type functions is determined by the powers of the Cartesian variables:

- a zeroth-order function has $a + b + c = 0$;
- a first-order function has a $a + b + c = 1$, and so on.

Replacing a Slater type orbital by a single Gaussian function leads to unacceptable errors which can be overcome if each atomic orbital is represented as a linear combination of Gaussian functions. Gaussian expansions contain two parameters, the coefficient and the exponent. The most flexible way to use Gaussian functions in *ab initio* molecular orbital calculations permits both of these parameters to vary during the calculation: uncontracted or primitive Gaussians, but these calculations require a significant computational effort and so basis sets that consist of contracted Gaussian functions are most commonly employed. In a contracted function the contraction and exponents are pre-determined and remain constant during the calculation.[92]

- **A minimal basis set** is a representation that contains just the number of functions that are required to accommodate all the filled orbitals in the atoms. The basis sets STO-3G, STO-4G, etc, (in general, STO-nG) are all minimal basis sets in which *n* Gaussian functions are used to represent each orbital. A minimal basis set cannot describe non-spherical aspects of the electronic distribution. For instance, for carbon the only functions that incorporate any anisotropy are the $2p_x$, $2p_y$, and $2p_z$ functions. As the radial components of these functions are required to be the same, no component can differ from another.

- **Double zeta basis set**. This can provide a solution to the anisotropy problem because it is then possible to have different linear combinations for the p_x, p_y and p_z orbitals. Linear combination of a "contracted" function and a "diffuse" function gives an overall result that is intermediate between the two. The basis set coefficients of the contracted and the diffuse functions are automatically calculated by the SCF procedure, which thus determines whether a more contracted or a more diffuse representation of that particular orbital is required.

- **Split valence double zeta basis sets.** An alternative to the double zeta basis approach is to double the number of functions used to describe the valence electrons but to keep a single function for the inner shells. The rationale for this approach is that the core orbitals, unlike the valence orbitals, do not affect chemical properties very much and vary only slightly from one molecule to another. The notation used for such split valence double zeta basis sets is exemplified by 3-21G. In this basis set three Gaussian functions are used to describe the core orbitals. The valence electrons are also represented by three Gaussians: the contracted part by two Gaussians and the diffuse part by one Gaussian.

- **Polarization basis function.** The use of split valence basis sets can help to surmount the problems with non-isotropic charge distribution but not completely. The charge distribution about an atom in a molecule is usually perturbed in comparison with the isolated atom. The most common solution to this problem is to introduce polarization functions into the basis set. The polarization functions have a higher angular quantum number and so correspond to *p* orbitals for hydrogen and *d* orbitals for the first and second row elements.

  For the [n]CPP molecules, formed by carbon and hydrogen atoms, the most appropriate and so the basis set we use is the 6-31G (d,p).

- **Diffuse functions.** A deficiency of the basis sets described so far is their inability to deal with species which have a significant amount of electron density away from the nuclear centers such as anions and molecules containing lone pairs. This failure arises because the amplitudes of the Gaussian basis functions are rather low far from the nuclei. Highly diffuse functions can be added to the basis set. These basis sets are denoted using a "+"; thus the 3-21+G basis sets contains an additional single set of diffuse s- and p-type Gaussian functions. "++" indicates that the diffuse functions are included for hydrogen as well as for heavy atoms.

2.6.6. Restricted and Unrestricted Formalisms, Spin Contamination and Electron Density[71,91]

When dealing with cations and dications in open shell configuration, these need to be treated differently to their neutral analogs with closed shell electronic configurations, in chapter 5 we will used all these terminologies and concepts here explained.

To deal with open-shell systems two approaches have been devised:

- **Spin restricted Hartree-Fock (RHF)**: uses combinations of singly and doubly occupied molecular orbitals. The doubly occupied orbitals use the same spatial functions for the electrons of both α and β spin.
- **Spin unrestricted Hartree-Fock (UHF)** is the alternative approach which uses two sets of molecular orbitals: one for electrons α spin and the other for electrons of β spin. So that two matrices are involved for each type of spin. Thus α_{occ} +β_{occ} equals to the total number of electrons in the system, equation 31. UHF uses two density matrices, the full density matrix being the sum of these two:

$$P_{\mu\nu}^{\alpha} = \sum_{i=1}^{\alpha_{OCC}} c_{\mu i}^{\alpha} + c_{\nu i}^{\alpha};\ P_{\mu\nu}^{\beta} = \sum_{i=1}^{\beta_{OCC}} c_{\mu i}^{\beta} + c_{\nu i}^{\beta} \rightarrow P_{\mu\nu} = P_{\mu\nu}^{\alpha} + P_{\mu\nu}^{\beta} \tag{31}$$

Two different approaches are widely used for open-shell states. In the restricted open-shell Hartree-Fock (ROHF) method, the electrons that are paired with each other are given the same spatial orbital function. While the UHF gives all different spatial orbitals for spin α and spin β.

2.6.6.1. Spin Contamination

The main problem with the UHF wave function is that it is not an eigen function of the spin operator $\hat{S}^2$ (it cannot be made an eigen function of $\hat{S}^2$ by taking a linear combination of a few UHF)., whereas the true wave function and the ROHF wave function are eigen functions of $\hat{S}^2$. When a UHF wave function is found, one calculates the $\langle \hat{S}^2 \rangle$ for the UHF. If the deviation of $\langle \hat{S}^2 \rangle$ from $S(S+1)\hbar^2$, the UHF wave function should be viewed with suspicion of being spin contaminated.[71,93]

2.6.6.2. Electron Density

In a closed-shell Hartree-Fock wave function the distribution of electron spin is zero everywhere because the electrons are paired. In an open-shell system, however, there is an excess of electron spin that can be expressed as the spin density, analogous to the electron density, equation 32. The spin density can be viewed as an output in any unrestricted calculation.[71]

$$\rho^{spin}(r) = \rho^{\alpha}(r) - \rho^{\beta}(r) \tag{32}$$

2.6.7. Charge Distribution, Atomic Charges, Population Analysis[79,91]

An atomic charge is not a physical observable, regardless of the great importance chemists place on this intuitively appealing property. There are several properties that correlate well with atomic charges, whichever manner they are defined, but such definitions remain arbitrary, because in quantum mechanics there is no operator that corresponds to an atomic charge.
Here we use a single doubly occupied orbital in HF for illustration. Assume a diatomic molecular orbital with only to atomic orbitals contributing:

$$\varphi(x,y,z) = a\chi_1 + b\chi_2 \tag{33}$$

where a and b are variational coefficients, and $\chi_1 \; and \; \chi_2$ are the two atomic orbitals assumed to be normalized. Normalization of the molecular orbitals requires that

$$\iiint |\varphi(x,y,z)|^2 dV = 1 \tag{34}$$

This leads to the normalization condition,

$$a^2 + b^2 + 2S_{1,2} = 1 \tag{35}$$

Where $S_{1,2}$ is the overlap between $\chi_1 \; and \; \chi_2$. Mulliken had the idea to look at this equation differently, and before integration:

$$|\varphi(x,y,z)|^2 = a^2\chi_1^2 + b^2\chi_2^2 + 2ab\chi_1\chi_2 \tag{36}$$

The key point is that the three terms represent three different charge distributions from which Mulliken realized that the third term can be assigned to correspond to the bond region. This is not precise since mathematically both $\chi_1 \; and \; \chi_2$ extend far from the molecule, their product is largest in the bond region but it is not zero elsewhere. The assignment of the third term as bond (or overlap) density is a practical one. Three natural contributions to the charge distribution are obtained:

- First term centered on atom 1 so a^2 is assign to atom 1
- Second term centered on atom 2, so b^2 I sassing to atom 2
- Third term is the overlap density, $2S_{1,2}$ is assign to the bond (overlap).

These three terms add up to 1. The above decomposition of the charge of each electron can be done. What remains to be computed, are the different contributions from all the orbitals and all the atoms. Net atomic populations and overlap populations (for each atom pair whether they are bonded or not). Overlap populations of non-bonded atom pairs tend to be small, because the respective overlaps are small, but these small contributions are needed to make sure that the gross total of populations adds up to the total number of electrons. The final step in a Mulliken population's analysis is to divide the overlap populations in such a manner as to obtain atomic charges only. This is done by dividing equally the overlap populations between the two atoms involved. This is arbitrary and has been criticized, especially for polar bonds. Note that the term is "population" and not "charge", emphasizing that this is not claiming to determine atomic charges, which one cannot do unequivocally. The process is basis set dependent, because the coefficients a and b as well as the overlap integral $S_{1,2}$ depend on the basis set. When diffuse functions are added to the basis set, the overlap density becomes $2ab\chi_1\chi_2$more diffuse and less assignable to the atom pair 1 and 2 making the concept less useful. In practical applications atomic gross populations are very consistent within one given model chemistry.

In chapter 6 of this work we will study cationic and dicationic forms of the [n]CPP for which Mulliken charges will be analyzed to obtain the charge distribution picture along the molecules.

2.6.8. Potential Energy Surfaces (PES)[91]

One of the most important steps in a quantum calculation is to find the right configurational structure to work with, so from that any properties estimation can be done. An equilibrium structure is a point one multidimensional potential energy surface for which all first energy derivatives with respect to the individual geometrical coordinates are zero, and for which the diagonal representation of the matrix of second energy derivatives has all positive elements. In the one-dimensional case, this means that the first derivative of the potential energy with respect to the reaction coordinate is zero:

$$\frac{\partial V}{\partial R} = 0 \tag{37}$$

The same must be true in dealing with a many-dimensional potential energy diagram. Here all the partial derivatives of the energy with respect to each of the 3N-6 (N atoms) independent geometrical coordinates (R_i) are zero:

$$\frac{\partial V}{\partial R_i} = 0 \;\; i = 1,2,3.....3N-6 \tag{38}$$

In the one-dimensional case, reactants and products are energy minima and are characterized by a positive second energy derivative:

$$\frac{\partial^2 V}{\partial R^2} > 0 \tag{39}$$

The transition state is an energy minimum and is characterized by a negative second energy derivative:

$$\frac{\partial^2 V}{\partial R^2} < 0 \tag{40}$$

In the many-dimensional case each independent coordinate, R_i, gives raise to 3N-6 second derivatives:

$$\frac{\partial^2 V}{\partial R_i R_1}, \frac{\partial^2 V}{\partial R_i R2}, \frac{\partial^2 V}{\partial R_i R3}, \ldots \frac{\partial^2 V}{\partial R_i R_{3N-6}} \tag{41}$$

This leads to a matrix of second derivatives, the so-called Hessian

$$\begin{bmatrix} \frac{\partial^2 V}{\partial R_1^2} & \frac{\partial^2 V}{\partial R_1 R_2} & \ldots \\ \frac{\partial^2 V}{\partial R_2 R_1} & \frac{\partial^2 V}{\partial R_2^2} & \ldots \\ \ldots & \ldots & \frac{\partial^2 V}{\partial R_{3N-6}^2} \end{bmatrix} \tag{42}$$

In this form, it is not possible to say whether any given coordinate corresponds to energy minimum, energy maximum, or neither. To see the correspondence, the original set of geometrical coordinates (R_i) is replaced by a new set of coordinates B_i which leads to a matrix of second derivatives that is diagonal

$$\begin{bmatrix} \frac{\partial^2 V}{\partial B_1^2} & 0 & 0 \\ 0 & \frac{\partial^2 V}{\partial B_2^2} & 0 \\ 0 & 0 & \frac{\partial^2 V}{\partial B_{3N-6}^2} \end{bmatrix} \tag{43}$$

The B_I are unique and referred to as normal coordinates. Stationary points for which all second derivatives (in normal coordinates) are positive are energy minima:

$$\frac{\partial^2 V}{\partial B_i^2} > 0 = 1,2,3....3N-6 \tag{44}$$

These correspond to equilibrium forms (reactants and products). Stationary points, where all but one of the second derivatives are positive, are so-called (firs-order) saddle points and may correspond to transition states. If they do, the coordinate for which the second derivative is negative is referred to as the reaction coordinate B_p

$$\frac{\partial^2 V}{\partial B_p^2} < 0 \tag{45}$$

2.6.8.1. Geometry Optimization[91]

Many systematic mathematical procedures (algorithms) exist to find a local minimum of a function of several variables. These procedures will find a local minimum in the PES in the neighborhood of the initially assumed molecular geometry. The energy and energy gradient (first derivatives with respect to all geometrical coordinates) are calculated for the initial geometry, and this information is the used to project a new geometry. This process needs to continue until the lowest energy optimized geometry is reached. Three criteria must be satisfied before a geometry is accepted as optimized:

- Successive geometry changes must not lower the energy by more than a specified value
- The energy gradient must closely approach zero
- Successive iterations must not change any geometrical parameter by more than a specified value

For a molecule with several conformations, one must repeat the local-minim search procedure for each possible conformation, so as to locate the global minimum. Geometry optimization does not guarantee that the final geometry will have a lower energy than any other geometry of the same molecular formula. All that it guarantees is that the geometry will correspond to a local minimum, that is, a geometry the energy of which is lower than that of any similar geometry. The full collections of local minima are referred to as conformers. Geometry optimization is an iterative process.

In 2010 Segawa et al[94] collected a whole series of conformers for [n]CPPs by simple rotations between neighboring rings, demonstrating that for even ns the global minimum was around alternated twisting between neighboring phenyls. So that in this work special attention will be paid to all the optimized structure to relate geometrical and electronic parameters with spectroscopic observables, so that an exhaustive effort has been made to find global minimum for each [n]CPPs.

2.6.9. Vibrational Spectroscopy

The prediction of frequencies and intensities generates a simulated spectrum, which can be plotted as a series of bands (Lorentzian band shaped is used in this work). The maximum of each Lorentzian curve is fixed at the value of predicted frequency, and its integrated area is fixed according to the computed transition intensity. Band widths can be fixed for all the transitions, or adapted in such a way to obtain a better qualitative agreement with the experimental spectrum.

A “synthetic” spectrum can be directly compared with the experimental one in order to gain an idea of the quality of the prediction, before proceeding to the analysis of the eigenvectros, which is of great help in order to establish the vibrational assignment of the observed features. This process allows one to associate an Raman band to a given normal mode of vibration, which in turn helps the assignment of the transition to localized or collective motions. Moreover on identifies the atoms or groups involved in the vibration and the kind of deformations they undergo, namely the extent of bond stretching, the bending of valence angles, and torsional displacements. Last but not least, a vibrational assignment allows assignment of the symmetry species to which the mode belongs.

2.6.9.1. PES and Vibrations[91]

The vibrational frequency for a diatomic molecule A-B is given by:

$$\nu = \frac{1}{2\pi}\sqrt{\frac{k}{\mu}} \tag{46}$$

where, k is the force constant, which is in fact the second derivative of the potential energy, V, with respect to the bond length, *R*, at its equilibrium position

$$k = \frac{\partial^2 V(R)}{dR^2} \tag{47}$$

and μ is the reduced mass

$$\mu = \frac{m_A m_B}{m_A + m_B} \tag{48}$$

Polyatomic systems are treated in a similar manner. Here the force constant is the elements in the diagonal representation of the Hessian. Each vibrational mode is associated with a particular motion of atoms away from their equilibrium positions on the potential energy surface. Low frequencies correspond to motion in sallow regions of the surface, whereas high frequencies correspond to motions in steep regions. Note that one of the elements of the Hessian for a transition state will be a negative number, meaning that the corresponding frequency will be imaginary.

2.6.9.2. Calculation of Frequencies[95]

DFT provides better results for frequency calculations than HF. In this work any frequency calculation will be carried out by B3LYP hybrid functional with scaling factors as suggested by Scott-Random.[96] The calculation of vibrational frequency is made for the isolated molecule (i.e. in vacuum) under the hypothesis that the intramolecular potential is well described by the harmonic approximation, that is, by a quadratic function of the vibrational degrees of freedom (Cartesian or internal displacements of the nuclei, taken form a well-defined equilibrium molecular geometry). Following the classical treatment which starts from a set of differential equation describing the time evolution of degrees of freedom of the nuclei, the 3N-6 vibrational frequencies are obtained through diagonalization of the dynamical matrix, which can be written on basis of the 3N atomic Cartesian displacement coordinate (r_i) according to the eigenvalues equation

$$M^{-1}F^{\times}A^{\times} = A^{\times}\Lambda \tag{49}$$

M^{-1} is the diagonal matrix containing the inverse of the atomic masses, $F^{\times}$ is the Cartesian force constant matrix $F^{x}_{i,j} = \left(\partial^2 V / \partial x_i x_j\right)_0$, Λ is the diagonal matrix of the frequency parameters, ν_k is the wavenumber, $\lambda_k = \omega_K^2 = 4\pi^2 c^2 \nu_k^2$. The k-th column of the eigenvector matrix $A_k^{\times}$ describes the amplitudes of oscillation of the set of Cartesian coordinates during the k-th normal mode, with harmonic time evolution. So the vibrational frequencies are computed by determining the second derivatives of the energy with respect to the Cartesians nuclear coordinates and then transforming to mass-weighted coordinates. Then it is required to compute frequencies following a previous geometry optimization using the same method.

The prediction of vibrational frequencies of a molecule requires the knowledge of several parameters, such as the set of molecular force constants and the geometrical parameters. Therefore an accurate knowledge of the molecular bond lengths and angles is a prerequisite for the vibrational analysis. High-level DFT calculations often allow predicting frequencies that fit the experimental ones with deviations not exceeding 10-15 cm^{-1}. The Gaussian program we used yields as a standard output the harmonic vibrational potential, frequencies and normal modes which are directly calculated by equation 51 by the same program. The results can be routinely visualized thanks to a graphical interface, which directly shows the “animation” of normal modes.

2.6.9.3. Calculation of Intensities[95]

Under the double (mechanical and electrical) harmonic approximation, the problem of the prediction of IR and Raman intensities can get reduced to the calculation of the relevant "electrical" parameters responsible for Raman fundamental transitions, $\partial\alpha/\partial L_j$ (the derivate of the molecular polarizability tensor with respect to the normal mode displacements L_j). The intensity of the Raman associated with the j-th transition is given by:

$$I_j = kI_0(\nu_s)^4 \sum_{\rho,\sigma} \left|(\alpha_{\rho\sigma})_j\right|^2 \tag{50}$$

$$(\alpha_{\rho\sigma})_j = \left(\frac{\partial\alpha_{\rho\sigma}}{\partial L_j}\right)_0 \langle 1_j|L_j|0_j\rangle = \left(\frac{\partial\alpha_{\rho\sigma}}{\partial L_j}\right)_0 \left(\frac{h}{8\pi^2 c\,\nu_j}\right)^{\frac{1}{2}} \tag{51}$$

where ν_s is the wave number of the scattered beam and ν_j is the vibrational wavenumber, *h* the Planck constant, and *c* the speed of light in "vacuo.. Raman intensities depend on a collective response of the electronic cloud, which in several cases cannot be modeled by localized transferable parameters.

2.6.10. Electronic Spectra Calculation

If a molecule is subjected to a linear electric filed E that is fluctuating such that

$$E = \mathrm{r}\cos(\omega t) \tag{52}$$

Where *r* is the position vector in one dimension, *t* is time, and ω is the frequency of the fluctuation; it can be shown that the frequency-dependent polarizability is well approximated by

$$\langle\alpha\rangle_\omega = \sum_{i\neq 0}^{states} \frac{\left|\langle\psi_0|\mathrm{r}|\psi_i\rangle\right|^2}{\omega - (E_i - E_0)} \tag{53}$$

where the numerator of each term in the sum is a so-called transition dipole moment and the denominator involves the frequency and the energies of the excited states and the ground state. Note that if the frequency corresponds exactly to the difference in energy between an excited state and the ground state, there is a pole in the frequency – dependent polarizability, it diverges since the denominator goes to zero.

When an electronic transition occurs from the ground state to an excited state, the much greater mass of the nuclei than that of the electrons means that the excited state has the greatest probability to be produced in a geometry that is close to the equilibrium geometry of the ground electronic state (the Frank-Condon principle), even though this geometry is not likely to be the equilibrium geometry of the excited estate. The excited state is thus produced in a high vibrational level. Hence the observed maximum-intensity frequency ν_{max} in the electronic absorption spectrum corresponds to a change in geometry. The energy change $h\nu_{max}$ is called the vertical excitation energy.

Time dependent density functional theory (TDDFT), provides enough information to support the most intense absorption bands.[97,98] TDDFT can be used as well for different oxidized states of the same system under study. TDDFT was implanted in 1984 by Runge ang Gross.[99] Any molecular system is considered to be in its electronic ground state, and to obtain the absorption spectra when light interacts with the system driving it to its electronic excited state. TDDFT considers that this is a time dependent system perturbation which occurs modelling its external potential. In this regard, dynamic polarizability $\overline{\alpha}(\omega)$ discrete dipolar moment respond against a time dependent electric field whose frequency is defined as $\omega(t)$:[100]

$$\overline{\alpha}(\omega) = \sum_I \frac{f_I}{\omega_I^2 - \omega_0^2} \tag{54}$$

This is extended over all the excited states (I), ω_I represents the excitation energy, E_I-E_0, and f_I corresponds to the oscillator strength. So that once the polarizability is known from the density calculated from DFT, the electronic spectrum can be calculated. Within the Khon-Sham scheme the time dependent KS equation can be derived in a manner that the time dependent electron density is provide by the summation of the time dependent KS orbitals, the adiabatic approximation is used obtain the time dependent exchange energy. The time dependent exchange potential is approximated to the time independent one but being evaluated with respect to the electron density at a time, *t*:

$$V_{xc}[\rho(r,t)] \approx \frac{\partial E_{xc}[\rho]}{\partial \rho_t(r)} = V_{xc}[\rho(r)] \tag{55}$$

As in DFT the calculation precision depends on the functional used to estimate the exchange correlation energy. The functional broadly used providing good results are B3LYP and PBE. [101] TDDFT results provide the probability of vertical one electron transitions between different molecular orbitals and the energy involved in that transition. Then these results will be directly used to explain the nature of experimental electronic absorption bands.

2.6.11. Nuclear Independent Chemical Shifts[75]

Nucleus-Independent Chemical Shifts (NICS), can be used as an aromaticity criteria.[102] The magnetic field induced by the ring current is opposed to the external field inside the ring in a parallel on the outside giving rise to an upfield nuclear magnetic resonance (NMR) shifts of have been calculated in this thesis for [n]CPPs at different positions within their cavities, specified in chapter 6. To do so ghost atoms were inserted to specify the positions at which we wanted to obtain the NICS values.

NMR measurements assess the energy difference between a system in the presence and absence of an external magnetic field. For a chemical shift measured on a given nucleus, there are two magnetic field of interest: the external field of the instrument and the internal field of the nucleus. The chemical shift is proportional to the second derivative of the energy with respect to these two fields, and it can be computed using second-derivatives. However the integrals in question are more complex than those used for vibrational calculations because, unlike the electric field, which perturbs the potential energy term of the Hamiltonian, the magnetic field perturbs the kinetic energy term (it is the motion of the electrons that generates electronic magnetic moments). The nature of the perturbed kinetic energy operator is such that an origin must be specified defining a coordinate system for the calculation. This origin is called the “gauge origin”.

The magnetic field is independent of the choice of the gauge origin. Many are the computed magnetic properties if the wave function used is exact. Regrettably, we are not often afforded the opportunity to work with exact wave functions; we work with DFT B3LYP, which provides acceptable results. To reduce artifact associated with the gauge origin, the old method gauge including atomic orbitals (GIAOs) is used as a basis set. By a clever incorporation of the gauge origin into the basic functions themselves, all matrix elements involving the basis functions can be arranged to be independent of it. An alternative is the “individual gauge for localized orbitals (IGLO) method, where different gauge origins are used for each localized MO in order to minimize error introduced by having the gauge origin far from any particular MO. of the two methods, modern implementations of GIAO are more robust, so we follow this procedure.

In the area of NMR calculations has been carried out with very large basis sets, and recommendations have tended to call for at least triple Zeta quality with diffuse and polarization functions abundantly. Following this recommendation we used the 6-311++G(2df,p)basis set which uses a single zeta core and triple zeta valence representation with additional diffuse function for all atoms. The (2df, p) indicates two sets of d functions and one set of *f* functions for first row atoms and one set of *p* functions for hydrogen.

2.6.12. Working Stations and Computational Programs Used in This Work

This work has been carried out mostly using Malaga's university stations, and also during my stay in Georgetown University, their working stations were used as well:

- **PICASSO**. This is a SGI origin-2000 computer with one hundred and twenty eight MIPS R10000 processors at 196 MHz. The main memory shared between all the processors is of 400 GB. It counts with a parallelization program which enables the shared use of the memory and processors for the calculations with the Gaussian 09 program. It is place in the super computation and bioinformatics center (SCBI) of Malaga University.
- **QUIFI7.** Cluster which counts with sixteen i7 2600 k nodes, with 8 nuclei and 16 GG of RAM DDR memory at 1333 MHz. It has a hard driver of 500 GP SATAII for the system and two 2 TB SATAII for the scratch. This cluster belongs to molecular spectroscopy group from Malaga University and it is placed in the Central Services of research support of the university (SCAI).
- **Medusa**. Medusa is a High Performance Computing (HPC) Cluster for researchers at Georgetown University.

Among the used programs are:

- **Gaussian 09**.[1] Package of programs implemented to conduct different calculations. It includes different calculations methodologies as DFT methods used in this thesis.
- **GaussView 5.0.8**. Graphic interface designed to prepare the Gaussian 09 inputs and to visualize and pictorially examine their outputs.
- **Chemcraft**.[103] Graphic interface designed to prepare the Gaussian 09 inputs and to visualize and pictorially examine their outputs.
- **Gaussum**.[104] Program application that can analyze the Gaussian output to extract and calculate useful information. This includes the progress of the SCF cycles, geometry optimization, UV-Vis/IR/Raman spectra, MO levels.
- **ChemDraw Ultra 7.0.** Program used to generate chemical structures in 2D and 3D.
- **Mercury**. Program which enables the analysis and extraction of molecules within the crystal structure registered in the Cambridge Data Base.

2.7. References

1 Gaussian 09, Revision A.02, M. J. Frisch, G. W. Trucks, H. B. Schlegel, G. E. Scuseria, M. A. Robb, J. R. Cheeseman, G. Scalmani, V. Barone, B. Mennucci, G. A. Petersson, H. Nakatsuji, M. Caricato, X. Li, H. P. Hratchian, A. F. Izmaylov, J. Bloino, G. Zheng, J. L. Sonnenberg, M. Hada, M. Ehara, K. Toyota, R. Fukuda, J. Hasegawa, M. Ishida, T. Nakajima, Y. Honda, O. Kitao, H. Nakai, T. Vreven, J. A. Montgomery, Jr., J. E. Peralta, F. Ogliaro, M. Bearpark, J. J. Heyd, E. Brothers, K. N. Kudin, V. N. Staroverov, R. Kobayashi, J. Normand, K. Raghavachari, A. Rendell, J. C. Burant, S. S. Iyengar, J. Tomasi, M. Cossi, N. Rega, J. M. Millam, M. Klene, J. E. Knox, J. B. Cross, V. Bakken, C. Adamo, J. Jaramillo, R. Gomperts, R. E. Stratmann, O. Yazyev, A. J. Austin, R. Cammi, C. Pomelli, J. W. Ochterski, R. L. Martin, K. Morokuma, V. G. Zakrzewski, G. A. Voth, P. Salvador, J. J. Dannenberg, S. Dapprich, A. D. Daniels, O. Farkas, J. B. Foresman, J. V. Ortiz, J. Cioslowski, and D. J. Fox, Gaussian, Inc., Wallingford CT, (2009).

2 F. A. Cotton, *Chemical Applications of Group Theory*, John Wiley & Sons, New York (1989).

3 E. B. Wilson, J. C. Decius, P. C. Cross, *Molecular Vibrations, The theory of Infrared and Raman Vibrational Spectra*, Dover Publications, New York (1995).

4 G. W. Chantry, *Polarizability Theory of the Raman Effect*, in *The Raman Effect. Vol. 1. Principles*, edited by A. Anderson, M. Dekker, New York (1971).

5 C. Castiglioni, M. Gussoni, G. Zerbi, *Synth. Met.* **29**, E1-E6 (1989).

6 S. Krichene, J. P. Buisson, S. Lefrant, *Synth. Met.* **17**, 589-594 (1987).

7 E. del Corro, M. Taravillo, J. González, V. G. Baonza, *Carbon* **49**, 973-979 (2011).

8 http://www.scai.uma.es/servicios/area_microscopia/afm/afm.html browsed on October 26th, 2015.

9 http://www.scai.uma.es/servicios/aqcm/evi/evi.html browsed on October 26th, 2015.

10 http://www.nanocarbon.cz/instruments.html browsed on October 26th, 2015.

11 E. Ehrenfreund, Z. Vardeny, O. Brafman, B. Horovitz, *Phys. Rev. B* **36**, 1535 (1987).

12 B. Horovitz, *Phys. Rev. Lett*. **47**, 1491 (1981).

13 B. Horovitz, *Solid State Commun. Colloq*. **41**, 729 (1982).

14 C. Castiglioni, M. Gussoni, J. T. Lopez Navarrete, G. Zerbi, *Solid State Commun*. **65**, 625-630 (1988).

15 C. Castiglioni, M. Del Zoppo, G. Zerbi, *J. Raman Spectrosc*. **24**, 485-494 (1993).

16 H. E. Schaffer, R. R. Chance, R. J. Silbey, K. Knoll, R. R. Schrock, *J. Chem. Phys*. **94**, 4161 (1991).

17 F. Maurice, G. Froyer, M. Minier, M. Gauneau, *J. Phys. Lett*. **42**, 425 (1981).

18 D. M. Ivory, G. G. Miller, J. M. Sowa, L. W. Shacklette, R. R. Chance, R. H. Baughman, *J. Chem. Phys*. **71**, 1506 (1979).

19 M. Endo, Y. Nishimura, T. Takahashi, K. Takeuchi, M. S. Dresselhaus, *J. Phys. Chem. Sol.* **57**, 725 (1996).

20 G. Zannoni, G. Zerbi, *J. Chem. Phys*. **82**, 31 (1985).

21 L. Cuff, M. Kertesz, *Macromol.* **27**, 762 (1994).

22 M. Rumi, G. Zerbi, K. Müllen, G. Müller, *J. Chem. Phys*. **106**, 1 (1997).

23 G. Louarn, L. Athouël, G. Froyer, J. P. Buisson, S. Lefrant, *Synth. Met*. **55**, 4762 (1993).

24 H. Ohtsuka, Y. Furukawa, M. Tasumi, *Spectrochim. Acta A* **49**, 5/6, 731–737 (1993).

25 G. Heimel, D. Somitsch, P. Knoll, E. Zojer, *J. Chem. Phys*. **116**, 10921 (2002).

26 A. Marucci, M. A. Pimenta, S. M. D. Brown, M. J. Matthews, M. S. Dresselhaus, M. Endo, *J. Mater. Res*. **14**, 3447–3454 (1999).

27 V. Hernandez, C. Castiglioni, M. Del Zoppo, G. Zerbi, *Phys. Rev. B* **50**, 9815-9823 (1994).

28 G. Leising, T. Verdon, G. Louarn, S. Lefrant, *Synth. Met*. **41–43**, 279 (1991).

29 M. S. Dresselhaus, P. C. Eklund, *Adv. Phys.* **49**, 705-814 (2000).

33 H. Kataura, Y. Kumazawa, Y. Maniwa, I. Umezu, S. Suzuki, Y. Ohtsuka, Y. Achiba, *Synth. Met.* **103**, 2555 – 2558 (1999).

34 R. B. Weisman, S. M. Bachilo, *Nano Lett.* **3**, 1235-1238 (2003).

35 http://www.photon.t.u-tokyo.ac.jp/~maruyama/kataura/kataura.html, browsed on October 7th, 2015.

37 http://www.photon.t.u-tokyo.ac.jp/~maruyama/kataura/kataura.html browsed on October 26th, 2015.

38 T. Chang, *Acta Mech. Sinica* **23**, 159–162 (2007).

39 V. N. Popov, P. Lambin, *Phys. Rev. B* **73**, 085407 (2006).

40 L. Li, T. Chang, G. Li, *Carbon* **49**, 4412-4419 (2011).

41 P. T. Araujo, P. B. C. Pesce, M. S. Dresselhaus, K. Sato, R. Saito, A. Jorio, *Physica E* **42**, 1251–1261 (2010).

42 C. Thomsen, S. Reich, *Topics Appl. Phys*. **108**, 115-232 (2007).

43 T. M. G. Mohiuddin, A. Lombardo, R. R. Nair, A. Bonetti, G. Savinini, R. Jalil, N. Bonini, D. M. Basko, C. Galiotis, N. Marzari, K. S. Novoselov, A. K. Geim, A. C. Ferrari, *Phys. Rev. B* **79**, 205433 (2009).

44 A. Jorio, G. Dresselhaus, M. S. Dresselhaus, M. Souza, M. S. S. Dantas, M. A. Pimenta, *Phys. Rev. Lett.* **85**, 2617(2000).

45 A. Jorio, A. G. Souza Filho, G. Dresselhaus, M. S. Dresselhaus, A. K. Swan, M. S. Ünlü, B. B. Goldberg, M. A. Pimenta, J. H. Hafner, C. M. Lieber, R. Saito, *Phys. Rev. B* **65**, 155412 (2002).

46 A. M Rao, E. Richter, S. Bandow , B. Chase, P. C. Eklund, K. A. Williams, S. Fang , K. R. Subbaswamy, M. Menon, A. Thess, R. E. Smalley, G. Dresselhaus, M. S. Dresselhaus, *Science* **275**, 187–191 (1997).

47 J. S. Park, K. Sasaki, R. Saito, W. Izumida, M. Kalbac, H. Farhat, G. Dresselhaus, M. S. Dresselhaus, *Phys. Rev. B* **80**, 081402 (2009).

48 H. Farhat, H. Son, Ge. G Samsonidze, S. Reich, M. S. Dresselhaus, J. Kong, *Phys. Rev. Lett.* **99**, 145506 (2007).

56 H. W. Kroto, J. R. Health, S. C. O'Brien, R. Curl, R. E. Smalley, *Nature* **318**, 162 (1985).

57 A. L. Balch, M. M. Olmstead, *Chem. Rev*. **98**, 2123–2165 (1998).

58 M. S. Dresselhaus, G. Dresselhaus, P. C. Eklund, *J. Raman Spectrosc*. **27**, 351-371 (1996).

59 P. C. Eklund, P. Zhou, K. A. Wang, G. Dresselhaus, M. S. Dresselhaus, *J. Phys. Chem. Sol.* **53**, 1391-1413 (1992).

60 P. C. Eklund, A. M. Rao, P. Zhou, Y. Wang, J. M. Holden, *Sol. Films* **257**, 185-203 (1995).

61 D. R. McKenzie, C. A. Davis, D. J. H. Cockayne, D. A. Muller, A. M. Vassallo, *Nature* **355,** 622 (1992).

62 K. Hedberg, L. Hedberg, M. Buhl, D. S. Bethune, C. A. Brown, R. D. Johnson, *J. Am. Chem. Soc.* **119**, 5314-5320 (1997).

63 P. J. Evans, E. R. Darzi, R. Jasti, *Nature Chem.* **6**, 404-408 (2014).

64 L. Guan, H. Li, Z. Shi, L. You, Z. Gu, *Solid Stat. Comm*. **133**, 333-336 (2005).

65 G. Sun, M. Kertesz, *J. Phys. Chem. A* **106**, 6381 (2002).

66 V. Schettino, M. Pagliai, G. Cardini, *J. Phys. Chem. A* **106**, 1815 (2002).

67 D. Jing, Z. Pan, *Eur. J. Mech. A Sol*. **28**, 948 (2009).

68 www.roditi.com browsed on October 26th, 2015.

69 V. G. Baonza, M. Taravillo, A. Arencibia, M. Cáceres, J. Núñez, *J. Raman Spectrosc.* **34**, 264–270 (2003).

71 I. N. Levine, *Quantum Chemistry*, Pearson Advanced Chemistry Series, Boston (2014).

72 D. R. Hartree, *Proc. Cambridge Phil. Soc*. **24**, 89, 111, 426 (1928).

73 V. A. Fock, *Z. Phys*. **15**, 126 (1930).

74 J. C. Slater, *Phys. Rev*. **35**, 210 (1930).

75 C. J. Cramer, *Essentials of Computational Chemistry: Theories and Models*, John Wiley & Sons, Chichester (2004).

76 A. Meckler, *J. Chem. Phys*. **21**, 1750 (1953).

77 C. Møller, M. S. Plesset, *Phys. Rev*. **46**, 618 (1934).

78 J. Čížek, *J. Chem. Phys.* **45**, 4256 (1966).

79 A. R. Leach, *Molecular Modelling Principles and Applications*, Addison Wesley Longman Limited, Harlow (1997).

80 J. L. McHale, *Molecular Spectroscopy*, Prentice-Hall, New Jersey (1999).

81 E. R. Davidson, D. Feller, *Chem. Rev*. **86**, 681 (1986).

82 P. Hohenberg, W. Kohn, *Phys. Rev*. **136**, B864-B871 (1964).

83 W. W. Kohn, L. J. Sham, *Phys. Rev*. **140**, A1133-A1138 (1965).

84 K. Burke, J. P. Perdew, M. Levy, *Modern Density Functional Theory: A Tool for Chemistry*, edited by J. M. Seminario, P. Politzer, Elsevier, Amsterdam (1995).

85 A. D. Becke. *Phys. Rev. A* **38**, 3098-3100 (1988).

86 C. Lee, W. Yang, R. G. Parr, *Phys. Rev. B* **37**, 785 (1988).

87 A. D. Becke. *J. Chem. Phys.* **98**, 1372–1377 (1993).

88 J. P. Perdew, M. Ernzerhof, K. Burke, *J. Chem. Phys.* **105**, 9982–9985 (1996).

89 P. J. Stevens, J. F. Devlin, C. F. Chabalowski, M. J. Frisch, *J. Phys.Chem*. **98**, 11623 (1994).

90 A. D. Becke. *J. Chem. Phys.* **98**, 5648–5652 (1993).

91 T. Engel, P. J. Reid, *Quantum Chemistry and Spectroscopy*, Pearson, Boston (2013).

92 E. R. Davidson, D. Feller, *Chem. Rev*. **86**, 681 (1986).

93 F. Jensen, *Introduction to Computational Chemistry*, John Wiley &Sons, Chichester (1999).

94 Y. Segawa, H. Omachi, K. Itami, *Org. Lett.* **12**, 2262-2265 (2010).

95 C. Castiglioni, *Theory of Vibrational Spectroscopy of Polymers* in *Vibrational Spectroscopy of Polymers: Principles and Practice*, edited by N. J. Everall, P. R. Griffiths, J. M. Chalmers, Wiley (2007).

96 A. P. Scott, L. Radom, *J. Phys. Chem*. **100**, 16502 (1996).

97 R. Pou-Amérigo, E. Ortí, M. Merchán, M. Rubio, P. M. Viruela, *J. Phys. Chem. A* **106**, 631 (2002).

98 R. Pou-Amérigo, P. M. Viruela, R. Viruela, M. Rubio, E. Ortí, *Chem. Phys. Lett*. **352**, 491 (2002).

99 E. Runge, E. K .U. Gross, *Phys. Rev. Lett.* **52**, 997 (1984).

100 W. Koch, M. Holthausen, *A Chemist´s Guide to Density Functional Theory*, Wiley-VCH, Weinheim (2001).

101 J. P. Perdew, K. Burke, M. Enzerhof, *Phys. Rev. Lett*. **78**, 1396 (1997).

102 Z. Chen, C. S. Wannere, C. Corminboeuf, R. Putcha, P. V. R. Schleyer, *Chem. Rev*. **105**, 3842-3888 (2005).

103 http://www.chemcraftprog.com/ browsed on October 26th, 2015.

104 http://gausssum.sourceforge.net/ browsed on October 26th, 2015.

Chapter 3

Phys. Chem. Chem. Phys. DOI:10.1039/C5CP05500H (2015)

From Linear to Cyclic Oligoparaphenylenes: Electronic and Molecular Changes Traced in the Vibrational Raman Spectra and Reformulation of the Bond Length Alternation Pattern Section

M. Peña Alvarez, L. Qiu, M. Taravillo, V. G. Baonza,
M. C. Ruiz Delgado, S. Yamago, R. Jasti,
J. T. López Navarrete, J. Casado, M. Kertesz

Cyclic paraphenylenes, [n]CPPs, and linear paraphenylenes, [n]LPPs, formed by *n* benzenes, are investigated by Raman spectroscopy for *n* = 5 to 12 and density functional theory (DFT) for *n* = 4 to 20. The information on the experimental Raman frequencies and intensities, combined with DFT computations and reported X-ray diffraction structures, provides a consistent interpretation of the Raman spectra and allows establishing relevant structure-property trends. Structural and electronic effects such as benzene ring bending, inter-ring torsions, π–conjugation (aromaticity) and orbital energy gaps as a function of the linear elongation in [n]LPP versus macrocyclic curvature in [n]CPPs and of the molecular size (i.e., polymer limit) are systematically analyzed on the basis of the vibrational Raman properties. Changes in the BLA as an indicator of the degree of quinonoid character are analyzed and linked to the Effective Conjugation Coordinate (ECC) model. The BLA patterns involved in twisted and non-twisted conformations and in different species (bipolarons, quinonoid tautomers, and the ECC active modes) are compared and their differences are discussed. This paper offers a unified interpretation of structural and electronic aspects in relation to the evolution from linear 1D π–systems to cyclic 2D structures.

Introduction

Cyclic [n]paraphenylenes ([n]CPPs, Fig. 1) are closed macrocyclic molecules formed by *n* benzene units in a fashion that could be considered as the shortest slice of an armchair carbon nanotube (CNT).[1-13] [n]CPPs are capable of encapsulating guest molecules,[14] their electronic properties are size-tunable[14-16] and markedly differ from those of CNTs.[17] They furthermore provide a link between small oligomers and polymers of phenylenes. Various [n]CPPs have been characterized by X-ray diffraction (XRD), vibrational and electronic spectroscopy and electrochemistry.[4,5,18-23] Computational modeling based on density functional theory has also been used to interpret the experimental data.[12] An important underlying question in all these studies concerns the structural and electronic features that make [n]CPPs singularly different to linear [n]paraphenylenes ([n]LPPs, Fig. 2). It is well known that linear π–conjugation shapes the structures of [n]LPPs in competition with ring aromaticity. One therefore wonders if in [n]CPPs a similar cyclic π–conjugation effect exists and what are its structural and spectroscopic marks. In chemical terms, the issue of π–conjugation has been addressed by the degree of aromatic (A) vs. quinonoid (Q) structural character.[2,4,24,25] A and Q are illustrated in Fig. 1 for [6]CPP (for the same A the twisted and non-twisted versions are also shown). For instance, Bachrach and Stück showed by using DFT at the B3LYP/6-31G(d)[26] level that the Q structure, called "bond-shift", can be found as a local metastable minimum on the potential energy surface (PES) for *n* = 3-6.

In this scenario, [n]LPPs will aid the interpretation of the properties of their cyclic cousins.[27,28] The alternative A (twisted and non-twisted) and Q structures for [n]LPPs are also illustrated in Fig. 2.

A way to quantify the aromatic/conjugation or A/Q interconversion deals with the bond length alternation (BLA) pattern which involves rather different deformations on linear and cyclic cases, one along the [n]CPP perimeter and another along the linear [n]LPP chain. In fact this paper shows some of these differences in the BLA patterns for the two series. However, generally in the literature, any A to Q change has been quantitatively described by the same BLA parameter[29] using the following formula and the definitions in Fig. 3:

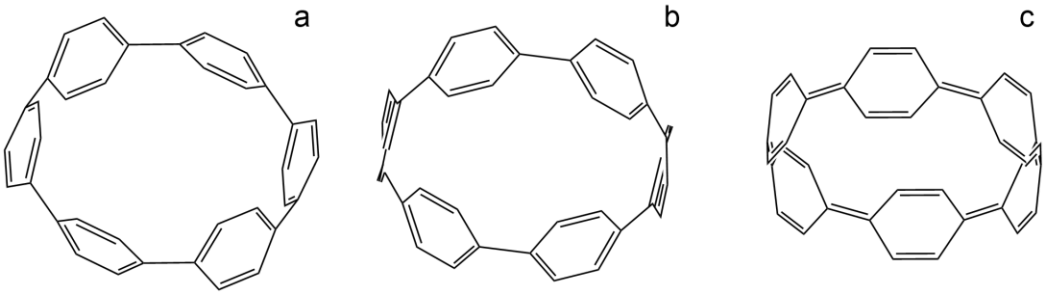

Fig. 1 Schematics of structural isomers of [6]CPP: a) aromatic D_{3d}, twisted conformation; b) aromatic D_{6h}, non-twisted conformation; and c) quinonoid D_{6h}, non-twisted conformation.

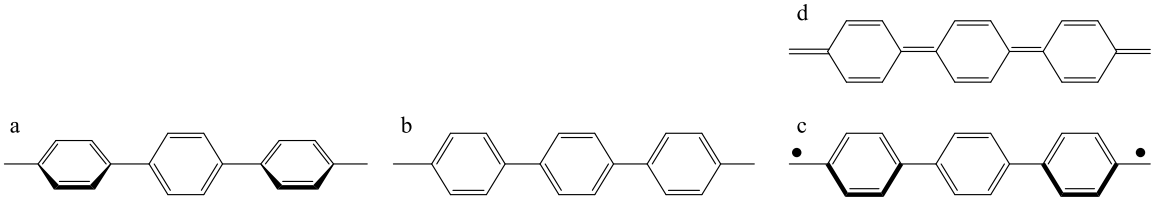

Fig. 2 Structural isomers of [3]LPP. a) Aromatic C_{2v}, twisted conformation; b) aromatic D_{2h}, non-twisted conformation; c) diradical aromatic C_{2v}, non-twisted conformation; and d) quinonoid D_{2h} non-twisted conformation.

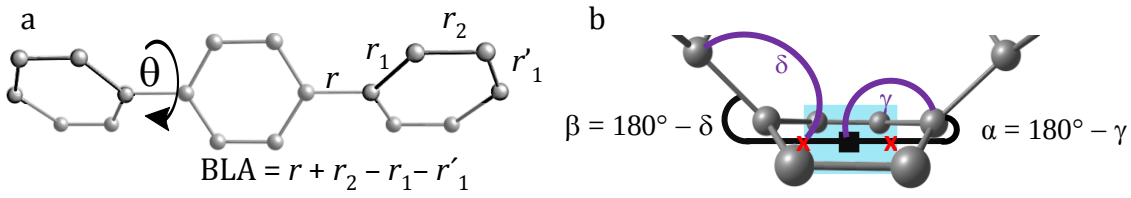

Fig. 3 a) Torsional angle (θ) between two neighboring benzene units; and the C–C bond distances (r, r_1 and r_2). b) Out-of-plane bending angles α and β are defined as α = 180° – γ; β= 180° – δ. Different centroids are indicated by X and ■ and are used to calculate the out-of-plane deformation of the benzene units. For [n]LPPs, α = β = 180°.

$$\mathrm{BLA} = r + r_2 - r_1 - r_1' = r + r_2 - 2r_1 \quad (1)$$

when the inter-ring bond (r) is long, and r_1 and r_2 are close in value, the structure is aromatic with BLA > 0. For [n]CPPs $r_1 = r_1'$. When r is short, and $r_1 > r_2$, then BLA < 0 and the structure is quinonoid.

The different orbital patterns of the relevant HOMO and LUMO frontier molecular orbitals in Scheme 1 are the fundamental reasons why the BLA changes significantly in the A → Q direction when the occupancy between HOMO and LUMO is switched. For this reason the HOMO-LUMO bandgap strongly depends on the degree of BLA as shown in the literature.[29,35] As a consequence, the strong vibronic coupling between some A_g-like symmetry vibrations (mimicking BLA stretching modes) and the HOMO-LUMO bandgap is responsible for the main bands of the Raman spectra which are thus associated with vibrational coordinates that involve a certain degree of BLA distortion. In other words, due to this strong coupling of the BLA-like deformation and the gap, the Raman intensities and frequencies are spectroscopic markers of the BLA changes, a connection that is emphasized in the Effective Conjugation Coordinate (ECC) theory.[29-31]

ECC theory defines a totally symmetric stretching vibration corresponding to the in-phase shrinking/stretching of the C-C/C=C consecutive bonds (ECC mode) in such a way that their vibrational amplitudes match the A↔Q geometrical transformation, or BLA deformation.[31-33] Since the ECC mode is not a vibrational eigenfunction, its intensity appears to be distributed among the few symmetric C-C/C=C stretching normal modes of the vibrational Raman spectrum (ECC-like bands). The frequency and intensity behavior of these ECC-like bands give insights into the BLA alteration in the A/Q context: for example, an ECC band frequency downshift is related to the variation of the BLA value towards zero (to the transition from A to Q or vice versa).[31,32]

Here we focus on the [n]-dependence of BLA for both [n]CPP and [n]LPP series together for the first time in connection with linear and cyclic π–conjugation and with the A↔Q transformation.[33,34] Additional open questions we attempt to solve here are:

1. Is this quinonoidization effect in [n]CPPs a result of valence tautomerization, *i.e.*, are there two different local minima on the electronic ground state PES?[35]

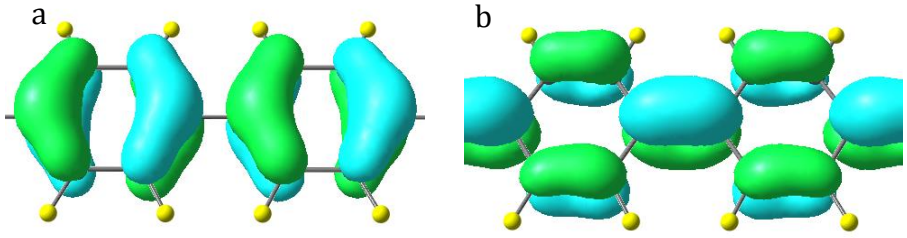

Scheme 1. Orbital pattern for the HOMO (a) and the LUMO (b) of a section of oligoparaphenylenes. H atoms are in yellow.

2. The ground state structures of highly doped [n]LPPs and poly-p-phenylenes (PPPs) are generally understood to have bipolarons, which have a structure containing quinonoid characteristics, as expressed by a negative BLA. Is this kind of quinonoidization similar to that argued in [n]CPPs?
3. It has been shown that the strong Raman A_{1g} vibrations of [n]LPPs present a large BLA component. Do the main Raman bands of [n]CPPs also involve a strong BLA component?

To address these points, we obtain and compare the geometries of [n]CPPs and [n]LPPs as a function of *n* paying attention to the distinctive electronic effects (i.e., hybridization, electronic delocalization due to the loss of local planarity in Fig. 3b etc.) in both series in order to highlight the differences between linear and cyclic π–conjugation. The discussion is particularly important in the limit of highly strained [n]CPPs (those with smaller *n* values). Then we address the main features of the Raman spectra, and the connections of the Raman active modes to the BLA pattern and to the A/Q interplay. A unified vision of linear *versus* cyclic π–conjugation is given in the Conclusions section. Along the paper, when possible, computed structures are compared with the available XRD data. Furthermore, we also present new experimental data on the Raman spectra of [5]CPP.

Methods

[n]CPPs with *n* = 7-12 were synthesized by using a synthetic strategy through multinuclear arylplatinum complexes,[36] while [5]CPP and [6]CPP were synthesized through Suzuki–Miyaura cross-coupling.[4,5] For comparison of the cyclic and linear oligomers, we recorded the Raman spectra of [5] and [6]LPP (samples were purchased from TCI and studied without further purification).

All reported energy values and geometrical parameters refer to the geometry-optimized structures using the B3LYP/6-31G(d,p) method. We have also carried out DFT calculation with an extended basis set B3LYP/6-311+G(2df,p), and with two further functionals with dispersion content (wB97xD and B3LYP-D3/6-31G(d,p)). The latter two provided essentially the same results as B3LYP/6-31G(d,p) which was therefore chosen in all presented computations as a good comprise between computational cost and accuracy. Validation data are provided in Tables S1-S3 (Appendix 1).

Unless noted otherwise, all geometries were optimized without constraints, and all minima were confirmed by vibrational calculations with all frequencies being real. The exceptions are: planar [n]LPPs and non-twisted [n]CPPs, which were optimized by keeping the D_{2h} and D_{nh} symmetry, respectively. Raman frequencies have been scaled: the factor 0.97 was used for the 450-900 cm^{-1} region and 0.9675 for the region between 1100-1700 cm^{-1}. The assignments of the bands refer to normal modes and symmetry labels of the respective high symmetry conformation, D_{nh}. Vibrational Raman intensity for a given *j*th vibrational normal mode, in the non-resonant approximation, is proportional to I_j as given by:[32]

$$I_j = 45\alpha'^2 + 7\gamma'^2 \quad (2)$$

where α'^2 and γ'^2 are the derivatives with respect to the *j*th normal mode displacements of the trace and anisotropy of the polarizability term, respectively.

Raman measurements under room conditions of different [n]CPPs were conducted with an Invia Reflex Raman RENISHAW microscope with 785 nm excitation wavelength, with a spectral resolution of 0.5–1 cm^{-1}. A Senterra dispersive micro Raman spectrometer from Bruker with 785 nm excitation wavelength was used for the characterization of [5]CPP and [5] and [6]LPPs at room temperature with a standard spectral resolution of 3 cm^{-1}. [5]CPP was measured in an inert atmosphere. Experimental intensities are quoted as their heights when fitted with Lorentzian profiles with FWHM ranging between 6 and 15 cm^{-1}, depending on the band, but constant for each band regardless of *n*. Crystal structures have been taken from the CSD database, see Table 1. The XRD data for [11]CPP[25] were not used because of spurious H atoms in the structure. Similarly the structures of [9]CPP and [12]CPP were not used in our comparisons due to their large *R*-factors.

Table 1. XRD data reported for [n]CPPs and [n]LPPs used.

***n* =**	**5**	**6**	**7**	**8**	**9**	**10**	**12**	**[3]LPP**	**[4]LPP**
Ref-code[a]	HIYLIM	LAXKOM	RIRYEY	QEBKAL	VAMWOX	QEBKEP	ONIZIV	TERPHE15	QUPHEN
Ref.	4	5	18	19	20	21,22	23	37	38, 39
***R* %**	4.86	5.06	6.48	4.14	9.52	5.05	9.04	3.2	4.5

[a]Cambridge Structural Database (CSD).

We have calculated using B3LYP/6-31G(d,p) the non-resonant Raman spectra of the [n]CPPs. The most intense bands are the A_{1g} modes for molecules with D_{nh} or $D_{n/2,d}$ symmetry while for molecules with lower symmetries we will refer to them as A_{1g}-like normal modes.

The normal mode displacement vectors, $\overrightarrow{L_j}$, can be decomposed into modes expressed in internal coordinates, $\overrightarrow{B_k}$:

$$\overrightarrow{L_j} = c_{j,1}\overrightarrow{B_1} + \sum_{k>1} c_{j,k}\overrightarrow{B_k} \tag{3}$$

here mode $k = 1$ corresponds to that special BLA mode, denoted $\overrightarrow{B_1}$, which carries most of the Raman intensities according to the ECC model and this mode has been called the amplitude mode (AM) or Я- or ECC mode.[31,32,40] $c_{j,1}$ is the coefficient of the B_1 component of the jth normal mode. Vector $\overrightarrow{B_1}$ is a displacement vector with A_{1g} (or approximate A_{1g}) symmetry.

Under these conditions, vibrational Raman intensity theory describes the non-resonant Raman intensity of the jth A_{1g} mode, coupled with the $\overrightarrow{B_1}$ one, as approximately proportional to the square of that component's coefficient:

$$I_j \propto \left|c_{j,1}\right|^2 \tag{4}$$

The ECC model has been used to obtain insights into the dominant A_{1g} Raman modes for a variety of conjugated systems even though the specific nature of the special $\overrightarrow{B_1}$ mode is rather unknown.[31-33] It is clear however that the BLA mode is fully delocalized over the complete sequence of C-C/C=C bonds which represents a normalized displacement that is proportional to a sum over all repeat units of the following displacement vectors, for the notation of Fig. 3a:

$$\overrightarrow{B_{BLA}} = \sum\left(\delta r + \delta r_2 - \delta r_1 - \delta r'_1\right) \tag{5}$$

This mode is referred to as the $k = 1$ mode, $\overrightarrow{B_1}$, in eqn. (3). Based on eqns. (3) and (4), we can estimate the displacements of this special AM or ECC mode from the sum of the product between the square root of the intensity of the A_{1g} modes and the respective displacement vectors:

$$\overrightarrow{B_1} = c_1 \sum_{i\in A_{1g}} \pm I_i^{1/2}\overrightarrow{L_i} \tag{6}$$

where c_1 is the normalization factor and the sign of each term is chosen to ensure that all contributions are in phase.

Results

I. Energies and Topologies of the PES

I.1. Aromatic-Quinonoid Transition

[n]CPPs have received much attention in this regard, since with decreasing size and increasing strain, the benzene rings become deformed, and benzene aromaticity along the bonds designated as r_1 in Fig. 3 is inhibited due to an increasing sp^3 character which provokes a certain degree of quinonoid character in the rings.

Scheme 2a shows the general shape of the potential energy curve for the small [n]CPPs (n = 4 and 5) between the quinonoid and the aromatic local minima as a function of the bond length alternation (BLA) coordinate. The respective numerical values are summarized in Table 2. For instance, the BLA of the [5]CPP from its quinonoid (Q) to its aromatic conformation (A) varies from -0.185 Å to 0.064 Å. This change is accompanied by significant changes in the bending angles indicating a significant loss of benzene aromaticity leading to highly localized exo-double bonds in the quinonoid configuration, explaining its higher energy compared to the aromatic form.

The transition state (TS) for [4]CPP connecting the quinonoid local minimum and the aromatic absolute minimum of the PES was located by Bachrach and Stück.[26] In [5]CPP through a rigid scan (where the C-C distances are modified along a linear grid connecting the A and Q structures without relaxation[41]), we find a tentative non-twisted TS with an energy barrier of about 39 kcal mol^{-1} from A to Q. The real TS obtained by relaxation should give an even lower energy barrier but we were unable to obtain the exact structure of this TS even though both minima are characterized by 3N-6 real vibrational frequencies. However, we are not able to find a quinonoid tautomer for any [n]CPP with n>5. This suggests that [5]CPP is the limiting size for the existence of the quinonoid structure as a valence tautomer. Table 2 summarizes our calculated A/Q parameters of the structures for n = 4-6. The geometries and energies behave as expected. The E(Q) – E(A) difference increases with increasing size. The larger degree of bending of the benzene units in the smaller [n]CPPs appears with a concomitant larger pyramidalization of all carbons.[26] It appears that it is this pyramidalization that assists in the development of inter-ring double bonds and makes the quinonoid structure energetically competitive, but only for very small [n]CPPs.

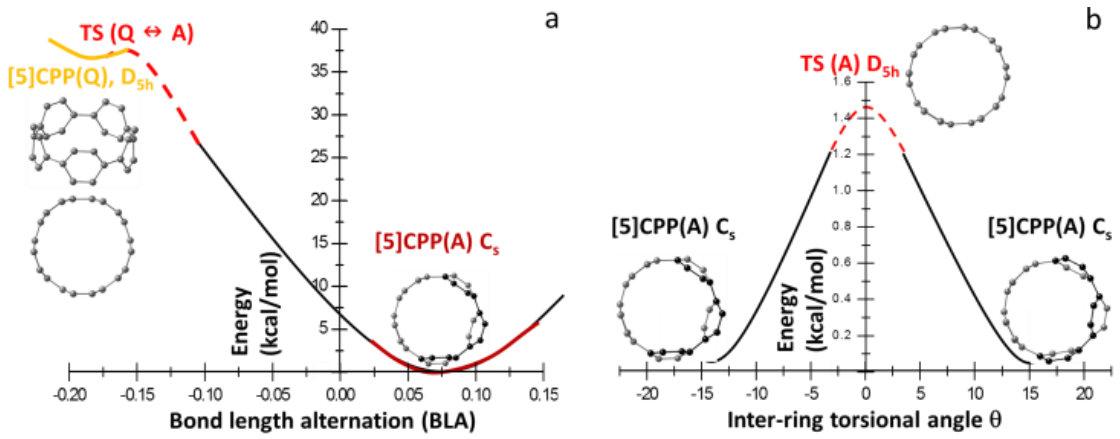

Scheme 2. a) Schematic potential energy curves for [5]CPP, TS: transition state. b) Schematic of the potential energy curve for [5]CPP indicating the conformational pathway between two degenerate structures through its non-twisted D_{5h} structure.

Table 2. Energy differences between the quinonoid local minimum (Q) and the aromatic minimum (A), barriers and selected structural data for [n]CPPs. E_B is the energy barrier relative to E_Q; energies are in kcal mol^{-1}, distances are in Å, angles are in degrees.

n	Sym. (Q)	Sym. (A)	$E_Q - E_A$	E_B	A BLA	Q BLA	BLA for TS (A↔Q)	αA	αQ	βA	βQ
4	D_{4h}	D_{2d}	10.4	9.9	0.074	-0.222	-0.105	20	29	25	16
5	D_{5h}	C_s	37.5	0.7	0.064	-0.185	-0.153	16	22	20	13
6	-	D_{3d}	-	-	0.062			14		16	

I.2. Twisted to Non-Twisted Aromatic Transition

Now we focus on the barriers between the two energetically competitive aromatic structures, the low (twisted, $D_{n/2,d}$) and high (non-twisted, D_{nh}) symmetry conformations in Scheme 2b which further illustrates the barrier between them. The per-ring energy difference [kcal (mol ring)$^{-1}$] between these is shown in Fig. 4a as a function of *n*. For both [n]CPP and [n]LPP series, these energy differences increase with increasing size towards a common value around 1.6 kcal (mol ring)$^{-1}$. Furthermore these differences are larger in [n]LPPs, for instance, [4]LPP requires about +1.3 kcal (mol ring)$^{-1}$ for planarization, while only about +0.2 kcal (mol ring)$^{-1}$ for [4]CPP due to the strong bending in the smaller [n]CPPs.[24] The numerical values are provided in Tables S4 and S5 (Appendix 1).

Since the non-twisted D_{nh} structures are unstable, they are characterized by imaginary frequencies which are shown in Fig. S1a and b (Appendix 1) as a function of *n*. Interestingly, they follow a pattern as a function of size depending on whether the molecule is cyclic or linear. For even [n]CPPs, there are ((n/2)-1) different ways the structure can deviate from a non-twisted geometry, and for odd [n]CPPs there are ((n-1)/2) ways (degeneracies are observed). The lowest energy displacement corresponds to the largest imaginary frequency and it corresponds to an alternating in-out displacement which represents the largest possible avoidance of H...H non-bonded repulsions. This is significant because it means that there are ((n/2)-1) different conformers for the even [n]CPPs and ((n-1)/2) for the odd [n]CPPs.

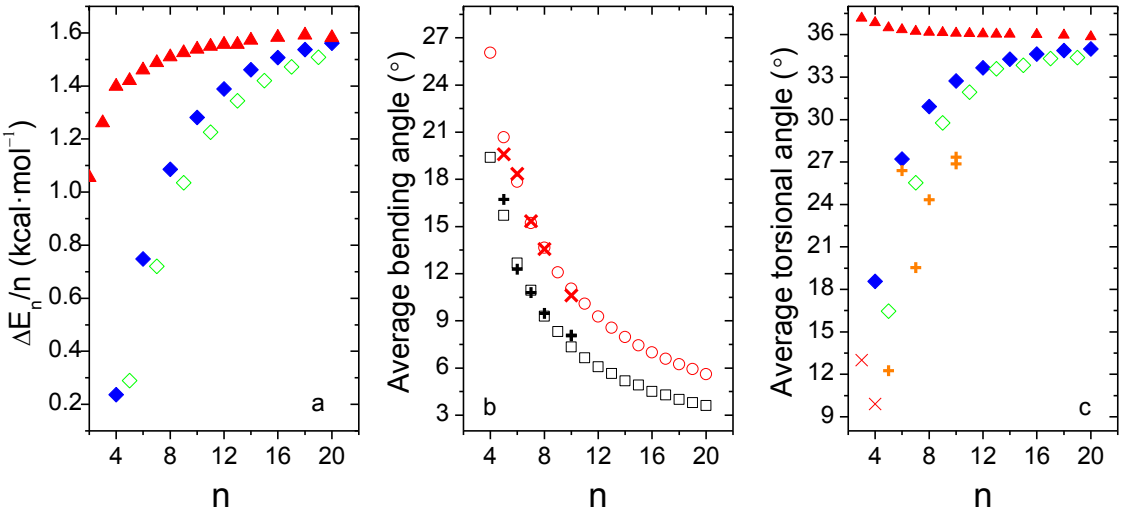

Fig. 4 B3LYP/6-31G(d,p) data: a) Energy difference per phenyl unit between the twisted and non-twisted conformations, $\Delta E_n/n$, as a function of *n*. ◆ and ◇ represent the even and odd CPPs, respectively, while ▲ is for [n]LPPs. b) Computed average bending angles as a function of *n*: □ and ○ for α and β respectively; + and × are for XRD data.[4,5,18-23] c) Torsional angles between neighboring benzenes, ▲ for LPPs, ◆ and ◇ correspond to even and odd [n]CPPs, respectively. + refers to XRD data for [n]CPPs[4,5,18,20-23] and × for [n]LPPs.[37-39]

II. Geometrical and Electronic Parameters

II.1. Bending and Torsions

While in [n]LPPs the benzene rings remain planar, in [n]CPPs they are bent.[11,12] In Fig. 4b we have plotted the experimental and theoretical bending angles of [n]CPPs, as defined in Fig. 3b, as a function of *n*. In agreement with results previously reported in the literature,[12,26] out of plane six member ring deformations grow dramatically when the [n]CPP becomes smaller. Fig. 4c shows the computed inter-ring torsional angles of [n]LPPs and [n]CPPs. Even and odd [n]CPPs follow an alternating pattern of ±torsions, however this undulating distribution of torsions in odd [n]CPPs is not uniform (Fig.4c thus shows average torsional values). The [n]LPPs have torsional angles that are slightly higher for smaller *n* and they trend towards a constant value, around 36°, for the larger *n* values.[42] Our data are in agreement with those of Chen et al.[9]

II.2. Computed Bond Length Alternation

In Fig. 5a and d we have presented the BLA dependence on *n* for both [n]CPPs and [n]LPPs obtained from our optimized structures and from literature XRD data. In the case of the [n]CPPs, the agreement between theory and experiment is excellent.

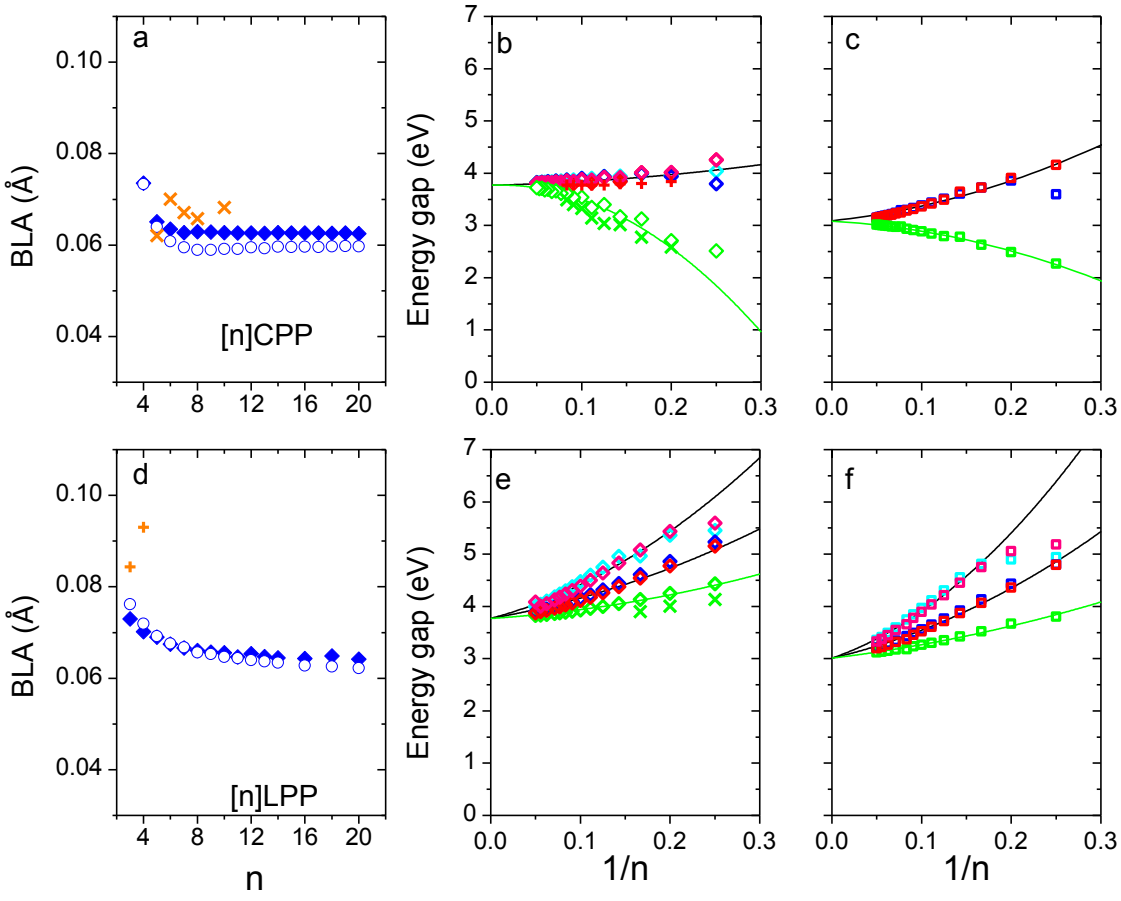

Fig. 5 Bond length alternation as a function of *n*: a) [n]CPP; d) [n]LPP. ○ and ◆ stand for B3LYP/6-31G(d,p) non-twisted and twisted conformational data, respectively; × and + stand for [n]CPP and [n]LPP XRD data.[4,5,18,20-23,37-39] Energy gaps, versus 1/n for: b) twisted [n]CPPs, c) non-twisted [n]CPPs, e) twisted [n]LPPs, and f) non-twisted [n]LPPs. ◇ corresponds to twisted conformations and □ to non-twisted conformations. Green symbols for HOMO-LUMO values, red symbols for HOMO-LUMO+1 and HOMO-1→LUMO and blue symbols for the HOMO→LUMO+2 and HOMO-2→LUMO. × and + for experimentally assigned HOMO-LUMO and the HOMO-LUMO+1 bands for [n]CPPs respectively.[4,5,18,20-23] × for experimentally assigned HOMO-LUMO bands in [n]LPPs.[43]

There are only few experimental data reported in the literature for [n]LPPs which precludes an extensive analysis. The comparison of theBLAs between [n]LPP and [n]CPP shows that both systems have very similar values for $n > 8$, in line with the decreasing bending of the benzene rings. BLAs behave very similarly in the twisted and non-twisted [n]CPPs and none of these show any significant quinonoid character. The BLA values for the non-twisted conformers are slightly smaller compared to the twisted analogues in line with some gain of aromatic character in the latter.

II.3. BLA and Energy Gaps

There is a striking difference between the energy gaps as a function of *n* for [n]LPPs and [n]CPPs in Fig. 5. The higher bending and lower torsion in [n]CPPs have a concomitant impact on the HOMO-LUMO gaps[44] which clearly decrease with increasing size in [n]LPPs.[44] However, the HOMO–LUMO gap behavior on the [n]CPPs becomes one of the most distinctive features regarding [n]LPPs because it becomes narrow with decreasing size. The energy gap data, fitted to a second order polynomials in n^{-1}, converge to a common limiting value of 3.77 eV for twisted [n]CPPs, and around 3.05 eV for non-twisted [n]CPPs as $n \rightarrow \infty$. In this limit, non-twisted [n]CPPs and [n]LPPs converge to the same value in concert with the idea that they approach the edges of the bands of the respective infinite chains (the energy gap of PPP is around these limits, at 3.4 eV).[45,46]

This discussion on the structural and electronic features of [n]CPPs establishes their distinctive behavior compared to the [n]LPPs especially for smaller *n* (see Fig. S2, Appendix 1). Further insights into this comparison are obtained in the next sections by the analysis of the BLA in terms of Raman shifts and intensities, and the discussion of the ECC model as it is related to the A/Q transformation and Raman data.

III. Vibrational Spectra and Structures

In this section we discuss those aspects of the Raman spectra concerning the most intense bands with A_{1g} (A_{1g}-like) symmetry on the basis of the DFT computations. Table 3 summarizes our assignments for [6]CPP and [6]LPP.

According to the ECC model, these bands show significant intensities because their displacements contain a large component of the ECC mode as described by eqn. (3). In general the non-twisted [n]CPP structures give rise to simpler spectra, thus we first describe their strongest Raman bands and extrapolate the assignments to the twisted (i.e., lower symmetry) homologues on the basis of the very close similarity among the respective normal modes.

III.1. The 450-900 cm^{-1} Low Frequency Region

In Fig. 6 and Table 3 we gathered the experimental and computational results obtained for [6]CPP and [6]LPP between 450 cm^{-1} and 900 cm^{-1}, while Figs. S3 to S7 (Appendix 1) show the experimental and theoretical spectra of [n]CPPs and [n]LPPs from $n = 4$ to 20.

The spectrum of [6]CPP presents four major A_{1g} bands, one around 500 cm^{-1} and the other three at around 800 cm^{-1}. [6]LPP however has only one strong A_{1g} band at around 800 cm^{-1} (similar differences occur for all *n* in Figs. S3–S7, Appendix 1). The 500 cm^{-1} band is due to a breathing-type motion of the CPP ring as a whole where the C_{ipso}-C_{ipso} bonds move outward relative to the center while the C_{ortho}-C_{ortho} bonds move inward, thus resulting in a vibration along the [n]CPP perimeter, which we will refer as radial flexing mode or RFM.[8,9] In linear paraphenylenes the parent mode has B_{2u} symmetry and is not Raman active. The three 750 - 850 cm^{-1} bands in twisted [n]CPPs correspond to three A_{1g} modes arising from C_{ipso}-C_{ortho}-C_{ipso} bending modes coupled with antisymmetric phenyl breathing modes and the RFM mode. The computed frequencies of these A_{1g} bands show an upshift of 20 cm^{-1} from $n = 4$ to $n = 9$ for the twisted conformers. This shift is 35 cm^{-1} for the non-twisted conformations, as shown in Figs. S6 and S7 (Appendix 1).

Table 3. Experimental and theoretical wavenumbers (in cm^{-1}) for [6]CPP and [6]LPP, species of symmetry (non-twisted D_{nh} conformation) and the vibrational assignment in terms of internal coordinates.

[6]CPP				[6]LPP		
Exp.	Theor.	Sym.	Vibrational description	Exp.	Theor.	Sym.
504	499	**A_{1g}**	RFM	--	--	--
	770	**A_{1g}**	β(CC)+ $\beta_{antisym}$(phenyl) + RFM (for CPPs) + β(C-H)	--	--	--
	784	**A_{1g}**		--	--	--
804	804	**A_{1g}**		770	772	A_g
1192	1179	E_{2g}	β(phenyl)+ ν(C-C)+ ω(CH)	--	--	--
1200	1185	**A_{1g}**	β(C-H) + ν(C-C)$_{interring}$	1219	1222	A_g
1252	1244	E_{2g}	β(phenyl) + ν(C-C)$_{interring}$ + β(C-H)	1269	1263	A_g
1263	1245	**A_{1g}**	β(phenyl) + ν(C-C)$_{interring}$ +β(C-H)	1278	1278	A_g
1269	1264	E_{1g}	ν(C-C) + ω(CH) + β(phenyl)	--	--	--
1504	1496	E_{2g}	G_{io}: ν(C_{ipso}-C_{ortho})	1486	1485	A_g
1567	1576	A_{1g}	G_{A1g}: ν(C-C)$_{transversal}$	1593	1594	A_g
1584	1592	E_{2g}	G_{E2g}: ν(C-C)$_{trans}$ + ν(C-C)$_{long}$	--	--	--

RFM: radial flexural mode or C_{ipso}-C_{ipso} bond vibration with motion outward relative to the center of the macrocycle and the C_{ortho}-C_{ortho} bond motion inward; **β(C-C)**: C-C bond bending mode; **$\beta_{antisym}$(phenyl)**: antisymmetric phenyl breathing mode, C_{ortho}-C_{ortho} with motion inward relative to the benzene center, C_{ipso} outward. **β(phenyl):** symmetric phenyl breathing mode; **ω(CH)**: C-H wagging mode; **ν(C-C)$_{interring}$**: C-C inter-ring stretching mode; **β(C-H)**: C-H bending mode; **ν(C_{ipso}-C_{ortho})**: C_{ipso}-C_{ortho} inter-ring stretching mode; **ν(C-C)$_{transversal}$**: C-C stretching mode along the transversal direction of the macrocycle; **ν(C-C)$_{long}$**: C-C stretching mode along the longitudinal direction of the ring.

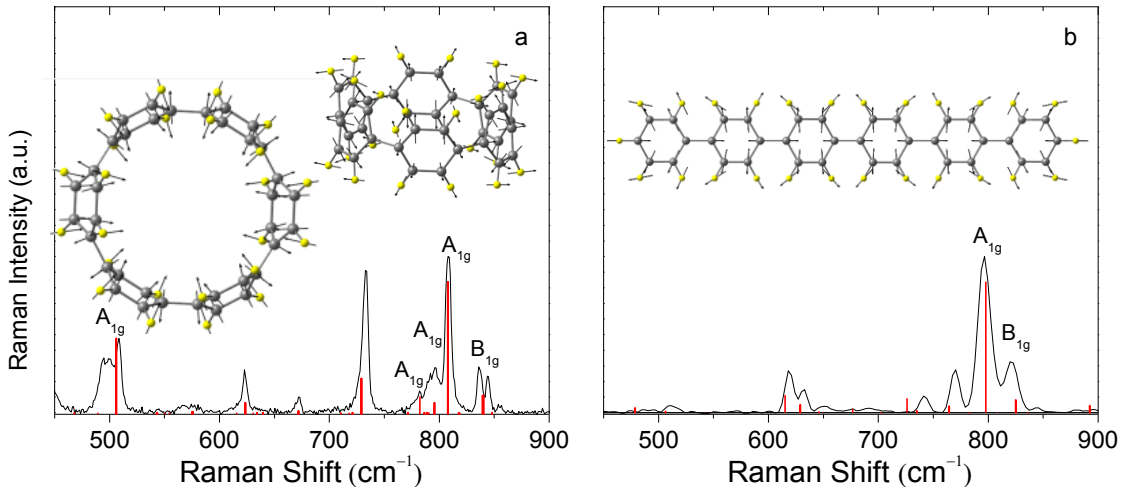

Fig. 6 Raman spectra (black lines) in the region 450–900 cm^{-1} region of a) [6]CPP and b) [6]LPP. Red vertical bars are the B3LYP/6-31G(d,p) calculated spectra for D_{3d} [6]CPP and non-twisted D_{2h} [6]LPP. Theoretical frequencies are scaled by a factor of 0.97. Insets show the displacement vectors of the strongest A_{1g} bands. a) Left: RFM mode. b) Right: C_{ipso}-C_{ortho}-C_{ipso} bending mode.

III.2. The 1100-1300 cm^{-1} Region

Fig. 7 shows the experimental spectra in the 1100 - 1300 cm^{-1} region for [6]CPP (see Figs. S8 - S11, Appendix 1, for the experimental and theoretical spectra for the rest of compounds).

In the 1200 cm^{-1} region two main A_{1g} bands dominate the spectrum with the assignment given in Table 3. These are correlated with the bands at 1220 cm^{-1} and 1280 cm^{-1} of [n]LPPs.[24,34,42,47] A discussion of the non- A_{1g} modes is given in the Appendix 1. In regard of these two A_{1g} Raman bands, their intensity ratio ($I1280_{A_{1g}}/I1220_{A_{1g}}$) has been correlated with the domain-size of linear π–conjugation in [n]LPPs and torsional angles (see Figs. S12-S15, Appendix 1).[33,42] In the next section we discuss the behavior of this ratio for linear versus cyclic PPs in the context of ECC theory.

III.3. The BLA Modes in the 1500 -1600 cm^{-1} Region

The most intense Raman bands of the spectra appear in this range and are shown in Fig. 7. The displacements associated with these bands contain a large component of the totally symmetric BLA mode similar to the [n]LPPs.[30,31] A prominent feature at around 1600 cm^{-1} with two components at lower and higher frequencies, denoted G_{A1g} and G_{E2g}, stands out in this region. The G terminology refers to the C-C stretching band characteristic of graphitic materials and CNTs.[8,9,24] The most intense of these two components comes from an A_{1g} mode related to the collective C-C stretching mode that follows the BLA pattern, while the shoulder at higher frequencies is an E_{2g} mode also related to C-C stretching bands.[24] A weak band at around 1500 cm^{-1} assigned to the C_{ipso}-C_{ortho} stretching mode, hereafter referred to as G_{io}, is observed (of E_{2g} and E_2 symmetry for even and odd *n*, respectively, see Fig. S16 and S17, Appendix 1).[8,9] Given that this G_{A1g} band is the most intense of the spectra, its intensity and Raman shift are of particular importance for π-conjugation in the context of the ECC model.[30-32,48,49]

In Fig. 8 we show the G_{A1g} frequencies as a function of *n* from which we deduce the following:

i) For twisted [n]LPPs, the G_{A1g} mode slightly downshifts with increasing *n* while this change is more pronounced for the non-twisted conformers of [n]LPPs.

ii) In the [n]LPP and [n]CPP series, the G_{A1g} Raman bands are always at higher frequency values for the twisted conformers than for the non-twisted conformers.

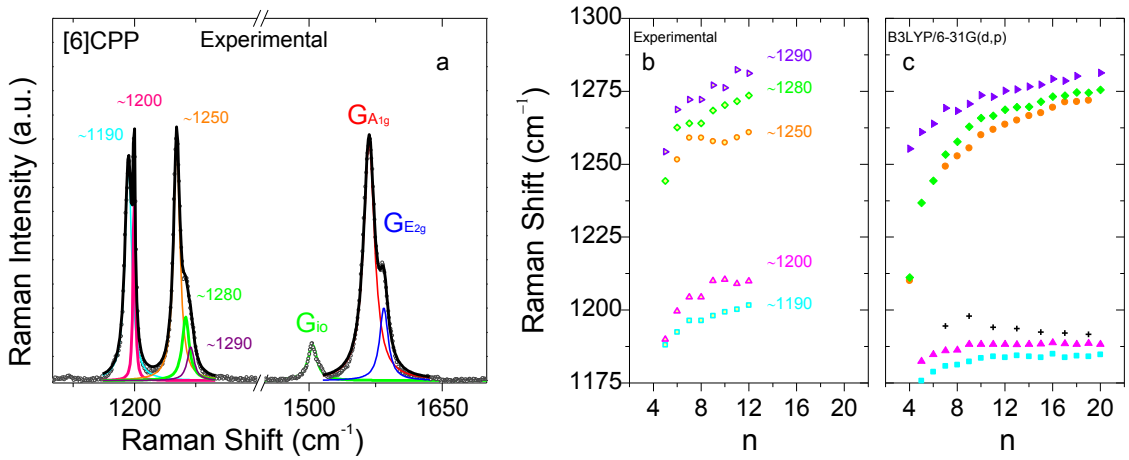

Fig. 7 a) Raman spectrum (black lines) of [6]CPPs in the 1100-1700 cm^{-1} region. The band deconvolutions are shown in color. Evolution of Raman frequencies of the main bands in the 1175-1300 cm^{-1} region. b) Experimental data. c) Calculated for twisted [n]CPPs; theoretical frequencies are scaled by 0.9675.

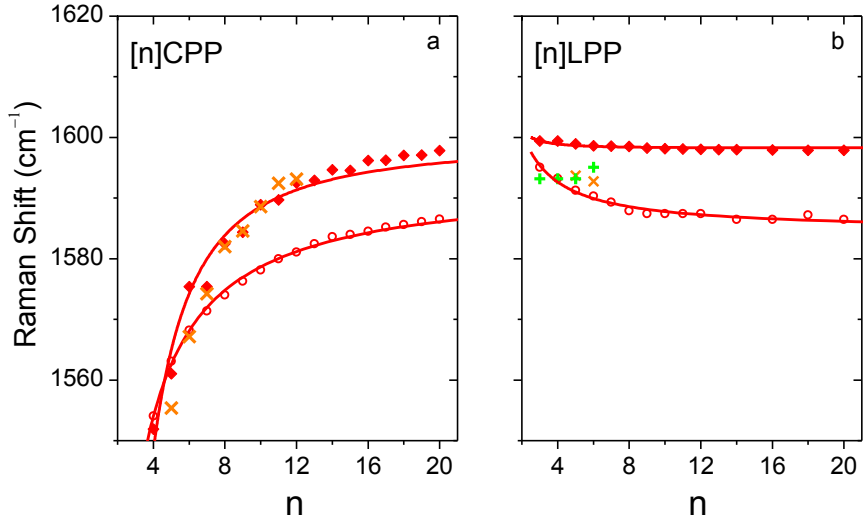

Fig. 8 G_{A1g} band Raman shift vs. *n* for: a) [n]CPPs and b) [n]LPPs. ○ for non-twisted computed data and ◆ for twisted data. × for [n]CPP experiments. + for [n]LPPs experiments.[50] Lines are provided to guide the eye.

iii) For both [n]LPP and [n]CPP series, the frequency of the G_{A1g} bands converge to similar values in the polymeric limit[33,51] (n→∞) in accordance with the reduction of the curvature which unifies the linear and cyclic behaviors.

iv) It is well known that in [n]LPPs the electron confinement of electron density by aromaticity in the phenyl rings precludes extensive inter-ring π-conjugation, and so small Raman shift variations are observed from molecule to molecule.[43] In concordance with this Raman shift – π–conjugation relationship, the Raman frequencies of the non-twisted [n]LPPs are more downshifted with respect to their twisted counterpairs.

v) Both in the twisted and non-twisted models of the [n]CPP series these G_{A1g} bands show a much larger frequency variation as a function of *n* compared to [n]LPPs. This large frequency dispersion is attributed to the strong bending of the benzene rings which breaks down its aromaticity and allows a larger π–conjugation for [n]CPPs, especially for smaller *n*.[24] (Fig. 5). It can also be attributed to the absence of terminal constraints in [n]CPPs.

vi) Interestingly, the signs of the dispersion shifts with increasing size in [n]CPPs and [n]LPPs are opposite. In [n]LPPs it is known that when adding more phenyl units to the chain the conjugation is increased, so it explains why G_{A1g} downshifts with increasing *n*.[43] On the other hand, in [n]CPPs the increasing strain on the smaller units leads to considerably lower torsions which favor the conjugation between phenyl units developing through space orbital interactions.[52] Thus this explains the opposite trends in the shifts between [n]CPPs and [n]LPPs.

III.4. Size Dependence of the Intensities of Selected A_{1g} Modes

We now address the intensity evolution of the A_{1g} bands as a function of *n* in Fig. 9.

The calculated non-resonant Raman intensities were plotted relative to that of the G_{io} band, as its intensity remains almost unaltered with the molecular size (Fig. S17, Appendix 1, shows the experimental Raman spectra normalized to their G_{io} bands). The first observation is that the relative intensity of the G_{A1g} band increases superlinearly with increasing *n*. The experimental $I(G_{A1g})/I(G_{io})$ intensity ratios are in satisfactory agreement with computations.

Fig. 10 shows the intensity ratio between the two A_{1g} bands at 1200 cm^{-1} and 1280 cm^{-1} relative to the G_{A1g} band in both [n]CPPs and [n]LPPs. For larger *n*, as the ring strain is reduced, these intensity ratios in the two series converge to a similar value. For smaller *n* the significantly different intensity ratios represent another manifestation of the particular electronic structure promoted by ring bending and dearomatization.[43]

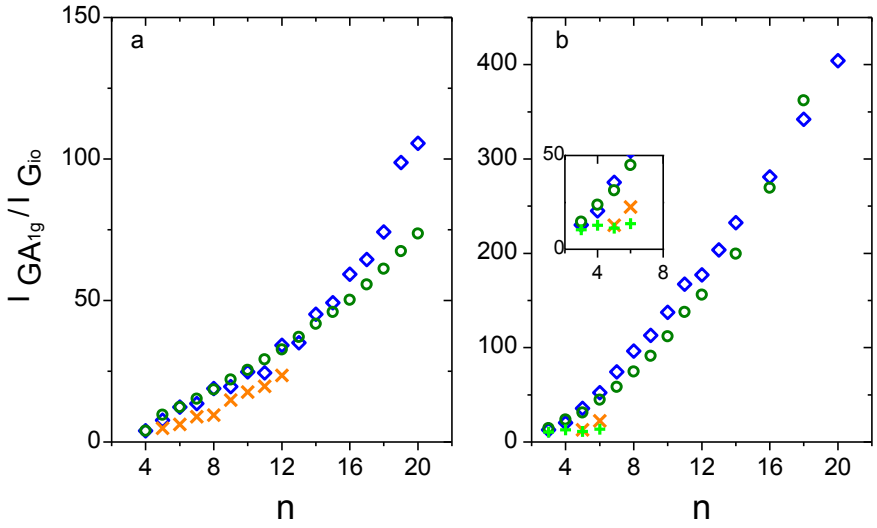

Fig. 9 Relative Raman Intensities of the G_{A1g} band as a function of *n* compared to the respective G_{io} band intensity. a) [n]CPPs and b) [n]LPPs. ○ for B3LYP/6-31G(d,p) non-twisted conformations, ◇ for B3LYP/6-31G(d,p) twisted ones and × for experiments. + for experimental data for [3]LPP to [6]LPP.[50]

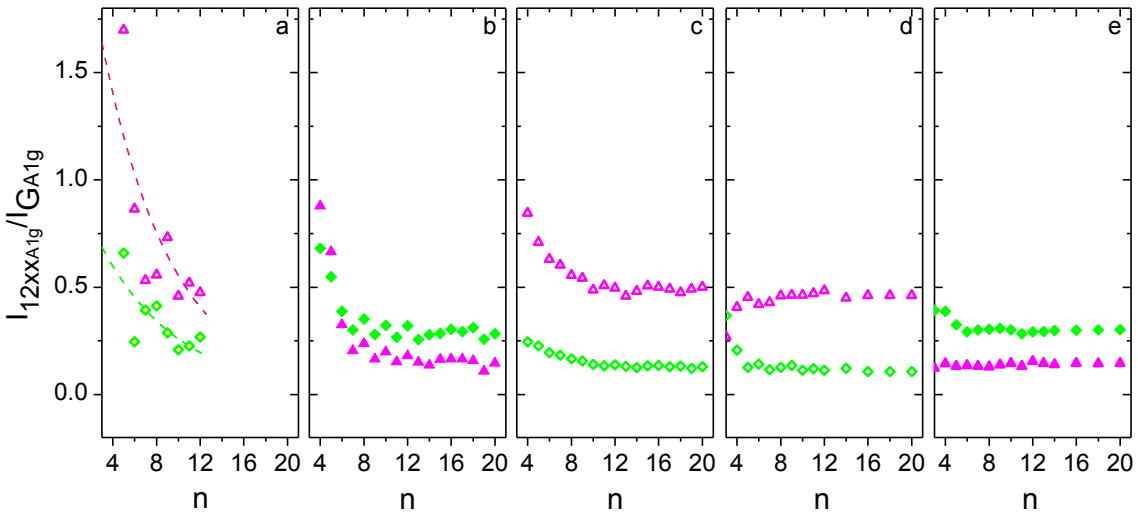

Fig. 10 $I_{12xxA1g}/I_{GA1g}$ as a function of *n*, where $I_{12xxA1g}$ stands for the intensity of the 1200 and 1280 cm^{-1} A_{1g} bands with respect to their corresponding G_{A1g} band. a) Experimental [n]CPPs (lines are to guide the eye). Data from B3LYP/6-31G(d,p); b) twisted [n]CPPs; c) non-twisted [n]CPPs; d) non-twisted [n]LPPs; and e) twisted [n]LPPs.

III.5. BLA and Raman Active A_{1g} Modes

This section is aimed at addressing the Q/A character directly from the analysis of the changes in the bond distances as a new way to analyze the different BLA characteristics that occur in [n]CPPs and [n]LPPs. The conventional way of addressing the quinonoid/aromatic character connects the BLA values with the aromatic character if BLA > 0 and to the quinonoid character if it is < 0. We also use this important indicator. In addition to the BLA value, we have additional data from the theoretical computations regarding the normal mode displacement vectors for each [n]CPP (one is illustrated in Fig. 11a) as well as their computed non-resonant Raman intensities. This provides an opportunity to compute an approximate amplitude mode displacement vector via eqn. (6). We applied this formula to the non-twisted D_{nh} [n]CPPs which requires the summation over all the A_{1g} modes with significant intensity. We limited the summation to the following modes: ~500 cm^{-1} [RFM], 800 cm^{-1}, ~1200 cm^{-1}, ~1280 cm^{-1}, ~1580 cm^{-1} [G_{A1g} mode]; and 3200 cm^{-1} (C-H A_{1g} mode). The displacement parameters for the resulting modes are depicted in Fig. 11b. Since displacement vectors are normalized, there are no absolute values associated with the BLA-like geometry change along the vibrational coordinate. For this reason, we use ratios of displacements and compare those with the traditionally obtained geometry changes associated with BLA changes along the aromatic/quinonoid geometry changes.

In Fig. 11b the displacements involved in C-C stretching are characterized by the changes in the three parameters, as per Fig. 3a: δr, δr_1 and δr_2. The signs are the same for δr and δr_2 and the opposite for δr_1. In an attempt to compare them and being able to define the aromatic/quinonoid geometry change, in Fig. 11c the ratios $\delta r/\delta r_2$ and $\delta r_1/\delta r_2$ are presented against n. It can be observed that the ratio $\delta r/\delta r_2$ is ~ 2 and its value becomes larger as n decreases. On the other hand, the ratio $\delta r_1/\delta r_2$ remains nearly constant at about −0.87 for any n. The positive $\delta r/\delta r_2$ and the higher ratio for the smaller [n]CPPs clearly show the strengthening of the C-C force constant along r, with the intensification of the quinonoid character as n decreases. Note that this trend is gradual, without showing a critical n value.

There is no requirement that the C-C bond lengths added together along the carbon skeleton of [n]LPPs or [n]CPPs, (R, in eqn. (7)) should be constant and thus we cannot assume that the BLA mode should obey approximately such a condition:

$$R = r + r_2 + r_1 + r'_1 = \text{constant} \tag{7}$$

However, this geometrical restriction on R does not apply for the $\overrightarrow{B_1}$ mode displacement vectors (accounted in δR) as shown in Fig. 11c for all n values. For further and unbiased characterization of the displacements, we define two relative displacement parameters:

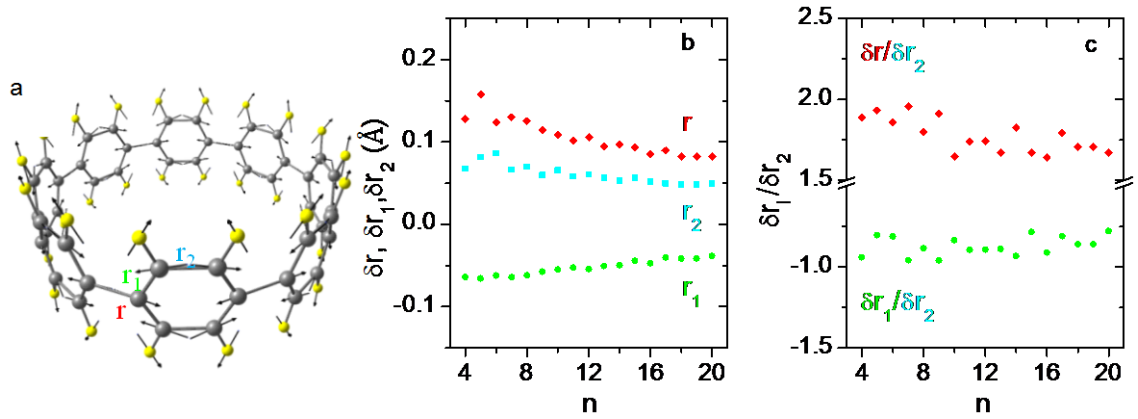

Fig. 11 Normalized ($\overrightarrow{B_1}$) amplitude modes of [n]CPPs as evaluated by eqn. (6). a) Displacement pattern for [8]CPP. b) Components of the amplitude mode in terms of δr, δr_1 and δr_2 as a function of n (the signs comply with the BLA pattern); and c) BLA parameters defined in eqn. (8), as a function of n, evaluated from the components shown in (b).

$$\Delta = -\delta r/\delta r_1 \quad (8a)$$

$$\Delta_2 = -\delta r_2/\delta r_1 \quad (8b)$$

where δr, δr_1, and δr_2 refer to the changes of the respective bond lengths. A large Δ indicates a large change in r, a large Δ_2 indicates a large change in r_2 both compared to the changes in r_1.

In Fig. 12, pairs of Δ and Δ_2 values from three different sources of changes in the BLA pattern are collected: (i) from the analysis of the geometry changes due to oxidation or reduction based on [5]CPP$^+$, [5]CPP^{2+}, [5]CPP^{2-}, and [3], [4], [5]LPP^{2+}, (ii) from the analysis of the BLA displacement vectors based on eqn. (6) in the neutral [n]CPPs, and (iii) from the comparison of the A and Q structures in the valence tautomers of [n]CPPs with n = 4 and 5. We also show in Fig. 12 the geometry changes that are possible in compliance with eqn. (5) and eqn. (7).

To our surprise we find some variations, although not very large, of the BLA patterns (defined from displacement parameters) regarding the expected changes from the narrowly defined BLA mode of eqn. (5). Interestingly, the changes are classified by groups and are even more subtle from molecule to molecule. Overall for each of these three groups, the changes in r are about twice in magnitude compared with the changes in r_1 while changes in r_2 are comparable to changes in r_1. These changes however are not evenly distributed among r, r_1 and r_2. The important implication therefore is that various structural modifications can be characterized and distinguished in terms of the qualitative aromatic (A) vs. quinonoid (Q) structural change using these new parameters ($\Delta = -\delta r/\delta r_1$ and $\Delta_2 = -\delta r_2/\delta r_1$) which are sensitive to geometrical changes along the A to Q transition. This two dimensional characterization shows much more detail than the BLA change as defined in eqn. (5) and shown in Fig. 5a. Accordingly, the A vs. Q geometry change is dominated by the change of the inter-ring distance, δr, which is approximately twice compared to δr_1 and δr_2 in the three discussed groups. For this reason one can identify a change of direction from an A to a Q structure even if such a quinonoid structure cannot be identified experimentally or theoretically as a local minimum for a given system.

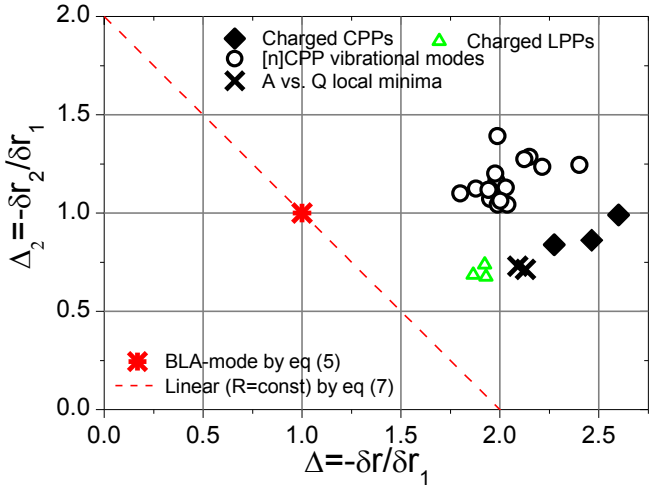

Fig. 12 Variations of the relative values of Δ and Δ_2 displacement parameters. Black diamonds are values for the oxidized/reduced [n]CPPs and [n]LPPs; circles are values obtained from our analysis using eqn. (6) for all [n]CPPs discussed in this work. The red dashed line indicates no change in the overall sum along the conjugation path as per eqn. (7). X refers to values of the [n]CPP with n = 4 and between their A and Q local minima on their respective PESs (Scheme 2). Red star refers to the BLA mode that satisfies eqn. (5).

Conclusions

In this paper, for the first time, a systematic study of the structural and electronic properties of the [n]CPP series in comparison with their linear analogues, oligoparaphenylenes, is conducted. Particular emphasis is placed on the structural differences and their different behaviors as a function of molecular size obtained from Raman spectroscopy and DFT computations. Benzene ring bending angles, inter-rings torsions, BLA patterns and HOMO-LUMO gaps are carefully compared for both series. The distinctive evolution of these structural parameters indicates the presence of a particular type of π–electron delocalization associated with the cyclic geometry which is absent in the linear congeners, or cyclic π–conjugation. Cyclic π–conjugation is manifested by the large benzene ring bending, minimal inter-ring torsions and small HOMO-LUMO gaps. In contrast, linear π–conjugation produces no phenyl deformation, minimal inter-ring torsion and slightly reduced HOMO-LUMO gaps. The strong difference that activates cyclic π–conjugation is the partial rupture of benzene aromaticity that liberates electrons from the ring confinement towards a more quinonoid configuration and facilitates cyclic delocalization. In contrast, aromaticity in [n]LPPs mostly inhibits linear π–conjugation. Compared with [n]LPPs, we find several Raman spectroscopic marks directly attributed to cyclic π–conjugation such as larger intensity distribution along all the A_{1g} modes, with not only the G_{A1g} as in [n]LPPs but also larger frequency shifts with size for the detected Raman bands. We have found that a generalized definition of BLA in terms of displacement parameters provides more insights into this particular aromatic-quinonoid balance in the cyclic π–structures. A way of obtaining such displacement parameters is obtained from the ECC mode vibrational eigenvectors extracted from the vibrational analysis associated with the most intense bands of the Raman spectra.

We also conclude that the concept of a quinonoid-like structure is not limited to situations where such a tautomeric structure can be computationally identified as a local minimum. Quinonoid structures provide useful tools for the analysis of structural changes upon Raman active vibrations even if such a quinonoid structure is not present as a local minimum.

In summary, an exhaustive analysis of the differences and similarities between [n]LPPs and [n]CPPs is carried out revealing different aromatic/quinonoid characters of the benzene rings. At the end, we extract clear differences between linear π–conjugation and cyclic π–conjugation.

References

1 H. Omachi, T. Nakayama, E. Takahashi, Y. Segawa, K. Itami, *Nature Chem*. **5**, 572–576 (2013).

2 R. Jasti, J. Bhattacharjee, J. B. Neaton, C. R. Bertozzi, *J. Am. Chem. Soc*. **130**, 17646–17647 (2008).

3 T. Sisto, M. R. Golder, E. S. Hirst, R. Jasti, *J. Am. Chem. Soc.* **133**, 15800–15802 (2011).

4 P. J. Evans, E. R. Darzi, R. Jasti, *Nature Chem.* **6**, 404–408 (2014).

5 J. Xia, R. Jasti, *Angew. Chem. Int. Ed.* **51**, 2474–2476 (2012).

6 M. Fujitsuka, C. Lu, T. Iwamoto, E. Kayahara, S. Yamago, T. Majima, *J. Phys. Chem. A* **118**, 4527–4532 (2014).

7 S. E. Lewis, *Chem. Soc. Rev.* **44**, 2221–2304 (2015).

8 H. Chen, M. R. Golder, F. Wang, S. K. Doorn, R. Jasti, S. Tretiak, A. K. Swan, *J. Phys. Chem. C* **119**, 2879–2887 (2015).

9 H. Chen, M. R. Golder, F. Wang, R. Jasti, A. K. Swan, *Carbon* **67**, 203–213 (2014).

10 N. Toriumi, A. Muranaka, E. Kayahara, S. Yamago, M. Uchiyama, *J. Am. Chem. Soc.* **137**, 82–85 (2015).

11 B. M. Wong, *J. Phys. Chem. C* **113**, 21921–21927 (2009).

12 (a) Y. Segawa, A. Fukazawa, S. Matsuura, H. Omachi, S. Yamaguchi, S. Irle, K. Itami, *Org. Biomol. Chem.* **10**, 5979-5984 (2012). (b) Y. Segawa, H. Omachi, K. Itami, *Org. Lett.* **12**, 2262–2265 (2010).

13 S. Yamago, E. Kayahara, T. Iwamoto, *Chem. Rec.* **14**, 84–100 (2014).

14 T. Iwamoto, Y. Watanabe, T. Sadahiro, T. Haino, S. Yamago, *Angew. Chem. Int. Ed.* **50**, 8342–8344 (2011).

15 M. R. Golder, B. M. Wong, R. Jasti, *Chem. Sci*. **4**, 4285–4291 (2013).

16 E. Kayahara, T. Kouyama, T. Kato, H. Takaya, N. Yasuda, S. Yamago, *Angew. Chem. Int. Ed*. **52**, 13722–13726 (2013).

17 E. H. Hároz, J. G. Duque, X. Tu, M. Zheng, A. R. Hight Walker, R. H. Haige, S. K. Doorn, J. Kono, *Nanoscale* **5**, 1411–1439 (2013).

18 F. Sibbel, K. Matsui, Y. Segawa, A. Studer, K. Itami, *Chem. Commun.* **50**, 954–956 (2014).

19 S. Yamago, Y. Watanabe, T. Iwamoto, *Angew. Chem. Int. Ed.* **49**, 757–759 (2010).

20 Y. Segawa, P. Šenel, S. Matsuura, H. Omachi, K. Itami, *Chem. Lett*. **40**, 423–425 (2011).

21 E. Kayahara, Y. Sakamoto, T. Suzuki, S. Yamago, *Org. Lett*. **14**, 3284–3287 (2012).

22 J. Xia, J. W. Bacon, R. Jasti, *Chem. Sci.* **3**, 3018–3021 (2012).

23 Y. Segawa, S. Miyamoto, H. Omachi, S. Matsuura, P. Senel, T. Sasamori, N. Tokitoh, K. Itami, *Angew. Chem. Int. Ed.* **50**, 3244–3248 (2011).

24 M. Peña-Alvarez, P. M. Burrezo, M. Kertesz, T. Iwamoto, S. Yamago, J. Xia, R. Jasti, J. T. López Navarrete, M. Taravillo, V. G. Baonza, J. Casado, *Angew. Chem. Int. Ed*. **53**, 7033–7037 (2014).

25 E. R. Darzi, R. Jasti, *Chem. Soc. Rev*. **44**, 6401–6410 (2015).

26 S. M. Bachrach, D. Stück, *J. Org. Chem*. **75**, 6595–6604 (2010).

27 M. Banerjee, R. Shukla, R. Rathore, *J. Am. Chem. Soc.* **131**, 1780–1786 (2009).

28 a) P. A. Irvine, D. C. Wu, P. J Flory, *J. Chem. Soc., Faraday Trans. 1* **80**, 1795–1806 (1984). (b) K. N. Baker, A. V .Frai, T. Resch, H. C. Knachel, W. W. Adams, E. P. Socci, B. L. Farmer, *Polymer* **34**,1571–1587 (1993). c) M. Rinke, H. Gusten, H. J. Ache. *J. Phys. Chem.* **90**, 2666–2669 (1986).

29 a) J. L. Bredas, R. R. Chance, R. Silbey, *Phys. Rev. B* **26**, 5843–5854 (1982); (b) T. A. Skotheim, *Handbook of Conducting Polymers*, Dekker, New York (1986). (c) J. L. Bredas and R. R. Chance, *Conjugated Polymeric Materials*, Kluwer Academic, Dordrecht, (1990); (d) Y. S. Lee, M. Kertesz, R. L. Elsenbaumer, *Chem. Mater*. **2**, 526–530 (1990).

30 (a) B. Horovitz, *Solid State Commun.* **41**, 729–734 (1982); (b) E. Ehrenfreund, Z. Vardeny, O. Brafman, B. Horovitz, *Phys. Rev. B: Condens. Matter Mater. Phys*. **36**, 1535–1553 (1987).

31 G. Zerbi, M. Gussoni, C. Castiglioni, in *Conjugated Polymers,* ed. J. L. Bredas and J. Silbey, Kluwer, New York, p. 435 (1991).

32 M. G. Gussoni, W. B. Person, G. Zerbi, in *Vibrational Intensities in Infrared and Raman Spectroscopy* ed. W. B. Person and G. Zerbi, Elsevier: Amsterdam, 221–238 (1982).

33 L. Cuff, C. Cui, M. Kertesz, *J. Am. Chem. Soc.* **116**, 9269–9274 (1994).

34 A. Marucci, M. A. Pimenta, S. D. M. Brown, M. J. Matthews, M. S. Dresselhaus, M. Endo, *J. Mater. Res.* **14**, 3447–3454 (1999).

35 M. Kertesz, C. H. Choi, S. Yang, *Jpn. Chem. Rev.* **105**, 3448–3481 (2005).

36 T. Iwamoto, Y. Watanabe, Y. Sakamoto, T. Suzuki, S. Yamago, *J. Am. Chem. Soc.* **133**, 8354–8361 (2011).

37 A. P. Rice, F. S. Tham, E. L. Chronister, *J. Chem. Crystallogr.* **43**, 14–25 (2013).

38 Y. Delugeard, J. Desuche, J. L. Baudour, *Acta Crystallogr Sect. B: Struct. Crystallogr. Cryst. Chem.* **32**, 702–705 (1976).

39 J. L. Baudour, *Acta Crystallogr Sect. B: Struct. Crystallogr. Cryst. Chem.* **47**, 935–949 (1991).

40 H. Kuzmany, A. Imhoff, D. B. Fitchen, A. Sarhangi*. Phys. Rev. B* **26**, 7109–7112 (1982).

41 http://www.gaussian.com/g_tech/g_ur/k_scan.htm

42 G. Heimel, D. Somitsch, P. Knoll, J. L. Bredas, E. Zojer, *J. Chem. Phys.* **122**, 114511 (2005).

43 V. Hernandez, C. Castiglioni, M. Del Zoppo, G. Zerbi, *Phys. Rev. B: Condens. Matter Mater. Phys*. **50**, 9815–9823 (1994).

44 N. I Nijegorodov, S. W. Downey, M. B. Danailov, *Spectrochim. Acta, Part A* **56**, 783–795 (2000).

45 C. X. Cui, M. Kertesz, Y. Jiang, *J. Phys. Chem*. **94**, 5172–5179 (1990).

46 L. W. Shacklette, H. Eckhardt, R. R. Chance, G. G. Miller, D. M. Ivory, R. H. Baughman, *J. Chem. Phys.* **73**, 4098–4120 (1980).

47 G. Zannoni, G. Zerbi, *J. Chem. Phys.* **82**, 31–38 (1985).

48 G. Zerbi, B. Chierichetti, O. Inganas, *J. Chem. Phys*. **94**, 4637–4645 (1991).

49 G. P. Brivio, E. Mulazzi, *Phys. Rev. B* **30**, 876–882 (1984).

50 H. Ohtsuka, Y. Furukawa, M. Tasumi, *Spectrochim. Acta, Part A* **49**, 731–737 (1993).

51 Y. Pelous, G. Froyer, C. Herold, S. Lefrant, *Synth. Met.* **29**, E17–E22 (1989).

52 L. Adamska, I. Nayyar, H. Chen, A. K. Swan, N. Oldani, S. Fernandez-Alberti, M. R. Golder, R. Jasti, S. K. Doorn, S. Tretiak, *Nano Lett*. **14**, 6539–6546 (2014).

Chapter 4

Angew. Chem. Int. Ed. **53**, 7033-7037 (2014)

Properties of Sizeable [n]Cycloparaphenylenes as Molecular Models of Single-Wall Carbon Nanotubes Elucidated by Raman Spectroscopy: Structural and Electron-Transfer Responses under Mechanical Stress

M. Peña Alvarez, P. M. Burrezo, M. Kertesz, T. Iwamoto,
S. Yamago, J. Xia, R. Jasti, J. T. López Navarrete,
M. Taravillo, V. G. Baonza, J. Casado

[n]Cycloparaphenylenes behave as molecular templates of "perfectly chemically defined" single-wall carbon nanotubes. These [n]CPP molecules have electronic, mechanical, and chemical properties in size correspondence with their giant congeners. Under mechanical stress, they form charge-transfer salts, or complexes with fullerene, by one-electron concave–convex electron transfer.

A given [n]cycloparaphenylene ([n]CPP) can be considered as the shortest length cylindrical version of (n,n) armchair single-wall carbon nanotubes (SWCNTs; Figure 1). The unique tubular shape of SWCNTs is key for their outstanding optical, electronic and mechanical properties, which are the basis of their applications as unique nanomaterials.[1,2] However, a full understanding of the molecular foundation of these outstanding characteristics is still incomplete, which is due, among other factors, to difficulties in the chemical definition of SWCNTs, a drawback which is intimately related to current syntheses and the absence of orthodox methods for their bottom-up chemical preparation.[2] In this regard, [n]CPPs are perfectly-defined hydrocarbon compounds envisioned as the cyclization of long linear oligo[n]paraphenylenes,[3-9] and have been already prepared by well-established organic synthetic reactions.[3-9] Very recently, significant progress has been made with the demonstration of the preparation of SWCNTs using [n]cycloparaphenylene molecules as templates.[2a,10]

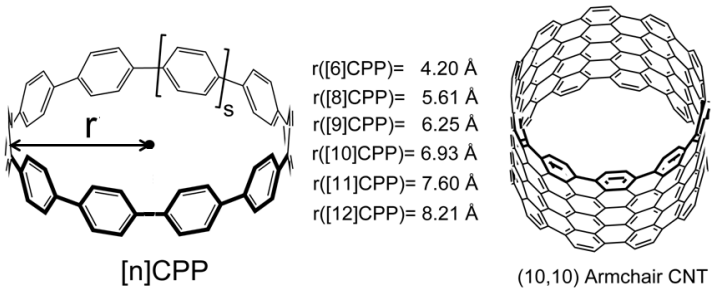

Figure 1. Chemical structure of [n]CPP, n = 6-12, with n = 10–s and s = 4, 3, 2, 1, 0, –1 and –2. r = [n]CPP radius. Radii are taken from ref. 3-9.

In our interest of exploring possible mechanical, chemical and spectroscopic analogies between [n]CPPs and SWCNTs, we here study [n]CPPs in an oligomeric approach to SWCNTs. Furthermore, the study of the [n]CPPs might provide relevant insights about the exclusive properties imparted by their unique *belt*-shape or *nanohoop* structure and relate them to known properties of SWCNTs. Furthermore, [n]CPPs are significant on their own right given their salient optoelectronic and structural properties,[3-9,11] and their host-guest ability to form supramolecular assemblies[7,12] (van der Waals nanotubes). The sizeable radius of the [n]CPPs together with their bendable peripheral cyclic π–electron delocalization provides us with an excellent opportunity to study their electronic, structural and mechanical properties as a function of the precise chemical structure.

Raman spectroscopy has been established as the most suitable tool to probe the molecular and electronic structure of sp^2-carbon nanostructures[13] and to establish structure-property relationships in SWCNTs allowing the formulation of structural-spectroscopic correlations. In particular, the frequency of the radial breathing mode (RBM), ν(RBM), is used to estimate the diameter distribution in SWCNTs based on its linear trend with the inverse of the tube diameter d.[14] Herein, we use Raman spectroscopy to probe the molecular level changes in the electronic structure of [n]CPPs as a function of their sizes/diameters (Figure 1) from [6]CPP to [12]CPP, aiming to get new structural and chemical insights within the context of molecular strain, peripheral or cyclic π–electron delocalization, mechanical flexibility, and host-guest properties. The latter aspect deserves special mention, as we have realized a novel full charge-transfer host-guest complex between [10]CPP and C_{60} promoted under high pressure, which contrasts with that well-known supramolecular complex solely formed by π···π van der Waals concave-convex interactions.[7] The interpretation of these phenomena is guided by quantum-chemical calculations that included full geometry optimizations and frequency and intensity (Raman and IR) calculations at the B3LYP/6-31G* level. Frequencies were scaled with the uniform scaling factor of 0.97.

Figure 2 shows the 785 nm excitation Raman spectra for the seven [n]CPP compounds. The low wavenumber regions of [10]CPP and [12]CPP are clearly dominated by single bands at 286 and 242 cm^{-1}, respectively, that would belong in principle to RBM radial-like modes. To check this hypothesis,

we have carried out quantum chemical calculations of the vibrational Raman spectra for the most stable conformers of the [n]CPPs (Appendix 2, see section S1). We noticed that the two bands above are predicted at 274 and 233 cm^{-1} in [10]CPP and [12]CPP (Appendix 2, see Figures S2.1, S3.1, and S.4.1 and Tables S2.1, S3.1 and S4.1); however, correspond to E_{2g} or E_2 symmetry modes, thus not representing true RBM modes, which are totally symmetric modes. In the shorter [n]CPPs, the low frequency region is much more complex, and only with the help of the predicted theoretical spectra we are able to assign the E_{2g} or E_2 modes in the Raman spectra at 258, 323, 356, 404, and 442 cm^{-1} in [11]-, [9]-, [8]-, [7]- and [6]CPP, respectively. Interestingly, as the radii of these molecules are known (Figure 1), we found a clear linear dependence of their frequencies on $1/d$ (Scheme 1a), which is a unique property of the RBM modes in SWCNTs, so we suggest to label them as pseudo-RBM modes. The calculated spectra also permit to assign the true totally symmetric RBM modes to those bands at 153, 165, 189, and 231 cm^{-1} in [9]-, [8]-, [7]- and [6]CPP, respectively. Interestingly, fitting the frequencies of these modes against $(1/d)$, we obtain a very similar slope (197 nm cm^{-1}) to that typically found in SWCNTs (227 nm cm^{-1}; Scheme 1).

The nearly cylindrical shape of the [n]CPPs implies a strain component on its formation energy which accounts for the positive work owing to rolling and cycling a linear oligophenylene of the same

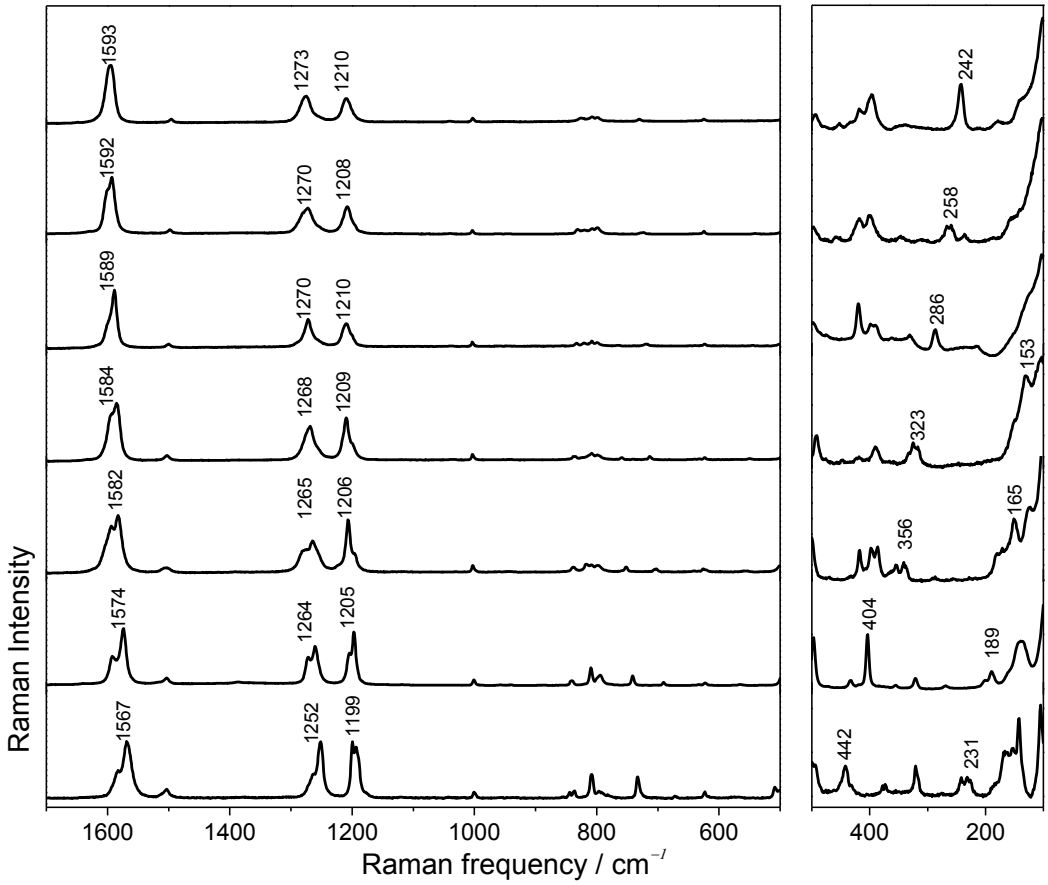

Figure 2. 785 nm Raman spectra of the compounds in solid state at room temperature. From bottom to top: [6]CPP to [12]CPP.

$$\omega_{p-RBM}(cm^{-1}) = (8 \pm 3) + \frac{(375 \pm 3)}{d(nm)} \quad \text{(a)}$$

$$\omega_{RBM}(cm^{-1}) = (-3 \pm 6) + \frac{(197 \pm 5)}{d(nm)} \quad \text{(b)}$$

$$\text{Strain Energy}(kJ/mol) = (14 \pm 7) + (0.74 \pm 0.04) * \omega_{p-RBM}(cm^{-1}) + (3.2 \pm 0.6) \cdot 10^{-4} * \omega^2_{p-RBM}(cm^{-2}) \quad \text{(c)}$$

Scheme 1. $\nu(cm^{-1})$–$(1/d)$ fits for the pseudo-RBM (a), and RBM (b) in [n]CPPs. Strain energy as a function of the pseudo-RBM Raman frequency. See the Appendix 2, Figure S4.2 for details.

size.[15] We have represented in Figure 3 the variation of the strain energy and the pseudo-RBM frequency with the number of rings. As both energetic and spectroscopic parameters display the same trend, the pseudo-RBM frequencies in the [n]CPPs (and the RBM frequencies in SWCNTs) can be considered as experimental observables of the strain energy according to the expression given in Scheme 1. In Figure 3, taking [12]CPP as a reference, we compare both the [n]CPPs pseudo-RBM frequencies and the corresponding RBM ones of (n,n) armchair SWCNTs divided by that of the [12]CPP (E_2) and (12, 12) SWCNTs (A_{1g}), respectively. We observe a good match between these ratios, suggesting that [n]CPPs again mimic the relevant structural properties of SWCNTs, despite their different chemical constitution.

In the 1560-1600 cm^{-1} range the most intense Raman bands appear at 1567 cm^{-1} in [6]CPP, 1574 cm^{-1} in [7]CPP, 1582 cm^{-1} in [8]CPP, 1584 cm^{-1} in [9]CPP, 1589 cm^{-1} in [10]CPP, 1592 cm^{-1} in [11]CPP, and 1593 cm^{-1} in [12]CPP. These bands originate from totally symmetric vibrations arising from collective CC stretching modes of the benzenoid rings along the transversal tube axis direction (Appendix 2, Figures S2.1 and S3.1, and Tables S2.1 and S3.1). All of the [n]CPPs show sub-bands at higher frequencies (1600-1610 cm^{-1}) owing to localized transversal modes, which reside on alternant rings. The transversal character of both bands resemble that of G^+ band in armchair SWCNTs.[16,17] However, no G^- modes are recognized owing to the absence of a well-defined longitudinal direction in the [n]CPPs (Appendix 2, Tables S2.1 and S3.1).[17] These modes derive from 8a mode in benzene, what allows us to analyze the benzoquinonoid nature of such molecular structures. It is well known that 8a mode frequencies around 1600 cm^{-1} are characteristic of benzo-aromatic moieties, while down-shifted frequencies are typical of benzoquinonoid moieties.[18] Such a correlation between Raman frequencies and aromatic-quinonoid character is further corroborated by the oxidation of [10]CPP to its radical cation ([10]CPP$^{\bullet+}$; Figure 5), which unequivocally provokes ring quinonoidization, and shows the main Raman band at 1569 cm^{-1}. The detection of the G bands between 1565-80 cm^{-1} in the shorter [n]CPP indicates that their rings are partially quinonoidized, or that benzene aromaticity is partially broken due to two main effects: 1) The inter-ring connecting carbons become pyramidalized ($sp^2 \rightarrow sp^3$ evolution) and 2) the rings are slightly bent to accommodate the macrocyclic curvature and to mitigate ring strain. The Raman band at 1567 cm^{-1} indicates a benzo-quinonoid structure and strong cycle strain in [6]CPP, while that at 1595 cm^{-1} in [12]CPP reveals a slightly curved macrocycle with a ring aromatic character similar to that of linear oligoparaphenylenes (Appendix 2, Figure S5.1 and Table S5.1). The behavior of these bands has been further investigated as a function of the temperature and irradiation time, allowing interesting conformational properties of the [n]CPPs to be deduced (Appendix 2, Section S8).

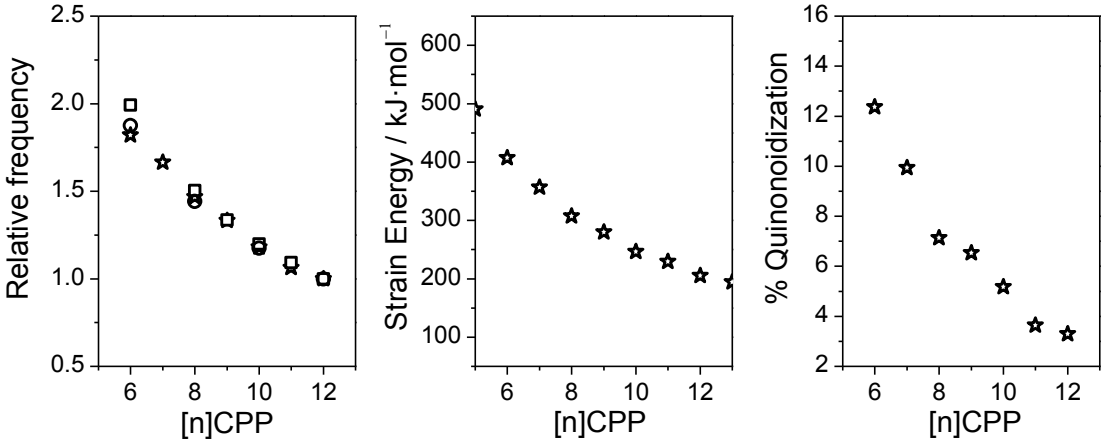

Figure 3. Left: Relative frequency (ν ([n]CPP *pseudo*-RBM *modes*)/(ν ([12]CPP *pseudo*-RBM *mode*) experimental (stars) and theoretical (circles); and (ν((n,n) SWCNT–RBM modes) / ν((12,12) SWCNT-RBM modes) with square symbols) as a function of *n*, SWCNTs data.[16] Middle: Variation of the strain energy[15] of the [n]CPP as a function of *n*. Right: Variation of the per-ring quinonoid character as a function of *n* (see Appendix 2, Section S6 for details).

The force field of a given molecule is the true connection between its vibrational observables (frequencies) and the electron density. A force constant analysis of the 1600 cm^{-1} Raman modes allows us to quantify a degree of quinonoidization close to 12 % per ring for the smallest [6]CPP (Figure 3; Appendix 2, Section S6). This indicates that quinonoidization and $sp^2 \rightarrow sp^3$ re-hybridization owing to the curvature take place only in a moderate degree, which is sufficient to maintain the prevalent aromatic character of the rings as a condition to preserve chemical stability, even in the more strained member of the series [6]CPP. This distinctive partial quinonoid character might provoke an incipient activation for cycloaddition reactions, which would support the demonstration that SWCNTs grow by vertical condensation of [n]CPPs.[2]

Analyzing the bands appearing around 1190-1220 cm^{-1}, it is seen that they mainly emerge from in plane CH bending modes, β(CH), and those around 1260-1270 cm^{-1}, corresponding to ring breathing modes, ν(CC) (Appendix 2, Figure S7.1). The relative Raman intensity ratio, $I_{\nu(C\text{-}C)}/I_{\beta(CH)}$, in linear oligophenylenes has been related to the π–conjugation domain-size as a function of the torsional angle (θ) between neighbouring rings (that is, a larger ratio means higher torsional angle or smaller conjugation).[19] We have obtained $I_{\nu(C\text{-}C)}/I_{\beta(CH)}$ for each [n]CPP (Appendix 2, Figure S7.2) and noticed that it progressively increases with increasing the [n]CPP size. This might reveal smaller conjugation in the largest [12]CPP, thus confirming that in the larger [n]CPPs the behavior is closer to linear oligoparaphenylenes: thus, [12]CPP can be viewed as a collection of short linear oligophenylenes cyclically embedded to form a macrocycle. In this regard, large [n]CPPs behave as nearly equivalent to linear oligoparaphenylenes, which is in agreement with: 1) the almost full aromatic character of the rings in these relatively long compounds; and 2) the exponential variation of the ring strain with size, with a strong attenuation effect starting in [11]-[12]CPP.

Table 1 shows selected data from the optimized theoretical geometries. The inter-ring CC bonds are rather large for [6]CPP, revealing an inefficient orbital overlap between the $2p_z$ orbitals of adjacent benzenes. The rings disclose a typical quinonoidal character ($r_1 < r_2$) that decreases with increasing *n*. The θ inter-ring torsional angle increases with *n*, approaching those predicted for the linear parents. The γ angle (180° in [n]LPP) reveals that the curvature of the macrocycle is attained by forcing it from 180° what further interferes the coupling between vicinal $2p_z$ orbitals. This suggests that cyclic conjugation in the [n]CPPs has a different nature than standard linear conjugation, which is always driven by a maximal inter-ring p_z orbital overlap.

Internal strain can be modulated by application of external stresses or pressures, and such experiments have revealed key information about the structural and mechanical properties of SWCNTs.[20] We have therefore performed series of pressure-dependent Raman experiments using an anvil cell device[21] on the largest and smallest members, [6]CPP to [12]CPP; maximum pressures around 8-10 GPa were achieved. Figure 4 compares the Raman spectra measured at ambient conditions, high pressure, and after pressure release. In [12]CPP, pressure does not seem to cause any irreversible change, in clear contrast to that observed in [6]CPP, where significant frequency and spectral changes are found: the pseudo-RBM mode of [6]CPP shifts to lower values, and the 1600

Table 1. B3LYP/6-31G* optimized geometries of the [n]CPP.[a]

[n]CPP	$r(CC)_{interring}$	$r_1(CC)_{ring}$	$r_2(CC)_{ring}$	θ	γ	θ[b]
6	1.490	1.393	1.410	27.1	150	36.0
8	1.487	1.391	1.407	30.7	157	-
10	1.485	1.392	1.407	32.8	162	-
12	1.484	1.390	1.406	33.5	165	35.9

[a] See the Appendix 2, Section S1 for the definition of the bond distances (Å) and angles (°). [b] [n]LPP

cm^{-1} region is completely modified. The first observation suggests ovalization of the cycle (flattening) and formation of two pseudo-linear segments, more aromatic, which would be responsible of the bands at 1605 cm^{-1}. Such irreversibility in [6]CPP reveals that the cyclic shape collapses below 8 GPa and remains quenched in a sandwiched-like structure when the pressure is released to ambient conditions (see insert in Figure 4), a phenomenon already found in SWCNTs.[22,23] Similar pressure experiments are presented in Appendix 2, Figure S9 for the [n]CPP molecules; changes before and after the pressure cycle are progressively smaller as the size increases, presumably because less strained molecules would require higher pressures to undergo an equivalent permanent deformation.

We have also conducted two challenging experiments under pressure. First, we used a 1:1 [6]CPP and [12]CPP mixtures aiming to encapsulate [6]CPP into [12]CPP just to emulate a ultrashort double walled CNT (DWCNT).[24(a)] The Raman spectra of the mixtures before and after the pressure cycle are displayed in the Appendix 2, Figure S10.1. Very small changes are observed in the Raman spectrum, thus indicating that pressure could promote encapsulation of [6]CPP into the internal cavity of [12]CPP, and thus preventing [6]CPP to collapse. This observation is in good agreement with previous results observed in DWCNTs, where the outer tube acts as pressure protector of the inner tube.[24]

The success of the [6]CPP encapsulation into [12]CPP under pressure, together with the fact that some [n]CPPs can also accommodate C_{60}-fullerene into their internal cavities, led us to explore the properties of C_{60}+[n]CPPs complexes, which is also in clear analogy with the "SWCNT+C_{60} peapods".[25,26] It is π–π interactions that are responsible for the assembly of some [n]CPPs with C_{60}, giving rise to the formation in solution of 1:1 stoichiometric supramolecular complexes driven by a surprisingly high exo-thermicity.[7] In particular, concave-convex π–π interactions are strongly promoted in these complexes owing to the natural curvature adjustment between the [n]CPP host and the C_{60} guest. We prepared 1:1 powdered mixtures of [10]CPP and C_{60} and applied pressures up to 10 GPa, which are well below the 22 GPa limit of chemical stability found for C_{60}.[27] Figure 5 displays the Raman spectra of the mixture recovered at ambient conditions after a pressure cycle. In the spectral range around 1460-1470 cm^{-1} we observe the two strongest Raman bands, one at the same frequency as pristine C_{60}, and another one at 1463 cm^{-1}. In the [10]CPP region at 1570-1600 cm^{-1} we observe a new band at 1569 cm^{-1} while the band at 1589 cm^{-1} disappears. Interestingly, the changes of these Raman bands in the C_{60}@[10]CPP complex formed in solution are very small, in accordance with π–π interactions that are unable to produce appreciable changes in the electronic structure of the individual components (supramolecular effect). Our observations in the experiment

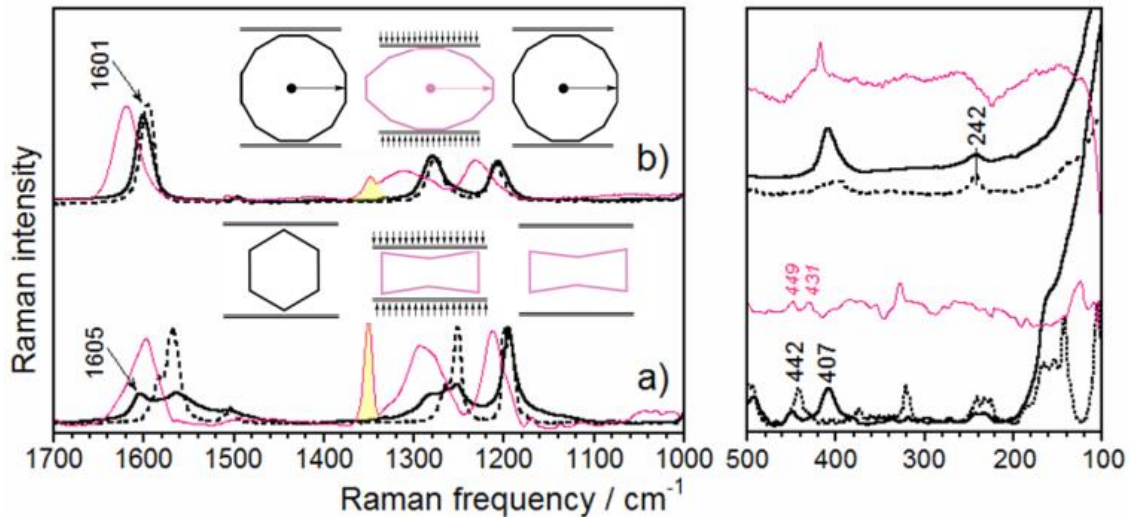

Figure 4. 785 nm Raman spectra of: a) [6]CPP and b) [12]CPP, before (solid line), with an applied pressure around 6 GPa (grey line) and after the pressure release (dotted line). Bands with asterisks correspond to the diamond used as pressure sensor. Inserted schemes represent (from left to right) the molecular models before applied pressure, with applied pressure, and after release.

with pressure substantially differ from that described for the C_{60}@[10]CPP solution complex; as seen in Figure 5, pressure promotes the appearance of new Raman bands that correlate perfectly with those of the C_{60} radical anion ($C_{60}^{\bullet-}$)[27] and [10]CPP radical cation ([10]CPP$^{\bullet+}$).

The straightforward interpretation is that the application of pressure produces the releasing of one electron from the donor [10]CPP to the acceptor C_{60} yielding a charge-transfer charge-separated complex, or a $C_{60}^{\bullet-}$@[10]CPP$^{\bullet+}$ salt. We can reasonably assume that, as already demonstrated herein, pressure might induce flattening of the [10]CPP that approaches the electron-donor surface to the acceptor one to a distance feasible for the electron transfer, which is a situation that is unlikely to occur in solution. This electron-transfer reaction is a good example of the chemical reactivity in the electronic polarized cavity of [n]CPP provided that a suitable sandwiched transition state is formed.

We have also analyzed the frequency of the pseudo-RBM in the $C_{60}^{\bullet-}$@[10]CPP$^{\bullet+}$ complex which upshifts by 8 cm^{-1} (296 cm^{-1}). According to the ($1/d$) frequency dependence, this shift indicates a slight reduction of the [10]CPP size in the complex, or that the [10]CPP$^{\bullet+}$ is "compressed" owing to the loss of one electron and quinonoidization of the structure with the concomitant decrease of the radius (the pseudo-RBM mode in [10]CPP$^{\bullet+}$ alone was undetected). The C_{60} band at 270 cm^{-1} scarcely shifts in the complex, in agreement with the barely observable displacement of just +1 cm^{-1} in K_3C_{60} ($C_{60}^{\bullet3-}$).[27]

Finally, similar complexation experiments of C_{60} under pressure have been carried out with [9]CPP and [11]CPP (Appendix 2, Figure S11.1). In the former case, the 1585 cm^{-1} band is displaced to 1561 cm^{-1}, in agreement with the formation of a radical cation quinonoidal structure. Noticeably, this band is displaced to lower frequencies relative to [10]CPP$^{\bullet+}$, as a sign of the attainment of a larger quinonoidization in the shorter phenylene core. No appreciable spectral changes were observed in the experiment of C_{60} under pressure with [11]CPP, which is probably due to a lack of size matching.

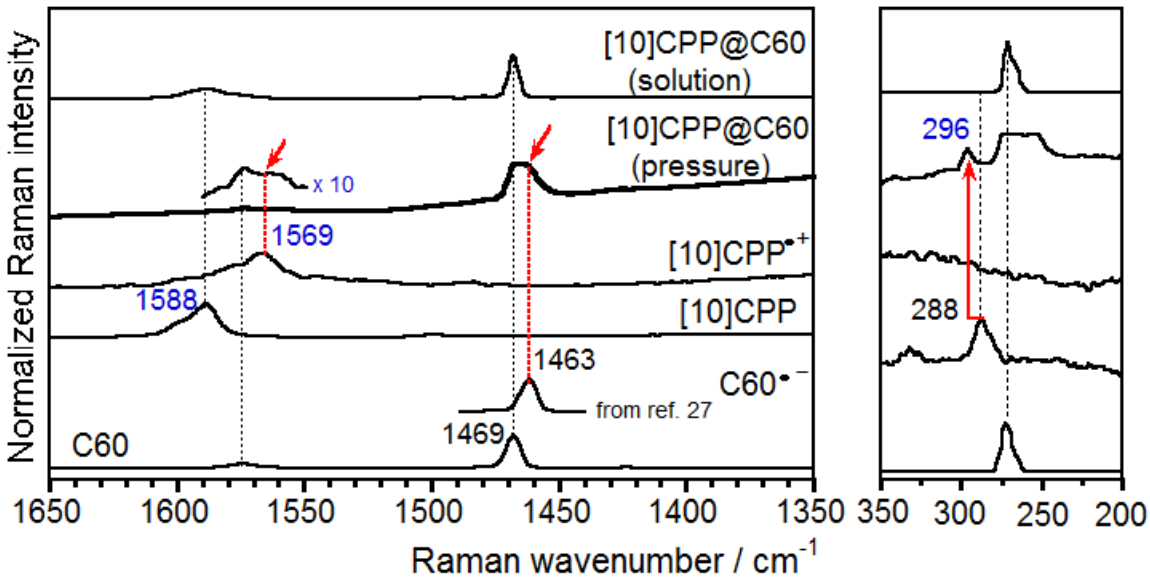

Figure 5. 785 nm Raman spectra of 1:1 $CHCl_3$ solution mixtures of [10]CPP and C_{60} and in solid state after the application of a 6 GPa pressure. The spectra of the neutral C_{60} and [10]CPP together with those of the C_{60} anion and of CPP radical cation are also shown.

In summary, we have performed a thorough study of the Raman properties of [n]cycloparaphenylenes, which can be considered as the first molecularly well-defined models of SWCNTs. We provide with some spectroscopic-structural relationships between: 1) the parallel behavior and dependence of the pseudo-RBMs in [n]CPPs with those RBM of (n,n) armchair SWCNTs;

2) the ring cyclic strain, molecular-level benzene quinonoidization and ring size; and 3) the transformation of "pure" cyclic π–electron conjugation into *pseudo*-linear conjugation (cyclically embedded). On the other hand, high-pressure studies allow: 1) new insights on the plastic and conformational properties of these nanohoop-shaped systems; and 2) proposal of the formation of a charge transfer complex, $C_{60}^{\bullet-}$@[10]CPP$^{\bullet+}$, as a further progress relative to the already-known π–π van der Waals C_{60}@[10]CPP supramolecular analogue. Overall, our study is a complete initiative to correlate structural, spectroscopic and chemical properties in well-defined [n]CPP models and to relate such properties with those of SWCNTs.

References

1 M. J. O´Connell, *Carbon Nanotubes: Properties and Applications*, Taylor&Francis, Boca Raton (2006); P. J. F. Harris, *Carbon Nanotube Science: Synthesis, Properties and Applications,* Cambridge University Press, Cambridge (2009).

2 (a) *Carbon nanotubes and Related structures. Synthesis, Characterization, Functionalization and Properties* (Eds.: N. Martín, D. M. Guldi), Wiley-VCH, Weinheim (2010). (b) R. Saito, G. Dresselhaus, M. S. Dresselhaus, *Physical Properties of Carbon Nanotubes,* Imperial College Press, London (1998).

3 R. Jasti, J. Bhattacharjee, J. B. Neaton, C. R. Bertozzi, *J. Am. Chem. Soc.* **130**, 17646–17647 (2008).

4 J. Xia, R. Jasti, *Angew. Chem. Int. Ed.* **51**, 2474–2476 (2012); T. J. Sisto, M. R. Golder, E. S. Hirst, R. Jasti, *J. Am. Chem. Soc.* **133**, 15800–15802 (2011); T. J. Sisto, R. Jasti, *SynLett.* **23**, 483–489 (2012); E. S. Hirst, R. Jasti, *J. Org. Chem.* **77**, 10473–10478 (2012); R. Jasti, C. R. Bertozzi, *Chem. Phys. Lett*. **494**, 1–7 (2010); J. Xia, J. W. Bacon, R. Jasti, *Chem. Sci.* **3**, 3018–3021 (2012).

5 M. R. Golder, B. M. Wong, R. Jasti, *Chem. Sci*. **4**, 4285–4291 (2013); E. Kayahara, T. Kouyama, T. Kato, H. Takaya, N. Yasuda, S. Yamago, *Angew. Chem. Int. Ed.* **52**, 13722–13726 (2013); A. V. Zabula, A. S. Filatov, J. Xia, R. Jasti, M. A. Petrukhina, *Angew. Chem. Int. Ed.* **52**, 5033–5036 (2013).

6 T. Iwamoto, Y. Watanabe, Y. Sakamoto, T. Suzuki, S. Yamago, *J. Am. Chem. Soc.* **133**, 8354–8361 (2011); S. Yamago, Y. Watanabe, T. Iwamoto, *Angew. Chem. Int. Ed.* **49**, 757–759 (2010); E. Kayahara, Y. Sakamoto, T. Suzuki, S. Yamago, *Org. Lett.* **14**, 3284–3287 (2012).

7 T. Iwamoto, Y. Watanabe, T. Sadahiro, T. Haino, S. Yamago, *Angew. Chem. Int. Ed.* **50**, 8342–8344 (2011).

8 H. Omachi, S. Matsuura, Y. Segawa, K.Itami, *Angew. Chem. Int. Ed.* **49**, 10202–10205 (2010).

9 H. Takaba, H. Omachi, Y. Yamamoto, J. Bouffard, K. Itami, *Angew. Chem. Int. Ed.* **48**, 6112–6116 (2009); Y. Segawa, S. Miyamoto, H. Omachi, S. Matsuura, P. Senel, T. Sasamori, N. Tokitoh, K. Itami, *Angew. Chem. Int. Ed.* **50**, 3244–3248 (2011); H. Omachi, Y. Segawa, K. Itami, *Acc. Chem. Res.* **45**, 1378–1389 (2012); Y. Ishii, Y. Nakanishi, H. Omachi, S. Matsuura, K. Matsui, H. Shinohara, Y. Segawa, K. Itami, *Chem. Sci.* **3**, 2340–2345 (2012).

10 H. Omachi, T. Nakayama, E. Takahashi, Y. Segawa, K. Itami, *Nat. Chem.* **5**, 572–576 (2013).

11 Y. Segawa, A. Fukazawa, S. Matsuura, H. Omachi, S. Yamaguchi, S. Irle, K. Itami, *Org. Biomol. Chem.*, *10***,** 5979–5984 (2012); C. Camacho, T. A. Niehaus, K. Itami, S. Irle, *Chem. Sci.* **4**, 187–195 (2013); T. Nishihara, Y. Segawa, K. Itami, Y. Kanemitsu, *J. Phys. Chem. Lett.* **3**, 3125–3128 (2012).

12 U. H. F. Bunz, S. Menning, N. Martín, *Angew. Chem. Int. Ed.* **51**, 7094–7101 (2012); S. Schrettl, H. Frauenrath, *Angew. Chem. Int. Ed.* **51**, 6569–6571 (2012).

13 M. S. Dresselhaus, A. Jorio, R. Saito, *Annu. Rev. Condens. Matter Phys*. **1**, 89–108 (2010).

14 C. Thomsen, S. Reich, *Light Scattering in Solid IX, Topics Appl. Physics*, **108***,* 115–232 (2007).

15 Y. Segawa, H. Omachi, K. Itami, *Org. Lett.* **12**, 2262–2265 (2010).

16 E. H. Haroz, J. G. Duque, X. Tu, M. Zheng, A. R. Hight Walker, R. H. Hauge, S. K. Doorn, J. Kono, *Nanoscale* **5**, 1411–1439 (2013).

17 A. Jorio, A. G. Souza Filho, G. Dresselhaus, M. S. Dresselhaus, A. K. Swan, M. S. Ünlü, B. B. Goldberg, M. A. Pimenta, J. H. Hafner, C. M. Lieber, R. Saito, *Phys. Rev. B* **65***,* 155412 (2002).

18 L. Cuff, C. Cui, M. Kertesz, *J. Am. Chem. Soc.* **116**, 9269–9274 (1994); J. Casado, S. Patchkovskii, M. Z. Zgierski, L. Hermosilla, C. Sieiro, M. M. Oliva, J. T. López Navarrete, *Angew. Chem. Int. Ed.* **47***,*

1443–1446 (2008); S. R. González, Y. Ie, Y. Aso, J.-T. López Navarrete, J. Casado, *J. Am. Chem. Soc.* **133**, 16350–16353 (2011).

19 G. Heimel, D. Somitsch, P. Knoll, J. L. Brédas, E. Zojer, *J. Chem. Phys.* **122**, 114511 (2005).

20 A. San-Miguel, *Chem. Soc. Rev*. **35**, 876–889 (2006).

21 V. G. Baonza, M. Taravillo, A. Arencibia, M. Cáceres, J. Núñez, *J. Raman Spectrosc.* **34**, 264–270 (2003).

22 Z. S. Zhao, X. F. Zhou, M. Hu, D. L. Yu, J. L. He, H.-T. Wang, Y. J. Tian, B. Xu, *J. Superhard Mater.*, **34**, 371–385 (2012).

23 M. Yao, Z. Wang, B. Liu, Y. Zou, S. Yu, W. Lin, Y. Hou, S. Pan, M. Jin, B. Zou, T. Cui, G. Zou, B. Sundqvist, *Phys. Rev. B* **78**, 205411 (2008).

24 (a) E. del Corro, J. González, M. Taravillo, E. Flahaut, V. G. Baonza, *Nano Lett*. **8**, 2215–2218 (2008). (b) A. L. Aguiar, E. B. Barros, R. B. Capaz, A. G. Souza Filho, P. T. C. Freire, J. Mendes Filho, D. Machon, Ch. Caillier, Y. A. Kim, H. Muramatsu, M. Endo, A. San-Miguel, *J. Phys. Chem. C* **115**, 5378–5384 (2011).

25 B. Anis, F. Börrnert, M. H. Rümmeli, C. A. Kuntscher, *J. Phys. Chem. C* **117**, 21995–22001 (2013).

26 B. W. Smith, M. Monthioux, D. E. Luzzi, *Nature* **396**, 323–324 (1998).

27 M. S. Dresselhaus, G. Dresselhaus, P. C. Eklund, *J. Raman Spectrosc*. **27**, 351–371 (1996).

Chapter 5

Faraday Discussions **173**, 157-171 (2014)

Chameleon-like Behaviour of Cyclo[n]paraphenylenes in Complexes with C_{70}. On their Impressive Electronic and Structural Adaptability as Probed by Raman Spectroscopy

M. Peña Alvarez, P. M. Burrezo, T. Iwamoto, L. Qiu,
M. Kertesz, M. Taravillo, V. G. Baonza,
J. T. López Navarrete, S. Yamago, J. Casado

A series of four 1:1 host-guest supramolecular complexes of [n]CPPs and C_{70} have been analyzed by Raman spectroscopy in solid state and complemented with the analysis of their spectroscopic responses under mechanical and thermal stresses. By following the frequency behaviour of the G and RBM modes we have found that [10]CPP in the C_{70}@[10]CPP complex displays a more "ordered" structure. However, in C_{70}@[11]CPP, the nanoring becomes oval-shaped with closer contacts with the C_{70} poles and less conformational restriction in the flattened region. By mechanical and thermal stresses we are able to modify the lying conformation of C_{70}@[10]CPP towards a standing orientation. C_{70}@[11]CPP resists pressure changes, although it tends to shift from the standing to the lying orientation by heating. As for the crystal cell, the [n]CPPs occupy the residual empty spaces while the main crystallographic positions are reserved for C_{70}. These are new examples of the impressive adaptability of the [n]CPP molecules to different physico-chemical environments, a chameleon-like property which reveals the delicate equilibrium provided by cyclic conjugation and ring strain.

A Introduction

Cyclo[n]paraphenylenes (abbreviated as [n]CPP, see Fig. 1) are a class of conjugated pure-hydrocarbon molecules featuring a cyclic disposition of 1,4 substituted benzenes with the p_z carbon orbitals oriented towards the macroring center. Given their aesthetic shape, they attracted the interest of chemists for a long time.[1] It was in 2008 when Jasti and Bertozzi[2] were able to synthesize cyclo[n]paraphenylene compounds for the first time, [8]CPP, [12]CPP and [18]CPP, paving the way for the preparation of [n]CPP of almost all sizes, [6]- to [18]CPP, in a beautiful competition race mainly between the groups of Itami,[3] Yamago[4] and Jasti.[5] Very recently, the smallest member of the series, [5]CPP, has been successfully prepared almost simultaneously by Yamago and Jasti.[6]

The analogy between [n]CPPs and armchair single wall carbon nanotubes (SWCNT) is straightforward: the [n]CPP can be considered as the shortest version of arm-chair SWCNTs and, as such, can be considered as their molecular models. While the chemical lack of definition of SWCNTs is an insurmountable obstacle for the full understanding of their properties, the perfect knowledge of the chemical structures of the [n]CPP series allows researchers to evaluate the evolution of their electronic, structural and optical properties as a function of the [n]CPP size, thus permitting the first *oligomeric approach* to the physical properties of SWCNT. But [n]CPPs have been also used as templates for the chemical synthesis of SWCNT via a controlled vertical condensation of [n]CPP, as reported by Itami,[7] which is considered the first successful preparation of nanotubes by using an orthodox synthetic organic approach. In their own way, the [n]CPPs display very interesting optoelectronic properties as well thanks to the co-existence of rather unusual effects such as molecular strain and cyclic conjugation. Cyclic strain increases with the decrease of the number of benzenes[8] and produces in these rings some slight deformations from planarity and their partial benzo-quinonoidization.[9] On the other hand, cyclic conjugation, which is provided by these p_z orbitals contained in the circumferential molecular plane, further stabilizes the whole cyclic arrangement. As a result, these appealing molecules contain highly polarisable electronic shapes in the belt which originate other interesting chemical properties such as the ability to form host-guest π–π and van der Waals supramolecular complexes. These complexes are the focus of this article.[10]

We have recently reported on the dependence of the structural and electronic properties of the [n]CPPs (from [6]CPP to [12]CPP) with their size, and established robust relationships between quinonoidization, cyclic strain, cyclic conjugation and [n]CPP dimension, using Raman spectroscopy as the revealing tool.[11] Another structural feature of significance is their conformational effect that makes these [n]CPPs irregular cylinders with the successive benzenes canted or staggered with opposite angles.[8,9] We have also addressed the structural flexibility of the whole nanohoop which, for the larger compounds, is able to undergo reversible ovallisation under strong mechanical stress.[11] The ability to re-adapt their shapes, their inner empty cavity, and the capacity to promote favourable surrounding π–π electronic interactions, are the basis for the formation of the 1:1 stoichiometric complexes.[10]

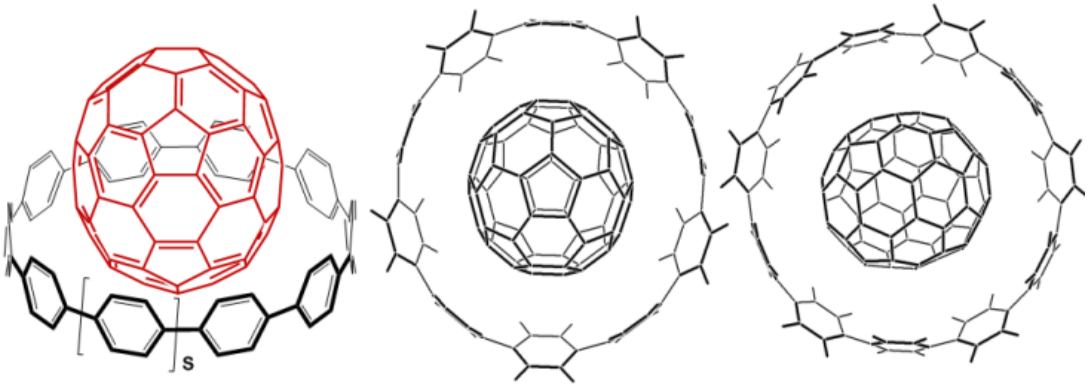

Fig. 1 Left: chemical structures of the [n]CPP compounds (s = 0 for [9]CPP, s = 1 for [10]CPP, s = 2 for [11]CPP and s = 3 for [12]CPP). Middle: lying disposition for C_{70}@[10]CPP. Left: standing disposition for C_{70}@[11]CPP.

In this paper, we go a step further in these studies of [n]CPPs and address in detail the conformational and electronic effects of new [n]CPP complexes with a new guest, such as C_{70}.[12] The oval shape of this fullerene will allow us to get new insights of the connection between [n]CPP shape, its conformational plasticity and the electronic properties of the formed complexes. The whole study will be carried out by using Raman spectroscopy as the structural and electronic diagnostic tool. Raman spectroscopic properties will be investigated as a function of mechanical stress (pressure dependent measurements) and thermal stress (temperature dependent measurements). With this study we aim to provide new features of the particular physical and chemical properties of [n]CPP resulting from their impressive propensity to reshape their structures.

B Experimental Procedures and Technical Details

The syntheses of the [n]CPP and of their complexes with C_{70} have been published elsewhere.[12] The samples were studied as pure solids, and these were well characterized by different analytical and crystallographic techniques.

Raman measurements were carried out with a Senterra dispersive micro-Raman spectrometer from Bruker with a 785 nm laser as the excitation source. The Raman scattering radiation was collected in a back–scattering configuration with a standard spectral resolution of 3 cm^{-1}, a spatial resolution of 0.5 μm, and a spot size of about 3 μm.

High pressure studies were conducted in a sapphire anvil cell (SAC) with a culet diameter of 400 μm and a gold gasket.[13,14] No pressure transmitting medium was used and diamond chips were placed as the pressure calibrants. The Raman experiments were carried with the same Senterra microscope with 785 nm laser excitation. The recovered samples, after pressure cycles, were also analyzed, taking several spectra on different sample points to confirm the reproducibility on the same sample and to ensure whether the transformation of the samples is complete or not.

Laser excitation time dependent measurements were carried out in the micro-Raman spectrometer (BWTEK Voyage™ BWS435-532SY) with an excitation wavelength of 532 nm. These experiments were repeated at different temperatures ranging from 298 to 523 K. The [8]CPP sample was placed in a Pt crucible and situated inside the high temperature stage system (Linkam TS1500 with a T95 system controller). This system can heat within a temperature range from ambient up to 773 K, allowing us to observe and characterize samples through its quartz lid window. The high temperature stage system was equipped with a Pt/Rh thermocouple in direct contact with the ceramic heating element to detect and control the sample temperature. During the experiments, the temperature was stabilized within ± 0.1 degrees. It was necessary to wait between 10 and 15 minutes for the sample to have a uniform temperature. Variable temperature Raman experiments on the complexes were carried out in the same Linkam TS1500 device but the excitation laser used was the 785 nm of the Senterra dispersive micro-Raman spectrometer from Bruker.

C Vibrational Raman Antecedents on [n]CPPs

The Raman spectra of [n]CPPs are characterized by the existence of four main Raman bands which constitute the fingerprint of their structure and electronic shapes.[11] For our discussion in this paper we will focus only in two: i) the strongest band of the spectrum at 1580-1600 cm^{-1} which corresponds to the analogue G mode in SWCNTs (in our [n]CPP we call it as G mode as well) and is described as a CC stretching mode along the tangential direction of the tube. This G mode is composed of two sub-bands, the so-called G_1 and G_2 modes (see Fig. 2 and Fig. S1 of Appendix 3). The frequency of the G_1 band in the [n]CPPs has been related to the degree of quinonoidization of the benzene units due to the cyclic strain. And ii) the pseudo-radial breathing modes in our [n]CPPs which are related with the radial breathing vibrational mode of SWCNTs, a molecular motion that takes place along the radial direction of the tube and appears in the 400-100 cm^{-1} range. From a structural-spectroscopy relationship, the frequency of this pseudo-RBM band is quite sensitive to the cyclic radius (and therefore size) of the [n]CPP.

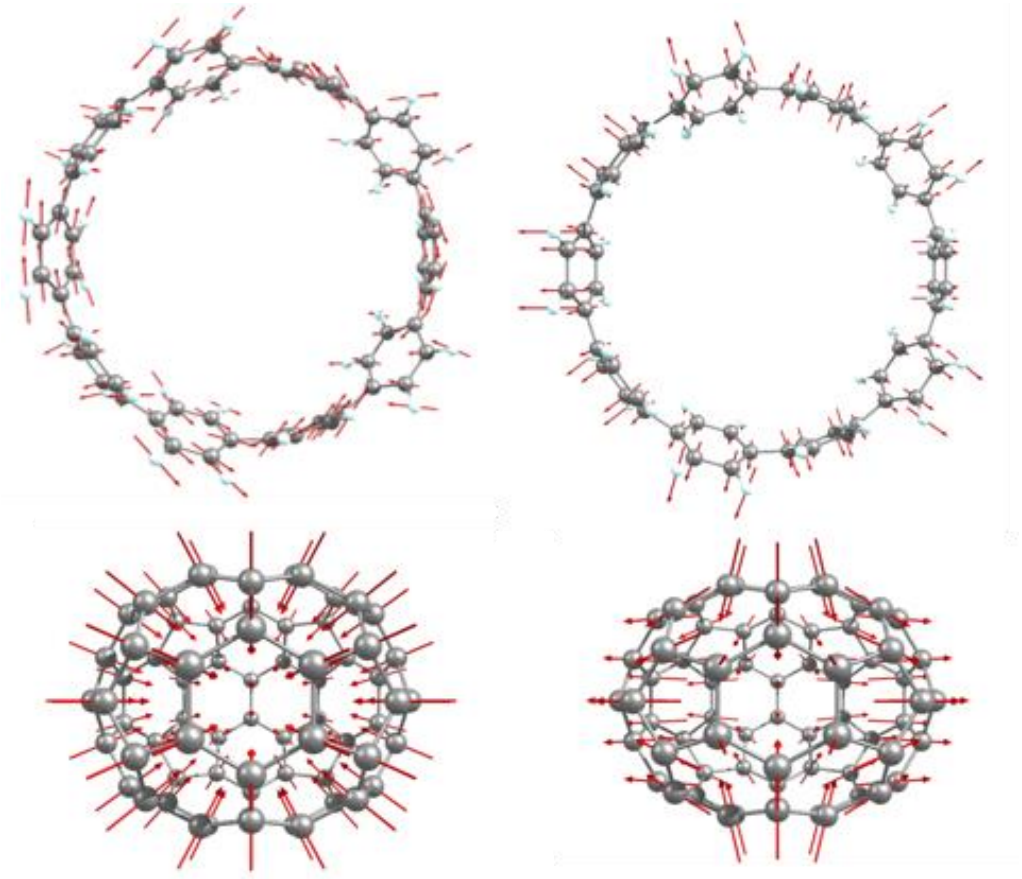

Fig.2 Top: vibrational modes associated with the G_1 band of [10]CPP (left) with its pseudo radial breathing mode (right) from reference 11. Bottom: radial breathing mode (left) and radial-like breathing mode (right, squashing mode) of C_{70}, in the experimental spectrum these modes are observed at 456 and 256 cm^{-1}, respectively.

It is interesting to note the nature of the main Raman bands of the Raman spectrum of C_{70}, or those at: i) 1564 cm^{-1} which is due to a tangential CC stretching mode or G-like mode; ii) 456 cm^{-1} which is the radial breathing mode with slightly more vibrational amplitudes along the *long* axial direction of the ellipsoid. And iii) 256 cm^{-1} which also corresponds to a sort of breathing radial-like mode (squashing mode) featuringthe main vibrational amplitudes in the atoms placed in the equatorial segment of C_{70}.[15] Fig. 2 depicts the normal modes associated to most of these relevant bands (see Fig. S2 of Appendix 3 for further information).

D Conformational Studies

In this section we will address the analysis of the conformational properties of the [n]CPP as individual entities with the objective of understanding them before the CPP assemblies with C_{70} fullerene. To this end, we have studied the effect that simultaneous thermal and laser excitation stresses cause on the [n]CPP spectra. Fig. 3 shows the time evolution of the Raman spectra of [8]CPP, as a prototypical example, at 25 °C by exciting with the 2.33 eV laser. It must be indicated the same experiments with low energy Raman excitation at 1064 nm did not produce any spectral change.

Changes in the spectra are clearly visible resulting in a new peak at 1604 cm^{-1}. The time growth of the integrated area of this band (relative to that at 1582 cm^{-1}) allows us to obtain the rate constant for the process which, studied as a function of the temperature, gives us the activation barriers associated with the conversion towards the structure responsible for the new Raman component. For the growth of the 1604 cm^{-1} band a value of E_a = (19.9 ± 1.3) kJ mol^{-1} is determined. This activation energy is different depending on the [n]CPP size, for instance, in [12]CPP the strongest 1594 cm^{-1}

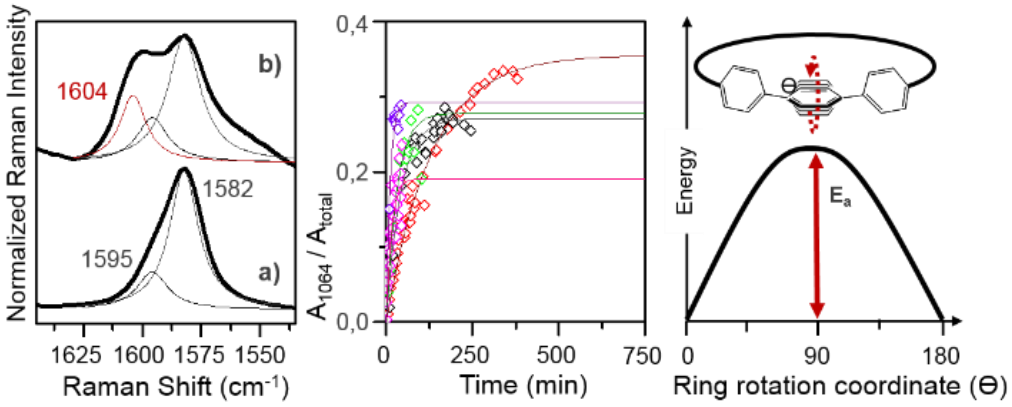

Fig.3 532 nm Raman spectra of [8]CPP. a) Deconvoluted spectrum at the start at 298 K; b) deconvoluted spectrum recorded after exposition time to the laser radiation of about 300 min at 298 K. Middle: ratio between the area of the 1604 cm^{-1} band and the total area of these features as a function of the exposition time to the laser radiation at several temperatures; red (298.15 K), black (348.15 K), green (373.15 K), violet and pink (423.15 K). Right: representation of the ring rotation with its energy barrier.

band also evolves into the new band at 1604 cm^{-1} with a value of E_a = (22.0 ± 2.0) kJ mol^{-1}.[8,9] These experimental activation energies are in excellent agreement with those energy barriers calculated for the full rotation of a given benzene regarding their vicinal rings around the inter-ring C-C bonds. As a result, the energy barriers for the conversion into a species with a new band up-shifted (1604 cm^{-1} bands) with regards to the original ones is consistent with the transformation into a more distorted or staggered conformation among the successive rings of the cycle, where these barriers might be viewed as the maximal energy costs for full rotation (Fig. 3). We speculate that the need of assistance by high energy radiation to develop the conformational effect can be explained by the formation after light absorption of an excited state closely related with the transient state of this internal rotation.

E Complexation of [n]CPP with C_{70}: the 1:1 Complexes

On the Interpretation of the G Modes of the [n]CPP

Fig. 4 and 5 display the Raman spectra of the 1:1 complexes, [10]CPP and [11]CPP; [9]CPP and [12]CPP, respectively. The solid state structures of [10]CPP and [11]CPP have been fully characterized by X-ray diffractometry in the solid state and by UV-Vis electronic absorption spectroscopy in solution.[12] For the shorter and larger complexes, no crystallographic data are available. At a first sight, in comparison with the respective [n]CPP, complexation induces much larger changes on the Raman spectra of [10]CPP and [11]CPP compared to those of [9]CPP and [12]CPP.

For C_{70}@[10]CPP, the G_1 mode frequency of [10]CPP changes from 1589 cm^{-1} to 1581 cm^{-1} in the complex. We have previously assigned the down-shift behaviour of the G_1 band in [n]CPP to the quinonoidization effect of the benzene rings that simultaneously brings the formation of less staggered structures between successive benzene rings (this effect is called below the "ordering" effect in the belt). A decrease in the number of benzene rings producing more effective cyclic conjugation gives also rise to a more quinonoid less staggered alternating ring sequence. A clear example of the connection between Raman down-shifts and quinonoidization is shown in the oxidation of a given cycloparaphenylene compound to its radical cation.[11] Therefore, the –8 cm^{-1} down-shift of the G_1 band on [10]CPP → C_{70}@[10]CPP can be attributed to the "ordering" effect on the cycloparaphenylene structure as a result of the template effect that the C_{70} fullerene exerts on it, mediated by the attractive π–π forces established between both compounds in the complex. Solid state studies on C_{70}@[10]CPP reveal that the C_{70} fullerene occupies the internal cavity of the

cycloparaphenylene with the CPP belt surrounding the shortest axis or equatorial segment of the fullerene ellipsoid, or *lying* disposition (see Fig. 1).[12] The size of this short axis of C_{70} is 0.712 nm which, compared with the diameter of [10]CPP, 1.380 nm, anticipates a favourable interaction between the two units with very suitable 0.33 nm van der Waals distances. As a result of the interaction on the circular equator, [10]CPP does not deform its cyclic shape which, together with the better alignment of the consecutive rings, favours cyclic electron delocalization as the origin of the Raman down-shift (lower torsional angles than in the pristine molecules, see Fig. S3a in Appendix 3).

The Raman behaviour in the case of the C_{70}@[11]CPP complex is different. The G_1 band, at 1592 cm^{-1} in the individual [11]CPP, up-shifts to 1596 cm^{-1}, by +4 cm^{-1}. In contrast to the case of C_{70}@[10]CPP, we should associate these changes also to the conformational effect, but in this case caused by a more staggered benzene ring distribution in the cycloparaphenylene (higher torsional angles between neighbouring benzenes, supported by the 1200 cm^{-1} spectral region behaviour, see Fig. S3b in Appendix 3). We have also shown that the formation of this more inter-ring distorted shape induces the diminishing of the quinonoidal character, reverting towards a more aromatic form, justifying the up-shift of the G_1 band. The size of the C_{70} long axis is 0.796 nm while the [11]CPP diameter is 1.51 nm, thus it anticipates the two structures will interact by van der Waals interactions along the long C_{70} axes. Indeed, the solid state structure of C_{70}@[11]CPP has been resolved, in which C_{70} adopts a *standing* conformation (see Fig. 1) where the maximal coupling is through the two poles of C_{70} with the CPP rings of the belt all residing along the long axis of the ellipsoidal fullerene (this contrasts with the coupling through the equatorial part in C_{70}@[10]CPP).[12] As a result of this disposition, the [11]CPP undergoes a deformation of the cylindrical shape towards a more ellipsoidal flattened shape. This description is nicely in agreement with: i) our previous publication[11] where we have described the great flexibility of the CPP compounds in a series of detailed studies as a function of variable pressure. We have shown that by applying mechanical stress to the samples these reversibly deformed into oval or flattened shapes. This mechanical deformation was followed by Raman spectroscopy which probed a frequency up-shift, in two linear regimes, with the increment of pressure such as observed here for the same G modes on [11]CPP → C_{70}@[11]CPP; ii) the argument that in order to stabilize the standing conformation the benzenes placed in the equatorial side, given its unsuitable disposition for π–π coupling, would prefer to slightly rotate in order to promote energetically favourable hydrogen-C_{70} or H····π interactions[16] which might result again in a more staggered disposition for these benzenes also contributing to the Raman up-shift. This explanation would support an increment of entropy in the complexation reaction regarding the [11]CPP and C_{70} reactants, such as deduced experimentally, thus allowing us to understand the entropy controlled regime for the exergonic formation reaction of this complex.[12]

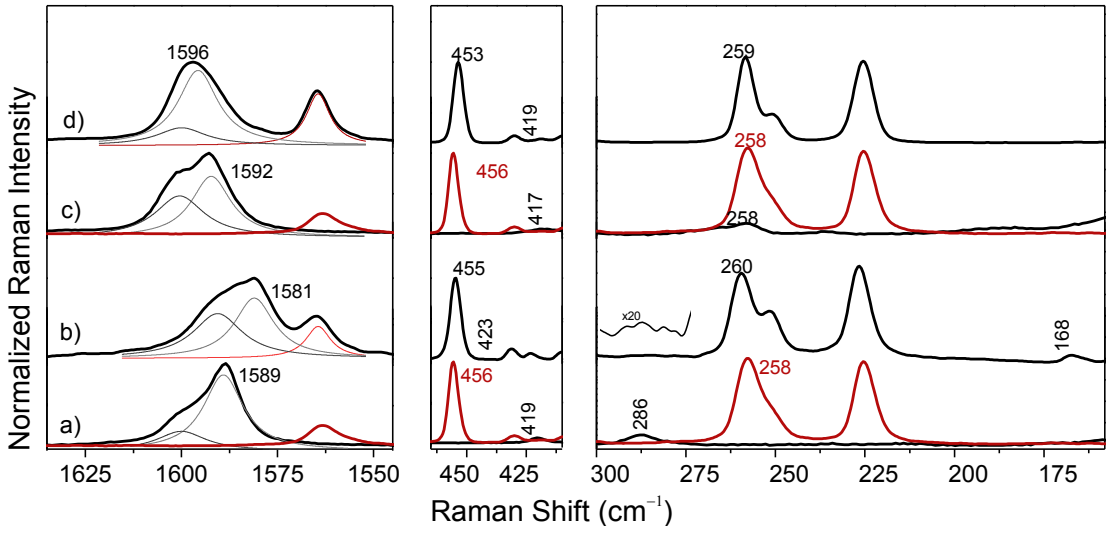

Fig.4 Solid state 785 nm Raman spectra at 25 °C of: a) [10]CPP (black) and C_{70} (red); b) C_{70}@[10]CPP; c) [11]CPP (black) and C_{70} (red); d) C_{70}@[11]CPP. Thin lines correspond to the deconvoluted bands.

On the Interpretation of the [n]CPP RBMs

The low frequency region 500-100 cm^{-1} of the Raman spectra of the [n]CPPs is important because of the presence of the pseudo-RBM modes (see Fig. 2) whose frequencies also account for the alteration of their donut-like cylindrical shape with the formation of the complexes in the solid state. In [10]CPP and [11]CPP the pseudo-RBMs were assigned to the bands at 286 cm^{-1} and 258 cm^{-1} respectively, while the RBM modes were not detected in their Raman spectra.[11] After formation of the complexes in the low frequency region, the spectra are clearly dominated by the C_{70} Raman bands which mostly mask the Raman fingerprint of the cycloparaphenylene unit. In spite of this, three main findings need to be mentioned: i) the pseudo-RBM modes, which seemingly disappear after complexation; ii) in C_{70}@[10]CPP a completely new feature appears in the spectrum at 168 cm^{-1}; and iii) in the region around 500-400 cm^{-1} there is a band at 423 cm^{-1} in C_{70}@[10]CPP which evolves from the [10]CPP one at 419 cm^{-1} and at 419 cm^{-1} in C_{70}@[11]CPP from that at 417 cm^{-1} in [11]CPP. It seems that the interaction in the complex drastically alters the dynamics of the pseudo-RBM modes provoking their disappearance. Simultaneously, the same electronic effect might give extra-intensity to the formerly weak (undetectable) RBM modes which emerges in the complex at 168 cm^{-1} (in the individual [n]CPP this mode would be expected to appear below 150 cm^{-1}). It might be argued that the slight symmetrical compression of [10]CPP around C_{70} could provoke a slight reduction of its diameter and, as a consequence, an increase of the RBM frequency given the reciprocal relationship between the RBM frequency and the diameter of the cylinder. Similar reasons can account for the frequency up-shifts of the 430-400 cm^{-1} bands from the unperturbed CPPs.

On the Interpretation of the C_{70} Fullerene Modes

Complexation has a much smaller impact on the Raman frequencies of the C_{70} fullerene, given its rigidity, which contrasts with the elasticity of the CPPs. However, there are two interesting features in the spectra of the complexes compared to that of C_{70} alone: i) the analogue radial breathing mode of C_{70} at 456 cm^{-1} (main atomic displacements lie along the long axis and on the poles of the ellipsoid, see Fig. 2) changes by –1 cm^{-1} in C_{70}@[10]CPP and by –3 cm^{-1} in C_{70}@[11]CPP, the latter being the

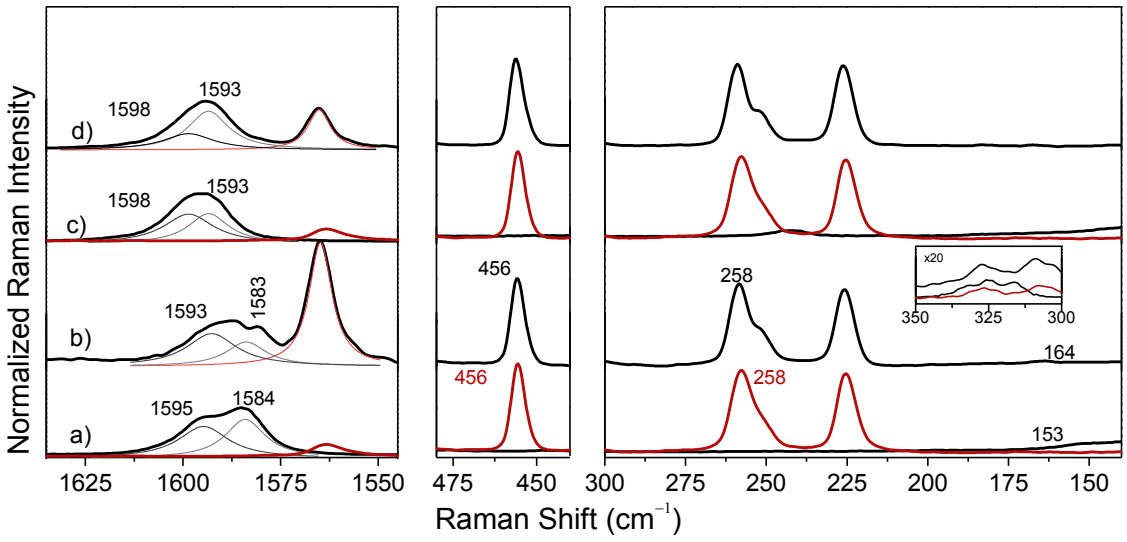

Fig.5 Solid state 785 nm Raman spectra at 25 °C of: a) [9]CPP (black) and C_{70} (red); b) C_{70}@[9]CPP; c) [12]CPP (black) and C_{70} (red); d) C_{70}@[12]CPP. Thin lines correspond to the deconvoluted bands.

greatest in agreement with the formation of the standing complex where the strongest interaction between [11]CPP and C_{70} goes through these polar regions of the ellipse; and ii) another radial breathing mode of the C_{70} is that at 256 cm^{-1} (squashing mode, with main atomic displacements on the equator of the ellipse, see Fig. 2) which appear at +2 cm^{-1} in C_{70}@[10]CPP and at +1 cm^{-1} in

C_{70}@[11]CPP, the former being the greatest in agreement with the formation of the lying complex where the strongest interaction between [10]CPP and C_{70} goes through the equatorial belt of the fullerene. These are remarkable observations, since in SWCNTs peapods of C_{70}, not significant observations have been achieved on the C_{70} orientation changes along the SWCNT, due mainly to the lack of diameter, and thus of conformational, purity in the SWCNT samples. However, it is straightforward that C_{70} it is vibrationally affected by its orientation inside the tube cavity, as observed on CPPs.

The Spectra of C_{70}@[9]CPP and C_{70}@[12]CPP

Their Raman spectra in Fig. 5 display small, but appreciable, differences regarding the superposition spectrum of the individual components. In spite of the fact that their innermost cavities are either too small or large to accommodate C_{70} ([9] and [12]CPP have diameters of 1.23 nm and 1.66 nm, respectively), the differences in the spectra seem to indicate some new insights. The G_1 and G_2 bands at 1584 cm^{-1} and 1595 cm^{-1} in [9]CPP move to 1583 cm^{-1} and 1593 cm^{-1} in C_{70}@[9]CPP. As in the C_{70}@[10]CPP, this down-shift emerges from a less inter-ring staggered conformer (see Fig. S4 of Appendix 3), resulting from the template-ordering effect of C_{70} on the [9]CPP shape. The C-C stretching modes of C_{70} fullerene are all up-shifted by 1-2 cm^{-1}. Although the internal volume of [9]CPP is unable to accommodate the C_{70} fullerene, it could be thought in a partial encapsulation, possibly through one of the two poles or through the corannulene segments of the fullerene "egg", forming a proto-complex. Due to the formation of this pseudo-complex, a new RBM band at 164 cm^{-1} (from that at 153 cm^{-1} in [9]CPP) is detected. Simultaneously, the C_{70} RBM bands (456 cm^{-1} and 256 cm^{-1}) change both by +0.5 cm^{-1}. The changes in the Raman spectrum of the C_{70}@[12]CPP from its components are certainly smaller in accordance with the mismatch of their relative sizes for the stabilization of any persistent concave-convex interaction in the internal cavity of the cycloparaphenylene.

F Spectral Responses of the [10]- and C_{70}@[11]CPP Complexes under Thermal and Mechanical Stresses

Variable Pressure Raman Experiments

Fig. 6 and 7 display the Raman spectra of C_{70}@[10]CPP and C_{70}@[11]CPP under pressure and on heating. Both thermal and mechanical treatments lead to rather different behaviour such as it will be discussed below.

The application of pressure to C_{70}@[10]CPP induces an overall up-shift of the whole spectrum together with the typical spectral broadening as exerted by the increment of the intermolecular contacts in the pressed sample. The G_1 band up-shifts from 1581 cm^{-1} at room pressure to 1592 cm^{-1} at 2 GPa, a significant shift which might be justified, not only because of the increasing frequency effect of pressure, but also because of the additional flattening of the [10]CPP structure towards a more oval shape.[11] This change is accompanied by a similar +12 cm^{-1} displacement (from 1564 cm^{-1} at room pressure to 1576 cm^{-1} at 2 GPa) of the tangential CC stretching mode of fullerene. The C_{70} bands associated to the RBM modes also experience big up-shifts such as are displayed in Fig. 6. After pressure release the spectrum does not recover its original aspect, hence the G_1 band maximum is at 1584 cm^{-1} while the C_{70} tangential mode band is displaced to 1567 cm^{-1}.

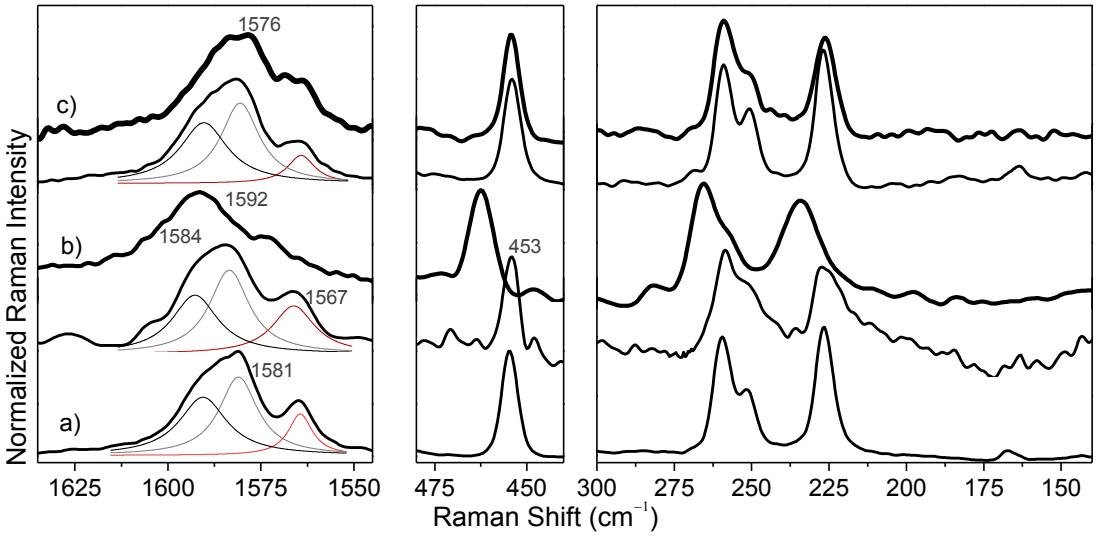

Fig.6 785 nm Raman spectra of C_{70}@[10]CPP: a) at room temperature and pressure; b) thick black line corresponds to the spectrum at high pressure (≈ 2.0 GPa) and thin black line corresponds to the recovered spectrum after pressure cycle; both spectra taken at 25 °C; c) thick black line corresponds to the spectrum at high temperature (140 °C) and thin black line corresponds to the recovered spectrum after thermal cycle. Both spectra are taken at room pressure. Thin lines correspond to the deconvoluted bands.

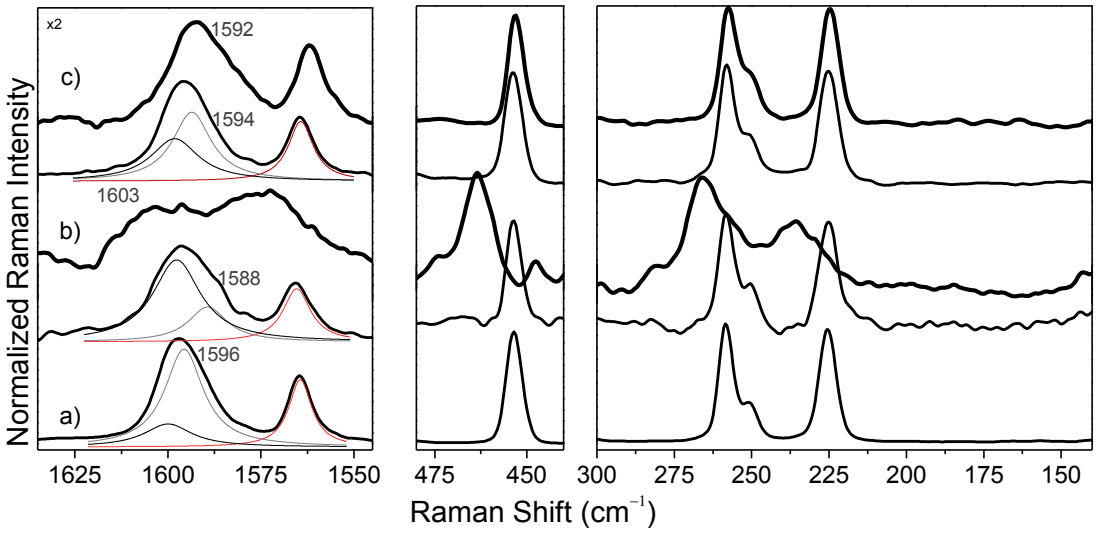

Fig.7 785 nm Raman spectra of C_{70}@[11]CPP: a) at room temperature and pressure; b) thick black line corresponds to the spectrum at high pressure (≈ 2.0 GPa) and thin black line corresponds to the recovered spectrum after pressure cycle, both spectra taken at 25 °C; c) thick black line corresponds to the spectrum at high temperature (140 °C) and thin black line corresponds to the recovered spectrum after thermal cycle. Both spectra are taken at room pressure. Thin lines correspond to the deconvoluted bands.

In the case of the C_{70}@[11]CPP, the application of pressure again produces an up-shift of its G mode frequency from 1596 cm^{-1} to 1603 cm^{-1} which is smaller than in C_{70}@[10]CPP (+11 cm^{-1}) corroborating the connection between frequency up-shifts and structural flattening as this varies from sample to sample. The smaller change in C_{70}@[11]CPP comes from the fact that the [11]CPP structure is already partially flattened in the standing complex at room pressure so that the space for further deformations is smaller. This could be due to the fact that the π–π contacts in the molecular region around the equatorial segment are not optimal leaving the possibility of a further ovallization. Similarly to C_{70}@[10]CPP, the C_{70} fullerene bands undergo ≈+10 cm^{-1} frequency displacements with pressure. The back to room pressure spectrum has suffered a significant down-shift on the CPPs' G

bands, confirming the formation of a more staggered form to achieve better π–π contacts with C_{70}, but the low frequency C_{70} remains as in the pristine complex indicating the prevalence of the complex in its standing orientation.

The fact that C_{70}@[10]CPP, does not recover the original aspect would be indicating that the [10]CPP could have slightly rotated from the lying disposition towards a situation closer, but not identical, to the standing form. After pressure release this high pressure structure would result in a meta-stable kinetically blocked species. Fig. 8 represents the evolution of the main Raman band frequencies of C_{70}@[10]CPP with pressure. In general, the G bands of the cycloparaphenylenes follow a different variation pattern compared to that of fullerene. These G bands of [10]CPP linearly shift up to a critical pressure, 0.6 GPa, at which they stay constant with the increment of pressure up to 1.6 GPa from which a second linear region is detected. However, the tangential CC stretching mode of fullerene follows a continuous linear regime in the whole range of pressure. This behavior on the cycloparaphenylene fragment could be related to a re-orientational effect from the lying to standing shape in the first linear regime, while for the second linear segment, at higher pressures, the CPP undergoes a flattening process (see Fig. S5 and Fig. S7 in Appendix 3 for further information). The existence in the recovered spectrum of an up-shift (from 1581 cm^{-1} to 1584 cm^{-1}) tells us about the reorientational movement in the complex which is the same effect found going on from a lying form in C_{70}@[10]CPP (1581 cm^{-1}) to the standing shape in C_{70}@[11]CPP (1592 cm^{-1}). In addition, the combination of both effects, reorientation plus flattening, imparts the observed irreversibility of the whole cycle. In the case of C_{70}@[11]CPP, the differentiation of the two frequency-pressure regimes is much less clear and the almost continuous behaviour before and after 1 GPa should be related to the predominance of the flattening process in the whole cycle process.

The second aspect of relevance is that while from complex to complex at room conditions the main Raman spectral changes are observed for the CPP bands, here in the experiments at variable pressure, the C_{70} fullerene frequencies are those mainly altered (see Fig. S8 in Appendix 3). This could reveal that in the solid the relevant crystallographic positions are occupied by C_{70} while the [n]CPPs might mostly fill the empty space among them, with the result that the main transmitters of the pressure in the solid are the C_{70} molecules which thus undergo the greater frequency changes.

These changes of the Raman frequencies of the [n]CPP in the complex by pressure in terms of re-orientational and flattening arguments are in agreement with the Raman data on the literature reported for analogous binary systems of C_{70} inside SWCNTs, or peapods.[17,18]

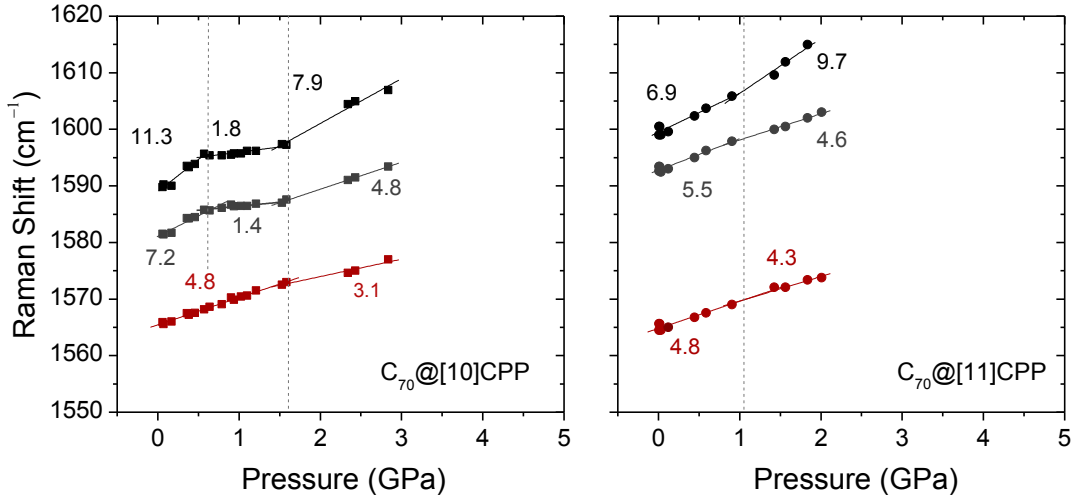

Fig. 8 Evolution of the Raman frequencies of the G modes of the C_{70}@[10]CPP and C_{70}@[11]CPP samples as a function of pressure. Inserted values correspond to the pressure coefficients of each linear trend expressed in units of $cm^{-1}GPa^{-1}$. Black and grey dots correspond to the G_1 and G_2 bands of the [n]CPPs, respectively, while red points correspond to the 1565 cm^{-1} band of C_{70}. (see Fig. S7 of Appendix 3 for the C_{70} RBMs).

Variable Temperature Raman Experiments

Fig. 4 and 5 also display the spectra within the thermal stress cycle. The spectrum of C_{70}@[10]CPP at 140 °C is slightly different to that at room conditions, with the G band displaced −2 cm^{-1}. The formation process of this complex is exothermic meaning that heating would produce the rupture of the interaction in the complex leading to exactly the inverse effect of the G frequencies. Thus we argue that temperature only imparts a bulk effect with no effecton the molecular structure of the complex, an interpretation corroborated by the spectrum when the complex is taken back to room temperature which is exactly identical to the original one. In contrast, for C_{70}@[11]CPP it turns out that the G mode band is scarcely changed at 140 °C (−0.5 cm^{-1}) while the recovered spectrum at room temperature shows the G band at 1592 cm^{-1}, which is unexpectedly similar to that of [11]CPP alone, 1592 cm^{-1}. A possible explanation is that heating would rotate the cycloparaphenylene from the standing situation towards the lying around the equatorial belt of the fullerene where the π–π distances increase, the π–π interaction is apparently interrupted and the [11]CPP starts to behave as an isolated entity (again this would be a kinetically blocked state in the solid after thermal template).

As for the C_{70} bands, is concerned, temperature scarcely affects them by −1 cm^{-1} in all cases in the range of temperature analyzed, an observation that contrasts with their significant changes in the pressure experiments.

G Structural Responses of the [9]- and C_{70}@[12]CPP Complexes under Mechanical and Thermal Stresses

Fig. 9 displays the Raman spectra of C_{70}@[9]CPP under pressure. Given the small volume of the innermost cavity of [9]CPP, we have inferred from the Raman changes in the complex the formation of a species of proto-complex. The Raman spectrum of C_{70}@[9]CPP as a function of pressure in the initial stages of the compression displays the typical frequency up-shift inherent to the increment of intermolecular contacts; however, at around ≈2 GPa, the spectrum evolves by showing a dominant low frequency component at 1579 cm^{-1} together with another feature at 1604 cm^{-1}. These changes at high pressure persist after pressure release, the G bands down-shift 2 cm^{-1}, what might be interpreted by arguing that the application of pressure further helps the formation of the supramolecular complex, a compound that it is not formed directly from solution. Nonetheless, the binary system formed from solution is in a suitable disposition to progress with pressure towards the final complex where it is likely that the [9]CPP more effectively surrounds the corannulene fragments of the fullerene.

In the case of C_{70}@[12]CPP, the increment of pressure up to ≈2 GPa scarcely affects the frequencies of cycloparaphenylene unit, likely due to the moderate pressure increment. Again the largest changes are detected for the fullerene bands in agreement with these molecular entities supporting the transmission of the mechanical stress.

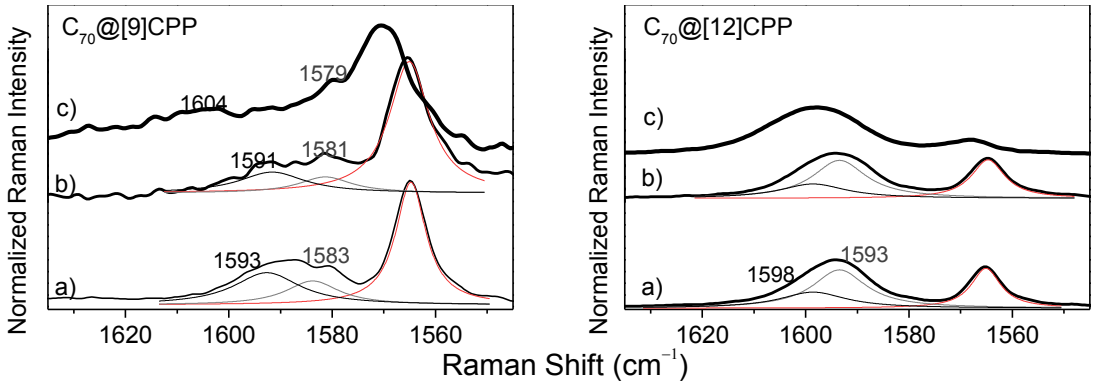

Fig.9. Left: 785 nm Raman spectra of C_{70}@[9]CPP: a) at room temperature and pressure; b) black line corresponds to the spectrum at high pressure (≈ 2.0 GPa); and c) the recovered spectrum after pressure cycle. Both spectra taken at 25 °C. Thin lines correspond to the deconvoluted bands. Right: the same for C_{70}@[12]CPP.

F Conclusions

The electronic and structural properties of host-guest supramolecular 1:1 complexes of [n]CPPs and C_{70}, C_{70}@[n]CPP with n = 9,10, 11 and 12, have been thoroughly analyzed by using Raman spectroscopy. We have found that the vibrational Raman spectra, and in particular the bands associated with the CC stretching tangential G modes and with the radial breathing modes of both [n]CPP and C_{70}, contain the relevant electronic and structural information resulting from complexation. Depending on their sizes, the [n]CPPs have been shown to be able to adapt their structures to form stable couplings with C_{70}: in C_{70}@[10]CPP the fullerene is surrounded by the [10]CPP by its equatorial part, or lying orientation, a situation that we now further characterize as having a less staggered structure for the CPP. In C_{70}@[11]CPP the fullerene is wrapped up through its long ellipsoidal axis, or standing orientation, where the nanoring becomes oval-shaped with close contacts in the C_{70} poles and less conformational restriction in the flattened region.

Under mechanical stress, the largest frequency changes are found for the fullerene bands revealing that the [n]CPPs, as for the unit cell of the solid is concerned, occupy the empty spaces, with the C_{70} molecules in the prevalent sites. In addition, pressure produces the modification of the lying structure of the C_{70}@[10]CPP complex towards a more standing-like conformation followed by the flattening of its structure, a dual process that overall renders an irreversible structural mechanical cycle. C_{70}@[11]CPP, however, resists in its standing position the applied pressure, and it is by heating that the CPP ring seems to rotate towards a lying disposition by finally recovering its “isolated” spherical aspect. All in all, these data display the great adaptability of the [n]CPPs to the shape of C_{70} and also to the crystalline structure in the fullerene solid. C_{70} molecules are encapsulated in SWCNTs forming the well-known peapods where the fullerene molecules might adopt both lying and standing positions existing in many cases as mixtures of both. Here, in the analysis of the [n]CPP as models of SWCNTs, the characterization by Raman of these well-defined complexes might help us to understand the complexity of these peapods between fullerene and SWCNT.

The main message of this study is the impressive structural versatility and adaptability of the [n]CPP molecules to different physico-chemical environments, a chameleon-like property provided by the conjunction of unusual effects such as cyclic conjugation and ring strain cylindrical shape which form a delicate ground electronic state equilibrium easily modifiable through external physical and chemical inputs.

References

1 V. C. Parekh and P.C. Guha, *J. Indian Chem. Soc.* **11**, 95 (1934).

2 R. Jasti, J. Chattacharjee, J. B. Neaton and C.R. Bertozzi, *J. Am. Chem. Soc.* **130**, 17646 (2008).

3 H. Omachi, S. Matsuura, Y. Segawa and K. Itami, *Angew. Chem. Int. Ed.* **49**, 10202 (2010); H. Takaba, H. Omachi, Y. Yamamoto, J. Bouffard and K. Itami, *Angew. Chem. Int. Ed.* **48**, 6112 (2009); Y. Segawa, S. Miyamoto, H. Omachi, S. Matsuura, P. Senel, T. Sasamori, N. Tokitoh and K. Itami, *Angew. Chem. Int. Ed.* **50**, 3244 (2011); H. Omachi, Y. Segawa and K. Itami, *Acc. Chem. Res.* **45**, 1378 (2012); Y. Ishii, Y.Nakanishi, H. Omachi, S. Matsuura, K. Matsui, H. Shinohara, Y. Segawa and K. Itami, *Chem. Sci.* **3**, 2340 (2012).

4 E. Kayahara, T. Kouyama, T. Kato, H.Takaya, N. Yasuda and S. Yamago, *Angew. Chem. Int. Ed.* **52**, 13722 (2013); T. Iwamoto, Y. Watanabe, Y. Sakamoto, T. Suzuki and S. Yamago, *J. Am. Chem. Soc.* **133**, 8354 (2011); S. Yamago, Y. Watanabe, T. Iwamoto, *Angew. Chem. Int. Ed.* **49**, 757 (2010); E. Kayahara, Y. Sakamoto, T. Suzuki and S. Yamago, *Org. Lett.* **14**, 3284 (2012).

5 J. Xia and R. Jasti, *Angew. Chem. Int. Ed.* **51**, 2474 (2012); T. J. Sisto, M. R. Golder, E. S. Hirst and R. Jasti, *J. Am. Chem. Soc.* **133**, 15800 (2011); T. J. Sisto and R. Jasti, *SynLett.* **23**, 483 (2012); E. S. Hirst and R. Jasti, *J. Org. Chem.* **77**, 10473 (2012); R. Jasti, C. R. Bertozzi, *Chem. Phys. Lett*. **494**, 1 (2010); J. Xia, J. W. Bacon and R. Jasti, *Chem. Sci.* **3**, 3018 (2012); M. R. Golder, B. M. Wong and R. Jasti, *Chem. Sci*. **4**, 4285 (2013); A. V. Zabula, A. S. Filatov, J. Xia, R. Jasti and. M. A. Petrukhina, *Angew. Chem. Int. Ed.* **52**, 5033 (2013*)*.

6 E. Kayahara, V. K. Patel and S. Yamago, *J. Am. Chem. Soc.* **136**, 2284 (2014); P. J. Evans, E. R. Darzi and R. Jasti, *Nat. Chem.* **6**, 404 (2014).

7 H. Omachi, T. Nakayama, E. Takahashi, Y. Segawa and K. Itami, *Nat. Chem.* **5**, 572 (2013).

8 Y. Segawa, H. Omachi and K. Itami, *Org. Lett.* **12**, 2262 (2010).

9 See papers in references 2-5 where the molecular structures of some [n]CPPs are resolved by x-ray diffraction. In addition: S. Taubert, D. Sundholm and F. Pichierri, *J. Org. Chem*. **75**, 5867 (2010); U. H. F. Bunz, S. Menning and N. Martín, *Angew. Chem. Int. Ed.* **51**, 7094 (2012); S. Schrettl and H. Frauenrath, *Angew. Chem. Int. Ed.* **51**, 6569 (2012).

10 T. Iwamoto, Y. Watanabe, T. Sadahiro, T. Haino and S. Yamago, *Angew. Chem. Int. Ed.* **50**, 8342 (2011).

11 M. Peña-Alvarez, P. M. Burrezo; M. Kertesz, T. Iwamoto, S. Yamago, J. Xia, R. Jasti, J. T. López Navarrete, M. Taravillo, V. G. Baonza and J. Casado, *Angew. Chem. Int. Ed*. **53**, 7033-7037. (2014).

12 T. Iwamoto, Y. Watanabe, H. Takaya, T. Haino, N. Yasuda and S. Yamago, *Chem. Eur. J.* **19**, 14061 (2013).

13 V. G. Baonza, M. Taravillo, A. Arencibia, M. Cáceres and J. Núñez, *J. Raman Spectrosc.* **34**, 264 (2003).

14 E. del Corro, J. González, M. Taravillo, E. Flahaut and V. G. Baonza, *Nano Lett*. **8**, 2215-18 (2008).

15 G. Sun and M. Kertesz, *J. Phys. Chem. A* **106**, 6381 (2002). V. Schettino, M. Pagliai, G. Cardini, H. *J. Phys. Chem. A*, 2002, **106**, 1815. D. Jing, Z. Pan, *Eur. J. Mech. A/Sol*. **28**, 948 (2009).

16 S. Tsuzuki, K. Honda, T.Uchimaru, M. Mikami, K. Tanabe, *J. Am. Chem. Soc.* **124**, 104-112 (2002).

17 C. Caillier, D. Machon, A. San-Miguel, R. Arenal, G. Montagnac, H. Cardon, M. Kalbac, M. Zukalova, L. Kavan, *Phys. Rev. B* **77**, 125418 (2008).

18 P. M. Rafailov, C. Thomsen, H. Kataura, *Phys. Rev. B* **68**, 193411 (2003); A. N. Khlobystov, R. Scipioni, D. Nguyen-Manh, D. A. Britz, D. G. Pettifor, G. A. D. Briggs, S. G. Lyapin, A. Ardavan and R. J. Nicholas, *Appl. Phys. Lett.* **84**, 772 (2004).

Chapter 6

The Raman Fingerprint of Cyclic Conjugation: The Case of the Stabilization of Cations and Dications in Cycloparaphenylenes

Radical cations and dications of [n]CPPs from n = 5 to n = 12 have been studied by Raman spectroscopy and Density Functional Theory. Small [n]CPP dications owe their stability to the closed-shell electronic structure imposed by cyclic conjugation surpassing the destabilizing effect of ring strain and of the electron deficiency of the charged states. Large [n]CPP dications mitigate cyclic strain by forming diradicals. The Raman spectra reflect the balance among cyclic conjugation, cyclic strain and biradicaloid stabilization by finding an unexpected turning point in the frequency behavior of the G vibrational modes as a function of size. These Raman data represent the vibrational fingerprint of this rare form of conjugation which is central to stabilize both cations and dications of [n]CPP macrocycles.

Cycloparaphenylenes ([n]CPPs with *n* the number of phenyl rings) were suggested in 1934[1] and first synthesized in 2008 by Beztozzi and Jasti.[2] In only seven years the whole [n]CPP series from [5]CPP to [18]CPP has been prepared.[2,3,4] Nowadays the [n]CPP saga is now greatly diversified by many different types of functionalizations, however, "pure" [n]CPPs still represent the best molecular models to address important issues concerning the electronic structure of these outstanding cyclic π–conjugated molecules.[5]

The main distinctive features of [n]CPPs are the circular deformation of the π–electron structure and the cyclic strain imparted by the same curvature. In fact, in this [n]CPP series, [5]CPP accumulates an impressive cyclic strain energy of 119 kcal/mol as the 360^0 curvature is shared only by five rings, yet neutral [5]CPP is fairly stable.[4] A larger degree of destabilization is expected in their oxidized states (radical cations, $[n]CPP^{\bullet+}$, and dications, $[n]CPP^{2+}$) by removing bonding electrons; however, they are also quite stable as shown for $[8]CPP^{\bullet+}$ and $[8]CPP^{2+}$.[6,7] Considering this, the fundamental question that arises is: why are the smallest [n]CPP molecules in the oxidized states stable despite the increasing accumulation of ring strain compounded by the reduced number of available π-electrons? Recently, Yamago and Uchiyama addressed this issue in $[8]CPP^{2+}$ by considering the [4n]annulene character of neutral [n]CPPs. Accordingly, they argued that $[8]CPP^{2+}$ is a 4(n-1)+2 π–electron system and obtaining additional aromatic stabilization, which the authors described as in-plane aromaticity following the terminology based on [4n+2] annulene dications.[8] Nonetheless, the stabilizing energy component provided by annulenoid aromaticity in these dications is expected to be small and therefore, a priori, it seems insufficient to justify the chemical robustness of the $[n]CPP^{2+}$ series, especially for the highly strained smaller members, such as *n* = 5 and 6. Further in line with these energetic considerations, we also present evidence that [n]CPP monocations show intermediate behavior between neutrals and dications. Whether or not in-plane aromaticity is the main factor, the basic question is if there is any direct or indirect experimental proof linked to the outstanding stabilization of smaller $[n]CPP^{\bullet+}$/$[n]CPP^{2+}$ cations and that could allow us to further decipher its nature and origin. Our conclusion is that we deal with a particular case of cyclic conjugation[9] which is a rare form of thermodynamic stabilization and hence of interest in several fields of chemistry.

Yamago and Jasti[6,7] have recently reported the properties of oxidized [8]CPP and other even members of the series mainly focusing on the electronic absorption spectra, ESR, VT-NMR and electronic structure calculations.[10,11] Here, we analyze the complete, odd and even, cationic and dicationic series of [n]CPPs from *n* = 5 to 12. This work provides a unified perspective of the evolution of the electronic and molecular structures of these oxidized species based on Raman spectroscopy. This technique is highly valuable for the diagnosis of the π–conjugated and π–aromatic structures (as already described for neutral [n]CPPs)[12,13] and enables us to characterize the specific stabilizing factors responsible for the unique stability of the π–electronic structure of small $[n]CPP^{\bullet+}$ cations and $[n]CPP^{2+}$ dications. The approach relies on the size evolution of Raman data and structural (cyclic ring strain) and electronic (aromaticity) parameters.

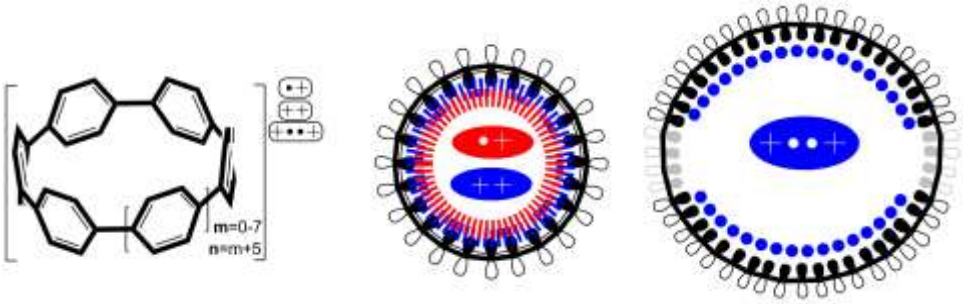

Scheme 1. a) [n]CPPs (n = m+5, m = 0-7) denoting the forms of the oxidized species analyzed. b) Top view of the $2p_z$ orbital orientation for cyclic conjugation in small [n]CPPs together with that in large [n]CPP radical cations. c) Symmetry breaking indicated for biradicals. Red: radical cations, blue: dications.

The UV-Vis-NIR spectra of [8]CPP$^{\bullet+}$ and [8]CPP^{2+} (Fig. S1-S3 of Appendix 4) show that their Raman spectra are taken in near-resonance thus providing the unique vibrational fingerprint of each individual oxidized species. These experimental Raman spectra for [8]CPP$^{\bullet+}$/[8]CPP^{2+} are compared in Fig. S3 (Appendix 4) with the (U)B3LYP/6-31G(d,p) predictions: the very good theory-experiment correlation supports the accuracy of the electronic structure calculations in terms of energetics and of molecular structures as it will be discussed below. All [n]CPP$^{\bullet+}$/[n]CPP^{2+} systems (n = 5-12) were thus characterized by UV-Vis-NIR electronic absorption spectroscopy and their bands assigned with TDDFT modeling.

In the Raman spectra of [8]CPP$^{\bullet+}$/[8]CPP^{2+} the main bands at around 1600 cm^{-1} arise from CC vibrational modes describing an alternating stretching/shortening pattern of the consecutive CC bonds along the tangential direction of the macrocycle (G-type vibrations in carbon nanotubes) which are referred to here for the [n]CPPs as G-like modes.[12] These have two contributions, G_{A1g} and G_{E2g}, the former being a collective CC stretching vibration completely delocalized along the perimeter of the molecule (without vibrational nodes) and therefore highly sensitive to variations of the π–electron structure around the belt of the macrocycle (Fig. S5, Appendix 4). These G bands are our Raman probes for inquiring about molecular shapes and electronic structures in oxidized [n]CPPs.

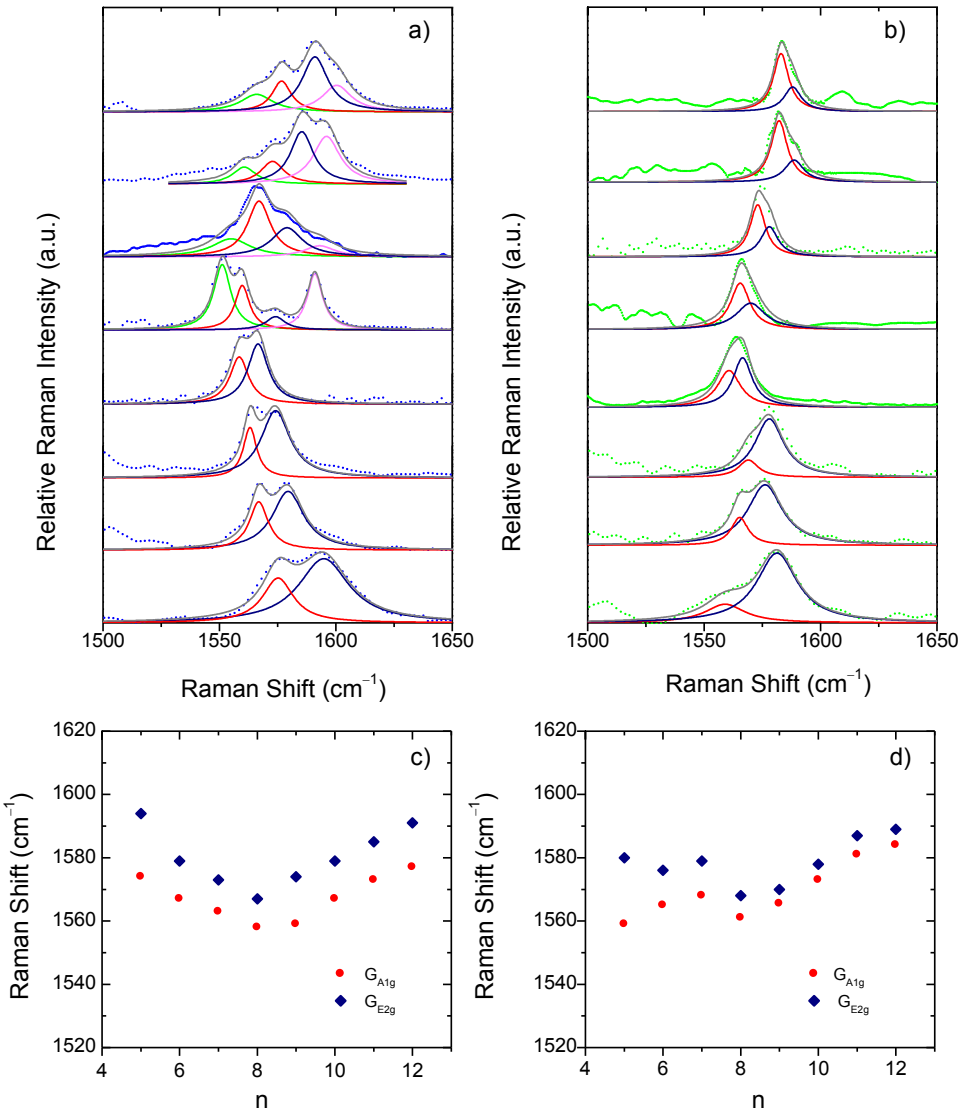

Figure 1. a) G bands in the near-resonant Raman spectra in solution of [5]CPP^{2+} to [12]CPP^{2+} from the bottom to the top. Red and blue lines are the GA_{1g} and GE_{2g} Lorentzian deconvolutions, respectively. b) The same for [n]CPP$^{\bullet+}$. c) and d) GA_{1g} and GE_{2g} shifts as a function of n.

The evolution of the G bands in the Raman spectra of the neutral [n]CPPs (going from n = 12 to 6) has been already reported by us showing a continuous frequency downshift with decreasing n.[12] This behavior has been ascribed to the continuous increase of quinonoidization on the benzenes as a result of their bending imposed by the strain in the macrocycle as its size decreases.[12] In contrast to the neutral [n]CPPs, we present in Figure 1 for the first time two distinctive and surprising trends on the G band frequencies for the dications: i) the spectra for the large [n]CPP^{2+}, [9]CPP^{2+} to [12]CPP^{2+}, display several Raman bands (up to 4 in [12]CPP^{2+}) whereas from [8]CPP^{2+} to [5]CPP^{2+} the spectra are simpler (two bands in [5]CPP^{2+}); and ii) the G_{A1g}/G_{E2g} shifts follow a surprising V-shape behavior consisting of a progressive frequency downshift from [12]CPP^{2+} to [8]CPP^{2+} and from [5]CPP^{2+} to [8]CPP^{2+} with [9]CPP^{2+} being at the turning point.

Linear oligoparaphenylenes ([n]LPPs) in their oxidized, cationic ([n]LPP$^{\bullet+}$) and dicationic ([n]LPP^{2+}) states are known to develop well-defined quinonoidal structures along the π–conjugation path called polarons.[14,15] These polarons have diagnostic Raman bands.[16] Shorter [n]LPP^{2+} dications (i.e., n < 4) have closed-shell singlet ground electronic states (S_0), while larger ones with n > 4 start to stabilize an open-shell singlet structure driven by the re-aromatization of the innermost benzene rings giving way to a singlet diradicaloid pseudo-aromatic species.[16] This behavior is reflected in the Raman spectra of [n]LPP^{2+} dications by the G band splitting shown in Figure S11 (Appendix 4). Concomitantly to the appearance of this diradicaloid character, there exists a singlet-triplet gap (ΔE_{ST}) which nearly vanishes for n > 8 owing to the large inter-radical distance. No experimental spectral Raman proofs of this closed-shell → open-shell transition in [n]LPP^{2+} dications can be provided given the limited number of available dicationic samples. However, this transformation of the quinonoidal structure into a pseudo-aromatic singlet biradical has been demonstrated in a series of neutral quinonoidal tetracyano oligo(N-annulated perylene)quinodimethanes.[17]

Figure 2 shows the variation of the energy difference between the closed-shell and open-shell configurations of the [n]CPP^{2+} series. The behavior is qualitatively similar to [n]LPP^{2+} but quantitatively different. In Figure 2a we observe that for n < 8, the closed-shell S_0 state is by far the most stable configuration with a ΔE_{ST} gap to the first triplet excited state of ≈20 kcal/mol. For larger [n]CPP^{2+}, n > 9, the open-shell biradical form becomes the S_0 ground electronic state with a small but non-vanishing ΔE_{ST} gaps revealing how the cyclic structure, in contrast to [n]LPP^{2+}, avoids terminal spin accumulation. These data support the biradical character of the ground state as suggested by Yamago et al. for [10]CPP^{2+} and [12]CPP^{2+} based on H-NMR.[10]

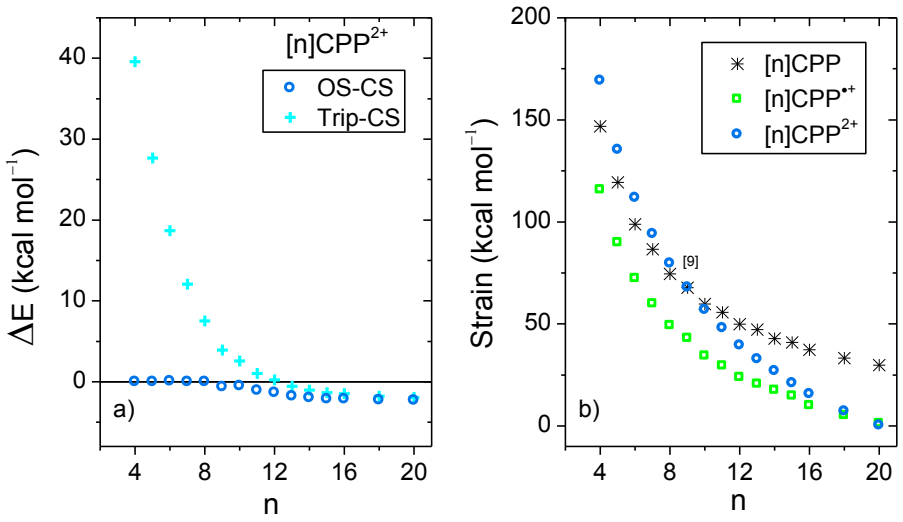

Figure 2. a) DFT/(U)B3LYP/6-31G(d,p) relative energies (ΔE) between the closed-shell singlet and open-shell singlet (E_{OS} - E_{CS}), and the triplet and open-shell singlet (E_{Trip} - E_{CS} = ΔE_{ST}) of the [n]CPP^{2+} series. b) (U)B3LYP/6-31G(d,p) strain energies calculated from the homodesmotic reaction in Scheme 2 and Fig. S11 (Appendix 4).[18]

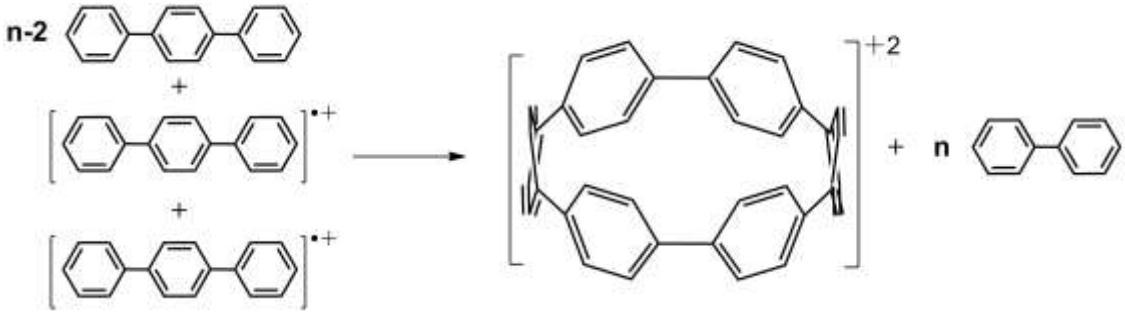

Scheme 2. Homodesmotic reaction for the calculation of strain energies of [n]CPP^{2+}.

In Figure 2b we present the calculated macrocyclic strains of the [n]CPP^{2+} dications which have been calculated considering the corresponding homodesmotic reaction, as shown in scheme 2 and Fig. S11 (Appendix 4) adapted from a similar procedure for the neutral [n]CPPs.[18] In our case for the dications, we consider two radical cations in the reactants which thus include the +2 ionic state for the final dication. Interestingly, while the $n < 9$ [n]CPP^{2+} dications have larger strain energies, by +20 kcal/mol than the neutrals, for $n \geq 9$, the biradical [n]CPP^{2+} dications have less strained structures compared to the neutral molecules. This difference can be explained in terms of the bending of the six-member rings: in the neutrals, cyclic strain energy is proportional to the reduction in aromaticity of the benzene units. For the dications, oxidation itself causes a partial reduction of the aromaticity of the benzene rings and consequently the energy cost of the local deformation is smaller. For $n < 9$, the reason for the energy strain being larger in the dications is associated with the repulsive electrostatic term which is not present in the neutrals. These repulsive interactions are larger in the smaller molecules where the two positive charges are more confined. Nonetheless, this additional electrostatic term in these small dications provides a challenge for understanding their unexpected stability. Comparing the size dependent behavior of strain and biradical formation in Figure 2b, we deduce that in larger [n]CPP^{2+} dications the formation of the diradicaloid configuration takes place concomitant with the mitigation of the ring strain. Both the stability switch over in the strain values and the sudden appearance of diradical character occur at the same critical $n = 9$ size which is also the turning point for the frequency behavior for the structurally sensitive Raman G bands.

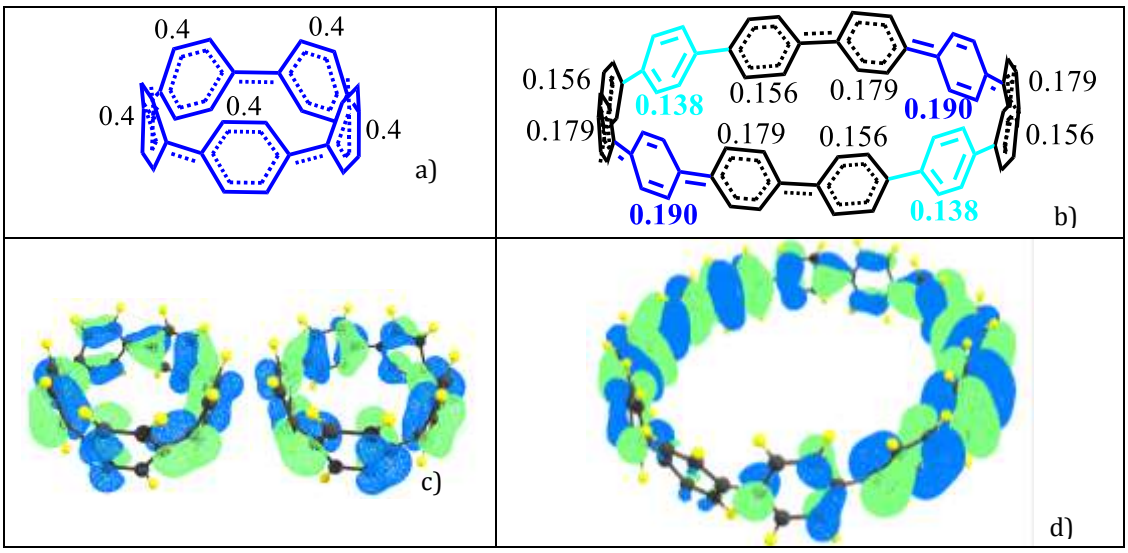

Figure 3. DFT-(U)B3LYP/6-31G(d,p) data: Per ring charge distribution and valence bond structures from optimized molecular geometries for a) [5]CPP^{2+} and b) [12]CPP^{2+}. c) Degenerate HOMO and HOMO-1 orbital topologies for [5]CPP^{2+}, and d) HOMO of [12]CPP^{2+}.

The transition as a function of size of the macrocycle from small and highly strained (singlet closed-shell) to large and less strained (open-shell) has a significant impact on the molecular geometries as represented in Figure 3 for the two extreme cases of $[5]CPP^{2+}$ and $[12]CPP^{2+}$. In the smaller $[n]CPP^{2+}$ dications all six member rings are very nearly equivalent, whereas from $[9]CPP^{2+}$ on the macrocycles show domains with different aromatic-quinonoid characters in the CC bond length alternation pattern resulting in an overall symmetry loss of the circular shape towards an oval structure with increasing *n* (see Table S3 and Fig. S13 for the geometries of the whole series, Appendix 4). Similar symmetry breaking has been observed for dicationic cyclic oligothiophenes.[19] The relevant frontier molecular orbitals shown in Figure 3 further reveal the transition between small and large $[n]CPP^{2+}$ dications: the HOMO/HOMO-1 degeneracy which is present for $n < 9$ is broken for $n \geq 9$ (Table S4, Appendix 4).

Another relevant structural feature of [n]CPPs is the distribution of conformations between neighboring benzene rings provoked by the hydrogen-hydrogen steric repulsions forcing phenyl to phenyl torsions (θ) in the neutral molecules. These produce an alternating pattern for even *n* values.[13] Compared to the neutral series, the situation in the $[n]CPP^{2+}$ series is substantially different. The evolution of the average torsions in Figure 4a displays a significant change by oxidation, decreasing from neutrals to cations and even more from cations to dications. Thus, the smaller dications ($[4]CPP^{2+}$–$[6]CPP^{2+}$) have θ close to zero increasing up to 14° in $[8]CPP^{2+}$. This is important since smaller torsions enhance π-conjugation between neighboring benzenes consistent with a larger double bond character for the interring bond, *r*. Figure 4b shows negative BLA values indicative of a significant quinonoid character for $n < 9$ in the dication series. It is this BLA decrease that shows up in the Raman shifts providing the experimental evidence.

The unusual experimental Raman spectral behavior described in Figure 1 is nicely explained by taking into account all these structural effects: i) the existence of an increased number of Raman bands in larger $[n]CPP^{2+}$ dications is the result of the appearance of aromatic and quinonoidal domains lowering the molecular symmetry leading to new Raman-active bands. ii) The overall $[12]CPP^{2+} \rightarrow [9]CPP^{2+}$ frequency downshift corresponds to the gradually increasing contributions of the local quinonoidal structure of the benzene rings with decreasing *n*, similar to the structural and Raman spectroscopic behavior described for the neutral [n]CPP series.[12,13] For instance, in $[12]CPP^{2+}$ the strain and bending effects are small and the G frequency therefore is the highest among $n = 9$-12 members of the series. iii) When moving from $[8]CPP^{2+}$ to $[5]CPP^{2+}$ the closed-shell structure is stabilized (the open shell diradical character essentially disappears leading to the increase in absolute value of the bond length alternation as seen in Figure 4b) provoking the collective circumferential C=C/C–C vibration G mode frequencies to upshift as *n* decreases from $n = 9$ to $n = 5$.

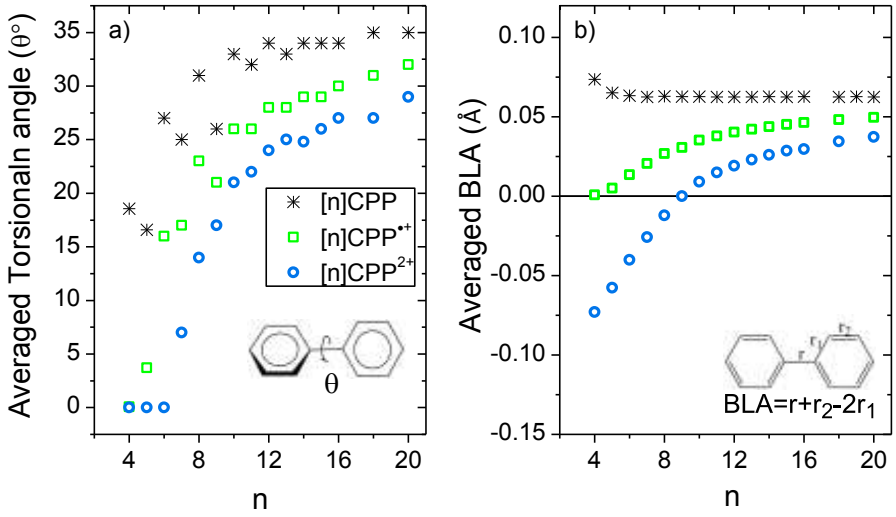

Figure. 4. a) Size evolution of the interring torsional angles (θ, see insert). b) Size evolution of the averaged BLA parameter (see insert for the definition of BLA).

As already mentioned before, in the π–electronic structures of [n]CPP, *cis-trans* [4n]annulene[7] substructures can be identified (i.e., considering 4 π–electrons per benzene, 4n in total) and from this point of view the $[n]CPP^{2+}$ annulenic-like dications feature 4n-2=4(n-1)+2 Hückel π–electrons in a conjugated circuit referred to as in-plane aromaticity, a concept also known as superaromaticity.[20] Under this hypothesis, we observe that the triplet states of $[n]CPP^{2+}$ dications represent electronic configurations with 4(*n*-1) π–electrons so the ΔE_{ST} gap of >20 kcal/mol for $[5]CPP^{2+}$ in Figure 2a emerges as a result of the energy required to break its closed-shell structure. As the macrocycle size decreases its ΔE_{ST} gap increases denoting the effective strength of the bonding within the superaromatic conjugated π–electrons.

The radical cations, $[n]CPP^{\bullet+}$, have been also characterized by UV-Vis-NIR (Fig. S4, Appendix 4) and Figure 1 also display their resonant or near-resonant Raman spectra where, similarly to the dications, a close to a V-shape behavior in the G frequency bands as a function of *n* is found. The turning point is also between $[8]CPP^{\bullet+}$ and $[9]CPP^{\bullet+}$. From theoretical calculations in Figure 4 we see that for the larger $[n]CPP^{\bullet+}$ cations (*n* > 8), their average dihedral interring torsion angles are larger than in the smaller analogues meaning that an increasing tendency to localize the charge within the benzene rings is expected which would cause the Raman bands to upshift going from $[9]CPP^{\bullet+} \rightarrow [12]CPP^{\bullet+}$. This trend is to be contrasted with the *n* < 9 cases where the frequency upshifts of the radical cations originate from the cyclic delocalization of the charge over the whole molecular cylinder (Table S5, Appendix 4). This full delocalization, such as in the dications, reinforces the C=C/C-C bond alternation path (see BLA evolution in Figure 4b) and leading again to the Raman upshift going from $[8]CPP^{\bullet+}$ to $[5]CPP^{\bullet+}$. In regard to strain energies, the behavior 4n-1 $[n]CPP^{\bullet+}$ cations is intermediate between 4n neutrals and 4(n-1)+2 dications showing some aspects of both.

Finally, it is interesting to jointly analyze in Figure 4b the evolution of the bond length alternation (BLA) as a function of *n* for neutral, cationic and dicationic [n]CPPs. The BLA of neutrals is positive indicating an overall aromatic character of their benzene units, which barely changes with *n.* The BLA in small $[n]CPP^{\bullet+}$ cations reaches a value showing an intermediate structure. The dications display more pronounced BLA changes. For *n* > 9 the BLA is positive indicating an overall pseudo-aromatic structure in line with the open-shell biradical state. For $[9]CPP^{2+}$ the BLA = 0 Å represents the turning point towards a negative BLA value. For smaller *n* < 9 the BLA attains larger negative values indicating an increased double bond character for the interring bond (*r*) due to electron pair localization in the closed-shell configuration. Comparing the absolute values, an increasingly bond length alternating π–conjugated structure is in consonance with the upshift of the Raman frequencies of the dication from $[9]CPP^{2+}$ to $[5]CPP^{2+}$. These results are complemented by the calculations of the Nucleus-Independent Chemical Shifts (NICS) for each [n]CPP at the cavity center, NICS(C) (shown in Fig. S16, Appendix 4). There is a rapid decrease of NICS(C) with the incremental addition of the positive charge (neutral, radical cation and dication) and with the decreasing of *n* reaching NICS (C) values of −20 ppm for $[5]CPP^{2+}$, from which it can be inferred that a strong ring current is being induced in the cavity due to the efficiency of the cyclic conjugation.

Taking the data in the cation and dication series together, a similar V-shape Raman frequency behavior is found for both. However, while $[n]CPP^{2+}$ dications correspond to the 4(n-1)+2 Hückel aromatic formula, $[n]CPP^{\bullet+}$ cations are formally non-aromatic, so the stabilizing effect that would be able to compensate the macrocyclic strain in the $[n]CPP^{\bullet+}$ cations cannot be aromatic stabilization alone but it must be partly the result of charge delocalization over the macrocycle. In-plane conjugation as used by other authors[7] in the literature seems to be ambiguous because a plane of conjugation does not exist for [n]CPPs (the effect spreads out over the whole nearly cylindrical molecule). Therefore, the stabilizing charge delocalization effect occurring in cations and dications here, we think, is a manifestation of C=C/C-C conjugation in a cyclic geometry, or cyclic conjugation.[8]

In summary, the complete series of cations and dications of [n]CPPs from *n* = 5 to *n* = 12 have been studied. Small $[n]CPP^{2+}$ dications owe their stability to the closed-shell structure imposed by the efficient cyclic conjugation which softens the impressive increase in ring strain. In this regard, these

small [n]CPP^{2+} dications are real models for studies of cyclic conjugation instead of the purely theoretically constructed cyclacenes.[21] As the size of the [n]CPP increases, cyclic conjugation vanishes and large [n]CPP^{2+} dications mitigate cyclic strain by forming biradicaloid structures. The balance between cyclic conjugation, cyclic strain and biradicaloid transformation is evidenced in the Raman spectra by the detection of a surprising V-shape behavior of the G band frequencies.

Experimental Section

Oxidation titrations. $Et_3O^+SbCl_6^-$ was used to generate the cations and dications in 10^{-4} M solution of [n]CPP in CH_2Cl_2. Oxidations were monitored by UV-Vis-NIR absorption using a Cary 5000 spectrophotometer.

Raman spectroscopy. Raman measurements at room conditions of [n]CPP$^{\bullet+}$ and [n]CPP^{2+} were selected in resonant and near resonant conditions with the 532 nm, 785 nm or 1064 nm laser Raman excitations, using an Invia Reflex Raman RENISHAW and a Ram II Bruker FT-Raman spectrometers. The bands have been fitted with Lorentzian curves (FWHM = 12 and 15 cm^{-1}).

Theoretical calculations. Density Functional Theory (DFT) quantum-chemical calculations were performed as implemented in the Gaussian 09.[22] Energy values and geometrical parameters refer to the geometry-optimized structures using the B3LYP/6-31G(d,p) method, the minima were checked by frequency calculations. The unrestricted (U)B3LYP/6-31(d,p) approach was used for open shell cations and dications. For open shell ground-state of the dications, broken symmetry spin-unrestricted theory with the guess=mix keyword was used. TDDFT computations were done for the UV-vis absorption spectra using TD-(U)B3LYP/6-31G(d,p), and NICS calculations were done at the (U)B3LYP/6-311++G(2df,p) GIAO level.

References

1 V. C. Parekh, P. C. Guha, *J. Indian Chem. Soc.* **11**, 95–100 (1934).

2 R. Jasti, J. Bhattacharjee, J. B. Neaton, C. R. Bertozzi, *J. Am. Chem. Soc*. **130**, 17646–17647 (2008).

3 a) T. Iwamoto, Y. Watanabe, Y. Sakamoto, T. Suzuki, S. Yamago, *J. Am. Chem. Soc.* **133**, 8354–8361 (2011); b) T. J. Sisto, M. R. Golder, E. S. Hirst, R. Jasti, *J. Am. Chem. Soc.* **133**, 15800–15802 (2011); c) J. Xia, R. Jasti, *Angew. Chem. Int. Ed.* **51**, 2474 –2476 (2012).

4 a) E. Kayahara, V. Kumar Patel, S. Yamago, *J. Am. Chem. Soc.* **136**, 2284–2287 (2014); b) P. J. Evans, E. R. Darzi, R. Jasti, *Nat. Chem*. **6**, 404–408 (2014).

5 a) H. Omachi, Y. Segawa, K. Itami, *Acc. Chem. Res.* **45**, 1378–1389 (2012); b) H. Omachi, T. Nakayama, E. Takahashi, Y. Segawa, K. Itami, *Nat. Chem.* **5**, 572–576 (2013); c) T. Nishihara, Y. Segawa, K. Itami, *Angew. Chem. Int. Ed.* **54**, 3707–3711 (2015); d) F. E. Golling, M. Quernheim, M. Wagner, T. Nishiuchi, K. Müllen, *Angew. Chem. Int. Ed.* **53**, 1525–1528 (2015); e) S. Hitosugi, W. Nakanishi, T. Yamasaki, H. Isobe, *Nat. Commun.* **2**, 492 (2011).

6 a) M. R. Golder, B. M. Wong, R. Jasti, *Chem. Sci*. **4**, 4285–4291 (2013); b) E. Kayahara, T. Kouyama, T. Kato, H. Takaya, N. Yasuda, S. Yamago, *Angew. Chem. Int. Ed.* **52**, 13722–13726 (2013).

7 N. Toriumi, A. Muranaka, E. Kayahara, S. Yamago, M. Uchiyama, *J. Am. Chem. Soc*. **137**, 82–85 (2015).

8 J. Chandrasekhar, E. D. Jemmis, P. v. R. Schleyer, *Tetrahedron Lett*. **39**, 3707–3710 (1979).

9 H. S. Choi, K. S. Kim, *Angew. Chem. Int. Ed*. **38**, 2256-2258 (1999). b) R. Herges, *Chem. Rev.* **106**, 4820–4842 (2006). c) E. S. Hirst, F. Wang, R. Jasti, *Org. Lett.* **13**, 6220–6223 (2011).

10 E. Kayahara, T. Kouyama, T. Kato, S. Yamago*, J. Am. Chem. Soc*. **138**, 338–344 (2016).

11 M. R. Talipov, R. Jasti, R. Rathore, *J. Am. Chem. Soc*. **137**, 14999–15006 (2015).

12 M. Peña-Alvarez, P. M. Burrezo, M. Kertesz, T. Iwamoto, S. Yamago, J. Xia, R. Jasti, J. T. López Navarrete, M. Taravillo, V. G. Baonza, J. Casado, *Angew. Chem. Int. Ed.* **53**, 7033–7037 (2014).

13 M. Peña Alvarez, L. Qiu, M. Taravillo, V. G. Baonza, M. C. Ruiz Delgado, S. Yamago, R. Jasti, J. T. López Navarrete, J. Casado, M. Kertesz, *Phys. Chem. Chem. Phys* DOI:10.1039/C5CP05500H (2015).

14 L. Cuff, C. Cui, M. Kertesz, *J. Am. Chem. Soc*, **116**, 9269–9274 (1994).

15 S. A. Brazovskii, N. N. Kirova, *JETP Lett.* **33**, 4–8 (1981).

16 J. L. Bredas, R. R. Chance, R. Silbey, *Mol. Cryst. Liq. Cryst*. **77**, 319–332 (1981).

17 Z. Zeng, M. Ishida, J. L. Zafra, X. Zhu, Y. Mo Sung, N. Bao, R. D. Webster, B. Sun Lee, R.-Wei Li, W. Zeng, Y. Li, C. Chi, J. T. López Navarrete, J. Ding, J. Casado, D. Kim, J. Wu, *J. Am. Chem. Soc.* **135**, 6363–6371 (2013).

18 Y. Segawa, H. Omachi, K. Itami, *Org. Lett*. **12**, 2262–2265 (2010).

19 M. Iyoda, K. Tanaka, H. Shimizu, M. Hasegawa, T. Nishinaga, T. Nishiuchi, Y. Kunugi, T. Ishida, H. Otani, H. Sato, K. Inukai, K. Tahara, Y. Tobe, *J. Am. Chem. Soc.* **136**, 2389–2396 (2014).

20 J. Aihara, *Chem. Phys. Lett.* **381**, 147–153 (2003).

21 a) T. M. Krygowski, M. K. Cyrański, *Chem. Rev*. **101**, 1385–1419 (2001); b) T. Kawase, M. Oda, *Angew. Chem. Int. Ed*. **43**, 4396–4398 (2004).

22 Gaussian 09, Revision A.02, M. J. Frisch, G. W. Trucks, H. B. Schlegel, G. E. Scuseria, M. A. Robb, J. R. Cheeseman, G. Scalmani, V. Barone, B. Mennucci, G. A. Petersson, H. Nakatsuji, M. Caricato, X. Li, H. P. Hratchian, A. F. Izmaylov, J. Bloino, G. Zheng, J. L. Sonnenberg, M. Hada, M. Ehara, K. Toyota,

R. Fukuda, J. Hasegawa, M. Ishida, T. Nakajima, Y. Honda, O. Kitao, H. Nakai, T. Vreven, J. A. Montgomery, Jr., J. E. Peralta, F. Ogliaro, M. Bearpark, J. J. Heyd, E. Brothers, K. N. Kudin, V. N. Staroverov, R. Kobayashi, J. Normand, K. Raghavachari, A. Rendell, J. C. Burant, S. S. Iyengar, J. Tomasi, M. Cossi, N. Rega, J. M. Millam, M. Klene, J. E. Knox, J. B. Cross, V. Bakken, C. Adamo, J. Jaramillo, R. Gomperts, R. E. Stratmann, O. Yazyev, A. J. Austin, R. Cammi, C. Pomelli, J. W. Ochterski, R. L. Martin, K. Morokuma, V. G. Zakrzewski, G. A. Voth, P. Salvador, J. J. Dannenberg, S. Dapprich, A. D. Daniels, O. Farkas, J. B. Foresman, J. V. Ortiz, J. Cioslowski, and D. J. Fox, Gaussian, Inc., Wallingford CT, (2009).

Chapter 7

High Pressure Response of [n]CPPs: Mechanical Modulation of their Cross Section

In this chapter we present a high pressure, Raman study on [n]CPPs of different members ranging from [5]CPP to [12]CPP and with pressures up to 12 GPa by means of a sapphire anvil cell. We aim to analyse the size dependent mechanical properties of these molecular systems and their reversible or irreversible behaviour towards deformation. Moreover, among the main objectives of this chapter is to provide a better understanding of certain analogies and differences between the strain response of [n]CPPs and either SWCNTs or LPPs. It has been broadly discussed in this thesis how the increasing strain on the [n]CPPs with decreasing *n* is responsible for the unique [n]CPPs properties. Subsequently there is a remaining question left: will the [n]CPPs high pressure response modulated by such initial structural strain? We will attempt to disclose any possible configurational or conformational alterations that pressure may induce on these systems. In the cases that such alterations occurred it is essential to know if they would be reversible or irreversible and in which extent these would affect to the properties of [n]CPPs. In this regard the formation of unreachable configurations at room conditions by convectional synthetic routes will be suggested, such as quinonoid or peanut shaped [n]CPPs. Additionally, we would like to highlight that all these studies have been performed in the solid state, so the formation of any unconventional conformation of [n]CPPs should have the advantage of being an environmentally clean route to achieve them.

7.1. Introduction

It is known that high pressure can be used as modulating tool of interactions, and also to trigger reaction paths otherwise not reachable at room conditions. This is why high pressure is becoming a leading tool for manipulating and inducing reactions in very specific directions. Even though high pressure may be seen as a very convenient tool, not much has been explored in this field. Becoming the latter an important drawback since, no much information can be found in the literature. An additional disadvantage is that very extreme conditions, not easily scalable to high quantities, may be necessary for such transformations.

One of the highest attractions of [n]CPPs is that they have been thought as ideal candidates for the bottom up synthesis of armchair SWCNTs.[1] The mechanical response of SWCNTs has been widely studied, since along their long dimension they are among the strongest materials.[2,3] However within their cross sectional directions, SWCNTs are softer as their diameter increases, reaching even collapsed configurations.[4] Such changes may have influences on the CNTs properties, so it is important to have them well controlled and characterized to do a fine use of the system in future applications.[5,6,7] In addition, it is known that pressure-dependent Raman experiments provide key information about the bond anharmonicity and the mechanical strength of CNTs.[8,9] There are few high-pressure experimental works which study their properties while taking their size into consideration.[10] The lack of studies on single diameters SWCNTs, together with the fact that the pressure also modulates their resonance conditions, as mentioned in section 2.1, makes that results could be more conclusive if those studies were done with single diameters SWCNTs. Likewise, it can be considered that the high pressure response of [n]CPPs could assist providing answers to some of the open questions of CNTs.

On the other hand, optical studies under high pressure of molecular systems allow to correlate how intermolecular interactions and structural changes affect photo-physical properties without modifying their chemical composition.[11,12] In this regard, there is an open window to explore about how [n]CPPs would evolve, since such properties are still unexplored. Nevertheless the high pressure response of their linear analogs (linear paraphenylenes, [n]LPPs) is quite known.[13,14] As said in previous sections, [n]LPPs depict torsions between neighboring rings to minimize steric repulsions between ortho hydrogens. When pressure is applied over these systems they follow a large planarization in the sense that the torsions between neighboring benzene rings diminish towards zero. For instance, at room temperature at pressures higher than 1.5 GPa, the planarization of para-hexaphenyl has been described described.[14] Nothing is known about if [n]CPPs would respond to high pressure in a similar fashion, with a decrease in their torsions towards higher inter phenyl conjugation. Therefore we aim to find that possible connection between the two oligomeric systems.

Along this thesis, it has been shown how the properties of [n]CPPs are tremendously *n* strain dependent. Such dependence is modulated by two main factors: strain and cyclic conjugation. We wonder if the compression of [n]CPPs would lead to the formation of different configurations triggered by their initial strain. Moreover, so far all the studied [n]CPP properties are very size dependent, so it we could speculate that the further strain gain during compression would reveal that [n]CPPs mechanical properties are very *n* dependent as well. By means of the high pressure Raman spectra behavior of the different [n]CPPs, we aim to explore their mechanical properties. We will conduct a detailed analysis of the most important vibrational modes as function of *n*. Then we will compare our results with those of SWCNTs, and with those of their molecular cousins, [n]LPPs. This analysis will enable us to provide the first study on mechanical properties of [n]CPPs.

This chapter will be divided in different sections. It starts with a preliminary analysis of the high pressure response of SWCNTs and LPPs, which will be used as reference for the next sections. Then it will continue with a detailed study of the [n]CPPs high pressure behavior which will allow us to characterize the [n]CPPs mechanical properties. We will finish this chapter studying the recovered samples, once pressure has been released, to analyze pressure as modulating tool in a reversible or irreversible fashion.

7.2. Experimental

SWCNTs. In the search of the analysis of how high pressure affects to CNTs we conduct high pressure Resonant Raman experiments on SWCNTs. Studied sample was purchased in Sigma Aldrich Inc. (SWeNT® SG-76). It was produced by a CoMoCAT® Catalytic Chemical Vapor Deposition (CVD) method, using a flow of pure carbon monoxide at a pressure of 1–10 atm. The nanotubes were grown by CO disproportionation at 700–950 °C in the presence of a unique Co-Mo catalyst. Factory assays guarantee the following characteristics: ≥ 77% is carbon as SWCNT, with diameters ranging between 0.7 and 1.1 nm, >50% of the sample has a (7,6) chirality. Ideally armchair pure nanotubes would have been more appropriated for the comparison with the high pressure response of [n]CPPs, but these are not commercially available and the purification process is a very tedious method[15] and out of the scope of this work. We used a 488 nm excitation line, resonant with the diameters of our SWCNTs, 0.7 and 1.1 nm (see chapter 2 for Kataura plot).[16-18] The experiments were done with a LabRAM HR spectrometer (Horiba Jobin-Yvon) using a 1800 grooves mm^{-1} grating and an Ar/Kr laser (488.0 nm). We conduct high pressure experiments by means of a sapphire anvil cell (SAC) with anvils with a diameter culet of about 400 μm. A partially drilled gasket of gold is utilized, but to avoid uncontrolled interactions no pressure transmitting medium is charged. With the employed configuration no stress marker, as diamond, was required as its Raman shift would be overlapped by the SWCNTs D band. As already done in other cases in the literature,[19,20] we use the Raman shift of the sapphire anvil (bands at 417 and 750 cm^{-1}, A_{1g} and E_g modes, respectively[21,22]) as pressure indicator.

[5]- and [6]LPP were purchased from TCI. The former was measured at room and high pressure conditions with a Bruker Senterra dispersive Raman spectrometer with the 785 nm as excitation wavelength and a spectral resolution of 3 cm^{-1}. [6]LPP measurements were done by using a Spectra-Physics solid state laser operating at 532 nm, coupled to a micro-Raman spectrometer with an HR460 monochromator. Pressure studies were conducted in a SAC with anvils with a diameter culet of 400 μm, pressures up to 12 GPa were reached. No pressure transmitting medium was charged and diamond chips were used as pressure calibrant.[23]

[5]- to [12]CPP. [n]CPPs with n = 8, 9, 10, 11 and 12 were provided by Yamago et al., and were synthesized by using a synthetic strategy through multinuclear arylplatinum complexes.[24] [5]CPP, [6]CPP and [7]CPP were provided by Jasti et al., synthesized through Suzuki–Miyaural cross-coupling/macrocyclization to macrocycles and their consecutive reduction routes.[25,26] Raman measurements at room and high pressure conditions of the different [n]CPPs were conducted with a Senterra dispersive Raman spectrometer from Bruker with a 785 nm excitation wavelength with a standard spectral resolution of 3 cm^{-1}. Pressure studies were conducted in a SAC with anvils with a diameter culet of 380 μm. Pressures up to 12 GPa were reached, although for each [n]CPP the maximum pressure achieved was slightly different. No pressure transmitting medium was used and diamond chips were employed as pressure calibrant.[23] In the case of [5]CPP all the sample manipulation was done in an glove box under a nitrogen atmosphere.

For all the Raman spectra the background has been removed setting the baseline at zero before any spectral analysis is done. As already mentioned, in section 2.1., from the Raman spectra of each one of the samples at every pressure point we study the Raman shift and intensities of the main bands. Second derivative analyses of the spectra have been done to obtain the peaks maxima, ω. Those peaks maxima are used as initial values of the fitting with a sum of Lorentzian curves, as it was already explained elsewhere.[27] In the Lorentzian fitting of the peaks, the full width half maximum (FWHMs) ranges between 8 and 40 cm^{-1}. During the Lorentzian peak fitting, the FWHMs are firstly fixed at the room conditions values, between 8 and 15 cm^{-1}, and then let freely iterate. As intensities we consider the area of the bands.

7.3. Systems Related with [n]CPPs

7.3.1. Single Walled Carbon Nanotubes

Single Walled Carbon Nanotubes (SWCNTs) have attracted much attention from the scientific community because their interesting one-dimensional properties and for their potential applications.[28,29] It has been suggested that these one dimensional systems conduct structural transitions during compression in which their cross section changes from circular to oval and then to a peanut shape.[30,31] The concomitant diameter decrease with compression leads to high increment over the structural energy. Such cross section decrease leads to size dependent structural transitions in a manner that nanotubes with diameters above 2.6 nm at room conditions are defined to be stable into their collapsed configurations.[32] In line with those observations, the mechanical properties along the cross sectional directions have been related with the SWCNTs diameters, being these softer as higher their diameters are. The pressure at which the structural transition occurs is referred as pressure of collapse or pressure transition and it is very size dependent in the sense that it is larger for the smaller CNTs.[33] For instance, Elliott et al.[30] observed a pressure transition around 6.6 GPa for nanotubes of diameters around 0.8 nm, while for bigger nanotubes with diameters of 1.2 nm they reported that their pressure transition was around 2.1 GPa.

To better illustrate this behavior a B3LYP/6-31G(d,p) methodology was here used to calculate how the energy of a (10,10) SWCNT of finite length, with 200 carbon atoms, changes when this is constrained within its cavity, as shown in Figure 1. Based on those results discussed in the literature, we assume that pressure induced such kind of deformation within the SWCNT cross section. In this representation we see how the energy, respect the non-constrained geometry, exponentially increases while the SWCNT is being deformed towards ovallization and to its final peanut shape. Pressure would be responsible for such energy increase and the resulting tubular deformation.

Raman spectroscopy is a widely used tool for the characterization of carbon based materials. As anticipated in the section 2.2.2 valuable structural information can be obtained, such as the diameters of the measured tubes with a given excitation line. In particular, during the study of SWCNTs high pressure response it has been considered as one of the most important characterization tool and testing ground for theoretical predictions. Raman spectroscopy allows studying the high pressure

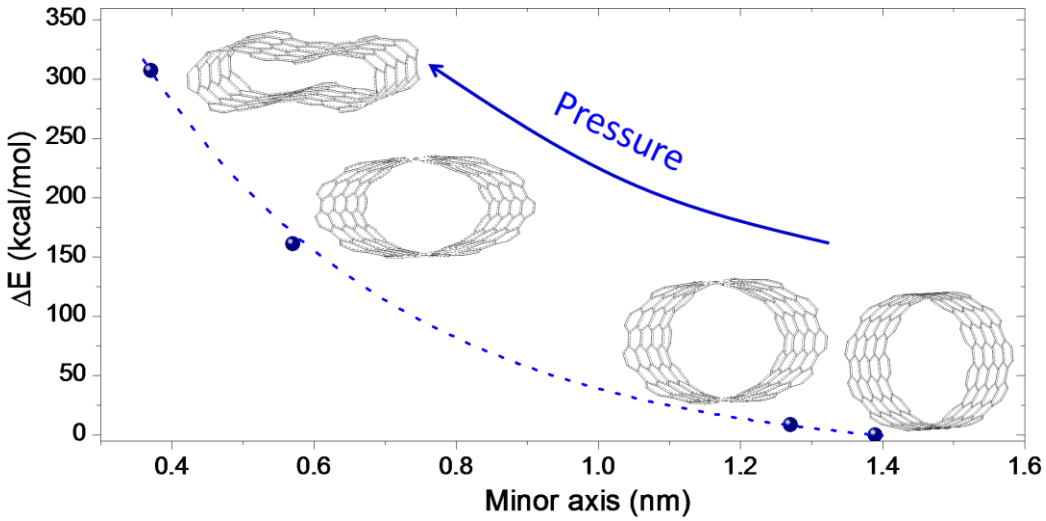

Figure 1. DFT-B3LYP/6-31G(d) energy variation of a (10,10)SWCNT with finite length, 200 carbon atoms, when its cavity diameter is constrained, taking as zero energy that of the non-constrained optimized geometry. "Minor axis" distance corresponds to the shortest diameter along which constrain has been set. Optimizations have been done freezing the coordinates of those atoms involved in the diameter cross section.

dependence of their shape within their cross sections.[34,35,36] In principle the Radial Breathing Modes (RBMs) and the G modes are those whose Raman shifts and intensities trends have been related with their mechanical properties and with their possible structural transition.[37,38,39] When the tubes are deformed a change in their cross section occurs leading to a change into their resonance conditions, thus the intensity decrease of the RBMs has been related with such deformation.[40,41] About the G bands, it has been observed that, regardless the SWCNT nature, G modes are intimately affected by strain.[39] The G bands show a linear upshift with pressure which is broken towards another linear trend with different slope once a structural transition occurs. In the literature,[35,41,42,43] such structural transition has been assigned to the mentioned ovallization within the cross sectional direction, as pictured in Figure 1. In the next section we are going to show our Raman study at high pressure of a commercial sample of SWCNTs.

7.3.1.1. High Pressure Behavior of Single Walled Carbon Nanotubes

Resonant Raman spectroscopy is among the most common ways to be selective to study SWCNTs of certain diameters when the sample is not totally of a single diameter. When the laser energy is resonant with electronic transition energy in a nanotube, the Raman signal can be intense enough to observe spectra from an individual isolated SWCNT.[44]

In Figure 2a we plot the Raman spectra at selected pressures in the RBMs region when the spectra are normalized to the G band. Measurements were done with the 488 nm excitation line. Indications provided from the factory about the composition of this sample say that is formed by tubes with diameters between 0.7 and 1.1 nm and enriched with the (7,6) SWCNTs. Therefore using the Kataura plot, see chapter 2,[16] we conclude that the 488 nm is the most adequate excitation to probe these tubes.[16,18] The bottom spectrum corresponds to the pristine sample at room conditions, this depicts several low frequency bands corresponding to large diameters (grey bands). However, once the sample is placed in the high pressure cell the latter are not visible any more. With the requirement that all the RBMs must have the same FWHM,[45] we fit the remaining RBMs to six different contributions, represented with different colored Lorentzian curves in Figure 2a. The Raman shift of these contributions ranges from 216 to 300 cm^{-1} approximately, so the diameters range between 0.76 and 1.05 nm (see Table 1).

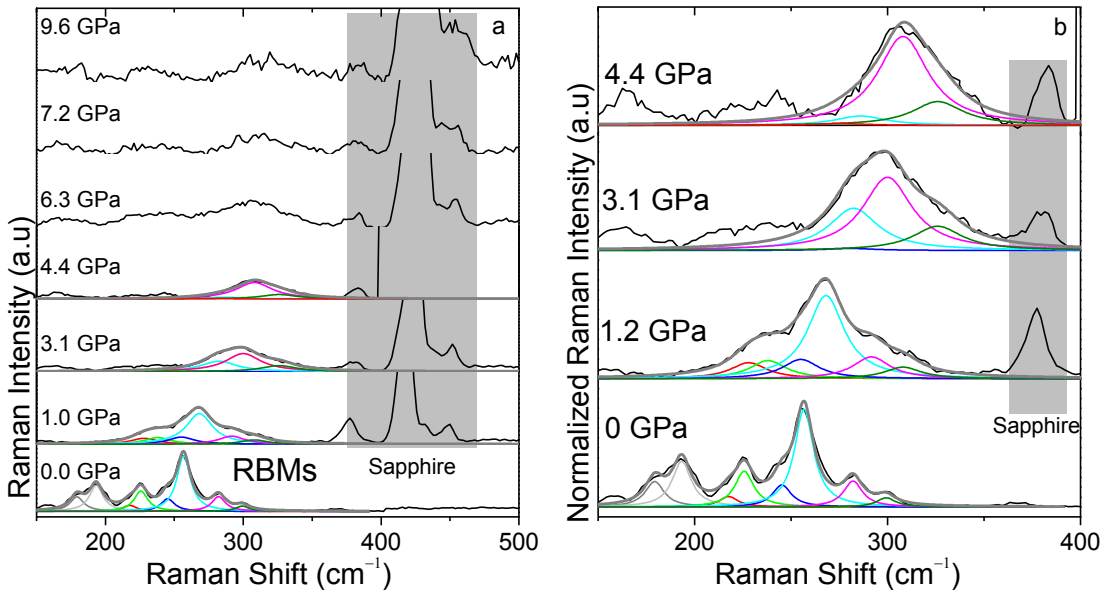

Figure 2. Raman spectra of SWCNTs at selected pressures in the RBMs region, obtained by using the laser excitation energy of 2.54 eV. a) Normalized to the G band. b) Normalized to the most intense RBM. Colored curves below the spectra represent the Lorentzian peaks of the different RBMs and grey curve is the sum of these Lorentzians. Shadow region corresponds to sapphire Raman peaks used as anvils.

estimated from equation 1,[45] already described in the methodology chapter:

$$d(nm) = \frac{227}{\omega_{RBM}(cm^{-1})} \quad (1)$$

We can assign the most intense band around 256 cm^{-1}, in light blue, to tubes with a diameter of 0.88 nm, meaning that the sample is mainly constituted by those tubes. In addition, we can use other estimation of the diameter from equation 2:[46]

$$d = \frac{a_0}{\pi}\sqrt{n^2 + nm + m^2} \quad (2)$$

where a_0 is proportional to the C-C distance and equals to 2.494 Å, and n and m correspond to the chiral parameters. So that, if we use the chiral parameters provided by the factory (n = 7, m = 6), we calculate a diameter of 0.88 nm, in agreement with the value reported in Table 1.

In Figure 2a it can be seen that with increasing pressure the RBMs become negligible at pressures above 4 GPa. This is probably due to the loss of resonance with the cross section deformation.[40] To better illustrate this behavior in Figure 2b we represent the Raman spectra in the RBMs region when these are normalized to the most intense RBM band. A general broadening is observed which makes difficult the SWCNT assignment. If we follow the intensity of the band assigned to (7,6) tubes, in light blue, this seems to decrease with increasing pressure. This intensity decrease is generally observed in all the RBMs, and it could then be related to the pressure induced cross section deformation, as exemplified in Figure 1, leading to a change into their resonance characteristics.[40,41]

In Figure 3a we show the Raman shift of the different RBMs as a function of the applied pressure. These follow linear trends with very similar slopes summarized in Table 1. In Figure 3b we plot the pressure coefficients that we obtain together with those reported in the literature as a function of the Raman shift of each tube at room conditions. It can be seen that these slopes are a bit larger for RBMs of lower shifts, i.e. for bigger and thus softer SWCNTs. Our results are in good agreement with those values described in the literature.[10,47-54]

Finally, in Figure 4 we represent how the intensities of the assigned RBMs vary with increasing pressure. We can clearly see the already described intensity decreasing of the RBMs. Therefore, we can conclude that a cross section deformation has been induced by pressure at values higher than 4.4 GPa.

Table 1. ω_0: Raman shift at room pressure of the observed RBMs. Diameters were estimated from equation 1 and the ω_0 values. S_1: pressure coefficient of the RBMs of the analyzed sample of SWCNTs. This sample was characterized in the factory as having tubes with diameters ranging between 0.7 and 1.1 nm.

	ω_0 (cm^{-1})	Diameter using eq. 1 (nm)	S_1 $d\omega/dP$ ($cm^{-1}GPa^{-1}$)
This work	300	~0.76	5.6 ± 0.4
	285	~0.80	5.0 ± 0.4
	256	~0.88	6.6 ± 0.4
	245	~0.95	5.6 ± 0.9
	225	~1.01	6.0 ± 1.0
	216	~1.05	6.0 ± 1.0

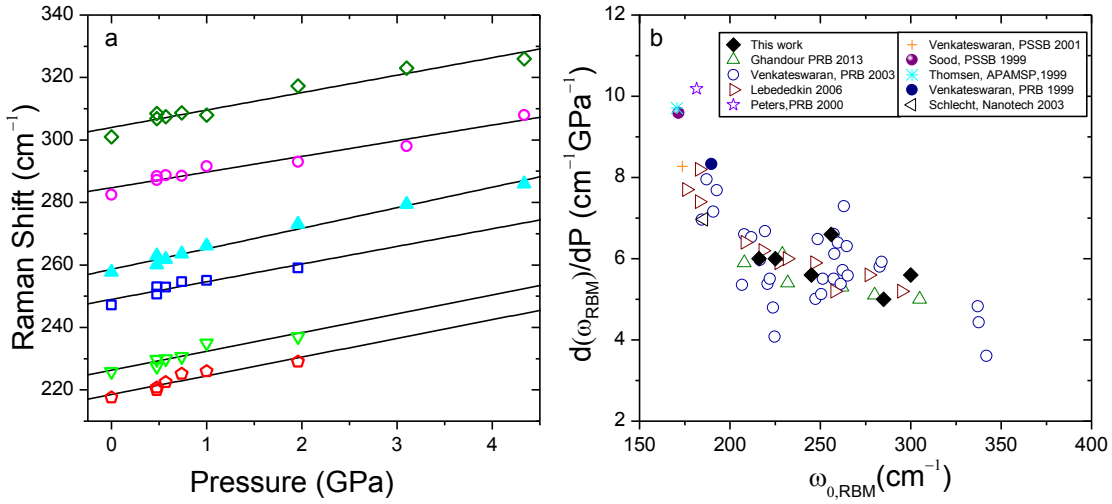

Figure 3. a) Raman shift pressure dependence of the RBMs observed between 216 and 300 cm^{-1} at room conditions. b) Pressure coefficients of the circumferential modes represented against their Raman shift at room conditions. (◆) this work; (△) Ghandour et al. [10]; (⬠) Venkateswaran et al. [47]; (▷) Lebedkin et al. [48]; (☆) Peters et al. [49]; (+) Venkateswaran et al. [50]; (●) Sood et al. [51]; (✳) Thomsen et al. [52]; (●) Venkateswaran et al. [53]; (◁) Schlecht et al. [54].

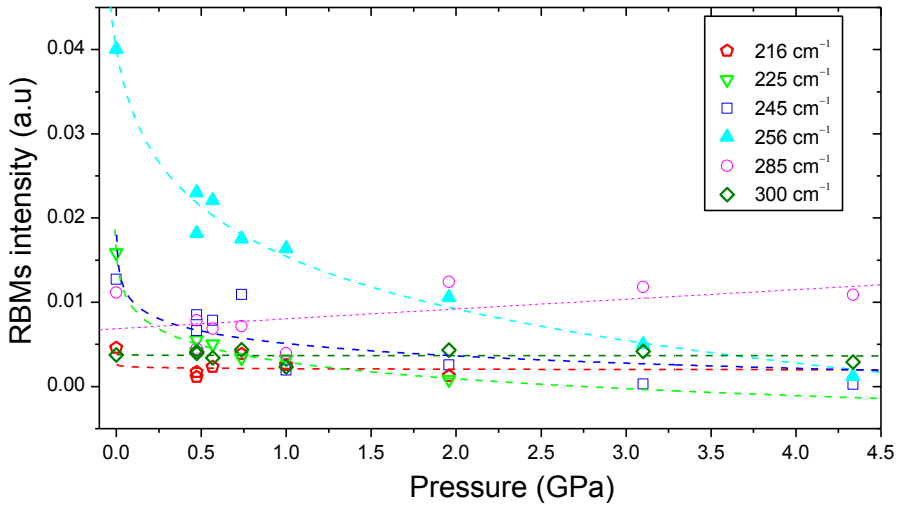

Figure 4. RBMs intensity, normalized to G band, as a function of pressure. Colored symbols correspond with the color of the Lorentzian peaks of Figure 2. Colored dashed lines correspond to the fitting of the intensity of each band as a function of pressure. The fitting function used is I=a+bLn(P+c), where a, b and c are the fitting parameters. The color of each dashed line matches the corresponding color assigned to each band.

In Figure 5 we plot the Raman spectra at selected pressures in the high frequency region, 1200 – 1800 cm^{-1}. The bottom spectrum of the Figure 5a corresponds to the pristine sample. The G profile can be described by at least six Lorentzian contributions, then we are dealing mainly with metallic chiral nanotubes.[55,56] It can be observed how, regardless the contribution, these bands broaden with the increasing pressure. In Figure 5b we have represented the Raman shift of these contributions as a function of pressure, together with the values for the defect related D band. These bands follow a double linear trend depicting a clear kink around 5 GPa. This deviation appear in all the bands, but due to the defect relationship of the D band, such kink is more abrupt in this band, with a change in slope from 12.6 cm^{-1}GPa^{-1} to 1.9 cm^{-1}GPa^{-1}, Table 2. The Raman shift of these bands have been fitted to a double linear trend,

$$\begin{aligned} \omega &= a + S_1 p && \text{if } (p < PT) \\ \omega &= a + (S_1 - S_2)PT + S_2 p && \text{if } (p > PT) \end{aligned} \qquad (3)$$

where S_1 and S_2 correspond to the slopes of the linear trends before and after the kink or pressure transition (*PT*), and *a* corresponds to the intercept before pressure transition. Then, we have for each band four parameters (*a*, S_1, S_2, *PT*), although *PT* is the same for all the bands, since to the set data of the seven bands has been fitted globally sharing a parameter, *PT*. The fitting lines have been depicted in the Figure 5b and the corresponding fitting parameters are summarized in Table 2. In the literature a similar behavior has been described,[30,41,57] and values for *PT*, S_1 and S_2 are in agreement with those here observed. For instance, Ghandour et al.[10] obtained a coefficient of 4.56 $cm^{-1}GPa^{-1}$ for the G band of nanotubes with diameters around 0.84 nm. We can also indicate that these values are around the same magnitude than those obtained for the graphite G band, 4 $cm^{-1}GPa^{-1}$.[58]

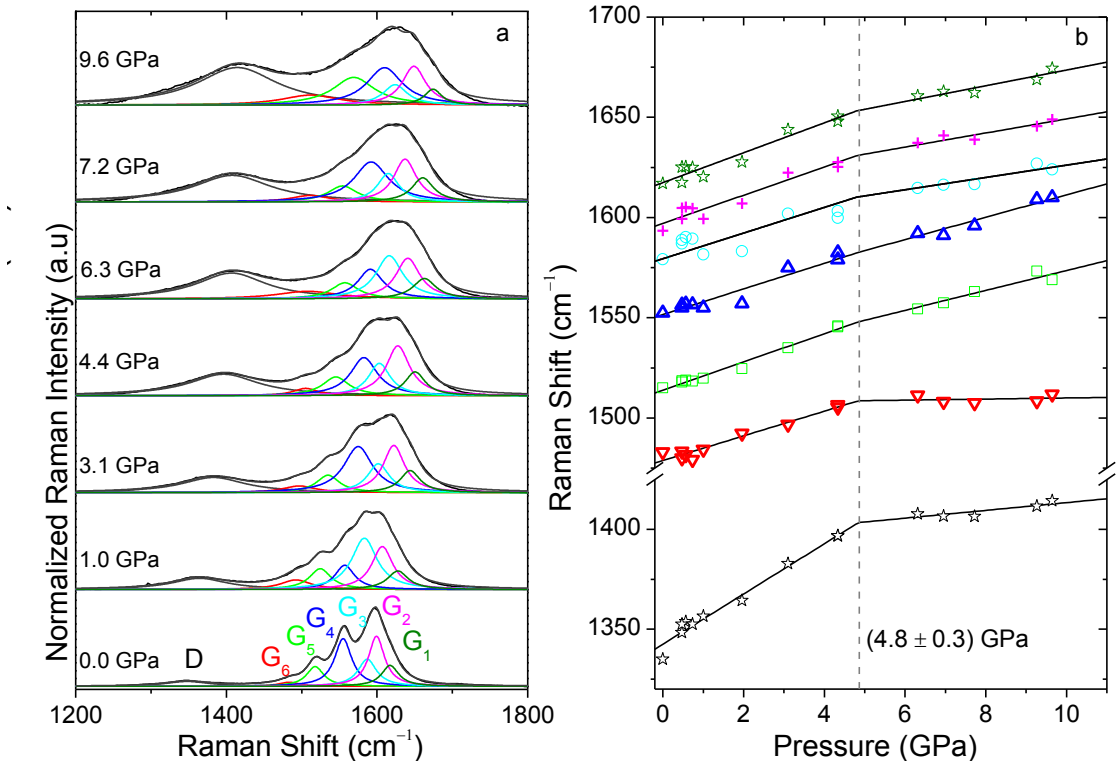

Figure 5. a) Raman spectra of SWCNTs at selected pressures normalized to the most intense band. Laser excitation energy = 2.54 eV. Curves below the spectra represent the Lorentzian peaks of different G contributions. b) Raman shift of the G bands as a function of pressure, colored symbols correspond with the color of the Lorentzian peaks; black stars correspond to the D band.

Table 2. ω_0: Raman shift at room pressure of the G and D bands of the analyzed sample of SWCNTs. Laser excitation line: 488 nm. Pressure coefficients: S_1, before pressure transition and S_2, after pressure transition (*PT*). Last lines summarize results taken from Ref. [30].

	Diameter nm	*PT* GPa	Band	ω_0 cm^{-1}	S_1 $d\omega/dP$ $cm^{-1}GPa^{-1}$	S_2 $d\omega/dP$ $cm^{-1}GPa^{-1}$
This work	0.7 – 1.1	4.8 ± 0.3	G_1	1620 ± 1	7.4 ± 0.6	3.9 ± 0.7
			G_2	1599 ± 1	7.0 ± 0.6	3.5 ± 0.7
			G_3	1583 ± 2	6.4 ± 0.6	3.1 ± 0.8
			G_4	1552 ± 1	6.4 ± 0.5	5.6 ± 0.5
			G_5	1515 ± 1	7.0 ± 0.2	5.0 ± 0.5
			G_6	1483 ± 2	6.2 ± 0.6	0.3 ± 0.7
			D band	1342 ± 2	12.6 ± 0.6	1.9 ± 0.9
Ref. [30]	0.8	6.6 ± 0.8	G^+	1595	6.8	4.9
	1.4	2.1 ± 0.2	G^+	1594	8.8	5.9

The double linear trend observed in the shifts with pressure of the G bands has been related with the pressure effect on the tubular system:

- Firstly, before *PT*, in principle pressure affects mainly molecular bonds and in a minor degree molecular angles.
- After *PT*, pressure affects mostly bond angles towards ovallization of the tube and C-C bonds remain almost unaltered, as depicted in Figure 1.

Such description is in agreement with the behavior followed by the G bands, C-C stretching bands: these in the first regime depict larger coefficients than in the second regime. C-C bonds are harder and more rigid than bond angles; then, the first regime is referred as hard phase and the second one as soft phase of the tube.[59]

As observed, the pressure at which the slope changes is around 4.8 GPa, this is of the same magnitude to that observed by Elliott et al. for SWCNTs with diameters about 0.8 nm.[30] Interestingly, the D band is the one which depicts the largest slope change. This is consistent with the fact that D band has a relationship with defects density. Therefore it is expected that from ovallization not only its intensity would increase, but also a larger frequency dependence on this deformation. We tried to compare this marked dependence on the D band with deformation with results from the literature, but due to the overlap with the Raman signal of diamond used as anvil in the majority of the works, in our knowledge, no data are reported about the behavior of the D band for SWCNTs. However, reports on double walled CNTs provide pressure coefficients for the external tube slightly lower than ours: 5.1 $cm^{-1}GPa^{-1}$ given by del Corro et al.[27] and 7.1 $cm^{-1}GPa^{-1}$ given by Arvanitidis et al.[60] The only stated information about the D band behavior of SWCNTs with pressure is the observation of a significant intensity increase on the D band of the recovered samples after compressed (at a maximum pressure around ~35 GPa).[61]

Because of the diameter heterogeneity in our SWCNT ,sample we cannot say anything else about the behavior of those less abundant tubes. However, we can be certain that pressure has induced changes in the cross sectional shape of the most abundant diameter, with a physical origin similar to that described in the literature. Because of the large number of peaks of the G band and their lower diameter selectivity, compared with the RBMs; and because of the RBM broadening with increasing pressure, not much information can be extracted apart from:

- In our commercial sample (majority diameter ~ 0.88 nm) there is a pressure transition around 4.8 GPa. From this pressure the Raman shifting with increasing pressure varies, so different slopes are observed. Also around this value the resonance of the pristine sample varies with the concomitant RBM intensity decrease.

However, these results are enough to be used as reference in case an analogue behavior is observed for the high pressure response of[n]CPPs. therefore, in this chapter we attempt to establish the connection between the mechanical response of [n]CPPs and SWCNTs within its cavity. In this regard, a truly analysis of the size tubular high pressure dependence can be conducted. Therefore, this will configure the first real exploration of how diameter influences the deformability of nanotubular systems.

As mentioned along this work, the Raman spectra of [n]CPPs is modulated by their strain within the cycle, providing valuable information about the electronic properties and π conjugation In connection with [n]CPPs, SWCNTs share the tubular shape and a strong Raman shift dependence as a diameter function. Subsequently, we wonder if pressure will increase strain in [n]CPPs in an analogues manner than it does in SWCNTs, with the sub-sequential cyclic deformation. In such situation, one would expect analogues shifting on the studied [n]CPPs G and RBMs bands.

On the other hand, we consider is that high pressure may induce the formation of different [n]CPPs configurations. This would establish a totally new ambit in the CNTs field: it has been studied how high pressure might increase reactivity of systems hosted in their cavity,[62] but nothing has been explored about the reactivity of a SWCNT with itself further than its ovallization.

7.3.2. [5]- and [6]- Lineal Paraphenylenes

The other systems related with [n]CPPs are linear para-phenylenes, [n]LPPs, their linear oligomeric analogues. In this section we will explore the [n]LPPs response for [5] and [6]LPP. With this preliminary study we aim to provide the reader with a general background of how [n]LPPs behave with high pressure. Therefore, together with the already explored high pressure behavior of SWCNTs, we will count with enough information to conduct a precise analysis of the [n]CPPs high pressure response.

[n]LPPs are known as ladder compounds. These oligomeric systems are gaining importance in the conjugated polymeric materials, being used for applications in electronic and photo-electronic devices.[63] These are perfect candidates for π conjugated materials in a tentative bottom up synthesis.[64] [n]LPPs at room conditions and in their ground state have a non-planar configuration presenting torsional angles between neighboring benzenes, with twisted structures, becoming planar in their excited electronic states.[65] The high pressure response of these molecules has already been studied, and it is well known that they planarize,[14,66,67] being such planarization favored by the stabilization energy gain from larger π-conjugation. Guha et al.[14,68] interpreted such pressure-induced conformational change as a modification into the energy potential curve which separates the planar and twisted conformers, as it is depicted in Figure 6b. At room conditions those would be separated by an energy barrier, W shaped potential curve. With pressure this energy barrier would considerably decrease adopting an U shaped potential curve along the torsional energy surface. These authors estimated that for the [6]LPP the energy barrier was about 0.045 eV and for the poly para-phenylene (PPP) about 0.065 eV.[68] Raman spectroscopy seems to be again the most suitable tool to follow those effects since, as explained in chapter 2, intensity ratios of several bands can be related with those conformational variations.

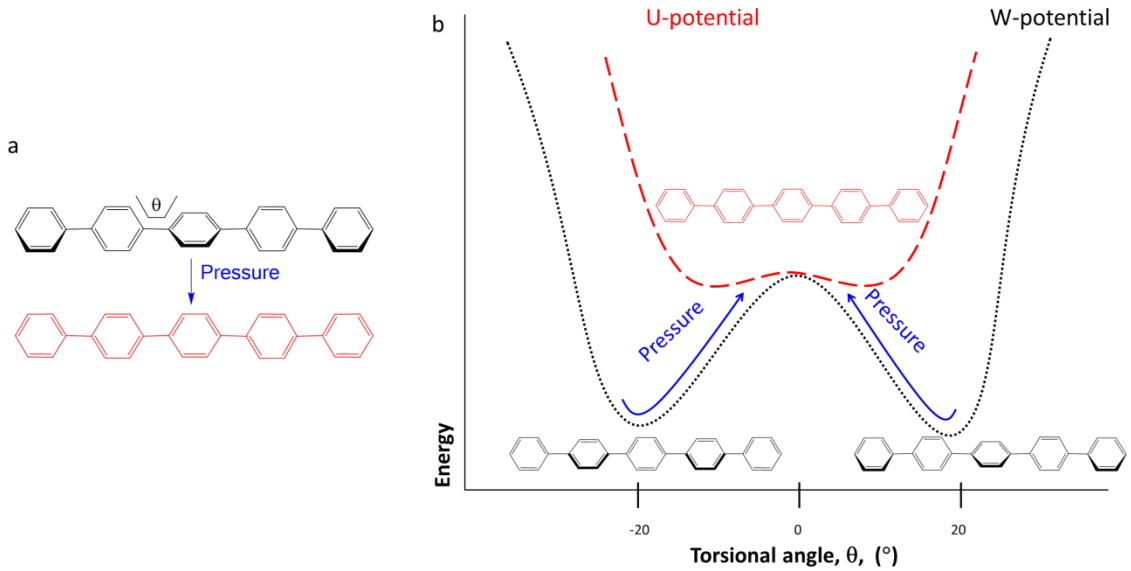

Figure 6. a) Scheme of effect of pressure on [5]LPP torsional angles (θ). b) Schematic of the potential energy versus averaged torsional angle. Dotted line represents the potential energy of a twisted configuration at ambient pressure, and dashed line symbolizes potential energy of a planar configuration at high pressure. Change of the potential energy from "W" to "U" shape is based on ref. [14].

The Raman spectra of [n]LPPs have already been very well characterized, being the most intense bands three A_{1g} bands:[69,70] the 1200 cm^{-1} mode, assigned to the C-C interring stretching mode coupled to a CH bending mode; the 1280 cm^{-1} mode, related to the phenyl breathing and the GA_{1g} mode, around 1600 cm^{-1}, corresponding to the C-C stretching mode of the benzoid rings. Around 1500 cm^{-1} appears a low intensity band with E symmetry, which is assigned to the C_{ortho}-C_{ipso} stretching bond in LPPs. the As studied in previous chapters, the intensity ratio between the 1280 and 1200 cm^{-1} bands is related with the torsional angle between neighboring rings. For instance, for [3]LPP at room conditions an average torsional angle of 13° is described[71] and an intensity ratio of 3.9 is given.[72,73]

Below we are going to describe our own results for [5]- and [6]LPP samples, analyzing their Raman spectra at high pressure. These experiments were conducted by different Raman devices: [5]LPP with a Senterra and 785 nm as excitation line, and [6]LPP with an ISA HR460 monochromator and 532 nm as excitation line. The increasing fluorescence observed on the [6]LPP experiments hindered the further pressure increase, so only experiments up to 6.8 GPa are shown.

In Figure 7 we have gathered Raman spectra of [5]- and [6]LPP at selected pressures. The bottom spectrum corresponds to the pristine sample. It can be seen how in both cases the intensity ratio between the 1280 and 1200 cm^{-1} A_{1g} bands quickly decreases with increasing pressure. Apart from that, the A_{1g} bands of both LPPs upshift with increasing pressure. In Figure 8 the Raman shifts of the A_{1g} bands as a function of pressure have been represented for both. In Figure 8b we have compared for [6]LPP experimental results with those obtained by Guha et al.[68] It is also clear that the 1280 cm^{-1}, 1500 cm^{-1} E and 1600 cm^{-1} A_{1g} bands follow a linear trend with pressure regardless *n*. Nevertheless, a clear slope change is observed for both LPPs for the 1200 cm^{-1} band: at ~ 1.2 GPa for [5]LPP and [6]LPP. The pressure at which the slope varies has been obtained by the fitting of the 1200 cm^{-1} experimental data to equation 3. In the [6]LPP case, we have used for the fitting our experimental data together with those provided by Guha et al.[68]

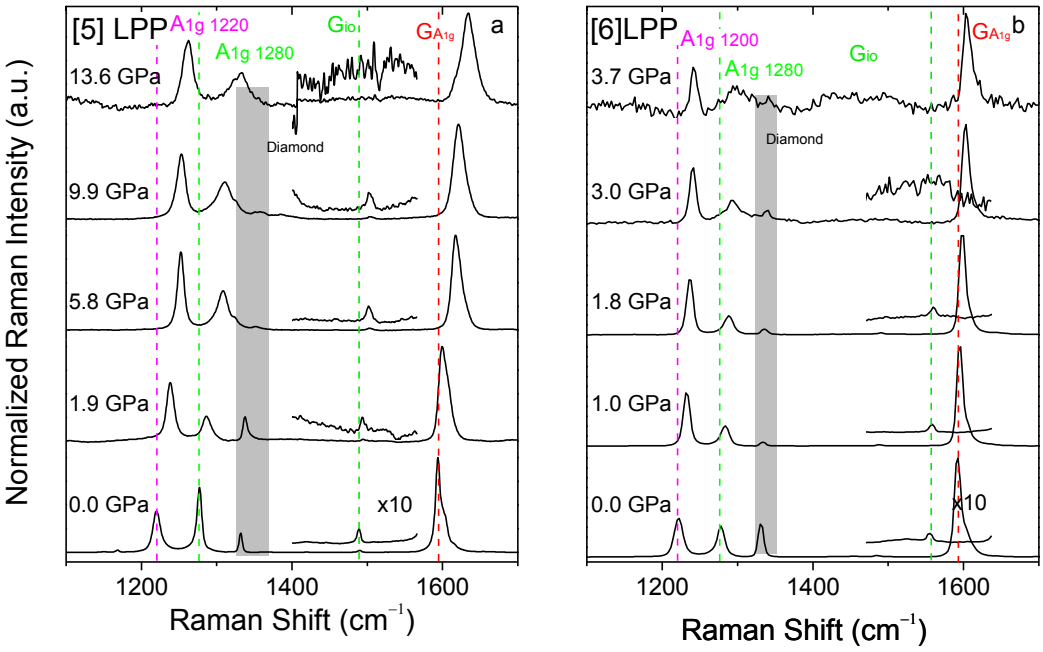

Figure 7. Raman spectra in the 1100-1700 cm^{-1} region at selected pressures, measured with the 2.33 eV excitation line. a) [5]LPP, b) [6]LPP. All the spectra have been normalized to the GA_{1g} band. Marked peaks have been fitted to Lorentzian peaks. Shadow region corresponds to the Raman band of the diamond used as pressure marker.

Table 3. Summary of the main bands of the linear para-phenylenes: data from this work for the [5]- and [6]LPP; data taken from ref [13] for [3]-, [4]- and [6]LPP and data obtained fitting the Raman shifts of ref. [13]; and data for the polymer poly-paraphenylene (PPP) from ref. [74]. ω_0: the value at zero pressure of the Raman shift of the band; S_1 are the pressure coefficients of the 1280, 1500 and 1600 cm^{-1} bands. For the 1200 cm^{-1} band S_1 and S_2 are the pressure coefficients before and after planarization.

			A_{1g} 1200 cm^{-1}			A_{1g} 1280 cm^{-1}		Gio		A_{1g} 1600 cm^{-1}	
	n	***PT*** **GPa**	ω_0 cm^{-1}	S_1 $cm^{-1}GPa^{-1}$	S_2 $cm^{-1}GPa^{-1}$	ω_0 cm^{-1}	S_1 $cm^{-1}GPa^{-1}$	ω_0 cm^{-1}	S_1 $cm^{-1}GPa^{-1}$	ω_0 cm^{-1}	S_1 $cm^{-1}GPa^{-1}$
This work, 300 K	***5***	1.2 ± 0.5	1220 ± 1	17.1 ± 0.1	1.9 ± 0.1	1283 ± 1	3.1 ± 0.2	1491 ± 1	1.6 ± 0.1	1594 ± 1	3.1 ± 0.1
	6	1.2 ± 0.5	1221 ± 1	13 ± 1	2.9 ± 0.2	1278 ± 1	4.6 ± 0.2	1278 ± 1	2.6 ± 0.2	1591 ± 1	3.9 ± 0.3
Martin et al. [13]	***3***	1.0 ± 1.5	1223	19 ± 2	2.7 ± 0.2	1275	4.2 ± 0.3	--	--	1596	4.2 ± 0.2
	4	0.9 ± 0.2	1214	26 ± 2	2.7 ± 0.2	1274	4.8 ± 0.1	--	--	1592	4.0 ± 0.1
	6	1.3 ± 0.1	1217	18 ± 1	3.2 ± 0.1	1281	5.0 ± 0.4	--	--	1596	4.4 ± 0.2
Hanfland et al. [74]	***PPP***	1.0	1230	10.3	2.7	--	--	--	--	1597	3.5

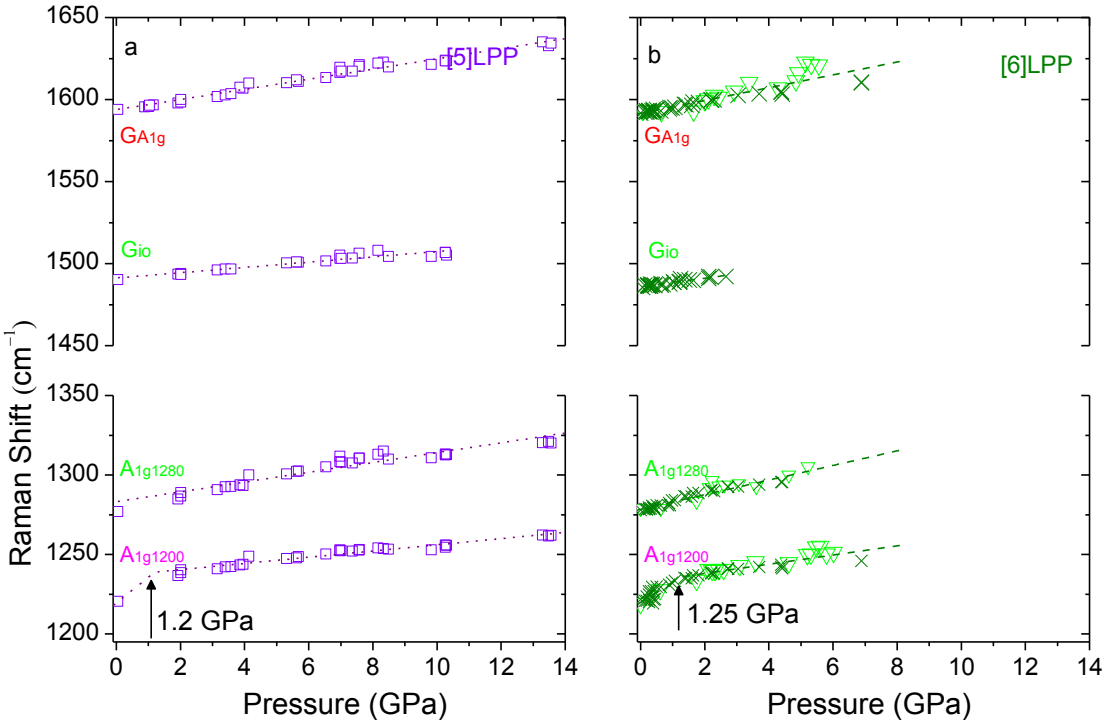

Figure 8. Raman shift of the A_{1g} 1200 cm^{-1}, A_{1g} 1280 cm^{-1} and GA_{1g} bands as a function of pressure. a) [5]LPP; b)[6]LPP. (×) this work, (△) data from Guha et al. [68]. Violet dotted and green dashed lines correspond to the fittings of the A_{1g} 1200 cm^{-1} data to the equation 3; for the A_{1g} 1280 cm^{-1} and GA_{1g} bands a single straight line has been used.

In Table 3 we have collected the slopes of the different bands for each [n]LPP. Our results are close to the already observed by Martin et al.[13] for [3]-, [4]- and [6]LPP. Hence we can conclude that the agreement between our results and those described in the literature is good and so the methodology here used is appropriate. The pressure coefficients of each band are very close to each other when comparing between the different oligomeric lengths. The differences observed between the different lengths might be attributed to experimental errors and not the oligomeric size. For

instance, the GA_{1g} band has a pressure coefficient between 3.9 and 4.4 $cm^{-1}GPa^{-1}$ for [6]LPP, and of about 3.5 $cm^{-1}GPa^{-1}$ for PPP.

Comparing our experimental results for the Gio and the GA_{1g} band we obtained pressure coefficients for the Gio band of about 1.6 $cm^{-1}GPa^{-1}$ and 2.6 $cm^{-1}GPa^{-1}$, for [5]- and [6]LPP respectively, while t or the GA_{1g} band, pressure coefficients of the [5]- and [6]LPP are a bit larger, 3.1 $cm^{-1}GPa^{-1}$ and 3.6 $cm^{-1}GPa^{-1}$. Assuming that pressure induces the [n]LPP torsional planarization, differences in the Gio and GA1g coefficients indicate that he stretching of the C_{ortho}-C_{ortho} and C_{ipso}-C_{ipso} are more sensitive to torsions than the C_{ipso}-C_{ortho}. This appreciation is in agreement with the B3LYP/6-31G(d,p) predictions described in chapter 3, appendix 1 Figure S16. With torsions and size (conjugation length) the GA_{1g} is the most sensitive, while the Gio is more sensitive to torsions than it is to size. Comparison between the Raman shifts of these bands for twisted and non-twisted configurations, shows how the Gio band slightly upshifts in the non-twisted configurations, while the GA_{1g} downshift with torsional planarization, and [n]LPP. Therefore the larger coefficients of the GA_{1g} band would be in agreement with the pressure induced planarization.

Regarding the pressure transition (*PT*) between the non-planar and planar configurations it seems that it is exhibited around 1.0 and 1.2 GPa in short oligophenylenes regardless *n*, as Martin et al. described.[13] We have also estimated the *PT* and the pressure coefficients from the PPP results given by Hanfland et al.[74] From the fitting of their Raman shifts of the 1200 cm^{-1} band to equation 3 a *PT* around 1 GPa is obtained. Therefore it looks like pressure planarization is not strongly *n* dependent.

On the other hand, Hanfland et al.[74] suggested the possibility that high pressure drove interlinks formation for PPP at pressures higher that 5 GPa. This would be promoted from the 1D planar configurations that get close enough to interact along their π skeleton with the growing pressure.[74] Although their study is based mainly in the observed energy gap evolution and the a,b,c crystal parameters with pressure, a certain deviation of a lineal trend can be observed around 5 GPa as well. In our study of the [5]- and [6]LPP we see that in our pressure range that change is not appreciated. Moreover, Raman evidences would not be enough to assume that chains interlinks. To reach similar conclusion about the behavior of [5]- and [6]LPPs further studies would be required. For instance, Raman work should be complemented by the analysis of the optical gap or infrared spectra as a function of pressure.

Regarding the intensity ratio, $I1280A_{1g}/I1200A_{1g}$, we have represented them in Figure 9 for [5]LPP and [6]LPP. It can be seen that both LPPs follow a quick decrease up to 1.2 GPa for [5]- and [6]LPP. From these pressure values, the intensity ratios remain approximately constant, around 0.4 units, in good agreement with the results from the literature for [6]LPP.[14,68] As mentioned, these changes in the intensity ratio together with the change in the pressure coefficients of the 1200 cm^{-1} A_{1g} band have been related with the decrease of the torsional angles between neighboring benzenes. It has been suggested that a change into the torsional potential energy curve occurs with pressure and so the non-twisted configuration becomes an energy minimum at high pressure, as depicted in Figure 5.

In this section we have analyzed the high pressure response of [n]LPPs to be used as reference in the study of the high pressure behavior of [n]CPPs. Moreover, pressure doesn't seem to induce any electronic rearrangement rather than the pi conjugation enhancement along the oligomeric unit. The pressure coefficients of the different bands and the kink of the $I1280A_{1g}/I1200A_{1g}$ intensity ratio, are size independent. Therefore it can be concluded that pressure modulates the [n]LPPs torsional planarization regardless *n* at pressures higher than 1.2 GPa. However, such π conjugation enhancement does not cause any C-C bond rearrangement, since the kink of the $I1280A_{1g}/I1200A_{1g}$ intensity ratio is not coupled to any change in the slope of any of the C-C stretching bands.

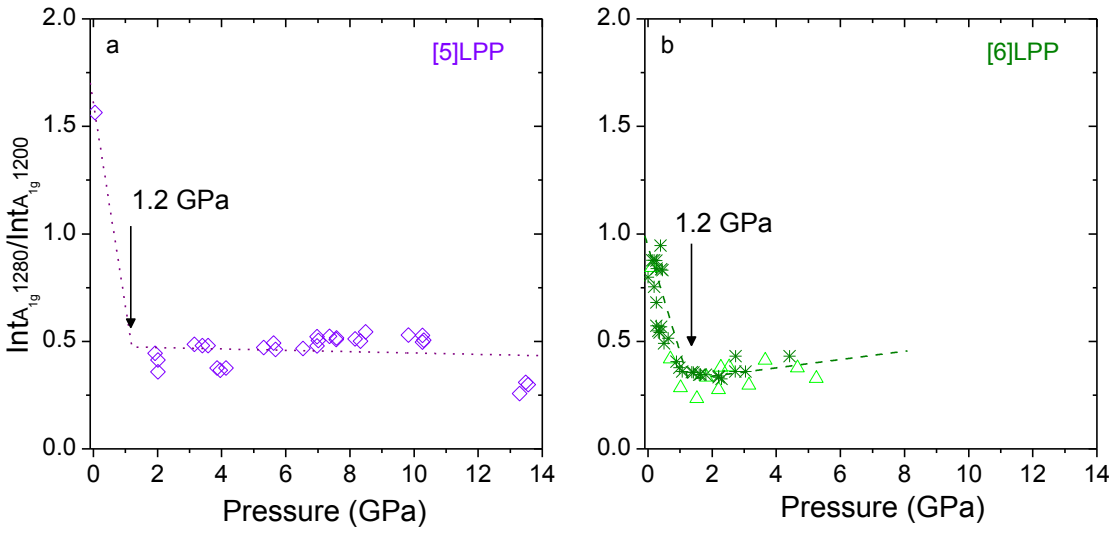

Figure 9. Pressure dependence of the I1280A_{1g}/I1200A_{1g} intensity ratio: a) [5]LPP; b) [6]LPP. (×) this work, (△) data from Guha et al. [68]. Violet dotted and green dashed lines correspond to fittings to equation 3.

Regarding the LPPs structure, only limited data are available in the literature of their solid structure at room temperature. For instance, the average torsions for [3]LPP and [4]LPP are 15° and 10°, respectively.[71,75,76] These are about 30°-25° below the predicted values as isolated single molecules, because LPPs intermolecular packing in the solid state, counteracting the H…H repulsions which generate the torsion.[71,75,76] In addition, torsions of [5]- and [6]LPPs systems are described at isolated molecules to be around 35°.[77] However in solid state these torsional angles should diminish to values which can be estimated from their ratio ($IA_{1g}1280/IA_{1g}1200$) compared with the values of [3]- and [4]LPP. Hence torsions around 10° and 15° at room conditions should be expected for [5]- and [6]LPP. At higher pressures than 1.2 GPa, pressure may induce further torsion decrease towards a planar configuration.

We know that [n]CPPs do present torsional angles between neighboring phenyl units, which as in [n]LPPs are lower at room conditions than those measured by XRD at 100 K (see chapter 3). In contrast to [n]LPPs, in [n]CPPs torsional angles are strongly affected by their increasing strain with the decreasing *n*. Torsions are hindered by strain, rotation of phenyl units are more energetic, and consequently torsions decrease with decreasing size. We wonder if high pressure will induce the planarization of [n]CPPs as in [n]LPPs. Moreover, we attempt to resolve how strain might be involved in such planarization pressure induced process.

As in [n]LPPs, a torsion decrease would enhanced the π conjugation between phenyl units. Because of the lower torsional angles of the smaller [n]CPPs, we could consider that the pressure required to reduce their torsional angle might be low. However, in this line we do not take into account the effect of strain, which certainly might play an important role. As seen in chapter 6, torsions in [n]CPPs are directly related with the stabilization provided by cyclic conjugation. Would such conjugational effect induce a rapid high pressure torsional decrease? Then, will the high pressure response of [n]CPPs in terms of torsions size dependent, or size independent as in [n]LPPs?

In the next section of this chapter we will explore the high pressure response of [n]CPPs in terms of how it might modulate their cross sectional shape, in line with SWCNTs, and in terms of torsional angles, in line with [n]LPPs. We will analyze how strain of [n]CPPs might be responsible of any of the [n]CPP high pressure modulations.

7.4. High Pressure Behavior on [n]CPPs

One of the aims of the previous high pressure experiments with SWCNTs and LPPs was to confirm the suitability of our experimental settings to the study the response to pressure of these systems. We see that for SWCNTs much purer tubes would be need to obtain more conclusive results as a function of diameter and chirality. However, when preparation of the systems follows a bottom up route, as it is in the organic synthesis of LPPs, the results are much more straightforward and promising in terms of no possible misleading products can be interfering. Here we focus on the [n]CPPs to approach several open questions:

1. Are [n]CPPs as deformable as SWCNTs within its cross section direction?
2. Will pressure induce a decrease in the torsional angle between neighboring phenyls as in their linear analogues? Could exist a competitive response between the cross section tubular deformation and the torsional angle decrease towards [n]CPPs more symmetric non-twisted configurations?
3. Are those highly strained [n]CPPs going to behave as those less strained, in other words, small [n]CPPs will behave as the bigger ones? How would pressure affect to those highly strained [n]CPPs?
4. Can we do a comprehensive analysis of the [n]CPP mechanical properties? Will these be closer either to their linear analogues, to SWCNTs or nothing to do with any of them?
5. It has already been described in previous sections how the conjugated character along the cavity is enhanced in the smaller [n]CPPs with n<9. Will pressure induce any alteration of that pattern?
6. Will pressure effects be reversible? In the case they were not, would it lead to unreachable configurations at room conditions?

In this section we aim to resolve these open questions considering any possible high pressure response in molecular terms. DFT theoretical calculations carried out along this thesis have considered a single molecule without any intermolecular interaction. As mentioned, at the end of this chapter we have collected significant views of the crystal structure of each of the studied molecular systems with the aim to provide support to the results discussion. It should be pointed out that theoretical calculations conducted with programs which have into account the solid crystal (Quantum Expresso)[*] obtain similar results to those with single molecule ones. DFT results have provided us with substantial support for the assignment of certain Raman bands and then the interpretation of their experimental high pressure response. A computational work at high pressures over these molecules is out of the scope of this thesis.

Finally, we want to clarify that along this chapter Raman spectra at four selected pressures for each [n]CPP will be shown, so the section does not excessively lengthen. But those are not the only measurements, in Table 4 we summarize the number of runs for each [n]CPP, pressure range reached and the total number of points measured.

Previous sections of this work aim to assign the origin of the main Raman contributions of the spectra and how strain, torsions and geometrical parameters are in charge of the spectrum modulation. So we are now in disposition to study the pressure effect on the [n]CPPs Raman spectra, analyzing different spectral regions. In Figure 10 we show the Raman spectra of [6]CPP at room conditions together with the predicted spectrum for the optimized structure at the B3LYP/6-32G(d,p) level. We have marked with different colored bars the most remarkable bands: from the G modes up to the radial breathing modes (RBMs). From these we will study the high pressure

[*] Quantum Expresso calculations have been done for several [n]CPPs by the group headed by Prof. Miklos Kertesz, Georgetown University.

response only of the most intense and informative bands, which will be detailed along the next sections.

Once the analysis of the high pressure behavior is done, we will use several models to obtain the mechanical properties of these conjugated molecular systems in terms of bulk modulus along the cross section. Finally we have carried out a striking study of the recovered samples, once pressure is released.

Table 4. Number of measured runs for each [n]CPP, pressure range and total number of points measured.

n	Runs	Pressure range/GPa	Total number of points measured
5	3	~10	50
6	2	~8	75
7	2	~11	60
8	2	~10	50
9	1	~7	25
10	1	~8	30
11	1	~6	33
12	2	~10	55

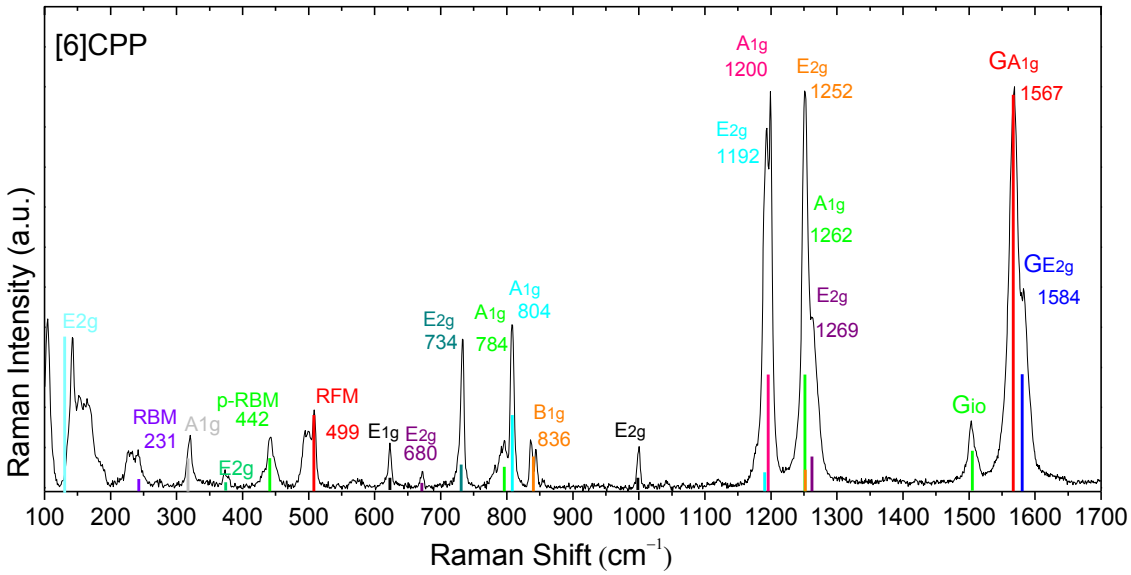

Figure 10. Raman spectrum of [6]CPP at room conditions in the 100 -1700 cm^{-1} region. Black line corresponds to the experimental spectrum, taken with the 785 nm excitation line. Colored bars correspond to the theoretical Raman spectrum at the B3LYP/6-31G(d,p) level, scaled with 0.965. Raman shifts marked correspond to the experimental values for each band.

7.4.1. High Pressure Behavior of the [n]CPPs GA_{1g} and GE_{2g} Bands

As studied in previous chapters in the 1550 - 1600 cm^{-1} region [n]CPPs depict the bands referred as G modes, in analogy to CNTs.[15] In Figure 11 we show this region for [6]CPP in which, as already discussed, two intense bands come from an A_{1g} mode related to the collective C-C stretching mode, while the shoulder at higher frequencies is an E_{2g} mode also related to C-C stretching mode but the vibration is not as good localized along the radial direction as in the case of the A_{1g} mode, as depicted in Table 5. Because of these bands are among those of higher intensity of the whole spectrum, as seen in Figure 10 so, in general, these are those with the mayor precision to obtain their Raman shift. Because of this and also because their defined origin over the C-C backbone, the high pressure dependence of these will represent the main diagnostic tool to analyze the changes and the pressure transitions.

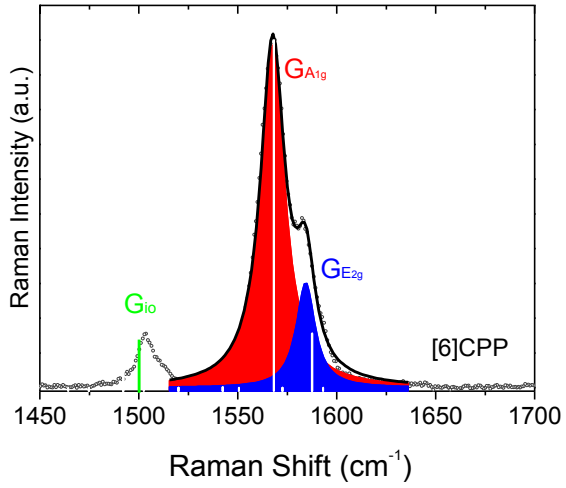

Figure 11. Raman spectrum of [6]CPP at room conditions in the 1450 -1700 cm^{-1} region. Grey dots correspond to the experimental spectrum, taken with the 785 nm excitation line. Black line is the fitting with the sum of two Lorentzians, corresponding to the GA_{1g} and GE_{2g} bands, plotted as the red and blue areas. Vertical white lines correspond to the theoretical Raman spectrum at the B3LYP/6-31G(d,p) level, scaled with 0.965.

Table 5. Vibrational eigenvectors associated with the Gio, GA_{1g} and GE_{2g} bands of the Raman spectrum of [6]CPP, obtained from DFT calculations with B3LYP/6-31G(d,p) level.

Gio	GA_{1g}	GE_{2g}
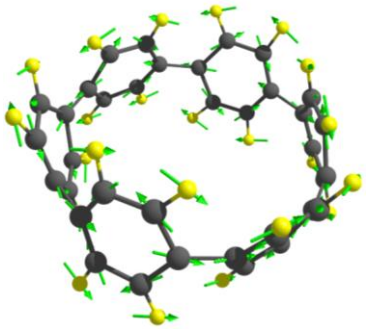	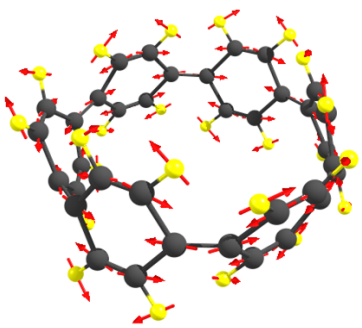	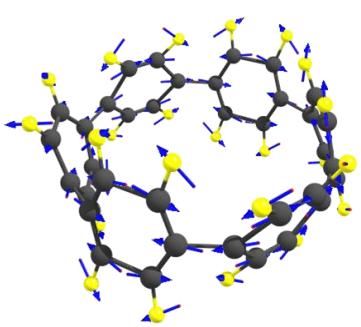
Mostly due to the stretching of C_{ipso}-C_{ortho} bonds	C_{ortho}-C_{ortho} and C_{ipso}-C_{ipso} bonds stretching along the transversal direction of the macrocycle	C_{ortho}-C_{ortho} and C_{ipso}-C_{ipso} bonds stretching along the longitudinal and transversal direction of the ring.

In Figure 12 we show the high pressure dependence of the Raman spectra around the 1600 cm^{-1} region of all the [n]CPPs at selected pressure values, all of them have been scaled to the normalized GA_{1g} band. In these spectra we observe, independently on the CPP size, the G bands broadens with compression. This broadening can be assigned to the splitting of the GE_{2g} band as a result of symmetry loss towards an oval configuration.[35] In the case of [7]CPP, at pressures higher than ~ 2 GPa we observe a new band around 1604 cm^{-1}, pictured in light blue, whose intensity increases with increasing pressure. On the other [n]CPPs, apart from [5]CPP, although the bands considerably broaden, no new features can be resolved. For [5]CPP the broadening of the GA_{1g} and splitting of the GE_{2g} is also visible, but two additional contributions grow with increasing pressure around 1450 cm^{-1}, green area, and 1600 cm^{-1}, orange area. All these [5]CPPs bands upshift with pressure, following an analogous behavior between each other but at different rates. We hypothesize about the possibility of a mechanically induced transition towards a quinonoid distorted configuration. In such case, the 1450 cm^{-1} band would correspond with the localized C=C stretching, and the 1600 cm^{-1} one with the single C-C bond stretching, in agreement with our previous description of the effect of the quinonoidization in the Raman shift of such strained [n]CPP.[78]

In Figure 13 we represent the pressure dependence of the GA_{1g} and GE_{2g} modes for each [n]CPP under study, and in Figure 14 we plot the Gio shift as a function of pressure. In the latter due to the low intensity of this mode and the increasing fluorescence with pressure, the visibility becomes worse with pressure, so we do not have as many data points as we do for the GA_{1g} and GE_{2g} band. These G modes clearly shift linearly over two regimes with a change in the slope around a pressure value which is higher as the CPP diameter is lower, ranging from 0.6 GPa for [12]CPP to 5.8 GPa for [5]CPP. We have fitted to a double linear trend with equation 3, leaving the pressure transition for each *n* as a shared parameter for all the bands of the spectrum, not only the G bands. The resulting pressure coefficients of the Gio, GA_{1g} and GE_{2g} bands before (S_1) and after (S_2) pressure transition, have been gathered together in Table 6 together with such pressure transitions.

Table 6. Experimental interceptions and pressure coefficients of the linear variation with pressure of the G bands for each [n]CPP before (S_1) and after (S_2) pressure transition (*PT*). Experimental results of diameters have been taken from the indicated references.

			G_{io}			GA_{1g}			GE_{2g}		
n	**Diameter nm**	***PT* GPa**	ω_0 cm^{-1}	S_1 $cm^{-1}GPa^{-1}$	S_2 $cm^{-1}GPa^{-1}$	ω_0 cm^{-1}	S_1 $cm^{-1}GPa^{-1}$	S_2 $cm^{-1}GPa^{-1}$	ω_0 cm^{-1}	S_1 $cm^{-1}GPa^{-1}$	S_2 $cm^{-1}GPa^{-1}$
5	0.69 [25]	5.8 ± 0.5	1504	5.8 ± 0.2	---	1555	4.5 ± 0.2	-4.0 ± 0.5	1573	4.9 ± 0.2	-6.1 ± 0.4
6	0.81 [26]	4.7 ± 0.5	1504	2.6 ± 0.2	---	1567	5.1 ± 0.2	1.0 ± 0.6	1584	4.7 ± 0.2	1.4 ± 0.7
7	0.98 [79]	3.5 ± 0.5	1504	2.1 ± 0.2	0.0 ± 0.4	1574	3.6 ± 0.3	2.6 ± 0.2	1591	4.0 ± 0.3	2.4 ± 0.2
8	1.09 [80]	2.2 ± 0.5	1505	4.0 ± 0.5	1.0 ± 0.4	1582	3.7 ± 0.3	2.6 ± 0.1	1595	4.9 ± 0.8	3.1 ± 0.1
9	1.24 [81]	1.4 ± 0.5	1503	5.0 ± 1.0	1.2 ± 0.7	1585	4.2 ± 0.8	3.0 ± 0.3	1596	5.2 ± 0.4	3.5 ± 0.3
10	1.39 [82,83]	1.2 ± 0.5	1500	4.0 ± 1.0	1.1 ± 0.2	1589	4.5 ± 0.5	2.9 ± 0.1	1598	5.9 ± 0.5	3.6 ± 0.1
11	1.54 [84]	0.9 ± 0.5	1498	3.1 ± 0.9	1.4 ± 0.2	1592	5.0 ± 1.0	2.7 ± 0.2	1602	8.0 ± 1.0	3.5 ± 0.2
12	1.65 [85]	0.6 ± 0.5	1496	2.0 ± 1.0	1.8 ± 0.1	1595	7.0 ± 2.0	3.4 ± 0.1	1602	9.0 ± 2.0	3.9 ± 0.1

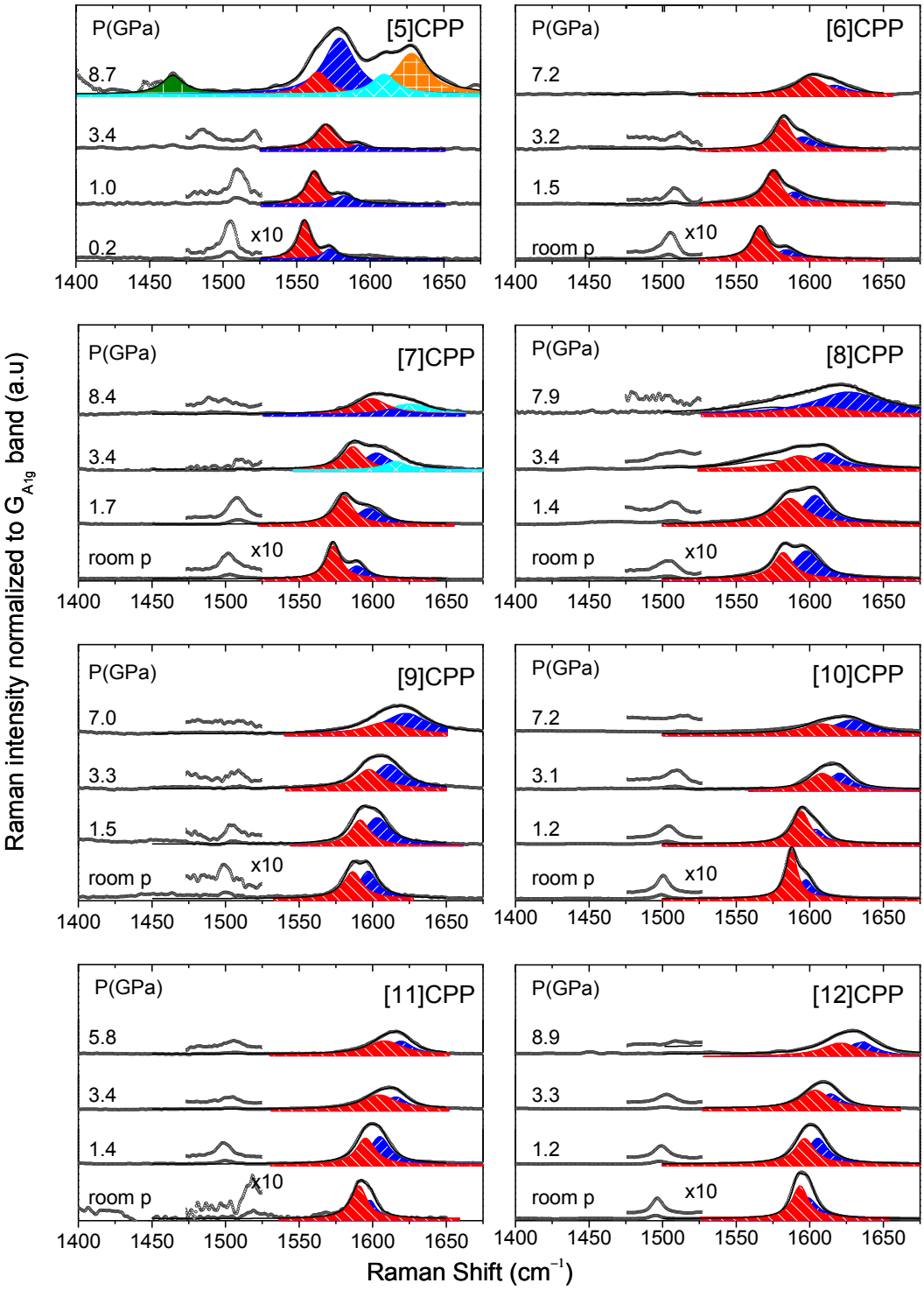

Figure 12. [n]CPPs Raman spectra at selected pressures normalized to the area of the GA_{1g} band. Grey dots correspond to the experimental spectra, taken with the 785 nm excitation line. Black line is the fitting with the sum of Lorentzians peaks. Red area: GA_{1g} mode contribution. Blue area: GE_{2g} mode contribution. Cyan additional features have been fitted for [7]CPP (see text). Inserts correspond to the x10 amplifications around the G_{io} band. In [5]CPP glowing additional features have been fitted to the Lorentzian peaks colored as green, cyan and orange areas (see text).

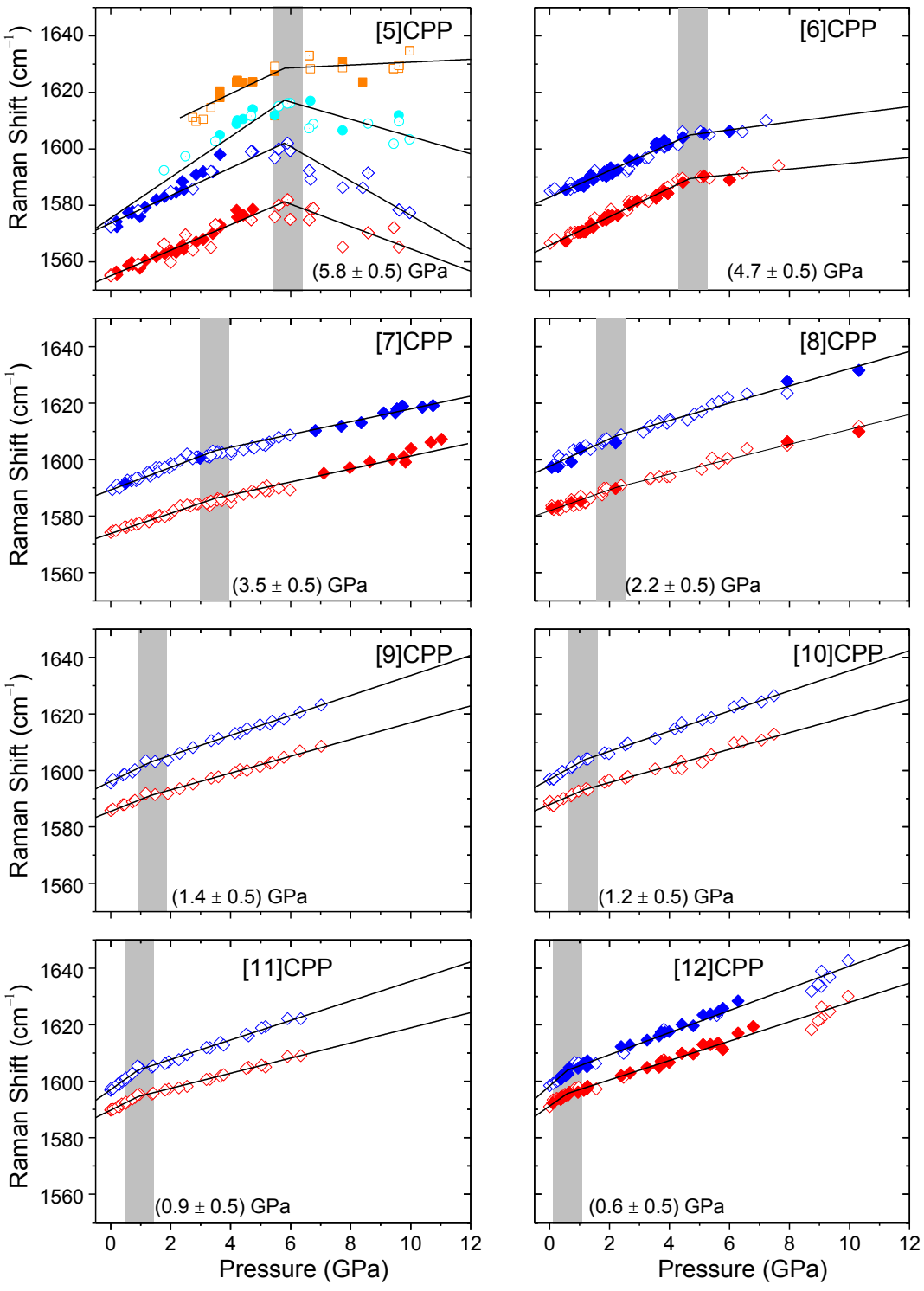

Figure 13. Pressure dependence of the Raman shifts of G modes for the [n]CPPs. Red diamonds correspond to the GA_{1g} band and blue diamonds to the GE_{2g} band, closed and open symbols correspond to different measured runs. In [5]CPP the additional contributions are drawn as cyan (GE_{2g} split), and orange around 1600 cm^{-1} band. Solid lines correspond to the data fitting to equation 3. For each [n]CPP fittings are done together for all the bands following a double linear trend, considering PT as a shared parameter. The fitting of the [5]CPP E_{2g} band splitting, in cyan, has been forced to the same frequency origin than the E_{2g} at room conditions. This setting is done to keep on with the fact that both of the E_{2g} bands are together degenerated at room pressure. Grey shadow regions represent the pressure of the transition between the two linear regimes, whose value is indicated for each [n]CPP in its panel.

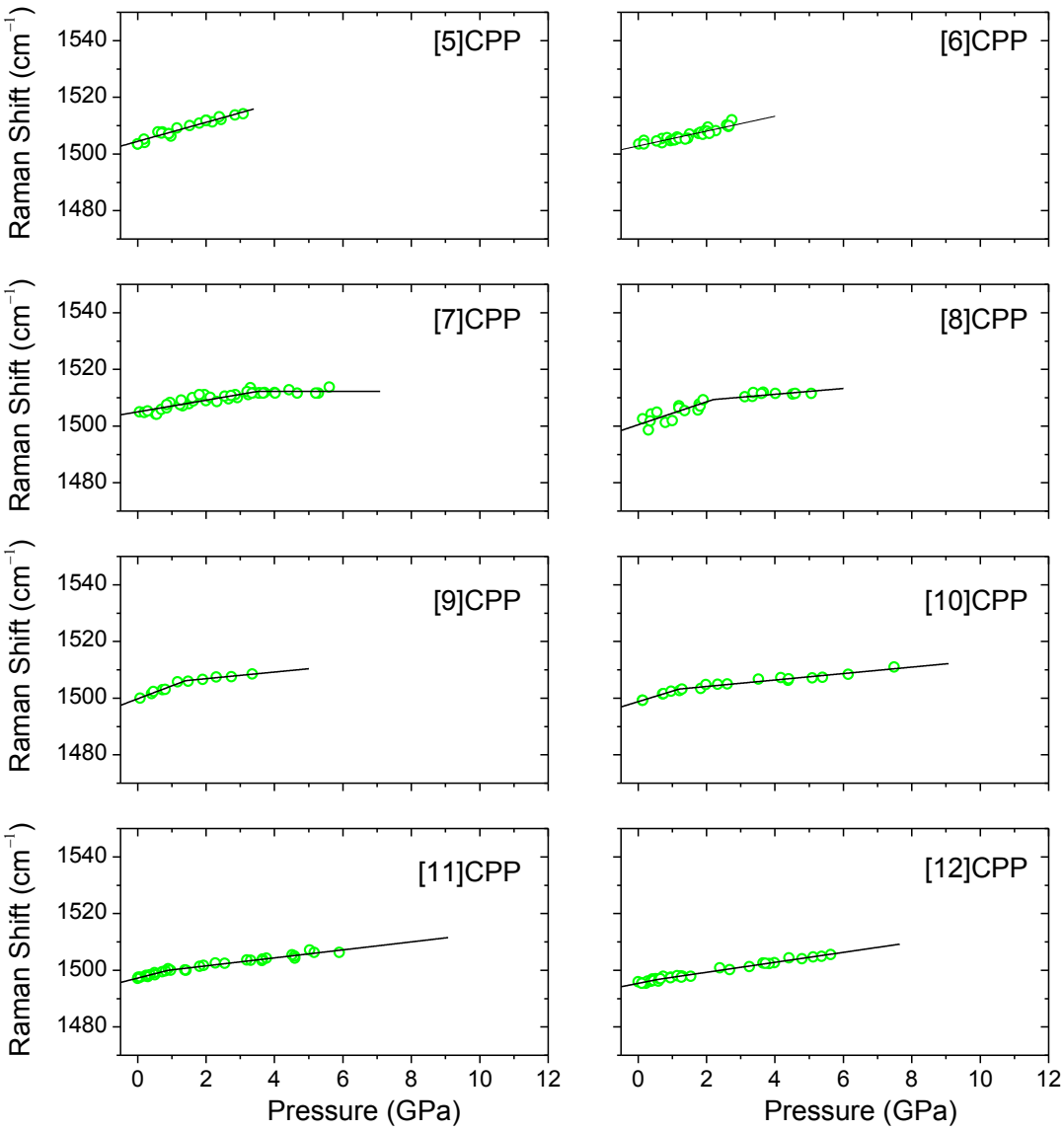

Figure 14. Pressure dependence of the Raman shifts of Gio modes for the [n]CPPs. Due to the low intensity of this mode and the growing fluorescence with increasing pressure the Gio peaks are difficult to resolve. Therefore, these are visible along a lower pressure range compared with the more intense G bands, Figure 13. In the [5]CPP and [6]CPP the Gio intensity becomes negligible at pressures below PT. Black lines correspond to the fitting to equation 3 of the Raman shifts of the Gio band for each [n]CPP. Fittings are done for each [n]CPP together for all the bands following a double linear trend, considering PT as a shared parameter.

As already described, Raman shift of the G bands of CNTs[35,86] show a slope change of the linear trend. This is related with their loss of their cylindrical shape, from circular to oval. We suggest that such behavior is followed by [n]CPPs which become more oval with the incoming pressure, as represented in Figure 15 for [10]CPP. This deformation is in agreement then with the new peak observed on the [7]CPP around 1605 cm^{-1} due to the GE_{2g} splitting from the corresponding symmetry rupture. The GE_{2g} splitting probably also occurs in the other [n]CPPs, but unfortunately due to the broadening we are not able to resolve it. In [5]CPP the new features report an analogous double linear trend, but the 1450 cm^{-1} band has not been represented here to not disturb the scale. In any case, the linear trends have much higher slopes than after the so called here, pressure transition, *PT*. This is in agreement with a change from a regime at which pressure alters mainly bonds, large frequency upshift, towards another at which the bonding is not affected as much but bending angles are, as depicted in Figure 15 for [10]CPP.

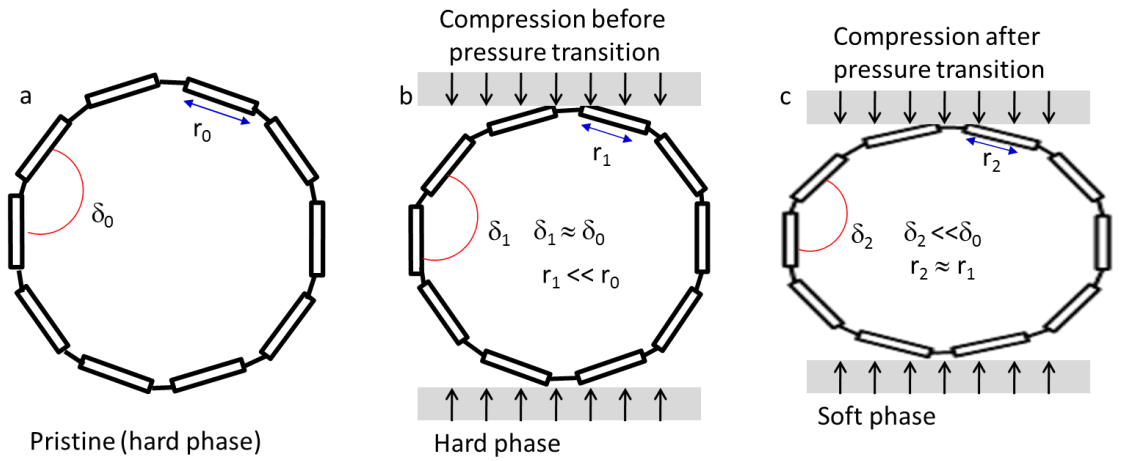

Figure 15. Scheme of the suggested for the [10]CPP about the evolution of its cross section and angles with increasing pressure. *r* denotes the C-C bond lengths and δ denotes the bending angles. Subscripts 0, 1 and 2 are used to refer to the different marked stages: a) Pristine, b) compression before deformation at pressure transition, and c) after pressure transition.

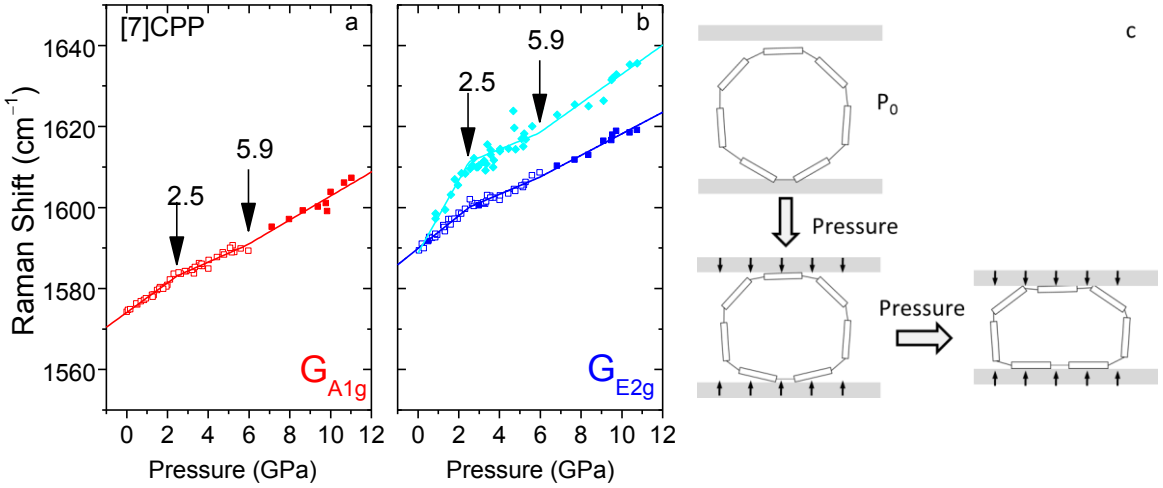

Figure 16. a) [7]CPP Raman shift pressure dependence of G modes for the: a) GA_{1g} band; b) GE_{2g} bands; closed and open symbols correspond to different measured runs. Experimental data have been fitted to a triple linear trend; solid lines correspond to such fit. Marked pressures correspond to the changes in slope. c) Scheme representing pressure response of [7]CPP configuration along the three regimes.

As already mentioned, in [7]CPP we are able to quantitatively distinguish GE_{2g} splitting, observable from about 2 GPa. In Figure 16a we plot the GA_{1g} Raman shift with pressure and in Figure 16b the GE_{2g} bands. We see that for the GA_{1g} and for both of the GE_{2g} contributions their Raman shifts as a function of pressure can be divided into three regions instead of two. We have fitted these values to a linear variation with two kinks, sharing the pressure values of those kinks for the three bands. The pressure transitions for these regions are at 2.5 and 5.9 GPa, dividing the regions with different slopes. The first region would have larger coefficients than the second one and the second lower coefficients than the third. In Table 7 we summarize the pressure coefficients of each band along each of the regimes. The high pressure coefficients for all of the G bands in the first regime indicate that, initially C-C bonds would be mostly altered. Then, along the second regime with much lower coefficients mainly bond angles would be altered. Finally the slight increase in the coefficients along the third regime shows that in this, C-C bonds are being deformed together with the bond angles. Herein, this behavior is interpreted as a pressure induced transition firstly to oval shape and secondly towards peanut shape, as depicted in Figure 16c.

Table 7. Pressure coefficients of the linear variation with pressure of the G bands for [7]CPP. First regime, before (S_1) pressure transition (*PT*), second regime (S_2) between PT_1 and the second pressure transition (PT_2) and third regime (S_3) after PT_2.

	GA_{1g}	GE_{2g}	GE_{2g}
S_1 ($cm^{-1}GPa^{-1}$)	3.9 ± 0.2	4.4 ± 0.2	8.0 ± 0.2
S_2 ($cm^{-1}GPa^{-1}$)	2.3 ± 0.1	2.2 ± 0.1	2.0 ± 0.1
S_3 ($cm^{-1}GPa^{-1}$)	3.1 ± 0.1	2.7 ± 0.1	3.7 ± 0.1
***PT_1* (GPa)**	2.5 ± 0.5		
***PT_2* (GPa)**	5.9 ± 0.9		

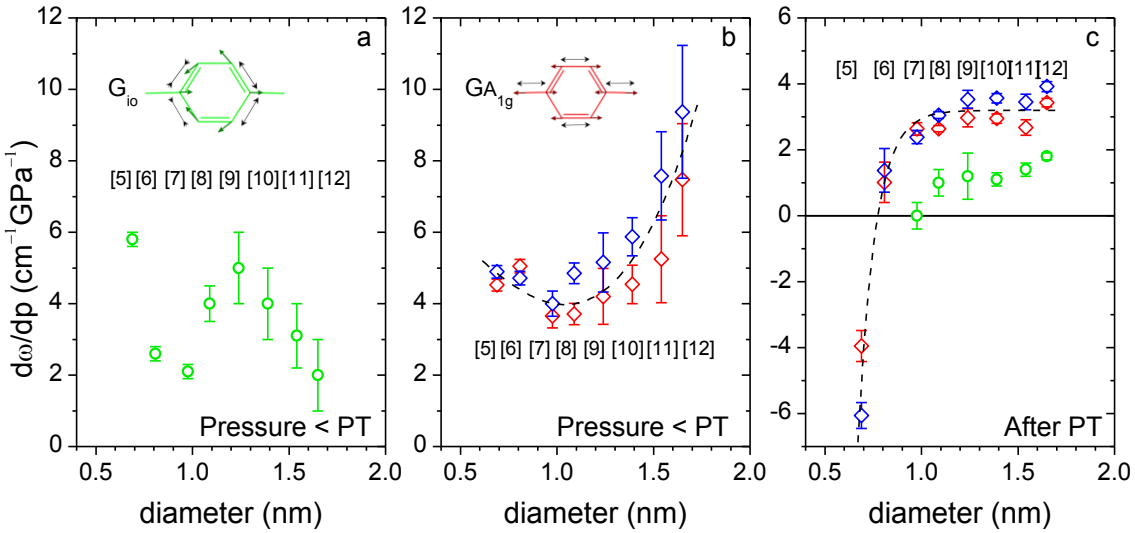

Figure 17. Diameter dependence of the pressure coefficients of the G modes, (○)Gio, (◇)GE_{2g} and (◇)GA_{1g} modes for [5-12]CPPs. a) Gio before pressure transition; a) GA_{1g} and GE_{2g} before pressure transition b) Gio, GA_{1g} and GE_{2g} after pressure transition. Dashed lines are guide to the eye.

Large positive pressure coefficients are related with larger deformations, i.e. those vibrations involved in that mode are being further affected. In Figure 17 we have the pressure coefficients followed by the Gio, GA_{1g} and GE_{2g} bands as a function of the [n]CPP diameters, before and after the *PT*. In Figure 17a we see how pressure coefficients of the Gio band increase from [6] to [9]CPP, 2.6 cm^{-1} GPa^{-1} to 5 cm^{-1} GPa^{-1}; and from [9] to [12]CPP, the Gio pressure coefficients decrease from 5 cm^{-1} GPa^{-1} to 2 cm^{-1} GPa^{-1}. In this analysis we exclude [5]CPP, with the largest Gio pressure coefficient, we will explain it separately below. Figure 17b shows how generally the GA_{1g} mode presents slightly lower coefficients than the GE_{2g}, probably because the non-accounted GE_{2g} splitting. As in the Gio, for the GA_{1g} and GE_{2g}, there exists dependence between the pressure coefficients for the different *n* and the diameter, however the size dependence is opposite: [7]-[8]- [9]CPP represent a minimum instead of a maximum. Pressure coefficients of [n]CPPs with diameter lower or larger than [7]-[8]- [9]CPP linearly grow increasing and decreasing diameters. For [n]CPPs with $n \geq 7$, the pressure coefficients of the GE_{2g} band grow at a rate of (6.4 ± 0.9) nm^{-1} cm^{-1} GPa^{-1}, and those of the GA_{1g} band grow as well with a rate of (4.2 ± 0.7) nm^{-1} cm^{-1} GPa^{-1}.

Differences in the behavior followed by the Gio band and GA_{1g} as a diameter function are interesting, since the former comes mainly from the C_{ortho}-C_{ipso} stretching mode, while the latter comes from the C_{ipso}-C_{ipso} and C_{ortho}-C_{ortho} stretching mode. As mentioned, in the Gio around [9]CPP there is a maximum 5 $cm^{-1}GPa^{-1}$, while for the GA_{1g}, GE_{2g}, around [7]- [8]CPP there is a minimum. 2.6 $cm^{-1}GPa^{-1}$, 4.9 $cm^{-1}GPa^{-1}$, respectively. In the previous section we already explained how the GA_{1g}

band, and so the GE_{2g} band with common vibrational modes, are more sensitive to planarization, than the Gio band is. Additionally, in chapter 3 we studied how the GA_{1g} band is strongly strain sensitive. Thus, lower coefficients of the GA_{1g} band than the Gio band in the middle sized [n]CPPs, indicate that these are tougher against stress and deformation in the [n]CPP transversal direction, C_{ipso}-C_{ipso} and C_{ortho}-C_{ortho}. But its larger Gio pressure coefficient indicates that their deformation involves torsional rearrangement in larger extent. Thus, it can be interpreted as that pressure may be modulating torsional angles as the same time that it deforms the [n]CPPs cross section. When comparing the pressure coefficients between [n]CPPs and [n]LPPs, in the latter this increase with the lengthngin of the oligomer, while in the former the pressure coefficient of the Gio band is more than twice larger for [5]CPP than it is for [6]CPP As seen, the analysis of the intensity ratio $IA_{1g}1280/IA_{1g}1200$ can provide more detailed information, so it will be one of the main items to address in the next section.

The [n]CPPs higher pressure coefficients of the GA_{1g} and GE_{2g} with the growing *n*, evidences that CPPs are softer as bigger they are. The fact that [5]- and [6]CPP depict larger GA_{1g} and GE_{2g} coefficients than [8]CPP could be justified because of their large strain. If strain is too high, [n]CPPs could need to rearrange towards more relaxed configurations when they are compressed. Such rearrangement could involve redistribution within their π electronic configuration. [6]CPP steeply rearranges towards a more benzoid structure, with lower conjugation between neighboring benzenes. However, [5]CPP seems more favorable to move towards a different configuration. The larges Gio pressure coefficient indicates that C_{ipso}-C_{ortho} stretching bonds are softer in [5]CPP than in any other [n]CPP. This fact might be in agreement with a transition towards a more bent configuration, quinonoid.

Concerning the slopes followed by the different G bands after *PT*, it is seen in Figure 17c that these as well are strongly depending on *n* but in a different manner than before *PT*, being much lower than in the previous phase. So it can be said that, as anticipated, in this regime C-C bonds are less altered, and are the bond angles those mostly modulated. The low intensity of the Gio band makes impossible the characterization of the PT and so we do not have data for the Gio band PT pressure coefficients or [5]- and [6]CPP. The Gio pressure coefficients follow a parallel trend with sized to the GA_{1g} and GE_{2g}. Approximately from [8]- to [12]CPP, pressure coefficients remain constant with *n* at about 2 cm-1GPa-1 for the G_{io} and 3 cm^{-1} GPa^{-1} for the GA_{1g} and GE_{2g}. From[6]- and [5]CPP these coefficients rapidly decrease up to -4 and -6 $cm^{-1}GPa^{-1}$ for the GA_{1g} and GE_{2g} bands, respectively.

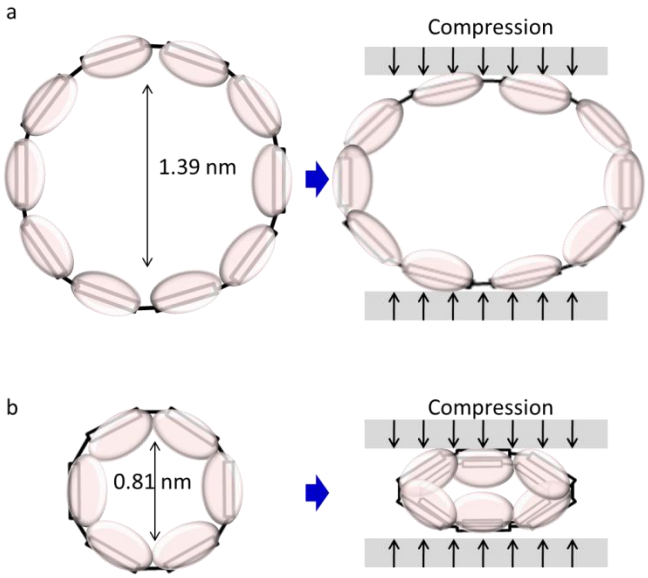

Figure 18. Scheme of the π electron density modulation with pressure along the CPP cross section, a) [10]CPP, b)[6]CPP.

The after *PT* GA_{1g} and GE_{2g} lower coefficients for [6]CPP than in bigger [n]CPPs, but remaining positive could indicate that changes are done in a higher extent only over the angles. It is very likely that [6]CPP because of its small diameter, as shown in Figure 18b, once it turns oval rapidly goes towards a peanut shape. Therefore the intermediate oval-step observed in [7]CPP is not present in [6]CPP. Such high pressure behavior of [6]CPP is favored because of the induced van der Waals interactions between opposite CPP walls, as already predicted for small diameter carbon nanotubes.[87] However in higher diameter tubes or rings, the transition towards peanut shape requires higher pressures to be completed, Figure 18a.[88] In such a way in [7]CPP it is observed a second *PT* which should appear for the larger [n]CPPs at higher pressures. That second *PT* should increase with the [n]CPPs diameter, because larger cross sectional deformation would be required to a van der Waals stabilized peanut shape to become energetically favored.

[5]CPP behaves differently to the others with negative pressure coefficients of the GA_{1g} and GE_{2g} bands after *PT.* Negatives slopes in vibrational shifting are generally related with reorganization into the structural backbones. So as already intuited by the glowing of the 1450 and 1600 cm^{-1} bands, the downshift of these bands was related with higher quinonoid contributions.[78] Thus it seems that pressure induces a transition towards a distorted, oval, quinonoid configuration, in [5]CPP.

For SWCNTs it has been stated that the physical deformations of their cross section are strongly diameter dependent, easier with larger diameters (lower pressures are need to induce them).[30,59,89] In Figure 19a we have compared the limited available SWCNTs G bands pressure coefficients before *PT* as a function of diameter,[10] with our [n]CPPs results. Interestingly, the G bands of SWCNTs and [n]CPPs follow a similar behavior with pressure and diameter. These SWCNTs coefficients increase with their diameter, with a rate of 6.8 nm^{-1} cm^{-1} GPa^{-1}, close those obtained for [n]CPPs. These results confirm the similarities in the radial response between CPPs and SWCNTs, with the advantage that the controlled CPPs synthesis presents and controlled diameter analysis. Experimental results on armchair CNTs of such small diameter are not yet resolved. However, it seems that the [5]CPP high pressure response is uniquely due to its molecular character. Thus, it remains unknown how such thin SWCNTs would respond to compression. To compare the behavior followed by the LPPs and CPPs, in Figure 19b we have the pressure coefficients of the LPPs' C-C tensile mode, taken from this work and the literature.[13] Since the PPP coefficient is about 4.5 cm^{-1} GPa^{-1},[90] the LPPs coefficients can be considered approximately constant with their phenyl number.

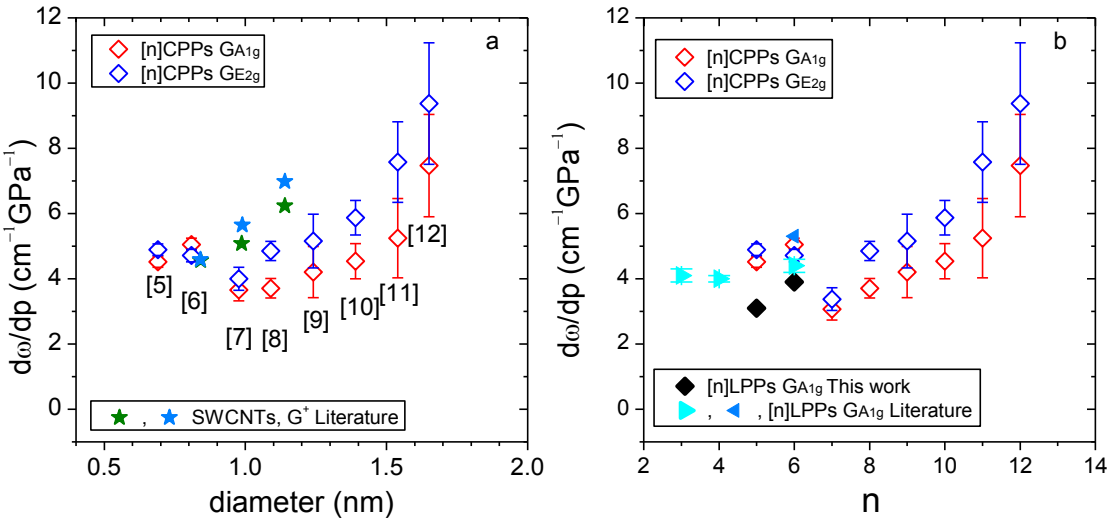

Figure 19. Pressure coefficients of the G modes, (◇)GE_{2g} mode and (◇)GA_{1g} mode for [5-12]CPPs before *PT* plotted against a) diameter and b) number of benzenes which form the [n]CPP and [n]LPP. Data from SWCNTs: (★) and (★) G^+ band from Ghandour et al. [10]. Data from [n]LPPs: (◆) this work for [5]- and [6]LPP, (▶) from Martin et al. [13] for [3]-, [4]- and [6]LPP, and (◀) from Guha et al. [68] for [6]LPP.

7.4.2. Discussion about the Assignment of the G like Bands for [n]CPPs

Although the assignment of the two [n]CPPs bands as GA_{1g} and GE_{2g} modes seems very clear, we want to leave it out of any controversy, because LPPs also present in this region a low intensity resonant Raman band, resulting from a combination of the 610 and 990 cm^{-1} bands,[91] next to the C-C stretching mode of the benzoid rings. In Figure 20 we have analyzed the pressure dependence of the sum of the [n]CPPs following bands: 624 cm^{-1} band, benzene ring deformation with constant C-C bond lengths and the 1000 cm^{-1}, band benzene breathing with constant C-H bond lengths.[92] We represent the resulting values against the pressure dependence of the GE_{2g} mode of the [n]CPPs. We find that for the case of [10]CPP, this variation follow a linear trend with a slope equals to 0.50 ± 0.02. For the remaining [n]CPPs, the variation is also linear with slopes ranging from 0.45 to 0.70 depending on the [n]CPP. Therefore, the GE_{2g} mode of [n]CPPs is not analogous to the combination band presented by the LPPs and it is clearly closer to the TO band of the SWCNTs.

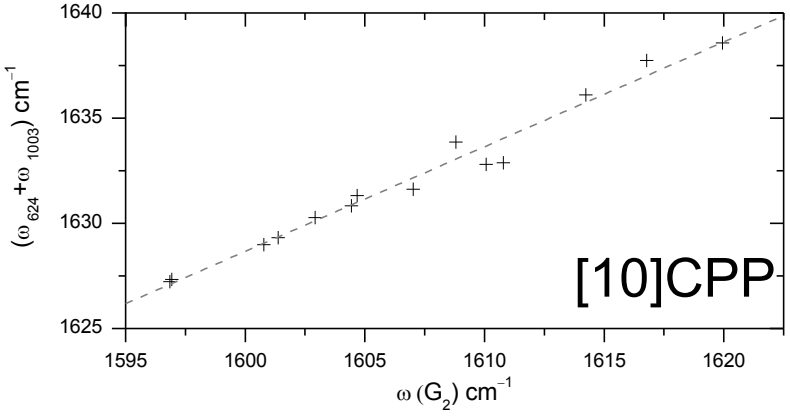

Figure 20. Frequency combination of the Raman shift of the 624 cm^{-1} band (benzene ring deformation with constant C-C bond lengths) and the 1000 cm^{-1} band (benzene breathing with constant C-H bond length) as a function of the frequency of the GE_{2g} band. Data evaluated for [10]CPP. The parameters from obtained from the linear fitting are: ω_0 equals to (832 ± 36) cm^{-1}, and the slope equals to 0.50 ± 0.02.

7.4.3.High Pressure behavior of the [n]CPPs 1100 – 1300 cm^{-1} Spectral Region

One of the most interesting sections of the [n]CPP Raman spectra is the 1100-1300 cm^{-1} region. In this region it is possible to characterize two A_{1g} bands whose intensity ratio provides valuable information. In [n]LPPs the intensity ratio between the 1280 and 1200 cm^{-1} A_{1g} bands ($I1280A_{1g}/I1200A_{1g}$) has been used as an indicator of the conjugation length. Consequently, an increase in conjugation length would lead to a decrease in the intensity ratio. In Figure 21 we plot the experimental and theoretical spectra in the 1150-1375 cm^{-1} region for [6]CPP. The assignment of the bands as well as their symmetry labels refer to the high symmetry conformations, D_{nh}. The region has been decomposed into different contributions: 1192 cm^{-1} band corresponds to E_{2g} combination mode between phenyl breathing, C-C stretching and CH wagging; 1200 cm^{-1} band corresponds to an A_{1g} mode, C-H bending mode coupled to C-C interring stretching mode; 1252 cm^{-1} band to an E_{2g} symmetry mode, from a contribution of the symmetric phenyl breathing mode coupled to C-C interring stretching mode and C-H bending mode; 1262 cm^{-1} band corresponds to an A_{1g} mode, phenyl breathing mode coupled to C-C interring stretching mode and C-H bending mode; 1269 cm^{-1} band corresponds to an E_{1g} combination mode between phenyl breathing, C-C stretching and CH wagging. To generalize the way to talk about these bands for all the [n]CPPs we will refer to them as 1190, 1200, 1250, 1280 and 1290 cm^{-1} bands. In previous chapters it was already explained how at room conditions the Raman spectra of [n]CPPs in this middle region was modulated by strain and torsional angles. Therefore, not only frequencies depend on strain, but also intensities of the different contributions. To facilitate the analysis of these bands at high pressures in Table 8 we have summarized the vibrational modes of the five different mentioned modes.

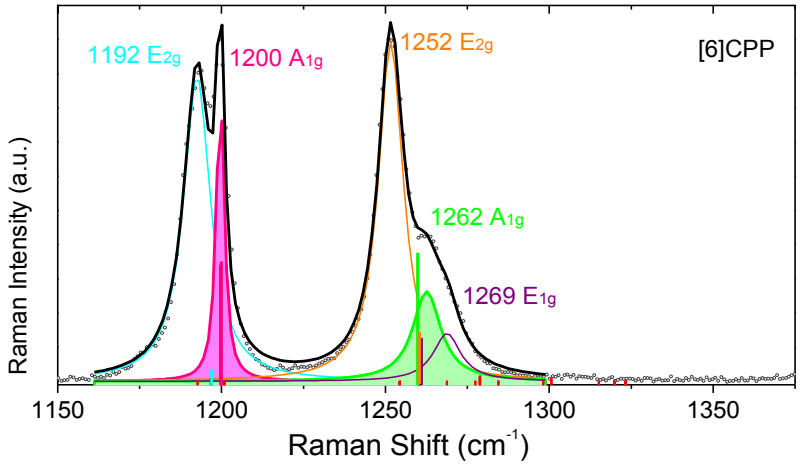

Figure 21. Raman spectrum of [6]CPP at room conditions in the 1150 -1375 cm^{-1} region. Grey dots correspond to the experimental spectrum, taken with the 785 nm excitation line. Black line is the fitting with the sum of five Lorentzians, corresponding to the 1192 cm^{-1} E_{2g}, 1200 cm^{-1} A_{1g}, 1252 cm^{-1} E_{2g}, 1262 cm^{-1} A_{1g}, and 1269 cm^{-1} E_{1g} bands. Pink and green areas correspond to the 1200 and 1262 cm^{-1} bands (to which we will refer in the text as 1200 and 1280 cm^{-1} A_{1g} bands, to generalize to any *n*). Vertical colored lines correspond to the theoretical Raman spectrum at the B3LYP/6-31G(d,p) level, scaled with 0.97.

Table 8. [n]CPPs bands in the 1100-1300 cm^{-1} region: symmetry, vibrational assignment in terms of generic internal coordinates and intensity description in terms of torsions and strain. Raman shifts are approximately those corresponding to [6]CPP at room conditions, and in brackets are the calculated by B3LYP/6-31G(d,p) methodology scaled with 0.97.

Raman shift (cm^{-1})	Symmetry	Vibrational description	Intensity description
1190 (1197)	E_{2g}	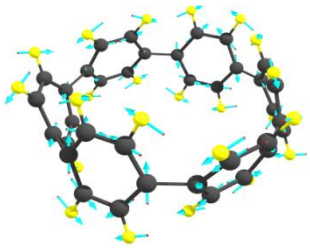 β(phenyl)+ ν(C-C)+w(C-H)	Intensity decreases lower strain, larger *n*.
1200 (1200)	A_{1g}	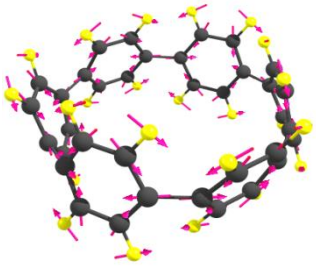 β(C-H)+ν(C-C)$_{interring}$	Higher intensity ratio: I1280$_{A1g}$/I1200$_{A1g}$ → Higher torsional angle
1250 (1259)	E_{2g}	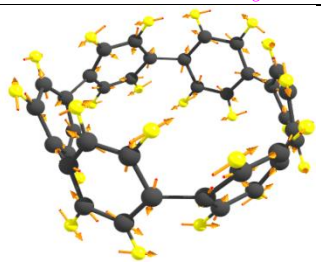 β(phenyl)+ν(C-C)$_{interring}$+β(C-H)	Intensity grows with the decreasing *n*. Connected with the C-H hindering of the lower torsions in smaller CPPs
1280 (1260)	A_{1g}	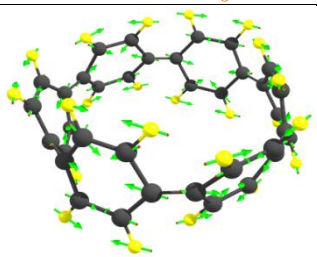 β(phenyl)+ν(C-C)$_{interring}$+β(C-H)	Higher intensity ratio: I1280$_{A1g}$/I1200$_{A1g}$ → Higher torsional angle
1290 (1261)	E_{1g}	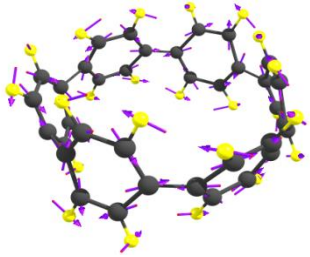 ν(C-C) + w(C-H) + β(phenyl)	Requires from bending and torsions to becomes be active

β(phenyl): symmetric phenyl breathing mode; **w(C-H)**: C-H wagging mode; **ν(C-C)$_{interring}$**: C-C inter-ring stretching mode; **β(C-H)**: C-H bending mode; **ν(C-C)**: C_{ipso}-C_{ortho} stretching mode.

In Figure 22 we can see Raman spectra at selected pressures for the different [n]CPPs. In these a general upshift is observed for all the contributions and, as occurred on the higher frequency region, these are broadened with the increasing pressure. We are analyzing five contributions, being three of them E bands, so it is expected that such broadening might be caused by the symmetry loss, i.e. by the E bands degeneracy breaking. Unfortunately our experimental settings and spectral resolution does not allow us to quantitatively resolve it. It is a general effect caused by compression that the E bands gain intensity regardless *n,* but unfortunately for the non-accounted E splitting we are not capable to quantitatively analyze such effect. These contributions are related with distortions out of the linear configuration from the linear analogues; so their intensity increase is totally related with the growing distortion:

- The E_{2g} band around 1190 cm^{-1}, light blue contribution, whose intensity on the pristine [n]CPPs was higher on the more strained structures, suffers a logical intensity enhancement with the increasing pressure, larger in those with higher initial strain, lower *n.*
- The E_{2g} band around 1250 cm^{-1}, orange contribution, at room conditions requires large strain to have a significant intensity, so it is visible at room conditions for the lower *n*. We see how with compression we are significantly increasing the strain because of the intensity of the 1250 cm^{-1} band steeply grows.
- The E_{1g} band around 1290 cm^{-1}, which requires from bending and torsions to be active, and it is higher as higher the torsion is. The pressure effect on it is more difficult to be defined since it grows with pressure, but its intensity grows more steeply in smaller [n]CPPs than in bigger ones.

All these bands need from cyclization of the LPPs to become intense. The growing intensity of these bands evidences the suggested prediction about a mayor change on the bond angles after pressure transitions.

- A_{1g} bands. As mentioned in previous chapters, the intensity ratio $I1280_{A_{1g}}/I1200_{A_{1g}}$ is a parameter directly related with torsions. It seems like the intensity of the 1280 cm^{-1} A_{1g} band decreases with pressure. Later on this section we will qualitatively analyze this trend as a function of pressure and also *n*.

In Figure 23 we gather the high pressure response of all these bands for the different [n]CPPs. As happened with the G bands, these also depict a linear upshift with pressure whose slope changes at a certain pressure value, *PT*. Bear in mind that the 1200 cm^{-1} A_{1g} band in [n]LPPs showed a kink at which the linear upshift with pressure changed its slope. However, in [n]LPPs that kink is related with a change in the torsional angle towards planarization. In contrast to [n]LPPs,[13] in [n]CPPs all the bands in the 1200 cm^{-1} region depict a kink in the Raman shift pressure dependence. Moreover, the pressure coefficients of the five bands depend on *n*, unlike those for [n]LPPs which are approximately constant regardless *n*. Thus, in [n]CPPs the pressure coefficients before and after *PT* give us information about a change from a hard to soft stage. In Table 9 and Table 10 the pressure coefficients before and after *PT* for each band have been summarized. It can be observed that for any *n* larger coefficients are observed in these bands before *PT*. As mentioned in the previous section, during the hard phase, pressure mainly modulates C-C bonds rearrangement, thus larger coefficients are expected. Once systems go to a soft stage, the pressure coefficients of these bands are lower, meaning that are the angles those which are mostly affected. The deformation through the angles also would explain the intensity growth observed on the E bands after *PT*.

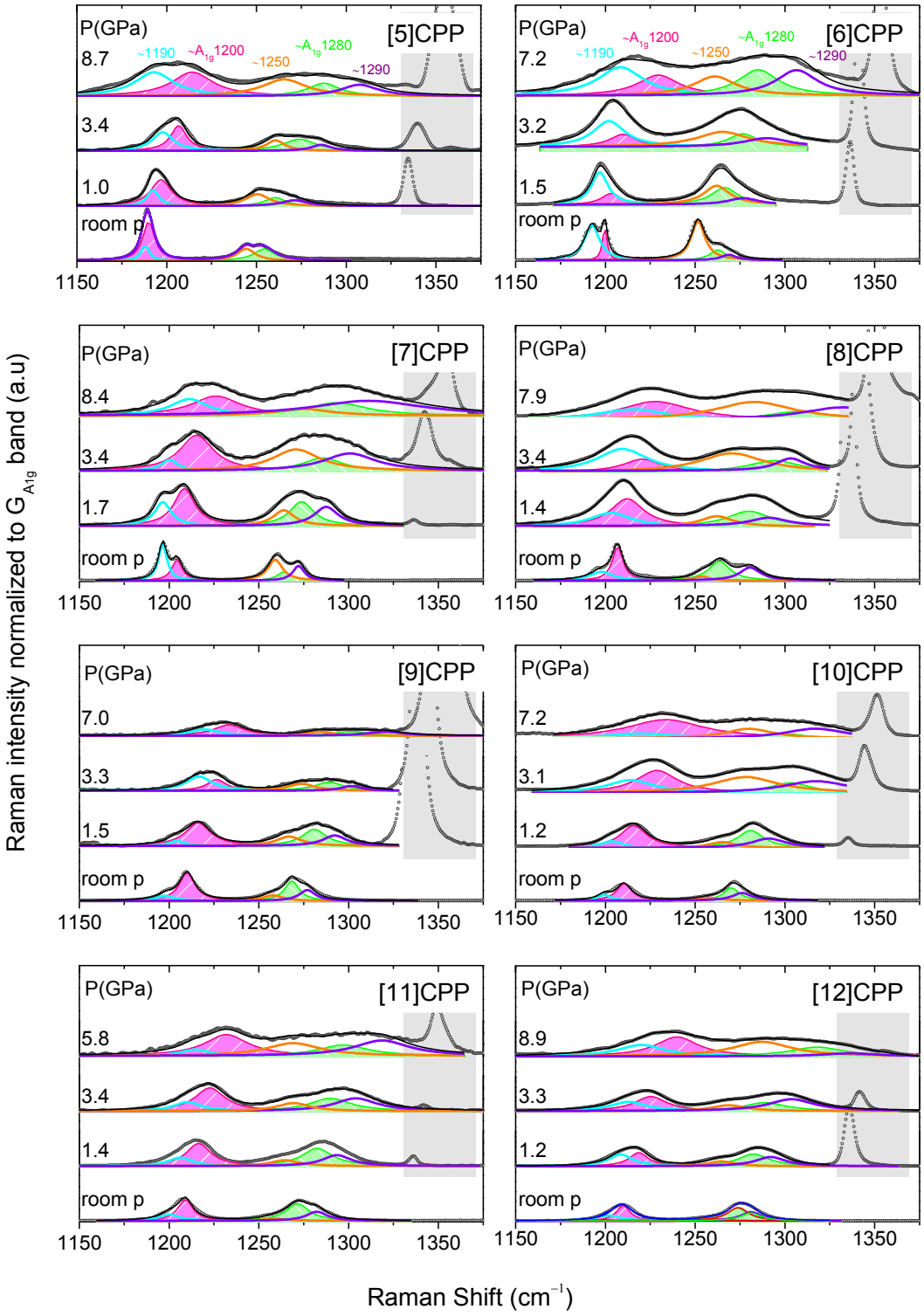

Figure 22. Raman spectra of [n]CPPs at selected pressure values in the 1150-1375 cm^{-1} region. All spectra have been scaled to the normalized GA_{1g} band. Grey dots correspond to the experimental spectra, taken with the 785 nm excitation line. Black lines are the fitting with the sum of five Lorentzians. Colored lines are the Lorentzian peaks corresponding to the 1190 cm^{-1} E_{2g}, 1200 cm^{-1} A_{1g}, 1250 cm^{-1} E_{2g}, 1280 cm^{-1} A_{1g}, and 1290 cm^{-1} E_{1g} bands. Pink and green areas correspond to the so-called 1200 and 1280 cm^{-1} bands. Grey shadow region corresponds to the diamond band used as pressure sensor.

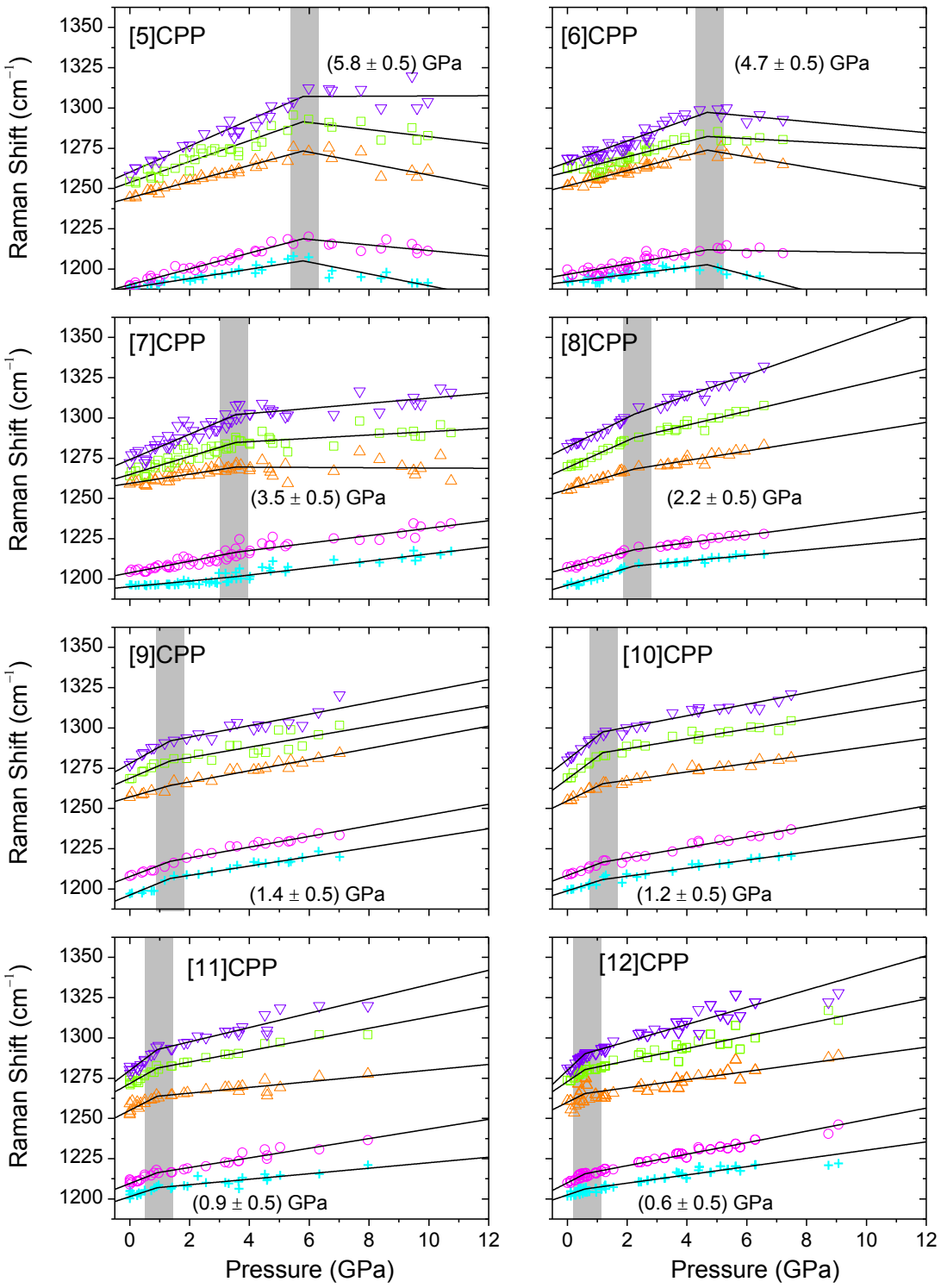

Figure 23. Pressure dependence of the Raman shifts in the 1200-1300 cm^{-1} region for the [n]CPPs: (+) 1190 cm^{-1} E_{2g}; (○) 1200 cm^{-1} A_{1g}; (△) 1250 cm^{-1} E_{2g}; (□) 1280 cm^{-1} A_{1g}; (▽) 1290 cm^{-1} E_{1g}. Solid lines correspond to the data fitting to equation 3. For each [n]CPP fittings are done together for all the bands following a double linear trend, considering PT as a shared parameter Grey shadow regions represent the pressure of the transition between the two linear regimes.

Table 9. Experimental interceptions and pressure coefficients of the [n]CPPs 1200 cm^{-1} bands before (S_1) and after (S_2) pressure transition (*PT*).

		E_{2g} 1190 cm^{-1}			A_{1g} 1200 cm^{-1}		
n	***PT*** **GPa**	ω_0 cm^{-1}	S_1 $cm^{-1}GPa^{-1}$	S_2 $cm^{-1}GPa^{-1}$	ω_0 cm^{-1}	S_1 $cm^{-1}GPa^{-1}$	S_2 $cm^{-1}GPa^{-1}$
5	5.8 ± 0.5	1188	2.9 ± 0.2	-3.7 ± 0.4	1190	4.9 ± 0.2	-1.7 ± 0.4
6	4.7 ± 0.5	1193	2.3 ± 0.2	-4.9 ± 1.2	1200	3.3 ± 0.2	-0.3 ± 0.7
7	3.5 ± 0.5	1196	1.8 ± 0.3	2.2 ± 0.2	1204	3.6 ± 0.3	2.3 ± 0.2
8	2.2 ± 0.5	1196	5.3 ± 1.8	0.2 ± 0.2	1204	5.1 ± 0.3	2.4 ± 0.2
9	1.4 ± 0.5	1198	7.6 ± 1.0	2.9 ± 0.3	1210	7.0 ± 1.0	3.3 ± 0.3
10	1.2 ± 0.5	1199	5.9 ± 0.8	2.5 ± 0.2	1210	7.0 ± 0.8	3.2 ± 0.2
11	0.9 ± 0.5	1200	6.1 ± 0.9	1.7 ± 0.2	1209	7.3 ± 1.0	3.0 ± 0.2
12	0.6 ± 0.5	1202	6.3 ± 1.9	2.6 ± 0.1	1210	9.5 ± 1.9	3.6 ± 0.1

In some cases the given number of digits exceeds the number of significant digits in order to avoid possible rounding errors.

Table 10. Experimental interceptions and pressure coefficients of the [n]CPPs 1280 cm^{-1} bands before (S_1) and after (S_2) pressure transition (*PT*).

		E_{2g} 1250 cm^{-1}			A_{1g} 1280 cm^{-1}			E_{1g} 1290 cm^{-1}		
n	***PT*** **GPa**	ω_0 cm^{-1}	S_1 $cm^{-1}GPa^{-1}$	S_2 $cm^{-1}GPa^{-1}$	ω_0 cm^{-1}	S_1 $cm^{-1}GPa^{-1}$	S_2 $cm^{-1}GPa^{-1}$	ω_0 cm^{-1}	S_1 $cm^{-1}GPa^{-1}$	S_2 $cm^{-1}GPa^{-1}$
5	5.8 ± 0.5	1240	5.0 ± 0.3	-3.5 ± 0.5	1244	6.5 ± 0.3	-2.2 ± 0.5	1254	8.1 ± 0.3	0.1 ± 0.5
6	4.7 ± 0.5	1252	4.7 ± 0.2	-3.1 ± 0.8	1263	4.7 ± 0.2	-1.0 ± 0.8	1269	6.6 ± 0.2	-1.7 ± 0.8
7	3.5 ± 0.5	1259	2.9 ± 0.3	-0.1 ± 0.2	1264	5.6 ± 0.3	1.0 ± 0.2	1272	7.9 ± 0.3	1.6 ± 0.2
8	2.2 ± 0.5	1259	5.7 ± 0.3	3.0 ± 0.2	1264	8.4 ± 0.3	4.4 ± 0.2	1272	9.1 ± 0.3	6.5 ± 0.2
9	1.4 ± 0.5	1258	5.3 ± 0.9	3.5 ± 0.3	1268	8.0 ± 1.0	3.2 ± 0.3	1277	10.4 ± 1.0	3.6 ± 0.3
10	1.2 ± 0.5	1257	9.0 ± 0.9	2.6 ± 0.2	1270	13.9 ± 1.0	3.0 ± 0.2	1276	14.5 ± 1.0	3.6 ± 0.2
11	0.9 ± 0.5	1259	9.5 ± 1.1	1.8 ± 0.2	1272	10.4 ± 1.0	3.5 ± 0.2	1282	14.1 ± 1.1	4.4 ± 0.2
12	0.6 ± 0.5	1261	9.3 ± 1.9	2.5 ± 0.1	1274	12.6 ± 2.0	3.8 ± 0.1	1281	17.5 ± 2.1	5.3 ± 0.2

In some cases the given number of digits exceeds the number of significant digits in order to avoid possible rounding errors.

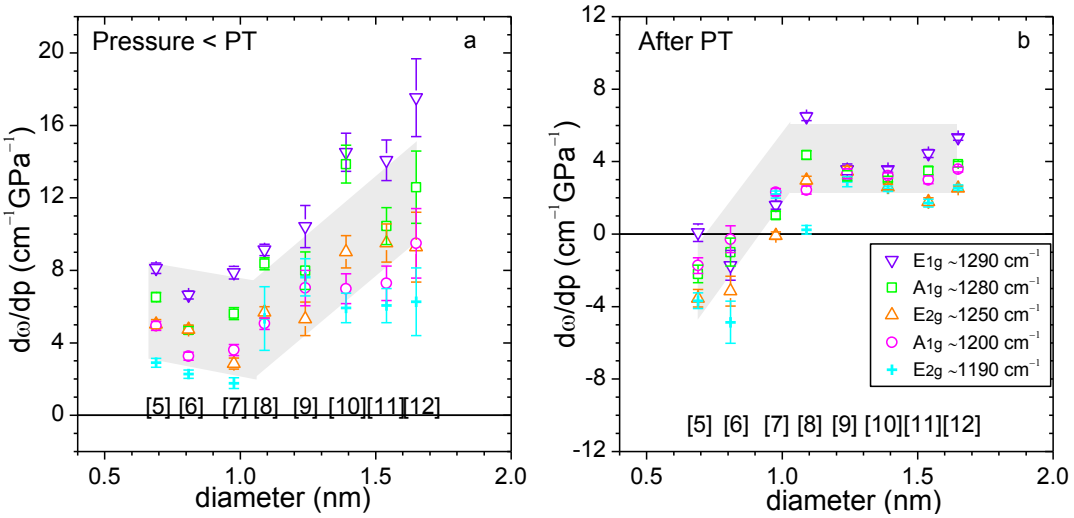

Figure 24. Diameter dependence of the pressure coefficients band in the the 1200-1300 cm^{-1} region, for [5-12]CPPs. a) before pressure transition; b) after pressure transition. ○ 1200 cm^{-1} A_{1g} mode; □ 1280 cm^{-1} A_{1g} mode; + 1190 cm^{-1} E_{2g} mode; △ 1250 cm^{-1} E_{2g} mode; ▽ 1290 cm^{-1} E_{1g} mode. Dashed lines are used as guide to the eye.

In Figure 24 we represent the pressure coefficients of the different Raman contributions as a function of diameter before and after *PT*. We have already described the vibrational origin of these bands, and in all of them there is certain contribution of the C-C stretching. Then, it is comprehensible that these follow analogous behavior than the G bands, purer C-C stretching modes. In Figure 24a we see that before *PT* the highest pressure coefficients correspond to the biggest [n]CPPs. Therefore vibrations involved in these modes are being further affected in the bigger [n]CPPs than in the smaller ones. As occurred with the G-like bands, [7]- and [8]CPP represent a minimum in the coefficients trend. From this minimum the coefficients obtained for all the 1200 cm^{-1} bands are higher, i.e. smaller and bigger [n]CPPs depict larger coefficients. It could be argued, that [6]CPP depicts larger coefficients than [7]CPP because the former is more deformed. The [6]CPP deformation would be promoted by the stabilization provided by incoming π-π interactions. On the other hand, [5]CPP would evolve differently towards a quinonoid configuration.

Regarding the analysis of the pressure coefficients after *PT*, we see in Figure 24 b, as in the G bands, these are approximately constant with *n* at about 3 cm^{-1} GPa^{-1} from *n*>8. For *n*<8 these coefficients rapidly decrease with decreasing *n* towards negative values. This indicates that from *PT* for *n*>8 pressure keeps distorting the structure with similar contributions towards C-C rearrangement and bond angle change. However, for *n*<8, C-C rearrangement is lower with decreasing *n*, and bond angle perturbations are largely affected. Interestingly, in the cases of [5]- and [6]CPP depict negative coefficients, indicating that these modes are susceptible to the configurational changes induced by pressure. The [5]CPP different trend will be explained by interpretation of all the high pressure evidences, which so far seem to converge towards the formation of a more quinonoid configuration. In the [6]CPP case, the negative coefficients after *PT*, obtained for all the 1200 cm^{-1} bands, support the hypothesized formation of a peanut configuration. Further analysis of the behavior of these two systems will be done at the end of this chapter.

In Figure 24 it is observed how the E_{1g} band around 1290 cm^{-1} is the one with largest coefficients for any [n]CPP, even higher than those of the G bands. This behavior is observed for all the [n]CPPs before and after *PT*. The E_{1g} band, ~1290 cm^{-1}, results from the combination between phenyl breathing mode and C-H wagging. When the [n]CPPs are compressed, the molecules are squeezed against each other therefore the C-H wagging is largely hindered. Regardless the intramolecular configuration, intermolecular compression remains with increasing pressure. Hence, pressure hinders the C-H wagging in both regimes, which explains why the E_{1g} band depicts the largest pressure coefficients.

A major interest in the Raman spectra of [n]CPPs comes from the analysis of the intensity ratio between the 1280 and 1200 cm^{-1} bands ($I_{1280A1g}/I_{1220A1g}$). In [n]LPPs, the diminution of this ratio has been correlated to the increase in the conjugation.[91,93,94] In the Figure 25 we have represented the progress of the ratio $I_{1280A1g}/I_{1220A1g}$ as a function of pressure for the different [n]CPPs. It should be pointed out that in [n]LPPs this ratio progresses with pressure following an exponential decrease towards a low constant value, about 0.26. In contrast, in [n]CPPs it is observed that with increasing pressure there is a first region in which the intensity ratio grows up to a maximum at a certain pressure, which depends on *n*. From that intensity ratio maximum, with increasing pressure this ratio then exponentially decreases, as happened in [n]LPPs. To analyze this behavior we have fitted the intensity ratios for each *n* to a combined linear with an exponential fitting which converge at a certain pressure, which we will refer as of torsional limit (TL):

$$\begin{aligned} &\text{if } (p < p_{TL}):\ \omega = \omega_0 + S_1 p && \text{Linear growth} \\ &\text{if } (p > p_{TL}):\ \omega = (\omega_0 + S_1 p_{TL})\exp\{-d(p - p_{TL})\} && \text{Exponential decrease} \end{aligned} \quad (4)$$

where p_{TL} corresponds to the pressure at the kink to which we will refer as pressure torsional limit; *d* is a fitting parameter of the exponential side; S_1 is the slope of the linear trend and ω_0 is the Raman shift at room conditions.

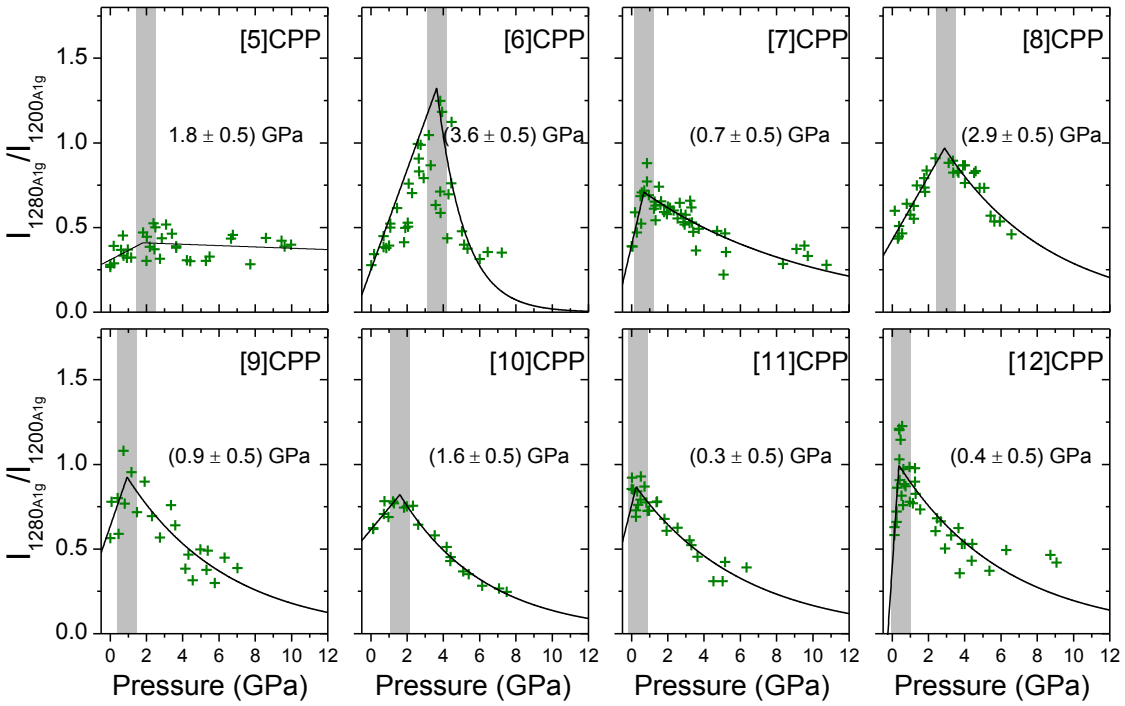

Figure 25. Intensity ratios, $I1280_{A_{1g}}/I1200_{A_{1g}}$ as a function of pressure for the different [n]CPPs. Black lines correspond to the fitting to equation 4. For each [n]CPP the value of pressure indicated is the pressure of torsional limit. Grey shadow bars mark the pressure region where the ratio exhibits its maximum value.

In Figure 25 it is seen that the first region, at which the intensity ratio linearly increases with pressure, becomes shorter for the largest [n]CPPs, being almost negligible for *n*=12. As said in previous chapters, with increasing *n* the [n]CPPs move towards the lineal polymeric limit. Then, it is understandable that as [n]CPPs become larger these behave more similarly to their linear analogues with no initial torsional increase.

On the other hand, the intensity ratio of [5]CPP after the pressure torsional limit remains almost constant with increasing pressure. This behavior is unique for [5]CPP, since [6]CPP responds with the largest intensity ratio, followed by an exponential decrease in the intensity ratio. The intensity ratios for all the other [n]CPPs decrease at approximately similar rate. The constant ratio for [5]CPP and the described behavior for [6]CPP indicate that a different pressure induced configurational change is being triggered between [5]CPP and the others.

In previous chapters we related this intensity ratio directly with the benzene torsional angles. We have performed calculations of geometry optimization based on a DFT methodology at the B3LYP/6-31G(d,p) level. In these optimized structures we calculated their Raman spectrum at the same theory level. In Figure 26a we have represented the $I_{1280A1g}/I_{1200A1g}$ of the [n]CPPs at room condition against the $I_{1280A1g}/I_{1200A1g}$ ratios obtained from the calculated spectra of the optimized structures. We see that there is a good correlation between experiments and calculations. The torsional angles of the optimized strucutres and the obtained $I_{1280A1g}/I_{1200A1g}$ ratios of the [n]CPPs from 4 to 20 are plotted in Figure 26b. Moreover, at this same theory level we optimized the [n]CPPs structures keeping their symmetry as D_{nh}, torsional angles equal to zero (non-twisted). In Figure 26b we also insert the corresponding $I_{1280A1g}/I_{1200A1g}$ ratios for these highly symmetric geometries. Additionally, for [6]CPP we have calculated how the $I_{1280A1g}/I_{1200A1g}$ ratio varies when torsions are changed in a controlled way, with torsional angles ranging from 0 to 40°. From those results in Figure 26b, we fit them to a second order polynomial.

$$\theta = -a + b\,(I_{1280A1g}/I_{1200A1g}) - c\,(I_{1280A1g}/I_{1200A1g})^2 \quad (5)$$

where θ represents the torsional angle between neighboring phenyl units, and a, b and c are fitting parameters. From the fitting of the data represented in Figure 26b we obtain that a, b and c are equals to 4.43°, 43.5° and 10.4°, respectively.

Through equation 5 thus we can estimate the torsional angle of [n]CPPs by using their experimental values for the intensity ratio $I_{1280A1g}/I_{1200A1g}$ at room conditions, reported in Table 11. Thus we have summarized the B3LYP/6-31G(d,p) torsional angles of the optimized structures with their corresponding $I_{1280A1g}/I_{1200A1g}$ ratios for the [n]CPPs. In this table the intensity ratios obtained for the non-twisted structures are also reported. Moreover we have added the experimentally observed ratios at room conditions, and the torsional angles given in the literature from XRD measurements conducted at around 100 K.

In Figure 26c we plot the estimated torsional angles of [n]CPPs at room conditions, which exponentially decrease with decreasing *n* due to their increasing strain.[92] In [n]LPPs it has been studied how the temperature modulates torsional conformations, so at room temperature the torsions are close to their lower limit before planarity, further planarization would be achieved only by high pressure.[68,72] Then it could be expected that the measured torsional angles at 100 K by x-ray diffraction[25,26,79-85] would be lower than torsions at room conditions. In Table 11 we see that indeed when we estimate torsions from the intensity ratio at room conditions these torsions are lower than the measured at 100 K. Regarding the differences between the estimated torsional angles from the measured $I_{1280A1g}/I_{1200A1g}$ at room conditons, and the obtained from the DFT B3LYP/6-31G(d,p) optimized structures in the global minimum, the latter are clearly higher. In this kind of calculations only one molecule is taken into account. As was earlier perceived, in [n]LPPs lower solid-state torsions than those DFT calculations were orbserved.[76] In [n]CPPs calculations their crystal environment is not considered, torsion reductions due to the neighboring molecules are not included. Therefore, as observed, predicted torsional angles are higher than the experimental ones, regardless the temperature of measurement. To have these torsional angles for [n]CPPs at room conditions is important because even though the value might not be precise, we know that this are lower than those described in the literature from x-ray diffraction measurements and DFT calculations. Then, these will be the starting point before compression.

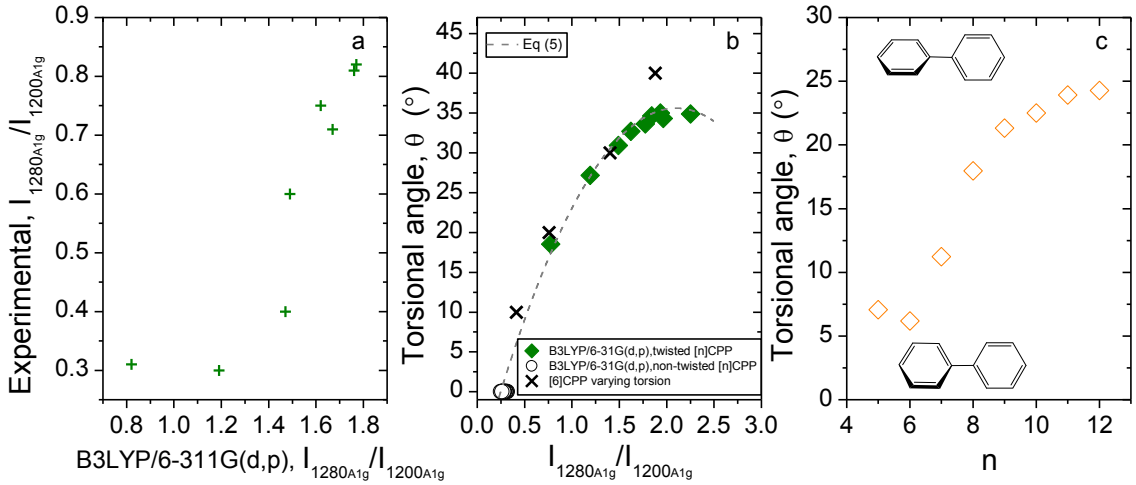

Figure 26. a) Room conditions experimental $I_{1280A1g}/I_{1200A1g}$ against calculated B3LYP/6-31G(d,p) $I_{1280A1g}/I_{1200A1g}$. b) Torsional angle calculated at the B3LYP/6-31G(d,p) level against the corresponding intensity ratio $I_{1280A1g}/I_{1200A1g}$ from the Raman spectra calculated at the same DFT level. (◆) For the optimized energy minimum structures, all twisted, and (○) for non-twisted structures with zero torsions. (✕) Intensity ratios estimated from geometry optimizations with fixed torsions (0°, 10°, 20°, 30°, 40°) for [6]CPP. Dashed line corresponds to a second order polynomial fitting of all the data. c) Estimated torsions from polynomial fitting of Figure 26c for the [n]CPPs at room conditions by using their experimental intensity ratio $I_{1280A1g}/I_{1200A1g}$.

From equation 5 and the measured intensity ratios at high pressures, we can estimate how torsions are affected during compression. In Figure 27 we plot those estimated torsional angles as a function of pressure for each [n]CPP. We see that the trend followed by the torsions is very similar to that of the intensity ratio. Interestingly, it seems as in none of the cases the torsions reached are below 7°, so pressure does not seem to induce the total reduction of torsions.

Table 11. [5]- to [12]CPP torsional angles calculated at the B3LYP/6-31G(d,p) level against the corresponding intensity ratios $I_{1280A1g}/I_{1200A1g}$ from the Raman spectra calculated at the same DFT level. Calculations for the optimized energy minimum structures, all twisted, and for non-twisted structures with zero torsions. Experimental intensity ratios and torsional angles obtained from x-ray diffraction measurements conducted at 100 K taken from the literature, references indicated in brackets. Torsional angles estimated with equation 5 from the experimental $I_{1280A1g}/I_{1200A1g}$ measured at room conditions.

	DFT/B3LYP-6-31G(d,p)				Experimental		
	Optimized structures at the global energy minimum		D_{nh} symmetry (non-twisted)				
n	$I_{1280A1g}/I_{1200A1g}$	θ (°)	$I_{1280A1g}/I_{1200A1g}$	θ (°)	$I_{1280A1g}/I_{1200A1g}$	θ (°) from X ray diffraction measurements at 100 K	θ (°) calculated from eq. 5
5	0.82	16.5	0.32	0	0.31	12.2 [25]	7.1
6	1.19	27.2	0.31	0	0.30	26.4 [26]	6.2
7	1.47	25.5	0.30	0	0.40	19.5 [79]	11.2
8	1.49	30.9	0.30	0	0.60	24.3 [80]	18.0
9	1.67	29.8	0.29	0	0.71	24.4 [81]	21.3
10	1.62	32.7	0.29	0	0.75	27.3/26.9 [82/83]	22.5
11	1.76	31.9	0.26	0	0.81	27.7[84]	23.9
12	1.77	33.7	0.28	0	0.82	23.3 [85]	24.3

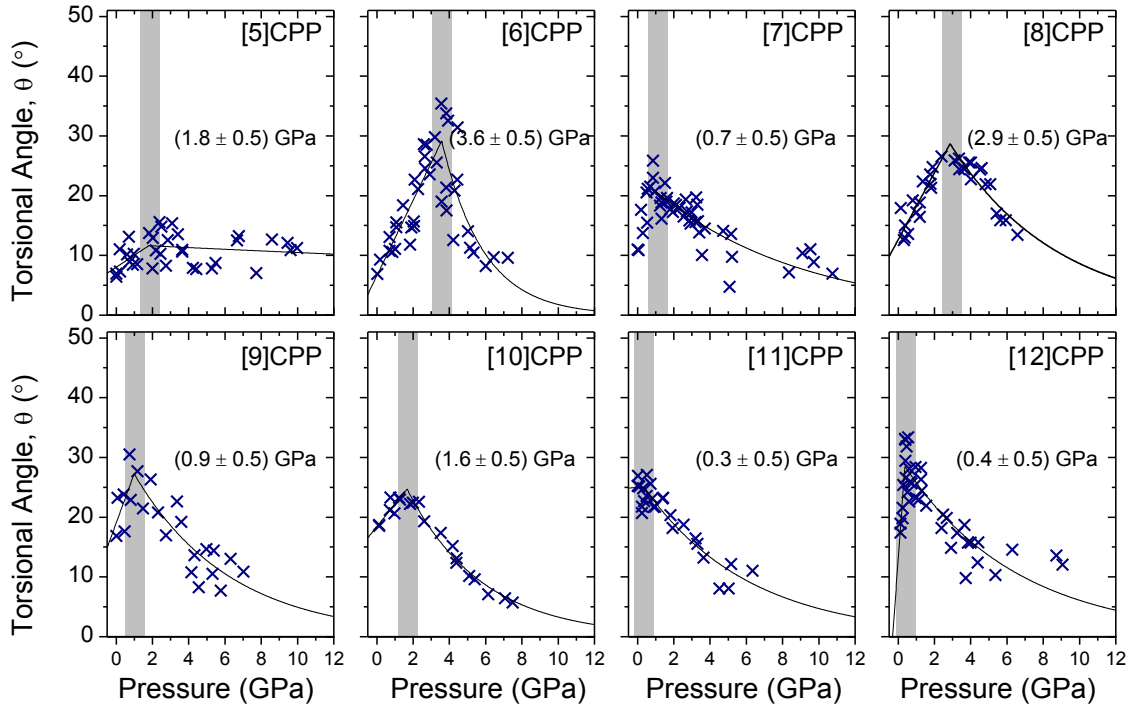

Figure 27. Estimated torsions from equation 5 as a function of pressure for the different [n]CPPs. Black lines correspond the fitting to equation 4. For each [n]CPP the value of pressure indicated is the pressure of torsional limit. Grey shadow bars mark the pressure region where the intensity ratio ($I_{1280A1g}/I_{1200A1g}$) exhibits its maximum value.

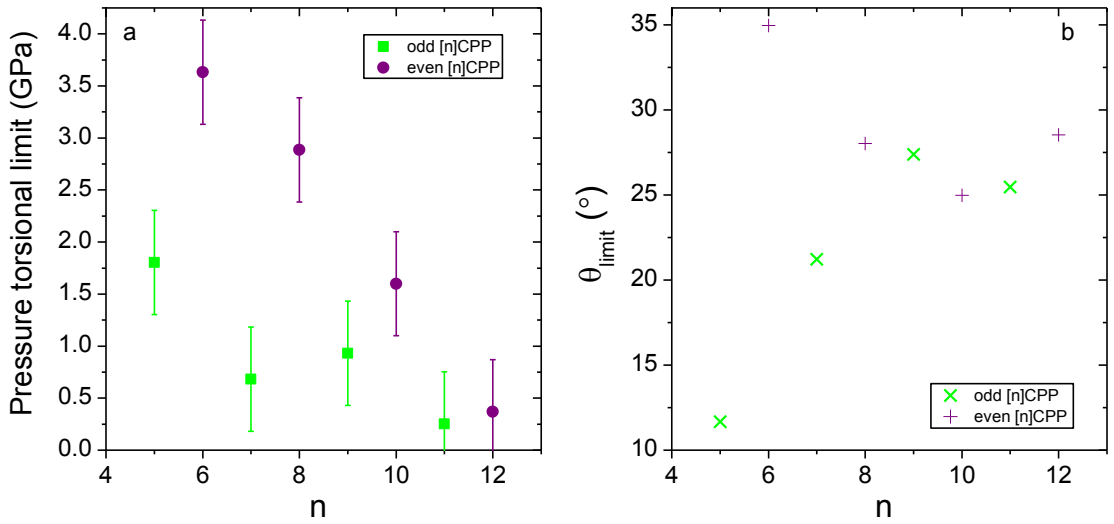

Figure 28. a) Pressure at the maximum of the $I1280A_{1g}/I1200A_{1g}$ ratio, referred as pressure of torsional limit as a function of *n*. b) Estimated torsional angles for those maximum $I1280A_{1g}/I1200A_{1g}$ ratio for each *n*, estimations are based on equation 5.

In Figure 28a we have represented the pressure at which the change in the intensity ratio trend occurs, coloring in green the odd [n]CPPs and in purple the even ones. Here there is an evident even-odd difference, being for the lower *n* larger in the even [n]CPPs converging (~0.5 GPa) almost with the linear poly-paraphenylene limit. In terms of torsions, which are the ones ruling these intensity ratios, the even [n]CPPs have larger freedom to be modulated in an alternated way during compression, so they can easily rearrange to accommodate the incoming stress. On the other hand, the odd [n]CPPs do not have the possibility to suffer such rearrangement, so once the upper limit is reached they do not have any other option but to decrease their torsional angle. In this regard, even [n]CPPs could be considered more torsional flexible.

In Figure 28b we have plotted the estimated maximum torsional angle as a function of *n*. For all [n]CPPs, except for [5]CPP, there is a common torsional limit (25-30°) from which at higher pressures a decrease of the torsional angles occurs. Thus torsional modulation can be interpreted as if pressure initially rearranged molecules with the consequential torsional increase up to achieve values of the TL. From pressures above the TL point, the molecular squeezing leads the torsional decrease together with the cycle ovallization. The different behavior followed by [5]CPP evidences once again that pressure drives its deformation through a different pathway at which torsions are not favored, as would be in its quinonoid configuration.

From the analysis of this spectral region two main conclusions can be reached, schematized in Figure 29:

- Raman shift in which C-C stretching modes and phenyl breathing modes are involved depict a double linear trend, as the G bands do. For the first range with larger pressure coefficients, higher C-C bond rearrangement exists. These pressure coefficients are larger for those bigger [n]CPPs, but there is a minimum at [7]CPP to increase again up to [5]CPP. The second pressure range, after transition, all the [n]CPPs have lower coefficients, being approximately constant from [8]- to [12]CPP, and negative for [5]- and [6]CPP. Thus indicating that smaller CPPs conduct a larger deformability and develop towards different configurations.

- Concerning the intensity ratios ($I1280A_{1g}/I1200A_{1g}$), these depict different behaviors to those observed in [n]LPPs. There is an initial increase up to a limiting torsional pressure, and then a steep exponential decrease, analogous to that observed in [n]LPPs. The initial torsional increase with pressure can be interpreted as a readjustment in torsions before torsion planarization. Such readjustment is more important for the smaller [n]CPPs, [5]- to [8]CPP,

as observed by their higher P_{TL}. For larger [n]CPPs at much lower pressures start rapidly a torsion decrease towards their non-twisted configuration.

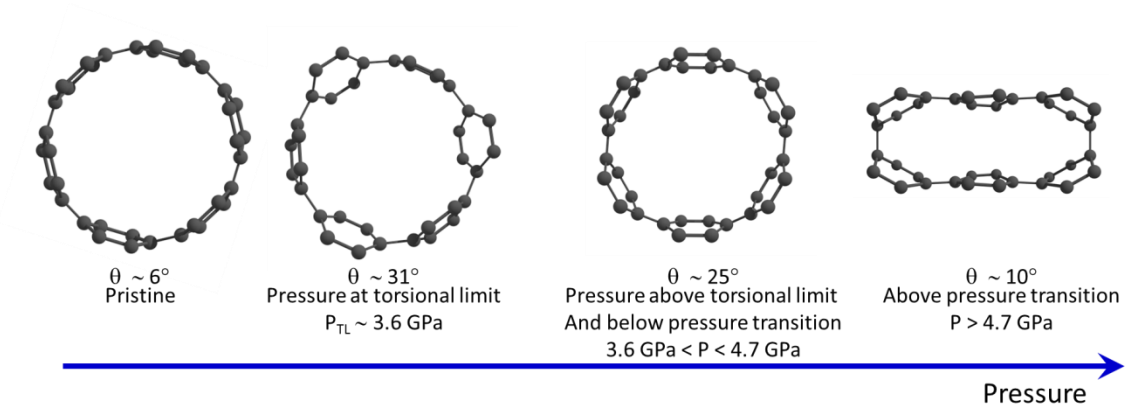

Figure 29. Scheme of the [6]CPP pressure evolution along its cross section from its pristine configuration with circular shape and torsional angle about 8°.

7.4.4.High Pressure Behavior of the [n]CPPs 450 – 1100 cm^{-1} Spectral Region

As seen in Figure 10 for [6]CPP this spectral region is characterized by medium intensity bands. In addition, the intensity of these diminishes with the increasing *n*, as already shown in a previous chapter. In Figure 30 we show the Raman spectrum of [6]CPP at room conditions in the 450 – 1100 cm^{-1} region. We have marked the bands that we will analyze during the high pressure study. At room conditions their intensity is low. With compression fluorescence increases and the ratio signal to noise decreases, hindering their identification, thus from certain pressures the recognition of these low intensity bands is no longer possible.

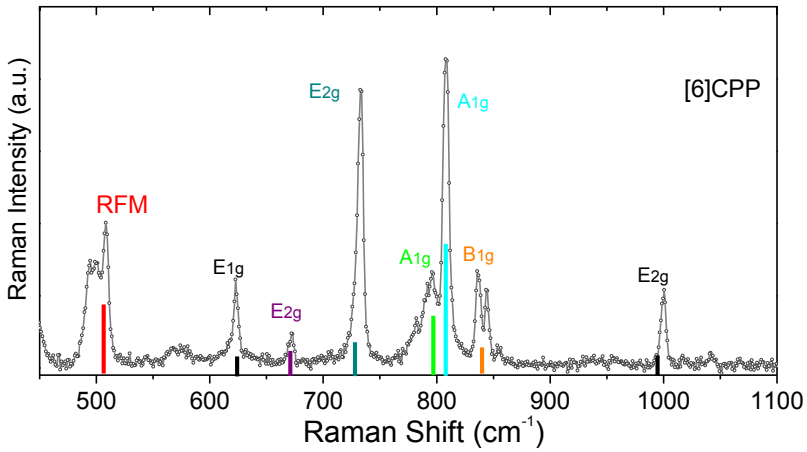

Figure 30. Raman spectrum of [6]CPP at room conditions in the 450-1100 cm^{-1} region. Grey dots correspond to the experimental spectrum, taken with the 785 nm excitation line. Vertical colored lines correspond to the theoretical Raman spectrum at the B3LYP/6-31G(d,p) level, scaled with 0.96.

In Figure 30 five bands between 650-850 cm^{-1} are highlighted. With the support of the B3LYP/6-31G(d,p) Raman calculations, (see Table 11), we assign them to the following vibrational modes: two with A_{1g} symmetry, two with E_{2g} symmetry and one with B_{1g} symmetry. Then, A_{1g} bands around 796 and 805 cm^{-1} for [6]CPP, represented in green and light blue respectively, result from the bending of the C_{ortho}-C_{ipso}-C_{ortho} bonds coupled to antisymmetric phenyl breathing and to the antisymmetric C_{ortho}-

C_{ipso}-C_{ortho} wagging. The E_{2g} band ~673 cm^{-1} and E_{2g} band ~730 cm^{-1}, represented in purple and dark green respectively, correspond to the combination of antisymmetric phenyl breathing mainly, with antisymmetric C_{ortho}-C_{ipso}-C_{ortho} bending. The B_{1g} mode in orange, around 836 cm^{-1} in [6]CPP, is a very low intensity mode which corresponds to the CH wagging. Unfortunately, as seen in Figures 30 and 31, we cannot study the five bands for all the [n]CPPs since they are too close to each other and their intensity with pressure decreases.

In the 500 cm^{-1} region, a single band appears, colored in red in Figure 30. This 500 cm^{-1} mode sets its origin on the flexural mode of benzene along one of its σ_d mirror planes. Thus the [n]CPP resultant has C_{ipso}-C_{ipso} bonds moving inwards while C_{ortho}-C_{ortho} move outwards, as represented in Table 11. Because it results into a vibration along the CPP perimeter, this is referred as Radial Flexural Mode (RFM) as Chen at al. reported elsewhere.[92]

Table 11. [n]CPPs bands in the 500-900 cm^{-1} region: symmetry, vibrational assignment in terms of generic internal coordinates. Raman shifts are approximately those corresponding to [6]CPP at room conditions, and in brackets are the calculated values by B3LYP/6-31G(d,p) methodology scaled with 0.96.

Raman shift (cm^{-1})	Symmetry	Vibrational description
504 (505)	A_{1g}	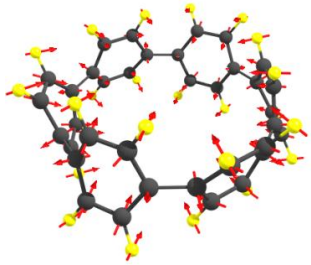 Radial Flexural Mode
623 (624)	E_{1g}	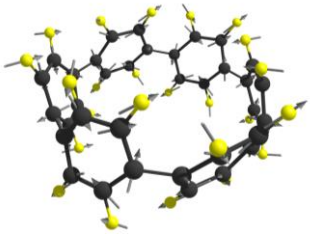 Phenyl deformation with constant bond lengths
673 (671)	E_{2g}	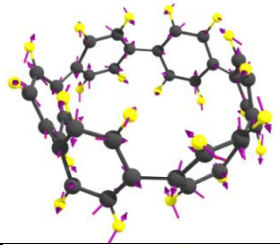 **β antisym (phenyl) + $RFM_{antisym}$**
730 (730)	E_{2g}	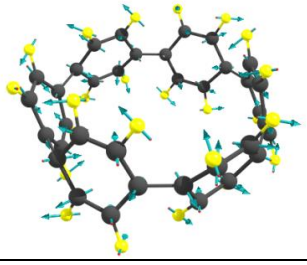 **β antisym (phenyl) + $RFM_{antisym}$**

796 (797)	A_{1g}	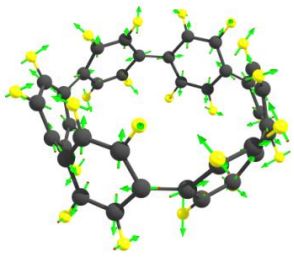	β antisym (Co-Ci-Co) + β antisym (phenyl) + ω antisym (Co-Ci-Co)
805 (808)	A_{1g}	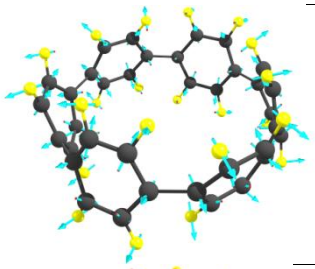	β antisym (Co-Ci-Co) + β antisym (phenyl) + ω antisym (Co-Ci-Co)
836 (840)	B_{1g}	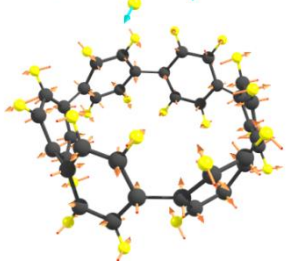	**ω(C-H)**
1006 (994)	E_{2g}	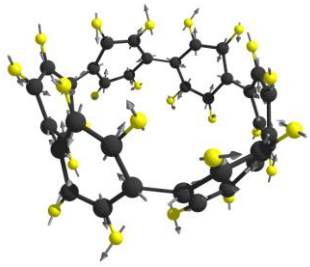	**Antisymmetric phenyl breathing mode**

RFM, radial flexural mode: C_{ipso}-C_{ipso} bond vibration with motion outward relative to the center and the C_{ortho}-C_{ortho} bond motion inward**, βantisym(phenyl)** antisymmetric phenyl breathing mode, C_{ortho}-C_{ortho} with motion inward relative to the benzene center. **β (Co-Ci-Co)**: C_{ortho}-C_{ipso}-C_{ortho} bending mode. **ω (Co-Ci-Co)**: C_{ortho}-C_{ipso}-C_{ortho} wagging mode. **ω(C-H)**: C-H wagging mode. A_{1g} ~ 790 cm^{-1} and A_{1g} ~ 800 cm^{-1}: from the bending of the C-C bonds coupled to antisymmetric phenyl breathing and antisymmetric RFM. E_{2g} ~ 700 cm^{-1} and E_{2g} ~ 740 cm^{-1}: combination of antisymmetric phenyl breathing with antisymmetric radial flexural mode. B_{1g} ~ 836 cm^{-1} corresponds to the CH wagging.

In Figure 31, we have the Raman spectra at selected pressure values of the different [n]CPPs in the spectral region under study. We are not able to assign the same modes for all [n]CPPs, as seen [10]CPP is the only [n]CPP showing all the mentioned bands. This is due to their different frequency shifts and intensity ratios. In Figure 31 we can observe how the quality of the spectra gets worse with increasing pressure. Therefore, for a given pressure value, different for the different [n]CPPs, the study of these bands was not possible any longer.

In Figure 32 we have represented the pressure dependence of the Raman shifts of the different [n]CPPs bands in the 650-900 cm^{-1} region. The shifts for each band with pressure have been obtained through a second derivative method. Because of the proximity between the different A_{1g} bands and the general low intensity of the spectrum our resolution in this region is slightly higher than before, about 5 cm^{-1}. In Figure 32 we see that the trends depicted by these bands could be defined as linear with the increasing pressure, because no significant changes in slope can be appreciated with the increasing pressure. It is only in some cases that a double linear trend could be appreciated, as in [11]CPP and [5]CPP. However, only in [5]CPP the quality of data is good enough to clearly show an

identifiable double linear trend, with a kink at 3.1 GPa. In Table 12 we have recorded the [n]CPPs pressure coefficients of each band. At first glance it can be observed that with the increasing *n* the slopes of the trends for the different bands increase as well.

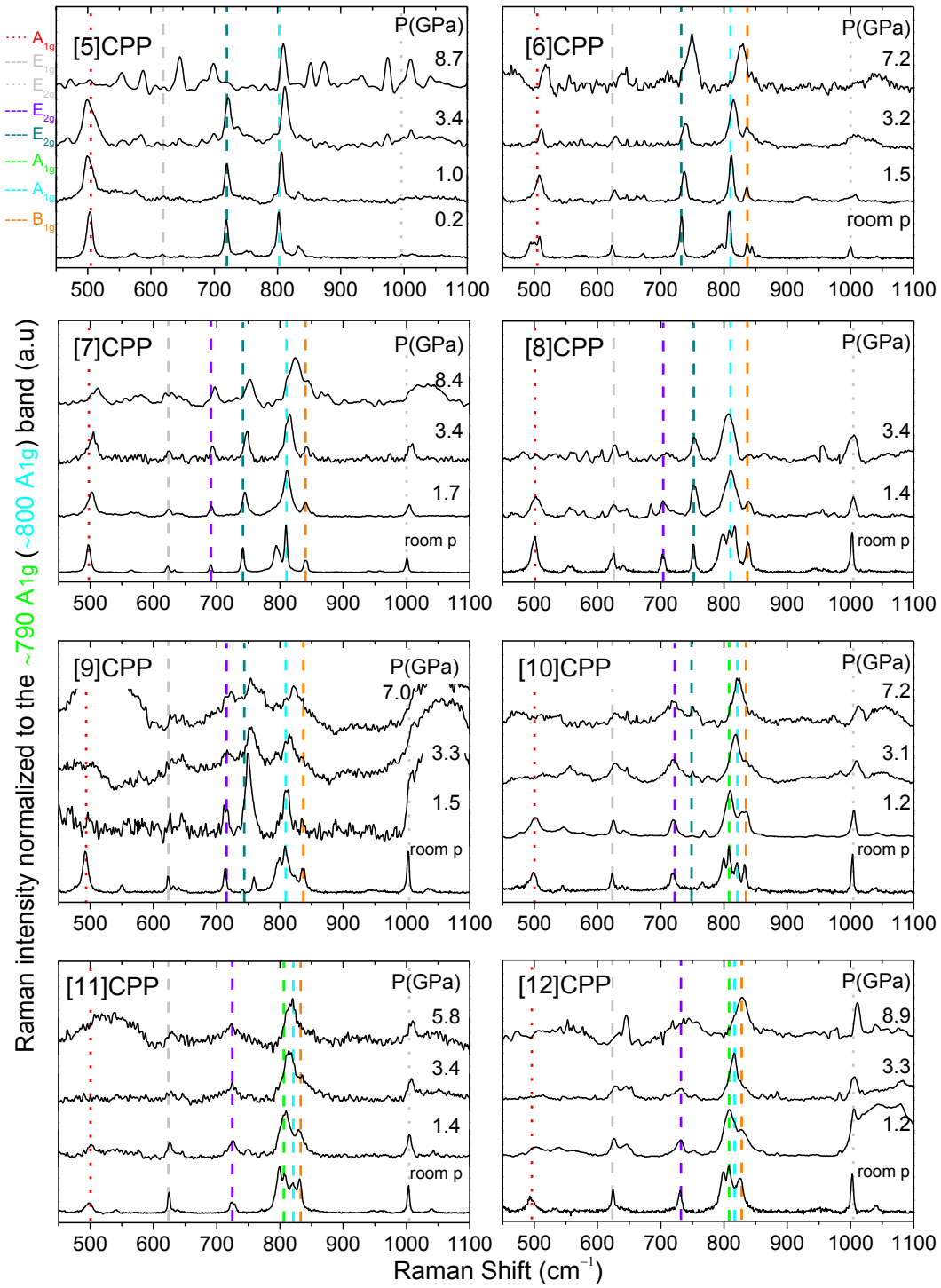

Figure 31. Raman spectra at selected pressures in the 450-1100 cm^{-1} region, *n*: 5-12. Colored vertical dashed lines are used to denote the different modes: red bar correspond to the RFM; purple and dark green bars to the 673 cm^{-1} and 750 cm^{-1} E_{2g} modes, respectively; light green and light blue bars are used for the 793 cm^{-1} and 805 cm^{-1} A_{1g} modes; and the orange one is used for the B_{1g} band. Raman spectra of [5]- to [9]CPP have been normalized to the ~800 cm^{-1} A_{1g} band and Raman spectra of [10]- to [12]CPP to the ~790 cm^{-1} A_{1g} band.

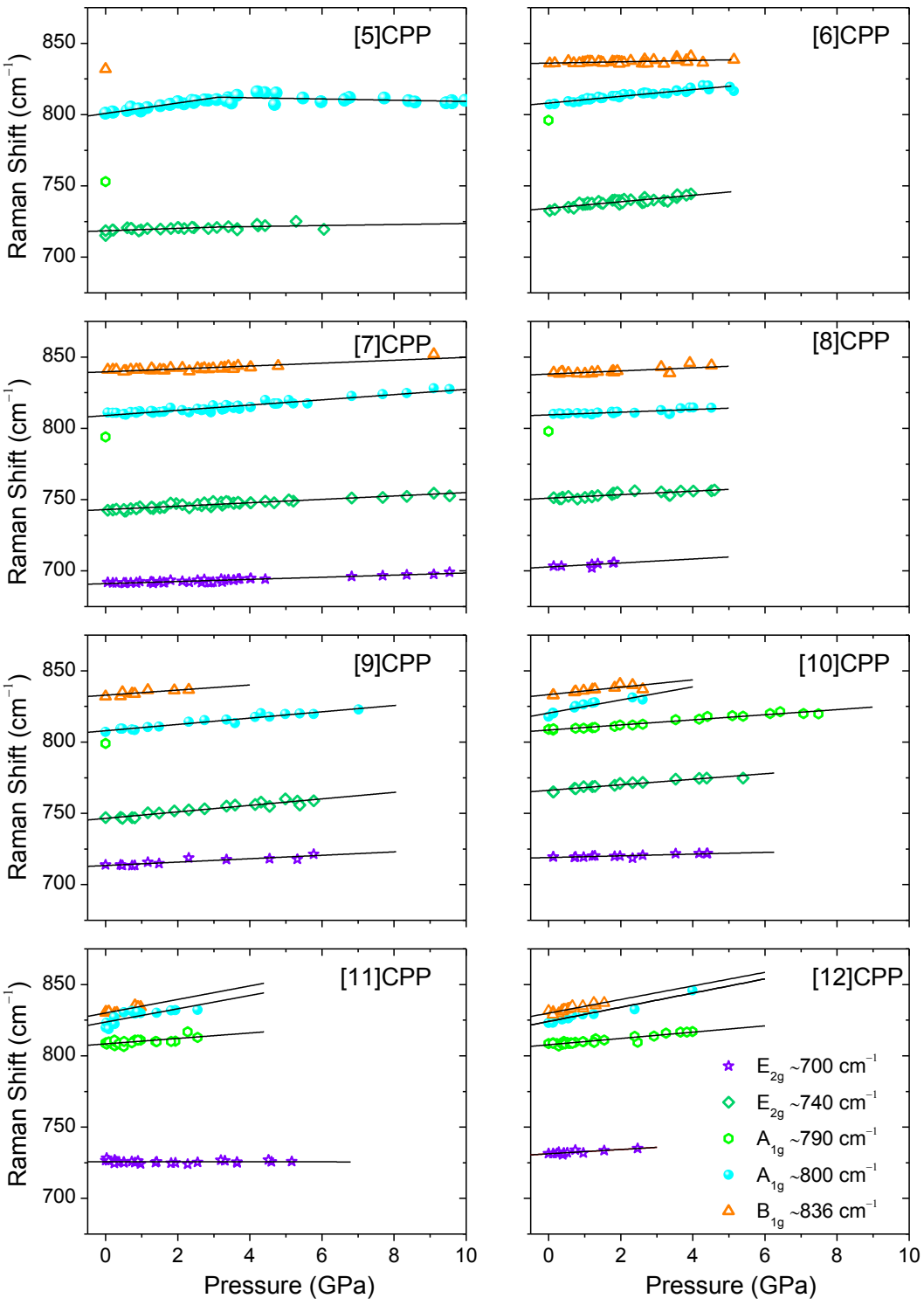

Figure 32. Pressure dependence of the bands between 650 and 900 cm^{-1}. Lines correspond to a linear fitting of the data, except in [5]CPP whose data have been fitted to equation 3.

Table 12. ω_0: Raman shifts at room conditions of the bands observed in the 650 – 840 cm^{-1} spectral region. S_1: Pressure coefficients of these bands. Only data for those bands followed with high pressure are reported.

	E_{2g} ~ 700 cm^{-1}		E_{2g} ~740 cm^{-1}		A_{1g} ~790 cm^{-1}		A_{1g} ~800 cm^{-1}		B_{1g} ~836 cm^{-1}	
n	ω_0 cm^{-1}	S_1 $cm^{-1}GPa^{-1}$	ω_0 cm^{-1}	S_1 $cm^{-1}GPa^{-1}$	ω_0 cm–1	S_1 $cm^{-1}GPa^{-1}$	ω_0 cm^{-1}	S_1 $cm^{-1}GPa^{-1}$	ω_0 cm^{-1}	S_1 $cm^{-1}GPa^{-1}$
5	--	--	715	0.8 ± 0.5	753	--	790	3.6 ± 0.5	832	--
6	--	--	734	1.9 ± 0.2	796	--	805	2.4 ± 0.2	836	0.5 ± 0.2
7	691	0.7 ± 0.1	743	1.2 ± 0.1	794	--	810	1.8 ± 0.1	841	1.0 ± 0.1
8	703	1.4 ± 0.7	751	1.2 ± 0.2	798	--	807	0.9 ± 0.2	838	1.1 ± 0.2
9	714	1.2 ± 0.2	747	2.3 ± 0.2	799	--	807	3.7 ± 0.3	833	1.8 ± 0.7
10	719	0.6 ± 0.2	765	1.9 ± 0.2	809	1.8 ± 0.1	815	4.6 ± 0.4	833	2.6 ± 0.4
11	726	0.0 ± 0.2	--	--	809	1.9 ± 0.5	818	4.7 ± 0.6	830	4.7 ± 1.5
12	731	1.5 ± 0.3	--	--	807	2.2 ± 0.2	818	5.0 ± 0.3	831	4.8 ± 0.5

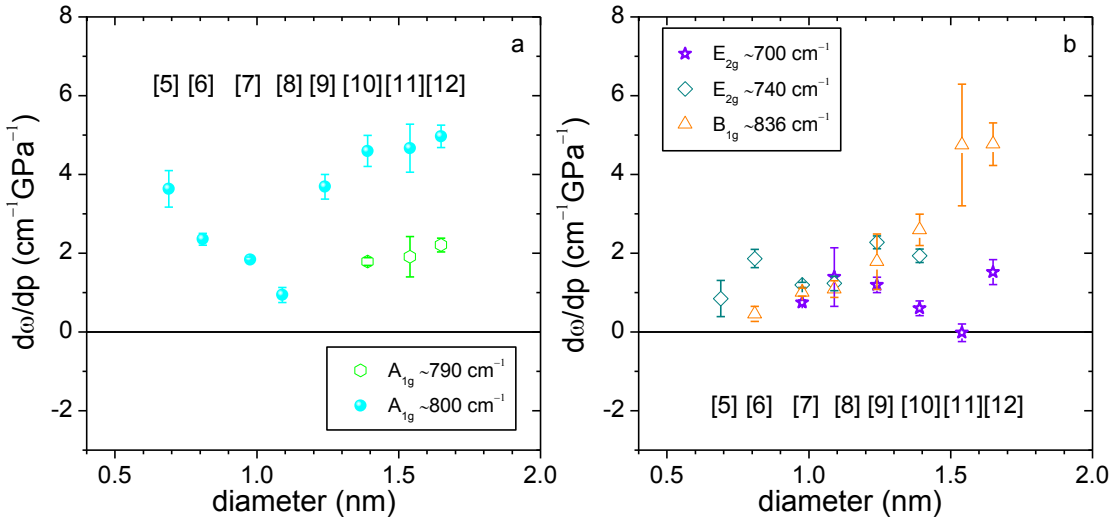

Figure 33. Diameter dependence of the pressure coefficients of the: a) A_{1g} bands in the 700-800 cm^{-1} region, b) E_{2g} and B_{1g} bands in the 650-900 cm^{-1} region.

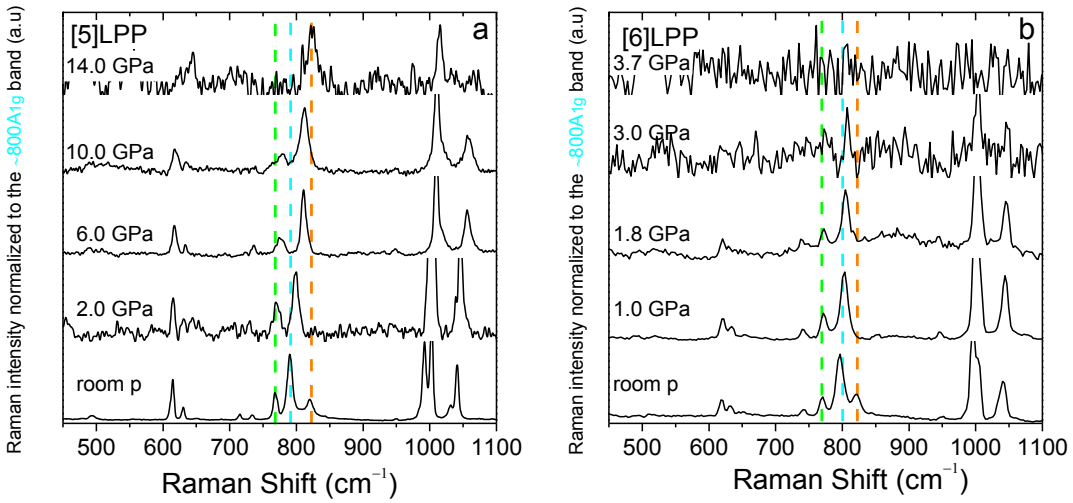

Figure 34. Raman spectra in the 450 -1100 cm^{-1} region of [5]- and [6]LPP at selected pressures. Vertical dashed lines are used to indicate two A_{1g} modes between 750 and 850 cm^{-1} resulting from the bending of the C-C bonds coupled to antisymmetric phenyl breathing, A_{1g} ~790 cm^{-1} in light green, and A_{1g} ~800 cm^{-1} in light blue. B_{1g} mode in orange corresponds to the C-H wagging.

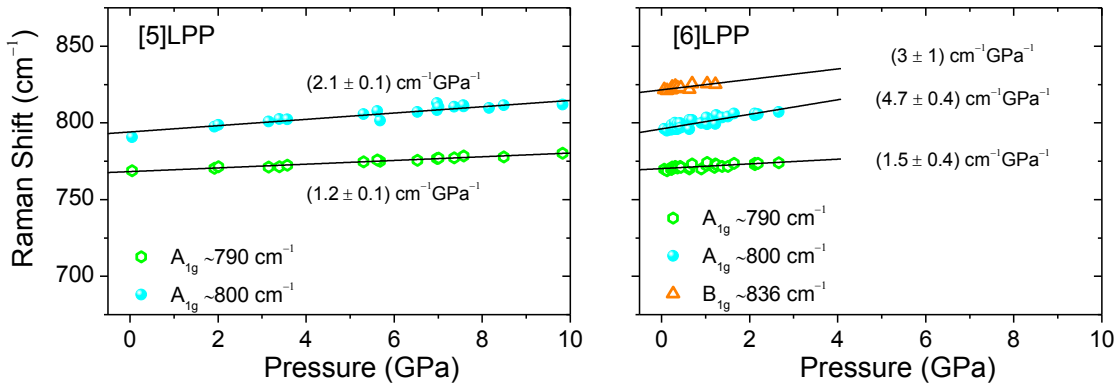

Figure 35. Pressure dependence of the Raman shifts of bands between 650 and 900 cm^{-1} for [5]- and [6]LPP. Black lines are linear fittings with the indicated slopes.

In Figure 33a and Figure 33b we have represented the pressure coefficients against the [n]CPP diameter for the A_{1g} bands, and for the E_{2g} and B_{1g} bands, respectively. For the A_{lg} bands the coefficients decrease with diameters from [5]- to [8]CPP to then increase again up to [12]CPP. In the case of the E_{2g} and B_{1g} bands, these depict a different trend at which coefficients grow with increasing diameter. It is important to mention that comparing the pressure coefficients of the bands in this middle region with those of the 1200 cm^{-1} or with the G bands, such values are much lower than the latter. So, within our experimental limits, the 1200 cm^{-1} and G bands provide us with much more valuable information.

Concerning the comparison of the behavior followed by [n]CPPs with SWCNTs, the latter do not depict important features in this region, but [n]LPPs do, so in Figure 34 we have presented the Raman spectra of [5]- and [6]LPP. In Figure 35 we see that [n]LPPs depict similar pressure coefficients regarding these bands, but in this case [5]- and [6]LPP respond differently to [5]- and [6]CPP. The pressure coefficient described by the A_{1g} ~800 cm^{-1} band, light blue, is twice larger for [5]CPP than it is for [6]CPP, while in [n]LPPs it is larger for [6]LPP than for [5]LPP. Such difference between [n]CPPs and [n]LPPs is another signal of the large radial π cyclic conjugation in the smaller [n]CPPs.

Regarding the RFM, the Raman shifts at high pressures of the different [n]CPPs have been represented in Figure 36a. These data are not available for [5]CPP because this band is very close to the p-RBM. Moreover in some cases because the RFM decaying intensity with increasing pressure we lose resolution very quickly so no data are available up to very high pressure values. We see in Figure 36a that the trends followed by this band can be fitted to a linear fit whose pressure coefficients have been recorded in Table 13, and no *PT* is appreciated.

In Figure 36b we have represented the obtained pressure coefficients as a function of the diameter. It is striking that they follow the same pattern we have been observing for other bands, i.e. there is a minimum in pressure coefficients around the diameters of [7]- and [8]CPP. The pressure coefficient of [8]CPP has a quite large error due to the low number of experimental data available. As mentioned along this section, the intensity of the band in this region diminishes with the increasing pressure, so in [8]CPP around 2.5 and 3 GPa the RFM is not identifiable. Additionally, the increase in the pressure coefficients of the RFMs from [7]- to [6]CPP is a bit larger than in the previous analyzed bands. Because of the nature of the RFM, this [6]CPP increment can be understood because an interaction between opposite benzenes might be induced, so the vibration responsible of this mode is going to be largely affected by pressure.

Table 13. Radial Flexural Modes (RFMs) for the different [n]CPPs, ω_0: Raman shift at room conditions and, S_1: pressure coefficient.

	RFM	
n	ω_0/cm^{-1}	$S_1/cm^{-1}GPa^{-1}$
5	505	--
6	504	2.3 ± 0.1
7	497	1.3 ± 0.1
8	501	1.3 ± 0.8
9	492	2.6 ± 0.4
10	499	2.8 ± 0.2
11	498	3.2 ± 0.7
12	493	3.6 ± 0.6

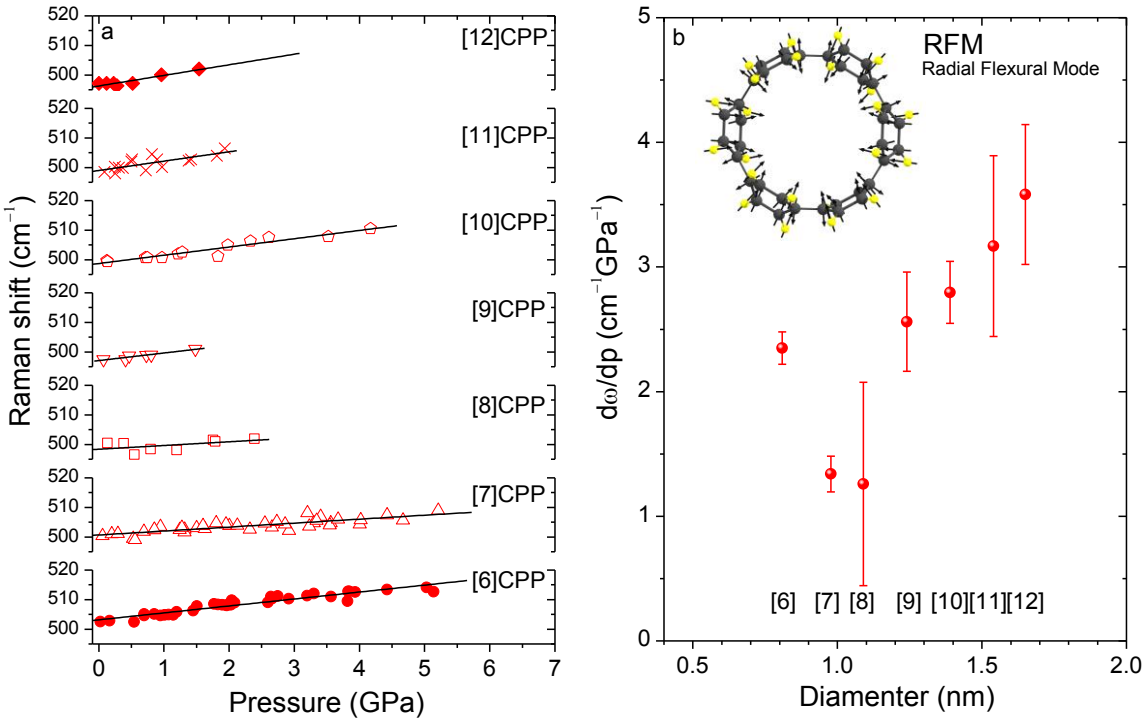

Figure 36. a) Pressure dependence of the radial flexural mode from bottom to top: [6]- to [12]CPP. Black lines are the resulting linear fittings to the corresponding data set. b) Pressure coefficients of the radial flexural mode as a function of diameter of the [n]CPP. Scheme inserted corresponds to the eigenvectors involved in this mode.

7.4.5. Radial Modes High Pressure Response

The low frequency region of the Raman spectra of [n]CPPs is dominated by several bands whose frequency is totally related with [n]CPP diameter, or in other words with strain. In Figure 37 we plot the Raman spectrum of [6]CPP in the 100-600 cm^{-1} region. We have marked in green the so-called pseudo-radial breathing mode (p-RBMs) and in purple the totally symmetric radial breathing mode (RBM). Their eigenvectors have been gathered in Table 14 together with the vibrational modes responsible for the other low intensity peaks present in this region. In chapter 4 we discussed that because the lower dimensions compared to CNTs, in length, the RBM appears at very low frequencies for the higher *n*, so it becomes experimentally inaccessible from *n*>8. However, we defined the p-RBMs with E_{2g} or E_2 symmetry which as RBMs show a clear linear dependence of their frequencies on $1/d$. This trend has been discussed in chapter 4, Figure 2 and scheme 1.

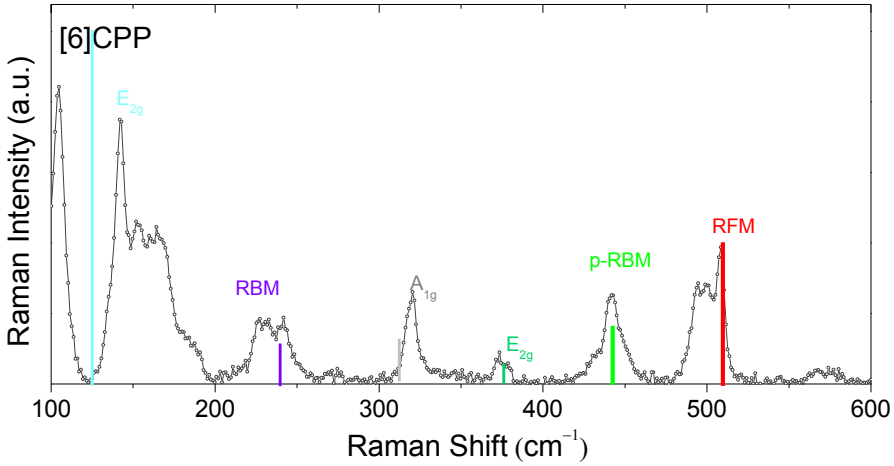

Figure 37. Raman spectrum of [6]CPP at room conditions in the 100-600 cm^{-1} region. Grey dots correspond to the experimental spectrum, taken with the 785 nm excitation line. Vertical colored lines correspond to the theoretical Raman spectrum at the B3LYP/6-31G(d,p) level, scaled with 0.96. Red bar corresponds to the RFM, green bar to the pseudo-radial breathing mode (p-RBM) and purple bar to the radial breathing mode (RBM).E_{2g} light blue bar around 125 cm^{-1} is assigned to the experimental peak around 142 cm^{-1}. This comes from phenyl twisting mode. As already discussed calculations overestimate the torsional angles, thus explaining the experimental upshift (lower torsions) compared to the computed one. The grey bar around 313 and greenish bar around 376 cm^{-1} match the experimental peaks around, 320 and 375 cm^{-1}. These correspond to vibrational modes with A_{1g} and E_{2g} symmetry, respectively. The 320 cm^{-1} A_{1g} band sets its origin at the rocking of a whole phenyl unit, its phenyls twits along the perimeter of the [n]CPP in a opposite direction to their direct phenyl neighbors. The E_{2g} band around 375 cm^{-1} is assigned to the wagging of the C_{ipso}-C_{ortho}-C_{ipso} atoms respect each phenyl center.

Table 14. Summary of the vibrational eigenvectors of the most relevant modes in the low frequency region. Raman shifts are those corresponding to [6]CPP at room conditions, and in brackets are the calculated values by B3LYP/6-31G(d,p) methodology scaled with 0.96.

Raman shift (cm^{-1})	Symmetry	Vibrational description
142 (126)	E_{2g}	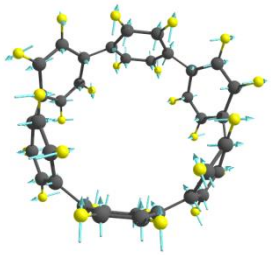 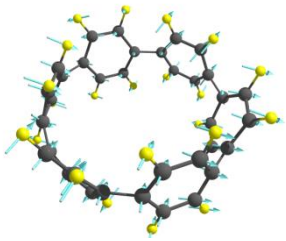 Phenyl twisting mode
231 (240)	A_{1g}	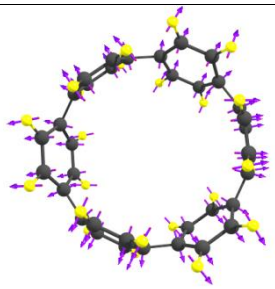 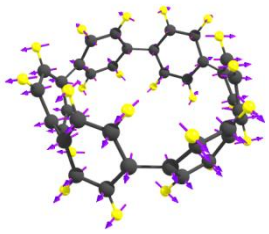 Radial breathing mode
320 (312)	A_{1g}	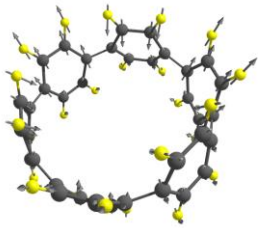 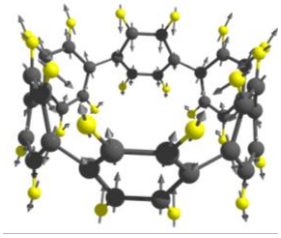 Rocking of a whole phenyl unit, its phenyls twits along the perimeter of the [n]CPP in a opposite direction to their direct phenyl neighbors
375 (375)	E_{2g}	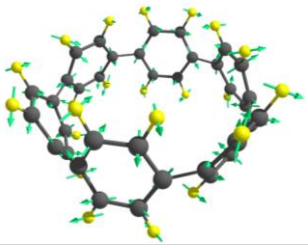 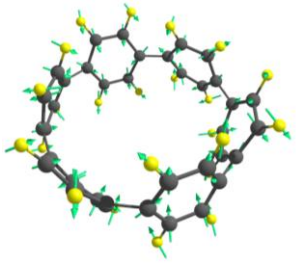 C_{ipso}-C_{ortho}-C_{ipso} wagging each phenyl unit center in phenyl plane and along the [n]CPP perimeter
442 (442)	E_{2g}	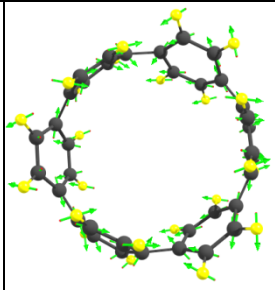 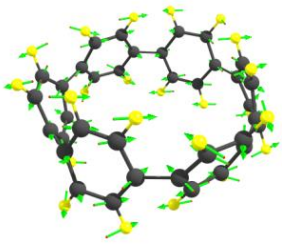 Pseudo-radial breathing mode

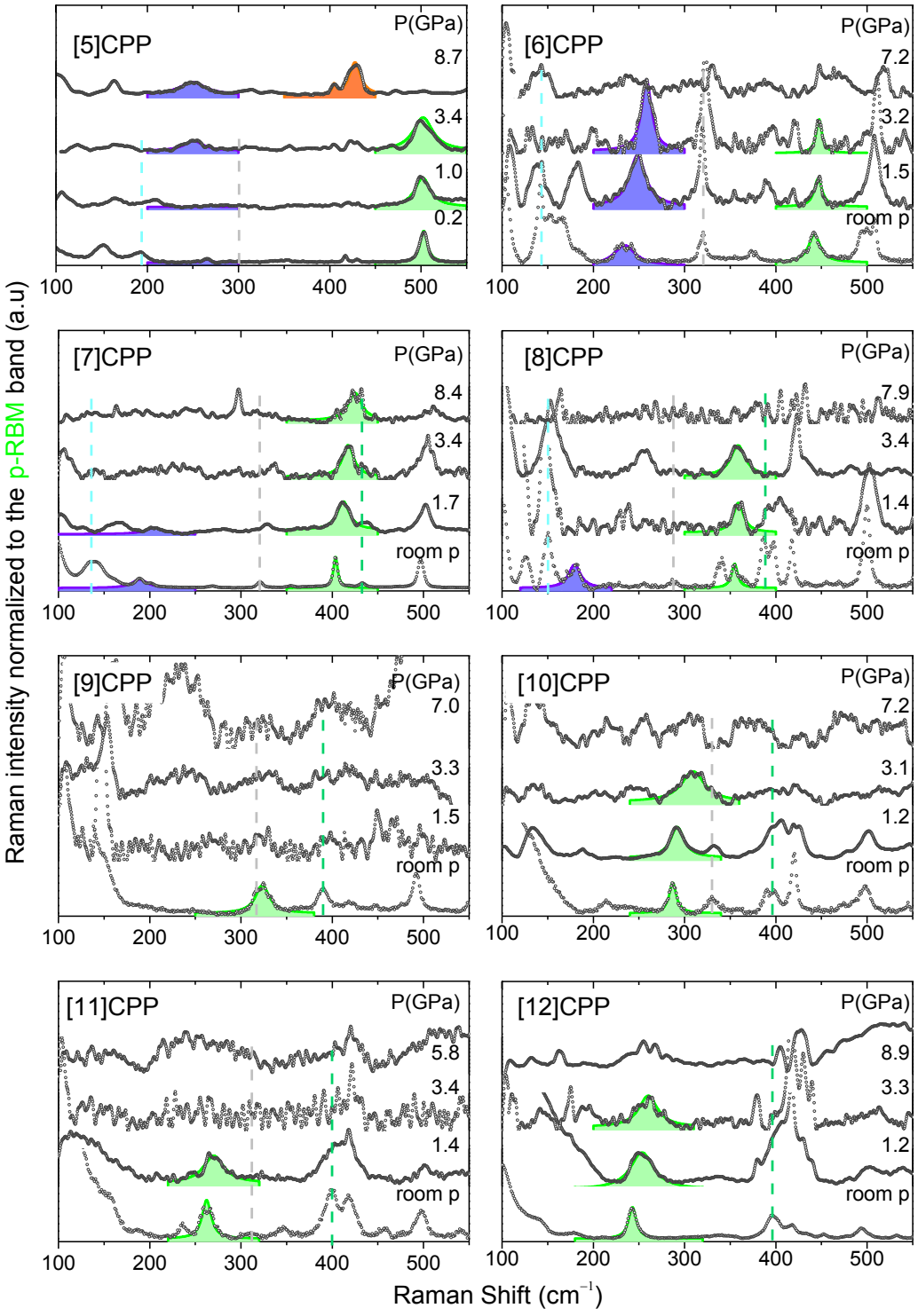

Figure 38. Raman spectra at selected pressures in the 100-550 cm^{-1} region, *n*: 5-12. Green areas correspond to the Lorentzian fitting of the corresponding p-RBMs. Purple areas correspond to the Lorentzian fitting of the RBMs, when is observed in our spectra. Orange area in the high pressure [5]CPP spectrum has been marked in a different color because of its important downshift from the p-RBMs. light blue bar correspond to the phenyl twisting band, grey bar to the Rocking of a whole phenyl unit, and the greenish bar to the C_{ipso}-C_{ortho}-C_{ipso} wagging. The low intensity of the latter peaks marked with bars, makes them very difficult to resolve so we will not study their behaviour with pressure.

Remember that RBMs of SWCNTs respond to high pressures by diminishing their intensity as consequence of their resonance loss, becoming negligible when the ovallization or collapse occurs.[35,95] As observed on Figure 38 for [n]CPPs, the p-RBM intensity decays with increasing stress. Nevertheless, since p-RBMs in [n]CPPs are not resonant, their intensity decay is not due to the loss of resonance resulting from the ovallization. We relate such diminishing intensity with the fluorescence increase induced by the stress, which hinders the analysis of the [n]CPPs weaker bands. In Figure 38 we have the Raman spectra of [n]CPPs at selected pressures. The p-RBMs have been coloured in green and the RBMs, when observable, in purple. In [5]CPP the intensity decrease of the p-RBMs occurs together with the growing of an incoming band around 400 cm^{-1}, which is clearly visible in the 8.7 GPa Raman spectrum.

In Figures 38a we have represented the pressure dependence for the p-RBMs. The data upshift with pressure following a double linear trend so these have been fitted to equation 3. Bear in mind that for each [n]CPP these fittings have been done together for all the bands. For each *n* the pressure transition has been left as a shared parameter within all the bands, and the slopes at lower and higher pressures than *PT* were left to freely fit. About the RBMs, Figure 39 b, we are able to measure the pressure dependence of those for [5]- to [7]CPP, but unfortunately due to their low intensity and the increasing fluorescence with pressure we are not able to follow them for a long pressure range, being then fitted to linear trends. The resulting pressure coefficients from these trends have been reported in Table 15. It is very interesting that while the available data for [6]- and [7]CPP upshift with pressure in a linear fashion, [5]CPP depicts a sudden decrease at around 2 GPa. This singularity might be related with a configurational change towards a more relaxed configuration with larger diameter, so lower wavenumbers would be justified.

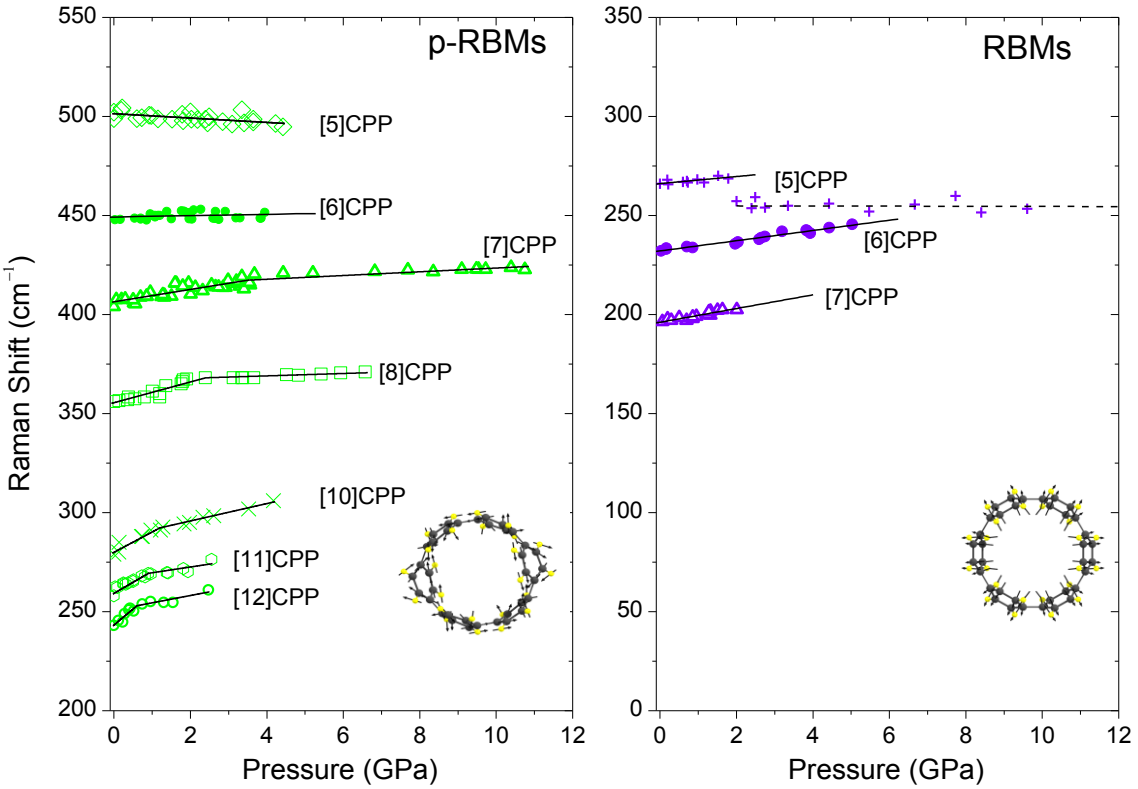

Figure 39. Pressure dependence of the Raman shifts for: a) p-RBMs, from top to bottom: [5]- to [12]CPP; b) RBMs observed for [5]- to [7]CPP. Lines correspond to the linear fittings of the Raman shifts of each mode. Inserted schemes correspond to the eigenvectors involved in these modes.

Table 15. ω_0: Raman shifts at room conditions of the bands observed in the 100 – 500 cm^{-1} spectral region, RBMs and p-RBMs. Pressure coefficients of these bands before and after pressure transition, S_1 and S_2 respectively. Only data for those bands followed with high pressure are reported.

		p-RBMs			RBMs	
n	***PT*** **GPa**	ω_0 cm^{-1}	S_1 $cm^{-1}GPa^{-1}$	S_2 $cm^{-1}GPa^{-1}$	ω_0 cm^{-1}	S_1 $cm^{-1}GPa^{-1}$
5	5.8 ± 0.5	502	-1.1 ± 0.3	--	266	2 ± 1
6	4.7 ± 0.5	442	0.3 ± 0.3	--	231	2.6 ± 0.1
7	3.5 ± 0.5	404	3.1 ± 0.2	0.9 ± 0.1	196	3.5 ± 0.4
8	2.2 ± 0.5	356	5.2 ± 0.3	0.6 ± 0.3	--	--
9	1.4 ± 0.5	323	--	--	--	--
10	1.2 ± 0.5	286	10 ± 1	4.4 ± 0.6	--	--
11	0.9 ± 0.5	258	11 ± 1	3 ± 1	--	--
12	0.6 ± 0.5	242	16 ± 3	3.7 ± 0.1	--	--

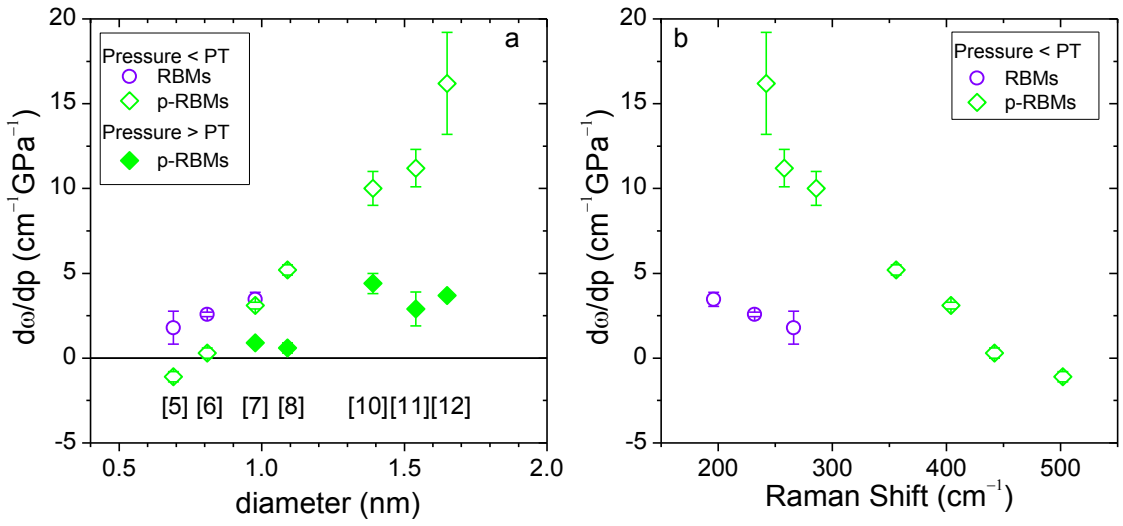

Figure 40. a) [n]CPPs diameter dependence of the pressure coefficients of the: a) (○) RBMs before pressure transition, (◇)p-RBMs before pressure transition and (◆) p-RBMs after pressure transition. b) Pressure coefficients before pressure transition against their ω_0 of the different modes of [n]CPPs.

In Figure 40 we represent the resulting pressure coefficients against their diameters, at pressures lower and higher than PT. We see that before pressure transition RBMs and p-RBMs pressure coefficients linearly increase with the increasing *n*. However, the p-RBMs depict larger increase than the RBMs. For pressure higher than *PT* we only have data available for the p-RBMs from [7]CPP to larger diameters. As occurred with the higher frequency bands, 1200 cm^{-1} and G bands, the pressure coefficients of the p-RBMs before *PT* are much lower after PT. Interestingly, the pressure coefficients after *PT* are almost constant with *n*, being slightly lower in the smaller [n]CPPs. In Figure 40b we have represented the pressure coefficients of the p-RBMs and RBMs before *PT* as a function of the Raman shift of each mode and each *n* at room conditions. We see that the largest coefficients are related with the lowest Raman shifts, this behavior was already observed in SWCNTs as shown in Figure 3b.

In order to compare the behavior followed by [n]CPPs with that known for SWCNTs in Figure 41 we have plotted together their RBMs pressure coefficients for pressures lower than *PT*. We have also compared with pressure coefficients given in the literature.[10,48] Pressure coefficients of the [n]CPPs and SWCNTs follow an analogue linear trend as a function of the diameter, with a very similar slope, about 5.3 $cm^{-1}GPa^{-1}nm^{-1}$, but different intercept, lower for [n]CPPs. Unfortunately we do not have data from the RBMs of the larger [n]CPPs, but from the smallest [n]CPPs coefficients, we could predict that [10]CPP and [12]CPP would have a pressure coefficient around 5.7 and 7.0 $cm^{-1}GPa^{-1}$, respectively.

On the other hand we are able to evaluate the p-RBMs as a function pressure for all the explored [n]CPPs. In Figure 41 we see that the p-RBMs also follow a trend with a linear increase of the coefficients with the increasing diameter. However, the slope of this line is about three times larger than for the RBMs. Thus, for [n]CPPs of largest diameters, p-RBMs are very sensitive to pressure.

Finally, the pressure coefficient of [5]CPP is negative, about –1.1 $cm^{-1}GPa^{-1}$. In chapter 4 S6, through a force constant analysis related the Raman shift of a totally aromatic configuration and a totally quinonoid configuration. We found that the ideal bond alteration mode from a quinonoid conformer would be 0.819 times downshifted from the aromatic configuration. Since the p-RBM band has certain contribution from the BLA, its downshift with increasing pressure could be indicating an aromatic – quinonoid transition. Moreover, in Figure 38 for [5]CPP it is seen how with increasing pressure the original p-RBM around 502 cm^{-1} becomes intensity negligible and a new feature around 420 cm^{-1} grows. Strikingly through the quinonoid-aromatic frequency relationship, 420 cm^{-1} is around the expected value for the p-RBM in the quinonoid [5]CPP. Consequently, the growth of the 420 cm^{-1} band with increasing pressure, is another signal showing that pressure might induce the transition from the aromatic [5]CPP to a quinonoidal distorted structure

From the high pressure behavior of the main [n]CPPs Raman bands we can conclude that [n]CPPs and SWCNTs respond similarly in terms of pressure coefficients diameter dependence and kinks on their Raman shift with high pressure. Subsequently, we can consider that pressure induces analogue effects on their tubular shape. In addition, [n]CPPs offer a wide possibility on the study of SWCNTs from a molecular approach with the advantage of their controlled synthesis.

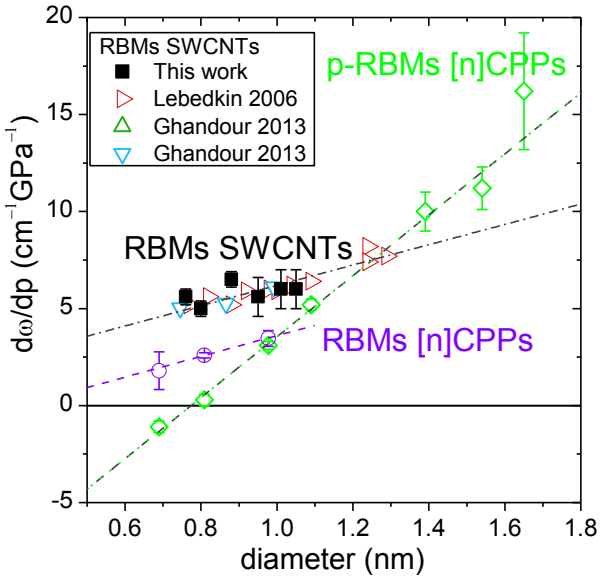

	Slope $cm^{-1}GPa^{-1}nm^{-1}$
RBMs SWCNTs	5.2 ± 0.4
RBMs [n]CPPs	5.3 ± 0.4
p-RBMs [n]CPPs	17.7 ± 0.6

Figure 41. Pressure coefficients of the circumferential modes represented against their diameter for [n]CPPs and SWCNTs. Data for the [n]CPPs: (◇) p-RBMs and (○) RBMs. Data for the RBMs of SWCNTs: (■) this work; (▷) Lebedkin et al. [48], and (△, ▽) Ghandour et al. [10]. Each data set has been fitted to a linear trend drawn as dashed lines and with the indicated slopes. SWCNTs data have been fitted to one single linear fit. Table at the right gathers the slopes of the SWCNTs, and [n]CPP pressure coefficients as diameter function linear trends.

[n]CPPs Radial Deformation Modulus

We have described the pressure effect on the [n]CPPs as a change in their cross sectional shape, from circular to oval, as depicted in Figure 42a. We have related such a deformation with the change of slope of certain Raman shifts as a function of pressure. More specifically, at a certain pressure the bands related with the C-C stretching mode revealed a kink in the pressure behavior. We have referred to the pressure at which the kink is observed as pressure transition, *PT*. However, so far we have not got into detail about the valuable information that such a pressure can provide about the mechanical properties of the system. This analysis is explained in this section.

Previously, the pressure dependences of the G and the 1200 cm^{-1} bands have been fitted together to equation 3, leaving the pressure transition as a common shared parameter for each *n*. From these fittings we have estimated a *PT* for each *n*. In Figure 42b we show the obtained *PT*s for the [n]CPPs as a function of their diameter. Comparison with some results of SWCNTs, from this work and also taken from the literature,[30,59,89] is also shown. As seen, the diameter dependence of *PT* for both of the systems, [n]CPPs and SWCNTs, behave analogously, *PT* decreases for larger diameters. This *PT* is related with the pressure at which deformation of their cross section starts: transition from circular to oval shape. The cross section circular-oval transition can be understood by the continuum theory of the buckling of elastic rings.[96-99]

The continuum theory of buckling of elastic rings suggests the use of accepted laws of physics, employed to model macroscopic properties and to predict the outcomes of the action of the external forces on microscopical bodies. It approaches the understanding of the mechanical behavior of materials modeled as a continuous mass rather than as discrete particles.[100] It assumes that straight lines normal to the mid-surface remain straight and normal to the mid-surface after deformation; and also that the thickness of the deformed surface does not vary during deformation either.[101] This theory relates the pressure at which a tube losses its circular cross section with the tube radius before any strain is applied, *R*. It is general for any order of magnitude of the tube diameter and it stablishes that *PT* follows a power law with $PT \propto R^{-3}$:

$$PT = \frac{3D}{R^3} \tag{6}$$

where *D* is the flexural (or bending) rigidity of the tube, which can be defined as the resistance offered by the tube while undergoing ovallization.

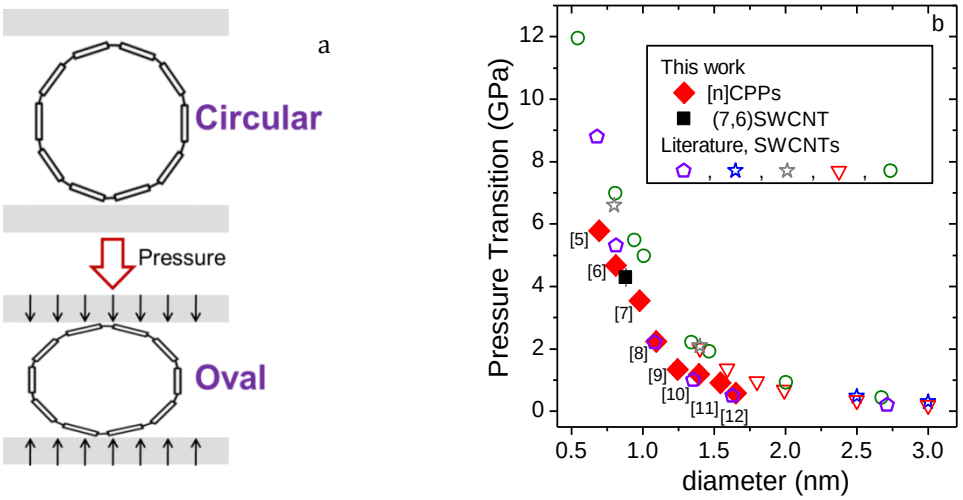

Figure 42. a) Scheme of the change over the cross section of [10]CPP due to the pressure induced ovallization. b) Pressure transition as a function of diameter of: (◆) [n]CPPs obtained from the Raman shift as a function of pressure of the G bands and 1200 cm^{-1} bands; (■) (7,6) SWCNTs, this work. SWCNTs data from the literature: (⬠) theoretical calculations from Sun et al. [59]; (○) theoretical and (☆) experimental data from Elliot et al. [30], (▽) circular to oval transition and (☆) collapse pressures from Hasegawa et al. [89].

As seen in Figure 42b, SWCNTs and [n]CPPs follow a similar *PT* diameter dependence. In Figure 43a we have plotted the experimental *PT*s as a function of the radius. In Figure 43b we represent the log of *PT* against the log of the radius. These logarithmic data have been fitted to a straight line (dashed black line) and the resulting slope is (−2.6 ± 0.2). Because this slope value is very similar to −3, the power described by equation 6, we have considered that this equation is also a good approach for the [n]CPPs. Therefore, as in SWCNTs,[60] the continuum theory of the buckling of elastic rings could be applied to obtain information about the [n]CPPs mechanical properties. Blue lines in Figure 43 correspond to the fittings of the experimental *PTs* of the [n]CPPs to equation 6, a *D* value equals to $(9.2 \pm 0.7)\cdot 10^{-20}$ J = (0.57 ± 0.04) eV can be obtained from our data.

In the literature there are several attempts to determine the circular-oval transition pressure of SWCNTs, as the values plotted in Figure 42b, being most based on theoretical calculations. From these data and with a similar analysis to above described for the [n]CPPs, we have obtained some *D* values for SWCNTs summarized in Table 6. In addition, there are several reported data for *D*:

- Sun et al.[59] provided a value of 0.76 eV, which was estimated by using both classical and *ab initio* constant-pressure molecular-dynamics simulations and continuum elastic theory analysis.
- Yakobson et al.[33] reported a value of 0.85 eV, which was computationally calculated using realistic molecular dynamics simulations of the axial compression of a nanotube.

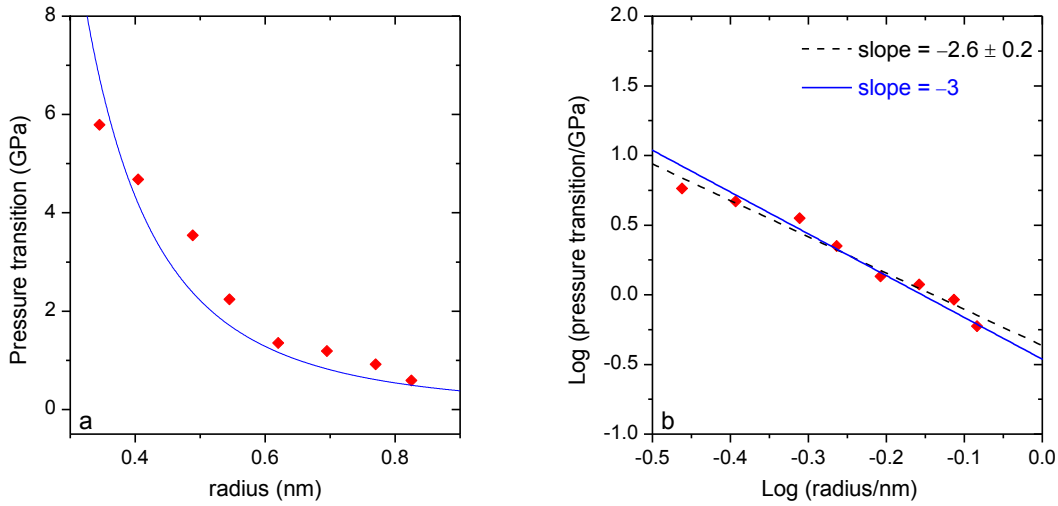

Figure 43. a) [n]CPPs pressure transition against their corresponding radius. Blue line is the variation given by equation 6 with $D = (0.092 \pm 0.007)$ GPa nm^3 = $(9.2 \pm 0.7)\ 10^{-20}$ J. b) Logarithmic pressure transition against logarithmic of the [n]CPP radius. Lines are two fits by fixing the slope to −3, blue solid line, or leaving it as a free fitting parameter, black dashed line.

Table 16. Flexural rigidity, *D*, of the equation 6, obtained from experimental data of [n]CPPs. It is compared with *D* values of carbon nanotubes.

		Flexural rigidity, *D* (eV)
[n]CPPs		**(0.57 ± 0.04)**
CNTs	Elliott et al.[30]	0.58
	Hasegawa and Nishidate[89]	1.44
	Sun et al.[59]	0.76
	Yakobson et al.[33]	0.85

Flexural rigidity is an important characteristic of any material and it is related with the dependence of the strain energy on its curvature along some direction. It is defined as follows:[99]

$$D = \frac{Yh^3}{12(1-\upsilon^2)} \tag{7}$$

D depends on *Y*, the Young's modulus, υ, the Poisson ratio, and *h*, the tube thickness. In case of dealing with layered materials flexural rigidity, *D*, is also referred as bending stiffness or elastic moduli of a layer. This bending stiffness has been studied for layered materials as graphene and graphite, being determined to be around 1.2 eV.[102,103] Moreover, it has been demonstrated that CNTs and nanotubes of different materials such as BN or C_2F show similar resistance against deformation.[104-108] Consequently, the bending curvature is the main responsible for the mechanical properties of the tubes.

In Table 16 we have compared the *D* value of the [n]CPPs with *D* values of SWCNTs. As expected because of the similar *PT* trends in [n]CPPs and SWCNTs, the *D* value for both systems stays in the same order of magnitude. However, in general the *D* value of the SWCNTs is about 30-50% higher than in [n]CPPs, so for the same diameter [n]CPPs require to deform a slightly lower pressure than a carbon nanotube. Nevertheless, as described along the text, pressure in the smaller [n]CPPs leads to configurational transformations, which may also justify their lower *PT*s and larger shape modulation compared with SWCNTs. On the other hand, the fact that [n]CPPs can deform similarly to SWCNTs makes us consider whether [n]LPPs and graphene could exhibit an equivalent behavior.

As we have already anticipated, in SWCNTs "Pressure transition", *PT*, is related not only with the loss of their circular shapes, but also with the pressure at which they suffer a change from a hard phase to a soft phase.[30] At pressures lower than *PT*, compression induces a shrinking of the circular shape, indicated by the high pressure coefficients in this pressure range. This shrinking takes place by means of a simultaneous bond length squeezing and bond angle increase, giving rise to a hard phase. On the other hand, at pressures higher than *PT*, the structures respond to external pressure by the altering their bond angles of an oval cross section, giving rise to a soft phase.[59,109]

Considering that [n]CPPs follow the same classical rules than CNTs do within their radial direction, we use the same models than those employed for the CNTs to estimate other mechanical properties of the [n]CPPs. One of such models is that proposed by Sun et al. which connects *PT* with the bulk moduli of the hard (B_h) and soft phase (B_s).[59]

$$\frac{B_h}{B_s} = \frac{12}{19}\left(\frac{R}{h}\right)^2 \tag{8}$$

$$B_s = \frac{19D}{2R^3} \tag{9}$$

$$B_h = \frac{6D}{h^2R} \tag{10}$$

Considering *h,* the tube thickness, 0.66 Å, as in SWCNTs,[59] for [n]CPPs we have estimated the radial compressibility of their hard and soft phases. In Figure 44a we plot the estimated B_h/B_s ratio as a function of the [n]CPPs radii. We see how this quotient importantly increases from 20 times up to 100 times from [5]- to [12]CPP. In Figure 44b we plot the estimated B_s using the value of 0.57 eV for the *D* parameter; and in Figure 44c, the obtained B_h modulus is shown. It can be seen that B_s is around tenths of GPa: ~1.6 GPa for [12]CPP and it rapidly increases to its higher value, 21 GPa for [5]CPP. On the other hand, the estimated bulk moduli for the hard phase of the [n]CPPs are around hundreds of GPa. B_h also increases for the smallest [n]CPP, ranging from ~150 GPa for [12]CPP to ~370 GPa for [5]CPP. However, as expected by the *R*-dependences of equations 9 and 10, the B_h growth with the radius decreasing is smoother than that shown by B_s.

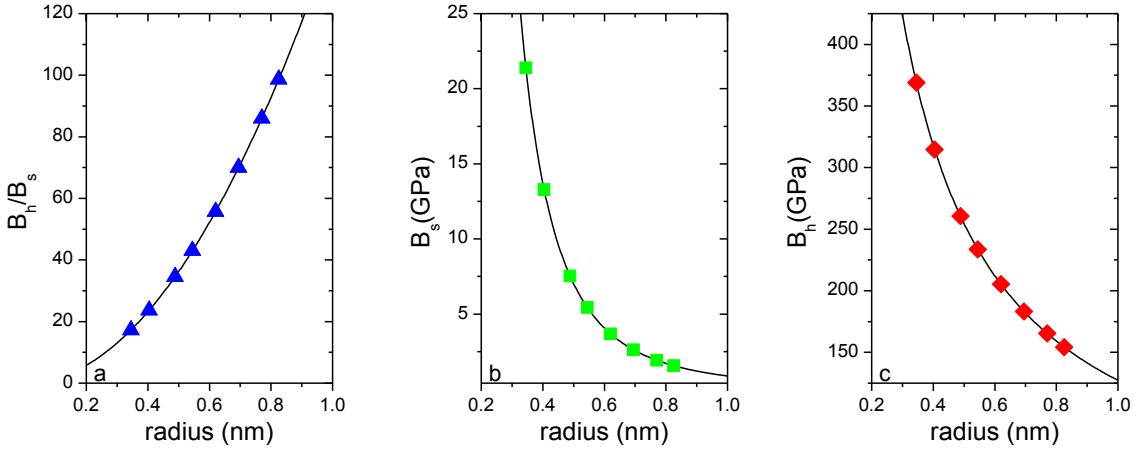

Figure 44. Radial moduli as a function of the [n]CPP radius. a) Radial moduli of the hard phase over the radial moduli of the soft phase. (b) Radial moduli of the soft phase. (c) Radial moduli of the hard phase. All these results have been estimated through the equations 8-10 and the parameters mentioned in the text.

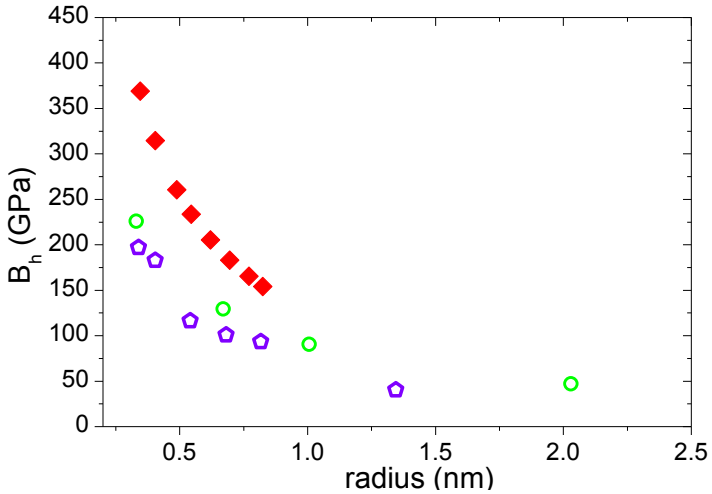

Figure 45. Radial moduli as a function of the [n]CPPs radius for the hard phases before deformation. (◆) [n]CPPs results estimated through the equations 8-10. Data from theoretical calculations for the bulk modulus of the hard phase of SWCNTs taken from: (⬠) Sun et al. [59], and (○) for armchair CNTs from Itami et al. [109].

[n]CPPs' bulk modulus of the hard phase represents the energy required for the compression before deformation to occur. On the other hand, the bulk modulus of the soft phase represents the energy required for deformation. Thus, the smallest [n]CPP need more energy to be compressed in both phases. Their smallest B_h/B_s quotients imply that these still are difficult to deform in their soft phase. However, the largest [n]CPP with the lowest B_h modulus is initially the most compressive of the series. Once ovallization occurs, [12]CPP is about 100 times easier to be compressed than in its hard phase, which might be related with its larger cross sectional deformation.

In order to compare the hard phase radial bulk modulus of [n]CPPs with that of SWCNTs in Figure 45 we represent the B_h of SWCNTs taken from the literature,[59,109] and our estimated [n]CPPs results It can be observed that the B_h of both of the systems are of the same order of magnitude. However, [n]cPPs B_h are about 200 GPa above for the smallest diameters and 100 GPa for the largest systems. As happens in CNTs, for [n]CPPs as the larger the diameters are, the more prominent the hardness transition is. These results show that while CPPs remain in their radial hard phase these can be even stiffer than SWCNTs.[109] Moreover, for [5]CPP, B_h is twice as large as those predicted for the smallest SWCNTs. Interestingly, the bulk modulus of [5]CPP is about 365 GPa, a value quite high and close to

the bulk modulus reported for diamond bulk (445 GPa).[110] This means that the bulk modulus of the smaller [n]CPPs are extremely high, comparable to that of the strongest material. This fact can be understood because of the high strain of the [5]CPP, about 114 kcal mol^{-1}, which provides it with large resistance to deformation and makes it a very rigid system.

In the literature, the great majority of works carried out on carbonaceous molecular systems are aimed to explore either their high pressure enhanced reactivity,[111] or to modulate their optical properties.[112] Due to the cyclic shape of the [n]CPPs, we were able to investigate their mechanical properties through the high pressure dependence of the Raman measurements of different [n]CPPs. We obtain that [n]CPPs flexural rigidity is close to that depicted by CNTs. Through the continuum theory of the buckling, we report that [n]CPPs molecular systems mechanical properties are of the same order of magnitude than those of the so far considered among the strongest materials.[113] Moreover, we estimate that the smallest of the [n]CPPs could be among the stiffest molecular systems. This property makes [n]CPPs even more valuable, since it is an added advantage to be considered together with their properties resulting from its large π radial cyclic conjugation.

7.4.6. Reversibility of the pressure induced effects

In previous sections we have studied how [n]CPPs behave when they are been subjected to extreme pressure conditions. In this section we are going to explore the nature of such [n]CPP high pressure response: its character elastic or plastic. To do so we are going to conduct an exhaustive analysis of the Raman spectra of the recovered samples, once the highest pressure reached for each [n]CPP was released. We will deeply compare these Raman spectra of the recovered samples with those of the samples before any perturbation was induced.

The Raman spectra of the recovered samples, provide us with very useful information about how the [n]CPPs respond to stress. In Figure 45 we depict the Raman spectra of the studied [n]CPPs in the 1100-1700 cm^{-1} spectral region, of the pristine sample and once the maximum pressure is released. In our previous work we already described how the elastic response of these molecular systems increased with their increasing diameter.[78] In agreement with this statement we see how the spectra of the recovered [9]- to [12]CPP are almost identical to that of the pristine samples. However, for the smallest samples, [5]- to [8]CPP, even though they keep their original GA_{1g} and GE_{2g} bands, they have developed a new feature at 1604 cm^{-1} (cyan area in recovered samples). As predicted by the GE_{2g} broadening during compression, this indicates that stress has leaded to a new conformational configuration with lower symmetry where the splitting of the GE_{2g} has occurred. In Figure 46 we have the Raman shifts of the G bands for pristine [n]CPPs compared with those of the recovered samples, Figure 46b. Additionally, in Figure 46c we represent the difference in ω from the pristine values to the recovered ones. This graph shows how from [7]- to [12]CPP the G bands, associated to the motions of C-C backbone of the structure, do not suffer any significant change, so these can be considered unaltered regarding their π bonding configuration.

In [5]- and [6]CPP it is clear that their GA_{1g} and the GE_{2g} bands considerably downshift. [5]CPP is the one with largest shifts, -30 and -50 cm^{-1} for the GA_{1g} and GE_{2g}, respectively. For [6]CPP these changes are much milder, about -10 and -2 cm^{-1} for the GA_{1g} and GE_{2g}, respectively. From the previous analysis during compression we would already expect the largest effects on the recovered ones of these two samples. It must be recalled that [5]CPP exhibited several soft modes with negative slopes, as the GA_{1g}. Interestingly, in [5]CPP the bands which grow with increasing pressure, remain in the recovered sample, indicating that a non-reversible configuration has been achieved. As explained in previous chapters,[78] the G-like bands of quinonoid and benzoid configurations are related by a 0.84 factor. Consequently, we speculate about a possible transition towards a quinonoid distorted structure, where the 1450 cm^{-1} band, which grows with the increasing pressure in [5]CPP, could correspond to the stretching of localized C-C double bonds, but further discussion will be done later over this.

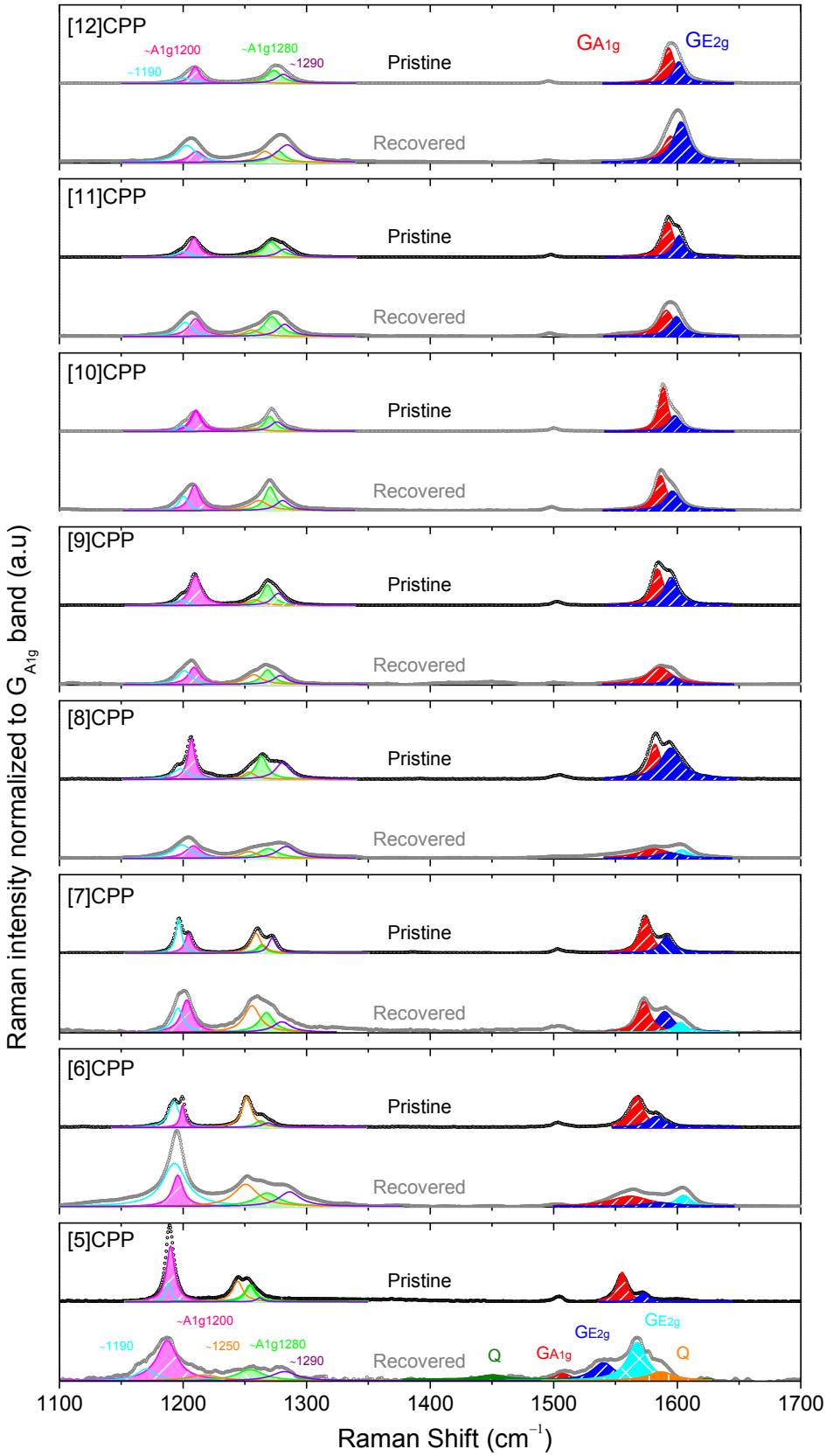

Figure 46. Raman spectra of [n]CPPs in the 1100-1700 cm^{-1} region: top, before pressure cycle, bottom, recovered samples. All spectra have been scaled to the normalized GA_{1g} band. Red area corresponds to the GA_{1g} band; dark blue area to the GE_{2g} band. Recovered samples, 1400-1600 cm^{-1} region: cyan area corresponds to the splitting of the GE_{2g}; orange area to high frequency quinonoid contribution; dark green to the C-C stretching of double bond of quinonoid contribution. 1100-1375 cm^{-1} region: cyan curve is the 1190 cm^{-1} E_{2g}, pink area the 1200 cm^{-1} A_{1g}, orange curve the 1250 cm^{-1} E_{2g}, green area the 1280 cm^{-1} A_{1g}, and purple curve the 1290 cm^{-1} E_{1g} bands.

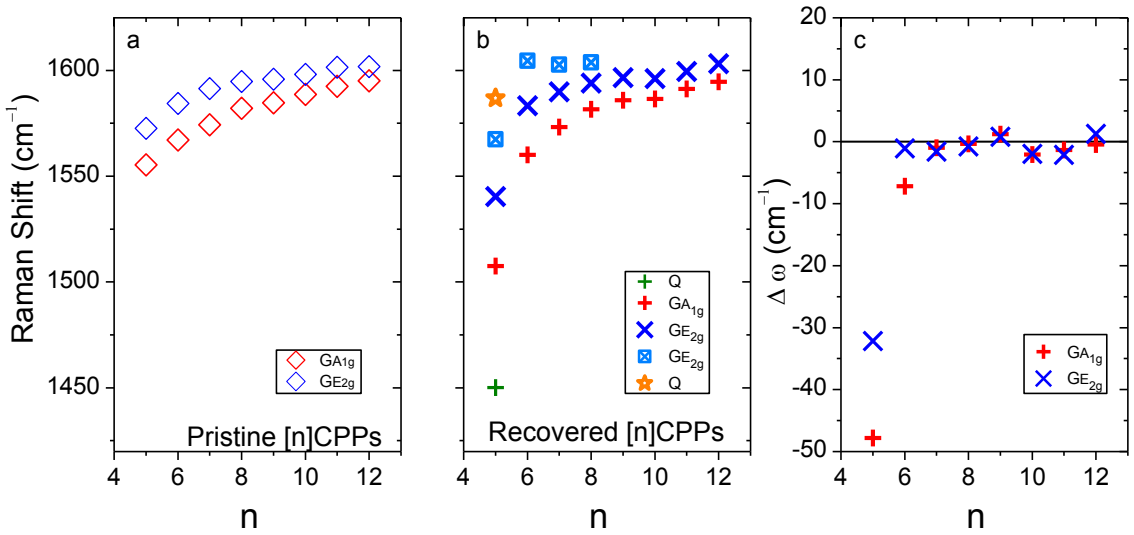

Figure 47. [n]CPPs Raman shifts of the G modes at room conditions as a function of *n*: a) Pristine samples; b) Recovered samples once pressure was released. c) Difference in the Raman shift of the GA_{1g} and GE_{2g} bands between that of the recovered sample and their corresponding pristine sample as a function of *n*, Δω = Raman shift of the recovered sample – Raman shift of the pristine sample. In this figure, once again, the different pressure response of [5]CPP is shown. The Raman shift of the [5]CPP recovered sample for the GE_{2g} and GA_{1g} enormously downshift respect the pristine sample, about -30 and -40 cm^{-1}, while the larger [n]CPPs G bands shift in a range between –8 and 2 cm^{-1}.

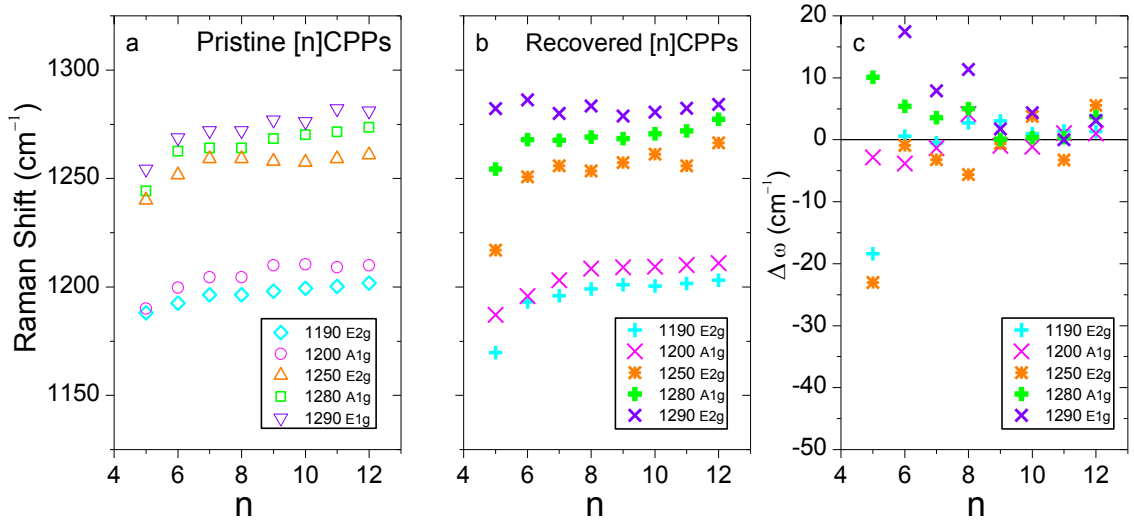

Figure 48. [n]CPPs Raman shift of the 1200 cm^{-1} bands at room pressure as a function of *n*: a) Pristine samples; b) Recovered sample once pressure is released. c) Difference in the Raman shift between that of the recovered sample and their corresponding pristine sample as a function of *n*, Δω= Raman shift of the recovered sample – Raman shift of the pristine sample. In the latter, Figure 48c, [5]CPP is the one with larger shifting in the recovered sample respect the pristine one.

In Figure 46 we have also analyzed the changes suffered by the 1200 cm^{-1} bands. The frequency analysis of these bands, shown in Figure 48, tells us that they remain upshifted for $n > 8$, but no remarkable changes are observed for lower *n* rather than those expected in [5]CPP. In addition, in Figure 47, it can be appreciated how for n > 8 pressure causes a general effect different to that for $n \leq 8$. For $n > 8$ the E bands around 1190, 1250 and 1290 cm^{-1} of the recovered samples increase their intensities compared to those of the pristine ones, indicating larger strain and torsions over the structures. However, non-quantitative information can be analyzed from this behavior since they result from the sum of several contributions. In contrast, for $n \leq 8$ the A_{1g} bands are those which seem to gain intensity. As was seen previously, intensity ratio I1280/I1200 is related with the torsional angle. In Figure 49 we see that all [n]CPPs (except [5]CPP) result in a higher ratio, what can be

interpreted as larger average torsions along the cycle. As is observed in Figure 49c, such torsional angle is between 4° and 8° higher in the recovered samples.

Thus so far we can conclude than in large [n]CPPs there is no configurational changes resulting from the high pressure treatment, rather than larger torsions resulting from the relaxed planarized structure. On the other hand, smaller [n]CPPs suffer irreversible modifications not only in torsions, larger as well, but also their Raman shifts indicate certain structural rearrangement, bigger as smaller the cycle is, so ovallization might remain. We might establish the boundary between a behavior and another in the [8]CPP.

Low frequency modes, especially the p-RBMs with E symmetry, are intimately related with the [n]CPP shape, so they can be a very good sensor about the elasticity of the process. In Figure 49 we have the Raman spectra centered between 200 and 1100 cm^{-1} for the pristine and recovered [n]CPPs. For $n > 8$ it is observed a certain bands broadening, but the spectra are nearly recovered in shape and frequency. Changes appear below that *n,* indicating some structural variations. Starting with [8]CPP, the p-RBM marked in green in the spectrum of the pristine sample seems to have completely vanished, instead there are two new features around 250 and 300 cm^{-1}, also there seems to be a new very weaker peak around 450 cm^{-1} (marked all in pink in the spectrum). Changes in the p-RBMs might be indicators of a loss of the circular shape toward a diameter distribution, ovallization which remains after pressure is released. Such effect has already been speculated for CNTs, explaining them the GE_{2g} splitting.[41]

Regarding [7]CPP, it seems that low frequency spectrum is not altered. It might be that the higher strain and the odd *n* prevents it to suffer such ovallization, however the clear splitting GE_{2g} band and the changes on the 1200 cm^{-1} bands indicate that there has been some configurational changes in terms of loss of symmetry. Then, it is reasonable think that the observed behavior is due to small circular deformation and larger torsions.

As seen in Figures 46 and 50, recovered [6]CPP Raman spectrum depicts wider modifications than in its bigger cousins. It is seen how apart from the broadening of the GA_{1g}, the GE_{2g} splitting and the 1200 cm^{-1} bands shifting, the low frequency region significantly changes. The p-RBM around 442 cm^{-1} in the pristine [6]CPP seems to have a splitting in the recovered sample, arising two newer features, around 409 and 933 cm^{-1}, marked in pink in Figure 50.

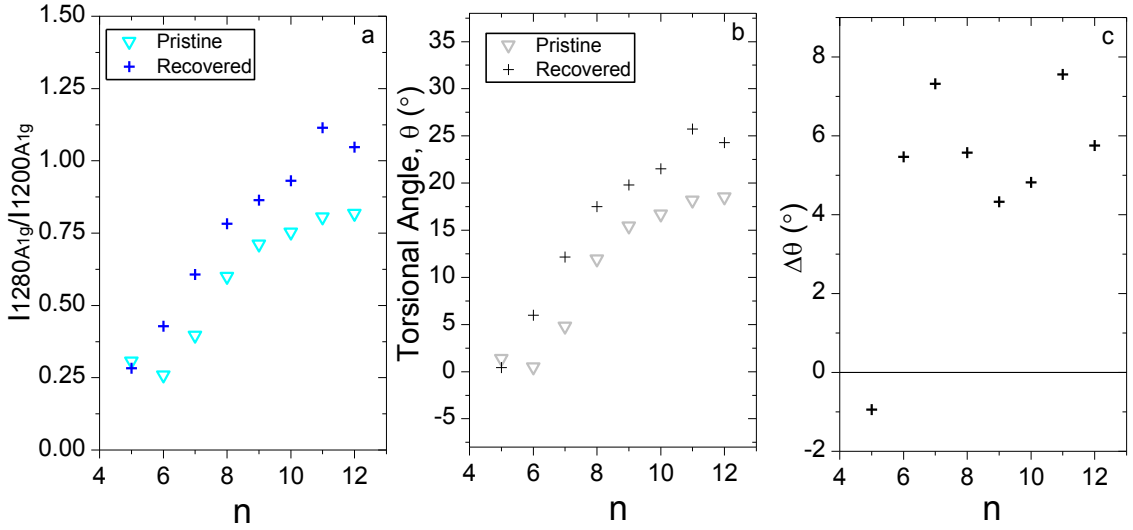

Figure 49. a) Intensity ratio, $I1280_{A_{1g}}/I1200_{A_{1g}}$, as a function of *n* for the pristine samples and recovered ones. b) Estimated average torsional angles between neighboring benzenes as a function of *n* obtained from equation 5 with the data from Figure 49a. (▽, ▽) Pristine sample, (+, +) recovered sample. c) Δθ: $\theta_{recovered} - \theta_{pristine}$; as a function of *n*, where it can be observed that from [6]CPP torsions of the recovered samples after pressure cycle are a bit larger respect the pristine sample. However, torsions in [5]CPP are a bit lower than in the pristine sample.

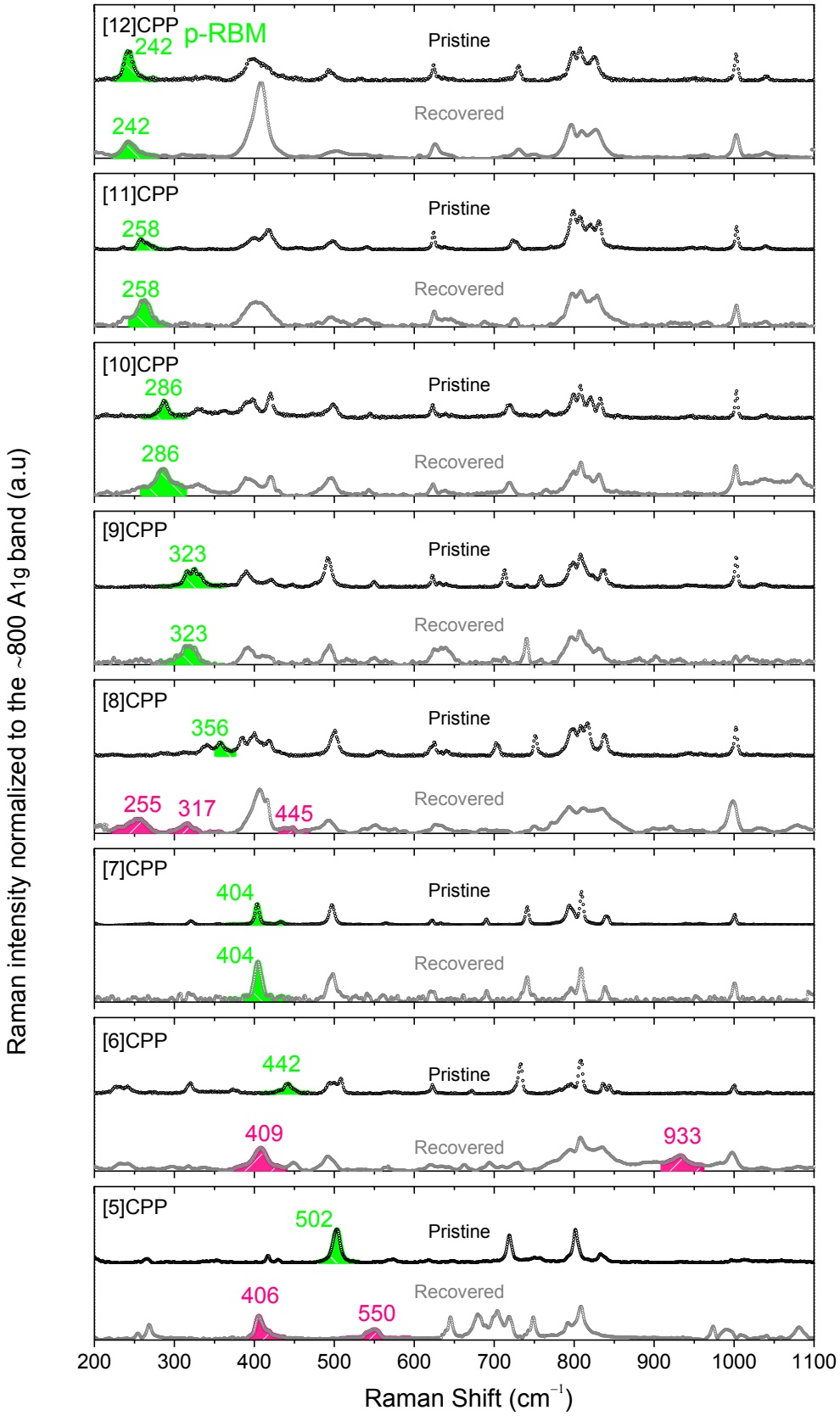

Figure 50. Low frequency region of the [n]CPPs Raman spectra all scaled to the normalized ~800 cm^{-1} A_{1g} band: top, before pressure cycle; bottom recovered sample after pressure is released. Green areas are used to assign the p-RBMs; pink areas are used to assign the new bands resulting from the splitting of the p-RBMs of the [5]-, [6]-, [8]CPP recovered samples.

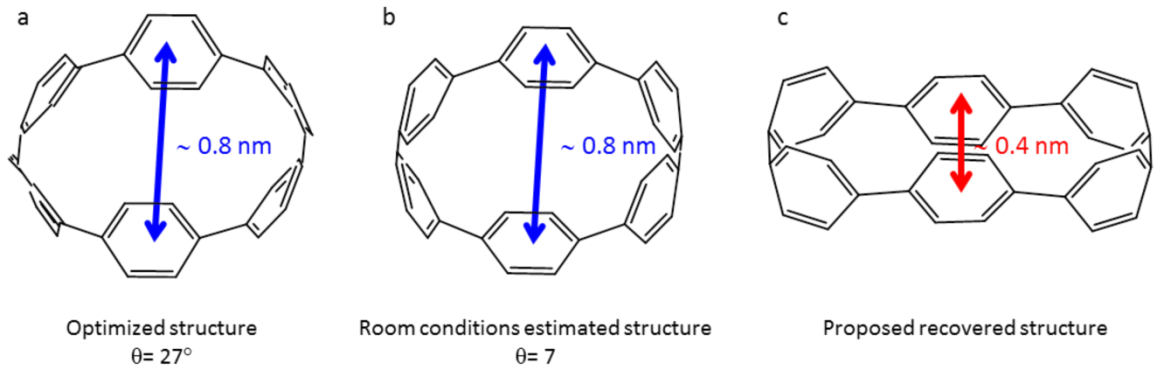

Figure 51. Schemes representing a molecule of [6]CPP: a) calculated optimizes structure at the B3LYP/6-31G(d,p) level. b) Estimated [6]CPP structure from the optimized one and applying equation 5 to estimate the torsional angle between neighboring phenyl units. c) Suggested structure for the recovered [6]CPP sample after 8 GPa pressure cycle, once the pressure is released.

In the previous chapter 4, we have related the diameter of the [n]CPP with the Raman shift of the p-RBMs as follows: [78]

$$\omega_{p-RBM}\left(cm^{-1}\right) = 8 + \frac{375}{d(nm)} \tag{12}$$

By using this equation and the values of the new features mentioned (409 and 933 cm^{-1}), diameters around 0.94 and 0.42 nm are obtained. It might be considered that the 933 cm^{-1} band corresponds to the mode of the collapsed interacting benzenes, and the 409 cm^{-1} to the resulting long diameter. This sketch is in agreement with the representations obtained by the Atomic Force Microscopy experiments on collapsed multiwalled CNTs by Yu et al.,[114] as well as with the predictions for SWCNTs from Yao et al. [35] and Cronin et al.[115]

Pristine [6]CPP has a strain of about 100 kcal mol^{-1},[116] so its deformation occurs at the higher *PT* than in other less strained CPPs. However, once it starts its distortion, since its opposite wall to wall distance is short enough, these walls approach and π-π interactions between them appear, leading the CPP towards a peanut shape. These interactions remain after pressure was released, explaining the resulting Raman spectra. We interpret the observed behavior as an irreversible cross section reduction as a result from the ovallization, the interaction between opposite benzenes might be induced, as represented in Figure 51.

Finally, we analyze [5]CPP, where larger spectral differences between the pristine and the recovered sample are observed. The low frequency range shows that many new features came up around 700 and 800 cm^{-1} and also at 1000 cm^{-1}. Moreover, the p-RBM totally vanishes while two new features around it emerge, at 406 and 550 cm^{-1}. This evidences once again that the effect that pressure has on this strained structure is different than that exhibited by its larger cousins. Apart from the splitting of the GE_{2g} mode, associated to loss of the circular cross section, it is seen how the new peaks around 1450 and 1604 cm^{-1} grow with the increasing pressure which come together with the significant Raman downshift of the GE_{2g} and GE_{2g} bands.

[5]CPP molecule has a high inherent strain and thus high bending angles, α = 16° and β = 20°, as is plotted in Figure 51a. Due to these values, close to those of a quinonoid configuration, Figure 51b, a quinonoid structure was suggested as possible conformation of its ground state. However, it has already demonstrated that such tautomer would involve a loss of electronic delocalization due to the double bond localization becoming a highly energetic and unfavorable structure, about 39 kcal mol^{-1} higher than the aromatic minimum.[117] On bigger CPP structures quinonoid-aromatic transition state was found and for larger [n]CPPs than [6]CPP, no quinonoid minimum was energetically available. The Raman downshift with pressure of the G bands and the other at which C-C bonds are involved, together with the change in the p-RBMs and finally the new features on the recovered [5]CPP

spectrum, confirm that a permanent transition towards a new configuration is being induced with the pressure.

We speculate about the possibility of leading the formation of a quinonoid distorted structure once [5]CPP starts deforming. As already discussed along this chapter with pressure a bond length alteration is being induced, but also bond angle deformation. Thus it could be more favorable than [5]CPP stands into its quinonoid configuration with larger α angle, rather than staying benzoid with such distorted shape. In Figure 53 we plot the calculated B3LYP/6-31G(d,p) Raman spectra of the aromatic and quinonoid [5]CPP minima, together with the experimental Raman spectra of the pristine and recovered [5]CPP, after a pressure of 10 GPa was reached. Raman spectrum of the quinonoid [5]CPP presents about four contributions on the G band regions, which could resemble the new features observed on the experimental spectra with increasing pressure and on that of the recovered sample. Also the decrease in intensity of the 1200 cm^{-1} A_{1g} bands is significant and analog to that of the quinonoid tautomer. Regarding the low frequency region, the calculated p-RBM for the quinonoid tautomer is about 80 cm^{-1} downshifted from the aromatic one, as already anticipated. In Figure 54 we have schematized the suggested shapes for the [5]CPP molecule at different configurations, showing the mechanically induced transition towards a deformed cyclic structure with higher quinonoidal character, involving double bond localization.

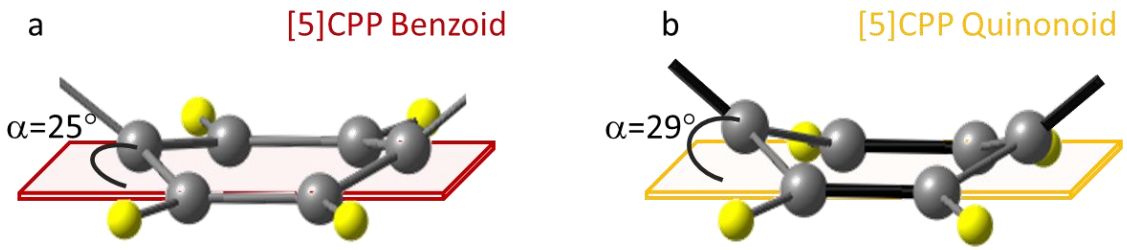

Figure 52. Side view of a phenyl unit in the [5]CPP optimized structures. DFT calculations at the B3LYP/6-31G(d,p) level. a) Benzoid configuration; b) Quinonoid configuration. The out of the phenyl plane bending angle has been marked.

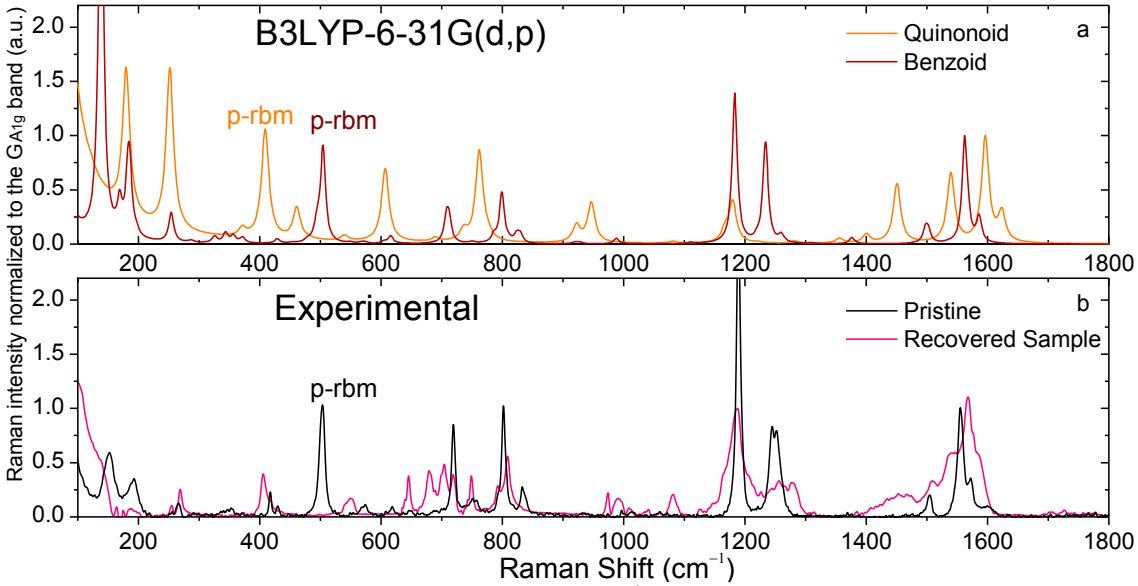

Figure 53. [5]CPP Raman spectra in the 100-1800 cm^{-1} region. a) Calculations for the optimized structures of the configuration: benzoid, brown line; quinonoid, orange line. Level B3LYP/6-31G(d,p), both spectra 0.97 scaled. b) Experimental Raman spectra for: the pristine sample (black line) and recovered sample once pressure is released (pink line).

As previously mentioned in other chapter, neutral [5]CPP depicts critical points into its electronic structure in the center of its cavity, so once compression modifies the structure, this electron density is modified as well leading to further electronic reorganization. So, we suggest as possible the deformation of [5]CPP-aromatic-configuration to an oval shape through a quinonoid configuration. As represented in Figure 54, this behavior means that the energy potential curve which joins the benzoid and quinonoid configurations is modified by pressure. The suggested path is possible considering that the initial volume of a quinonoid tautomer is a bit lower than the aromatic one, approximately 0.2 % lower, but it seems to be enough to be the driving force towards its formation

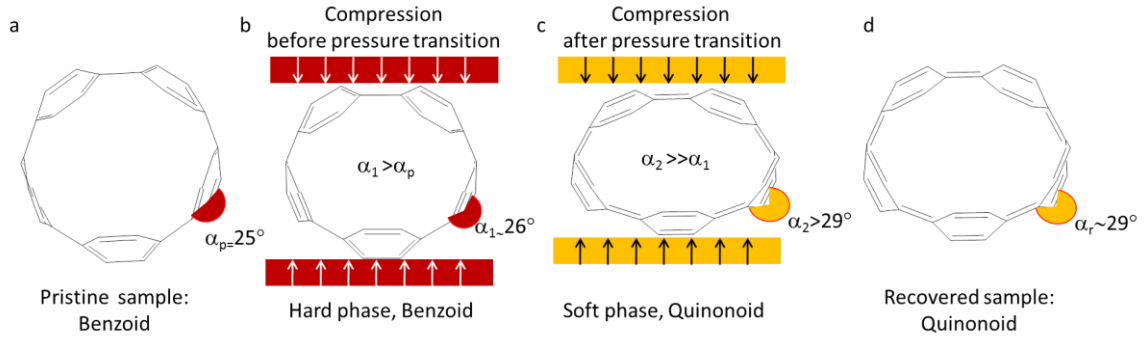

Figure 54. Scheme of how pressure modulates a [5]CPP molecule: a) pristine sample; b) compressed before pressure transition; c) compressed after pressure transition; c) recovered sample once pressure is released. Suggested bending angles are highlighted for each case.

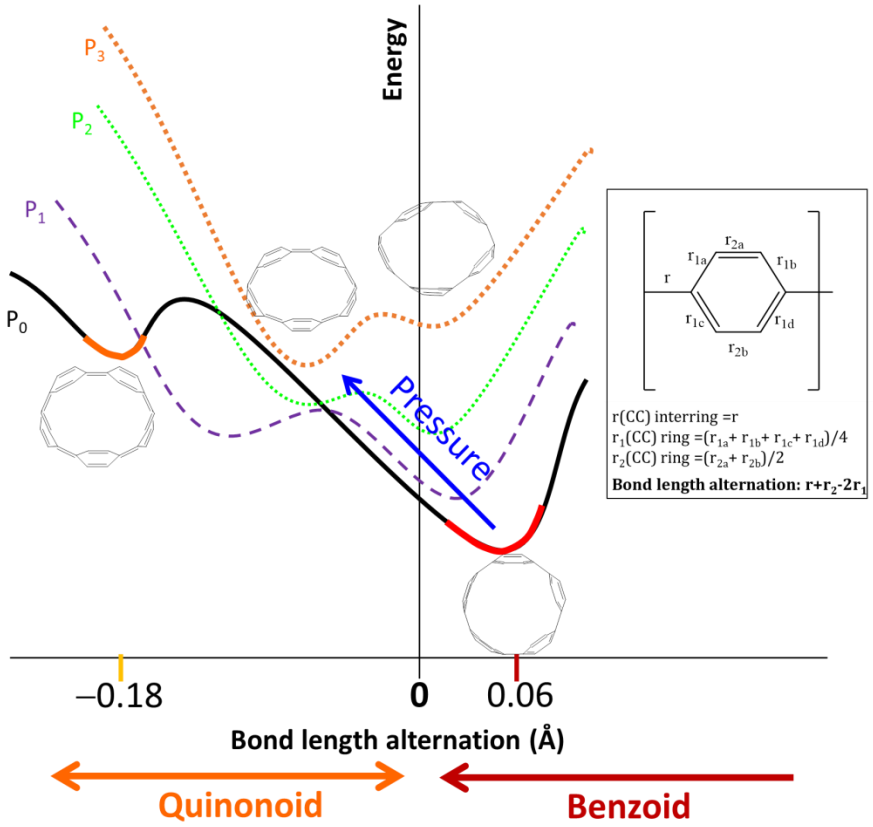

Figure 55. Scheme of how we hypothesize that pressure modulates the potential energy curve of [5]CPP along the bond length alternation (defined in the inserted scheme) path. Curves are shown at several pressures: $p_0 < p_1 < p_2 < p_3$.

With this in mind, it can be considered that being [5]CPP the most rigid structure, once it is deformed, an equilibria between the distorted oval quinonoid and aromatic tautomer can be resulting from the high pressure treatment. Finally, it can be mentioned that these studies open new perspectives in the field of mechano-chemistry,[118] which analyzes the application of mechanical force to induce the breaking and formation of chemical bonds.

7.4.7. Relationship Between [n]CPP Strain Energy and Pressure Induced Permanent Deformation

From the analysis of the recovered samples, we can conclude that being the smaller CPPs the ones which require higher energy –or pressure– to deform, this seems to be so far from the pristine energy minimum than once pressure is released they stand in that other configuration. With pressure we are introducing strain into the molecular systems by inducing their deformation and therefore their diameter reduction. Intuitively one may expect that at certain pressure this collapse between the CPPs walls should occur even in the largest [n]CPPs, but the energy required for that collapse to occur might be really far from the most favored minimum.

In Figure 55 we have done an estimation of how this pressure should be to observe the collapse of the different CPPs, obtaining that for the [12]CPP it should reach values of about 40 GPa. We have taken the strain energy data for the[n]CPPs from Iwamoto et al.,[24] and considering the next relations we have traduced the external pressure in strain energy terms, taken the carbon density in graphite,[119] to estimate the 1 carbon volume and not accounting hydrogen atoms:

$$1\,\text{GPa} = 10^9 \frac{N}{m^2} = 10^9 \frac{J}{m^3} \frac{1eV}{1.602176 \cdot 10^{-19} J} \frac{8.81 \cdot 10^{-30} m^3}{1\,\text{Carbon atom}} = 0.054987\ \text{eV/atom} \quad (13)$$

Then we are able to relate approximate how the strain energy gains with compression for each unit, and how it affects the diameter.

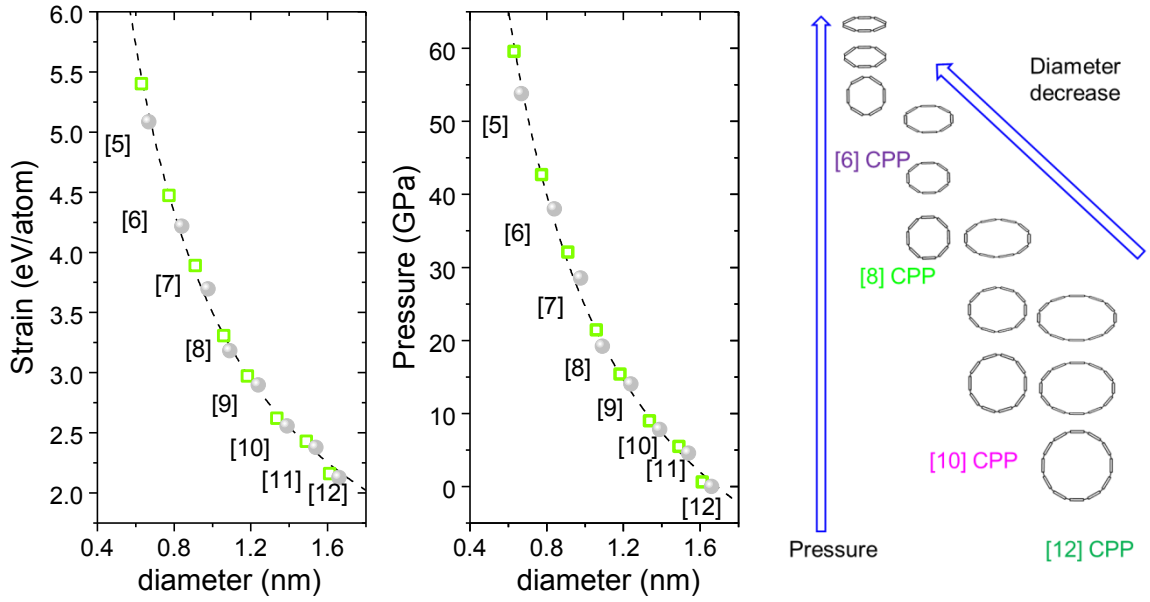

Figure 56. a) Strain energy for the [n]CPPs as a function of their diameter, (●) data taken from [24] at room conditions and (□) at their pressure transitions (change in units using equation 13). b) Pressure of the [n]CPPs related to that of [12]CPP, (●) at room conditions taken from Figure 56a (change in units using equation 13), and (□) the value of pressure transition has been summed to that resulting at room conditions. c) Scheme of pressure effect the measured even [n]CPPs.

In Figure 56a we have summed for each CPP studied the strain needed to initialize its ovallization. On the other side, on the Figure 56b we present the opposite transformation, the strain energy is presented in stress terms, in GPa, referring all of them to the [12]CPP as the cero pressure, and again summing to each CPP stress value the need for its transition to occur. Zang et al,[120] suggested that the transition oval-to peanut occurs always at a point defined by a universal constant in relation to the first transition, circular to oval, at which the aspect ratio remains constant independently on the radio and is about 0.46. In the [6]CPP the diminish in its diameter goes from 0.8088 to 0.74227 nm, assuming that the transition to peanut occurs at a point in which wall-to-wall van der Waals interactions are favored, then the CPP diameter, and therefore C-C bonds, should have been compressed about 8% respect their original distribution. From these representations we can conclude that, to achieve a final peanut shape on the [12]CPP where the wall to wall distance was about 0.34 nm, (at which the required bending energy could be compensated by the stabilizing van der Waals interactions) we should reach pressures as high as almost 40 GPa.

As bigger the CPP is, as less strained and easier to deform. However, not all the deformations guide to the same conformation. Before pressure transition most of the stress is employed in the ring shrinking, and after in a bond angle change. To achieve the peanut shape, the [12]CPP must shrink around one of its diameters by means of bond angles modifications, mainly, which as shown, must be high energy costly. On the other hand, [6]CPP, with the smallest of the diameters among the molecules here studied, in its hard phase al the external pressure is employed in diminishing its diameter, on such a way that when the ovallization occurs, the phases of the CPP are so close that it directly goes towards its peanut conformation. Moreover, as observed in its Raman spectra, this conformation results metastable, mainly because is stabilized by the van der Waals interactions between parallel CPP walls.

7.5. Conclusions.

- The use of the mechanical response to stress of the novel nano-molecular systems studied by Raman spectroscopy has allowed us to confirm that cyclic paraphenylenes behave along its cross sectional directions as "ultra-short Carbon nanotubes". As CNTs, CPPs respond to stress showing a circumferential deformation at *PT*, whose value varies depending on the CPPs size.
- The data reported here enable us to obtain the first pressure coefficients for the RBMs and G-like modes of CPPs. Pressure coefficients of RBMs show a diameter dependence similar to that presented by their analogous SWCNTs. However, the G bands depict a V-shape in their pressure coefficients as a function of diameter, with a minimum around [8]CPP. This V-shape is related with configurational changes utterly related with [n]CPPs as highly cyclic conjugated entities and not as ultra-short SWCNTs. [n]CPPs represent a unique entity by themselves, as the molecular unities with one of the highest mechanical strength.
- In the cyclic systems we observe that compression induces important changes in intensity ratio between the 1280 and 1200 cm^{-1} A_{1g} bands. However, in contrast to [n]LPPs in which the ratio rapidly decreases, in [n]CPPs there is an initial significant increase up to a limit about 30° (depends on *n*). Once that the torsional limit is reached, torsional angles between neighboring phenyl units rapidly decrease in analogy to [n]LPPs. With the increasing [n]CPP size *PTL* decreases towards zero. Consequently, during compression and in torsional terms, larger [n]CPPs trend to behave as [n]LPPs.
- As in SWCNTs, *PT*s depend on diameter (*d*) following approximately a $\boldsymbol{d}^{-3}$ dependence. Thus we assume that the deformation of [n]CPPs follow similar laws than CNTs around their radial direction. Through this approximation we estimate that the [n]CPPs flexural rigidity is about (0.57 ± 0.02) eV. Finding in the SWCNTs studies values of same magnitude order, 0.65 eV.
- This mechanical analysis allow us to estimate the bulk modulus along the radial direction of the [n]CPPs for their hard and soft phases.
- After pressure cycle, of about 10-12 GPa, for $n \geq 9$ the [n]CPP Raman spectra recover to its original shift and shape, with small variations which indicate increase in torsional angles. However for $n \leq 8$ with decreasing *n* Raman spectra become less reversible in frequency terms. Therefore pressure causes elastic ovallization from [9]- to [12]CPP, while for [5]- to [8]CPP the ovallization is less reversible. Hence, these smallest [n]CPPs can be considered to behave more plastically when compressed.
- We have been able to induce the permanent collapse of [6]CPP, forming stable π-π interactions between the phenylenes. In CNTs of these dimensions none plastic deformations have been described so far in the literature.
- [5]CPP, which in its pristine configuration has the largest bending angles, follows a different path with the increasing pressure. It seems like it is more favorable that it loss its benzoid configuration to be able to bend, increase bending angles, by means of attaining towards its oval quinonoid configuration. So, we mechanically control the formation of the [5]CPP quinonoid configuration, no classically synthetically approachable otherwise.
- The Raman high pressure response of the different [n]CPPs allow us to stablish a division in the [n]CPPs depending on their size.
    - For $n \geq 9$, with increasing *n*, we observe larger pressure coefficients before and after *PT.* there is a minimum as a function of diameter around [8] and [9]CPPs in the pressure coefficients of those bands involving C-C stretching bonds. Moreover, the Raman shifts of these [n]CPPs of the recovered samples after compression remain almost unchanged respect the corresponding spectra registered for the pristine [n]CPPs at room conditions. Hence, the high pressure cross sectional ovallization of

these large [n]CPP can be understood as reversible However, the from the comparison of the 1280-1200 cm^{-1} bands intensity ratio at room conditions, before and after compression a slight torsional angle between neighboring phenyl units can be interpreted. These observations indicates that electron density of phenyl units does not redistribute along the [n]CPP cavity, and it is slightly reinforced within each phenyl unit by the torsional angles increase.

- For $n \leq 8$ with decreasing *n,* pressure coefficients of those bands involved in C-C stretching bonds follow a V-shape with a minimum between [7]- and [8]CPP. After *PT* all the coefficients decrease towards negative values, having [5]CPP the minimum value. When analyzing the recovered samples, we see that these small [n]CPPs are not elastic, since slight alterations have being induced permanently. Such alterations are small for the largest, [7]- and [8]CPP, probably due to a permanent ovallization of the system together with the torsional angle increase. We conclude from these results that the large in plane conjugation present in the smallest [n]CPPs must play a role since the π conjugation might enhance the deformation of the circular shape towards the formation of π-π interactions in the cavity between confronted CPP sides.

7.6. Crystal structures of [n]CPPs

Here we summarize the crystal packing from x-ray diffraction results at 100 K of [n]CPP, from [5]- to [12]CPP in solid state. These have been taken from the literature references indicated in each case. We show on the left a side view of crystal packing mode and on the right a top down view illustrating the long range channels present. All the [n]CPPs except [5]- and [6]CPP have solvent molecules in their cavities, here those molecules have been omitted for clarity.

[5]CPP Ref. [25]	Space group	Orthorhombic, Pbca	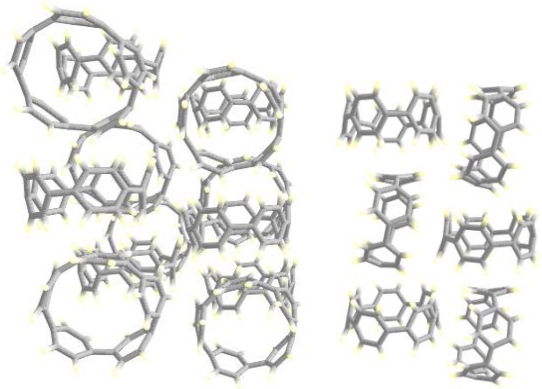
	a	9.8337 (2) Å	
	b	11.6263 (2) Å	
	c	35.5613 (2) Å	
[6]CPP Ref. [26]	Space group	Hexagonal, R-3	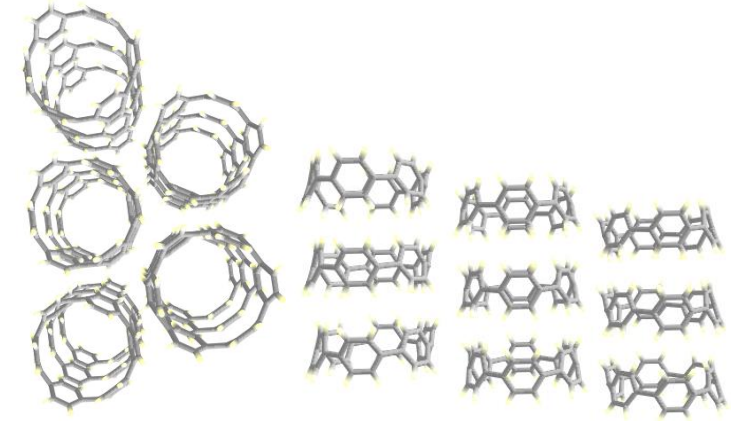
	a	19.3957 (4) Å	
	c	6.1998 (2) Å	
[7]CPP Ref. [79]	Space group	Orthorombic, Pnma	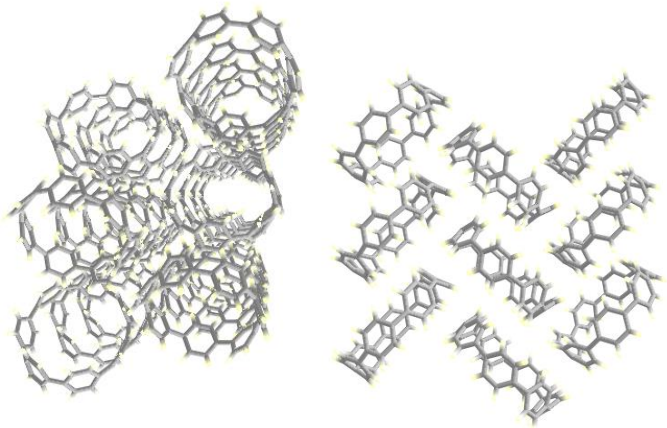
	a	18.340 (7) Å	
	b	22.335 (8) Å	
	c	8.218 (3) Å	

[8]CPP Ref. [80]	Space group	Monoclinic, $P2_1/n$	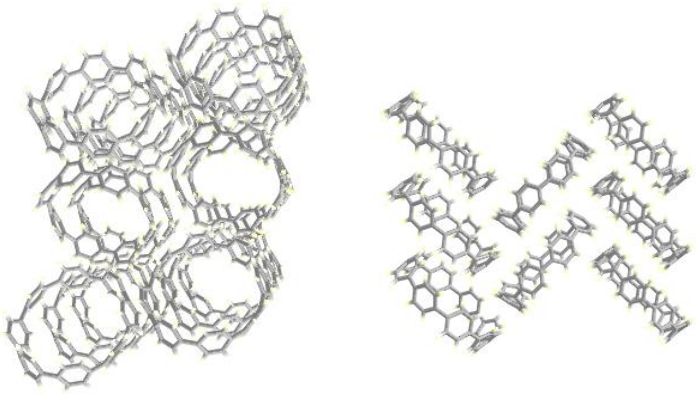
	a	12.9325 (2) Å	
	b	8.0103 (1) Å	
	c	19.3676 (3) Å	
[9]CPP Ref. [81]	Space group	Orthorhombic Pnma	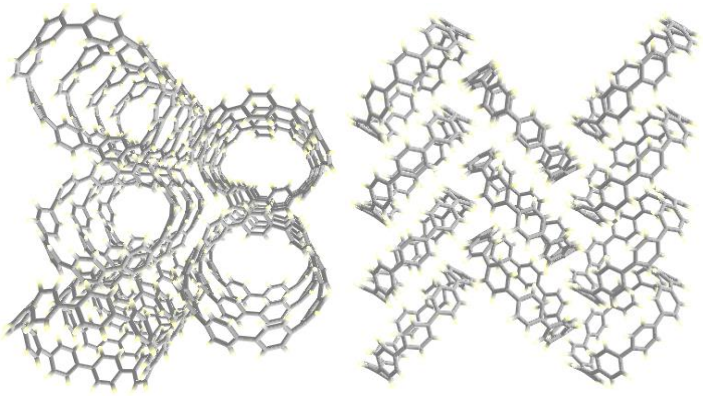
	a	20.9873(5) Å	
	b	26.5941(7) Å	
	c	8.0799(2) Å	
[10]CPP Ref. [82,83]	Space group	Monoclinic, $P2_1/c$	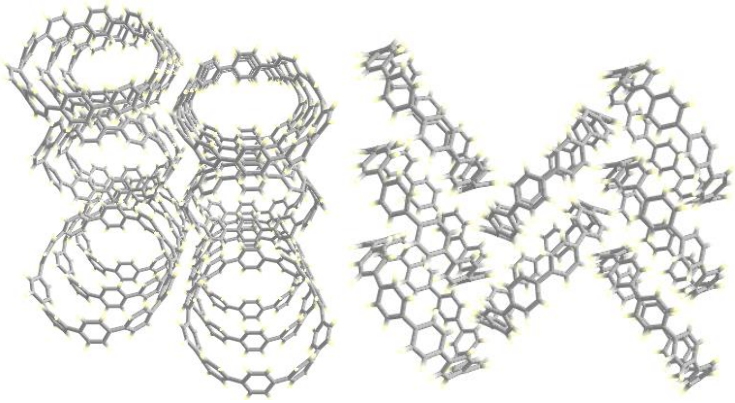
	a	15.9075 (4) Å	
	b	8.1405 (2) Å	
	c	20.74818 (6) Å	

[11]CPP Ref. [84]	Space group	Unknown	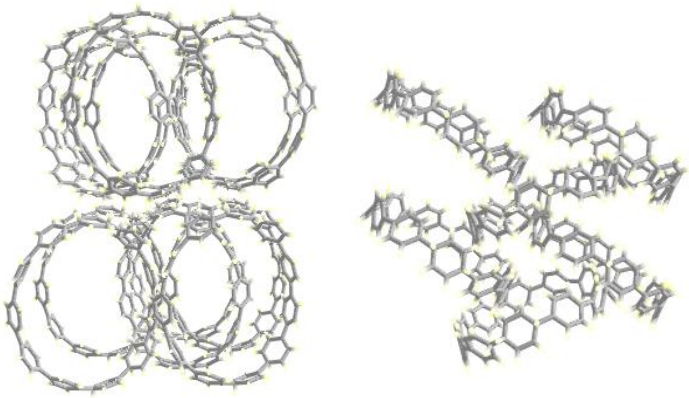
	a	36.8303(13) Å	
	b	13.7639(5) Å	
	c	10.2794(4) Å	
[12]CPP Ref. [85]	Space group	Monoclinic P 21/c	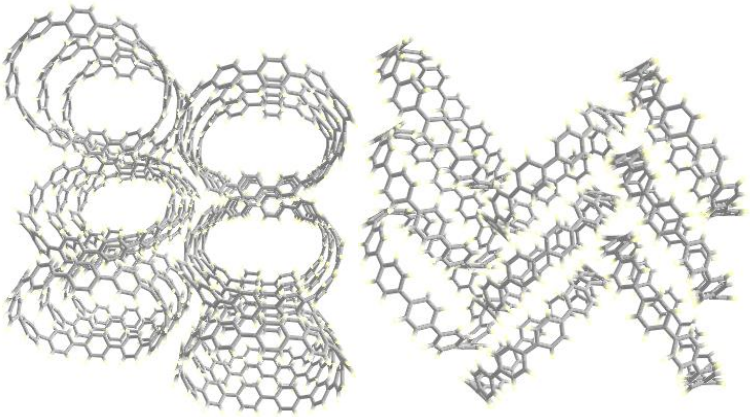
	a	18.5827(7) Å	
	b	8.1878(3) Å	
	c	23.6701(9) Å	

7.7. References

1 H. Omachi, T. Nakayama, E. Takahashi, Y. Segawa, K. Itami, *Nature Chem.* **5**, 572-576 (2013).

2 J. P. Lu, *Phys. Rev. Lett*. **79**, 1297-1300 (1997).

3 M. Meo, M. Rossi, *Comp. Sci. Tech.* **66**, 1597-1605 (2006).

4 Z. Chenguang, K. Bets, S. Soo Lee, Z. Sun, F. Mirri, V. L. Colvin, B. I. Yakobson, J. M. Tour, R. H. Hauge, *ACS Nano* **6**, 6023–6032 (2012).

5 D. Chen, T. Sasaki, J. Tang, L. C. Qin, *Phys. Rev. B* **77**, 125412 (2008).

6 K. Nishidate, M. Hasegawa, *Phys. Rev. B* **78**, 195403 (2008).

7 K. Nishidate, M. Hasegawa, *Phys. Rev. B* **81**, 125414 (2010).

8 O. Lourie, H. D. Wagner, *J. Mater. Res.* **13**, 2418-2422 (1998).

9 E. T. Thostenson, Z. Ren, T. W. Chou, *Comp. Sci. Tech.* **13**, 1899-1912 (2001).

10 A. J. Ghandour, I. F. Crowe, J. E. Proctor Y. W. Sun, M. P. Halsall, I. Hernandez, A. Sapelkin, D. J. Dunstan, *Phys. Rev. B* **87**, 085416 (2013).

11 S. R. Jezowski, L. Zhu, Y. Wang, A. P. Rice, G. W. Scott, C. J. Bardeen, E. L. Chronister, *J. Am. Chem. Soc.* **134**, 7459–7466 (2012).

12 R. Bini, M. Ceppatelli, M. Citroni, V. Schettino, *Chem. Phys.* **398,** 262–268 (2012).

13 C. M. Martin, Q. Cai, S. Guha, W. Graupner, M. Chandrasekhar, H. R. Chandrasekhar, *Phys. Stat. Sol.* **241**, 3339–3344 (2004).

14 S. Guha, W. Graupner, R. Resel, M. Chandrasekhar, H. R. Chandrasekhar, R. Glaser, G. Leising, *Phys. Rev. Lett*. **82**, 3625–3628 (1999).

15 E. H. Hároz, J. G. Duque, X. Tu, M. Zheng, A. R. Hight Walker, R. H. Haige, S. K. Doorn, J. Kono, *Nanoscale* **5**, 1411–1439 (2013).

16 H. Kataura, Y. Kumazawa, Y. Maniwa, I. Umezu, S. Suzuki, Y. Ohtsuka, Y. Achiba, *Synth. Met.* **103**, 2555 – 2558 (1999).

17 R. B. Weisman, S. M. Bachilo, *Nano Lett*. **3**, 1235–1238 (2003).

18 http://www.photon.t.u-tokyo.ac.jp/~maruyama/kataura/kataura.html, browsed on October 7th, 2015.

19 P. Loubeyre, F. Occelli, R. LeToullec, *Nature* **416**, 613-617 (2002).

20 B. J. Baer, M. E. Chang, W. J. Evans, *J. Appl. Phys*. **104**, 034504 (2008).

21 G. H. Watson Jr. W. B. Daniels, C. S. Wang, *J. Appl. Phys*. **52**, 956-958 (1981).

22 J. A. Xu, E. Huang, J. F. Lin, L. Y. Xu, *Amer. Mineral*. **80**, 1157-1165 (1995).

23 V. G. Baonza, M. Taravillo, A. Arencibia, M. Cáceres, J. Núñez, *J. Raman Spectrosc*. **34**, 264-270 (2003).

24 T. Iwamoto, Y. Watanabe, Y. Sakamoto, T. Suzuki, S. Yamago, *J. Am. Chem. Soc.* **133**, 8354-8361 (2011).

25 P. J. Evans, E. R. Darzi, R. Jasti, *Nature Chem*. **6**, 404-408 (2014).

26 J. Xia, R. Jasti, *Angew. Chem. Int. Ed.* **51**, 2474 –2476 (2012).

27 E. del Corro, M. Taravillo, J. González, V. G. Baonza, *Carbon* **49**, 973-979 (2011).

28 *Carbon Nanotubes: Synthesis, Structure, Properties and Applications*, edited by M. S. Dresselhaus, G. Dresselhaus, P. Avouris, Springer, Berlin, (2001).

29 L. Sun, F. Banhart, A. V. Krasheninnikov, J. A. Rodríguez-Manzo, M. Terrones, P. M. Ajayan, *Science* **312**, 1199-1202 (2006).

30 J. A. Elliott, J. K. W. Sandler, A. H. Windle, R. J. Young, M. S. P. Shaffer, *Phys. Rev. Lett*. **92**, 095501 (2004).

31 F. T. T. Cerqueira, B. Silvana, A. San-Miguel, M. A. L. Marques, *Carbon* **69**, 355–360 (2014).

32 C. Zhang, K. Bets, S. S. Lee, Z. Sun, F. Mirri, V. L. Colvin, B. I. Yakobson, J. M. Tour, R. H. Hauge, *ACS Nano* **6**, 6023–6032 (2012).

33 B. I. Yakobson, C. J. Brabec, H. J. Bernholc, *Phys. Rev. Lett.* **76**, 2511-2514 (1996).

34 U. D. Venkateswaran, D. L. Masica, G. U. Sumanasekara, C. A. Furtado, U. J. Kim, P. C. Eklund, *Phys. Rev. B* **68**, 241406R (2003).

35 M. Yao, Z. Wang, B. Liu, Y. Zou, S. Yu, W. Lin, Y. Hou, S. Pan, M. Jin, B Zou, T. Cui, G. Zou, B. Sundqvist, *Phys. Rev. B* **78**, 205411 (2008).

36 W. Yang, R. Z. Wang, Y. F. Wang, X.-M. Song, B. Wang, H. Yan, *Phys. Rev. B* **76**, 033402 (2007).

37 T. Chang, *Acta. Mech. Sinica* **23**, 159–62 (2007).

38 V. N. Popov, P. Lambin, *Phys. Rev. B* **73**, 085407 (2006).

39 L. Li, T. Chang, G. Li, *Carbon* **49**, 4412-4419 (2011).

40 G. Wu, X. Yang, J. Dong, *Appl. Phys. Lett*. **88**, 223114 (2006).

41 U. D. Venkateswaran, A. M. Rao, E. Richter, M. Menon, A. Rinzler, R. E. Smalley, P. C. Eklund, *Phys. Rev. B* **59**, 10928–10934 (1999).

42 M. J. Peters, L. E. McNeil, J. P. Lu, D. Kahn, *Phys. Rev. B* **61**, 5939–5944 (2000).

43 C. C. Ling, Q. Z. Xue, L. Y. Chu, N. N. Jing, X. Y. Zhou. *RSC Adv*. **2**, 12182–9 (2012).

44 A. Jorio, R. Saito, J. H. Hafner, C. M. Lieber, M. Hunter, T. McClure, G. Dresselhaus, M. S. Dresselhaus, *Phys. Rev. Lett*. **86**, 1118-1121 (2001).

45 P. T. Araujo, P. B. C. Pesce, M. S. Dresselhaus, K. Sato, R. Saito, A. Jorio, *Physica* **42***,* 1251–1261 (2010).

46 M. S. Dresselhaus, P. C. Eklund, *Advances in Physics* **49**, 705-814 (2000).

47 U. D. Venkateswaran, D. L. Masica, G. U. Sumanasekera, C. A. Furtado, U. J. Kim, P. C. Eklund, *Phys. Rev. B* **68**, 241406(R) (2003).

48 S. Lebedkin, K. Arnold, O. Kiowski, F. Hennrich, M. M. Kappes, *Phys. Rev. B* **73**, 094109 (2006).

49 M. J. Peters, L. E. McNeil, J. P. Lu, D. Kahn, *Phys. Rev. B* **61**, 5939-5944 (2000).

50 U. D. Venkateswaran, E. A. Brandsen, U. Schlecht, A. M. Rao, E. Richter, I. Loa, K. Syassen, P. C. Eklund, *Phys. Stat. Sol. B* **223**, 225-236 (2001).

51 A. K. Sood, P. V. Teradesai, D. V. S. Muthu, R. Sen, A. Govindaraj, C. N. R. Rao, *Phys. Stat. Sol. B* **215**, 393-401 (1999).

52 C. Thomsen, S. Reich, H. Jantoljak, I. Loa, K. Syassen, M. Burghard, G. S. Duesberg, S. Roth, *Appl. Phys. A* **69**, 309-312 (1999).

53 U. D. Venkateswaran, A. M. Rao, E. Richter, M. Menon, A. Rinzler Rinzler, R. E. Smalley, P. C. Eklund, *Phys. Rev. B* **59**, 10928-10934 (1999).

54 U. Schlecht, U. D. Venkateswaran, E. Richter, J. Chen, R. C. Haddon, P. C. Eklund, A. M. Rao, *J. Nanosci. Nanotech.* **3**, 139-143 (2003).

55 A. Jorio, M. A. Pimenta, A. G. S. Filho, R. Saito, G. Dresselhaus, M. S. Dresselhaus, *N. J. Phys.* **5**, 139.1–139.17 (2003).

56 E. Di Donato, M. Tommasini, C. Castiglioni, G. Zerbi, *Phys. Rev. B* **74**, 184306 (2006).

57 C. Thomsen, S. Reich, H. Jantoljak, I. Loa, K. Syassen, M. Burghard, G. S. Duesberg, S. Roth, *Appl. Phys. A* **69**, 309–312 (1999).

58 M. Peña-Álvarez, E. del Corro, V. G. Baonza, M. Taravillo, *J. Phys. Chem. C* **118**, 25132–25140 (2014).

59 D. Y. Sun, D. J. Shu, M. Ji, F. Liu, M. Wang, X. G. Gong, *Phys. Rev. B* **70**, 165417 (2004).

60 J. Arvanitidis, D. Christofilos, K. Papagelis, K. S. Andrikopoulos, T. Takenobu, Y. Iwasa, H. Kataura, S. Ves, G. A. Kourouklis, *Phys. Rev. B* **71**, 125404 (2005).

61 J. Y. Chen, M. Kim, C. S. Yoo, *Chem. Phys. Lett*. **479**, 91–94 (2009).

62 E. Hernández, V. Meunier, B. W. Smith, R. Rurali, H. Terrones, M. B. Nardelli, M. Terrones, D. E. Luzzi, J. C. Charlier, *Nano Letters*, 3, 1037–1042 (2003)

63 H. W. Furumoto, H. L. Ceccon, *J. Quant. Elec.* **6**, 262 (1970).

64 *The Importance of Pi-Interactions in Crystal Engineering: Frontiers in Crystal Engineering*, edited by E. R. T. Tiekink, J. Zukerman-Schpector, John Wiley and Sons, Chichester (2012).

65 V. Lukes, A. Justina, A. Aquino, H. Lischka, H. F. Kauffmann, *J. Phys. Chem. B* **111**, 7954-7962 (2007).

66 K. K. Zhuravlev, M. D. McCluskey, *J. Chem. Phys*. **114**, 5465-5467 (2001).

67 K. K. Zhuravlev, M. D. McCluskey, *J. Chem. Phys*. **120**, 1841-1845 (2004).

68 S. Guha, W. Graupner, R. Resel, M. Chandrasekhar, H. R. Chandrasekhar, R. Glaser, G. Leising, *J. Phys. Chem. A* **105**, 6203-6211 (2001).

69 G. Zannoni, G. Zerbi, *J. Chem. Phys.* **82**, 31-38 (1985).

70 A. Marucci, S. D. M. Brown, M. A. Pimenta, M. J. Matthews, M. S. Dresselhaus, K. Nishimura, M. Endo**,** *J. Mater. Res*. **14**, 1124-1131 (1999).

71 A. P. Rice, F. S. Tham, E. L. Chronister, *J. Chem. Cryst.* **43**, 14-25 (2013).

72 G. Heimel, P. Puschnig, Q. Cai, C. Martin, E. Zojer, W. Graupner, M. Chandrasekhar, H.R. Chandrasekhar, C. Ambrosch-Draxl, G. Leising, *Synth. Met.* **116** ,163-166 (2001).

73 H. Ohtsuka, Y. Furukawa, M. Tasumi, *Spect. Acta Part A* **49**, 731-737 (1993).

74 M. Hanfland, A. Brillante, K. Syassen, M. Stamm, J. Fink, *J. Chem. Phys.* **90**, 1930-1934 (1989).

75 Y. Delugeard, J. Desuche, J. L. Baudour, *Acta Cryst. B* **32**, 702-705 (1976).

76 J. L. Baudour, *Acta Cryst. B* **47**, 935-949 (1991).

77 K. N Baker, A. V. Fratini, T. Resch, H. C. Knachel, W. W. Adams, E. P. Socci, B. L. Farmer, *Polymer* **34**, 1571-1578 (1993).

78 M. Peña Alvarez, P. M. Burrezo, M. Kertesz, T. Iwamoto, S. Yamago, J. Xia; R. Jasti, J. T. López Navarrete, M. Taravillo, V. G. Baonza, J. Casado, *Angew. Chem. Int. Ed*. **53**, 7033-7037 (2014).

79 S. Yamago, Y. Watanabe and T. Iwamoto, *Angew. Chem. Int. Ed.* **49**, 757-759 (2010).

80 F. Sibbel, K. Matsui, Y. Segawa, A. Studer and K. Itami, *Chem. Commun*. **50**, 954-956 (2014).

81 Y. Segawa, P. Šenel, S. Matsuura, H. Omachi, K. Itami, *Chem. Lett*. **40**, 423-425 (2011).

82 E. Kayahara, Y. Sakamoto, T. Suzuki, S. Yamago, *Org. Lett*. **14**, 3247-3247 (2012).

83 J. Xia, J. W. Bacon, R. Jasti, *Chem. Sci*. **3**, 3018-3021 (2012).

84 E. R. Darzi, R. Jasti, *Chem. Soc. Rev* **44**, 6401-6410 (2015).

85 Y. Segawa, S. Miyamoto, H. Omachi, S. Matsuura, P. Senel, T. Sasamori, N. Tokitoh, K. Itami, *Angew. Chem. Int. Ed*. **50**, 3244 –3248 (2011).

86 J. Sandler, M. S. P. Shaffer, A. H. Windle, *Phys. Rev. B* **67,** 035417 (2003).

87 A. Merlen, P. Toulemonde, S. L. Floch, G. Montagnac, T. Hammouda, O. Marty, A. San-Miguel, *Carbon* **47**, 1643-1651 (2009)

88 J. Zang, A. Treibergs, Y. Han, F. Liu, *Phys. Rev. Lett.* **92**, 105501 (2004).

89 M. Hasegawa, K. Nishidate, *Phys. Rev. B* **74**, 115401 (2006).

90 M. Hanfland, A. Brillante, K. Syassen, M. Stamm, J. Fink, *J. Chem. Phys.* **90**, 1930–1934 (1989).

91 G. Heimel, D. Somitsch, P. Knoll, E. Zojer, *J. Chem. Phys.* **116**, 10921–10931 (2002).

92 H. Chen, M. R. Golder, F. Wang, R. Jasti, A. K. Swan, *Carbon* **67**, 203–213 (2014).

93 L. Cuff, C. Cui, M. Kertesz, *J. Am. Chem. Soc.* **116**, 9269–9274 (1994).

94 A. Marucci, M. A. Pimenta, S. D. M. Brown, M. J. Matthews, M. S. Dresselhaus, M. Endo, *J. Mater. Res*. **14**, 3447–3454 (1999).

95 A. L. Aguiar, R. B. Capaz, A. G. S. Filho, A. San Miguel, *J. Phys. Chem. C* **116**, 22637–22645 (2012).

96 M. Levy, *J. Math. Ser*. **3**, 7 (1884).

97 G. F. Carrier, *J. Math. Phys*. **26**, 94–103 (1947).

98 J. Chaskalovic, S. Naili, *Z. Angew. Math. Phys*. **46**, 149–155 (1995).

99 L. D. Landau, E. M. Lifshitz, *Elasticity Theory*, translated by J. B. Sykes and W. H. Reid, ed. Pergamon press, Oxford (1975).

100 M. E. Gurtin, A. I. Murdoch, *Archive for Rational Mechanics and Analysis* **57**, 291-323 (1975).

101 A. E. H. Love, *Phil. Trans. Roy. Soc*. **17** (1888).

102 R. Nicklow, N. Wakabayashi, H. G. Smith, *Phys. Rev. B* **5**, 4951–4962 (1972).

103 Q. Lu, M. Arroyo, R. Huang, *J. Phys. D: Appl. Phys*. **42**, 102002 (2009).

104 Z. C. Tu, Z. C. Ou-Yang, *Phys. Rev. B* **65**, 233407 (2002).

105 E. Hernández, C. Goze, P. Bernier, A. Rubio, *Phys. Rev. Lett.* **80**, 4502-4505 (1998).

106 J.-W. Jiang, Z. Qi, H. S. Park, T. Rabczuk, *Nanotech.* **24**, 435705 (2013).

107 D. Golberg, Y. Bando, C. Tang, C. Zhi, *Adv. Mater*. **19**, 2413–2432 (2007).

108 K. N. Kudin, G. E. Scuseria, B. I. Yakobson, *Phys. Rev. B* **64**, 235406 (2001).

109 A. N. Itami, V. K. Jindal, *Phys. Rev. B* **76**, 19544 (2007).

110 E. A. Belenkov, V. A. Greshnyakov, *J. Mater. Sci.* **50**, 7627–7635 (2015).

111 L. Ciabini, M. Santoro, F. Gorelli, R. Bini, V. Schettino, S.Raugei, *Nature Mat*. **6**, 39-43 (2007).

112 S. Fanetti, M. Citroni, L. Malavasi, G. A. Artioli, P. Postorino, R. Bini, *J. Phys. Chem*. *C* **117**, 5343–5351 (2013).

113 C. Lee, X. Wei, J. W. Kysar, J. Hone, *Science* **321**, 385–388 (2008).

114 M. F. Yu, T. Kowalewski, R. S. Ruoff, *Phys. Rev. Lett.* **86**, 87–90 (2001).

115 S. B. Cronin, A. K. Swan, M. S. Ünlü, B. B. Goldberg, M. S. Dresselhaus, M. Tinkham, *Phys. Rev. B* **72**, 035425 (2005).

116 Y. Segawa, H. Omachi, K. Itami, *Org. Lett*. **12**, 2262–2265 (2010).

117 M. Peña Alvarez, L. Qiu, M. C. Ruiz-Delgado, M. Taravillo, V. G. Baonza, S. Yamago, R. Jasti, J. T. López Navarrete, J. Casado, M. Kertesz, *Phys. Chem. Chem. Phys*. DOI:10.1039/C5CP05500H (2015).

118 M. M. Caruso, D. A. Davis, Q. Shen, S. A. Odom, N. R. Sottos, S. R. White, J. S. Moore, *Chem. Rev*. **109**, 5755-5798 (2009).

119 http://www.lookchem.com/Periodic-Table/Carbon/ browsed on October 7th, 2015.

120 J. Zang, A. Treibergs, Y. Han, F. Liu, *Phys. Rev. Lett.* **92**, 105501 (2004).

Chapter 8

Discussion

[n]CPPs

We started this thesis considering if [n]CPPs could be considered as polyaromatic systems classified within two groups:

- A first group characterized by linear chains of aromatic units linked to each other by single or quasi single C-C bonds, as in linear paraphenylenes.
- And a second group whose common feature is to have polycondensed aromatic rings, with no barriers to delocalization through the conjugated structural plane. In agreement with the PAH definition, [n]CPPs are suggested as molecular models for armchair SWCNTs.

As we have already broadly described, [n]CPPs consist of phenyl units connected to each other by single or quasi single C-C bonds, so they should belong to the first class. However, their cyclic configuration provides them with characteristics typical of largely conjugated systems. For instance, they have a low energy gap which shrinks with smaller *n* values. Thus, we have demonstrated here that [n]CPPs cannot actually be classified within a particular group. Our findings lead us to consider that [n]CPPs are real models for the understanding of the behavior of π systems regardless being classified into the first or the second class of aromatics. Therefore, [n]CPPs constitute completely new chemical entities with aromatic rings conjugated within a radial perimeter, which are flexible, and with an electron rich cavity able to stabilize charge and to host charged or neutral species.

Because of the high polarizability of any π system, Raman spectroscopy is a valuable tool to analyze any conjugational effect. This is why one of the principal targets of this work has been to conduct the assignment of the main Raman spectral contributions of the [n]CPPs. This strategy has allowed us to study structural and electronic characteristics of these systems, to understand their properties at the molecular level. We combine the information of the experimental Raman frequencies and intensities with the density functional theory (DFT) computations (at the B3LYP/6-31G(d,p) level) to provide a consistent interpretation of the [n]CPPs Raman spectra. We have found that the Raman spectra contain relevant electronic and structural information, in particular the bands associated with:

- C-C stretching tangential G modes.
- C-H bending modes (A_{1g} 1200 cm^{-1}) and phenyl breathing modes (A_{1g} 1280 cm^{-1}). Following previous works on LPPs and PPP, we have defined a general equation to directly relate the intensity ratios between the 1280 and 1200 cm^{-1} A_{1g} bands and the torsional angles between neighboring phenyls. For this purpose we employ the torsions obtained by DFT calculations of the [n]CPPs optimized geometries at different conformations, together with their corresponding Raman spectra.
- The low frequency region of the Raman spectra is dominated by low intensity bands which are highly diameter dependent. By means of a thorough analysis of the predicted modes and those experimentally observed peaks, we have been able to assign two main circumferential modes: Radial Breathing Modes, and pseudo-Radial Breathing Modes.

On the other hand, we have established similarities and differences between the Raman spectra of [n]CPPs and [n]LPPs, and between those of [n]CPPs and SWCNTs. In [n]CPPs, the G_{A1g} band derives from the 8a mode of benzene delocalized along the cycle. Therefore, this has a strong ring character enclosing the rich structural and electronic information of these systems.

- In [n]LPPs, it is known that, when adding more phenyl units to the chain, the conjugation is increased, so the G_{A1g} band downshifts with increasing *n*. Their conjugation lengthening has been directly related with the decrease in the $I_{1280A1g}/I_{1220A1g}$ ratio.
- In SWCNTs, the G_{A1g} band downshifts with decreasing diameter due to the larger bending of the parental graphene sheet, thus it is subjected to a larger tensile strain.
- In [n]CPPs, the G_{A1g} band significantly downshifts with decreasing *n*. We have concluded that the increasing strain on the smaller units leads to considerably lower torsions which favor the conjugation between phenyl units developing through space orbital interactions.

[n]CPPs and Cyclic π–Conjugation

In chapter 3 an exhaustive analysis of the differences and similarities between [n]LPPs and [n]CPPs was carried out, revealing different aromatic/quinonoid characters of the benzene rings. Benzene bending, inter-phenyl torsional angles, BLA patterns and HOMO-LUMO gaps were carefully compared for both series. The distinctive evolution of these structural parameters allowed us to conclude the presence of a particular type of π electron delocalization associated with the cyclic geometry. Cyclic π–conjugation is manifested by the large phenyl bendings, minimal inter-ring torsions and small HOMO-LUMO gaps. In contrast, linear π–conjugation produces no phenyl deformation, minimal inter-ring torsion and slightly reduced HOMO-LUMO gaps.

It has been broadly discussed in literature that changes in the bond length alternation (BLA) of conjugated polymers are directly related to changes in the energy gap.[1,2,3,4] In [n]LPPs, BLA increases linearly with an energy gap increase for smaller [n]LPPs.[5] However, we have found that for some [n]CPPs the behavior is the opposite, increases in the BLA lead to the energy gap decrease (see Figure S2 in Appendix 1). In [n]CPPs, from [4]- to [8]CPP, BLA decreases with the energy gap increase. From the minimum (around [8]- and [9]CPP) the BLA increases very slightly with the energy gap increase. We have concluded that this behavior is related with an enhanced cyclic π–conjugation. There seems that the size of [8]- or [9]CPP marks a limit diameter, and at higher diameters we will observe that the radial cyclic π–conjugation is dominated by in-plane p_z conjugation, towards the linear limit.

The strong difference between [n]CPPs and [n]LPPs that activates cyclic π–conjugation is the partial rupture of benzene aromaticity that liberates electrons from the ring confinement towards a more quinonoid configuration and facilitates cyclic π delocalization. At room conditions we have found several Raman signatures directly attributed to cyclic π–conjugation, such as larger intensity distribution along all the A_{1g} modes, with not only the G_{A1g} band as in [n]LPPs, but also larger frequency shifts with size for the observed Raman bands. In any case, the studied variations are gradual.

In addition, the limit size of [8]- and [9]CPP is strongly corroborated when analyzing the results of the [n]CPPs cationic and dicationic species. Even if the cyclic π–conjugation is already present in the neutral species, in the dicationic species it becomes more evident due to the concomitant structural and electronic changes, as shown in Figure 1. When two electrons are removed from the cyclic structure, the smaller [n]CPPs molecules in the oxidized states are stable despite the increasing accumulation of ring strain. The stabilization energy of such strained charged species is provided by the favorable electronic π–conjugation along the different phenyl units.

- In these charged species the balance between cyclic conjugation, cyclic strain and biradicaloid transformation is evidenced in the Raman spectra by the detection of a V-shape behavior of the G band frequencies as a function of the size of the [n]CPP, with a minimum around [8]- and [9]CPP. This fingerprint is driven by the in-plane cyclic alignment of the consecutive $2p_z$-lobes from neighboring units that face each other, preferred only for [n]CPPs with $n \leq 8$.
- As the [n]CPPs size increases, with $n \geq 9$, the extent of in-plane conjugation decreases and the large [n]CPPs dications mitigate cyclic strain by forming non-stable biradicaloid structures. Their behaviors approach to that of linear [n]LPPs dicationic species, which also exhibit a similar biradicaloid character.

Furthermore, we have conducted studies at high and low temperatures in [6]-, [8]- and [12]CPP (see Appendix 2). These show how, at low temperatures, torsions are maximized, and a high temperature reduces them. Moreover, the combination between temperature and laser excitation leads to configurations of higher torsions, so any conjugation between phenyl units is broken and the electron density of each of them is localized within each unit. Therefore no cyclic conjugation is possible. Data analysis allowed us to estimate the energy barrier for the benzene rotation in [8]CPP around 4.75 kcal mol^{-1} and for [12]CPP of 5.26 kcal mol^{-1}. Dividing this by *n*, we obtain a barrier of

about 0.6 and 0.4 kcal mol^{-1}, respectively. The larger barrier for [8]CPP evidences how cyclic conjugation holds phenyl units to lower torsions to get better p_z overlapping. In [12] CPP, due to its larger diameter, that p_z overlap is already minimized so torsions between phenyl units are not so disfavored.

We have also noted that the cyclic conjugation plays a role when analyzing the high pressure behavior of [n]CPPs as a size function. We have found that the compression of the [n]CPPs induces a deformation of their circular cross section towards a ovallized shape. We have observed that this phenomenon is exhibited by each [n]CPP at a different pressure, *PT*, whose value exponentially increases with the decreasing size. Therefore, in the studied pressure range, we proposed the existence of two solid phases:

1. A low pressure phase that is known as the hard phase because the registered pressure coefficients of the bands are higher. In this pressure range mainly are altered C-C bonds by compression. Moreover, we have observed that the pressure coefficients of the G bands show a V-shape as a function of *n*, with a minimum between [7]- and [8]CPP.
2. A high pressure phase or soft phase, in which compression induces the cycle deformation because bending angles are distorted, at such pressures the pressure coefficients are therefore lower.

   In terms of size dependence there is a clear *n* variation. While the pressure coefficients of the G bands of the larger [n]CPPs *(n* ≥ 9) are approximately constant, from *n* equals to 8 up to 5, these rapidly decrease up to below zero for the smallest. In the smallest [n]CPPs the better overlap between the p_z orbitals along the radius within the cavity triggers a different structural transition with other structural rearrangements.

Moreover, there is a notable difference on the possible reversibility of the changes induced by pressure, at least up to about 12 GPa, depending on *n*. For $n \geq 9$ their Raman spectra are almost totally reversible, with small variations which only indicate increase in torsional angles. However, for $n \leq 8$, with decreasing *n*, Raman spectra become less reversible in frequency terms. Therefore it seems that in those [n]CPPs with higher cyclic conjugation, the reversibility is less favored.

On regarding the behavior of [n]LPPs, our results have corroborated that the pressure of planarization (~1 GPa) is almost constant regardless of *n* and that the in-plane π–conjugation in [n]LPPs is considerably enhanced when these are compressed.

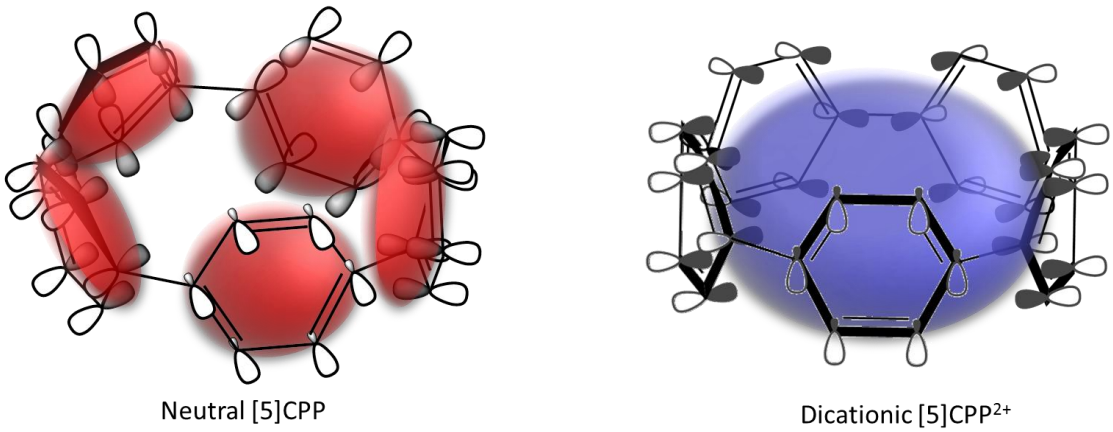

Figure 1. Scheme of [5]CPP under two configurations. Left: neutral, low interaction between the aromatic benzoid units, represented by the small red spheres localized in each phenyl unit. Right: dicationic $[5]CPP^{2+}$, which induces the radial cyclic π–conjugation, represented by the blue inner sphere.

However, in contrast to [n]LPPs, in the cyclic systems we have observed that compression induces different changes in the torsional angles between neighboring phenyl units. At low pressures, there is an initial significant increase up to a limit angle around 30° (this value depends on *n*). Once that torsional limit is reached, torsional angles rapidly decrease with pressure in analogy to [n]LPPs, so the interaction between p_z orbitals of different phenyl units is maximized. We have observed an even/odd dependence in the pressure of that torsional limit (PTL). The value of PTL is higher for the odd [n]CPPs, than for the even [n]CPPs. Nevertheless, there is a common trend for all the [n]CPPs, regardless of the even and odd fact: PTL decreases towards zero with increasing *n*, for [11]- and [12]CPP this is 0.3 and 0.4 GPa, respectively. Consequently, during compression and in torsional terms, larger [n]CPPs tend to behave as [n]LPPs.

All these observations point out that from [8]CPP to smaller *n,* the p_z overlap along the [n]CPP cavity is favored, thus providing [n]CPPs with different properties than those exhibited by the larger ones. When the H_{ipso}-H_{ipso} repulsion is overcome, by the [n]CPP oxidation or by mechanical compression, the cyclic conjugation is further evidenced. This work opens a broad variety of possibilities towards applications of [n]CPPs taking advantage of the cyclic conjugation. An issue which has not been approached before, neither experimentally and nor theoretically.

[n]CPPs and Quinonoidization

Along this work the quinonoidization term has referred in any discussion. Quinonoidization is expected as result from the [n]LPP closure because the inter-ring connecting carbons get pyramidalized ($sp^2 \rightarrow sp^3$ evolution). Phenyl units are slightly bent to accommodate the macrocyclic curvature and to mitigate ring strain. Through an exhaustive computational analysis we have found that quinonoid tautomers are not local minima for any [n]CPP with $n > 5$. [5]CPP is the limiting size for the existence of the quinonoid structure as a valence tautomer. We find that all [n]LPPs and [n]CPPs have an aromatic ground state structure, with a high energy lying quinonoid structure for the smallest [n]CPPs, only for [4]- and [5]CPP. The most used parameter to define quinonoid configurations is the bond length alternation, BLA, negative for the quinonoid forms and positive for the aromatic ones. Throughout this thesis we have widely demonstrated how the concept of a quinonoid-like structure is not limited to situations where such tautomeric structure can be computationally identified as a local minimum.

Quinonoid structures provide useful tools for the analysis of structural changes upon Raman active vibrations, even if such a quinonoid structure is not present as a local minimum. We have addressed the question of the partial quinonoid character of both [n]LPPs and [n]CPPs in various contexts. We have found small differences among three very different approaches:

(a) from the analysis of the geometry changes due to charge transfer for [n]LPPs and [n]CPPs;

(b) from the comparison of the A and Q structures of [4]CPP and [5]CPP;

(c) from the analysis of the displacement vectors based on the Effective Conjugation Coordinate model (ECC).[6,7,8]

We have concluded for all the groups that the aromatic-quinonoid geometry change is mainly dominated by the change of the inter-ring C-C distance, which should be approximately twice compared to the changes in C_{ortho}-C_{ipso} and C_{ipso}-C_{ipso}.

To address the Q/A character by Raman spectroscopy we have used the ECC model and the B3LYP/6-31G(d,p) computed Raman spectra to define the vibrational mode defined as total BLA. From the analysis of the resulting normalized displacement vectors, we have studied the BLA-like geometry change along the vibrational coordinate. We have found that as *n* decreases the C_{ortho}-C_{ortho} displacements are larger than those of the C_{ipso}-C_{ipso}. Such an effect clearly shows the strengthening of the C-C force constant along C_{ortho}-C_{ortho}, with the intensification of the quinonoid character as *n* decreases. Therefore BLA in terms of C-C lengths and C-C displacements along a vibrational mode provides more insights into this particular aromatic-quinonoid balance in the cyclic π structures.

From the experimental Raman shifts we have been able to quantify the effect of such quinonoidal contribution. We have considered that the GA_{1g} band to be with the largest BLA contribution. Therefore the GA_{1g} shifts can be used as connection with the electron density. Consequently, the broad Raman shift dispersion observed for the GA_{1g} band for the different [n]CPPs is a direct evidence of the changes in the BLA displacements as a function of *n*.

In addition, we have conducted a force constant analysis of the bonds involved in the GA_{1g} band (shown in chapter 4). Figure 2 is taken from chapter 4, but we here have also included the results obtained for [5]CPP, not available at the measurement time. In this figure we plot the estimated quinonoid percent as a function of *n*. As it is observed, the GA_{1g} band of [5]CPP at 1555 cm^{-1} indicates a benzo-quinonoid structure with almost 17% of quinonoidal character. However, in [12]CPP this band, at 1595 cm^{-1}, reveals a slightly curved macrocycle with a ring aromatic character similar to that existing in linear oligoparaphenylenes. This suggests that the quinonoidization and the $sp^2 \rightarrow sp^3$ re-hybridization due to the curvature take place only to a moderate degree, sufficient to maintain the prevalent aromatic character of the rings as a condition to preserve chemical stability, even in the most strained member of the series, the [5]CPP.

Of all the available [n]CPPs, [5]CPP is the only one which offers any possibility to study a real transition towards a quinonoid configuration; with a high energy lying quinonoidal state, about 39 kcal mol^{-1} above the aromatic ground state. However, at the same time [5]CPP is the one which depicts the largest radial π–conjugation, as demonstrated by the formation of its closed shell dication. Therefore, to reach such quinonoid conformation, the energy barrier that such conjugation provides should be overcome. The structural change from an A to Q structure involves a BLA change along the perimeter of the [n]CPP.

In this work we have considered that high pressure can be the driving force to cross the quinonoidization energy barrier. The BLA is not directly affected by pressure, since there are no changes in the conjugation length, no changes in the occupancy of the orbitals. Nevertheless, due to the expected changes of the torsions and planarity, some changes in the π-electronic structure are expected which should have an effect on the BLA.

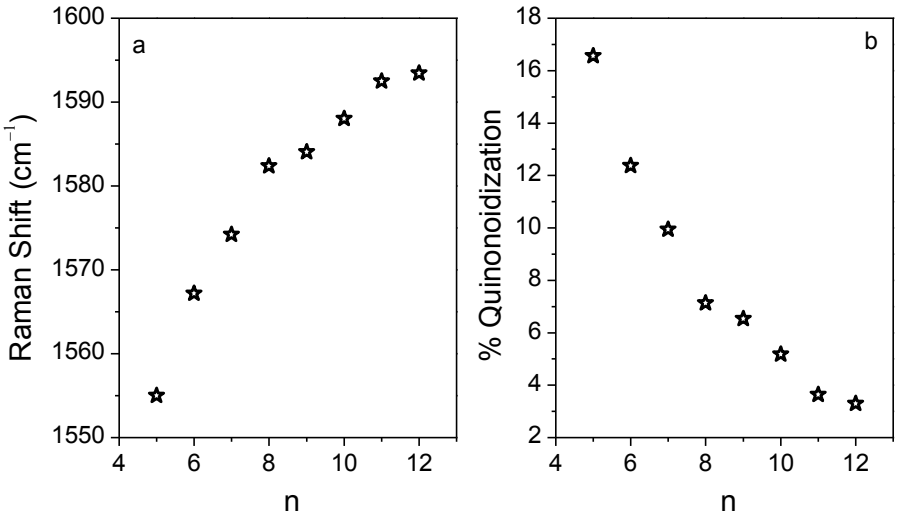

Figure 2. a) G_{A1g} band Raman shift against *n* for [n]CPPs. b) Variation of the [n]CPPs quinonoid character as a function of *n*.

We have explored the possibility of the [5]CPP quinonoidal tautomer formation triggered by high pressure. We have observed that high pressure induces the deformation of [5]CPP along its cross sectional direction, as in the other [n]CPPs. However, the larger pressure coefficients of their Raman features along the hard phase, together with its negative pressure coefficients along the soft phase are unique responses, only observed in [5]CPP. Moreover, with increasing pressure new Ramanfeatures grow around 1450 cm^{-1} and 400 cm^{-1}, which we have associated with the BLA and p-RBMs modes of the quinonoidal configuration, point supported by our force contestants analysis. The combination of these observations allow us to conclude that an oval quinonoid [5]CPP is being formed by the pressure. Thus, mechanical compression leads to its cylindrical deformation with a decrease in the barrier A-Q. So we are able to mechanically control the formation of the [5]CPP quinonoid configuration, no classically approachable by other conventional techniques.

Finally, to confirm the favored radial cyclic conjugation and also the quinonoid participation in the [n]CPPs ground state, in Figure 3 we compare the Raman spectra of the [6]CPP dication and neutral species with the tetrahydro [6]CPP (H_4[6]CPP). In the latter two phenyl units are diprotonated in the ipso positions, and consequently the pi cyclic conjugation must be disturbed. The Raman spectra of this structure is different to that of the neutral and dicationic [6]CPP. As seen in Figure 3, the 1500 cm^{-1} spectral region of the H_4[6]CPP spectrum is formed by two Raman bands, importantly upshifted respect the neutral and dicationic [6]CPP. The two H_4[6]CPP bands are: the 1610 cm^{-1} band corresponding to the C-C stretching of the phenyl units and the 1658 cm^{-1} band corresponding to the C=C stretching of the deprotonated phenyl units. As seen in Figure 3 these bands come from local vibrations, in contrast to what occurs in the neutral and dicationic [n]CPPs. Additionally, the important upshift observed for the H_4[6]CPP in the C-C stretching of the phenyl units, confirms the quinonoid contribution in neutrals due to the induced curvature, and the collective π conjugation.

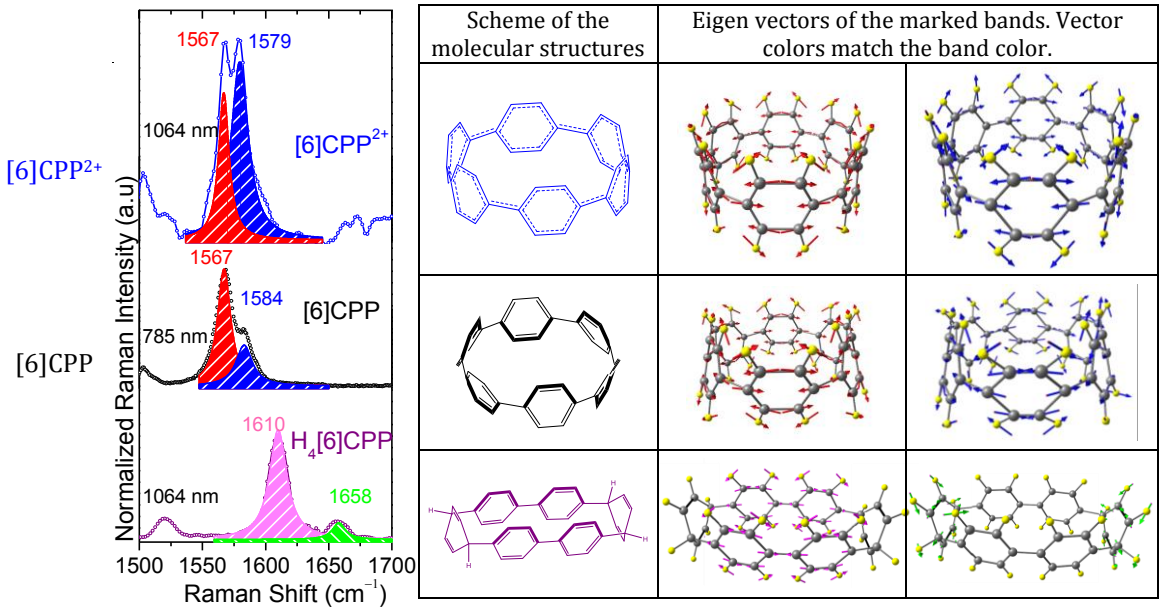

Figure 3. Left: Raman spectra in the 1500 cm^{-1} region of [6]CPP species, from bottom to top: [6]CPP2+, [6]CPP and tetrahydro [6]CPP. at the left of each spectrum the excitation wavelength used in each case is indicated. Right: corresponding structures scheme in the same order accompanied by the eigen vectors responsible for the marked bands. Colors of the marked bands of the spectra matches the colors of the eigen vectors.

[n]CPPs and Armchair SWCNTs

This work represents an initiative to correlate structural, spectroscopic and chemical properties in well-defined [n]CPPs and to relate such properties with those of SWCNTs. From the point of view of the [n]CPPs as molecular models of SWCNTs, this study contributes to clarify their amazing properties and to envisage new molecules with improved conjugation abilities. We have approached this issue through an exhaustive comparison between the Raman spectra of [n]CPPs and SWCNTs. Figure 4 shows the Raman shifts of several features for the [n]CPPs and SWCNTs as a function of their diameter (these data were already shown in chapter 4 and Appendix 2, and here data for the [5]CPP have been included).

We observe a parallel behavior and dependence of the circumferential pseudo-RBMs in [n]CPPs with those RBMs of (n,n) armchair SWCNTs. CNTs and [n]CPPs are the result of the bending of their parental structures, graphene layer and [n]LPPs, respectively. This curvature creates preferential vibrational directions along the tangential direction of the circumference, with a splitting in GA_{1g} and GE_{2g} modes. As seen in Figure 4c, both these bands show a distribution with diameter, analogously for [n]CPPs and armchair SWCNTs.

High pressure studies have also provided valuable information about differences and similarities between [n]CPPs and SWCNTs. Like SWCNTs, [n]CPPs conduct their circumferential deformation with compression which occurs gradually around a pressure value, here referred to as pressure transition (PT). Such pressure shows an exponential increasing with decreasing diameter. The data reported here enable us to obtain the first pressure coefficients for the main Raman peaks of [n]CPPs: pseudo–RBMs, RFMs, 700-900, 1200 cm^{-1} bands, and G-like modes. The resultant pressure coefficients for all the bands are strongly *n* dependent. When comparing the behavior followed by the RBMs and G modes of the [n]CPPs and SWCNTs, both of the systems depict parallel size dependences.

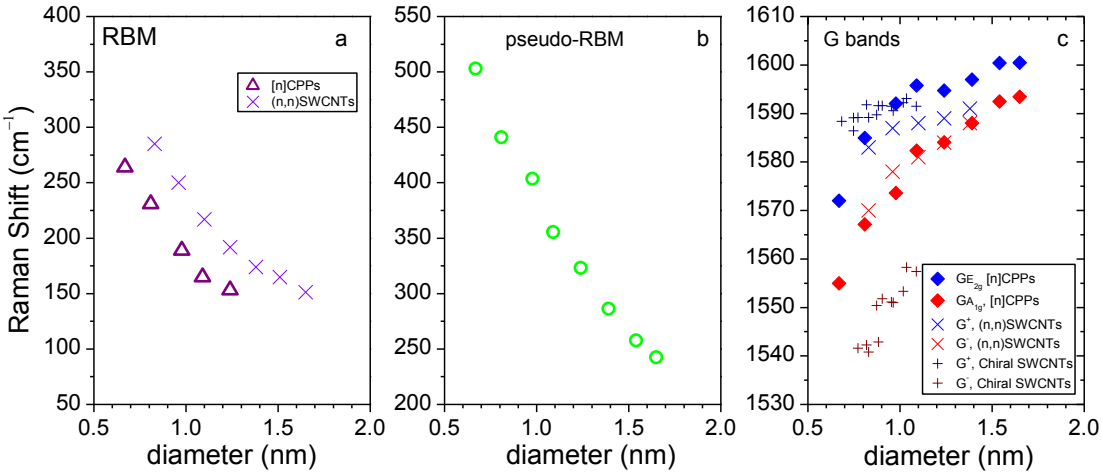

Figure 4. Diameter dependence of the Raman shifts of several features for the [n]CPPs and SWCNTs. a) RBMs. b) pseudo-RBMs. c) G-like modes. Data of armchair SWCNTs ranging from (6,6) to (10,10) are taken from ref. [9]. Data of chiral SWCNTs are taken from ref. [10, 11].

By means of the relationship between the *PT* and bulk modulus suggested by Sun et al,[12] we have estimated the radial compressibility of the [n]CPPs hard and soft phases (before and after deformation, respectively). Interestingly, like in SWCNTs, *PT*s of [n]CPPs depend on diameter (*d*) following approximately a d^{-3} dependence. Thus, we assume that the deformation of [n]CPPs around their radial direction follows the same classical rules as CNTs.[12,13] Therefore, the transition from circle to oval can be understood by the continuum theory of the buckling of elastic rings.[13] Through this approximation we have estimated that the [n]CPPs' flexural rigidity is about (0.57 ± 0.02) eV, the

same order of magnitude as in SWCNTs, 0.65 eV.[12] Using this approximation we have been able to estimate the bulk modulus along the radial direction of the [n]CPPs in their hard and soft phases. We have obtained that the bulk moduli are size dependent and in the hard phase of the same order of magnitude as those of SWCNTs, hundreds of GPa. In the soft phases these decrease by about two orders of magnitude.

Additionally, high-pressure studies have allowed for new insights on the reversibility of the deformability of these nanohoop-shaped systems, finding that they are quite elastic before *PT*. After *PT* (and at least up to 12 GPa) only the large [n]CPPs, $n \geq 9$, recover their initial shape but with larger torsional angles. Instead, we have observed that the pressure induces irreversible changes in [6]CPP and [5]CPP: a collapsed morphology in [6]CPP and the achievement of a quinonoid configuration in [5]CPP.

Finally, electronic and structural properties of host-guest supramolecular 1:1 complexes of [n]CPPs have been thoroughly analyzed using Raman spectroscopy. We have explored and demonstrated the ability of [n]CPPs to act both as a good guest and a good host. The main message of this study is the impressive structural versatility and adaptability of the [n]CPP molecules to different physico-chemical environments.

- We have studied the formation of [n]CPPs supramolecular complexes, achieving the first double nanohoop, [6]CPP@[12]CPP by using high pressure as mechanical triggering of the interactions.
- We have used high pressure to modulate molecular contacts between [n]CPPs and C_{60}, forming host-guest supramolecular 1:1 complexes of C_{60}@[n]CPP with n = 9,10, 11 and 12. We have proposed the formation of a charge transfer complex, $C_{60}^{\bullet-}$@[10]CPP$^{\bullet+}$, as a further progress relative to the already-known π–π van der Waals C_{60}@[10]CPP supramolecular analogue.
- Lastly, we have studied host-guest supramolecular 1:1 complexes of [n]CPPs and C_{70}, C_{70}@[n]CPP with n = 9, 10, 11. Depending on their sizes, the [n]CPPs have been shown to be able to adapt their structures to form stable couplings with C_{70}. While in C_{70}@[10]CPP the fullerene is surrounded by the [10]CPP by its equatorial part, or lying orientation, in C_{70}@[11]CPP the fullerene is enclosed through its long ellipsoidal axis, or standing orientation.

  Pressure produces the modification of the lying structure of the C_{70}@[10]CPP complex towards a more standing-like conformation followed by the flattening of its structure, a dual process that overall renders an irreversible structural mechanical cycle. Instead, C_{70}@[11]CPP, remains in its standing position when compressed, and it is by heating that the [11]CPP ring rotates towards a lying arrangement.

References

1 J. L Bredas, *J. Chem. Phys.* **82**, 3808–3811 (1985).

2 J. L. Bredas, F. Wudl, A. J. Heeger, *J. Chem. Phys*. **85**, 4673–4678 (1986).

3 Y. S. Lee, M. Kertesz, R. L. Elsenbaumer, *Chem. Mater.* **2**, 526–530 (1990).

4 C. H. Choi, S. J. Yang, *Chem. Rev*. **105**, 3448–3481 (2005).

5 Y. S. Lee, M. Kertesz, *J. Chem. Phys*. **88**, 2609**–**2617 (1988).

6 J. L. Bredas, R. R. Chance, R. Silbey, *Phys. Rev. B* **26**, 5843–5854 (1982).

7 B. Horowitz, *Phys. Rev. B* **36**, 1535 (1987).

8 G. Zerbi, M. Gussoni, C. Castiglioni, in *Conjugated Polymers,* ed. J. L. Bredas and J. Silbey, Kluwer, New York, p. 435 (1991).

9 E. H. Hároz, J. G. Duque, X. Tu, M. Zheng, A. R. Hight Walker, R. H. Haige, S. K. Doorn, J. Kono, *Nanoscale* **5**, 1411–1439 (2013).

10 O. Dubay, G. Kresse, H. Kuzmany, *Phys. Rev. Lett*. **88**, 235506 (2002).

11 H. Telg, J. G. Duque, M. Staiger, X. Tu, F. Hennrich, M. M. Kappes, M. Zheng, J. Maultzsch, C. Thomsen, S. K. Doorn, *ACS Nano* **6**, 904–911 (2012).

12 D. Y. Sun, D. J. Shu, M. Ji, F. Liu, M. Wang, X. G. Gong, *Phys. Rev. B* **70**, 165417 (2004).

13 L. D. Landau, E. M. Lifshitz, *Elasticity Theory*, translated by J. B. Sykes and W. H. Reid, ed. Pergamon Press, Oxford (1975).

Chapter 9

Conclusion

The backbone of this dissertation is based on the exhaustive analysis of the most interesting properties of the so-called [n]CPPs. These molecules with cyclic morphology are formed by phenylene units connected to each other in their *para* position by quasi-single bonds. As result of the partial bending of the phenylenes required to close the cycle, [n]CPPs display a high internal strain. The degree of deformation of such units exponentially increases with the decreasing cyclic size and, therefore, the smallest cycles exhibit a pronounced strain.

Due to the novelty of [n]CPPs, by the time this dissertation was started no work had been published about the [n]CPPs' Raman spectroscopic features. Consequently, one of the fundamentals of this thesis has been the experimental, theoretical and computational assignment of their main active Raman modes. Herein, we have approached the [n]CPPs' Raman spectra from a very fundamental level considering their size, shape and charge dependencies. Additionally, it must be noted that it has been essential the comparison with the structural and spectroscopic features of related compounds, such as the linear oligoparaphenylenes and the carbon nanotubes.

From the first studies in [n]CPPs it has been a challenge to know whether the deformation exerted by the cyclization is a driving force to the total or partial quinonoidization of the cycle. As was seen, in this work has been demonstrated that the closure of the cycle induces the out of plane bending of the phenyl units, hence it was also raised the possibility of the phenyl aromaticity rupture towards quinonoid species, with the consequent formation of localized double bonds between the C_{ortho}-C_{ortho} and C_{ipso}-C_{ipso} atoms. However, the analysis of the C-C distances from the XRD structural parameters of the literature demonstrates that such quinonoidization does not occur.

Here, we have explored the potential energy surface of the [n]CPPs, observing that the global minima of the [n]CPPs (with n = 4 – 20) are configured by totally benzoid units. Additionally, we do not find any quinonoid local minimum for [n]CPPs (with n = 6 – 20). Only for the most strained cycles, [4]- and [5]CPP, we find a high energetic quinonoid minimum.

Interestingly, a novel and notable result of this work has been the achievement of a distorted quinonoid configuration of [5]CPP at room conditions. This was reached by the compression of [5]CPP with the subsequent release pressure. Such a quinonoid configuration is the first purely quinonoid cyclic molecular structure, and to our knowledge comparable species have not been reported yet.

On the other hand, even if the ground state minima of the [n]CPPs are formed by benzoid phenyl units, the alteration of the planarity of the phenylenes must disturb the structural and electronic configuration. In this work we have quantified to which degree the quinonoidization is involved in those ground state energy minima. With this aim, we have conducted a force constants analysis for the vibrational modes involved in the mode approximated to be closest to the bond length alternation mode (BLA mode). Our results suggest that there is an increase of the quinonoidal character with the decreasing size, ranging from 3 % in [12]CPP to 17 % in [5]CPP.

Another issue that has received much attention in the [n]CPPs field is that these provide opportunity to study experimentally and theoretically the so-called cyclic π–conjugation. In the cyclic conjugation, the p_z orbitals are radially confined in the *xy* plane with their lobes radially oriented to *z* axis. However, neutral species of the [n]CPPs preserve the aromatic character of their phenyl units, and no delocalization within the cycle is observed. So, oxidized species of [n]CPPs, cations and dications, are candidates for this outstanding challenge.

For this reason, in this thesis the oxidized species of [n]CPPs (with *n* = 5-12) have been synthesized. Our findings reveal that the removal of one electron is enough to induce such an aromaticity rupture, being compensated by the stabilization of the radial cyclic π–conjugation. In addition, the removal of two electrons is even more favored since parity in the π electron number is reached. We have found that in the larger [n]CPPs, the cyclic conjugation becomes less preferred because of the lower p_z orbital overlap. Consequently, from [9]CPP^{2+} to larger diameters we detect the rupture of the cyclic symmetry, which is the result of a charge splitting towards a biradical character. Therefore, the smallest of the [n]$CPPs^{2+}$ constitute the first experimentally reachable models to explore the potential of the radial cyclic π–conjugation.

Furthermore, in this dissertation we make use of the temperature and pressure as modulating tools to explore several of the [n]CPPs' properties in comparison with those shown by the carbon nanotubes:

- Our results demonstrate that [n]CPPs are able to easily host in their cavity carbon systems with high electron density. The phenylenes high rotational freedom in the [n]CPPs allows them to morphologically adapt to their guest, guaranteeing the maximum interaction between both systems. In this line we have explored: charge transfer $C_{60}^{\bullet-}$@[n]$CPP^{\bullet+}$·complexes; the [n]CPPs capability to host C_{70} in different conformations, in analogy to the peapods; and the formation of the [6]CPP@[12]CPP complex, in analogy to the double walled carbon nanotubes.
- Through a high pressure study we have probed that [n]CPPs are as deformable as carbon nanotubes, transforming with the pressure towards an oval configuration. We have observed that ovallization occurs at low pressures in the larger [n]CPPs (< 1 GPa in [12]CPP). Thus, the smaller [n]CPPs exhibit a greater resistance to deformation, so higher pressures of transition are displayed.

In summary, in line with the title of this thesis, our work signifies a deep study of exceptional properties such as quinonoidization, radial cyclic π–conjugation and biradical character. Such terms can be exclusively related to [n]CPPs, and they are entirely linked to their diameter, molecular character and cyclic morphology. In addition, we have demonstrated that [n]CPPs and carbon nanotubes share several of their properties related with their tubular configuration. Among these shared properties are their capability to host systems with the appropriated size and their high radial bulk modulus.

Chapter 10

English Summary

Exceptional Properties of [n]CPPs: Why Molecular Morphology and Size Matter?

Ph. D. Student

Miriam Peña-Álvarez

Supervisors:

- Prof. Mercedes Taravillo Corralo
- Prof. Juan Casado Cordón
- Prof. Valentín García Baonza

Cycloparaphenylenes ([n]CPPs from now on), were firstly synthesized in 2008, and promptly joined the fascinating world of carbon nano-materials in their own right. These systems are formed by cyclic molecules with *n* phenyl units connected each other in their para-position, a configuration that resembles an ultra-short armchair single-wall carbon nanotube (SWCNT).

In this Ph. D. Thesis we put forward a systematic study on the electronic properties of [n]CPPs, providing a thoroughly link between [n]CPPs, SWCNTs and their linear analogues ([n]LPPs). Curvature, strain and electronic π–conjugation are the main characteristics of [n]CPPs that we will systematically study to examine their unexplored properties, and eventually their potential applications. In addition, we shall use [n]CPPs as models to realize the concept of radial cyclic electronic π–conjugation, which has been only theoretically considered so far.

Let us emphasize that we shall take advantage of the success of Raman spectroscopy for characterizing carbon-based materials. Raman spectroscopy is also among the most suitable tools to probe the electronic properties of such materials due to the high susceptibility of the π-electrons polarizability. In this Ph. D. Thesis we present a systematic study of a series of [n]CPPs considering all the geometrical parameters involved in their vibrational modes. We shall examine the influence of size on the Raman spectra of [n]CPPs, together with the effect of oxidation and mechanical compression on their molecular structures. Finally, we will explore the hosting capabilities of [n]CPPs as well as their mechanical properties relative to those of SWCNTs.

10.1 Introduction

Since the discovery of benzene as the first cyclic conjugated system,[1] major efforts have been made to understand the structural and electronic properties resulting from its in-plane p_z infinite conjugation.[2,3] Within this field, polyaromatic molecules became even more revolutionary due to their singular properties resulting from the large extent of p_z conjugation.[4] Within the polyaromatic systems there are two distinctions, linear chains units linked to each other by single or quasi single C-C bonds and polycondensed aromatic rings, the latter also being referred to as polycyclic aromatic hydrocarbons (PAHs). PAHs are substantially rigid over sizeable distances so there are no barriers to delocalization through the conjugated structural plane.

Nowadays, there is a whole scientific branch dedicated to the study of PAHs. This scientific field is rapidly growing due to the numerous applications of the carbon nanomaterials. Cycloparaphenylenes, or [n]CPPs, which were first synthesized in 2008, can also be included in this field. [n]CPPs are conjugated hydrocarbons with a cyclic disposition of 1,4-substituted benzenes, whose p_z orbitals are oriented towards the center of the macrocycle (see Figure 1b). After that first synthesis, [n]CPPs have been successfully prepared over a wide array of diameters[5-12] ranging from 0.669 nm in [5]CPP[6] to 2.4 nm in [18]CPP,[13] as shown in Figure 1a.

The properties of the polyaromatics molecules conjugated along the *xy* plane have been well studied. However, the potential effects caused by p_z orbitals orientational change towards a radial cyclic p_z configuration still remain unexplored. Theoretical cyclic systems with radially oriented π orbitals such as [n]cyclophenacenes,[14] and [n]cyclacenes[15] have been largely investigated.[16] Unfortunately, to our knowledge, the synthesis of those cyclic structures has not been achieved yet.[17] Recently, [n]CPPs have been suggested as models to explore the radial cyclic π–conjugation, however this concept has not been experimentally approached yet.[17-19] Therefore, a determinant factor of this work will be the analysis of the extent of the π delocalization or localization along the cyclic systems, considering size and configurational effects.

On the other hand, one of the main causes of interest in the [n]CPPs is that they are thought to be the shortest cylindrical version of (n,n) armchair SWCNTs (see Figure 2).[5,17,20-23] In this regard, significant progress has been made using [n]CPPs as templates for the controlled bottom-up synthesis of carbon nanotubes.[24-27]

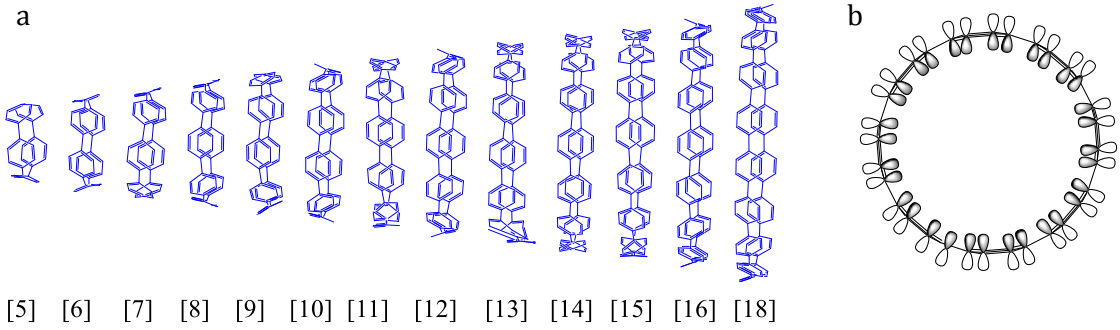

Figure 1. a) Side view of the molecular structures of all the [n]CPPs synthesized so far. b) Schematic representation of the radial π system of [8]CPP in its D_{8h} conformation.

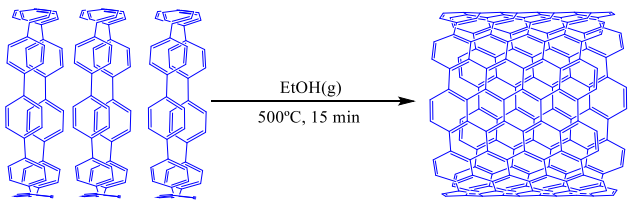

Figure 2. "Growth-from-template" strategy for the bottom-up synthesis of structurally uniform SWCNTs by using [12]- or [9]CPP as precursors.[27]

In this line, the study of the [n]CPPs might provide relevant insights about the exclusive properties imparted by their unique *cyclic*-shape and relate them to known properties of SWCNTs. In addition, [n]CPPs are significant on their own right given their salient optoelectronic and structural properties, and their host-guest ability to form supramolecular assemblies.[5,28-31] The sizeable radius of the [n]CPPs, together with their bendable peripheral cyclic π-electron delocalization provides us an excellent opportunity to study their electronic, structural and mechanical properties as a function of the precise chemical structure.

A systematic study of the structural and electronic properties of the [n]CPP series in comparison with their linear analogues, oligoparaphenylenes and SWCNTs, has been performed herein. Raman spectroscopy is controlled by the change in polarizability along the molecular vibrational modes.[32,33] Therefore, for these electron-rich systems, Raman spectroscopy is one of the most suitable diagnostic tools, allowing us to conduct an exhaustive investigation of the different electronic configurations.

10.1.1 Key Structural Parameters of the [n]CPPs

The number of π electrons which form the cycle increases with growing the number of phenyl units. However, in contrast to what occurs in their linear analogues, the energy gap of [n]CPPs is lower for smaller cycles, as shown in Figure 3. Consequently, one of the key characteristics of [n]CPPs is their size-tunable energy gap. Such different trend in the energy gap is justified by how radial cyclic configuration is modulated by the bending and the torsion of the phenyl units carrying the π–conjugation.

Both [n]LPPs and [n]CPPs, in their lowest energy conformation, depict torsions between neighboring phenyl units to minimize ortho hydrogen-hydrogen steric interaction, as shown in Figure 4. In [n]CPPs, torsional angles rapidly decrease with the decreasing size, up to 12° in [5]CPP,[6] while [n]LPPs depict also torsional angles almost constant with the oligomeric length: 36° was calculated for a long poly-paraphenelylene molecule.[34] Therefore, in the smaller [n]CPPs, torsion is strongly hindered by the cyclic configuration and the concomitant increasing strain.

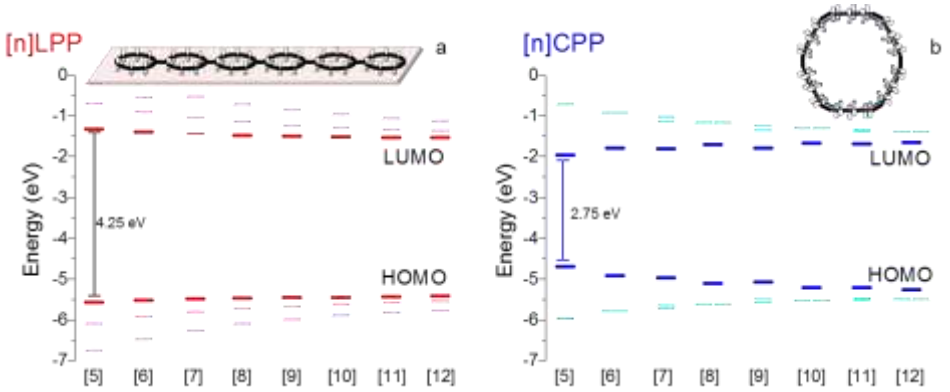

Figure 3. Schematic representation of the frontier molecular orbitals and their energies for the different oligophenylenes molecules: a)[n]LPPs; b) [n]CPPs. Red and dark blue correspond to the frontier orbitals HOMO and LUMO, and pink and light blue to HOMO-1, HOMO-2, LUMO+1 and LUMO+2, for [n]LPPs and [n]CPPs, respectively.[35-38]

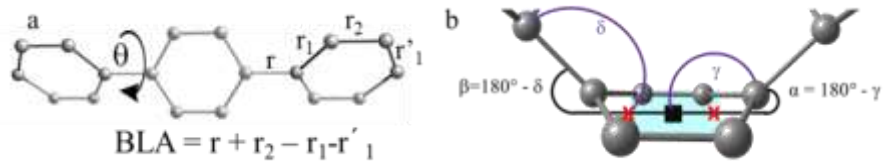

Figure 4. a) Torsional angle (θ) between two neighboring benzene units; and the C–C bond distances (r, r_1 and r_2). b) Out-of-plane bending angles α and β are defined as α = 180° – γ; β= 180° – δ. Different centroids are indicated by X and ■ and are used to calculate the out-of-plane deformation of the benzene units. For [n]LPPs, α = β = 180°.

Additionally, due to the increasing strain of the [n]CPPs with their decreasing diameter, it has been suggested that changes from a benzoid to a quinonoid configuration are possible. Such a configuration would be led by the large bending angle required from the phenyl units to close the cycle, as schematized in Figure 4.[9,39-41] In the literature any quinonoidal change has been quantitatively described by the same BLA parameter[42-45] using the following equation and the definitions in Figure 4a:

$$\mathrm{BLA} = r + r_2 - r_1 - r_1{}' = r + r_2 - 2r_1 \qquad (1)$$

where C_{ipso}-C_{ipso} bonds are marked as r, the C_{ipso}-C_{ortho} as r_1 and C_{ortho}-C_{ortho} as r_2. When the inter-ring bond (r) is long, and r_1 and r_2 are close in value, the structure is aromatic with BLA > 0. For [n]CPPs $r_1 = r_{1'}$. When r is short, and $r_1 > r_2$ then BLA < 0 and the structure is quinonoid. Subsequently, quinonoidization would be the result of a redistribution of the π electron density from the aromatic phenyl units: aromaticity would be disturbed to form local double bonds between C_{ipso}-C_{ipso} on one side and C_{ortho}-C_{ortho} on the other. In Figure 5 the aromatic and quinonoid conformers of [5]CPP are shown.

On the other hand, the cyclic configuration of the [n]CPPs joined to their high π electron density provide them with the ability to host other molecules with the proper size to fit within their inner cavity.[46,47] Hence, in analogy with SWCNTs, the resulting supramolecular structures would be stabilized by convex-concave π-π interactions.[48-50] For instance, in Figure 6b we show a peapod formed by C_{70} in its lying orientation in the cavity of a (10,10) SWCNT and in Figure 6a the corresponding ultra-short peapod of C_{70}@[10]CPP. As result of such a hosting capability several applications have been ascribed to these systems.[46,51] For instance, as light harvesting devices when they could form the so-called "Russian dolls": [n]CPPs of the appropriate size occupying the inner cavity of larger [n]CPPs;[52] or as funnels to purify fullerenes, endo or empty, of determined diameters from raw carbonaceous materials.[53,54]

The study of the potential properties of single diameter SWCNTs is still incomplete, a drawback which is intimately related to their current synthesis protocols and the absence of orthodox methods for their bottom-up chemical preparation.[55] In this regard, [n]CPPs with similar potentials in terms of morphological shape, could be used as models for those size dependent studies.

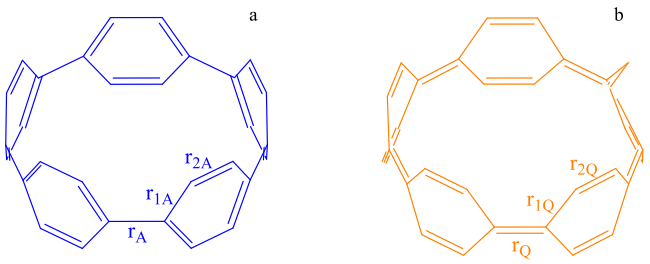

Figure 5. Scheme of the molecule of [5]CPP under two conformations: a) Benzoid conformation, BLA > 0. b) Hypothetical quinonoid conformation, BLA < 0.

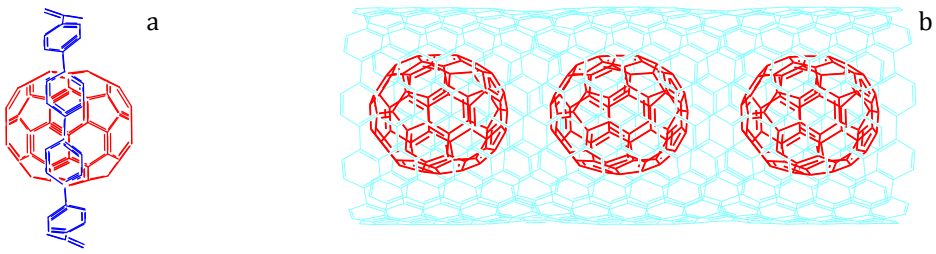

C_{70}@[10]CPP C_{70}@(10,10)SWCNT

Figure 6. a) Side view of the host-guest complex C_{70}@[10]CPP in lying orientation; b) Scheme of C_{70}@(10,10)SWCNT peapod in lying orientation.

10.2 Aims

With the support of calculations based on the density functional theory (DFT) methodologies, this work intends to conduct a deep analysis of the electronic and structural effects which configure the [n]CPPs Raman spectra. The information on the experimental Raman frequencies and intensities, combined with the DFT computations and reported X-ray diffraction structures, provides a consistent interpretation of the Raman spectra and allows us to establish relevant structure-property trends.

Structural and electronic effects such as benzene ring bending, inter-ring torsions, π conjugation (aromaticity) and orbital energy gaps as a function of the linear elongation in [n]LPP versus macrocyclic curvature in [n]CPP and of the molecular size (i.e., polymer limit) will be systematically analyzed on the basis of the vibrational Raman properties. In our interest of exploring possible mechanical, chemical and spectroscopic analogies between [n]CPPs and SWCNTs, we will here study [n]CPPs in an oligomeric approach to SWCNTs. This work offers a unified interpretation of structural and electronic aspects related with the evolution from linear 1D π systems to cyclic 2D structures.

Additionally, in this scenario, we will address the question of the partial quinonoid character of [n]CPPs in various contexts to understand if quinonoid configurations with local double bond localization could be real. We will explore the possibility of full quinonoid tautomers, and through a different approach to analyze the most characteristic Raman active modes, the involvement of quinonoid configurations into the aromatic ground state will be objectivized.

We will address the analysis of the conformational properties of the [n]CPPs in terms of torsional angles between neighboring phenyl units. With this aim a combination of temperature and laser excitation will be used to modulate different torsional conformations. In addition, DFT calculations of twisted and non-twisted conformations will be used to estimate different torsional conformers possible depending on *n*.

Besides, in this work we aim to amplify the understanding of the radial cyclic π-conjugation as a general stabilizing effect. This issue will be approached from an experimental and theoretical point of view for [n]CPPs from $n = 5$ to $n = 12$. Neutral and non-aromatic radical charged [n]CPPs, cations and dications, will be explored in terms of electronic conjugation. Subsequently, radical cations and dications of [n]CPPs, from $n = 5$ to $n = 12$, will been studied by Raman spectroscopy and by DFT calculations. The comprehensive analysis of the molecular and electronic properties of the charged [n]CPPs together with their Raman spectra will be the identification of the key factor intervening in the stabilization of these remarkable [n]CPP compounds.

Also, this work is directed to explore the possible usability that [n]CPPs provide to act as hosts and/or guests in the formation of supramolecular systems. With this intention in this work we will deal with the formation of π-π concave-convex interactions driven by high pressure, in solid state and with no solvent involved. Several solid state mixtures of [n]CPPs of different sizes and [n]CPP with C_{60} will be compressed and followed by high pressure. A series of four 1:1 host-guest supramolecular complexes of [n]CPPs and C_{70} will be analyzed by Raman spectroscopy in solid state and complemented with the analysis of their spectroscopic responses under mechanical and thermal stresses.

Finally, among the main goals of this dissertation is to analyze the size dependent mechanical properties of [n]CPPs and their deformability. This study will be envisioned to display analogies and differences between the mechanical properties of [n]CPPs and SWCNTs, with the latter being among the stiffest materials known. In this line, the formation of unreachable configurations at room conditions by convectional synthetic routes will be suggested, such as quinonoid or peanut shaped [n]CPPs. To accomplish these achievements we will present a high pressure-Raman study on [n]CPPs of different members ranging from [5]CPP to [12]CPP and with pressures up to 12 GPa by means of a sapphire anvil cell.

10.3 Results

10.3.1 Assignment of the Main [n]CPPs Raman Bands: Relationship between Molecular Morphology and Spectral Features

In Figure 7 we represent the Raman spectra of [n]CPPs, with *n* = 5-12, together with the spectrum of [6]LPP. The Raman spectra of [n]CPPs and [n]LPPs share many common features, mostly in the high frequency region, from 1000 to 1600 cm^{-1}. However, [n]CPPs spectra are more complex, with several contributions for the different bands and many peaks in the low frequency range which become increasingly intense with the decreasing *n*. Table 1 summarizes the bands marked in Figure 1 and their vibrational assignment is included.

In Figure 7, we have marked in green the so-called pseudo-radial breathing modes (p-RBMs) and in purple the totally symmetric radial breathing modes (RBMs). In analogy with SWCNTs both modes follow linear trends as a function of their diameter inverse. Such analogous trends suggest that [n]CPPs could mimic the relevant structural properties of SWCNTs, despite their different chemical constitution. We have related the diameter of the [n]CPPs to the Raman shift of the p-RBMs as follows:

$$\omega_{p-RBM}\left(cm^{-1}\right)=8+\frac{375}{d(nm)} \qquad (2)$$

One of the most interesting sections of the [n]CPP Raman spectra is the 1100-1300 cm^{-1} region. In this region it is possible to characterize two A_{1g} bands whose intensity ratio provides valuable information. In [n]LPPs the intensity ratio between the 1280 and 1200 cm^{-1} A_{1g} bands ($I1280A_{1g}/I1200A_{1g}$) has been used as an indicator of the conjugation length.[56] Consequently, an increase in conjugation length would lead to a decrease in the intensity ratio.

In the 1550 - 1600 cm^{-1} region [n]CPPs depict the bands referred as G modes, in analogy to CNTs.[57] In Figure 7 we see that the G band is formed by two intense contributions: the low frequency one assigned to the A_{1g} mode related to the collective C-C stretching mode within the circumferential direction; the high frequency contribution of lower intensity has E_{2g} symmetry and it is related to C-C stretching as well, but the C-C displacements are not as localized along the radial direction as in the case of the A_{1g} mode. Additionally, in Figure 7 we see how the intensity of the low frequency modes becomes relevant as size decreases. In contrast, when size increases intensity is mostly concentrated on the GA_{1g} band, as occurs in linear paraphenylenes regardless *n*. The G band splitting and the A_{1g} bands intensity distributions are marks directly attributed to cyclic configuration.

Table 1. Experimental and theoretical (B3LYP/6-31G(d,p) scaled ~0.97) wavenumbers (in cm^{-1}) for [6]CPP and [6]LPP, species of symmetry (non-twisted D_{nh} conformation) and the vibrational assignment in terms of internal coordinates.

[6]CPP				**[6]LPP**		
Exp.	Theor.	Sym.	Vibrational description	Exp.	Theor.	Sym.
231	240	**A_{1g}**	Radial Breathing Mode (RBM)	--	--	--
442	442	**E_{2g}**	Pseudo-Radial Breathing Mode (pseudo-RBM)	--	--	--
1192	1179	E_{2g}	β(phenyl)+ ν(C-C)+ ω (CH)	--	--	--
1200	1185	**A_{1g}**	β(C-H) + $\nu(C\text{-}C)_{interring}$	1219	1222	A_g
1252	1244	E_{2g}	β(phenyl) + $\nu(C\text{-}C)_{interring}$ + β(C-H)	1269	1263	E_{2g}
1263	1245	**A_{1g}**	β(phenyl) + $\nu(C\text{-}C)_{interring}$+β(C-H)	1278	1278	A_g
1269	1264	E_{1g}	ν(C-C) + ω(CH) + β(phenyl)	--	--	--
1567	1576	A_{1g}	G_{A1g}: $\nu(C\text{-}C)_{transversal}$	1593	1594	A_g
1584	1592	E_{2g}	G_{E2g}: $\nu(C\text{-}C)_{trans}$+ $\nu(C\text{-}C)_{longn}$	--	--	--

RBM: radial breathing mode; **p-RBM**: circumferential mode with radial breathing components, **β(C-C)**: C-C bond bending mode; **β(phenyl)** symmetric phenyl breathing mode; **ω(CH):** C-H wagging mode; **$\nu(C\text{-}C)_{interring}$**: C-C inter-ring stretching mode; **β(C-H)**: C-H bending mode; **$\nu s(C\text{-}C)_{transversal}$**: C-C stretching mode along the transversal direction of the macrocycle; **ν(C-C)long**: C-C stretching mode along the longitudinal direction of the ring.

In order to show the most obvious effects of cyclic configuration in Figure 8 we compare the Raman shift of the GA_{1g} bands for linear and cyclic configurations. We have also plotted the GA_{1g} frequencies of the [n]CPPs and [n]LPPs non-twisted configurations (zero torsional angles). It can be seen how the GA_{1g} bands of both twisted and non-twisted [n]CPP series show a much larger frequency shift as a function of *n* compared to [n]LPPs. This large frequency dispersion is attributed to the strong bending of the benzene rings which breaks down its aromaticity and allows larger π–conjugation for [n]CPP, especially for smaller *n*.[58] Interestingly, the sign of the dispersion shifts with increasing size in [n]CPP and [n]LPP are opposite. In [n]LPPs it is known that when adding more phenyl units to the chain the conjugation is increased, so it explains why the G_{A1g} downshifts with the increasing *n*.[59] Therefore, it can be concluded that cyclic configuration defines: larger shifts in frequency as size decreases for the detected Raman bands

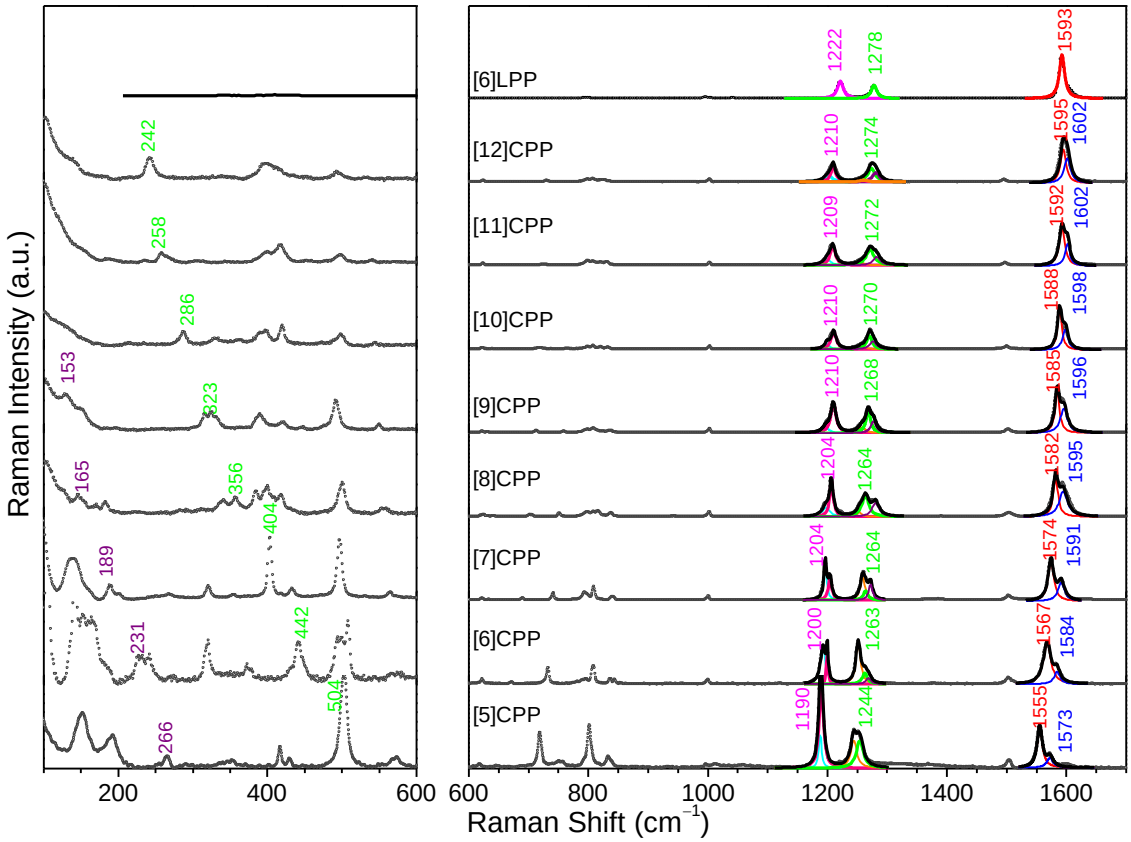

Figure 7. Raman spectra of [n]CPPs from [5]- to [12]CPP and [6]LPP in the 100 -1700 cm^{-1} region. All spectra have been normalized to the G_{A1g} mode around 1580 cm^{-1}. The assignment of the bands and contributions are specified in Table 1.

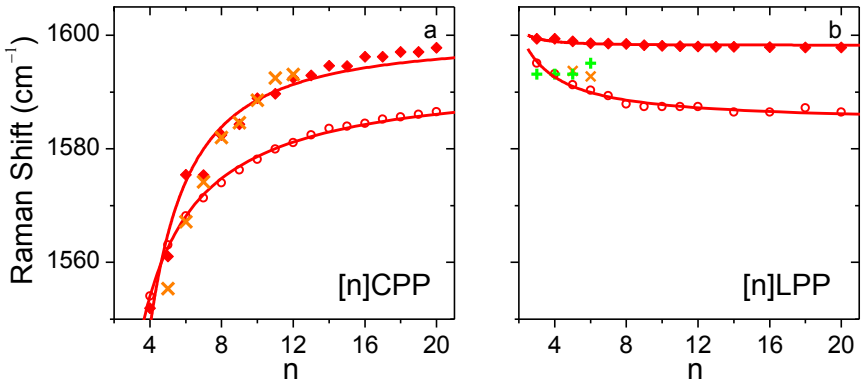

Figure 8. G_{A1g} band Raman shift against *n* for: a) [n]CPPs, b) [n]LPPs. Computed data for (○) for the non-twisted conformationsand (◆) for the twisted ones. (×) for [n]CPPs experiments. (+) for [n]LPPs experiments.[60] Lines are guides to the eye.

10.3.2 Exploring the Quinonoidization

As anticipated in the introduction quinonoid structures are characterized by strong negative bond length alternation patterns (BLA). In this regard, all available [n]CPPs depict positive BLA close to zero, indicative of bond length equalization. This is the main reason to figure out if a quinonoid configuration following such definition could be even real. A DFT computational approach is followed at the B3LYP/6-31G(d) level, finding that, in agreement with Bachrach and Stück results,[61] [n]CPPs, with *n* values ranging from 4 to 20, have an aromatic ground electronic state, and only for [4]- and [5]CPP we found a high energetic quinonoid state.

However, although the ground state minima of the [n]CPPs remain formed by aromatic phenyl units, the phenylene bending required to close the cycles must induce modifications in the structural and electronic configurations of the phenylenes. In this work we attempt to study how such electronic and structural reorganization occurs by identifying to in which degree the quinonoidization is involved in those ground state energy minima.

10.3.2.1 Effective Conjugation Coordinate Theory

The Effective Conjugation Coordinate (ECC) theory [42-45,62,63] defines a totally symmetric stretching vibration corresponding to the in-phase shrinking/stretching of the C-C/C=C consecutive bonds (ECC o BLA mode) in such a way that their vibrational amplitudes match the A ↔ Q geometrical transformation, or BLA deformation.[64] The BLA mode is not a vibrational eigenfunction, thus, the ECC establishes that the BLA intensity appears distributed among the few symmetric C-C/C=C stretching normal modes, A_g, of the vibrational Raman spectrum. From the ECC the displacements involved in the BLA mode (B_1) can be estimated as the sum of the product between the square root of the intensity of the A_{1g} modes and the respective displacement vectors $\overrightarrow{L_i}$ as defined in equation 3, where c_1 is the normalization factor:

$$\overrightarrow{B_1} = c_1 \sum_{i \in A1g} \pm I_i^{1/2} \overrightarrow{L_i} \qquad (3)$$

The Raman intensity of each A_{1g} mode and their corresponding displacement vectors for each mode can be obtained from the B3LYP/6-31G(d,p) Raman calculations. Thus in this work the BLA mode is generated for each [n]CPP with the D_{nh} symmetry. In Figure 9a the C-C displacements involved in the BLA mode are shown for [8]CPP. Since displacement vectors are normalized, there are no absolute values associated with the BLA-like geometry change along the vibrational coordinate. In Figure 9b the displacements involved in the C-C stretching are characterized by the changes of the three parameters, δr, δr_1 and δr_2. The signs are the same for δr and δr_2, and the opposite for δr_1. In an attempt to compare them and being able to define the aromatic/quinonoid geometry change, in Figure 9c the ratios ($\delta r/\delta r_2$) and ($\delta r_1/\delta r_2$) are represented against *n*. It can be observed that the ratio ($\delta r/\delta r_2$) is ~ 2 and its value becomes smaller as *n* increases. On the other hand, the ratio ($\delta r_1/\delta r_2$) remains nearly constant at about -0.87 for any *n*. The positive ($\delta r/\delta r_2$) and higher ratio for the smaller *n* shows the strengthening of the C-C force constant along *r*, so a concomitant increase of the quinonoid character.

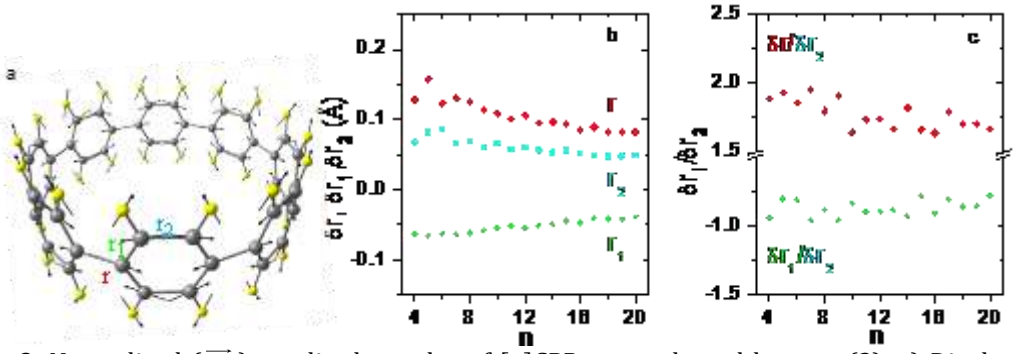

Figure 9. Normalized ($\overrightarrow{B_1}$) amplitude modes of [n]CPPs as evaluated by eqn. (3). a) Displacement pattern for [8]CPP. b) Components of the amplitude mode in terms of δr, δr_1 and δr_2 as a function of *n* (the signs comply with the BLA pattern). c) BLA ratios, ($\delta r_1/\delta r_2$) and ($\delta r/\delta r_2$), as a function of *n*.

10.3.2.2 Force Constant Analysis approximating the GA_{1g} Mode to the BLA Mode

The displacements analysis based on the ECC theory is only accessible from the computed Raman spectra. We cannot conduct an analogue quantitative analysis using the experimental spectra since we need not only the Raman shift, but also absolute Raman intensities, and the displacement vectors involved in each mode, experimentally not reachable. We have carried out an alternative approach to be able to experimentally quantify the quinonoid contribution in any molecular system through Raman spectroscopy. Within this model, we analyze the force constants involved in a hypothetical BLA mode under the two limiting configurations: totally benzoid and totally quinonoid, as described in Figure 10.

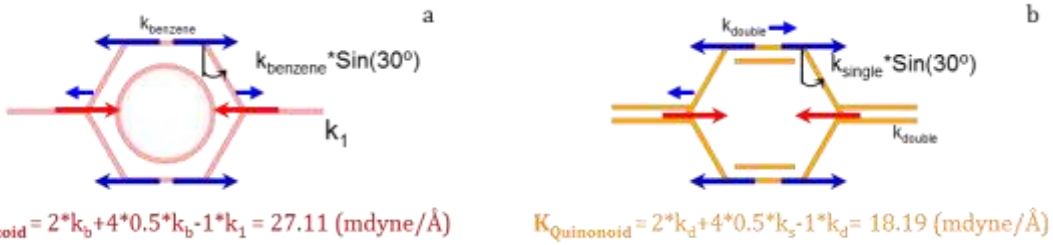

Figure 10. Vibrational pattern of the GA_{1g} mode of paraphenylene when: a) is totally benzoid and, b) totally quinonoid. Arrows indicate the carbon displacements, where in blue are the positive and in red the negative ones. We refer to vibrational amplitudes which are drawn in qualitative sizes so that we describe them as arbitrary relative displacements. K_B and K_Q represent the value of the total force constant of the arranged vibration on the circumferential axis when considered as totally benzoid and totally quinonoid, respectively. The used force constant values are summarized in Table 2.

Table 2. Force constant values used to estimate the total force constant of the BLA.

Ring with totally aromatic structure **0 % of quinonoidization** references taken from J. L. Jules et al. [65]		Ring with totally quinonoid structure **100 % of quinonoidization.** references taken from Y. Yamakita et al. [66]:	
$k_{benzoid}$ (k_b)	7.86 (mdyne/Å)	k_{double} (k_d)	7.875 (mdyne/Å)
k_1, C-C stretching of ethane	4.33 (mdyne/Å)	k_{single} (k_s)	5.156 (mdyne/Å)

With the structures of hypothetical totally quinonoid and benzoid phenyl units suggested in Figure 10 we get their relevant ring force constant in internal coordinates and according to the topology of the vibration we define the value of the force constant. We used reference force constants from the literature summarized in Table 2. From the values of $K_{Benzoid}$ or $K_{Quinonoid}$, the Raman shift, ω, for each limiting case can be estimated. A simple approximation to a diatomic molecule is used, equation 4, where K is the force constant and μ is the reduced mass:

$$\omega = \frac{1}{2\pi c}\sqrt{K/\mu} \tag{4}$$

$$\frac{\omega_{Quinonoide}}{\omega_{Benzoide}} = \sqrt{\frac{K_{Quinonoide}}{K_{Benzoide}}} = \sqrt{\frac{18.19}{27.11}} = \frac{1}{\sqrt{1.49}} = 0.819 \tag{5}$$

From the combination between the force constants ratio, equation 5, with equation 4, the frequency ratio benzoid/quinonoid can be calculated. Considering the same reduced mass for both tautomers and as ω_B that of 8a benzene mode, 1603 cm^{-1},[67,68] it can be estimated that:

100 % quinonoid → 1313 cm^{-1} **100 % benzoid → 1603 cm^{-1}**

The GA_{1g} mode involves all the rings of the structure, owing to the "rupture" of the bond length alternation pattern along the consecutive sequence of ---C=C-C=C-C=C--- bonds. We suspect that this mode has a strong ring character and therefore its frequency would mainly account for such character (i.e., quinonoidal). In this sense, the GA_{1g} mode could be approximated to the BLA mode and its Raman shift, represented in Figure 11, is valid to establish the degree of quinonoidization of the phenyl ring. The quinonoidization degree obtained is close to 3% per ring for [12]CPP, and about

17% in [5]CPP, thus showing that a highly aromatic character still remains. This indicates that there is certain $sp^2 \rightarrow sp^3$ re-hybridization due to the curvature, but that aromatic character remains.

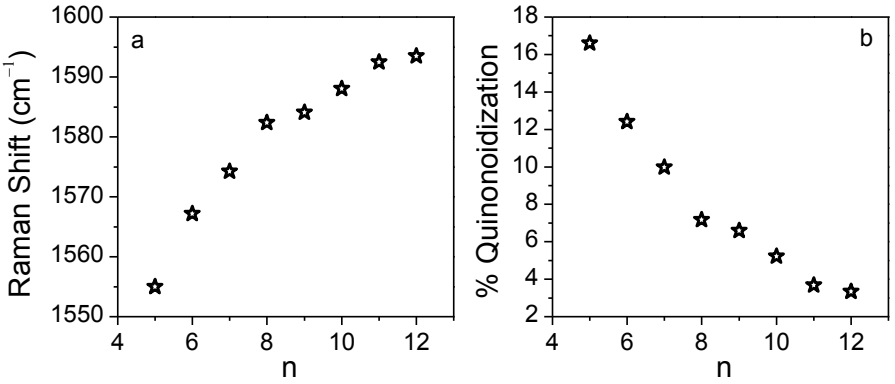

Figure 11. a) GA_{1g} band Raman shift as a function of *n* for the [n]CPPs. b) Variation of the quinonoid character of the [n]CPPs as a function of *n*.

10.3.2.3 Experimental Quinonoidization of [5]CPP

We have explored the energy difference between the two configurations, represented in Figure 12. At room conditions, [5]CPP is totally aromatic with the quinonoid configuration being a high energy minimum, about 37.5 kcal/mol above the aromatic one. We speculate about the possibility of leading the formation of a quinonoid [5]CPP structure. In order to reach such high energetic configuration we suggest the use of high pressure as modulating tool.[69] Therefore, high pressure was used to induce in [5]CPP the transition and to cross the A-Q energy barrier. Pressure induces bond length changes and more importantly also bond angle deformations. Thus, it could be more favorable than [5]CPP stands into its quinonoid configuration with larger α angle, rather than staying benzoid with such distorted shape.

In Figure 13 we plot the calculated B3LYP/6-31G(d,p) Raman spectra of the aromatic and quinonoid minima of the [5]CPP, together with the experimental Raman spectra of the pristine and recovered samples of [5]CPP, after a pressure of 10 GPa was reached. Computed Raman spectrum of the quinonoid [5]CPP presents about four contributions at the G band region, which could resemble the new features observed on the experimental spectrum of the recovered sample. Also the decreases in intensity of the 1200 cm^{-1} bands are significant and analog to those of the quinonoid tautomer. Regarding the low frequency region, the calculated p-RBM for the quinonoid tautomer is about 80 cm^{-1} downshifted from the aromatic one, as already anticipated. Consequently, we state that a configurational transition aromatic-quinonoid is induced by pressure in [5]CPP.

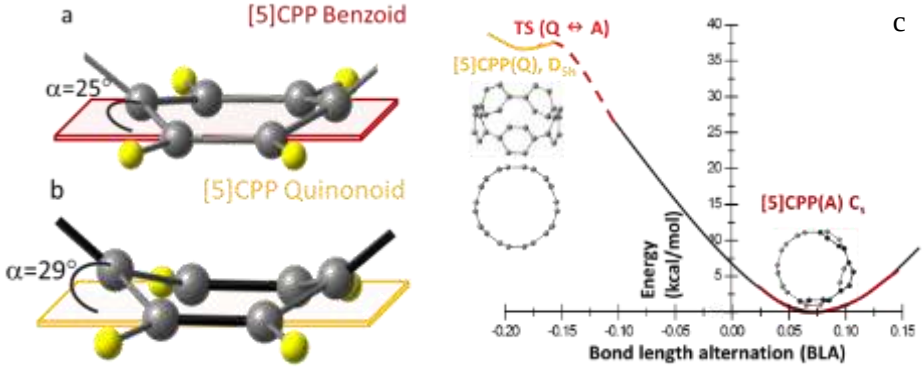

Figure 12. Side view of a phenyl unit in the [5]CPP optimized structures. DFT calculations at the B3LYP/6-31G(d,p) level. a) Benzoid configuration; b) Quinonoid configuration. The out of the phenyl plane bending angle has been marked. c) Schematic potential energy curves for [5]CPP, TS: transition state.

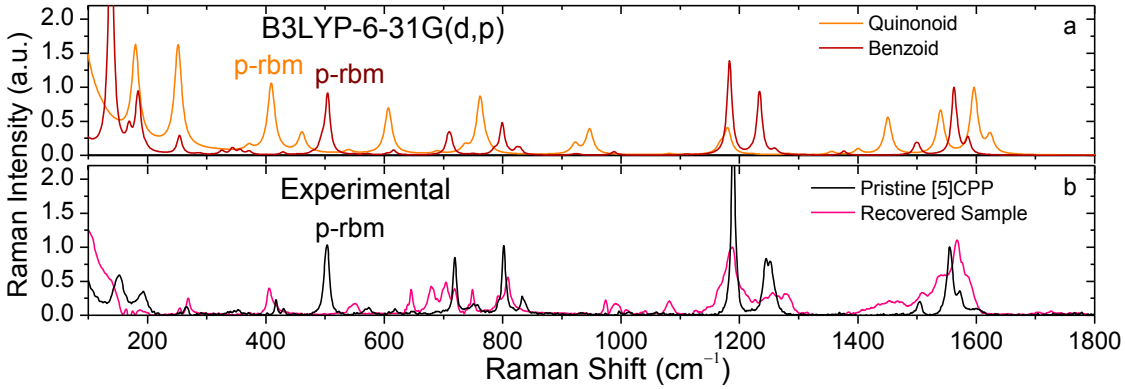

Figure 13. [5]CPP Raman spectra in the 100-1800 cm^{-1} region. a) Calculations for the optimized structures of the configuration: benzoid, brown line; quinonoid, orange line. Level B3LYP/6-31G(d,p), both spectra were sca3ed with 0.97. b) Experimental Raman spectra for: the pristine sample (black line) and recovered sample once pressure is released (pink line).

10.3.3 Conformational Studies of the [n]CPPs

We address the analysis of the conformational properties of the [n]CPPs as individual entities. Since the non-twisted D_{nh} structures do not correspond to global minimum, they are characterized by imaginary frequencies which follow a pattern as a function *n*. This allows us to relate the number or possible conformers with the number of imaginary frequencies of each D_{nh} mode. There are $((n/2)-1)$ different conformers for the even [n]CPPs and $((n-1)/2)$ for the odd [n]CPPs.

We have analyzed the energy difference between totally non-twisted configurations and the energy minimum twisted configuration. Such energy differences range in the order of 1 kcal/mol per phenyl ring, being in agreement with the energies barrier between torsional conformers suggested by Segawa et al.[36] Thus, non-twisted conformations in the larger [n]CPPs can be reachable by heating.

We have studied the effect that simultaneous thermal and laser excitation stresses cause on the [n]CPPs Raman spectra. Figure 14 shows the time evolution of the Raman spectra of [8]CPP, as a prototypical example, at 298 K by exciting with the 2.33 eV laser. Changes in the spectra are clearly visible resulting in a new peak at 1604 cm^{-1}. The time growth of the integrated area of this band (relative to that at 1582 cm^{-1}) allows us to obtain the rate constant for the process which, studied as a function of the temperature, gives us the activation barriers associated with the conversion towards the structure responsible for the new Raman component. A rotational energy barrier of 4.75 kcal/mol is determined for [8]CPP and of 5.26 kcal/mol for [12]CPP. These experimental activation energies are in excellent agreement with those energy barriers calculated for the full rotation of a given phenyl regarding their vicinal rings around the inter-ring C-C bonds. [5-12,29,36,517071]

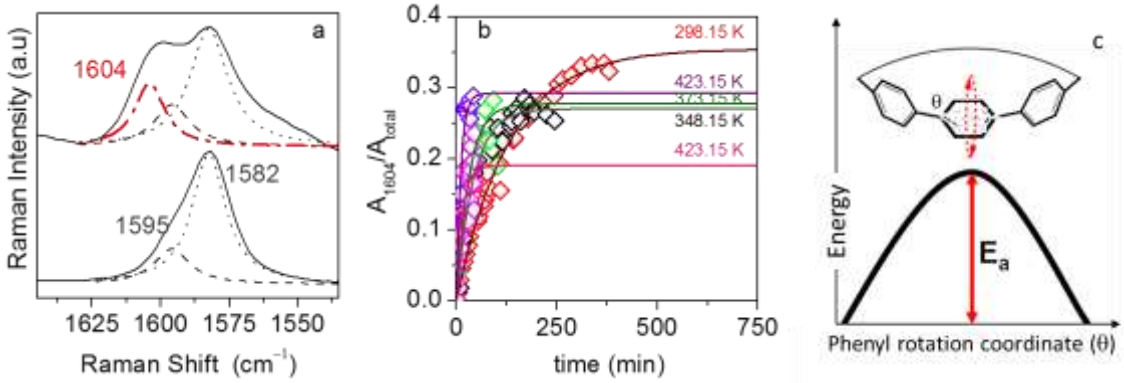

Figure 14. a) 532 nm Raman spectra of [8]CPP at 298 K. Top: initial spectrum; bottom: spectrum recorded after exposition time to the laser radiation of about 300 min. b) Ratio between the area of the 1604 cm^{-1} band and the total area of the features of this region as a function of the exposition time to the laser radiation; temperatures: red (298.15 K), black (348.15 K), green (373.15 K), violet (423.15 K) and pink (423.15 K). c) Scheme of the phenyl unit rotation with its energy barrier.

10.3.4 Study of the Radial Cyclic Conjugation

Besides, [n]CPPs can be used as models to understand the so far theoretical concept of radial cyclic electronic π conjugation. From the π cyclic conjugation terminology, we will analyze the required morphological parameters, and to which extent they may benefit the molecular properties. This understanding can provide us with the basic tools for future synthesis of molecular systems with desired properties.

However, as shown in the previous section, neutral species of the [n]CPPs preserve the aromatic character of their phenyl units, and delocalization within the phenyl units is small. So, oxidized species of [n]CPPs, cations and dications, are candidates for this interesting and challenging study. The removal of one electron is enough to induce the aromaticity rupture of the phenyl units, being compensated by the stabilization of the radial cyclic π–conjugation. For this reason, in this thesis the oxidized species of [n]CPPs (with *n* = 5-12) have been synthesized.

Figure 15 displays the near-resonant Raman spectra of the dications [n]CPP^{2+} and cations [n]CPP$^{\bullet+}$ in the G band region. In contrast to the neutrals, we observe two distinctive trends in the G bands:

- Raman spectra for the larger [n]CPP dications, [9]CPP^{2+} to [12]CPP^{2+}, display a larger number of features. For [8]CPP^{2+} to [5]CPP^{2+}, however, the spectra are similar to those of neutral ones.
- Raman shifts of the bands GA_{1g} and GE_{2g} of both cations and dications follow a V-shape as a function of *n*. It is observed that the species [8]CPP^{2+}/[8]CPP$^{\bullet+}$ exhibit the minimum value for these quantities. For the smaller cations, from [5]- to [8]CPP$^{\bullet+}$, it is observed that the Raman shifts are almost independent on *n*.

We have also conducted an exhaustive DFT analysis on neutral, cations and dications at the (U)B3LYP/6-31G(d,p) level. We find that while the smaller [n]CPPs^{2+} stay in a closed shell electronic configuration, around [9]CPP^{2+} there are changes towards an open shell electronic configuration. Thus, the smaller members of the series belong to the highest point group of symmetry with a homogenous charge distribution. The larger dications, from [9]CPP^{2+}, have a reduced symmetry, displaying domains with different charge and so, different aromatic-quinonoid character. Such symmetry rupture together with the existence of aromatic domains would explain why the Raman spectra of the larger dications become more complex. In Figure 16 molecular structures and computed charge distributions of [5]CPP^{2+} and [12]CPP^{2+} are schematized.

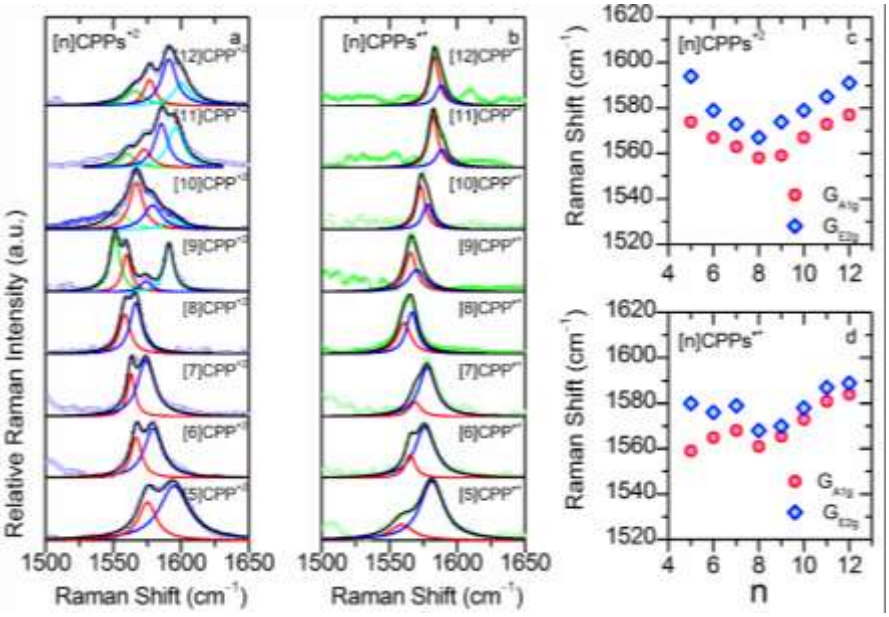

Figure 15. Raman spectra of the macrocycles in solution. a) [n]CPP^{2+} dicationic. b) [n]CPP$^{\bullet+}$ monocationic radicals. Red and blue lines are the GA_{1g} and GE_{2g} contributions, respectively. c) and d) G_{A1g} and G_{E2g} Raman shifts as a function of *n*.

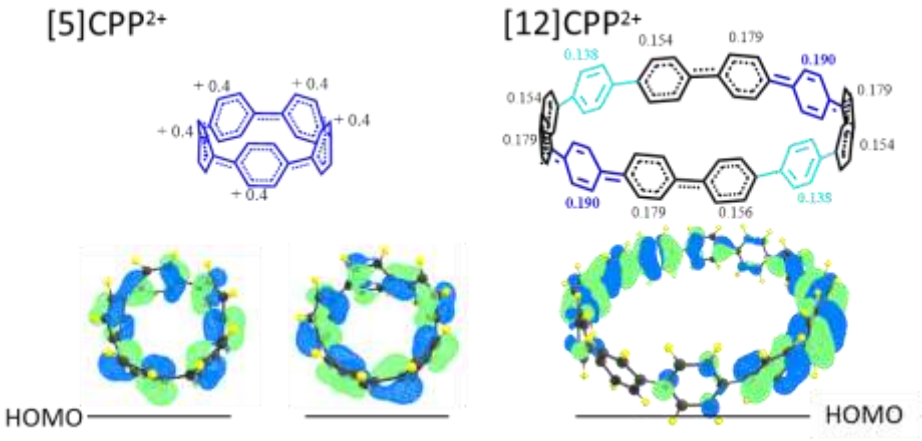

Figure 16. DFT-(U)B3LYP/6-31G(d,p) data. Top: per ring charge distribution of the dicationic species of *n* = 5 and *n* = 12. Bottom: HOMO orbital topologies ([5]CPP^{2+} is closed-shell singlet calculated at the DFT-B3LYP/6-31G(d,p) level, [12]CPP^{2+} is open-shell singlet calculated at the DFT-UB3LYP/6-31G(d,p) level).

Cyclic conjugation is related to the p_z overlap between neighboring units, so it is favored by smaller torsional angles between neighboring phenyl units. As shown in Figure 17a torsions in the smaller [n]CPP^{2+} with *n* from 5 to 8 are close to zero. Additionally in Figure 17b we observe that the BLAs change from neutrals to cations and even more to dications, BLA decrease with decreasing size. Dications smaller than [9]CPP^{2+} exhibit BLA negative, denoting the conjugational character along the structure. Consequently, we can conclude that the removal of electrons disrupts the phenyl aromaticity, facilitating electronic delocalization within the C-C skeleton.

We have complemented the structural analysis with calculations of the Nucleus-Indendent Chemical Shifts (NICS) at the (U)B3LYP/6-311+G(2df,p) level for each [n]CPP within its cavity.[72] As a reference we consider the benzene ring alone whose NICS(0) is –8 ppm in the center while NICS(1) calculated at 1 Å, indistinguishable above or below, amounts to –10 ppm. In Figure 17c, we summarize the obtained NICS values at the center of the cavity for each [n]CPP in neutral, cationic and dicationic state. In neutral [n]CPPs the NICS at the center are always non-zero. In the cations, NICS rapidly decrease with decreasing *n* towards –8 ppm for [5]CPP$^{\bullet+}$. Interestingly, for the dications NICS go to even lower values, –20 ppm for[5]CPP^{2+} and –5 ppm for [11]CPP^{2+}.

The conjunction of the computed results with the experimental Raman trends observed indicate that small [n]CPP^{2+}, from *n* < 9, are characterized by a totally different conjugation to that present in the neutral units. We can conclude that these small dications constitute a new experimentally available model of radial cyclic conjugation. This interpretation is supported by the EPR and NMR analysis of the dicationic species reported in the literature.[73]

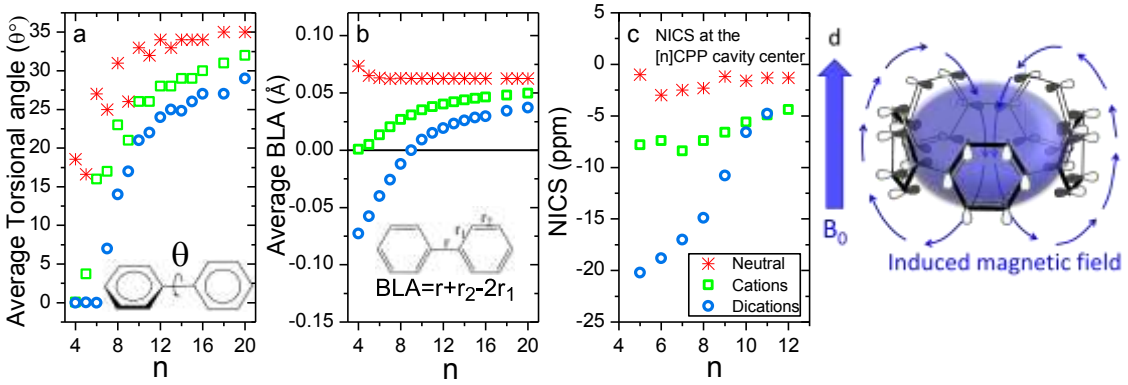

Figure 17. a) Size evolution of the interring torsional angles (θ, see inset). b) Size evolution of the average BLA parameter (see inset for the BLA definition). c) NICS at the center of the [n]CPP cavity as *n* function. d) Scheme representing the induced magnetic field in [5]CPP^{2+}.

10.3.5 Adaptability and Deformability of the [n]CPPs

[n]CPPs and SWCNTs are completely different systems but both are formed by conjugated units in a cylindrical fashion. Therefore, their properties that are intimately related with such electron rich cavities are the ones in which both of the systems converge. They are defined herein as follows: their pressure induced deformation towards peanut configuration and ability to host electron rich or electron poor π systems, stabilized by π-π concave-convex interactions. Due to the diameter purity, [n]CPPs offer the great advantage of control over all parameters that may interfere in any induced interaction. Moreover, given their purity, the characterization of any *in situ* procedure can be followed accurately.

10.3.5.1 Deformability of [6]CPP and [12]CPP

Internal strain can be modulated by application of external stresses or pressures, and such experiments have revealed key information about the structural and mechanical properties of SWCNTs. Thus, we have performed pressure-dependent Raman experiments using a sapphire anvil cell device to subject [n]CPPs at high pressures; maximum pressures around 8-10 GPa were achieved.

Figure 18a compares the Raman spectra of [6]CPP measured at ambient conditions, and after pressure was released. The 1600 cm^{-1} region is completely modified in terms of Raman shifts and number of contributions. The GE_{2g} mode around 1582 cm^{-1} splits into two contributions, while the GA_{1g} remains. These effects can be related with a pressure-induced deformation of the cycle towards a peanut configuration as depicted in Figure 18a. This permanent collapse of [6]CPP could be due to the formation stable of π-π interactions between the phenylenes. Similar deformations have been described for SWCNTs by Yao et al.[74] and by Cronin et al.,[75] and for MWCNTs by Yu et al.[76]

Additionally, significant frequency and spectral changes are found in the low frequency region as well. In Figure 18a we have marked the p-RBMs (E_{2g}) of the pristine sample and in pink those resulting in the recovered sample. It seems that there is an important splitting. By using the equation 2 and the values of the new features mentioned (409 and 933 cm^{-1}), diameters around 0.94 and 0.41 nm are obtained.

In Figure 18b we plot the Raman spectra of the pristine [12]CPP at room conditions and the recovered sample after a pressure cycle of about 10 GPa. It can be seen how the G bands, associated to the motions of C-C backbone of the structure, do not suffer any significant change, so these can be considered unaltered regarding their π bonding configuration. Additionally, the p-RBM remain unaltered and with a single contribution, indicating that non-permanent deformation might be induced along the pressure-cycle.

We conducted analogous studies for [n]CPPs from 5 to 12 finding that changes before and after the pressure cycle are progressively smaller as the size increases.

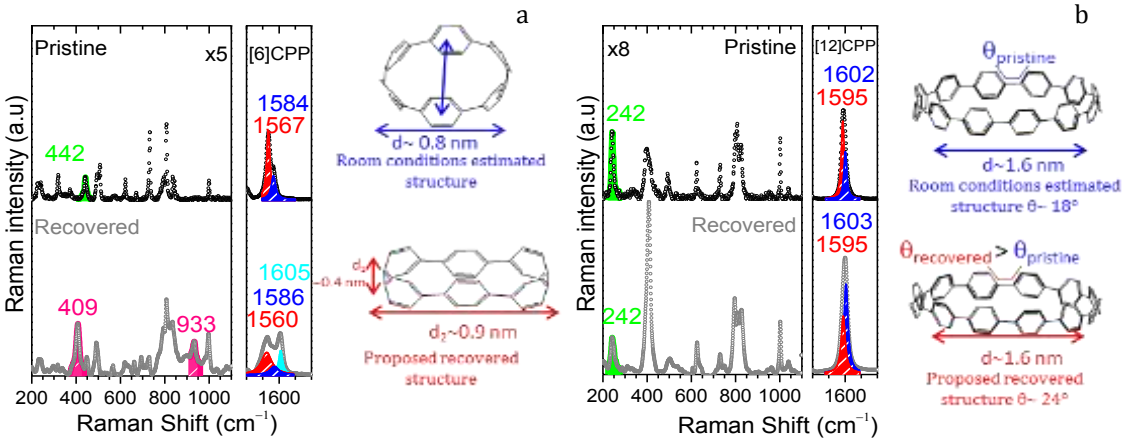

Figure 18. 785 nm Raman spectra of and suggested structures of: a) [6]CPP and b) [12]CPP, before, top and after, bottom, an applied pressure around 10 GPa.

10.3.5.2 Host-Guest Systems

We have used pressure to demonstrate the great adaptability of [n]CPPs that allows them to act as efficient guest and/or host molecules.

Synthesis of the First Double Nanohoop: [6]CPP@[12]CPP

First, we used 1:1 mixtures of [6]CPP and [12]CPP aiming to encapsulate [6]CPP by [12]CPP, just to emulate a ultrashort double walled CNT (DWCNT) or a "Russian doll", as called in the literature.[77] The mixture was subjected to a pressure of about 8 GPa and then released back to room pressure.

The Raman spectra of the [6]CPP - [12]CPP solid state mixture before and after the pressure cycle are displayed in Figure 19a. It is seen that while the initial sample presents the same features of the individual spectra of [6]CPP and [12]CPP, the spectrum of the recovered sample presents significant variations. There is a downshift in the bands of the 1600 cm^{-1} region, which may be caused by the van der Waals interactions between the [12]- and [6]CPP. Additionally, the p-RBM modes of both systems also slightly downshift which indicate that certain rearrangement between both of the structures might have been induced. Note that the distance between phenylenes of both [n]CPPs is slightly larger than the distance between layers of graphite, as seen in Figure 19b. Because all the facts described, it has been suggested that pressure induces the formation of intermolecular interactions between [6]CPP and [12]CPP, giving rise the double nanohoop, thus preventing [6]CPP to collapse. This observation is in good agreement with previous results observed in DWCNTs, where the outer tube acts as pressure protector of the inner tube.[78]

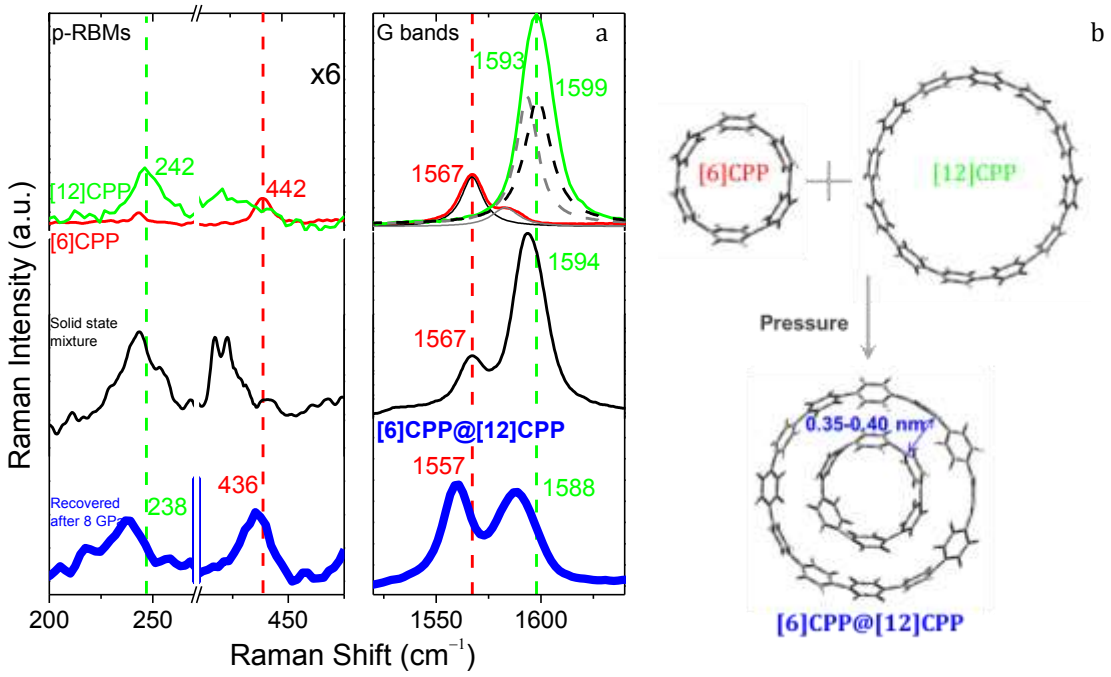

Figure 19. a) 532 nm Raman spectra. Top: [6]CPP and [12]CPP in red and green respectively. Middle spectrum corresponds to the solid state [6]CPP+[12]CPP mixture before any treatment. Bottom, [6]CPP and [12]CPP mixture after the pressure was released ([6]CPP@[12]CPP). b) Scheme of [6]CPP + [12]CPP molecular structures to form the double nanohoop: [6]CPP@[12]CPP.

Charge Transfer Complexes with Fullerene, $C_{60}^{\bullet-}$@[10]CPP$^{\bullet+}$

[n]CPPs can also accommodate C_{60} into their internal cavities, allowing us to explore the properties of [n]CPPs+C_{60} complexes, also in clear analogy with the "SWCNT+C_{60} peapods".[51,52] π–π interactions are responsible for the assembly of some [n]CPPs with C_{60}. Formation in solution of 1:1 stoichiometric supramolecular complexes driven by a surprisingly high exo-thermicity has previously been reported.[52]

We prepared 1:1 powdered mixtures of [10]CPP and C_{60} and applied pressures up to 10 GPa, which are well below the 22 GPa limit of chemical stability found for C_{60}.[79] Figure 20 displays the Raman spectra of the mixture recovered at ambient conditions after a pressure cycle. In the spectral range around 1460-1470 cm^{-1} we observe the two strongest Raman bands, one at the same frequency as pristine C_{60} and another one at 1463 cm^{-1}. In the [10]CPP region, at 1570-1600 cm^{-1}, we observe that the GA_{1g} band downshifts, from 1589 to 1569 cm^{-1}. Interestingly, our observations in the experiment with pressure substantially differ from those described for the formation in solution of the C_{60}@[10]CPP complex;[5,28] as seen in Figure 20, pressure promotes the appearance of new Raman bands that correlate perfectly with those of the C_{60} radical anion ($C_{60}^{\bullet-}$)[79] and [10]CPP radical cation ([10]CPP$^{\bullet+}$).

We have also observed changes in the region of the p-RBM. In the $C_{60}^{\bullet-}$@[10]CPP$^{\bullet+}$ complex, this mode upshifts by 8 cm^{-1} (296 cm^{-1}). According to the $(1/d)$ frequency dependence, this shift indicates a slight reduction of the [10]CPP size in the complex, or that the [10]CPP$^{\bullet+}$ is "compressed" owing to the loss of one electron and quinonoidization of the structure which the concomitant decrease of the radius. The C_{60} band at 270 cm^{-1} (cage squashing mode) scarcely shifts in the complex, in agreement with the barely observable displacement of just +1 cm^{-1} in K_3C_{60} ($C_{60}^{\bullet3-}$).[79]

The straightforward interpretation is that the application of pressure results in the release of one electron from the donor [10]CPP to the acceptor C_{60} yielding a charge-transfer charge separated complex, or a $C_{60}^{\bullet-}$@[10]CPP$^{\bullet+}$ salt.

Similar complexation experiments of C_{60} under pressure have been carried out with [9]CPP and [11]CPP, obtaining the corresponding supramolecular complexes.

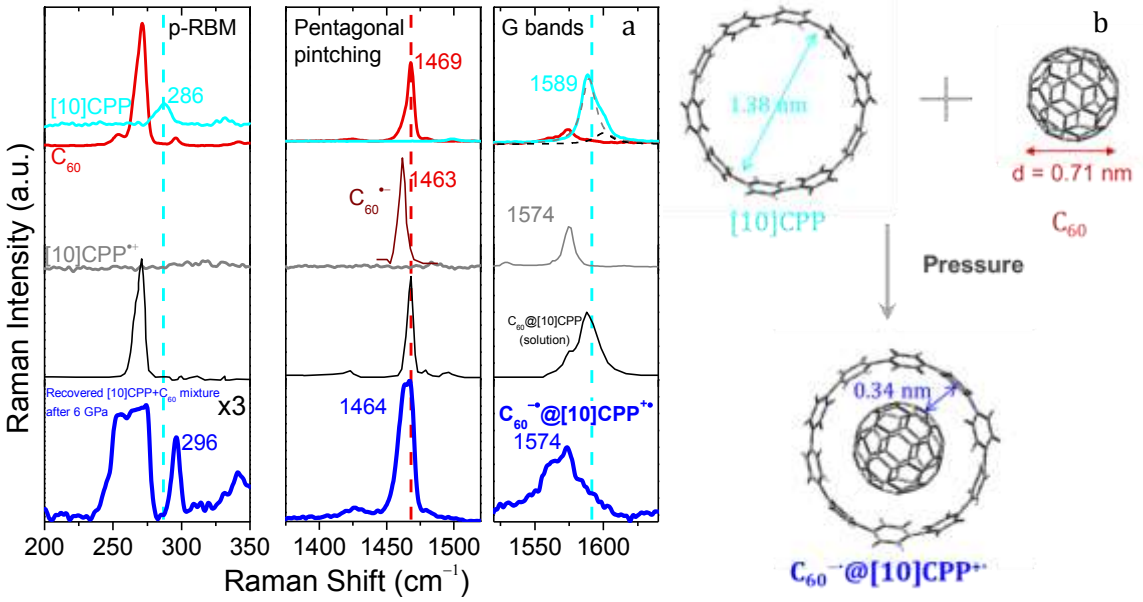

Figure 20. 785 nm Raman spectra of a) (top to bottom) C_{60} in solid state and [10]CPP in solid state; [10]CPP$^{+\bullet}$ and $C_{60}^{-\bullet}$ from Ref. [79]; C_{60}@[10]CPP formed in solution;[5,28] and $C_{60}^{-\bullet}$@[10]CPP$^{+\bullet}$ in solid state at room conditions after pressure release. b) Scheme of [10]CPP + C_{60} molecular structures to form $C_{60}^{-\bullet}$@[10]CPP$^{+\bullet}$ by one-electron concave-convex electron transfer.

Modulation of the C_{70} Orientation into the [10]CPP from Lying to Standing

The electronic and structural properties of host-guest supramolecular 1:1 complexes of [n]CPPs and C_{70}, C_{70}@[n]CPP with n = 9, 10, 11 and 12,[31] have been thoroughly analyzed by using Raman spectroscopy. We have found that the vibrational Raman spectra, and in particular the bands associated with the C-C stretching tangential G modes and with the radial breathing modes of both [n]CPP and C_{70}, contain the relevant electronic and structural information resulting from complexation.

Depending on their sizes, the [n]CPPs have been shown to be able to adapt their structures to form stable couplings with C_{70}: in C_{70}@[10]CPP the fullerene is surrounded by the [10]CPP by its equatorial part, or lying orientation, a situation that we now further characterize as having a less staggered structure for the CPP. In C_{70}@[11]CPP the fullerene is wrapped up through its long ellipsoidal axis, or standing orientation, where the nanohoop becomes oval-shaped with close contacts in the C_{70} poles and less conformational restriction in the flattened region.

The application of pressure to C_{70}@[10]CPP induces an overall up-shift of the whole spectrum together with the typical spectral broadening as exerted by the increment of the intermolecular contacts in the pressed sample. After pressure release the spectrum does not recover its original aspect, the GA_{1g} band up-shifts from 1581 to 1584 cm^{-1} while the C_{70} tangential mode band up-shifts from 1562 to 1567 cm^{-1}. The radial breathing mode of C_{70} at 456 cm^{-1} changes by –3 cm^{-1} as in the pristine C_{70}@[11]CPP, with standing orientation. This fact, together with the G bands evolution, let us consider that pressure might have induced the formation of the standing C_{70}@[10]CPP complex, where the strongest interaction between [10]CPP and C_{70} goes through these polar regions of the ellipse.

Additionally, analogue high pressure studies were conducted for C_{70}@[11]CPP. However, this complex resists in its standing position the applied pressure and it is by heating that the CPP ring seems to rotate towards a lying disposition by finally recovering its "isolated" spherical aspect.

These results evidence the [n]CPP outstanding chemical reactivity in their internal cavity, their flexibility, and their huge capability to adapt to many different physico-chemical environments. In addition, in the analysis of the [n]CPP as models of SWCNTs, the characterization by Raman of these well-defined complexes might help us to understand the complexity of these peapods between fullerene and SWCNTs.[80-82]

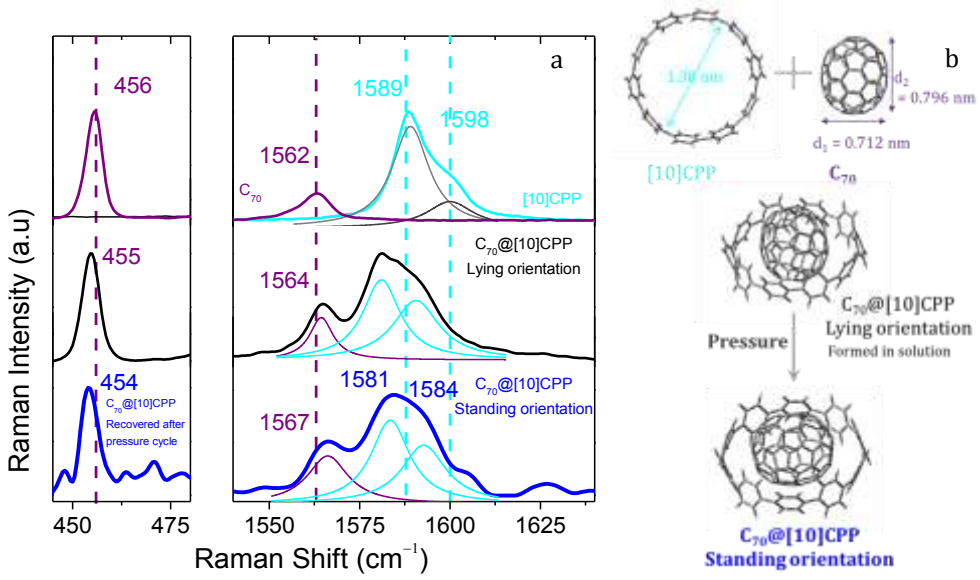

Figure 21. a) Solid state 785 nm Raman spectra in solid state at room conditions from top to bottom of: a) [10]CPP (cyan) and C_{70} (red); C_{70}@[10]CPP under its lying conformation before pressure cycle and; C_{70}@[10]CPP after pressure cycle. b) Scheme of C_{70}@[10]CPP under its lying conformation and suggested pressure effect on C_{70}@[10]CPP leading to its standing conformation.

10.3.6 Evaluation of the Mechanical Response of the [n]CPPs

This section summarizes the results about the Raman study on [n]CPPs under pressure. A sapphire anvil cell has been used for such studies. In the majority of the [n]CPPs maximum pressures of around 12 GPa were achieved.

10.3.6.1 Raman Spectroscopy of [n]CPPs under High Pressure

Valuable information can be extracted of the analysis of the pressure dependence of the Raman spectra. In Figure 22 Raman shifts of the GA_{1g} and GE_{2g} modes are plotted as a function of the pressure for each of the [n]CPPs under study. These G-like modes shift linearly over two regimes, with a change in gradient at a pressure transition which is higher as the [n]CPP diameter is lower, ranging from 0.6 GPa for the [12]CPP to 5.8 GPa for the [5]CPP. Interestingly, we observe a similar behavior in the Raman shift as a function of pressure for all the bands which involve C-C stretching modes. This behavior has been previously reported for the G bands of the CNTs,[74,83] and it has been related to the loss of their cylindrical shape and their ovallization. Thus, pressure effects could be described as:

- Firstly, at pressures lower than *PT*, pressure affects to molecular bonds and in a minor degree to molecular angles.
- At pressures higher than *PT*, pressure affects mostly bond angles towards ovallization of the tube and C-C bonds remain almost unaltered.

Such description is in agreement with the behavior followed by the G bands, C-C stretching bands: these in the first regime depict larger pressure coefficients than in the second regime. C-C bonds are harder and more rigid than bond angles; then, the first regime is referred as hard phase and the second one as soft phase of the tube.[84]

Moreover, these results allow us to obtain, for the first time, the pressure coefficients for the G-like bands and RBMs of the [n]CPPs. In Figure 23a we have plotted the pressure coefficients of the GA_{1g} and GE_{2g} bands as a function of the diameter. As seen, larger [n]CPPs exhibit the higher pressure coefficients. In addition, [5]- and [6]CPP depict larger pressure coefficients than [8]CPP. Such an issue could be justified because of their large strain, which makes that pressure-induced changes are quite different in the smaller cycles. With these findings and other results not shown in this summary, our conclusions are that [5]CPP under pressure is deformed towards a more bent configuration, quinonoid, and [6]CPP towards a permanent peanut configuration with a more benzoid structure.

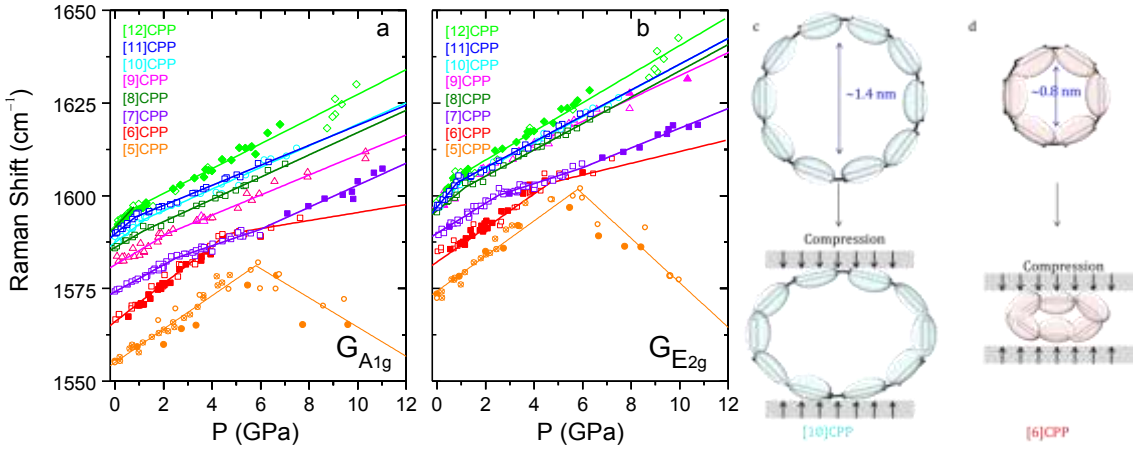

Figure 22. Pressure dependence of the Raman shifts of G modes for the [n]CPPs. a) GA_{1g} and b) GE_{2g} bands. Closed and open symbols correspond to different measured runs. Scheme of the π electron density modulation with pressure along the CPP cross section, c) [10]CPP, d) [6]CPP.

In Figure 23a we have compared with our [n]CPPs results the limited available pressure coefficients of the G bands of SWCNTs before *PT* as a function of diameter.[84] Interestingly, while the pressure coefficients of the G bands of the [n]CPPs depict an V-shape as a function of diameter, with a minimum around [8]CPP, the available pressure coefficients of SWCNTs show a linear growth with the increasing diameter. Consequently, this V-shape is related with configurational changes entirely related with [n]CPPs as highly cyclic conjugated entities and not as ultra-short SWCNTs. Unfortunately, to our knowledge, experimental results on armchair CNTs of such small diameter are not yet described, but it is expected that deformation observed in [5]CPP is uniquely due to its molecular character, thus it is probable that in CNTs other effects are induced by pressure.

Pressure coefficients of RBMs of the [n]CPPs show diameter dependence similar to that presented by their analogous SWCNTs. In Figure 23b we have plotted together the pressure coefficients of the RBMs and p-RBMs of the [n]CPPs for pressures lower than *PT*. We have also compared with pressure coefficients given in the literature for SWCNTs.[84,85] Pressure coefficients of the [n]CPPs and SWCNTs follow an analogue linear trend as a function of the diameter, with a similar slope. On the other hand, we see that the p-RBMs also follow a linear increase of their pressure coefficients with the increasing diameter. However, the slope of this line is about three times steeper than for the RBMs. Thus, for [n]CPPs of largest diameters, p-RBMs are very sensitive to pressure. Interestingly, while the observed trend of the pressure coefficients of the G bands is a common factor with all the bands which involve C-C stretching, the RBMs and p-RBMs are the only ones which follow a continuous linear increase with increasing size. This fact highlights the circumferential origin of the RBMs and p-RBMs modes. Differences in the pressure coefficient trends between [n]CPPs and SWCNTs are proof that [n]CPPs represent unique entities by themselves, different to carbon nanotubes.

Finally, from the high pressure behavior of the main [n]CPPs Raman bands we can conclude that [n]CPPs and SWCNTs share several common issues in terms of the diameter dependence of the pressure coefficients and kinks on their Raman shifts with pressure. Subsequently, we can consider that pressure induces analogue effects on their cylindrical shape, however, the fact that pressure coefficients have quite different values reveals the different structural nature of both systems.

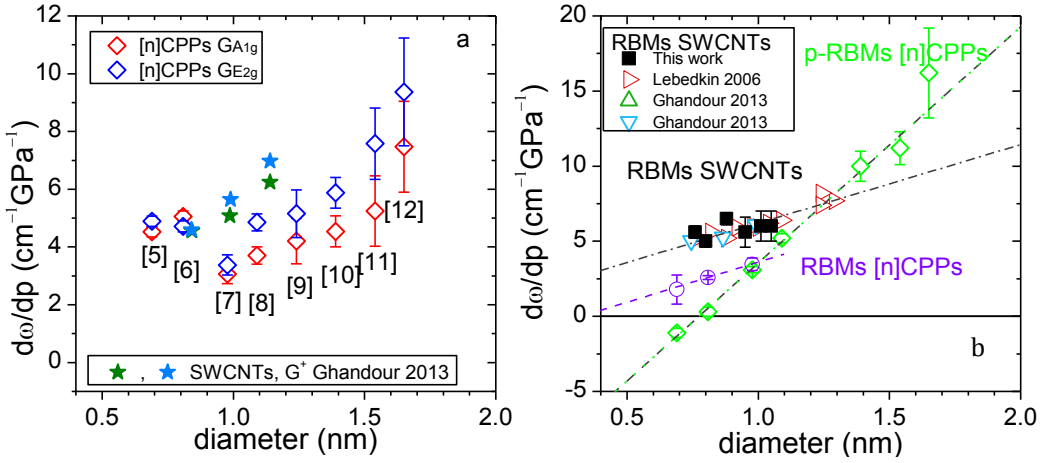

Figure 23. a) Pressure coefficients of the G modes, (◇) GE_{2g} mode and (◇) GA_{1g} mode for [5-12]CPPs before *PT* plotted against a) diameter and b) number of benzenes which form the [n]CPP and [n]LPP. Data from SWCNTs: (★) and (★) G^+ band from Ghandour et al. [85]. b) Pressure coefficients of the circumferential modes represented against their diameter for [n]CPPs and SWCNTs. Data for the [n]CPPs: (◇) p-RBMs and (○) RBMs. Data for the RBMs of SWCNTs: (■) this work; (▷) Lebedkin et al. [86], and (△, ▽) Ghandour et al. [85]. Each data set has been fitted to a linear trend.

10.3.6.2 Molecular Entities with one of the Highest Mechanical Strength

For SWCNTs it has also been reported that the physical deformations of their cross section are strongly diameter dependent, easier for the tubes of larger diameter, i.e., lower pressures are needed to induce the ovallization.[84,87,88] In Figure 24b we have the experimental pressures obtained for the [n]CPPs from the slope-changes of the results plotted in Figure 22a,b. Some data reported in the literature for SWCNTs are also shown as a function of diameter.[89,90]

Previous studies in SWCNTs have proposed that the transition from circular to oval can be understood by the continuum theory of the buckling of elastic rings.[91-95] This theory relates the pressure at which a tube losses its circular cross section with the tube radius before any strain is applied, *R*, and it stablishes that *PT* follows a power law:

$$PT = \frac{3D}{R^3} \tag{6}$$

where *D* is the flexural rigidity which is an important characteristic of any material and it is related with the dependence of the strain energy on its curvature along some direction. In case of dealing with layered materials this mechanical parameter is also referred as bending stiffness or elastic moduli of a layer. With our experimental results of *PT* of the Figure 24a and the equation 6 we have obtained a flexural rigidity equals to (0.57 ± 0.02) eV for [n]CPPs, in good agreement with the typical values of SWCNTs, ranging between 0.6 and 1.4 eV.[84,87,96]

Moreover, in SWCNTs "Pressure transition", *PT*, is related not only with the loss of their circular shape, but also with the pressure at which they change from a hard phase to a soft phase.[84,97] At pressures lower than *PT*, compression induces a shrinking of the circular shape. On the other hand, at pressures higher than *PT*, the structures respond to the external pressure by the modification of their bond angles for an oval cross section, giving rise to a soft phase. Considering that [n]CPPs follow the same classical rules as CNTs do within their radial direction, we use the model proposed by Sun et al. for SWCNTs which connects *PT* with the bulk modulus in the hard phase (B_h):[84]

$$B_h = \frac{6D}{h^2 R} \tag{7}$$

where we have taken *h*, the tube thickness, equals to 0.66 Å, as in SWCNTs.[84]

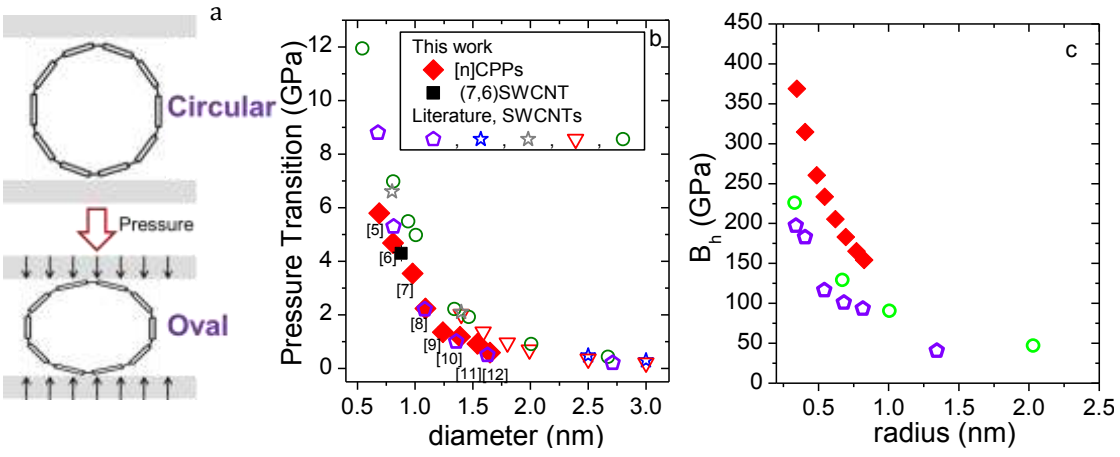

Figure 24. a) Scheme of the change over the cross section of [10]CPP. b) Pressure transition as a function of diameter of: (◆) [n]CPPs obtained from the Raman shift as a function of pressure of the G bands and 1200 cm^{-1} bands; (■) (7,6) SWCNTs, this work. SWCNTs data from the literature. c) Radial moduli as a function of the [n]CPP radius for the hard phases before deformation: (◆) [n]CPPs results estimated through the equations (6-7). (⬠) theoretical calculations from Sun et al. [84]; (○) theoretical and (☆) experimental data from Elliot et al. [87], (▽) circular to oval transition and (☆) collapse pressures from Hasegawa et al. [88] and (○) for armchair CNTs from Itami et al. [97].

In order to compare the hard phase radial bulk modulus of [n]CPPs with those of SWCNTs in Figure 24 we represent the B_h of SWCNTs taken from the literature,[84,97] and our estimated [n]CPPs results. It can be observed that both B_h values follow a similar behavior. However, the values for [n]cPPs are higher than those of SWCNTs,[97,98] ranging from ~150 GPa for [12]CPP to ~370 GPa for [5]CPP. These results show that while CPPs remain in their radial hard phase these can be even stiffer than SWCNTs. It can be highlighted the value B_h of [5]CPP, about 370 GPa, is twice as large as those of the smallest SWCNTs and it is close that of diamond, 445 GPa.[99] This means that the bulk moduli of the smaller [n]CPPs are extremely high, comparable to that of the strongest material. This fact can be understood because of the high strain of the [5]CPP, about 114 kcal mol^{-1}, which provides it with large resistance to deformation and makes it a very rigid system.

10.4 Conclusion

[n]CPPs exhibit exceptional properties exclusively related to their cyclic aromatic configuration such as quinonoidization, radial cyclic π–conjugation and biradical character. Furthermore, the fact that SWCNTs and [n]CPPs are formed by analogue backbone with the same shape confers them with shared properties related with their tubular configuration: a high capability to host systems with an appropriate size and their high radial bulk modulus.

10.5 Fundamental Contributions of this Ph. D. Dissertation

One of the fundamentals of this thesis has been the experimental, theoretical and computational assignment of the main [n]CPPs active Raman modes. Through a deep comparison between the shared features between [n]CPPs with SWCNTs and [n]LPPs, we provide relations which directly connect the bending and aromatic character with the Raman shift of the G bands of the [n]CPPs, the extent of the π delocalization with the intensity ratio of the 1200 cm^{-1} A_{1g} bands and their diameter with the Raman shift of the p-RBMs.

We demonstrate that in [n]CPPs the alteration of the planarity of the phenylenes must disturb the structural and electronic configuration, while conserving their aromatic character. In this work we establish and parametrize the increase of the quinonoidal character with the decreasing size involved in the [n]CPP aromatic ground state. Our results suggest that there is an increase of the quinonoidal character with the decreasing size, ranging from 3 % in [12]CPP to 17 % in [5]CPP.

Additionally, the exploration of the potential energy surface of the [n]CPPs shows that only the most strained cycles, [4]- and [5]CPP, have a highly energetic quinonoid minimum. By the compression of [5]CPP we reach the first purely quinonoid cyclic molecular structure, and to our knowledge comparable species have not been reported yet.

We have experimentally approached the so far theoretical concept of radial cyclic π–conjugation. We demonstrate that the removal of one electron and two electrons from small [n]CPPs (n < 9) induces the phenyl aromaticity rupture. The loss of aromaticity is totally compensated by the stabilization of the radial cyclic π–conjugation, and small dications with even electron number become the first experimentally reachable models to explore the radial cyclic π–conjugation.

Our results demonstrate that [n]CPPs are able to adapt in terms of shape and also electronic charge, so they are perfect to host in their cavity carbon systems with high electron density. We have also probed that [n]CPPs are highly deformable in terms of circular shape and torsional angles. Additionally, we have estimated that the smallest of the [n]CPPs could be among the stiffest molecular systems making [n]CPPs even more valuable molecular systems.

Summarizing, with this work we contribute to the fundamental knowledge of the [n]CPPs field as tentative models for cyclic π conjugation and quinonoidization. Additionally, our findings can contribute to their development as carbon nanomaterials exploring their mechanical resistance to deformation and the modulation of their structural and electronic properties with external parameters.

10.6 References

1 A. Kekulé, *Liebigs Ann.* **137**, 129–196 (1866).

2 G. Herzberg, *Infrared and Raman spectra of polyatomic molecules*, Van Nostrand, Princeton (1954).

3 C. R. Bailey, C. K. Ingold, H. G. Poole, C. L. Wilson, *J. Chem. Soc*. 222–235 (1946).

4 M. Kertesz, C. H. Choi, S. Yang, *Chem. Rev*. **105**, 3448–3481 (2005).

5 J. Xia, J. W. Bacon, R. Jasti, *Chem. Sci*. **3**, 3018–3021 (2012).

6 P. J. Evans, E. R. Darzi, R. Jasti, *Nature Chem.* **6**, 404–408 (2014).

7 J. Xia, R. Jasti, *Angew. Chem. Int. Ed.* **51**, 2474–2476 (2012).

8 F. Sibbel, K. Matsui, Y. Segawa, A. Studer, K. Itami, *Chem. Commun.* **50**, 954–956 (2014).

9 S. Yamago, Y. Watanabe, T. Iwamoto, *Angew. Chem. Int. Ed.* **49**, 757–759 (2010).

10 Y. Segawa, P. Šenel, S. Matsuura, H. Omachi, K. Itami, *Chem. Lett*. **40**, 423–425 (2011).

11 E. Kayahara, Y. Sakamoto, T. Suzuki, S. Yamago, *Org. Lett*. **14**, 3284–3287 (2012).

12 Y. Segawa, S. Miyamoto, H. Omachi, S. Matsuura, P. Senel, T. Sasamori, N. Tokitoh, K. Itami, *Angew. Chem. Int. Ed.* **50**, 3244–3248 (2011).

13 R. Jasti, J. Bhattacharjee, J. B. Neaton, C. R. Bertozzi, *J. Am. Chem. Soc*. **130**, 17646–7647 (2008).

14 Y. Matsuo, K. Tahara, M. Sawamura, E. Nakamura, *J. Am. Chem. Soc*. **126**, 8725–8734 (2004).

15 H. S. Choi, K. S. Kim, *Angew. Chem. Int. Ed*. **38**, 2256–2258 (1999).

16 R. Herges, *Chem. Rev.* **106**, 4820–4842 (2006).

17 E. S. Hirst, F. Wang, R. Jasti, *Org. Lett.* **13**, 6220–6223 (2011).

18 P. Li, T. J. Sisto, E. R. Darzi, R. Jasti, *Org. Lett.* **16**, 182–185 (2014).

19 K. Tahara, Y. Tobe, *Chem. Rev*. **106**, 5274–5290 (2006).

20 T. J. Sisto, M. R. Golder, E. S. Hirst, R. Jasti, *J. Am. Chem. Soc*. **133**, 15800–15802 (2011).

21 T. J. Sisto, R. Jasti, *Synlett* **23**, 483–489 (2012).

22 E. S. Hirst, R. Jasti, *J. Org. Chem*. **77**, 10473–10478 (2012).

23 R. Jasti, C. R. Bertozzi, *Chem. Phys. Lett*. **494**, 1–7 (2010).

24 B. D. Steinberg, T. L. Scott, *Angew. Chem. Int. Ed*. **48**, 5400–5402 (2009).

25 H. B. Li, A. J. Page, S. Irle, K. Morokuma, *Chem. Phys. Chem.* **13**, 1479–1485 (2012).

26 H. B. Li, A. J. Page, S. Irle, K. Morokuma, *J. Am. Chem. Soc*. **134**, 15887–15896 (2012).

27 H. Omachi, T. Nakayama, E. Takahashi, Y. Segawa, K. Itami, *Nature Chem*. **5**, 572–576 (2013).

28 T. Iwamoto, Y. Watanabe, T. Sadahiro, T. Haino, S. Yamago, *Angew. Chem. Int. Ed.* **50**, 8342–8344 (2011).

29 U. H. F. Bunz, S. Menning, N. Martín, *Angew. Chem. Int. Ed.* **51**, 7094–7101 (2012).

30 S. Schrettl, H. Frauenrath, *Angew. Chem. Int. Ed.* **51**, 6569–6571 (2012).

31 T. Iwamoto, Y. Watanabe, H. Takaya, T. Haino, N. Yasuda, S. Yamago, *Chem. – Eur. J*. **19**, 14061–14068 (2013).

32 M. Gussoni, C. Castiglioni, and G. Zerbi, *Spectroscopy of Advanced Materials*, edited by R. J. H. Clark, R. E. Hester ,Wiley, New York, Vol. 11, p. 251(1991).

33 E. Ehrenfreund, Z. Vardeny, O. Brafman, B. Horovitz, *Phys. Rev. B* **36**, 1535–1553 (1987).

34 H. Chen, M. R. Golder, F. Wang, R. Jasti, A. K. Swan, *Carbon* **67**, 203–213 (2014).

35 V. Hernandez, C. Castiglioni, M. Del Zoppo, G. Zerbi, *Phys. Rev. B* **50**, 9815–9823 (1994).

36 Y. Segawa, H. Omachi, K. Itami, *Org. Lett.* **12**, 2262–2265 (2010).

37 Y. Segawa, A. Fukazawa, S. Matsuura, H. Omachi, S. Yamaguchi, S. Irle, K. Itami, *Org. Biomol. Chem*. **10**, 5979–5984 (2012).

38 T. Iwamoto, Y. Watanabe, Y. Sakamoto, T. Suzuki, S. Yamago, *J. Am. Chem. Soc.* **133**, 8354–8361 (2011).

39 M. Rinke, H. Gusten, H. J. Ache. *J. Phys. Chem.* **90**, 2666–2669 (1986).

40 K. N. Baker, A. V .Frai, T. Resch, H. C. Knachel, W. W. Adams, E. P. Socci, B. L. Farmer, *Polymer* **34**,1571–1587 (1993).

41 P. A. Irvine, D. C. Wu, P. J Flory, *J. Chem. Soc., Faraday Trans. 1* **80**, 1795–1806 (1984).

42 J. L. Bredas, R. R. Chance, R. Silbey, *Phys. Rev. B* **26**, 5843–5854 (1982).

43 T. A. Skotheim, *Handbook of Conducting Polymers*, Dekker,New York, (1986).

44 J. L. Bredas and R. R. Chance*, Conjugated Polymeric Materials*, Kluwer Academic, Dordrecht, (1990).

45 Y. S. Lee, M. Kertesz, R. L. Elsenbaumer, *Chem. Mater*. **2**, 526–530 (1990).

46 S. E. Lewis, *Chem. Soc. Rev.* **44**, 2221–2304 (2015).

47 T. Iwamoto, Y. Watanabe, H. Takaya, T. Haino, N. Yasuda, S. Yamago, *Chem. – Eur. J*. **19**, 14061–14068 (2013).

48 T. J. Sisto, X. Tian, R. Jasti, *J. Org. Chem*. **77**, 5857–5860 (2012).

49 B. Anis, F. Börrnert, M. H. Rümmeli, C. A. Kuntscher, *J. Phys. Chem. C* **117**, 21995–22001 (2013).

50 B. W. Smith, M. Monthioux, D. E. Luzzi, *Nature* **396**, 323–324 (1998).

51 E. R. Darzi, R. Jasti, *Chem. Soc. Rev.* **44**, 6401–6410 (2015).

52 S. Fomine, M. G. Zolotukhin, P. Guadarrama, *J. Mol. Model.* **18**, 4025–4032 (2012).

53 H. Isobe, S. Hitosugi, T. Yamasaki, R. Iizuka, *Chem. Sci*. **4**, 1293–1297 (2013).

54 S. Hitosugi, R. Iizuka, T. Yamasaki, R. Zhang, Y. Murata, H. Isobe, *Org. Lett*. **15**, 3199–3201 (2013).

55 *Carbon nanotubes and Related structures. Synthesis, Characterization, Functionalization and Properties* (Eds.: N. Martín, D. M. Guldi), Wiley-VCH, Weinheim (2010).

56 G. Heimel, D. Somitsch, P. Knoll, J. L. Brédas, E. Zojer, *J. Chem. Phys.* **122**, 114511 (2005).

57 E. H. Haroz, J. G. Duque, X. Tu, M. Zheng, A. R. Hight Walker, R. H. Hauge, S. K. Doorn, J. Kono, *Nanoscale* **5**, 1411–1439 (2013).

58 M. Peña-Alvarez, P. M. Burrezo, M. Kertesz, T. Iwamoto, S. Yamago, J. Xia, R. Jasti, J. T. López Navarrete, M. Taravillo, V. G. Baonza, J. Casado, *Angew. Chem. Int. Ed*. **53**, 7033–7037 (2014).

59 L. W. Shacklette, H. Eckhardt, R. R. Chance, G. G. Miller, D. M. Ivory, R. H. Baughman, *J. Chem. Phys.* **73**, 4098–4120 (1980).

60 H. Ohtsuka, Y. Furukawa, M. Tasumi, *Spectrochim. Acta. Part A* **49**, 731–737 (1993).

61 S. M. Bachrach, D. Stück*, J. Org. Chem*. **75**, 6595–6604 (2010).

62 B. Horovitz, *Solid State Commun.* **41**, 729–734 (1982).

63 G. Zerbi, M. Gussoni, C. Castiglioni, in *Conjugated Polymers,* edited by J. L. Bredas and J. Silbey, Kluwer, New York, p. 435 (1991).

64 M. G. Gussoni, C. Castiglioni, G. Zerbi, *Spectroscopy of Advanced Materials*, edited by R. J. H. Clark, R. E. Hester, Wiley, New York, Vol. 11, p. 251(1991).

65 J. L. Jules, J. R. Lombardi, *J. Mol. Struc. (Theochem)* **255**, 664–665 (2003).

66 Y. Yamakita, M. Tamusi, *J. Phys. Chem.* **99**, 8524–8534 (1995).

67 E. B. Wilson, *Phys. Rev*. **45,** 706–714 (1934).

68 R. W. Wood, *Phys. Rev*. **36**, 1431-1434 (1930).

69 M. M. Caruso, D. A. Davis, Q. Shen, S. A. Odom, N. R. Sottos, S. R. White, J. S. Moore, *Chem. Rev*. **109**, 5755–5798 (2009).

70 S. Taubert, D. Sundholm, F. Pichierri, *J. Org. Chem*. **75**, 5867–5874 (2010).

71 S. Schrettl and H. Frauenrath, *Angew. Chem. Int. Ed.* **51**, 6569–6571 (2012).

72 Z. Chen, C. S. Wannere, C. Corminboeuf, R. Putcha, P. V. R. Schleyer, *Chem. Rev.* **105**, 3842–3888 (2005).

73 E. Kayahara, T. Kouyama, T. Kato, S. Yamago. *J. Am. Chem. Soc.* DOI: 10.1021/jacs.5b10855 (2015).

74 M. Yao, Z. Wang, B. Liu, Y. Zou. S. Yu, W. Lin, Y. Hou, S. Pan, M. Jin, B. Zou, T. Ciu, G. Zou, B. Sundqvist, *Phys. Rev. B* **78**, 205411 (2008).

75 S. B. Cronin, A. K. Swan, M. S. Ünlü, B. B. Goldberg, M. S. Dresselhaus, M. Tinkham, *Phys. Rev. B* **72**, 035425 (2005).

76 M. F. Yu, T. Kowalewski, R. S. Ruoff, *Phys. Rev. Lett*. **86**, 87–90 (2001).

77 E. del Corro, J. González, M. Taravillo, E. Flahaut, V. G. Baonza, *Nano Lett*. **8**, 2215–2218 (2008).

78 A. L. Aguiar, E. B. Barros, R. B. Capaz, A. G. Souza Filho, P. T. C. Freire, J. M. Filho, D. Machon, C. Caillier, Y. A. Kim, H. Muramatsu, M. Endo, A. San Miguel, *J. Phys. Chem. C* **115**, 5378–5384 (2011).

79 M. S. Dresselhaus, G. Dresselhaus, P. C. Eklund, *J. Raman Spectrosc*. **27**, 351–371 (1996).

80 C. Caillier, D. Machon, A. San-Miguel, R. Arenal, G. Montagnac, H. Cardon, M. Kalbac, M. Zukalova, L. Kavan, *Phys. Rev. B* **77**, 125418 (2008).

81 P. M. Rafailov, C. Thomsen, H. Kataura, *Phys. Rev. B* **68**, 193411 (2003).

82 A. N. Khlobystov, R. Scipioni, D. Nguyen-Manh, D. A. Britz, D. G. Pettifor, G. A. D. Briggs, S. G. Lyapin, A. Ardavan, R. J. Nicholas, *Appl. Phys. Lett.* **84**, 792–794 (2004).

83 J. Sandler, M. S. P. Shaffer, A. H. Windle, *Phys. Rev. B* **67,** 035417 (2003).

84 D. Y. Sun, D. J. Shu, M. Ji, F. Liu, M. Wang, X. G. Gong, *Phys. Rev. B* **70**, 165417 (2004).

85 A. J. Ghandour, I. F. Crowe, J. E. Proctor, Y. W. Sun, M. P. Halsall, I. Hernandez, A. Sapelkin, D. J. Dunstan, *Phys. Rev. B* **87**, 085416 (2013).

86 S. Lebedkin, K. Arnold, O. Kiowski, F. Hennrich, M. M. Kappes, *Phys. Rev. B* **73**, 094109 (2006).

87 J. A. Elliott, J. K. W. Sandler, A. H. Windle, R. J. Young, M. S. P. Shaffer, *Phys. Rev. Lett*. **92**, 095501 (2004).

88 M. Hasegawa, K. Nishidate, *Phys. Rev. B* **74**, 115401 (2006).

89 T. Chang, Acta. Mech. Sinica 23, 159–162 (2007).

90 C. Zhang, K. Bets, S. S. Lee, Z. Sun, F. Mirri, V. L. Colvin, B. I. Yakobson, J. M. Tour, R. H. Hauge, *ACS Nano* **6**, 6023–6032 (2012).

91 J. Zang, A. Treibergs, Y. Han, F. Liu, *Phys. Rev. Lett.* **92**, 105501 (2004).

92 M. Levy, *J. Math Ser.* **3**, 7 (1884).

93 G. F. Carrier, *J. Math. Phys*. **26**, 94–103 (1947).

94 J. Chaskalovic, S. Naili, Z. Angew. *Math. Phys*. 46, 149–155 (1995).

95 L. D. Landau, E. M. Lifshitz, *Elasticity Theory* (Pergamon, Oxford, 1986).

96 B. I. Yakobson, C. J. Brabec, H. J. Bernholc, *Phys. Rev. Lett*. **76**, 2511–2514 (1996).

97 A. N. Itami, V. K. Jindal, *Phys. Rev. B* 76, 19544 (2007).

98 C. Lee, X. Wei, J. W. Kysar, J. Hone, *Science* **321**, 385–388 (2008).

99 E. A. Belenkov, V. A. Greshnyakov, *J. Mater. Sci.* **50**, 7627–7635 (2015).

Chapter 11

Resumen en Español

Las Excepcionales Propiedades de los [n]CPPs: ¿Por Qué Importa Tanto el Tamaño y la Estructura Molecular?

Estudiante de Doctorado

Miriam Peña-Álvarez

Directores:

- Prof. Mercedes Taravillo Corralo
- Prof. Juan Casado Cordón
- Prof. Valentín García Baonza

Esta tesis doctoral tiene como eje fundamental el análisis exhaustivo de diversas propiedades de los compuestos denominados [n]ciclo-parafenilenos (desde ahora [n]CPPs). Estas moléculas cíclicas están formadas por fenilenos unidos en posición *para* mediante enlaces sencillos. Como consecuencia de la configuración cíclica, los [n]CPPs poseen un alto grado de tensión interna, dado que sus unidades fenilénicas se ven forzadas a doblarse parcialmente para poder cerrar el ciclo. Asimismo, esta configuración fenilénica cíclica hace que los [n]CPPs se hayan considerado como la mínima unidad de nanotubos de carbono con quiralidad única de tipo armchair.

El aspecto esencial de la tesis ha sido el estudio experimental y teórico de la espectroscopía Raman de los [n]CPPs, con un análisis de la dependencia de la misma con el tamaño, curvatura, tensión y conjugación electrónica. Por otro lado, también se ha estudiado la influencia de la temperatura, presión y la oxidación de los [n]CPPs en las variables espectroscópicas. Esto nos ha permitido explorar otras propiedades de los [n]CPPs como son: la conjugación electrónica, su deformabilidad y otras propiedades mecánicas, comparando el comportamiento observado en las mismas para los oligoparafenilenos lineales y los nanotubos de carbono. Por último, también se ha comprobado que los [n]CPPs y los nanotubos de carbono comparten propiedades relacionadas con su configuración tubular como son su habilidad para hospedar sistemas del tamaño apropiado.

11. 1. Introducción

Desde el descubrimiento del benceno como el primer sistema con conjugación cíclica,[1] la comunidad científica ha hecho grandes esfuerzos para entender sus propiedades electrónicas y estructurales resultantes de esa conjugación.[2,3] Dentro de este campo las moléculas poliaromáticas[4] han sido muy estudiadas debido a la gran extensión de su conjugación. Estos sistemas se pueden dividir en dos tipos: los que son lineales y sus unidades están unidas por enlaces simples C-C y los que presentan varios anillos aromáticos fusionados. Estos últimos se conocen comúnmente como hidrocarburos policíclicos aromáticos (*polycyclic aromatic hydrocarbons*, PAHs). Los PAHs suelen ser rígidos y no presentan barreras a la deslocalización electrónica en el plano estructural conjugado.

En la actualidad el estudio de los PAHs ha tenido un auge considerable debido a las numerosas aplicaciones de los nanomateriales de carbono (grafeno o nanotubos de carbono). Dentro de este campo pueden englobarse los cicloparafenilenos, [n]CPPs, hidrocarburos conjugados constituidos por bencenos unidos entre sí en sus posiciones 1 y 4 conformando un ciclo, de manera que sus orbitales p_z se encuentran orientados hacia el centro de la cavidad del macrociclo (véase la Figura 1b). Fueron sintetizados por primera vez en 2008[5] y desde entonces se han logrado diferentes tamaños,[5-13] con diámetros desde 0.669 nm en el [5]CPP[7] hasta 2.4 nm en el [18]CPP,[5] como se describe en la Figura 1.

En la actualidad las propiedades de los sistemas poliaromáticos conjugados en el plano *xy* son bien conocidas; sin embargo, el efecto que puede causar el cambio en la orientación de los orbitales hacia una configuración cíclica radial aún está poco explorado. Esto se debe a que experimentalmente no se han descrito sistemas con conjugación radial cíclica y, hasta el momento, únicamente existen predicciones teóricas[14] para sistemas moleculares no sintetizados aún[15] como los [n]ciclofenacenos[16] o los [n]ciclacenos.[17] Es en este ámbito donde toma importancia los [n]CPPs, como posibles modelos para analizar la conjugación π cíclica radial.[15-19] Por lo tanto, un aspecto muy importante de este trabajo será el análisis de la conjugación cíclica radial en función del tamaño y otras características conformacionales.

Por otro lado, un aspecto muy interesante de los [n]CPPs es su similitud estructural con los nanotubos de carbono de una pared (SWCNTs), de manera que podrían considerarse como la versión más corta de un nanotubo tipo armchair (n,n).[6,15,20-23] Así, se han realizado varios estudios donde se propone utilizarlos como plantillas para el crecimiento de nanotubos de quiralidad y tamaño definido, como se representa en la Figura 2.[24-27]

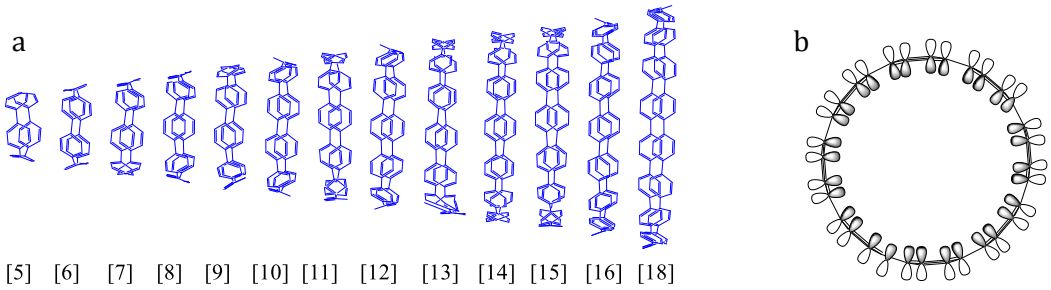

Figura 1. a) Vista lateral de las moléculas de todos los [n]CPPs sintetizados hasta ahora. b) Representación esquemática del sistema π radial del [8]CPP en su conformación con simetría D_{8h}.

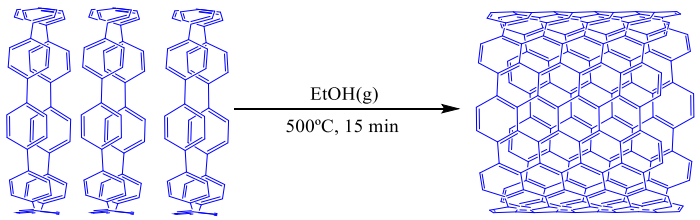

Figura 2. Esquema de la estrategia para la síntesis de SWCNTs usando [12]- ó [9]CPP como precursores.[27]

En esta línea, el estudio de los [n]CPPs permitirá comprender mejor las propiedades singulares que poseen, reflejo de su forma cíclica, relacionándolas además con las propiedades conocidas de los SWCNTs. Por otro lado, los [n]CPPs por si solos también son importantes, dadas sus sobresalientes propiedades optoelectrónicas y estructurales, así como por su capacidad de hospedar diferentes tipos de moléculas y formar complejos supramoleculares.[5,28-31] Por último, el amplio intervalo de diámetros disponibles en los [n]CPPs, junto con su modulable conjugación cíclica radial, ofrecen una oportunidad única para el estudio de sus propiedades electrónicas, estructurales y mecánicas en función de un tamaño definido.

En este trabajo se lleva a cabo un estudio sistemático de las propiedades estructurales y electrónicas de los [n]CPPs, en comparación con sus análogos lineales (desde ahora [n]LPPs) y los SWCNTs. Como es bien sabido la espectroscopía Raman depende de los cambios en la polarizabilidad.[32,33] Por lo que es una de las técnicas más apropiadas para el estudio de estos sistemas ricos en electrones π.

11.1.1 Principales Parámetros Estructurales de los [n]CPPs

Los [n]CPPs, como sus análogos lineales, están formados por *n* unidades fenilénicas, aumentando por tanto el número de electrones π con el número de unidades fenilénicas. Sin embargo, a diferencia de los [n]LPPs, donde el gap de energía entre los orbitales HOMO y LUMO disminuye con el aumento de unidades fenilénicas, en los [n]CPPs se observa la tendencia contraria: disminuyendo el gap al disminuir el número de unidades fenilénicas, tal y como se observa en la Figura 3. Por lo tanto, es evidente que la forma cíclica ejerce un papel fundamental en las propiedades de estos sistemas.

En términos de las propiedades estructurales, los [n]CPPs al igual que los [n]LPPs, en su conformación de menor energía, presentan ángulos de torsión entre sus unidades fenilénicas para minimizar la interacción entre los hidrógenos de unidades vecinas, como se describe en la Figura 4. Sin embargo, mientras que estos ángulos de torsión en los [n]LPPs son prácticamente constantes e independientes de *n*: un valor de 36° fue calculado para una molécula larga de poli-parafenileno,[34] en los [n]CPPs existe una enorme dependencia con *n*. Al disminuir el tamaño del ciclo, el ángulo disminuye hasta 12° en el [5]CPP.[7] Por lo tanto, en los [n]CPPs más pequeños la torsión se ve más impedida debido a que las unidades fenilénicas se deben doblar más para permitir el cierre del ciclo.

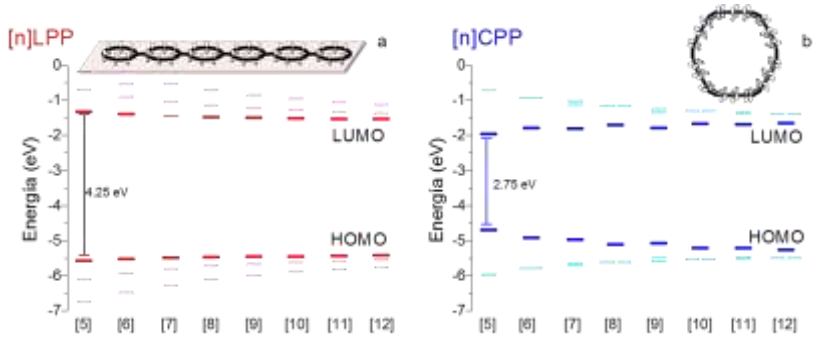

Figura 3. Representación esquemática de las energías de los orbitales moleculares frontera para las diferentes moléculas de oligofenilenos: a)[n]LPPs; b) [n]CPPs. Líneas en rojo y azul oscuro corresponden a los orbitales HOMO y LUMO, y en rosa y azul claro a HOMO-1, HOMO-2, LUMO+1 y LUMO+2, para [n]LPPs y [n]CPPs, respectivamente.[35-38]

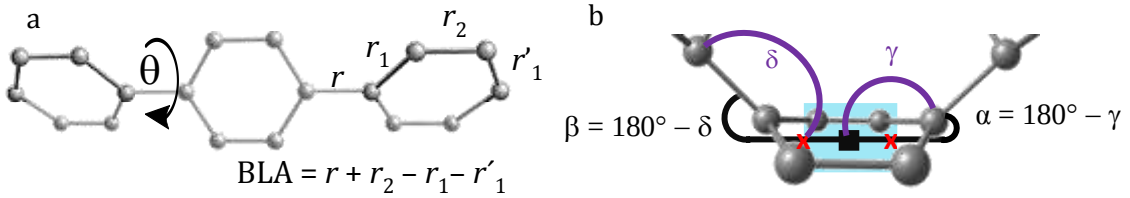

Figura 4. a) Ángulo torsional (θ) entre dos unidades fenilénicas vecinas; se indican las diferentes distancias C-C (*r*, r_1 y r_2). b) Los ángulos de deformación α y β se definen como α = 180° − γ; β = 180° − δ. Los diferentes centroides se indican con (X) y (■), se usan para calcular la deformación fuera del plano de las unidades fenilénicas. Para [n]LPPs, α = β = 180°.

Por otro lado, desde los primeros estudios en [n]CPPs, se describieron como especies moleculares con un alto grado de tensión interna, dado que sus unidades fenilénicas se ven forzadas a doblarse parcialmente para poder cerrar el ciclo,[10,39-41] Figura 4b. Esta deformación es mayor cuanto menor es el diámetro y, por tanto, la tensión interna también crece exponencialmente al disminuir el diámetro. Dado el alto grado de deformación fuera del plano de los [n]CPPs, se ha sugerido la posibilidad de una pérdida de aromaticidad en las unidades fenilénicas para formar especies quinonoides, con la consecuente localización de dobles enlaces entre C_{orto}-C_{orto} y C_{ipso}-C_{ipso}. En la literatura para describir de manera cuantitativa cualquier formación quinonoidal se usa el denominado parámetro BLA (*bond length alternation*):[42-45]

$$BLA = r + r_2 - r_1 - r_1' = r + r_2 - 2r_1 \quad (1)$$

donde r representa la distancia de enlace entre C_{ipso}-C_{ipso}, r_1 la distancia de enlace entre C_{ipso}-C_{orto} (para los [n]CPPs todas las r_1 son iguales por lo que $r'_1 = r_1$) y r_2 entre C_{orto}-C_{orto} (véase la Figura 4a). De este modo, cuando r es relativamente grande y r_1 y r_2 son muy parecidas, la estructura se define como aromática con un BLA > 0. Cuando r es corta y $r_1 > r_2$, entonces se obtiene BLA < 0 que definiría una estructura quinonoide. En la Figura 5 se representan las dos posibles conformaciones, aromática y quinonoide, del [5]CPP. Las distancias de enlace observadas en los [n]CPPs sintetizados hasta el momento definen sistemas aromáticos con BLA > 0 incluso para el más pequeño de los ciclos.

Por último, la configuración cíclica de los [n]CPPs junto con su alta densidad electrónica π les confiere la habilidad de hospedar en su cavidad interna sistemas del tamaño adecuado.[46,47] De este modo, en analogía con los SWCNTs, los [n]CPPs pueden formar sistemas supramoleculares estables debido a las interacciones π-π cóncavo-convexas.[48-50] Como ejemplo, en la Figura 6 se muestra un "*peapod*" formado por C_{70} en su posición vertical en el interior de la cavidad de un nanotubo (10,10) y su análogo "*peapod*" ultracorto formado por el mismo C_{70} y [10]CPP. En la literatura se han descrito varias aplicaciones de los sistemas supramoleculares formados a partir de los [n]CPPs.[51] Por ejemplo, como dispositivos de recolección de luz cuando se formaran las denominadas "muñecas rusas": [n]CPPs del tamaño apropiado ocupando la cavidad interna de [n]CPPs más grandes;[52] o para purificar fullerenos, endo- o vacíos, de diferentes tamaños a partir del material inicial de carbono.[53,54]

Aunque en principio, los SWCNTs podrían utilizarse también para estas aplicaciones de manera análoga, su síntesis y purificación con un tamaño y quiralidad definida es un factor limitante.[55] Por tanto, los [n]CPPs, donde el diámetro sí puede estar bien controlado, pueden ser utilizados como modelos para estos estudios donde se quieren analizar estas propiedades en función del tamaño.[46]

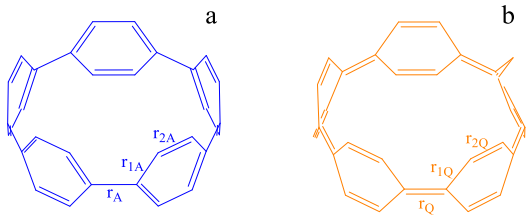

Figura 5. Esquema molecular de los dos tautómeros del [5]CPP: a) conformación benzoide con BLA > 0; b) conformación quinonoide con BLA < 0.

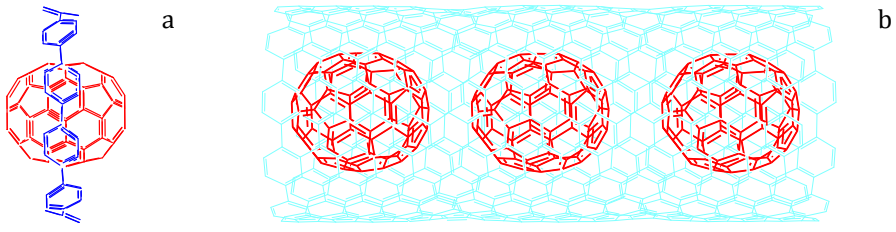

C_{70}@[10]CPP C_{70}@(10,10)SWCNT

Figura 6. a) Vista lateral del complejo supramolecular C_{70}@[10]CPP en orientación *lying*; b) Esquema del peapod C_{70}@(10,10)SWCNT en orientación *lying*.

11. 2. Objetivos

Este trabajo tiene como objetivo analizar los efectos electrónicos y estructurales que configuran el espectro Raman de los [n]CPPs. Para ello las medidas experimentales de espectroscopía Raman serán complementadas con cálculos teóricos basados en la teoría del funcional de la densidad (DFT). Al mismo tiempo, las frecuencias e intensidades Raman experimentales y teóricas se analizarán conjuntamente con otros parámetros estructurales y electrónicos (difracción de Rayos X de otros autores y espectroscopía UV-Vis), de manera que en su conjunto podamos establecer consecuencias relevantes sobre la tendencia estructura-propiedad.

A partir de un análisis sistemático de los modos Raman más significativos de los [n]CPPs en comparación directa con el comportamiento observado en los [n]LPPs y los SWCNTs, se estudiarán diferentes efectos estructurales y electrónicos en el espectro. De este modo se examinará la deformación parcial de los fenilenos, las torsiones de los fenilenos, la conjugación π y el gap de energía entre los orbitales HOMO y LUMO, tanto en función de la elongación lineal como en función de la curvatura. En este marco, se analizarán posibles analogías en las propiedades mecánicas, químicas y espectroscópicas de los [n]CPPs con los [n]LPPs por un lado y SWCNTs por otro. De este modo, este trabajo quiere ofrecer una interpretación unificada de los aspectos electrónicos y estructurales relacionados con la evolución de sistemas π 1D lineales a estructuras 2D cíclicas.

Además, queremos resolver la cuestión del carácter quinonoide parcial de los [n]CPPs, considerando contextos diferentes de manera que podamos clarificar si es posible que exista realmente una configuración totalmente quinonoide. Se explorarán, desde diferentes aproximaciones, los modos Raman activos que desvelarían en qué grado dichas configuraciones quinonoides pueden estar involucradas en un estado fundamental totalmente aromático.

También hemos tenido como objetivo analizar las propiedades conformacionales de los [n]CPPs en términos de los ángulos de torsión entre fenilenos vecinos. Para ello, se usarán cálculos DFT para estimar diferentes parámetros estructurales de las conformaciones más relevantes. Al mismo tiempo, se han realizado experimentos donde una combinación de irradiación láser en función del tiempo y temperatura se ha usado para acceder a diferentes conformaciones torsionales.

Otro objetivo ha sido analizar desde un punto de vista experimental la conjugación radia cíclica y entender qué factores la favorecen y estabilizan. Para ello se estudiarán experimentalmente y mediante metodologías DFT los [n]CPPs, con n = 5-12, en sus estados neutros, catiónicos y dicatiónicos. El análisis detallado de las propiedades moleculares y electrónicas de los sistemas oxidados será complementado con su espectroscopía Raman, que al mismo tiempo será la principal herramienta de evaluación y diagnóstico.

Asimismo, en este trabajo se analizará la capacidad de los [n]CPPs para formar complejos supramoleculares. Con esta intención se estudiarán mezclas en estado sólido de [n]CPPs de diferente tamaño y C_{60}. También se han probado sistemas supramoleculares 1:1 formados en disolución por [n]CPPs hospedando C_{70} con el objetivo de analizar cómo influían la presión y la temperatura en la configuración de los mismos.

Finalmente, entre los principales objetivos de este trabajo se encuentra el análisis de las propiedades mecánicas de los [n]CPPs. Su comparación con los SWCNTs permitirá establecer analogías y diferencias en su comportamiento. Se usarán celdas de tipo yunque con zafiros enfrentados para generar altas presiones y la espectroscopía Raman como técnica de diagnóstico. Además, se evaluará la posible reversibilidad de las deformaciones producidas, para reconocer si las configuraciones producidas pueden ser aptas para posibles aplicaciones futuras.

11. 3. Resultados

11.3.1 Asignación de las Principales Bandas Raman de los [n]CPPs

En la Figura 7 se representa el espectro Raman de los diferentes [n]CPPs, con *n* = 5-12, junto con el espectro Raman del [6]LPP. [n]CPPs y [n]LPPs presentan bastantes características comunes sobre todo en la región de alta frecuencia, desde 1000 a 1600 cm^{-1}. Sin embargo, a frecuencias menores de 1000 cm^{-1} el espectro Raman de los [n]CPPs es más complejo. En la Tabla 1 se resumen las bandas señaladas en los espectros de la Figura 7 y se describe su origen vibracional.

En la zona de bajas frecuencias de la Figura 7 se han señalado en morado los modos asignados a los denominados modos de respiración radial (RBMs) y en verde las bandas asignadas como pseudo modos de respiración radial (p-RBMs). En analogía con los RBMs de los SWCNTs, en los [n]CPPs la frecuencia Raman de ambos modos es directamente proporcional al inverso del diámetro del ciclo. En ecuación 2 se describe esta variación para el caso de los p-RBMs.

$$\omega_{p-RBM}\left(cm^{-1}\right)=8+\frac{375}{d(nm)} \qquad (2)$$

En la región espectral entre 1100-1300 cm^{-1} los [n]CPPs presentan varias contribuciones. Entre éstas es posible caracterizar dos bandas alrededor de 1280 and 1200 cm^{-1} con simetría A_{1g}, cuya ratio de intensidades ($I1280A_{1g}/I1200A_{1g}$), en analogía con los [n]LPPs, puede ser directamente relacionada con la extensión de la conjugación entre los fenilenos vecinos y, por tanto, con el ángulo de torsión entre ellos.[56] Una disminución en esta ratio señala un menor ángulo de torsión e indica, por tanto, una mayor conjugación entre bencenos vecinos.

En la región entre 1550 y 1600 cm^{-1} los [n]CPPs muestran dos contribuciones, las denominadas bandas G, llamadas así en analogía con los SWCNTs,[57] mientras que en el [6]LPP se observa una única contribución. La banda de menor frecuencia es la GA_{1g} y la de mayor es la GE_{2g} menos intensa. La primera resulta de la tensión colectiva de los enlaces C-C en la dirección circunferencial, mientras que la segunda tiene un origen vibracional similar, pero los desplazamientos C-C no están tan localizados en la dirección circunferencial. En la Figura 7 se observa también que la intensidad relativa de los modos de baja frecuencia aumenta al disminuir *n*, mientras que al aumentar *n* la bandas de mayor intensidad son las Gs, como sucede en los [n]LPPs. Así, el desdoblamiento en la banda G y la distribución de intensidades de las bandas A_{1g} son aspectos directamente relacionados con la configuración cíclica de los [n]CPPs.

Tabla 1. Asignación de los modos vibracionales, frecuencias (en cm^{-1}) experimentales y calculadas (B3LYP/6-31G(d,p) factor de escala ~0.97) para el [6]CPP y el [6]LPP, especies de simetría correspondientes a la conformación con ángulo de torsión nulo, D_{nh}.

[6]CPP				**[6]LPP**		
Exp.	Teor.	Simetría	Descripción vibracional	Exp.	Teor.	Sim.
231	240	**A_{1g}**	Radial Breathing Mode (RBM)	--	--	--
442	442	**E_{2g}**	Pseudo-Radial Breathing Mode (pseudo-RBM)	--	--	--
1192	1179	E_{2g}	β(phenyl) + ν(C-C) + ω (CH)	--	--	--
1200	1185	**A_{1g}**	β(C-H) + $\nu(C\text{-}C)_{interring}$	1219	1222	A_g
1252	1244	E_{2g}	β(phenyl)+ $\nu(C\text{-}C)_{interring}$ + β(C-H)	1269	1263	E_{2g}
1263	1245	**A_{1g}**	β(phenyl) + $\nu(C\text{-}C)_{interring}$ + β(C-H)	1278	1278	A_g
1269	1264	E_{1g}	ν(C-C) + ω(CH) + β(phenyl)	--	--	--
1567	1576	A_{1g}	GA_{1g}: $\nu(C\text{-}C)_{transversal}$	1593	1594	A_g
1584	1592	E_{2g}	GE_{2g}: $\nu(C\text{-}C)_{trans}$ + $\nu(C\text{-}C)_{long}$	--	--	--

RBM: Modo de respiración radial del anillo; **p-RBM**: modo circunferencial con componentes del RBM pero con simetría E_{2g}; **β(C-C)**: Flexión del enlace C-C; **β(phenyl)**: modo de respiración simétrica del fenilo; **ω(CH)**: flexión aleteo del C-H; **$\nu(C\text{-}C)_{interring}$**: tensión del enlace C-C entre anillos; **β(C-H)**: Flexión C-H; **$\nu_s(C\text{-}C)_{transversal}$**: tensión de los enlaces C-C en la circunferencia del macrociclo; **$\nu(C\text{-}C)_{long}$**: tensión de los enlaces C-C también en la dirección circunferencial, pero éstos no están tan localizados, observándose componentes hacia la parte superior e inferior del plano de los fenilenos.

En la Figura 8 se representan las frecuencias Raman de los modos GA_{1g} en función de *n* obtenidas experimentalmente y las calculadas mediante metodologías DFT al nivel B3LYP/6-31G(d,p) para los [n]CPPs y [n]LPPs. En ambos sistemas se han calculado para las estructuras de mínima energía y en las conformaciones con ángulo de torsión nulo. Se puede notar cómo la banda GA_{1g} de los [n]CPPs, independientemente de la conformación, se desplaza hacia menores frecuencias al disminuir el tamaño del ciclo, mientras que en los [n]LPPs estas frecuencias son prácticamente independientes de la longitud de la cadena. En cualquier caso, en los [n]LPPs se aprecia un leve desplazamiento hacia menores frecuencias al aumentar *n*, éste se relaciona con la creciente conjugación en el plano al añadir más unidades aromáticas.[58] Así, en los [n]CPPs la elevada variación con *n* se atribuye a la creciente deformación de los fenilenos, que en cierta medida interrumpe la aromaticidad dentro del fenileno, impide torsiones altas y permite una mayor conjugación radial en el ciclo.[59]

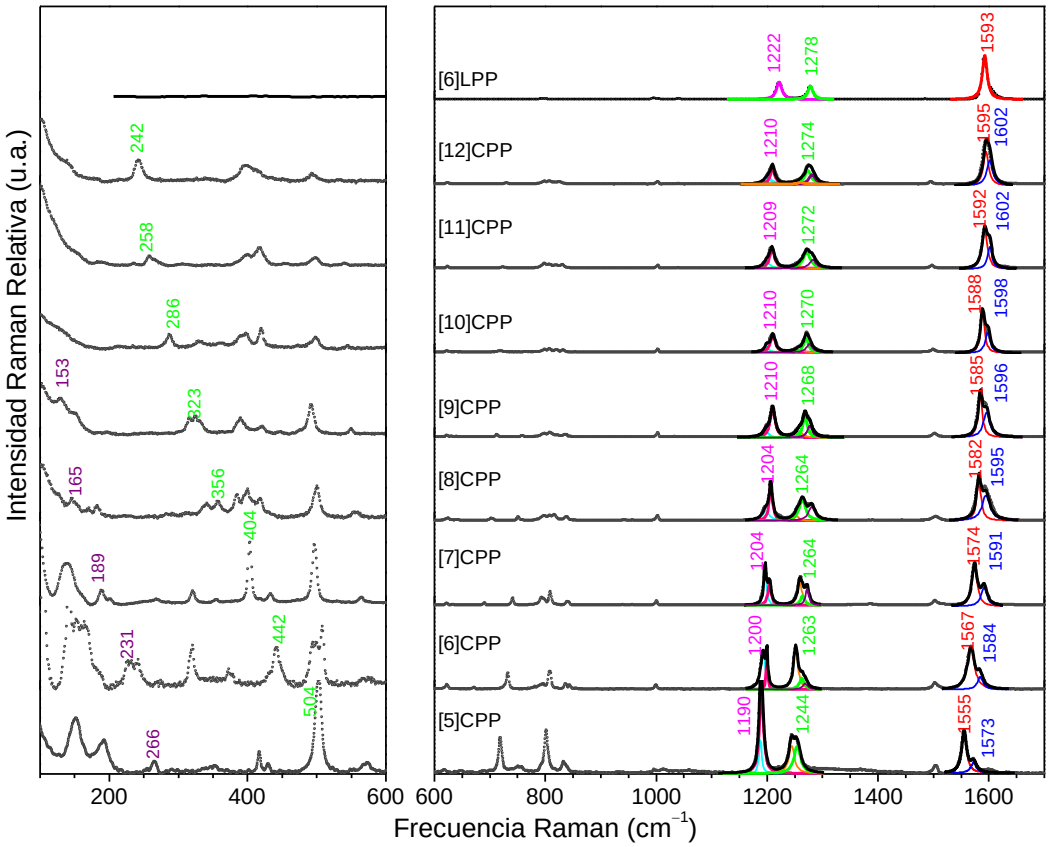

Figura 7. Espectros Raman de los [n]CPPs, con n = 5-12, y del [6]LPP, todos registrados con una longitud de onda de excitación de 785 nm. Todos los espectros han sido normalizados a su correspondiente banda GA_{1g}. Las asignaciones de las bandas marcadas se resumen en la Tabla 1.

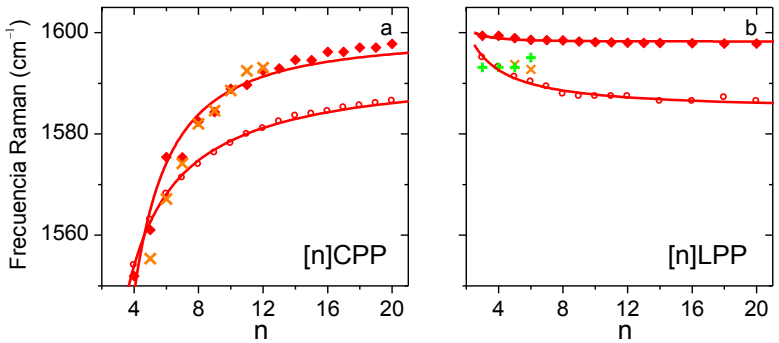

Figura 8. Frecuencia Raman de la banda GA_{1g} en función de *n* para: a) [n]CPPs, b) [n]LPPs. (×) Datos experimentales de los [n]CPPs y (+) de los [n]LPPs.[60] Datos calculados mediante metodologías DFT a nivel B3LYP/6-31G(d,p) (◆) para las conformaciones de mínima energía, con cierto ángulo de torsión entre los fenilenos, y (○) datos para las conformaciones con una torsión nula. Las líneas son únicamente una guía visual.

11.3.2 Explorando la Quinonoidización

Como ya se ha comentado las estructuras quinonoides están definidas por parámetros BLA negativos, pero todos los [n]CPPs tienen valores positivos cercanos a cero. En este trabajo se ha analizado si una configuración quinonoide puede existir en los [n]CPPs. Se han realizado cálculos con metodologías DFT a nivel B3LYP/6-31G(d,p) para obtener la estructura del estado electrónico fundamental. Hemos encontrado que en los [n]CPPs, con valores de n = 4-20, las estructuras con la mínima energía son aromáticas, con valores del parámetro BLA positivos y, únicamente para los más pequeños, [4]- y [5]CPP, se han hallado mínimos locales con una estructura quinonoide. Estos resultados están de acuerdo con los descritos previamente por Bachrach y Stück.[61]

Sin embargo, es cierto que aunque la estructura de mínima energía posea un BLA mayor que cero, la deformación fuera del plano de los fenilenos debe modificar en cierta medida esa distribución electrónica del fenileno. Por tanto, en este trabajo se ha buscado explicar y cuantificar en qué medida la reorganización estructural afecta a la configuración electrónica y, por tanto, qué grado de quinonoidización existe en la estructura del estado fundamental de mínima energía.

11.3.2.1 Análisis mediante la Teoría de la Coordenada de Conjugación Efectiva

La teoría de la coordenada de conjugación efectiva (ECC)[42-45,62,63] define una vibración totalmente simétrica correspondiente a la elongación/contracción de los enlaces consecutivos C-C/C=C (denominada modo ECC o BLA), donde la amplitud de esta vibración coincide con la transformación aromática ↔ quinonoide o deformación BLA.[64] Como el modo BLA no es una función propia vibracional, la teoría ECC establece que la intensidad BLA se distribuye entre los modos normales de tensión de simetría A_g, que involucran la elongación/contracción de los enlaces consecutivos C-C/C=C. A partir de la ECC se pueden estimar los desplazamientos atómicos involucrados en el modo BLA (B_1) a partir de la siguiente relación:

$$\vec{B_1} = c_1 \sum_{i \in A1g} \pm I_i^{1/2} \vec{L_i} \qquad (3)$$

donde c_1 es el factor de normalización, I_i es la intensidad de cada modo A_{1g} y $\vec{L_i}$ es el correspondiente vector de desplazamiento.

A partir de los cálculos a nivel B3LYP/6-31G(d,p) del espectro Raman de cada estructura optimizada con simetría D_{nh} se ha obtenido para cada modo A_{1g} tanto la intensidad Raman absoluta del modo como los vectores de desplazamiento de cada átomo. Con estos valores se ha generado para cada [n]CPP el modo de vibración BLA (véase el del [8]CPP en la Figura 9a). En la Figura 9b se representan los desplazamientos involucrados en la tensión C-C caracterizados mediante los cambios en los tres parámetros del modo BLA, δr, δr_1 y δr_2, de igual signo para δr y δr_2, y de signo contrario para δr_1. Para una mejor comparación en la Figura 9c se han representado las ratios ($\delta r/\delta r_2$) y ($\delta r_1/\delta r_2$) en función de n. Se observa que la ratio ($\delta r/\delta r_2$) es ~ 2 y que disminuye al aumentar n. Por otro lado, la ratio ($\delta r_1/\delta r_2$) tiene un valor casi constante alrededor de −0.87 y es independiente de n. Los valores positivos y mayores de la relación ($\delta r/\delta r_2$) para los ciclos más pequeños pone de manifiesto el fortalecimiento del enlace C_{ipso}-C_{ipso} o, lo que es lo mismo, el aumento del carácter quinonoide en los ciclos de menor tamaño.

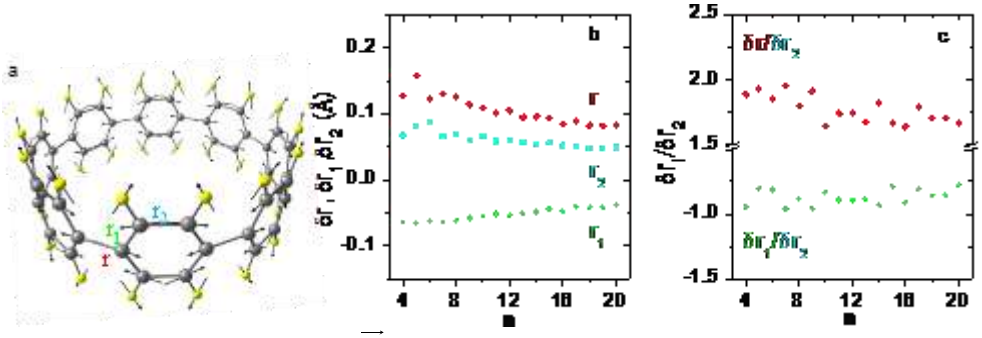

Figura 9. Modos BLA normalizados ($\vec{B_1}$) calculados a partir de la ecuación 3. a) Esquema de los desplazamientos de los átomos para el [8]CPP. b) Componentes del modo BLA en términos de δr, δr_1 y δr_2 en función de n. c) BLA ratios, ($\delta r_1/\delta r_2$) y ($\delta r/\delta r_2$), en función de n.

11.3.2.2 Análisis de Constantes de Fuerza Aproximando el Modo GA_{1g} al BLA

El análisis anterior mediante la teoría ECC sólo se puede realizar a partir de los espectros Raman calculados computacionalmente. No se puede llevar a cabo un análisis cuantitativo análogo con los espectros experimentales porque se requieren intensidades Raman absolutas y los vectores de desplazamiento involucrados en cada modo, lo que impide establecer una función de parametrización del grado de quinonoidización experimental. Por esta razón hemos buscado una aproximación alternativa para cuantificar espectroscópicamente en qué grado la estructura del estado fundamental de mínima energía tiene cierto carácter quinonoide. El modelo planteado es puramente geométrico (véase la Figura 10), analizando las constantes de fuerza de una unidad fenilénica en dos casos límite, totalmente benzoide y totalmente quinonoide.

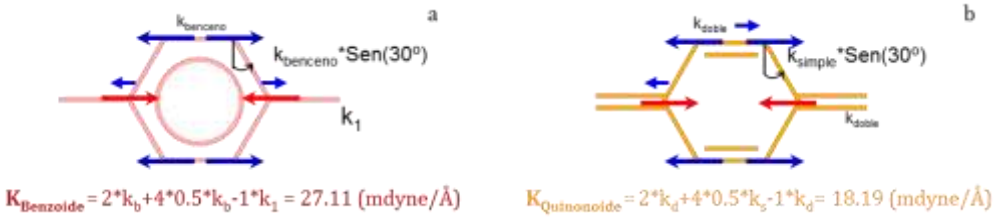

Figura 10. Patrón vibracional del modo BLA en un fenileno cuando: a) es totalmente benzoide (B), b) es totalmente quinonoide (Q). Las flechas indican los desplazamientos de los átomos de carbono, las rojas valores negativos y las azules positivos. K_B y K_Q representan las constantes de fuerza totales calculadas a partir de las relaciones geométricas entre las constantes de fuerza locales de la Tabla 2.

Tabla 2. Constantes de fuerza locales usadas para estimar los valores de K_B y K_Q de la Figura 10.

Fenileno totalmente aromático **0 % de quinonoidización** Datos tomados de J. L. Jules et al. [65]		Fenileno totalmente quinonoide **100 % de quinonoidización** Datos tomados de Y. Yamakita et al. [66]:	
$k_{benzoide}$ (k_b)	7.86 (mdina/Å)	k_{doble} (k_d)	7.875 (mdina/Å)
k_1, tensión C-C del etano	4.33 (mdina/Å)	k_{simple} (k_s)	5.156 (mdina/Å)

El cálculo descrito en la Figura 10 de la constante de fuerza global se realiza a través de las relaciones geométricas planteadas en dicha figura y utilizando las constantes de fuerza locales de la Tabla 2. A partir de las constantes de fuerza correspondientes ($K_{Benzoide}$ o $K_{Quinonoide}$) se puede estimar la frecuencia del modo de vibración de cada caso límite, ω. Para ello se ha utilizado una aproximación armónica para la frecuencia de vibración de una molécula diatómica, de manera que la relación entre la frecuencia de vibración ω y la constante de fuerza K viene dada por (donde μ es la masa reducida):

$$\omega = \frac{1}{2\pi c}\sqrt{K/\mu} \tag{4}$$

$$\frac{\omega_{Quinonoide}}{\omega_{Benzoide}} = \sqrt{\frac{K_{Quinonoide}}{K_{Benzoide}}} = \sqrt{\frac{18.19}{27.11}} = \frac{1}{\sqrt{1.49}} = 0.819 \tag{5}$$

Si consideramos que en ambos casos límite la masa reducida es la misma y que la frecuencia benzoide se corresponde con la frecuencia Raman del modo 8a del benceno (1603 cm^{-1})[67,68] se puede obtener que la frecuencia del caso límite quinonoide es:

100 % quinonoide → 1313 cm^{-1} **100 % benzoide → 1603 cm^{-1}**

El modo de vibración responsable de la banda GA_{1g} involucra a todos los fenilenos del ciclo, y se debe a la ruptura de la alternancia del patrón de la distancia de enlace en la secuencia de enlaces consecutivos –C=C-C=C–. Por tanto, este modo podría aproximarse al modo BLA y los posibles cambios en su frecuencia, con respecto a la del benceno, deben estar relacionados con el carácter quinonoide de la molécula. Esta aproximación permite cuantificar el grado de quinonoidización representado en la Figura 11b. Donde a partir de las frecuencias Raman de la banda GA_{1g} de los [n]CPPs (datos de la Figura 11a) se ha calculado su porcentaje de quinonoidización considerando los dos valores límite mencionados arriba. El grado de quinonoidización obtenido es mínimo en los ciclos de mayor tamaño, alrededor de un 3% en el [12]CPP, y aumenta con la diminución de *n*, llegando a ser aproximadamente de un 17 % para el [5]CPP. De modo que, como ya se ha descrito, existe una

cierta reorganización $sp^2 \rightarrow sp^3$ como consecuencia de la deformación fuera del plano, pero el carácter aromático permanece.

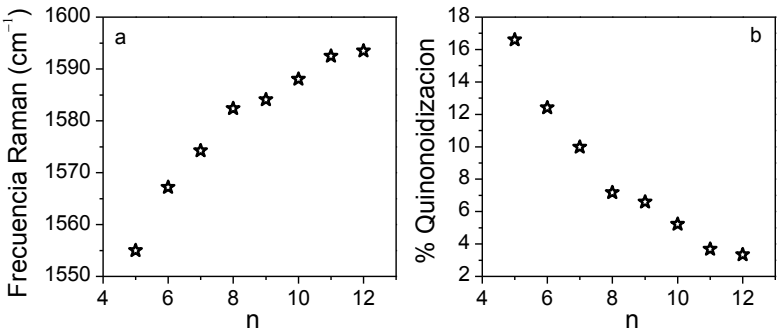

Figura 11. a) Frecuencia Raman de la banda GA_{1g} de los [n]CPPs en función de *n*. b) Valores calculados para el porcentaje de carácter quinonoide de los [n]CPPs en función de *n*.

11.3.2.3 Formación de un Tautómero Quinonoide

Se puede utilizar la presión para obtener especies de interés.[69] En nuestro caso hemos utilizado la presión para tratar de acceder a las estructuras quinonoides. Como ya se comentó en la estructura benzoide del [5]CPP el ángulo de deformación fuera del plano (α) es alrededor de 20°, Figura 12a, y en su conformación quinonoide hemos obtenido valores de α ~29°. Mediante cálculos computacionales hemos estudiado la superficie de energía potencial (PES) en función del parámetro BLA, encontrando un mínimo local con una estuctura quinonoide y con una energía de 37.5 kcal mol^{-1} superior a la del mínimo global benzoide, como se representa en la Figura 12c. Dado que en el [5]CPP se ha encontrado este mínimo quinonoide, es posible que como resultado de la presión se deforme considerablemente su estructura y sea más favorable que exhiba una configuración quinonoide con un mayor α, que encontrarlo en su configuración benzoide con una forma muy distorsionada.

En la Figura 13 se representan los espectros Raman calculados a nivel B3LYP/6-31G(d,p) para las estructuras optimizadas del [5]CPP aromático y quinonoide. Además, se muestran los espectros experimentales registrados en condiciones ambiente para el [5]CPP inicial puro y el de la muestra tras haber sido sometida a una presión de GPa. Se observa cómo el espectro Raman del recuperado a tras el ciclo de presión es diferente al espectro Raman de la muestra inicial, y además comparte ciertas características importantes con el espectro calculado para el confórmero quinonoide tales como, el mismo número de contribuciones en la banda G, que pasa de dos en el aromático a cuatro en el quinonoide, similar ratios de intensidades en las bandas de 1200 cm^{-1} y el desplazamiento significativo hacia menores frecuencias del modo p-RBM. Esto permite concluir que el tratamiento con alta presión conduce hacia la formación del [5]CPP deformado con configuración quinonoide.

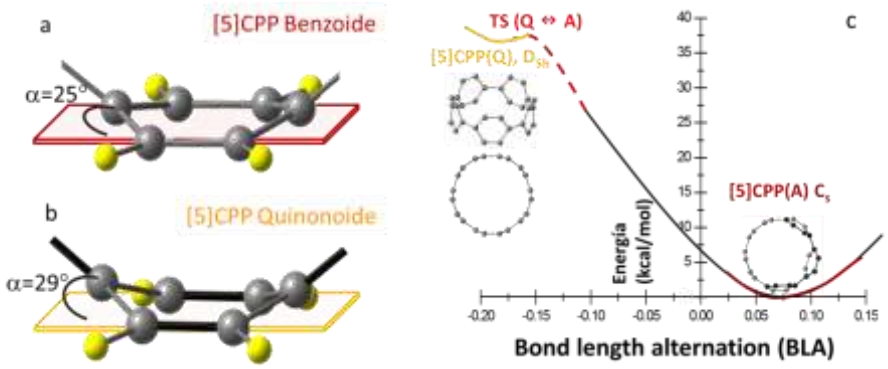

Figura 12. Vista lateral de una unidad fenilénica en las estructuras optimizadas a nivel B3LYP/6-31G(d,p) de los tautómeros del [5]CPP: a) benzoide, b) quinonoide. Se ha marcado el ángulo de deformación del fenileno fuera del plano, α. c) Esquema de la energía potencial en función del parámetro BLA para el [5]CPP. TS: estado de transición.

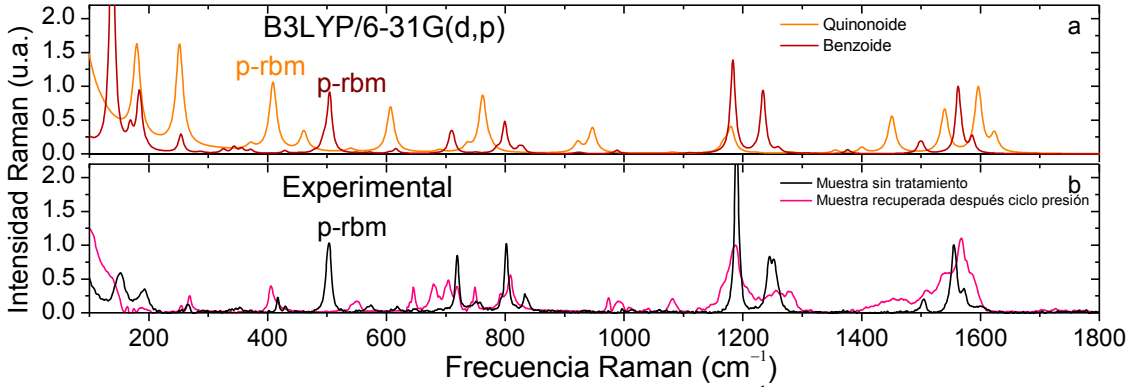

Figura 13. Espectros Raman del [5]CPP en la región 100-1800 cm^{-1}. a) Espectros calculados para las conformaciones benzoide (línea marrón) y quinonoide (línea naranja) a nivel B3LYP/6-31G(d,p) con un factor de escala de 0.97. b) Espectros registrados en condiciones ambiente con excitación a 785 nm. Espectro inicial (línea negra) y después (línea rosa) de ser sometido a una presión de 10 GPa.

11.3.3 Estudio Conformacional de los [n]CPPs

Los [n]CPPs en su conformación de mayor simetría, D_{nh}, con ángulos de torsión nulos, no se corresponden con la estructura de mínima energía. El espectro Raman calculado para estas conformaciones presenta frecuencias imaginarias. Así, el número de conformaciones posible para cada [n]CPP se ha relacionado con el número de dichos modos, de manera que se establece que: [n]CPPs con *n* par tendrán ((*n*/2)-1) posibles confórmeros y con *n* impar tendrán ((*n*-1)/2).

Además, la diferencia de energía entre los confórmeros de mínima energía y los correspondientes D_{nh} es del orden de 1 kcal mol^{-1} por fenileno, valores que son consistentes con las energías calculadas por Segawa et al.[36] Este valor indica que las conformaciones D_{nh} de los [n]CPPs pueden ser accesibles experimentalmente con un aumento de temperatura.

En la Figura 14a se muestra que la irradiación láser produce cambios en el espectro Raman del [8]CPP: una nueva banda aparece en torno a 1604 cm^{-1}. El análisis de esta banda en función del tiempo de irradiación a diferentes temperaturas, Figura 14b, ha permitido calcular la energía de activación del proceso asociado con la formación de la estructura responsable de la nueva contribución Raman. Nosotros hemos considerado que este proceso podría atribuirse a los cambios conformacionales mencionados arriba. Nuestros resultados dan una barrera energética de 4.75 kcal mol^{-1} para el [8]CPP y de 5.26 kcal mol^{-1} para el [12]CPP, valores que están en excelente acuerdo con los calculados para la rotación de un fenileno en los [n]CPPs.[6-13,29,51,3670,71]

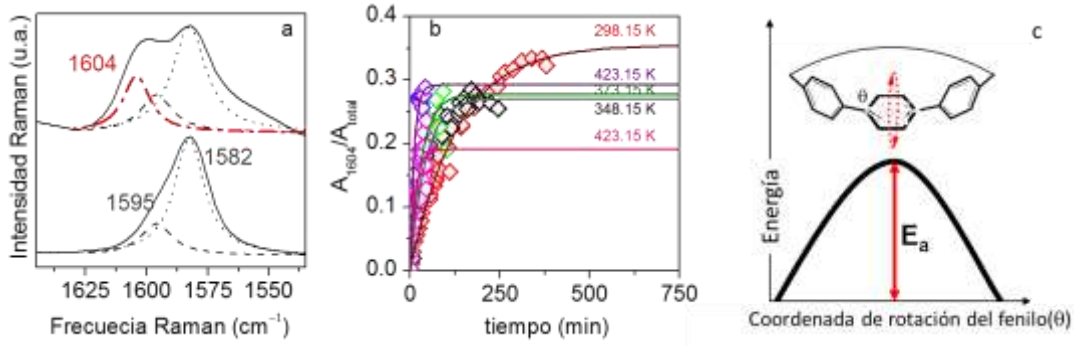

Figura 14. a) Espectros Raman del [8]CPP a 298 K. Inferior: antes de la irradiación; superior: tras 300 min de irradiación laser con una energía de 2.33 eV, se ha marcado en rojo la banda creciente con el tiempo. b) Relación entre el área de la banda creciente alrededor de 1604 cm^{-1} y el área total de las bandas en esta región en función del tiempo de exposición a la radiación láser. Temperaturas a la que se hizo la irradiación: rojo (298.15 K), negro (348.15 K), verde (373.15 K), violeta (423.15 K) y rosa (423.15 K). c) Esquema representando la barrera de energía involucrada en la torsión de un fenileno.

11.3.4 Estudio de la Conjugación Radial Cíclica

Otro aspecto que ha despertado gran atención en los CPPs radica en la oportunidad que suponen en el estudio de la denominada conjugación cíclica, tanto desde un punto de vista experimental como teórico. La *conjugación radial cíclica* se diferencia de la conjugación en el plano de un benceno, en la orientación y grado de confinamiento de los electrones π, de manera que los orbitales p_z se encuentran radialmente recogidos en el plano *xy* con sus lóbulos radialmente orientados hacia el eje *z*. Dado que las especies neutras de los [n]CPPs conservan en gran medida el carácter aromático de sus unidades fenilénicas, se ha considerado que las especies oxidadas, cationes y dicationes, serían mejores candidatos para este análisis.

Con el objeto de permitir la deslocalización radial en el ciclo se han sintetizado las especies oxidadas de los [n]CPPs, con *n* = 5-12. En la Figura 15 se representan los espectros Raman en la región de la banda G de las especies cargadas ([n]CPP^{2+} y [n]CPP$^{\bullet+}$). En comparación con los espectros de las especies neutras, se observa el siguiente comportamiento:

- Para los dicationes grandes, a partir del [9]CPP^{2+}, el espectro Raman en esta región presenta un mayor número de contribuciones, no sólo las bandas GA_{1g} y GE_{2g}.
- Los valores de las frecuencias Raman de las bandas GA_{1g} y GE_{2g} en función de *n*, tanto en los dicationes como en los cationes, describen claramente una tendencia en forma de V. Así, se observa un aumento de las frecuencias con el tamaño del ciclo a partir del [8]CPP^{2+}/[8]CPP$^{\bullet+}$, y también un aumento al disminuir el tamaño desde el [8]- hasta el [5]CPP^{2+}. Para los monocationes más pequeños no se observa una variación con *n*.

Combinado con el estudio experimental se ha desarrollado un análisis computacional DFT al nivel (U)B3LYP/6-31G(d,p) comparando los [n]CPPs neutros, cationes y dicationes y sus análogos lineales. Hay que destacar los resultados de la distribución electrónica de los dicationes. Se tienen evidencias de que cambia con el tamaño, de manera que los más pequeños tienen una configuración de capa cerrada como la más estable, mientras que en los más grandes, a partir del [9]CPP^{2+}, la configuración de capa abierta es la estable. Este cambio electrónico en los dicationes de capa abierta lleva asociado una ruptura de simetría en el sistema que revierte en una distribución de carga heterogénea y una consecuente distribución aromática-quinonoide en el ciclo. Sin embargo, los dicationes de menor tamaño con distribución electrónica de capa cerrada aumentan su simetría respecto a la especie neutra y, además, la distribución de carga es totalmente homogénea. Estas diferencias en simetría y la redistribución electrónica explicarían las nuevas contribuciones del espectro Raman en los dicationes de capa abierta y mayor tamaño. En la Figura 16 se han representado las estructuras moleculares y la distribución de carga calculada para los dicationes de menor y mayor tamaño, [5]CPP^{2+} y [12]CPP^{2+}.

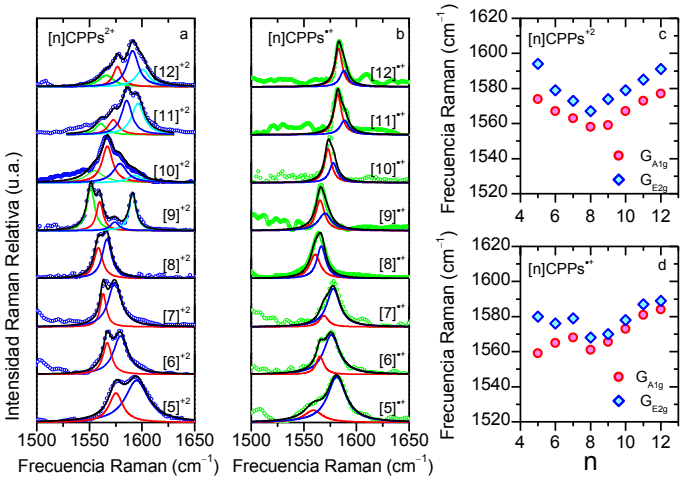

Figura 15. Espectros Raman de los macrociclos en disolución: a) [n]CPPs^{2+} dicatiónicos. b) Monocationes radicálicos. Las contribuciones roja y azul oscuro corresponden a las bandas GA_{1g} y GE_{2g}, respectivamente. c) y d) Frecuencia Raman de las bandas GA_{1g} y GE_{2g} en función de *n*: c) dicationes y d) monocationes radicálicos.

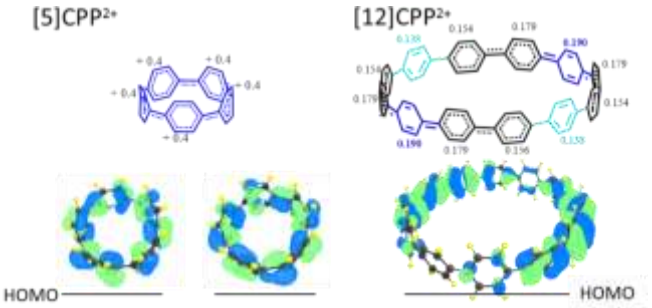

Figura 16. Representación a partir de cálculos DFT-(U)B3LYP/6-31G(d,p). Parte superior: Distribución de carga por anillo de [n]CPP^{2+} con *n* = 5 y *n* = 12. Parte inferior: topología de los orbitales HOMO. [5]CPP^{2+} tiene estructura electrónica de capa cerrada y [12]CPP^{2+} de capa abierta.

Se ha analizado la variación de los parámetros estructurales con la oxidación. En la Figura 17a se representan los ángulos de torsión para las especies neutras, catiónicas y dicatiónicas en función de *n*. Puede observarse cómo los ángulos de torsión disminuyen con la oxidación, siendo casi nulos en los dicationes más pequeños con *n* entre 5 y 8. También se ha analizado la evolución del parámetro BLA. Como se observa en la Figura 17b existe un claro cambio con la oxidación. Mientras en las especies neutras los BLA son positivos, casi constantes con *n*, en los cationes y dicationes, los BLA disminuyen al disminuir el tamaño del ciclo, de modo que los dicationes más pequeños que el [9]CPP^{2+} tienen BLA negativos. Por lo tanto, se puede concluir que la oxidación facilita la deslocalización electrónica en el esqueleto C-C.

El análisis estructural ha sido complementado con cálculos de los desplazamientos químicos independientes del núcleo (NICS, *Nucleus-Independent Chemical Shifts*), en el nivel (U)B3LYP/6-311+G(2df,p).[72] Como referencia se ha utilizado el valor calculado para el NICS del benceno en el centro, NICS(0), y a 1 Å por encima de su centro geométrico, NICS(1), cuyos valores han resultado ser −8 y −10 ppm, respectivamente. En la Figura 17c se muestran los resultados de los NICS en el centro de la cavidad para los diferentes [n]CPPs en función de *n* para las diferentes especies neutras, cationes y dicationes. En las especies neutras estos valores del NICS son en todos los casos no nulos, pero tal vez lo más interesante es que en los cationes y aún más en los dicationes los NICS disminuyen al disminuir *n*, alcanzando valores de −20 ppm para el [5]CPP^{2+} y −5 ppm para el [11]CPP^{2+}.

El conjunto de todos los parámetros analizados demuestra que los dicationes de menor tamaño están caracterizados por una conjugación totalmente diferente a la existente en las especies neutras, constituyendo un nuevo modelo experimental de la conjugación cíclica radial. La pérdida de un único electrón es suficiente para romper la aromaticidad de los fenilenos y favorecer la conjugación radial cíclica, pero la pérdida de dos electrones es aún más conveniente por el hecho de alcanzarse la paridad en el número de electrones π total en el sistema. Con el aumento del tamaño de los ciclos el efecto estabilizador de la conjugación π cíclica radial deja de ser favorable ya que disminuye el solapamiento entre los orbitales π, y a partir de [9]CPP^{2+} se observa un creciente carácter bi-radical con una separación de carga. Para esta interpretación también existen en la literatura evidencias en el análisis EPR y NMR de los dicationes.[73]

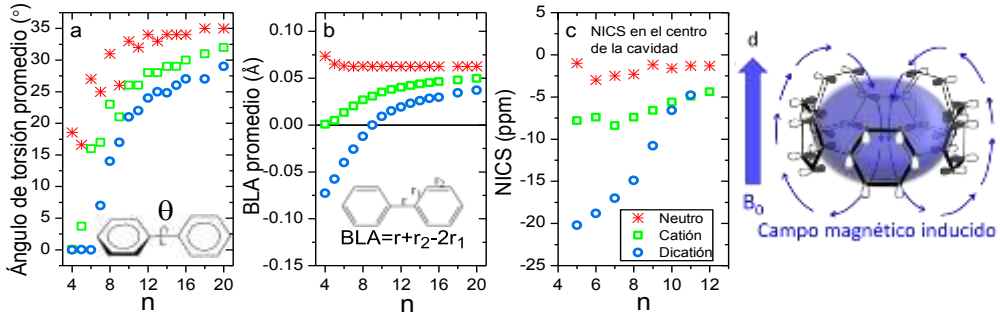

Figura 17. Evolución con *n* para los [n]CPPs neutros, catiónicos y dicatiónicos; a) ángulo de torsión entre fenilenos vecinos. b) Parámetro BLA promedio. c) NICS en el centro de la cavidad del [n]CPP. d) Esquema del campo magnético inducido en el interior del [5]CPP^{2+} por un campo externo, B_0.

11.3.5 Adaptabilidad y Deformabilidad de los [n]CPPs

Los [n]CPPs y los SWCNTs son sistemas completamente diferentes pero ambos están formados por unidades conjugadas con una forma cilíndrica. Por lo tanto, de todas sus propiedades las que están relacionadas con su cavidad rica en electrones son las que muestran en ambos un comportamiento convergente. Por ejemplo, su deformación inducida por la presión hacia formas ovalizadas. También su capacidad para hospedar sistemas con el tamaño adecuado en el interior de su cavidad. Los sistemas supramoleculares resultantes son estables ya que la alta densidad electrónica π les permite establecer interacciones de van der Waals. Dado el control en términos de tamaño y pureza de los [n]CPPs, la formación de sistemas supramoleculares es mucho más restrictiva y la caracterización de los procesos *in situ* puede ser evaluada de manera precisa.

11.3.5.1 Deformabilidad del [6]CPP al [12]CPP

El "strain" interno de los [n]CPPs puede modularse al someter los ciclos a altas presiones. En SWCNTs este tipo de experimentos han revelado propiedades mecánicas de los SWCNTs. Como dispositivo para generar la alta presión se ha utilizado una celda de yunques de zafiro alcanzándose presiones máximas de 10-12 GPa y la espectroscopía Raman como herramienta de diagnóstico.

En este apartado se va a analizar las muestras recuperadas tras un ciclo de presión. En la Figura 18a se compara el espectro Raman del [6]CPP medido en condiciones ambiente antes y después del ciclo de presión. Se puede observar que existe un desdoblamiento en las bandas Gs y que aparece una nueva contribución en 1600 cm^{-1}. Por otro lado en la zona de bajas frecuencias se observa que la banda p-RBM del [6]CPP antes del ciclo de presión desaparece tras ser sometido a presión y en su lugar aparecen dos contribuciones a menor y mayor frecuencias: 409 y 933 cm^{-1}. A partir de la ecuación 2 estos valores se pueden relacionar con unos diámetros alrededor de 0.94 y 0.41 nm. Hemos considerado que la presión induce la deformación permanente del [6]CPP hacia su configuración "peanut", estabilizada por interacciones π-π entre los lados opuestos del CPP, como se representa en la Figura 18a. Un comportamiento similar ha sido descrito anteriormente para los SWCNTs por Yao et al.[74] y Cronin et al.[75] y para CNTs multi-pared por Yu et al.[76]

En la Figura 18b se representa el espectro Raman de [12]CPP en condiciones ambiente antes y después del ciclo de presión. El efecto ejercido por la presión en este caso parece ser totalmente reversible ya que ninguna de las bandas Raman sufre cambios significativos.

Se han llevado a cabo estudios análogos para todos los [n]CPPs con *n* desde 5 a 12 encontrándose que la presión induce cambios asociados a deformaciones de la forma circular que resultan más reversibles conforme aumenta el tamaño del ciclo, de manera que a partir del [9]CPP se puede considerar que los [n]CPPs se recuperan tras el ciclo de presión.

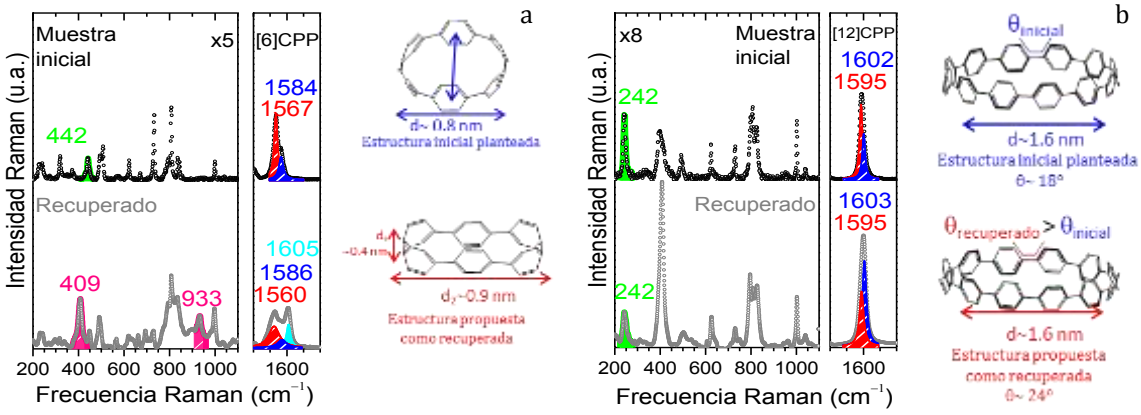

Figura 18. Espectros Raman registrados con 785 nm para: a) [6]CPP y b) [12]CPP. Espectros antes (superior) y después (inferior) del ciclo de presión (~10 GPa).

11.3.5.2 Sistemas Huésped-Anfitrión

Como ya se ha comentado anteriormente los [n]CPPs ofrecen la ventaja de poseer un diámetro y quiralidad definida frente a los SWCNTs, cuyas muestras comerciales se caracterizan por tener un diámetro más heterogéneo. En el siguiente bloque se resumen diferentes sistemas supramoleculares formados a altas presiones a partir de los [n]CPPs.

Síntesis del Primer Nanohoop Doble, [6]CPP@[12]CPP

En la introducción ya se mencionó que en la literatura se ha propuesto la formación a partir de [n]CPPs de las denominadas "muñecas rusas",[52] en las que un determinado [n]CPP ocuparía la cavidad interna de otro [n]CPP más grande. Además, dichos sistemas serían análogos a los nanotubos de carbono de pared doble (DWCNTs).[77] Aquí lo que se ha utilizado es la presión para formarlos. Así, primero se han mezclado en estado sólido dos tipos de [n]CPPs de diferente tamaño y cuyos diámetros son apropiados para formar un complejo como el descrito arriba. En concreto, hemos escogido [6]- y [12]CPP, y su mezcla equimolar en estado sólido se ha sometido a una presión máxima de unos 8 GPa para, a continuación, analizar el espectro Raman de la muestra recuperada en condiciones ambiente en comparación con los de los [n]CPPs individuales y el de la mezcla inicial.

En la Figura 19a se observa que, mientras que el espectro de la mezcla inicial [6]CPP - [12]CPP está formado por la superposición de los espectros de los compuestos individuales, en el espectro de la muestra recuperada se observan cambios significativos. Por ejemplo, en la zona de altas frecuencias de las bandas G, se aprecia que ambas bandas se desplazan significativamente hacia menores frecuencias. Por otro lado, en la zona de bajas frecuencias de las bandas p-RBMs de [6]- y [12]CPP, puede verse que en la muestra recuperada estas bandas se desplazan hacia menores frecuencias. Estos desplazamientos pueden relacionarse con la formación de interacciones de tipo van der Waals entre [6]- y [12]CPP, tal y como se representa en la Figura 19b. Sugerimos que la presión puede haber inducido la formación del doble nanohoop [6]CPP@[12]CPP, lo que evitaría además el colapso que sufriría el [6]CPP al ser comprimido a estas presiones. Estas observaciones están de acuerdo con resultados previos en DWCNTs, donde el nanotubo exterior actúa como protector del tubo interior, evitando así el colapso de este último.[78]

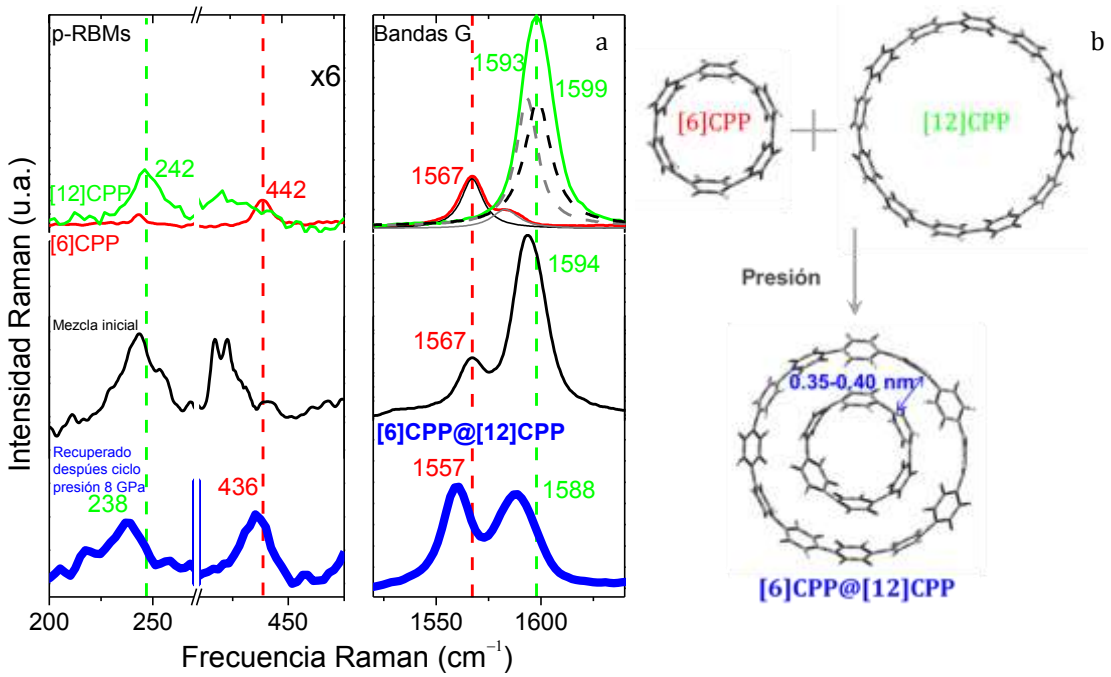

Figura 19. a) Espectros Raman registrados con 532 nm, en todos los casos en estado sólido. De arriba a abajo: [6]CPP y [12]CPP puros y separados; mezcla del [6]CPP y [12]CPP antes del tratamiento; mezcla del [6]CPP y [12]CPP recuperada tras el ciclo de presión (~8 GPa). b) Esquema de la formación del nanohoop doble [6]CPP@[12]CPP.

Complejos de Transferencia de Carga con C_{60}, $C_{60}^{\bullet-}$@[10]CPP$^{\bullet+}$

Por otro lado, los [n]CPPs son capaces de acomodar también moléculas de fullereno en su cavidad interna, formando así complejos supramoleculares C_{60}@[n]CPP, en analogía a los C_{60}@SWCNT *peapods*.[51,52] Interacciones π-π cóncavo-convexas son las responsables de inducir el autoensamblaje de las estructuras supramoleculares. Así, en la literatura se ha descrito la encapsulación en disolución del C_{60} por [10]CPP, formando el complejo C_{60}@[10]CPP en un proceso exotérmico.[52]

En este trabajo se ha querido investigar este tipo de complejo desde otra perspectiva diferente. Para ello se ha preparado una muestra en estado sólido compuesta por [10]CPP y C_{60} en relación 1:1, y se ha sometido esta mezcla alta presión, hasta unos 10 GPa, presión por debajo del límite de estabilidad del C_{60} (22 GPa).[79] La muestra recuperada a presión ambiente tras el ciclo de presión ha sido analizada mediante espectroscopía Raman. En la Figura 20 se comparan los espectros Raman de: los sistemas moleculares individuales, [10]CPP y C_{60}, la especie catiónica [10]CPP$^{\bullet+}$, el anión $C_{60}^{\bullet-}$[79], el complejo $C_{60}^{\bullet-}$@[10]CPP$^{\bullet+}$ formado en disolución, y la mezcla recuperada de [10]CPP y C_{60} tras el ciclo de presión.

Puede observarse que en el espectro de la muestra recuperada las bandas G del [10]CPP se desplazan hacia menores frecuencias, tal y como sucede en el radical catión [10]CPP$^{\bullet+}$. Al mismo tiempo, alrededor de 1469 cm^{-1}, donde aparece la banda correspondiente a la tensión C-C conocida como "*pentagonal pintching*" del C_{60}, se observa que en la muestra recuperada la banda se ha desplazado hacia 1464 cm^{-1}, valor cercano al definido para el radical anión $C_{60}^{\bullet-}$.[79] Por ultimo, en la zona de bajas frecuencias el p-RBM del [10]CPP se ha desplazado unos 10 cm^{-1} hacia mayores frecuencias. En esta zona también se observa a 270 cm^{-1} una banda característica del fullereno, que apenas se desplaza respecto su posición original, de acuerdo con la formación del $C_{60}^{\bullet-}$.[79]

El conjunto de todos estos resultados indica que la presión ha inducido la formación del radical anión ($C_{60}^{\bullet-}$) y el radical catión del [10]CPP ([10]CPP$^{\bullet+}$). Por tanto, hemos interpretado este fenómeno como la consecuencia de que la presión produce la donación de un electrón desde el [10]CPP al aceptor C_{60}, formándose un complejo de transferencia de carga, la sal $C_{60}^{\bullet-}$@[10]CPP$^{\bullet+}$.

En la tesis pueden encontrarse los detalles de otros experimentos análogos que se han realizado para inducir mediante la presión la encapsulación del C_{60} con [9]CPP y [11]CPP. A partir de los espectros medidos se ha podido concluir que se obtienen complejos supramoleculares semejantes.

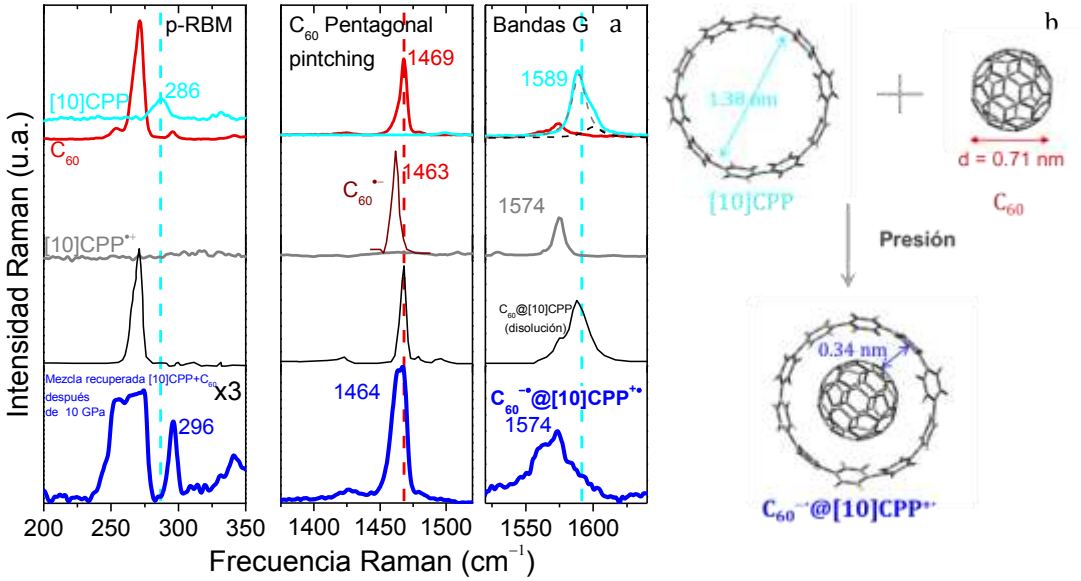

Figura 20. a) Espectros Raman registrados con 785 nm. De arriba a abajo: C_{60} y [10]CPP puros y separados en estado sólido; [10]CPP$^{+\bullet}$ y $C_{60}^{-\bullet}$ de la Ref. [79]; complejo C_{60}@[10]CPP formado en disolución; $C_{60}^{-\bullet}$@[10]CPP$^{+\bullet}$ en estado sólido y condiciones ambiente tras el ciclo de presión. b) Esquema de la formación de la sal $C_{60}^{-\bullet}$@[10]CPP$^{+\bullet}$ por transferencia de carga.

Modulación de la Orientación del C_{70} en la Cavidad del [10]CPP

En esta sección se resumen los estudios realizados en la tesis sobre las estructuras supramoleculares C_{70}@[n]CPP (con n = 9-12) formados en disolución.[31] En estos complejos se ha observado que el C_{70} se puede adaptar a la cavidad en diferentes orientaciones dependiendo del tamaño del [n]CPP, dado que el C_{70} tiene una forma elipsoidal. Con el [10]CPP adopta una orientación "*lying*" (su eje largo es perpendicular al plano radial del [10]CPP), y en cambio con el [11]CPP el eje largo de C_{70} se alinea de manera paralela al plano radial del [11]CPP, con una orientación denominada "*standing*". Aquí se ha estudiado mediante espectroscopía Raman el comportamiento bajo presión de estos complejos supramoleculares 1:1, analizando los posibles cambios de orientación del C_{70} en la cavidad del CPP. Por otro lado, la asignación de las diferencias espectroscópicas entre una conformación y otra podría servir como herramienta en el análisis conformacional de muestras de *peapods* en SWCNTs.

Los espectros de la Figura 21a muestran que la aplicación de presión sobre el complejo C_{70}@[10]CPP producen cambios significativos, de manera que la muestra recuperada del ciclo de presión presenta un espectro Raman ligeramente diferente al original. Así, la banda GA_{1g} del [10]CPP se desplaza a mayores frecuencias, desde 1581 a 1584 cm^{-1}. Al mismo tiempo el modo de la tensión C-C tangencial también se desplaza hacia mayores frecuencias, desde 1562 a 1567 cm^{-1}. Por otro lado, el modo de respiración radial del fullereno C_{70} se desplaza hacia menores frecuencias, desde 456 a 454 cm^{-1}. Este cambio se puede asociar a un cambio de orientación, sabiendo que en el C_{70}@[11]CPP este modo aparece a 453 cm^{-1}. Estos datos, junto con la dependencia de las frecuencias con la presión, indican que a una presión de unos 1.6 GPa se produce un cambio conformacional en el C_{70} dentro de la cavidad del [10]CPP, pasando de [10]CPP@C_{70} en orientación "*lying*" a orientación "*standing*", tal y como se ha esquematizado en la Figura 21b.

Un estudio análogo fue llevado a cabo con el complejo C_{70}@[11]CPP. Las observaciones muestran que la presión no induce ningún cambio espectral significativo y la orientación del C_{70} sigue siendo "*standing*". Por el contrario, al calentar este complejo supramolecular hasta aproximadamente unos 400 K se observan cambios que permanecen al disminuir la temperatura. El análisis espectroscópico de esta muestra recuperada indica que el C_{70} rotaría hacia una orientación "*lying*", configurando el C_{70}@[11]CPP en orientación "*lying*".

Estos resultados evidencian la capacidad de los [n]CPPs para amoldarse tanto química como conformacionalmente al sistema hospedado en su cavidad. Por último, en el análisis de los [n]CPPs como modelos de los SWCNTs, la caracterización Raman de estos complejos bien definidos podría ayudar a comprender la complejidad de estos *peapods* formados por fullerenos y los SWCNTs.[80-82]

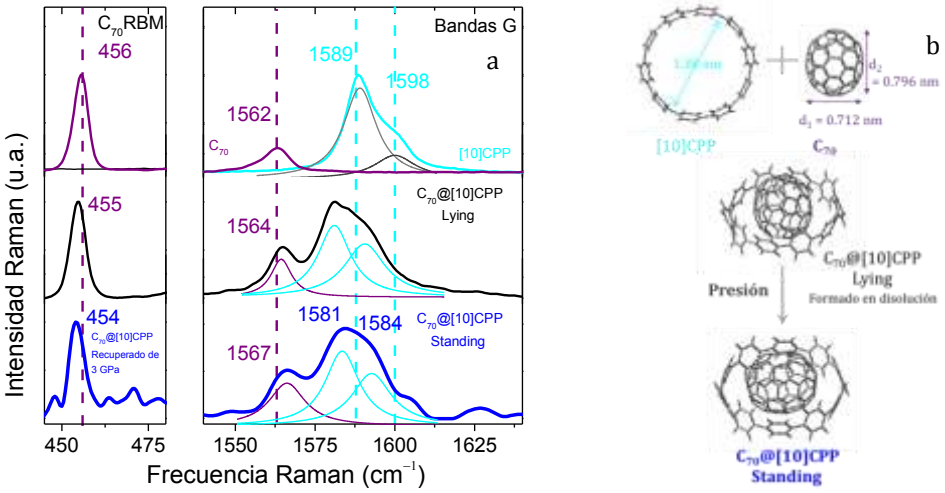

Figura 21. a) Espectros Raman registrados con 785 nm. De arriba a abajo: C_{70} y [10]CPP puros y separados en estado sólido; complejo C_{70}@[10]CPP formado en disolución; complejo C_{70}@[10]CPP en estado sólido y condiciones ambiente tras el ciclo de presión (~3 GPa). b) Esquema de la formación de C_{70}@[10]CPP y la transición del C_{70}@[10]CPP de una conformación "*lying*" hacia otra "*standing*".

11.3.6 Evaluación de la Respuesta de los [n]CPPs a la Compresión

En este apartado se resumen los resultados obtenidos sobre la evolución espectral Raman en función de la presión para los [n]CPPs puros. Se ha utilizado una celda de tipo yunque con zafiros enfrentados y en la mayoría de los [n]CPPs se han alcanzado presiones de hasta unos 12 GPa.

11.3.6.1 Espectroscopia Raman de los [n]CPPs a Altas Presiones

Del análisis de la variación con la presión de todas las bandas espectrales se puede extraer bastante información. Aquí mostramos únicamente los resultados más significativos. En la Figura 22 se muestra la frecuencia Raman de las bandas GA_{1g} y GE_{2g} en función de la presión para todos los [n]CPPs. Se observa que en ambos modos las frecuencias presentan dos regímenes lineales con la presión, con una mayor pendiente a bajas presiones. La presión donde se observa este cambio brusco en la pendiente se ha denominado presión de transición (*PT*). Su valor es mayor para los [n]CPPs de menor diámetro, siendo alrededor de 5.8 GPa en el [5]CPP y de 0.6 GPa en el [12]CPP. Esta tendencia se ha observado para todas las bandas que involucran la tensión del enlace C-C. Hay que señalar que este tipo de comportamiento ha sido previamente descrito en los nanotubos de carbono,[74,83] y se ha relacionado con la pérdida de su forma cilíndrica y su ovalización, de modo que:

- En el primer régimen, a presiones por debajo de *PT*, la presión afectaría principalmente a las distancias de enlace y en menor grado a los ángulos moleculares.
- A presiones superiores a *PT*, la presión afectaría principalmente a los ángulos moleculares, induciendo así la ovalización del sistema.

Esta descripción está de acuerdo con la observación de una mayor pendiente para las bandas G, a presiones por debajo de *PT*, y una menor pendiente por encima de *PT*. En el primer régimen las bandas G que involucran la tensión C-C sufren un mayor cambio por la presión, mientras que en el segundo régimen la modulación angular afecta en menor grado a las distancias de enlace C-C, con lo cual se justifica las menores pendientes observadas. El primer régimen se conoce en la literatura de nanotubos de carbono como la fase dura y el segundo como la fase blanda del tubo.[84]

Además, estos resultados nos permiten obtener por primera vez los coeficientes de presión de los [n]CPPs, tanto para las bandas G como para otros modos como los RBMs. En la Figura 23a se han representado en función del diámetro los coeficientes de presión para presiones por debajo de *PT* de las bandas GA_{1g} y GE_{2g}. Se puede observar que los [n]CPPs de mayor tamaño tienen los valores más altos, es decir, en estos ciclos más grandes la presión produce un cambio mayor en las frecuencias Raman, lo que significaría cambios mayores en las distancias de enlace.

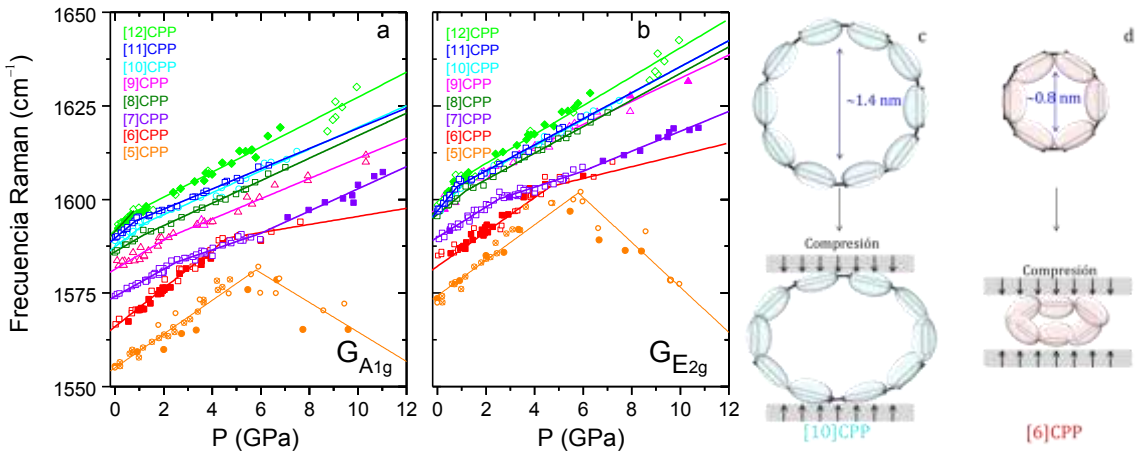

Figura 22. a) Variación con la presión de la frecuencia Raman de las bandas G para todos los [n]CPPs. a) GA_{1g} y b) GE_{2g}. Símbolos rellenos o vacíos para cada [n]CPP se corresponden con diferentes series de medidas. Esquema de los cambios con la presión de la forma molecular: c) [10]CPP y d) [6]CPP.

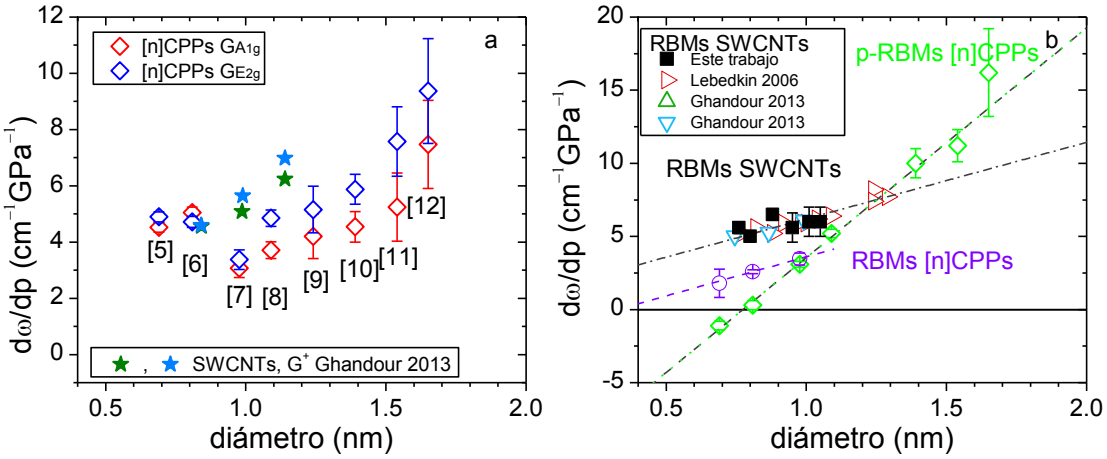

Figura 23. a) Coeficientes de presión en función del diámetro obtenidos para los [n]CPPs a presiones menores de *PT* para las bandas G, (◇) GE_{2g} y (◇) GA_{1g}. Datos de SWCNTs tomados de Ghandour et al. [85]: (★) , (★). b) Coeficientes de presión de los modos circunferenciales representados frente al diámetro para [n]CPPs y SWCNTs. [n]CPPs: (◇) p-RBMs y (○) RBMs. Para los RBMs de los SWCNTs: (■) este trabajo; (▷) Lebedkin et al. [86], y (△, ▽) Ghandour et al. [85].

En la Figura 23a también se muestra que los coeficientes de presión del [5]- y el [6]CPP son mayores que los del [8]CPP, lo que podría explicarse por la mayor tensión interna en los ciclos de menor tamaño, que hace que su respuesta a la presión sea bastante diferente a la que presentan el resto de [n]CPPs. Esto, junto con otros resultados no mostrados en el resumen, nos hacen concluir que en el [5]CPP con la presión se forma su configuración quinonoide y en el [6]CPP se obtiene una forma colapsada.

Por otro lado, en la literatura se ha establecido que la deformación de los SWCNTs depende de su diámetro, concluyendo que, al aumentar el tamaño del tubo, mayor es el coeficiente de presión de la banda G.[84,87,88] En la Figura 23a se comparan los coeficientes de presión a presiones por debajo de *PT* de la banda G de SWCNTs en función de su diámetro,[85] junto con los valores obtenidos para los [n]CPPs. Se observa que el comportamiento en ambos sistemas, SWCNTs y [n]CPPs, es análogo, con una pendiente con el diámetro similar. Hasta donde nosotros sabemos no se tiene información de cómo CNTs con diámetros pequeños como los de [5]- y [6]CPP responderían a la presión, pero es presumible que la deformación hacia una configuración quinonoide y la transformación hacia una configuración "*peanut*" están favorecidas en el caso de los CPPs por su estructura molecular, de modo que sería esperable que en los CNTs de ese tamaño la presión cause otro tipo de efectos.

En la Figura 23b se han representado los coeficientes de presión en función del diámetro de las bandas RBMs y p-RBMs de los [n]CPPs a presiones por debajo de *PT*, junto con los coeficientes de presión de los RBMs de los SWCNTs.[85,86] Se puede observar que los RBMs de los [n]CPPs siguen un comportamiento paralelo al descrito por los SWCNTs, esto es, cuanto mayor es el diámetro mayor es el coeficiente de presión. En el caso de los p-RBMs de los [n]CPPs se observa también un aumento de los coeficientes de presión con el diámetro, pero está claro que para estos modos la variación con el diámetro es mucho mayor, de manera que los p-RBMs de los [n]CPPs más grandes son muy sensibles a la presión. Hay que señalar que los coeficientes de presión de los modos RBMs y p-RBMs son los únicos que presentan este aumento lineal con el aumento del tamaño, reflejo de su origen radial, a diferencia de los modos donde la tensión C-C está involucrada, donde la tendencia con el tamaño siempre presenta un mínimo alrededor del [7]- y [8]CPP.

Por último, del comportamiento con la presión se puede concluir que aunque SWCNTs y [n]CPPs siguen tendencias similares, en términos de la dependencia no lineal con la presión de las frecuencias Raman y, por tanto, de las deformaciones sufridas por la presión, el hecho de que los coeficientes de presión tengan valores bastante diferentes también revela el diferente carácter estructural de ambos sistemas.

11.3.6.2 Propiedades Mecánicas de los [n]CPPs

Como se ha mencionado anteriormente en los SWCNTs se ha descrito que la presión produce deformaciones en la forma del tubo, más fácil cuanto mayor diámetro tienen los tubos, de manera que al disminuir el diámetro de los tubos mayor es la presión necesaria para inducir la ovalización, la presión denominada *PT*.[84,87,88]

En la Figura 24 se han comparado los resultados obtenidos en este trabajo para los [n]CPPs con valores de los SWCNTs recogidos en la literatura.[89,90] Se observa como ambos sistemas siguen un comportamiento similar donde *PT* aumenta exponencialmente con la disminución del diámetro. En estudios previos de SWCNTs se ha modelizado esta deformación circular–oval relacionada con *PT* mediante la teoría clásica del colapso de anillos elásticos.[91-95] Esta teoría relaciona la presión a la que un tubo pierde su forma circular con el radio del tubo antes de que se le aplique cualquier deformación, *R*, y establece que *PT* sigue una ley potencial con el radio del tubo:

$$PT = \frac{3D}{R^3} \tag{6}$$

donde *D* corresponde a la denominada rigidez flexural o "*bending stiffness*", que es una característica importante de cualquier material relacionada con la dependencia de la energía de "strain" con su curvatura. Además, en materiales laminares este parámetro mecánico mide la resistencia a doblar la lámina. Utilizando la ecuación 6 para ajustar los datos experimentales de *PT* de los [n]CPPs de la Figura 24a se ha obtenido un valor de $D = (0.57 \pm 0.02)$ eV. En el caso de los SWCNTs los diferentes autores han determinado valores comparables para *D*, entre 0.6 y 1.4 eV.[84,88,96]

Por otro lado, en los SWCNTs también se ha descrito que a la presión *PT* se produce una transición de una fase dura a una fase más blanda.[84,97] Esto se puede justificar desde el punto de vista de que a presiones por debajo de *PT* principalmente se modulan enlaces C-C, duros, y a presiones por encima de *PT* ángulos moleculares, más blandos. Sun et al.[84] han propuesto para los SWCNTs un modelo que relaciona el módulo de compresibilidad radial de la fase dura (B_h) con *D* y, por tanto, con la presión *PT*:

$$B_h = \frac{6D}{h^2 R} \tag{7}$$

donde *h* corresponde al espesor de la pared del tubo, considerado para SWCNTs como 0.66 Å.[84]

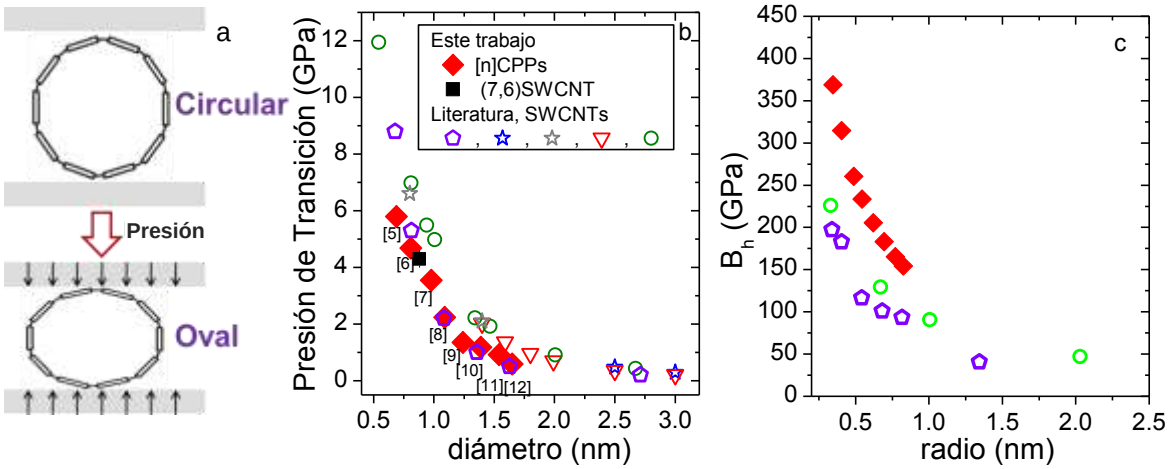

Figura 24. a) Esquema del cambio de la sección inducido por la presión en el [10]CPP. b) Presión de transición representada frente al diámetro para: (◆) [n]CPPs obtenido de la evolución de las frecuencias en función de la presión; (■) (7,6) SWCNTs, este trabajo junto con datos de SWCNTs tomados de la literatura. c) Módulo de compresibilidad radial en la fase dura en función del radio: (◆) [n]CPPs datos estimados a través de las ecuaciones (6-7). (⬠) Valores calculados por Sun et al. [84]. (○) datos calculados y (☆) experimentales de Elliot et al. [87], (▽) *PT* en la transición circular-oval y (☆) Presión de colapso dada por Hasegawa et al. [88] y (○) datos de B_h para SWCNTs con quiralidad armchair dados por Itami et al. [97].

Suponiendo que los [n]CPPs siguen las mismas leyes de deformación que los SWCNTs se puede estimar B_h para los [n]CPPs a partir de la ecuación 7 utilizando el mismo espesor, 0.66 Å. Estos resultados de B_h se han representado en la Figura 24c para los [n]CPPs junto con resultados tomados de la literatura para los SWCNTs.[84,97] Se puede observar que en ambos sistemas el hábito es similar, aumentando al disminuir el radio. Sin embargo, los valores de B_h de los [n]CPPs son ligeramente más altos que los de los SWCNTs,[97,98] con un valor de unos 370 GPa para el [5]CPP y de 150 GPa para el [12]CPP. Estos resultados demuestran que en su fase dura los [n]CPPs pueden ser incluso más rígidos que los SWCNTs. Es de destacar el dato encontrado para el [5]CPP, donde se ha estimado un valor bastante alto y cercano al del diamante, 445 GPa.[99] Esto significa que el módulo de compresibilidad de los [n]CPPs más pequeños es extremadamente alto, comparable al del material más duro. Este hecho podría justificarse por la alta tensión interna del [5]CPP, unos 114 kcal mol^{-1}, que le proporciona una gran resistencia a la deformación y hace que sea un sistema muy rígido.

11.4 Conclusión

En este trabajo se han mostrado las propiedades excepcionales de los [n]CPPs hasta ahora no puestas en manifiesto, tales como la quinonoidización parcial existente en los [n]CPPs neutros, la conjugación radial cíclica, el carácter biradical de las especies iónicas y sus singulares propiedades mecánicas, con módulos de compresibilidad radial por encima de los descritos para los SWCNTs. Además, se ha demostrado la enorme capacidad de los [n]CPPs para adaptarse a diferentes condiciones, siendo capaces de deformarse para hospedar en su cavidad a otros sistemas del tamaño apropiado, de manera que los complejos supramoleculares resultantes alcanzan su estabilidad gracias a interacciones π-π cóncavo-convexo y a interacciones electrostáticas.

11.5 Aportaciones Fundamentales de la Tesis Doctoral

Un aspecto esencial de la tesis ha sido el estudio experimental y teórico de la espectroscopía Raman de estos sistemas, de manera que se han asignado por primera vez los modos vibracionales más característicos de los [n]CPPs, así como su dependencia con el tamaño del ciclo y su carga. Hay que destacar que en este análisis ha sido fundamental la comparación realizada con la espectroscopía Raman de otros compuestos relacionados como son los oligoparafenilenos lineales y los nanotubos de carbono.

Por un lado se ha demostrado que existe un alto grado de deformación fuera del plano de las unidades fenilénicas, lo que induce una reorganización electrónica hacia la quinonoidización. Esta es mínima para los ciclos de mayor tamaño, alrededor de un 3 % en el [12]CPP, y es ligeramente más alta para los ciclos más pequeños, aproximadamente un 17 % para el [5]CPP.

Además, se ha demostrado que los tautómeros quinonoides son energéticamente desfavorables; sólo encontrándose un mínimo (no global) con una configuración quinonoide en la superficie de energía potencial para las especies más tensionadas, [4]CPP y [5]CPP. Un resultado notable de este trabajo ha sido la demostración de que la compresión del [5]CPP, a presiones del orden de GPa, permite acceder por primera vez a una configuración quinonoide cíclica distorsionada, configuración que no se ha podido obtener por otras vías.

Experimentalmente se ha accedido a sistemas con conjugación radial cíclica, convirtiéndose los [n]$CPPs^{2+}$ de menor tamaño en los modelos idóneos para explorar dicha conjugación. Se ha demostrado que la pérdida de un único electrón en los [n]CPPs es suficiente para romper la aromaticidad de los bencenos y favorecer la conjugación radial cíclica; pero la pérdida de dos electrones está aún más favorecida por el hecho de alcanzarse la paridad en el número total de electrones π. En los ciclos de mayor tamaño el efecto estabilizador de la conjugación π radial cíclica

deja de ser favorable ya que el solapamiento entre los orbitales π es menor observándose que, a partir del [9]CPP^{2+}, aparece una creciente separación de la carga y un mayor carácter biradical.

Los [n]CPPs exhiben una elevada libertad en el giro de los fenilenos vecinos y son altamente deformables de manera reversible en cuanto a su forma circular, por lo que son capaces de modelarse para adaptarse a entornos químicos y configuraciones diferentes y así hospedar diferentes sistemas del tamaño adecuado garantizando la máxima interacción entre ambos.

Asimismo, se ha observado que los [n]CPPS son tan deformables como los nanotubos de carbono en cuanto a su forma circular, observándose que la presión induce la formación en los [n]CPPs en una configuración oval análoga a las descritas en SWCNTs. Además, en su fase circular, dura, el módulo de compresibilidad radial de los [n]CPPs es mayor incluso que el de los SWCNTs, información que da incluso más valor a estos extraordinarios sistemas moleculares.

Finalmente, haciendo referencia al título de esta tesis doctoral, los conceptos aquí enumerados se pueden establecer exclusivamente en los [n]CPPS, y están ligados a su carácter molecular, a la morfología cíclica y a su diámetro. Además, se ha comprobado que los [n]CPPs y los nanotubos de carbono comparten propiedades relacionadas con su configuración tubular, como son su habilidad para hospedar sistemas del tamaño apropiado y su elevado módulo de compresibilidad radial.

11.6 References

1 A. Kekulé, *Liebigs Ann.* **137**, 129–196 (1866).

2 G. Herzberg, *Infrared and Raman spectra of polyatomic molecules*, Van Nostrand, Princeton (1954).

3 C. R. Bailey, C. K. Ingold, H. G. Poole, C. L. Wilson, *J. Chem. Soc*. 222–235 (1946).

4 M. Kertesz, C. H. Choi, S. Yang, *Chem. Rev*. **105**, 3448–3481 (2005).

5 R. Jasti, J. Bhattacharjee, J. B. Neaton, C. R. Bertozzi, *J. Am. Chem. Soc*. **130**, 17646–17647 (2008).

6 J. Xia, J. W. Bacon, R. Jasti, *Chem. Sci*. **3**, 3018–3021 (2012).

7 P. J. Evans, E. R. Darzi, R. Jasti, *Nature Chem.* **6**, 404–408 (2014).

8 J. Xia, R. Jasti, *Angew. Chem. Int. Ed.* **51**, 2474–2476 (2012).

9 F. Sibbel, K. Matsui, Y. Segawa, A. Studer, K. Itami, *Chem. Commun.* **50**, 954–956 (2014).

10 S. Yamago, Y. Watanabe, T. Iwamoto, *Angew. Chem. Int. Ed.* **49**, 757–759 (2010).

11 Y. Segawa, P. Šenel, S. Matsuura, H. Omachi, K. Itami, *Chem. Lett*. **40**, 423–425 (2011).

12 E. Kayahara, Y. Sakamoto, T. Suzuki, S. Yamago, *Org. Lett*. **14**, 3284–3287 (2012).

13 Y. Segawa, S. Miyamoto, H. Omachi, S. Matsuura, P. Senel, T. Sasamori, N. Tokitoh, K. Itami, *Angew. Chem. Int. Ed.* **50**, 3244–3248 (2011).

14 R. Herges, *Chem. Rev.* **106**, 4820–4842 (2006).

15 E. S. Hirst, F. Wang, R. Jasti, *Org. Lett.* **13**, 6220–6223 (2011).

16 Y. Matsuo, K. Tahara, M. Sawamura, E. Nakamura, *J. Am. Chem. Soc*. **126**, 8725–8734 (2004).

17 H. S. Choi, K. S. Kim, *Angew. Chem. Int. Ed*. **38**, 2256–2258 (1999).

18 P. Li, T. J. Sisto, E. R. Darzi, R. Jasti, *Org. Lett.* **16**, 182–185 (2014).

19 K. Tahara, Y. Tobe, *Chem. Rev*. **106**, 5274–5290 (2006).

20 T. J. Sisto, M. R. Golder, E. S. Hirst, R. Jasti, *J. Am. Chem. Soc*. **133**, 15800–15802 (2011).

21 T. J. Sisto, R. Jasti, *Synlett* **23**, 483–489 (2012).

22 E. S. Hirst, R. Jasti, *J. Org. Chem*. **77**, 10473–10478 (2012).

23 R. Jasti, C. R. Bertozzi, *Chem. Phys. Lett*. **494**, 1–7 (2010).

24 B. D. Steinberg, T. L. Scott, *Angew. Chem. Int. Ed*. **48**, 5400–5402 (2009).

25 H. B. Li, A. J. Page, S. Irle, K. Morokuma, *Chem. Phys. Chem.* **13**, 1479–1485 (2012).

26 H. B. Li, A. J. Page, S. Irle, K. Morokuma, *J. Am. Chem. Soc*. **134**, 15887–15896 (2012).

27 H. Omachi, T. Nakayama, E. Takahashi, Y. Segawa, K. Itami, *Nature Chem*. **5**, 572–576 (2013).

28 T. Iwamoto, Y. Watanabe, T. Sadahiro, T. Haino, S. Yamago, *Angew. Chem. Int. Ed.* **50**, 8342–8344 (2011).

29 U. H. F. Bunz, S. Menning, N. Martín, *Angew. Chem. Int. Ed.* **51**, 7094–7101 (2012).

30 S. Schrettl, H. Frauenrath, *Angew. Chem. Int. Ed.* **51**, 6569–6571 (2012).

31 T. Iwamoto, Y. Watanabe, H. Takaya, T. Haino, N. Yasuda, S. Yamago, *Chem. – Eur. J*. **19**, 14061–14068 (2013).

32 M. Gussoni, C. Castiglioni, and G. Zerbi, *Spectroscopy of Advanced Materials*, edited by R. J. H. Clark, R. E. Hester ,Wiley, New York, Vol. 11, p. 251(1991).

33 E. Ehrenfreund, Z. Vardeny, O. Brafman, B. Horovitz, *Phys. Rev. B* **36**, 1535–1553 (1987).

34 H. Chen, M. R. Golder, F. Wang, R. Jasti, A. K. Swan, *Carbon* **67**, 203–213 (2014).

35 V. Hernandez, C. Castiglioni, M. Del Zoppo, G. Zerbi, *Phys. Rev. B* **50**, 9815–9823 (1994).

36 Y. Segawa, H. Omachi, K. Itami, *Org. Lett.* **12**, 2262–2265 (2010).

37 Y. Segawa, A. Fukazawa, S. Matsuura, H. Omachi, S. Yamaguchi, S. Irle, K. Itami, *Org. Biomol. Chem*. **10**, 5979–5984 (2012).

38 T. Iwamoto, Y. Watanabe, Y. Sakamoto, T. Suzuki, S. Yamago, *J. Am. Chem. Soc.* **133**, 8354–8361 (2011).

39 M. Rinke, H. Gusten, H. J. Ache, *J. Phys. Chem.* **90**, 2666–2669 (1986).

40 K. N. Baker, A. V .Frai, T. Resch, H. C. Knachel, W. W. Adams, E. P. Socci, B. L. Farmer, *Polymer* **34**, 1571–1587 (1993).

41 P. A. Irvine, D. C. Wu, P. J Flory, *J. Chem. Soc., Faraday Trans. 1* **80**, 1795–1806 (1984).

42 J. L. Bredas, R. R. Chance, R. Silbey, *Phys. Rev. B* **26**, 5843–5854 (1982).

43 T. A. Skotheim, *Handbook of Conducting Polymers*, Dekker, New York, (1986).

44 J. L. Bredas, R. R. Chance*, Conjugated Polymeric Materials*, Kluwer Academic, Dordrecht, (1990).

45 Y. S. Lee, M. Kertesz, R. L. Elsenbaumer, *Chem. Mater*. **2**, 526–530 (1990).

46 S. E. Lewis, *Chem. Soc. Rev.* **44**, 2221–2304 (2015).

47 T. Iwamoto, Y. Watanabe, H. Takaya, T. Haino, N. Yasuda, S. Yamago, *Chem. – Eur. J*. **19**, 14061–14068 (2013).

48 T. J. Sisto, X. Tian, R. Jasti, *J. Org. Chem*. **77**, 5857–5860 (2012).

49 B. Anis, F. Börrnert, M. H. Rümmeli, C. A. Kuntscher, *J. Phys. Chem. C* **117**, 21995–22001 (2013).

50 B. W. Smith, M. Monthioux, D. E. Luzzi, *Nature* **396**, 323–324 (1998).

51 E. R. Darzi, R. Jasti, *Chem. Soc. Rev.* **44**, 6401–6410 (2015).

52 S. Fomine, M. G. Zolotukhin, P. Guadarrama, *J. Mol. Model.* **18**, 4025–4032 (2012).

53 H. Isobe, S. Hitosugi, T. Yamasaki, R. Iizuka, *Chem. Sci*. **4**, 1293–1297 (2013).

54 S. Hitosugi, R. Iizuka, T. Yamasaki, R. Zhang, Y. Murata, H. Isobe, *Org. Lett*. **15**, 3199–3201 (2013).

55 *Carbon nanotubes and Related structures. Synthesis, Characterization, Functionalization and Properties* (Eds.: N. Martín, D. M. Guldi), Wiley-VCH, Weinheim (2010).

56 G. Heimel, D. Somitsch, P. Knoll, J. L. Brédas, E. Zojer, *J. Chem. Phys.* **122**, 114511 (2005).

57 E. H. Haroz, J. G. Duque, X. Tu, M. Zheng, A. R. Hight Walker, R. H. Hauge, S. K. Doorn, J. Kono, *Nanoscale* **5**, 1411–1439 (2013).

58 L. W. Shacklette, H. Eckhardt, R. R. Chance, G. G. Miller, D. M. Ivory, R. H. Baughman, *J. Chem. Phys.* **73**, 4098–4120 (1980).

59 M. Peña-Alvarez, P. M. Burrezo, M. Kertesz, T. Iwamoto, S. Yamago, J. Xia, R. Jasti, J. T. López Navarrete, M. Taravillo, V. G. Baonza, J. Casado, *Angew. Chem. Int. Ed*. **53**, 7033–7037 (2014).

60 H. Ohtsuka, Y. Furukawa, M. Tasumi, *Spectrochim. Acta. Part A* **49**, 731–737 (1993).

61 S. M. Bachrach, D. Stück, *J. Org. Chem*. **75**, 6595–6604 (2010).

62 B. Horovitz, *Solid State Commun.* **41**, 729–734 (1982).

63 G. Zerbi, M. Gussoni, C. Castiglioni, en *Conjugated Polymers,* editado por J. L. Bredas, J. Silbey, Kluwer, New York, p. 435 (1991).

64 M. G. Gussoni, C. Castiglioni, G. Zerbi, *Spectroscopy of Advanced Materials*, editado por R. J. H. Clark, R. E. Hester, Wiley, New York, Vol. 11, p. 251(1991).

65 J. L. Jules, J. R. Lombardi, *J. Mol. Struct. (Theochem)* **255**, 664–665, (2003).

66 Y. Yamakita, M. Tamusi, *J. Phys. Chem.* **99**, 8524–8534 (1995).

67 E. B. Wilson, *Phys. Rev*. **45,** 706–714 (1934).

68 R. W. Wood, *Phys. Rev*. **36**, 1431–1434 (1930).

69 M. M. Caruso, D. A. Davis, Q. Shen, S. A. Odom, N. R. Sottos, S. R. White, J. S. Moore, *Chem. Rev*. **109**, 5755-5798 (2009).

70 S. Taubert, D. Sundholm, F. Pichierri, *J. Org. Chem*. **75**, 5867–5874 (2010).

71 S. Schrettl and H. Frauenrath, *Angew. Chem. Int. Ed.* **51**, 6569–6571 (2012).

72 Z. Chen, C. S. Wannere, C. Corminboeuf, R. Putcha, P. V. R. Schleyer, *Chem. Rev.* **105**, 3842–3888 (2005).

73 E. Kayahara, T. Kouyama, T. Kato, S. Yamago. *J. Am. Chem. Soc.* DOI: 10.1021/jacs.5b10855 (2015).

74 M. Yao, Z. Wang, B. Liu, Y. Zou. S. Yu, W. Lin, Y. Hou, S. Pan, M. Jin, B. Zou, T. Ciu, G. Zou, B. Sundqvist, *Phys. Rev. B* **78**, 205411 (2008).

75 S. B. Cronin, A. K. Swan, M. S. Ünlü, B. B. Goldberg, M. S. Dresselhaus, M. Tinkham, *Phys. Rev. B* **72**, 035425 (2005).

76 M. F. Yu, T. Kowalewski, R. S. Ruoff, *Phys. Rev. Lett*. **86**, 87–90 (2001).

77 E. del Corro, J. González, M. Taravillo, E. Flahaut, V. G. Baonza, *Nano Lett*. **8**, 2215–2218 (2008).

78 A. L. Aguiar, E. B. Barros, R. B. Capaz, A. G. Souza Filho, P. T. C. Freire, J. M. Filho, D. Machon, C. Caillier, Y. A. Kim, H. Muramatsu, M. Endo, A. San Miguel, *J. Phys. Chem. C,* **115**, 5378–5384 (2011).

79 M. S. Dresselhaus, G. Dresselhaus, P.C. Eklund, *J. Raman Spectrosc*. **27**, 351–371 (1996).

80 C. Caillier, D. Machon, A. San-Miguel, R. Arenal, G. Montagnac, H. Cardon, M. Kalbac, M. Zukalova, L. Kavan, *Phys. Rev. B* **77**, 125418 (2008).

81 P. M. Rafailov, C. Thomsen, H. Kataura, *Phys. Rev. B* **68**, 193411 (2003).

82 A. N. Khlobystov, R. Scipioni, D. Nguyen-Manh, D. A. Britz, D. G. Pettifor, G. A. D. Briggs, S. G. Lyapin, A. Ardavan, R. J. Nicholas, *Appl. Phys. Lett.* **84**, 792–794 (2004).

83 J. Sandler, M. S. P. Shaffer, A. H. Windle, *Phys. Rev. B* **67,** 035417 (2003).

84 D. Y. Sun, D. J. Shu, M. Ji, F. Liu, M. Wang, X. G. Gong, *Phys. Rev. B* **70**, 165417 (2004).

85 A. J. Ghandour, I. F. Crowe, J. E. Proctor Y. W. Sun, M. P. Halsall, I. Hernandez, A. Sapelkin, D. J. Dunstan, *Phys. Rev. B* **87**, 085416 (2013).

86 S. Lebedkin, K. Arnold, O. Kiowski, F. Hennrich, M. M. Kappes, *Phys. Rev. B* **73**, 094109 (2006).

87 J. A. Elliott, J. K. W. Sandler, A. H. Windle, R. J. Young, M. S. P. Shaffer, *Phys. Rev. Lett*. **92**, 095501 (2004).

88 M. Hasegawa, K. Nishidate, *Phys. Rev. B* **74**, 115401 (2006).

89 T. Chang, *Acta. Mech. Sinica* **23**, 159–162 (2007).

90 C. Zhang, K. Bets, S. S. Lee, Z. Sun, F. Mirri, V. L. Colvin, B. I. Yakobson, J. M. Tour, R. H. Hauge, *ACS Nano* **6**, 6023–6032 (2012).

91 J. Zang, A. Treibergs, Y. Han, F. Liu, *Phys. Rev. Lett.* **92**, 105501 (2004).

92 M. Levy, *J. Math Ser*. **3**, 7 (1884).

93 G. F. Carrier, *J. Math. Phys*. **26**, 94–103 (1947).

94 J. Chaskalovic, S. Naili, *Z. Angew. Math. Phys*. **46**, 149–155 (1995).

95 L. D. Landau, E. M. Lifshitz, *Elasticity Theory* (Pergamon, Oxford, 1986).

96 B. I. Yakobson, C. J. Brabec, H. J. Bernholc, *Phys. Rev. Lett.* **76**, 2511–2514 (1996).

97 A. N. Itami, V. K. Jindal, *Phys. Rev. B* **76**, 19544 (2007).

98 C. Lee, X. Wei, J. W. Kysar, J. Hone, *Science* **321**, 385–388 (2008).

99 E. A. Belenkov, V. A. Greshnyakov, *J. Mater. Sci.* **50**, 7627–7635 (2015).

Appendixes

Appendix 1

Phys. Chem. Chem. Phys. DOI:10.1039/C5CP05500H (2015)

Supporting Information:

From Linear to Cyclic Oligoparaphenylenes: Electronic and Molecular Changes Traced in the Vibrational Raman Spectra and Reformulation of the Bond Length Alternation Pattern Section

M. Peña Alvarez, L. Qiu, M. Taravillo, V. G. Baonza,
M C. Ruiz Delgado, S. Yamago, R. Jasti,
J. T. López Navarrete, J. Casado, M. Kertesz

DFT Calculation with Extended Basis Sets

In this section we are going to compare different computational methodologies based on the density functional theory (DFT).

Table S1. Computed main geometrical parameters and energy gap for [10]CPP optimized structure with different basis sets or functional.

Methodology	**BLA (Å)**	**Torsion, θ (°)**	**HOMO-LUMO gap (eV)**
B3LYP/6-31G(d,p)	0.0627	32.728	3.539
B3LYP-D3/6-31G(d,p)	0.0618	34.377	3.579
B3LYP/6-311+G(2df,p)	0.0652	33.033	3.472
wB97D/6-31G(d,p)	0.0750	36.714	7.003
Experimental from Ref [1,2]	0.0682	27.343	3.328

Table S2. Computed Raman shifts of the most intense bands for [10]CPP optimized structure with different basis sets or functional.

Methodology	G_{A1g} (cm^{-1})	GE_{2g} (cm^{-1})	1200 cm^{-1} A_{1g} (cm^{-1})	1280 cm^{-1} A_{1g} (cm^{-1})
B3LYP/6-31G(d,p)	1636	1649	1223	1297
B3LYP-D3/6-31G(d,p)	1646	1654	1239	1307
B3LYP/6-311+G(2df,p)	1624	1634	1219	1290
wB97D/6-31G(d,p)	1696	1697	1240	1326

Table S3. Scaled computed Raman shifts of the most intense bands for [10]CPP optimized structure with different basis sets or functional, and experimental Raman shifts for [10]CPP at room conditions.

	Scaling	G_{A1g} (cm^{-1})	GE_{2g} (cm^{-1})	1200 cm^{-1} A_{1g} (cm^{-1})	1280 cm^{-1} A_{1g} (cm^{-1})
B3LYP/6-31G(d,p)	0.9675	1590	1598	1188	1273
B3LYP-D3/6-31G(d,p)	0.9675	1592	1600	1199	1269
B3LYP/6-311+G(2df,p)	0.9800	1595	1601	1195	1264
wB97D/6-31G(d,p)	0.9400	1594	1595	1166	1246
Experimental	--	1589	1598	1210	1270

We can see that, between B3LYP/6-31G(d,p) and B3LYP-D3/6-31G(d,p), which inserts Grimme's dispersion damping function D3, results are very similar. BLA and torsions are even more over estimated. Regarding B3LYP with a larger basis set and adding diffusion, B3LYP/6-311+G(2df,p), results are also very similar to those obtained with B3LYP/6-31G(d,p). BLA and energy gap are a bit closer to the experimental ones, but frequency calculations are bit better with the lower bases set. Finally when comparing with a functional which includes diffusion, wB97D, this in general provides worse results than B3LYP.

[n]CPP and [n]LPP: Energy Difference Between Non-Twisted and Twisted Conformers

Table S4. The computed energy difference between non-twisted (D_{nh}) and global minimum twisted CPPs ($D_{n/2,d}$) for [n]CPP (*n* = 4-20) by the model chemistry B3LYP/6-31G(d,p). Right scheme represents the angle involved in torsions.

n	Energy difference / kcal mol^{-1}
20	31.22
19	28.65
18	27.67
17	25.02
16	24.12
15	21.30
14	20.46
13	17.48
12	16.66
11	13.49
10	12.81
9	9.31
8	8.68
7	5.04
6	4.49
5	1.45
4	0.95

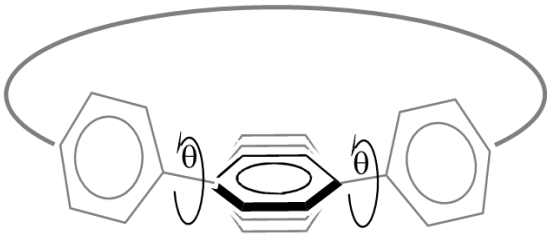

Table S5. The computed energy difference between non-twisted (D_{2h}) and global minimum twisted LPPs (C_{2v}) for [n]LPP (*n* = 4-20) by the model chemistry B3LYP/6-31G(d,p).

n	Energy difference / kcal mol^{-1}
20	31.64
18	28.65
16	25.33
14	22.02
13	20.23
12	18.68
11	17.05
10	15.39
9	13.73
8	12.07
7	10.42
6	8.76
5	7.10
4	5.59
3	3.78
2	2.11

D_{nh} [n]CPP and D_{2h} [n]LPP: Imaginary Frequencies

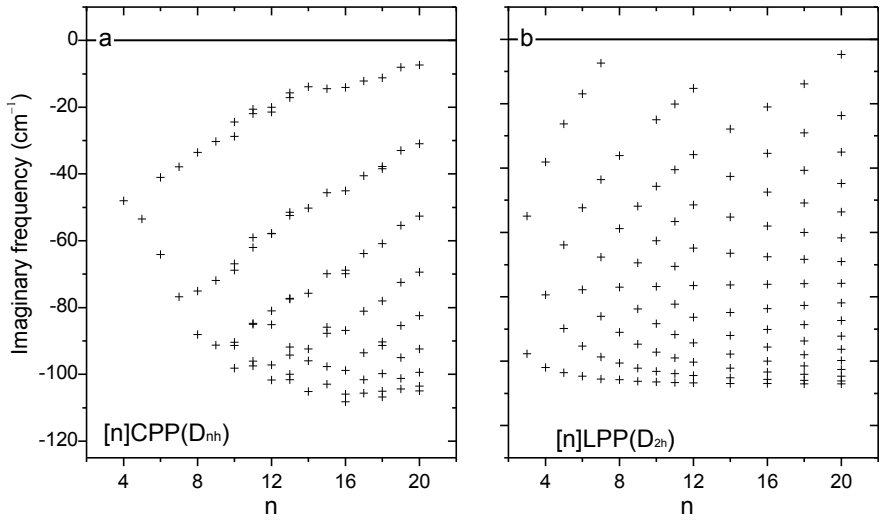

Fig. S1 Imaginary frequencies as a function of *n* for a) non-twisted [n]CPPs, D_{nh}, and for b) non-twisted [n]LPPs, D_{2h}.

Bond Length Alternation and Energy Gap

In the literature it has been broadly discussed that changes in the bond length alternation (BLA) of conjugated polymers are directly related to changes in the energy gap.[3] These changes are related to the Peierls distortion.[4] As we see in Fig. S2, in the [n]LPPs this is as expected and already predicted, increase on the BLA leads to increase on the energy gap.[5] However, in [n]CPPs the behavior is the opposite, increases in the BLA lead to the energy gap decrease. This different behavior is due to the high strain of the CPPs which strongly modulate their properties.[6] Interestingly, the behavior followed by BLA with HOMO-LUMO gap is not linear showing a minimum around [8]-[9]CPP. This needs to be further studied, but it could be related with the enhanced cyclic π conjugation with the smaller diameter, that does not lead to a decrease in the BLA, quinonoid behavior, but to an in-plane-conjugation with no negative but positive BLA. Such cyclic stabilization leads to a more stable configuration with the correspondent E_{gap} decrease.

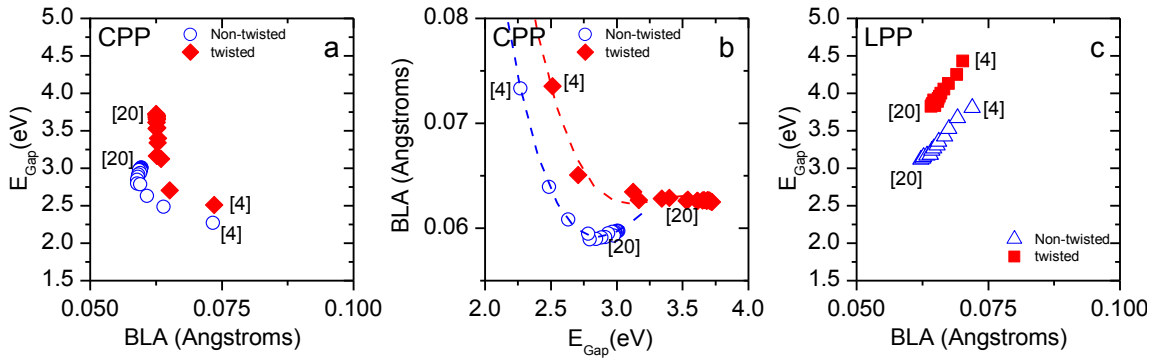

Fig. S2 a) HOMO-LUMO gap as a function of the BLA for [n]CPPs; b) [n]CPPs BLA vs HOMO-LUMO gap; c) HOMO-LUMO gap as a function of the BLA for [n]LPPs.

CPPs Experimental and B3LYP/6-31G(d,p) Raman Spectra: 450 – 900 cm^{-1} Region

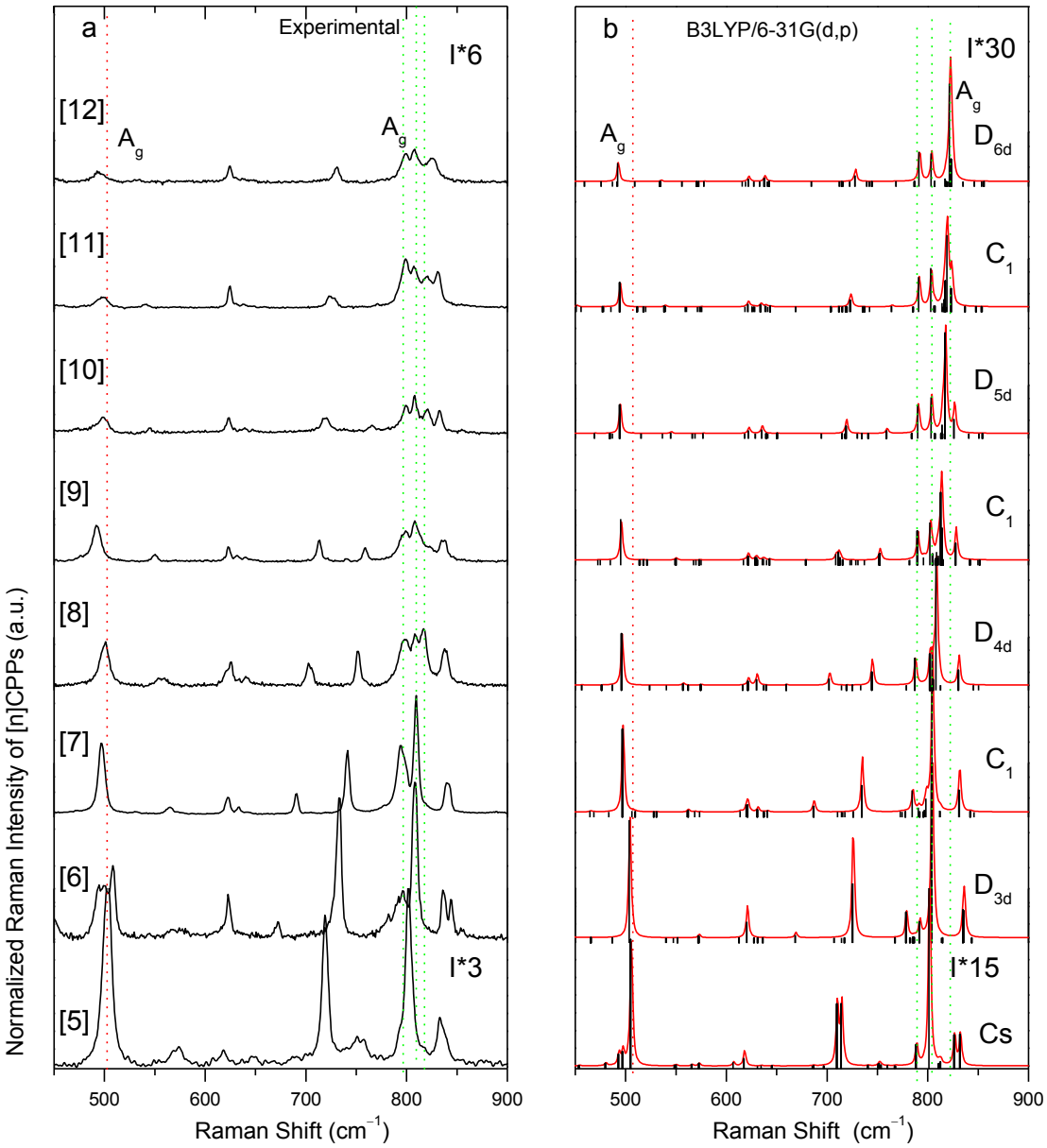

Fig. S3 Raman spectra of [n]CPPs from n = 5-12 between 450 – 900 cm^{-1}. a) Experimental spectra measured with a 785 nm excitation of solid state powder samples. b) Computed Raman spectra at the minimum energy optimized by B3LYP/6-31G(d,p) methodology. All bands have been normalized to the G_{A1g} mode. Theoretical Raman frequencies have been scaled with a factor of 0.97. Red and green vertical dotted lines mark the A_{1g} bands.

B3LYP/6-31G(d,p) Raman Spectra: 450 – 900 cm^{-1} Region

Twisted and Non-twisted Conformers of [n]CPPs

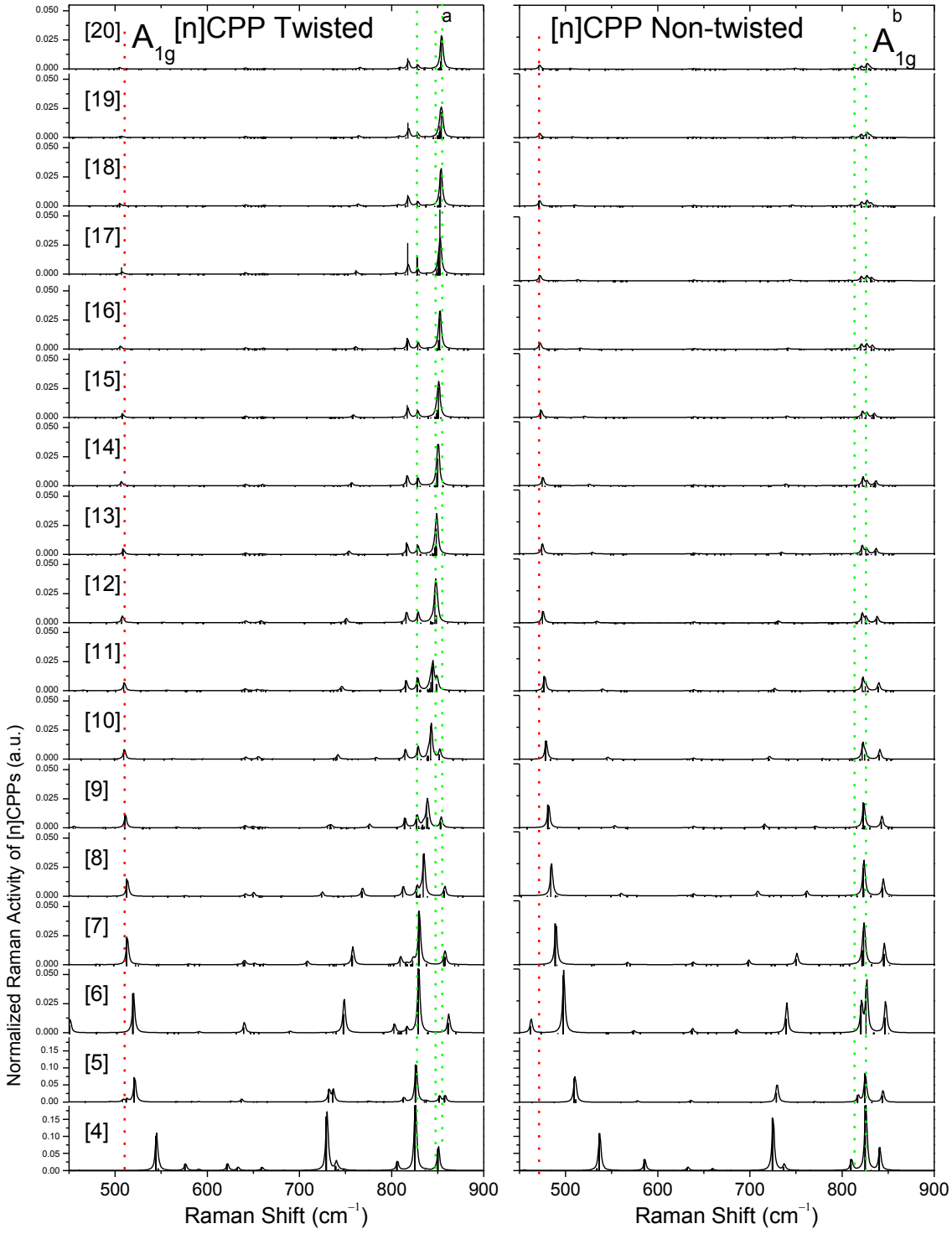

Fig. S4 B3LYP/6-31G(d,p) non-scaled Raman spectra of [n]CPPs in the low frequency region. Spectra have been normalized to the G_{A1g} band. Red and green vertical dotted lines mark the A_{1g} bands. Left: twisted conformers. Right: non-twisted conformers.

Twisted and Non-twisted Conformers of [n]LPPs

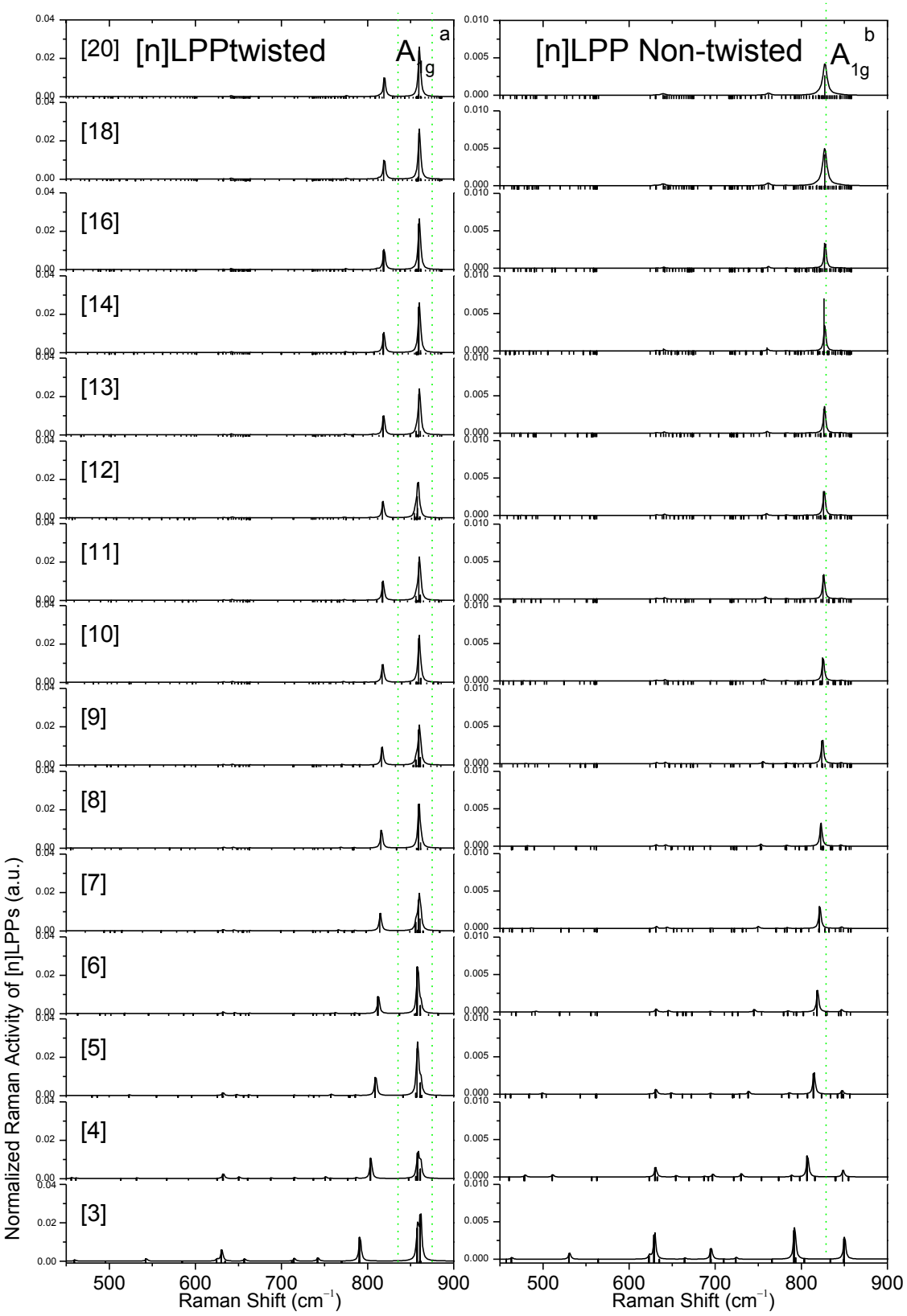

Fig. S5 B3LYP/6-31G(d,p) non-scaled Raman spectra of [n]LPPs in the low frequency region. Spectra have been normalized to the G_{A1g} band. Green vertical dotted lines mark the A_{1g} bands. Left: twisted conformers. Right: non-twisted conformers.

[n]CPP and [n]LPP Raman Shifts of the 450 – 900 cm^{-1} Region

In Fig. S6 we display the Raman frequencies of the A_{1g} bands against n in the 450-900 cm^{-1} region for both CPPs and LPPs.

In Fig. S7 we plot the same A_{1g} bands as a function of n^{-1} where the different trends with size might be better observed.

RFMs of the CPPs, contain a radial component explaining its downshift with the increasing size, as occurs with the RBMs and pseudo-RBMs.[20] For obvious reasons RFM are non-active in LPPs. In the non-twisted CPPs, this is about 30 cm^{-1} lower in frequency due to larger "strain" involved in this radial mode.

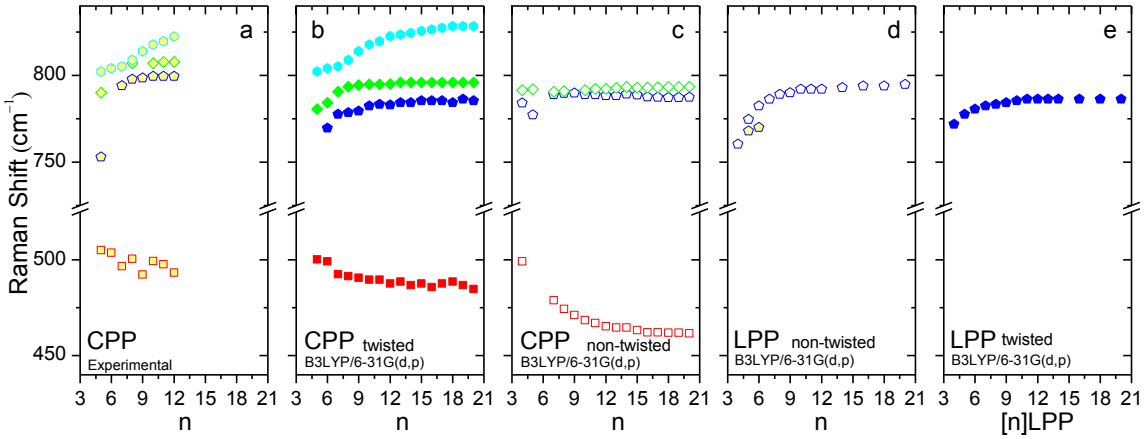

Fig. S6 Experimental and computed B3LYP/6-31G(d,p) Raman shifts as a function of n. a) Experimental values. Computed values for b) twisted CPPs; c) non-twisted CPPs; d) non-twisted LPPs; e) twisted LPPs. (□) Empty symbols correspond to non-twisted CPPs and LPPs, (■) one color filled symbols to twisted CPPs and LPPs and (⬟) two color filled symbols to experimental values. (□) Red squares are used for the 500 cm^{-1} band (A_{1g} band on CPPs). (⬟) Dark blue pentagons, (◆) green diamonds and (⬢) light blue hexagons correspond to the theoretical 800 cm^{-1} A_{1g} bands. Theoretical Raman frequencies have been scaled with a factor of 0.97.

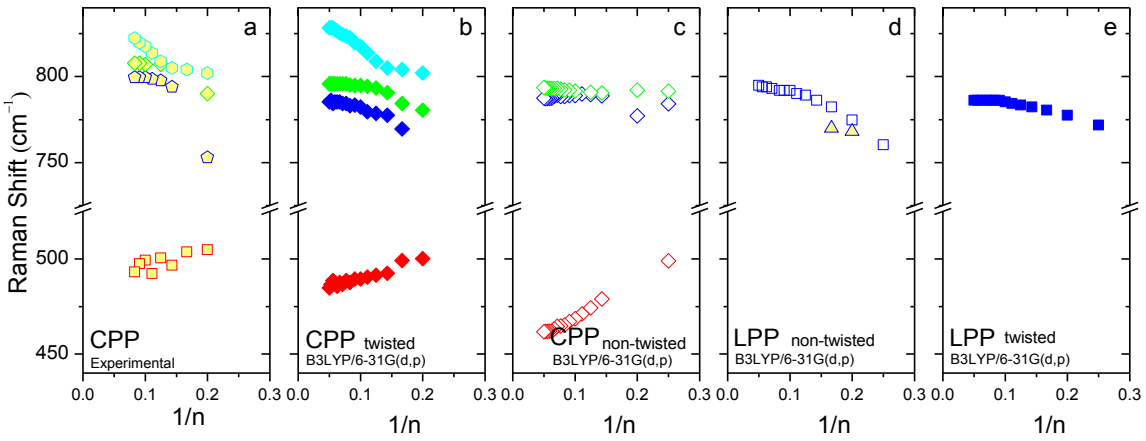

Fig. S7 Experimental and computed B3LYP/6-31G(d,p) Raman shifts as a function of n^{-1}. a) Experimental values. Computed values for b) twisted CPPs; c) non-twisted CPPs; d) non-twisted LPPs; e) twisted LPPs. (□) Empty symbols correspond to non-twisted CPPs and LPPs, (■) one color filled symbols to twisted CPPs and LPPs and (⬟) two color filled symbols to experimental values. (□) Red squares are used for the 500 cm^{-1} band (A_{1g} band on CPPs). (⬟) Dark blue pentagons, (◆) green diamonds and (⬢) light blue hexagons correspond to the theoretical 800 cm^{-1} A_{1g} bands. Theoretical Raman frequencies have been scaled with a factor of 0.97.

About the A_g 800 cm^{-1} bands, while as seen twisted CPPs present three bands in this region, non-twisted ones depict only two, being in any case the most intense one originated from the same in plane C-C vibration. As can be seen, for twisted and non-twisted CPPs respectively, the two lower frequency features appear approximately at the same frequency values than in the twisted [n]CPPs. All the Ag modes in this 800 cm^{-1} region, upshift about 23-40 cm^{-1} from [4-8]CPP and they remain approximately unaltered. However, in non-twisted CPPs these seem not to be affected by the different size, When comparing with their lineal analogues, we see that apart from the fact that LPPs only have one Ag mode in this region, now it is the non-twisted LPP which is affected most by the dimensional fact, with an upshift of about 35 cm^{-1} from [4] to [9] non-twisted LPP, while in the same range twisted LPP only upshift about 10 cm^{-1}. The 800 cm^{-1} bands of the CPP show a good agreement with the computed ones for twisted CPP.

B3LYP/6-31G(d,p) Raman Spectra: 1100 – 1700 cm^{-1} Region

Fig. S8 compares the experimental and theoretical spectra in the 1100 - 1700 cm^{-1} region for [5] to [12]CPP. Figs. S9 and S10 collect all the computed spectra in this region for [n]CPPs and [n]LPPs under their twisted and non-twisted conformations.

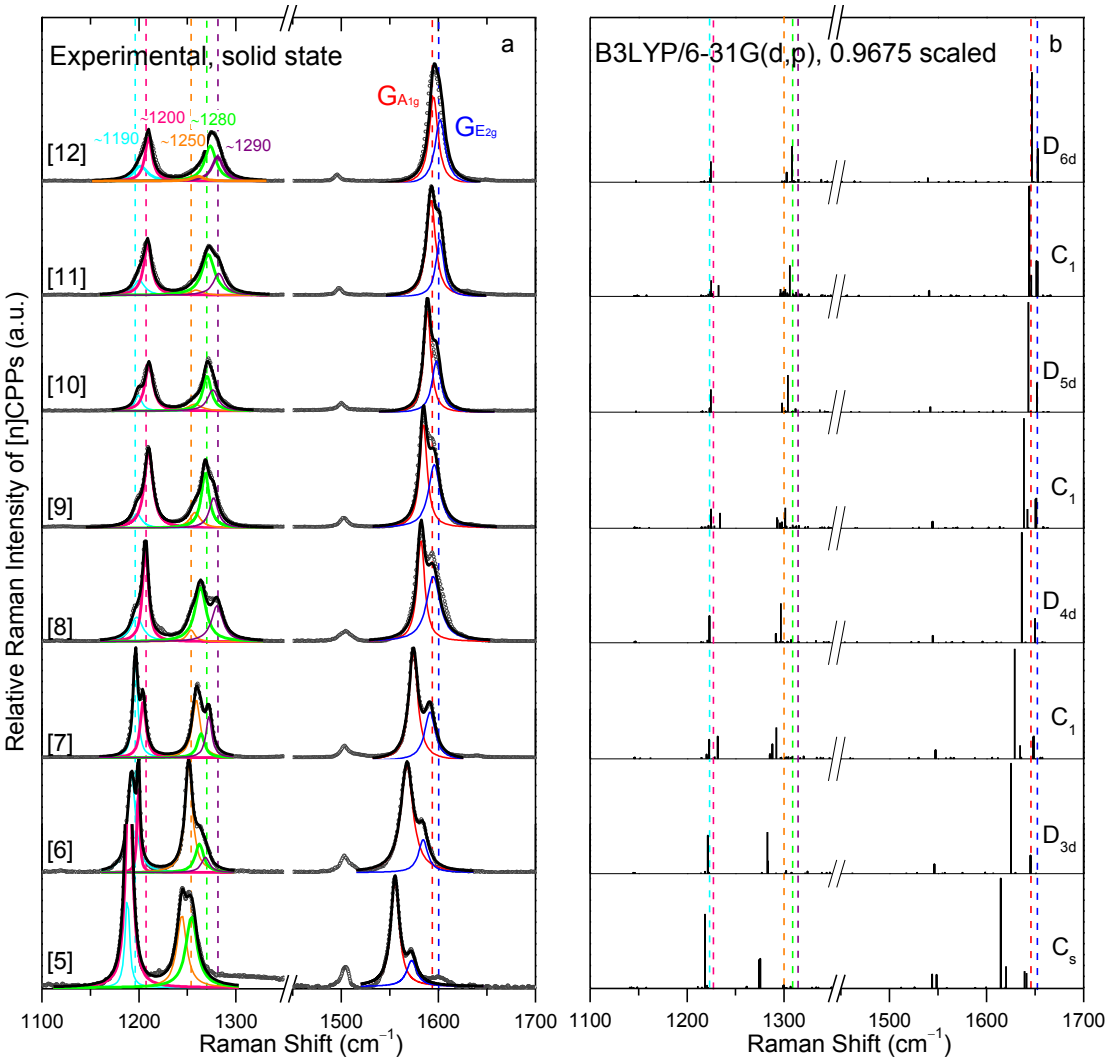

Fig. S8 Raman spectra of [n]CPPs from [6] to [12] CPP in the 1100 -1700 cm^{-1} region. a) Experimental spectra. b) Theoretical Raman spectra. All spectra have been normalized to the G_{A1g} mode around 1580 cm^{-1}. The 1150 -1350 cm^{-1} bands have been decomposed into different subband contributions, see text.

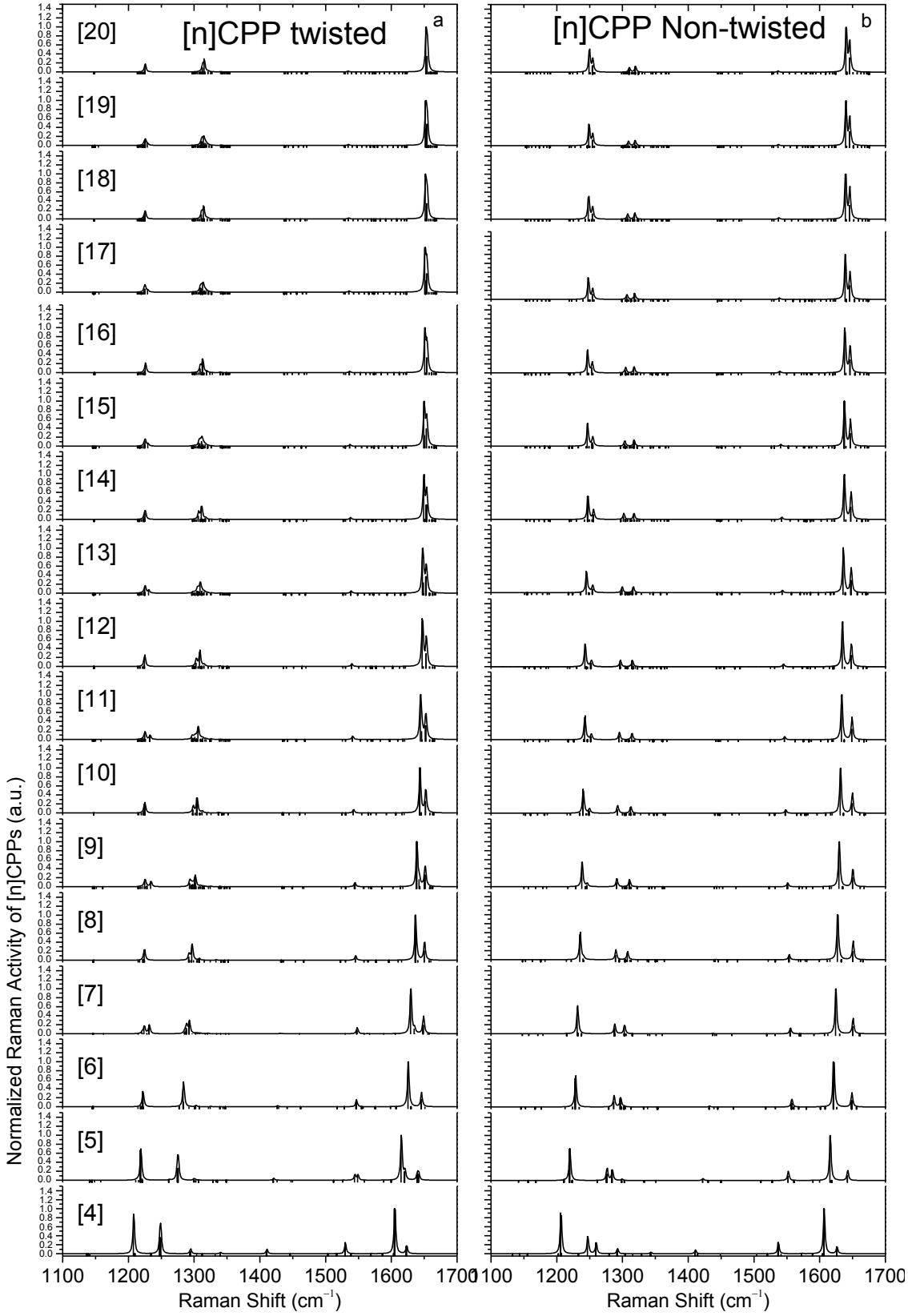

Fig. S9 B3LYP/6-31G(d,p) non-scaled Raman spectra of [n]CPPs in the 1100-1700 cm^{-1} region. Spectra have been normalized to the G_{A1g} band.

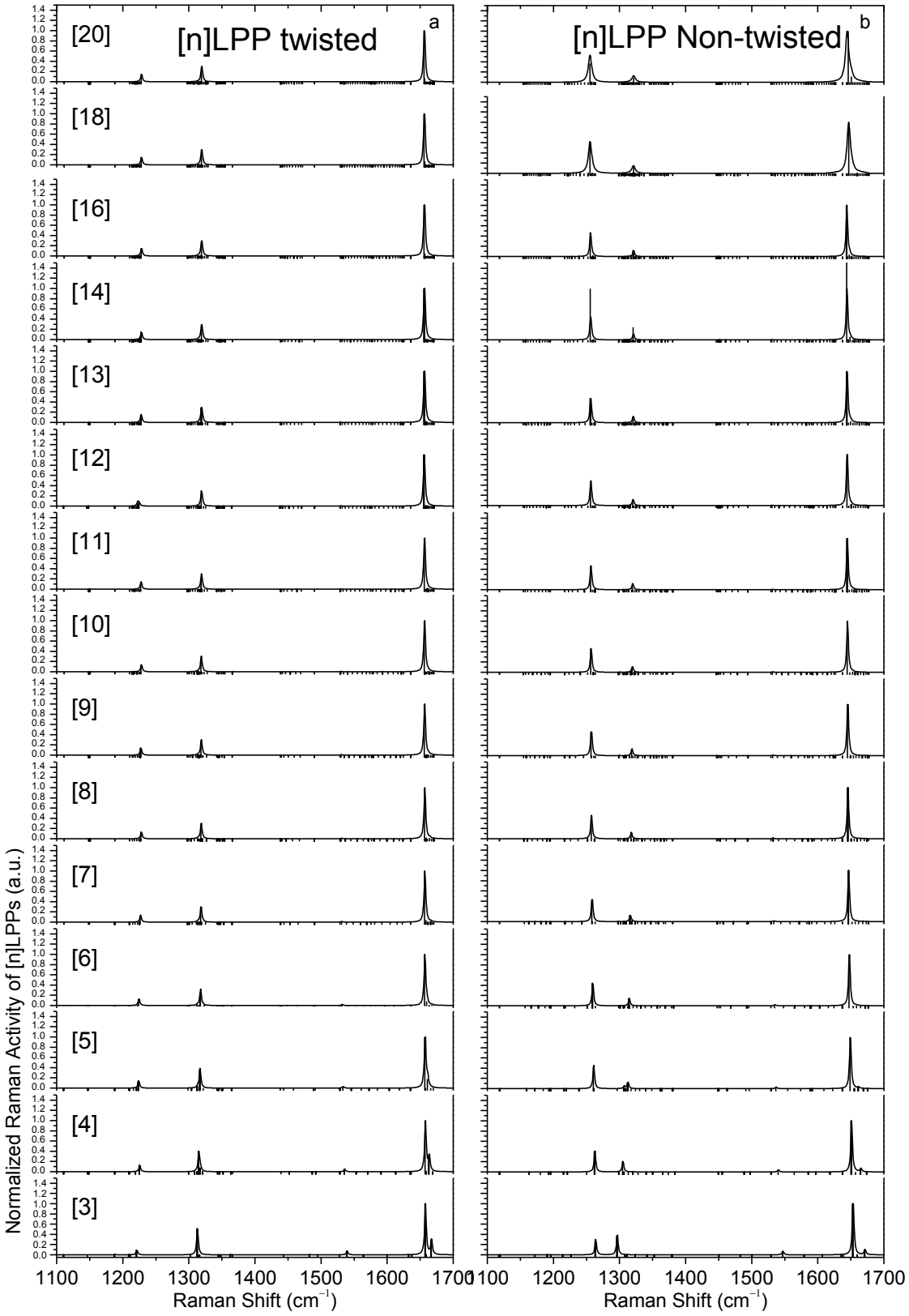

Fig. S10 B3LYP/6-31G(d,p) non scaled Raman spectra of [n]LPPs in the 1100-1700 cm^{-1} region. Spectra have been normalized to the G_{A1g} band.

[n]CPP and [n]LPP Raman Shift of the 1100 – 1300 cm^{-1} Region

Aside of the A_{1g} modes, other theoretical bands of importance in the context of the structure of the [n]CPP are those resulting from the benzene bending and from H···H interactions due to torsional angles between neighboring benzenes (Fig. S8 to S10). The E_{2g} band around 1190 cm^{-1} seems to be only influenced by the bending and much less by torsion. It is active in both of the CPP conformers and its intensity decreases as the bending decreases (as for larger [n]CPP). Computed odd twisted [n]CPP present an additional band around 1210 cm^{-1} (black crosses in Fig. 11b) which is not distinguishable in experimental spectra. The origin of the different features can be explained when comparing the Raman spectra of the different conformers, going from the simplest twisted [n]LPPs to the most complex, twisted [n]CPPs, as depicted in Fig. S11. While twisted [n]LPP display only the 1200 cm^{-1} and 1280 cm^{-1} bands, non-twisted [n]CPP show an additional feature around 1250 cm^{-1} (same nature as the E_{2g} symmetry modes of non-twisted [n]CPPs) and whose intensity grows with the decreasing *n* being almost negligible for [12]CPP revealing its connection with the C-H hindering of the lower torsions in smaller CPPs. Another interesting band in twisted [n]CPP is at 1285 cm^{-1}, of E_{1g} nature, and related with bending and torsion modes and that get more intense with higher torsions (Fig. S8), it is negligible in [5]CPP (small torsional angle) and becomes an important contribution in [12]CPP. The 1200 cm^{-1} A_{1g} band is for the non-twisted conformations of both [n]LPP and [n]CPP about 30 cm^{-1} at above that of the respective twisted conformers. The higher conjugation within the molecules on the non-twisted conformation increases the C-C interring force constant, explaining this upshift. In the case of the 1280 cm^{-1} A_{1g} band such a difference is missing.

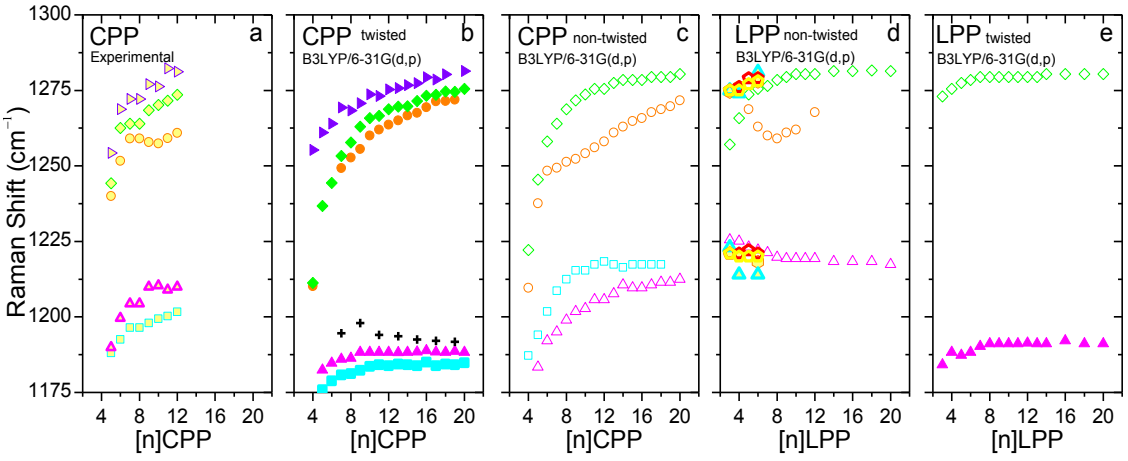

Fig. S11 Raman frequencies of the main contributions in the 1175-1300 cm^{-1} region. a) Experimental data. b) Calculated for twisted [n]CPPs; c) Calculated for non-twisted [n]CPPs; d) Calculated for non-twisted [n]LPPs; e) Calculated for twisted [n]LPPs. Experimental LPP values in d) are taken from Ohtsuka et al.[7] (green pentagons, ⬠), and from Heimel et al.[8] (red hexagons, ⬡) and from Martin et al. (blue triangles, △).[9] The theoretical Raman frequencies have been scaled with 0.9675.

On the $I1280A_{1g}/I1200A_{1g}$ Ratio and Structural Properties.

The intensity ratio between the A_{1g} modes related to C-H bending and phenyl breathing in linear oligophenylenes and PPP, $I1280A_{1g}/I1200A_{1g}$, has been related to the π–conjugation domain-size as a function of the torsional angle (θ) between neighbouring rings (i.e., larger ratio means higher torsional angle or smaller conjugation).[10,11,12] It has been observed for [n]LPPs that the ratio $I1280A_{1g}/I1200A_{1g}$, decreases with increasing the number of phenyl units, and also with decreasing torsion.[13,14] In this paper we extend this $I1280A_{1g}/I1200A_{1g}$ –π–conjugation correlation to the [n]CPPs. In Fig. S12 we have represented the theoretical and experimental intensity $I1280A_{1g}/I1200A_{1g}$ vs n^{-1} for [n]CPPs and [n]LPPs, which both follow the same trend. Differences between computed and experimental results are attributed to the variation in torsions between the crystal environment and the isolated computed molecules.

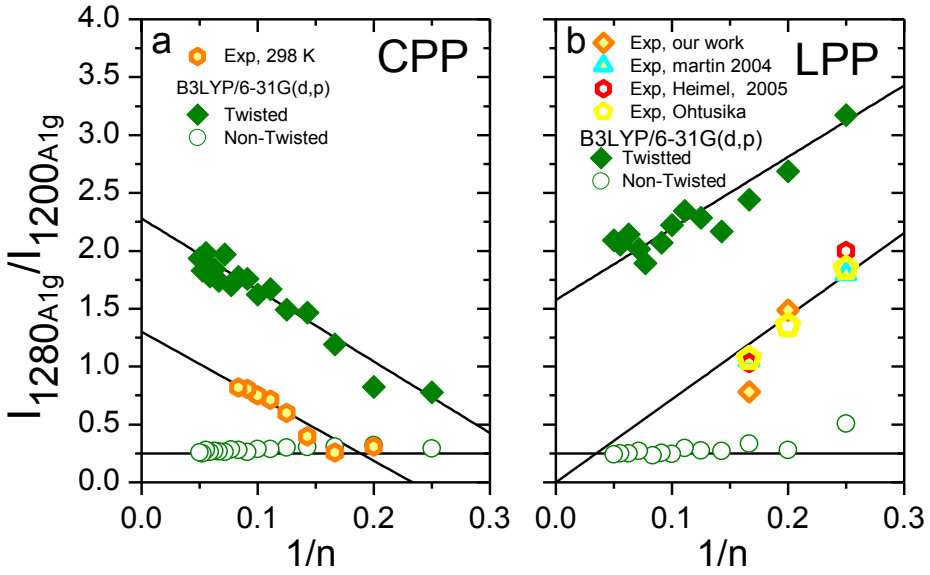

Fig. S12 Intensity ratios, $I1280A_{1g}/I1200A_{1g}$, as a function of $1/n$: a) [n]CPPs, b) [n]LPPs. (○) correspond to non-twisted CPPs and LPPs, (◆) correspond to twisted CPPs and LPPs; color filled hexagons (⬢) correspond to experimental ratios for CPPs, color filled diamonds (◆) correspond to experimental ratios for LPPs. Experimental LPP values were taken from Ohtsuka et al.[15] (⬟) and from Heimel et al.[8] (⬢), and from Martin et al. [913](▲).

We use the $I1280A_{1g}/I1200A_{1g}$ –π–conjugation correlation to analyze our temperature dependent spectra of [6] and [8]CPP (see Figs. S13 –S14) to obtain valuable insights on the conformation interplay of [n]CPP. The effects of temperature on the Raman spectra have been studied for [n]LPP for n =3-4 in references,[15,16,17,18] and for n =6 in references.[15,19]

Temperature Raman Spectra Dependence: [6] and [8]CPP

The FWHM used for the fittings of the bands in the 1200 - 1300 cm^{-1} region are, in order from left to right 14, (~7), (~8), (~11), 12 cm^{-1} from the 1190 cm^{-1}, 1200 cm^{-1}, 1250 cm^{-1}, 1280 cm^{-1} and 1290 cm^{-1} bands. The 1450-1700 cm^{-1} region present a 1500 cm^{-1}, and the 1600 cm-1 band deconvoluted in G_{A1g} and G_{E2g}, represented by red and blue lines respectively, being fitted to Lorentzian functions with FWHM of 10 and ~16 cm-1 respectively

In Figs.sS13c and S14c, the $I1280_{A1g}/I1200_{A1g}$ intensity ratios depict two different trends for [6]CPP and [8]CPP: the first from 100 to about 300 K, and the second range above 300 K. In the first range the intensity ratio diminishes with increasing temperature while Raman shift of all the contributions remains unchanged, meaning that only torsions are altered by temperature. In the second regime however intensity ratios seem to remain approximately constant, while whole Raman spectra downshifts with increasing temperature.

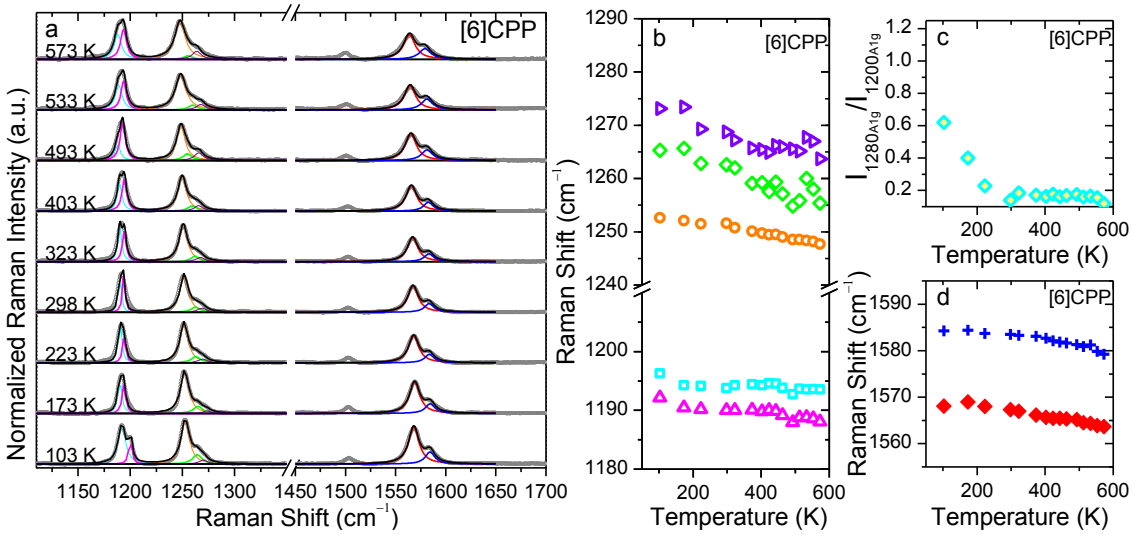

Fig. S13 a) Temperature dependent Raman spectra of [6]CPP, normalized to the G_{A1g} band. Measurements carried out with 785 nm excitation wavelength. b) Temperature evolution of the Raman shift for the 1200 cm^{-1} subbands. c) Temperature evolution of the Raman shift for the G_{A1g} and G_{E2g} bands. The colors in a) correspond to the colors in panels b) and c).

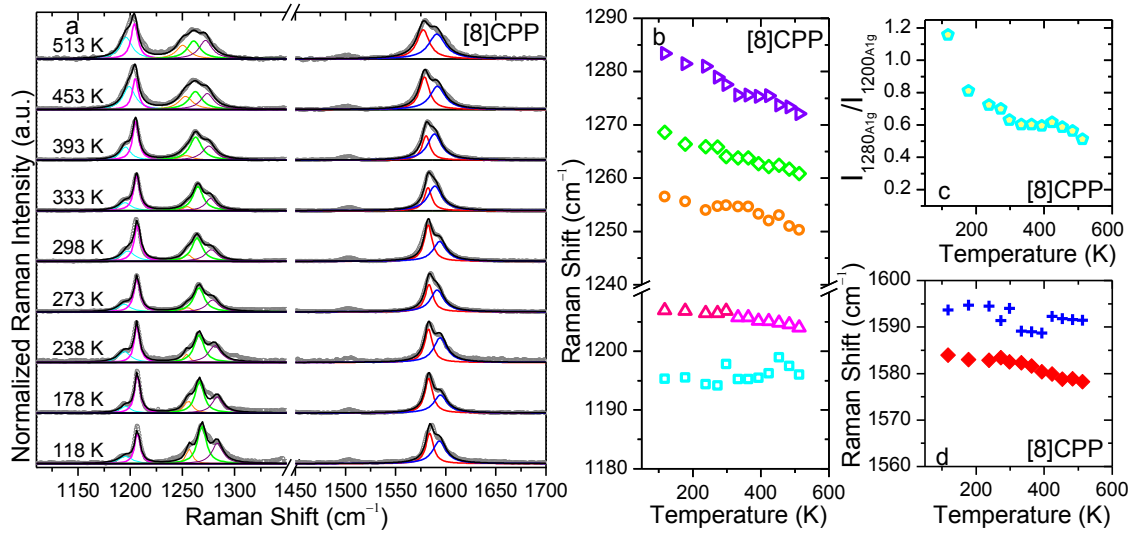

Fig. S14 a) Temperature dependent Raman spectra of [6]CPP, normalized to the G_{A1g} band. Measurements carried out with 785 nm excitation wavelength. b) Temperature evolution of the Raman shift for the 1200 cm^{-1} sub-bands. c) Temperature evolution of the Raman shift for the G_{A1g} and G_{E2g} bands. The colors in a) correspond to the colors in panels b) and c).

[n]CPP and [n]LPP Ratio and Torsional Angle

Fig. S15 shows the $I1280A_{1g}/I1200A_{1g}$ intensity ratios from various sources as a function of the torsional angle. We combined computed values for various [n]CPPs and the experimental low temperature values for [6] and [8]CPP. We also inserted results for [6]CPP and [6]LPP obtained from constrained geometry optimization as a function of the torsional angle. For the LPPs the correlation of the experimental data with the theoretical ones is weak, due to the already mentioned decreased torsions in solid state LPPs. The experimental ratios at 100 and 110 K for [6]CPP and [8]CPP respectively (blue diamonds) fit the theoretical predictions. It is seen now how there is a direct relationship between the torsional angle and the Raman intensity ration, regardless of whether the system is linear or cyclic. Moreover, this confirms that torsions at room conditions are lower than those at 110 K given by XRD data measurements. Based on this relationships one can estimate the torsional angles from the intensity ratios at room conditions to range approximately between 20° for [12]CPP and 5° for [5]CPP.

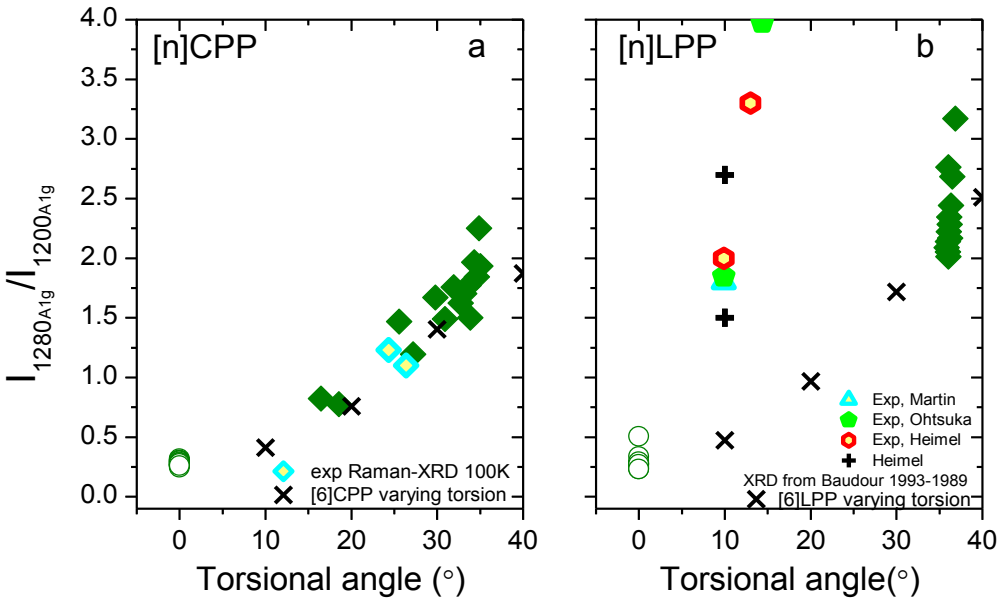

Fig. S15 Intensity ratios, $I1280A_{1g}/I1200A_{1g}$ as a function of the torsional angle, as a function of *n*. a) [n]CPPs, b) [n]LPPs. Computed ratios are (○) for non-twisted [n]CPPs and [n]LPPs, and (◆) for twisted [n]CPPs and [n]LPPs. (✕) corresponds to the intensity ratios estimated from geometry optimizations with fixed torsions for [6]CPP and [6]LPP. (◇) correspond to experimental ratios of CPPs at 100 K. Experimental LPP values were taken from the solid state measurements from Ohtsuka et al.[7] (⬠) and from Heimel et al.[8] (⬡), from Martin et al.[9] (△), and from the computed data from Heimel et al.[8] for *n*=3 and *n*=4 (+).

[n]CPP and [n]LPP Raman shifts in the 1450 – 1700 cm^{-1} region

In Fig. S16 we have plotted the computed and experimental Raman shift for CPPs and LPPs in their twisted and non-twisted conformations. We see that the frequencies of the A_{1g} bands in the non-twisted and twisted LPPs are approximately independent of the size, while the G_{io} slightly downshift. When comparing LPPs with CPPs we can see that the trends are different: for the CPPs the G band is formed by two contributions, G_{A1g} and G_{E2g},[20] which upshift with the increasing size and approach the linear paraphenylene limit, regardless of whether we consider the twisted or the not-twisted conformation. In the twisted CPPs, the Raman shift of the G_{A1g} modes is related to the size, as it is the band which suffers the strongest downshift caused by the increasing strain of the smaller CPPs due to the higher quinonoidal contribution resulting from the bending.[20] Since these modes are strongly affected by "quinonoid contributions", the non-twisted CPPs allow higher conjugation within the cycle, explaining their downshift and larger splitting between the G bands.

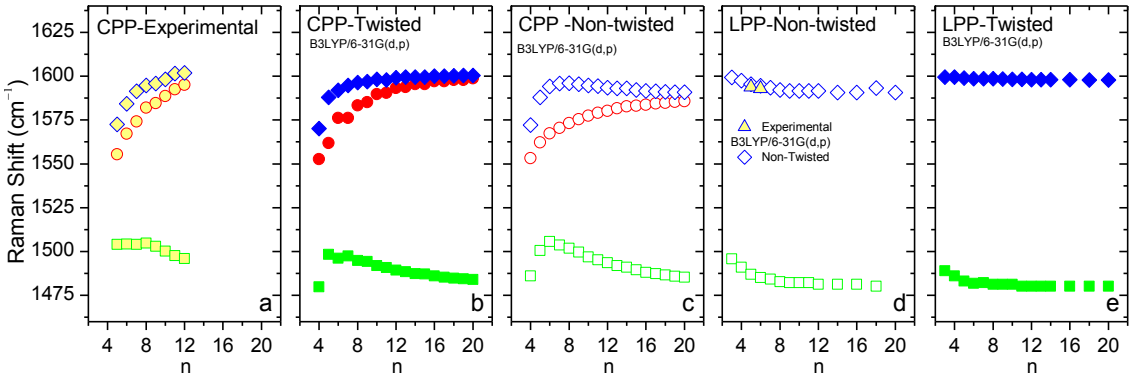

Fig. S16 Raman Shift of the (○)G_{A1g}, (◇)G_{E2g} (E_{2g} symmetry) and (□) G_{io} (E_{2g} symmetry) modes, red, blue and green symbols respectively. Experimental results are symbols with a yellow fill. a) Experimental CPPs; B3LYP/6-31g(d,p) of: b) twisted CPPs; c)non-twisted CPPs; d) non-twisted LPPs; e) twisted LPPs. Theoretical Raman shift have been scaled with a 0.9675 scaling factor.

[n]CPP: The 1200 and 1280 cm^{-1} Lines in the Experimental Raman Spectra Normalized to the G_{io} Band

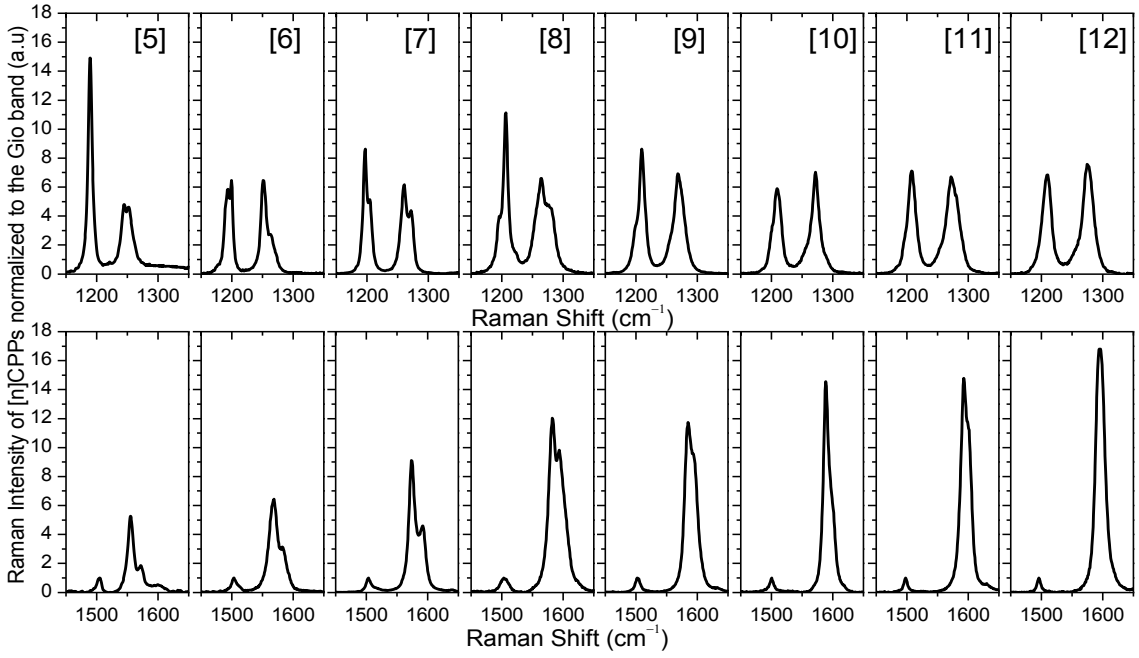

Fig. S17 Experimental Raman spectra run with the 785 nm excitation. The spectra are normalized to the 1500 cm^{-1} E_{2g} band (G_{io}).

[4]-, [5]- and [6]CPP Coordinates

[4]CPP, Aromatic Minimum D_{2d}

C	-0.87193900	-2.38491600	1.29915800
C	0.51604200	-2.48593400	1.29901100
C	1.23140400	-2.56823500	0.08656500
C	0.47789100	-3.03759100	-1.01402200
C	-0.91412100	-2.93579200	-1.01399900
C	-1.59165100	-2.36223700	0.08663900
H	-1.34907500	-2.06517600	2.22019000
H	1.03469000	-2.23855500	2.21989200
H	0.97240700	-3.29606100	-1.94716900
H	-1.44089200	-3.11933800	-1.94727700
C	2.93579200	-0.91412100	1.01399800
C	3.03759200	0.47789000	1.01402200
C	2.56823500	1.23140400	-0.08656500
C	2.48593400	0.51604300	-1.29901100
C	2.38491600	-0.87193900	-1.29915900
C	2.36223700	-1.59165100	-0.08663900
H	3.11933900	-1.44089200	1.94727600
H	3.29606200	0.97240700	1.94716800
H	2.23855400	1.03469000	-2.21989200
H	2.06517600	-1.34907500	-2.22019100
C	-2.48593400	-0.51604200	-1.29901100
C	-2.38491600	0.87193900	-1.29915900
C	-2.36223700	1.59165100	-0.08663900
C	-2.93579200	0.91412000	1.01399900
C	-3.03759200	-0.47789100	1.01402200
C	-2.56823500	-1.23140400	-0.08656600
H	-2.23855400	-1.03469000	-2.21989200
H	-2.06517600	1.34907500	-2.22019000
H	-3.11933900	1.44089200	1.94727700
H	-3.29606200	-0.97240800	1.94716800
C	0.87193900	2.38491600	1.29915900
C	1.59165100	2.36223700	0.08663900
C	0.91412100	2.93579200	-1.01399800
C	-0.47789100	3.03759200	-1.01402200
C	-1.23140400	2.56823500	0.08656600
C	-0.51604200	2.48593400	1.29901100
H	1.34907500	2.06517500	2.22019000
H	1.44089200	3.11933900	-1.94727600
H	-0.97240700	3.29606200	-1.94716800
H	-1.03469000	2.23855400	2.21989300

[4]CPP, Aromatic TS D_{4h}, ($D_{4h} \leftrightarrow D_{2d}$)

C	2.43171100	1.44640100	1.18624100
C	1.44640100	2.43171100	1.18624100
C	0.75300200	2.75758100	0.00000000
C	1.44640100	2.43171100	-1.18624100
C	2.43171100	1.44640100	-1.18624100
C	2.75758100	0.75300200	0.00000000

H	2.77226400	1.07861900	2.14965800
H	1.07861900	2.77226400	2.14965800
H	1.07861900	2.77226400	-2.14965800
H	2.77226400	1.07861900	-2.14965800
C	-1.44640100	2.43171100	1.18624100
C	-2.43171100	1.44640100	1.18624100
C	-2.75758100	0.75300200	0.00000000
C	-2.43171100	1.44640100	-1.18624100
C	-1.44640100	2.43171100	-1.18624100
C	-0.75300200	2.75758100	0.00000000
H	-1.07861900	2.77226400	2.14965800
H	-2.77226400	1.07861900	2.14965800
H	-2.77226400	1.07861900	-2.14965800
H	-1.07861900	2.77226400	-2.14965800
C	2.43171100	-1.44640100	-1.18624100
C	1.44640100	-2.43171100	-1.18624100
C	0.75300200	-2.75758100	0.00000000
C	1.44640100	-2.43171100	1.18624100
C	2.43171100	-1.44640100	1.18624100
C	2.75758100	-0.75300200	0.00000000
H	2.77226400	-1.07861900	-2.14965800
H	1.07861900	-2.77226400	-2.14965800
H	1.07861900	-2.77226400	2.14965800
H	2.77226400	-1.07861900	2.14965800
C	-2.43171100	-1.44640100	1.18624100
C	-2.75758100	-0.75300200	0.00000000
C	-2.43171100	-1.44640100	-1.18624100
C	-1.44640100	-2.43171100	-1.18624100
C	-0.75300200	-2.75758100	0.00000000
C	-1.44640100	-2.43171100	1.18624100
H	-2.77226400	-1.07861900	2.14965800
H	-2.77226400	-1.07861900	-2.14965800
H	-1.07861900	-2.77226400	-2.14965800
H	-1.07861900	-2.77226400	2.14965800

[4]CPP, Quinonoid, Local Minimum D_{4h}

C	2.41567400	1.46113800	1.23203400
C	1.46113800	2.41567400	1.23203400
C	0.68716800	2.64455600	0.00000000
C	1.46113800	2.41567400	-1.23203400
C	2.41567400	1.46113800	-1.23203400
C	2.64455600	0.68716800	0.00000000
H	2.93588600	1.19584400	2.14861800
H	1.19584400	2.93588600	2.14861800
H	1.19584400	2.93588600	-2.14861800
H	2.93588600	1.19584400	-2.14861800
C	-0.68716800	2.64455600	0.00000000
C	-1.46113800	2.41567400	1.23203400
C	-1.46113800	2.41567400	-1.23203400
C	-2.41567400	1.46113800	1.23203400
H	-1.19584400	2.93588600	2.14861800
C	-2.41567400	1.46113800	-1.23203400

H	-1.19584400	2.93588600	-2.14861800
C	-2.64455600	0.68716800	0.00000000
H	-2.93588600	1.19584400	2.14861800
H	-2.93588600	1.19584400	-2.14861800
C	-2.64455600	-0.68716800	0.00000000
C	-2.41567400	-1.46113800	1.23203400
C	-2.41567400	-1.46113800	-1.23203400
C	-1.46113800	-2.41567400	1.23203400
H	-2.93588600	-1.19584400	2.14861800
C	-1.46113800	-2.41567400	-1.23203400
H	-2.93588600	-1.19584400	-2.14861800
C	-0.68716800	-2.64455600	0.00000000
H	-1.19584400	-2.93588600	2.14861800
H	-1.19584400	-2.93588600	-2.14861800
C	0.68716800	-2.64455600	0.00000000
C	1.46113800	-2.41567400	-1.23203400
C	1.46113800	-2.41567400	1.23203400
C	2.41567400	-1.46113800	-1.23203400
H	1.19584400	-2.93588600	-2.14861800
C	2.41567400	-1.46113800	1.23203400
H	1.19584400	-2.93588600	2.14861800
C	2.64455600	-0.68716800	0.00000000
H	2.93588600	-1.19584400	-2.14861800
H	2.93588600	-1.19584400	2.14861800

[4]CPP, Quinonoid, TS (Q ↔ A) C_2

C	-1.99291200	1.99537100	1.21316000
C	-2.41609500	1.32446800	0.00084300
C	-0.03621300	2.82744600	0.00056900
H	-2.49288100	1.78894800	2.15453300
C	-2.82744600	-0.03621300	-0.00056900
C	-2.68626800	-0.81281200	-1.21054800
C	-1.99921800	-1.99537100	1.21040900
H	-3.01797400	-0.40257500	-2.16090100
C	-1.32446800	-2.41609500	-0.00084300
H	-1.79788400	-2.49920400	2.15084400
C	0.03621300	-2.82744600	0.00056900
C	1.99291200	-1.99537100	1.21316000
C	2.41609500	-1.32446800	0.00084300
H	2.49288100	-1.78894800	2.15453300
C	2.82744600	0.03621300	-0.00056900
C	2.68626800	0.81281200	-1.21054800
H	3.01797400	0.40257500	-2.16090100
C	1.99921800	1.99537100	1.21040900
C	1.32446800	2.41609500	-0.00084300
H	1.79788400	2.49920400	2.15084400
C	-1.99537100	-1.99291200	-1.21316000
C	0.81281200	-2.68626800	1.21054800
C	1.99537100	-1.99921800	-1.21040900
C	1.99537100	1.99291200	-1.21316000
C	-0.81281200	2.68626800	1.21054800
C	-1.99537100	1.99921800	-1.21040900

H	2.49920400	-1.79788400	-2.15084400
H	0.40257500	-3.01797400	2.16090100
H	1.78894800	2.49288100	-2.15453300
H	-2.49920400	1.79788400	-2.15084400
H	-1.78894800	-2.49288100	-2.15453300
H	-0.40257500	3.01797400	2.16090100
C	2.69009500	0.81535800	1.20830000
C	-0.81535800	2.69009500	-1.20830000
C	-2.69009500	-0.81535800	1.20830000
C	0.81535800	-2.69009500	-1.20830000
H	3.02694200	0.40813900	2.15818000
H	-0.40813900	3.02694200	-2.15818000
H	-3.02694200	-0.40813900	2.15818000
H	0.40813900	-3.02694200	-2.15818000

[5]CPP, Minimum C_s

C	0.77094700	-3.08384300	1.33439200
C	0.12156400	-3.50792100	0.15787700
C	-2.13404600	-2.91460500	1.15821900
C	-1.34667500	-3.25702000	0.03771300
C	-3.08696400	-1.90278100	1.07966100
C	-3.31103100	-1.20100800	-0.12514000
C	-3.48294500	1.01725100	1.08060100
C	-3.51249200	0.28117600	-0.12439000
C	-0.07570700	3.17586800	1.33420800
C	-2.83275900	2.24572000	1.15895100
C	-2.16421700	2.78455400	0.03848700
C	1.29146900	2.92852600	1.28594600
C	1.98377800	2.91205700	0.05956400
C	-0.81442100	3.41475500	0.15823900
C	3.64294700	1.19479000	0.95159700
C	3.00534300	1.83845300	-0.13135200
C	2.02399400	-2.48354000	1.28644100
C	3.83015000	-0.18657700	0.95170300
C	3.38695400	-0.97692000	-0.13119000
C	2.68708700	-2.28325100	0.06004300
C	0.95611800	-3.65849800	-0.97203800
C	-1.86488800	-2.84071400	-1.20554700
C	-2.83316200	-1.84576400	-1.28544200
C	-3.22359500	1.03015300	-1.28450200
C	-0.04969200	3.78100800	-0.97176400
C	-2.55419300	2.24647800	-1.20482700
C	1.32109900	3.53376800	-1.02076600
C	2.94103800	1.09802900	-1.32761600
C	2.21274500	-3.05770400	-1.02061700
C	3.12777700	-0.28016800	-1.32756900
H	0.21974100	-3.01809800	2.26653200
H	-1.89588200	-3.31757500	2.13863600
H	-3.53295500	-1.55516200	2.00676100
H	-3.82105500	0.56403500	2.00781100
H	-0.59005400	2.96514400	2.26587000
H	-2.70970200	2.69760900	2.13928000

H	1.76549800	2.53274100	2.17859000
H	3.85795800	1.74744200	1.86284700
H	2.37666200	-1.97761500	2.17967500
H	4.18426300	-0.66195800	1.86310000
H	0.57048700	-4.11705500	-1.87870900
H	-1.37826400	-3.14495700	-2.12700900
H	-3.06370600	-1.44979400	-2.26901400
H	-3.34083200	0.58710100	-2.26800200
H	-0.54319200	4.12174600	-1.87811000
H	-2.16627400	2.66936600	-2.12632600
H	1.84197200	3.68881400	-1.96240400
H	2.52458900	1.55198600	-2.22128500
H	2.75620800	-3.06898800	-1.96214100
H	2.84722500	-0.82841400	-2.22137900

[5]CPP, Quinonoid, Local Minimum D_{5h}

C	-1.46902200	3.17396200	1.22527700
C	-0.69341400	3.36027700	0.00000000
C	1.46902200	3.17396200	1.22527700
C	0.69341400	3.36027700	0.00000000
C	2.56466500	2.37793100	1.22527700
C	2.98153700	1.69785900	0.00000000
C	3.47257000	-0.41631500	1.22527700
C	3.41009000	0.37890700	0.00000000
C	0.67714400	-3.43125900	1.22527700
C	3.05407200	-1.70432000	1.22527700
C	2.53610500	-2.31094300	0.00000000
C	-0.67714400	-3.43125900	1.22527700
C	-1.41413800	-3.12610000	0.00000000
C	1.41413800	-3.12610000	0.00000000
C	-3.05407200	-1.70432000	1.22527700
C	-2.53610500	-2.31094300	0.00000000
C	-2.56466500	2.37793100	1.22527700
C	-3.47257000	-0.41631500	1.22527700
C	-3.41009000	0.37890700	0.00000000
C	-2.98153700	1.69785900	0.00000000
C	-1.46902200	3.17396200	-1.22527700
C	1.46902200	3.17396200	-1.22527700
C	2.56466500	2.37793100	-1.22527700
C	3.47257000	-0.41631500	-1.22527700
C	0.67714400	-3.43125900	-1.22527700
C	3.05407200	-1.70432000	-1.22527700
C	-0.67714400	-3.43125900	-1.22527700
C	-3.05407200	-1.70432000	-1.22527700
C	-2.56466500	2.37793100	-1.22527700
C	-3.47257000	-0.41631500	-1.22527700
H	-1.11044900	3.59583000	2.15971900
H	1.11044900	3.59583000	2.15971900
H	3.07669000	2.16727200	2.15971900
H	3.76298500	0.05507300	2.15971900
H	1.21520400	-3.56179300	2.15971900
H	3.01194800	-2.25638200	2.15971900

H	-1.21520400	-3.56179300	2.15971900
H	-3.01194800	-2.25638200	2.15971900
H	-3.07669000	2.16727200	2.15971900
H	-3.76298500	0.05507300	2.15971900
H	-1.11044900	3.59583000	-2.15971900
H	1.11044900	3.59583000	-2.15971900
H	3.07669000	2.16727200	-2.15971900
H	3.76298500	0.05507300	-2.15971900
H	1.21520400	-3.56179300	-2.15971900
H	3.01194800	-2.25638200	-2.15971900
H	-1.21520400	-3.56179300	-2.15971900
H	-3.01194800	-2.25638200	-2.15971900
H	-3.07669000	2.16727200	-2.15971900
H	-3.76298500	0.05507300	-2.15971900

[6]CPP, Aromatic Minimum D_{3d}

C	0.69513700	3.77518500	1.26278500
C	1.42314200	3.94838700	0.07061900
C	3.49339800	2.82119600	1.03566400
C	2.70783200	3.20667000	-0.07061900
C	3.61697500	-1.28558700	1.26278500
C	4.18992600	1.61477400	1.03566400
C	4.13097400	0.74171700	-0.07061900
C	2.92183800	-2.48959900	1.26278500
C	2.70783200	-3.20667000	0.07061900
C	4.13097400	-0.74171700	0.07061900
C	0.69652800	-4.43597000	1.03566400
C	1.42314200	-3.94838700	-0.07061900
C	-2.92183800	-2.48959900	1.26278500
C	-0.69652800	-4.43597000	1.03566400
C	-1.42314200	-3.94838700	-0.07061900
C	-3.61697500	-1.28558700	1.26278500
C	-4.13097400	-0.74171700	0.07061900
C	-2.70783200	-3.20667000	0.07061900
C	-4.18992600	1.61477400	1.03566400
C	-4.13097400	0.74171700	-0.07061900
C	-0.69513700	3.77518500	1.26278500
C	-3.49339800	2.82119600	1.03566400
C	-2.70783200	3.20667000	-0.07061900
C	-1.42314200	3.94838700	0.07061900
C	0.69652800	4.43597000	-1.03566400
C	2.92183800	2.48959900	-1.26278500
C	4.18992600	-1.61477400	-1.03566400
C	3.61697500	1.28558700	-1.26278500
C	3.49339800	-2.82119600	-1.03566400
C	0.69513700	-3.77518500	-1.26278500
C	-3.49339800	-2.82119600	-1.03566400
C	-0.69513700	-3.77518500	-1.26278500
C	-4.18992600	-1.61477400	-1.03566400
C	-3.61697500	1.28558700	-1.26278500
C	-0.69652800	4.43597000	-1.03566400
C	-2.92183800	2.48959900	-1.26278500

H	1.20613800	3.44295600	2.16107900
H	3.46601600	3.40863500	1.94998500
H	3.58475700	-0.67693200	2.16107900
H	4.68497300	1.29734000	1.94998500
H	2.37861900	-2.76602500	2.16107900
H	1.21895700	-4.70597600	1.94998500
H	-2.37861900	-2.76602500	2.16107900
H	-1.21895700	-4.70597600	1.94998500
H	-3.58475700	-0.67693200	2.16107900
H	-4.68497300	1.29734000	1.94998500
H	-1.20613800	3.44295600	2.16107900
H	-3.46601600	3.40863500	1.94998500
H	1.21895700	4.70597600	-1.94998500
H	2.37861900	2.76602500	-2.16107900
H	4.68497300	-1.29734000	-1.94998500
H	3.58475700	0.67693200	-2.16107900
H	3.46601600	-3.40863500	-1.94998500
H	1.20613800	-3.44295600	-2.16107900
H	-3.46601600	-3.40863500	-1.94998500
H	-1.20613800	-3.44295600	-2.16107900
H	-4.68497300	-1.29734000	-1.94998500
H	-3.58475700	0.67693200	-2.16107900
H	-1.21895700	4.70597600	-1.94998500
H	-2.37861900	2.76602500	-2.16107900

[6]CPP, Quinonoid, Local Minimum D_{6h}

C	-1.47415700	3.91176100	1.21980800
C	-0.69940300	4.07053700	0.00000000
C	1.47415700	3.91176100	1.21980800
C	0.69940300	4.07053700	0.00000000
C	4.12476300	0.67922300	1.21980800
C	2.65060600	3.23253800	1.21980800
C	3.17548700	2.64097000	0.00000000
C	4.12476300	-0.67922300	1.21980800
C	3.87489000	-1.42956800	0.00000000
C	3.87489000	1.42956800	0.00000000
C	2.65060600	-3.23253800	1.21980800
C	3.17548700	-2.64097000	0.00000000
C	-1.47415700	-3.91176100	1.21980800
C	1.47415700	-3.91176100	1.21980800
C	0.69940300	-4.07053700	0.00000000
C	-2.65060600	-3.23253800	1.21980800
C	-3.17548700	-2.64097000	0.00000000
C	-0.69940300	-4.07053700	0.00000000
C	-4.12476300	-0.67922300	1.21980800
C	-3.87489000	-1.42956800	0.00000000
C	-2.65060600	3.23253800	1.21980800
C	-4.12476300	0.67922300	1.21980800
C	-3.87489000	1.42956800	0.00000000
C	-3.17548700	2.64097000	0.00000000
C	-1.47415700	3.91176100	-1.21980800
C	1.47415700	3.91176100	-1.21980800

C	4.12476300	0.67922300	-1.21980800
C	2.65060600	3.23253800	-1.21980800
C	4.12476300	-0.67922300	-1.21980800
C	2.65060600	-3.23253800	-1.21980800
C	-1.47415700	-3.91176100	-1.21980800
C	1.47415700	-3.91176100	-1.21980800
C	-2.65060600	-3.23253800	-1.21980800
C	-4.12476300	-0.67922300	-1.21980800
C	-2.65060600	3.23253800	-1.21980800
C	-4.12476300	0.67922300	-1.21980800
H	-1.06644100	4.25983100	2.16374500
H	1.06644100	4.25983100	2.16374500
H	4.22234200	1.20635000	2.16374500
H	3.15590100	3.05348000	2.16374500
H	4.22234200	-1.20635000	2.16374500
H	3.15590100	-3.05348000	2.16374500
H	-1.06644100	-4.25983100	2.16374500
H	1.06644100	-4.25983100	2.16374500
H	-3.15590100	-3.05348000	2.16374500
H	-4.22234200	-1.20635000	2.16374500
H	-3.15590100	3.05348000	2.16374500
H	-4.22234200	1.20635000	2.16374500
H	-1.06644100	4.25983100	-2.16374500
H	1.06644100	4.25983100	-2.16374500
H	4.22234200	1.20635000	-2.16374500
H	3.15590100	3.05348000	-2.16374500
H	4.22234200	-1.20635000	-2.16374500
H	3.15590100	-3.05348000	-2.16374500
H	-1.06644100	-4.25983100	-2.16374500
H	1.06644100	-4.25983100	-2.16374500
H	-3.15590100	-3.05348000	-2.16374500
H	-4.22234200	-1.20635000	-2.16374500
H	-3.15590100	3.05348000	-2.16374500
H	-4.22234200	1.20635000	-2.16374500

References Supporting Information

1 E. Kayahara, Y. Sakamoto, T. Suzuki, S. Yamago, *Org. Lett*. **14**, 3284–3287 (2012).

2 J. Xia, W. Bacon, R. Jasti, *Chem. Sci.* **3**, 3018–3021 (2012).

3 (a) J. L. Bredas, *J. Chem. Phys.* **82**, 3808–3811 (1985). (b) J. L. Bredas, F. Wudl, A. J. Heeger, *J. Chem. Phys*. **85**, 4673–4678 (1986). (c) Y. S. Lee, M. Kertesz, *Int. J. Quantum Chem*. *Quantum Chem. Symp.* **32**, 163–170 (1987). (d) C. H. Choi, S. J. Yang, *Chem. Rev.* **105**, 3448–3481 (2005).

4 R. Peierls, *Quantum Theory of Solids*; Oxford: Oxford, p 108 (1955).

5 Y. S. Lee, M. Kertesz, *J. Chem. Phys*. **88**, 2609–2617 (1988).

6 Y. Segawa, A. Fukazawa, S. Matsuura, H. Omachi, S. Yamaguchi, S. Irle, K. Itami, *Org. Biomol. Chem*. **10**, 5979–5984 (2012).

7 H. Ohtsuka, Y. Furukawa, M. Tasumi, *Spectrochim. Acta. Part A* **49**, 731–737 (1993).

8 G. Heimel, D. Somitsch, P. Knoll, J. L. Bredas, E. Zojer, *J. Chem. Phys*. **122**, 114511 (2005).

9 C. M. Martin, Q. Cai, S. Guha, W. Graupner, M. Chandrasekhar, H. R. Chandrasekhar, *Phys. Stat. Sol*. **241**, 3339–3344 (2004).

10 L. Cuff, C. Cui, M. Kertesz, *J. Am. Chem. Soc*. **116**, 9269–9274 (1994).

11 G. Heimel, D. Somitsch, P. Knoll, J. L. Bredas, E. Zojer, *J. Chem. Phys.* **122**, 114511 (2005).

12 a) Y. Pelous, G. Froyer, C. Herold, S. Lefrant, *Synth Met.* **29**, E17–E22 (1989); b) L. Cuff, M. Kertesz, *Macromolecules* **27**, 762–770 (1994).

13 C. M. Martin, Q. Cai, S. Guha, W. Graupner, M. Chandrasekhar, H. R. Chandrasekhar, *Phys. Stat. Sol*. **241**, 3339 (2004).

14 S. Guha, W. Graupner, R. Resel, M. Chandrasekhar, H. R. Chandrasekhar, R. Glaser, G. Leising, *Phys. Rev. Lett.* **82**, 3625–3628 (1999).

15 H. Ohtsuka, Y. Furukawa, M. Tasumi, *Spectrochim. Acta. Part A* **49**, 731–737 (1993).

16 A. P. Rice, F. S. Tham, E. L. Chronister, *J. Chem. Crystallogr.* **43**, 14–25 (2013).

17 Y. Delugeard, J. Desuche, J. L. Baudour, *Acta Cryst*. **B32**, 702–705 (1976).

18 J. L. Baudour, *Acta Cryst.* **B47**, 935–949 (1991).

19 G. Heimel, P. Puschnig, Q. Caic, C. Martin, E. Zojera, W. Graupner, M. Chandrasekhar, H. R. Chandrasekhar, C. Ambrosch-Draxl, G. Leising, *Synth. Met*. **116**, 163–166 (2001).

20 M. Peña-Alvarez, P. M. Burrezo, M. Kertesz, T. Iwamoto, S. Yamago, J. Xia, R. Jasti, J. T. López Navarrete, M. Taravillo, V. G. Baonza, J. Casado, *Angew. Chem. Int. Ed*. **53**, 7033–7037 (2014).

Appendix 2

Angew. Chem. Int. Ed. **53**, 7033-7037 (2014)

Supporting Information:

Properties of Sizeable [n]Cycloparaphenylenes as Molecular Models of Single-Wall Carbon Nanotubes Elucidated by Raman Spectroscopy: Structural and Electron-Transfer Responses under Mechanical Stress

M. Peña-Alvarez, P. M. Burrezo, M. Kertesz, T. Iwamoto,
S. Yamago, J. Xia, R. Jasti, J. T. López Navarrete,
M. Taravillo, V. G. Baonza, J. Casado

General Information

Experimental Details

Nanorings with 8, 9, 10, 11 and 12 benzenes were synthesized by using a synthetic strategy through multinuclear arylplatinum complexes [1], whereas that [6]CPP was provided by Jasti et al. from Boston University [2]. [6]LPP sample was purchased from TCI.

Room Conditions Experiments

Raman measurements at room conditions of the different [n]CPPs were conducted with an Invia Reflex Raman RENISHAW microscope with 785 nm as excitation wavelength with a spectral resolution of 0.5-1 cm^{-1}.

High pressure measurements were carried out with a Senterra dispersive Raman spectrometer from Bruker with 785 nm as excitation, its Raman scattering radiation was collected in back–scattering configuration with a standard spectral resolution of 3 cm^{-1}, spatial resolution of 0.5 μm, and spot size of about 3 μm.

Temperature and excitation time dependent Raman measurements were carried out with a confocal micro-Raman spectrometer (BWTEK Voyage™ BWS435-532SY) coupled to an Olympus BX51 microscope, which allowed us to focus on the same sample spot for the registering of the spectra. The equipment has a solid-state laser with a wavelength of 532.0 nm. The spectral range available with this spectrometer is from 100 to 3750 cm^{-1} and the spectral resolution is about 3.8 cm^{-1}. All the spectra were run with a laser power of about 1.6 mW.

[6]LPP samples were also measured at room and high pressure conditions with a Spectra-Physics solid state laser operating at 532 nm coupled to a micro-Raman spectrometer with an HR460 monochromator.

High Pressure Experiments

High pressure studies were conducted in a sapphire anvil cell (SAC) [3,4] with a diameter culet of 400 μm and a gold gasket. No pressure transmitting medium was used and diamond chips were placed as the pressure calibrant. As mentioned, all the experiments were followed by Raman spectroscopy with a Senterra spectrometer and using the 785 nm excitation line. The recovered samples, after pressure cycles, were also analyzed, taking several spectra on different sample points to confirm the reproducibility on the same sample and to ensure whether the transformation of the samples is complete or not.

Laser Excitation Time and Temperature Dependent Experiments

Laser excitation time dependent measurements were carried out in the micro-Raman spectrometer (BWTEK Voyage™ BWS435-532SY) with an excitation wavelength of 532.0 nm. These experiments were repeated at different temperatures ranging from 298 to 523 K. [8]CPP and [12]CPP samples were placed in a Pt crucible and situated inside the high temperature stage system (Linkam TS1500 with a T95 system controller). This system can heat within a temperature range from ambient up to 773 K, allowing us to observe and characterize samples through its quartz lid window. The high temperature stage system was equipped with a Pt/Rh thermocouple in direct contact with the ceramic heating element to detect and control the sample temperature. During the experiments, the temperature was stabilized within ± 0.1 degrees. It was necessary to wait between 10 and 15 minutes for the sample to have a uniform temperature.

Computational Details

For all calculations the B3LYP density functional theory was used [5] in conjunction with the 6-31G* basis set [6]. All computations were done with Gaussian 09 [6]. Reported frequencies are harmonic frequencies and were uniformly scaling throughout with the scaling factor of 0.97 [7]. The intensities were not scaled. The energy minimization was performed with starting geometries of the [n]CPP molecules with even n, using an alternating starting torsional sequence. For odd n various local minima can be found and the relevant frequencies are not reported here. All minima were

confirmed by a vibrational frequency analysis: all computed frequencies were real. The minima correspond to the respective point groups as indicated in Table S4. The symmetry of the optimized geometry of [6]LPP was D_2. ChemCraf program was used for representing vibrational displacements [8]. Spectra were generated by the GaussSum-2.2.5 program with a broadening of 3 cm^{-1} [9].

S1. Parameters of the Optimized Geometries for [n]CPPs and [n]LPPs

Table S1.1 Ring torsions based on the optimized geometries, in degrees. θ: angle defined by the planes containing consecutive benzene rings. γ: angle formed by the inter-ring CC bond and the plane containing the benzene ring. See insert below for [6]CPP as an example. [n]LPP denotes the linear oligophenylenes.

n	θ [n]CPP: quasi-cylindrical	θ [n]CPP: non-cylindrical (D_{nd})	γ [n]CPP: non-cylindrical (D_{nd})	θ [n]LPP central torsion, (D_2)
2	-	-	-	41.1 (exp. 44.4)Ref [10]
4	0 (by definition)	18.4		36.0
6	0	27.1	150	36.0
8	0	30.7	157	-
10	0	32.8	162	-
12	0	33.5	165	35.9

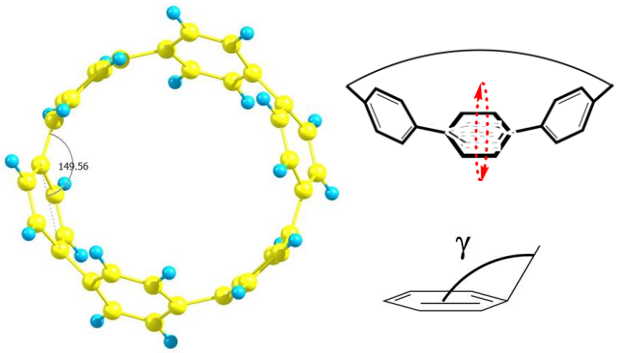

By increasing the size of the [n]CPP, the tilted angle between benzene increases approaching to the angles predicted for linear [12]LPP, so the θ values for the [n]CPPs clearly trend toward the same limiting value of 35.9°. By comparing [12]CPP and [12]LPP a small amount of strain and crowding is indicated by the difference between their tilted torsion angles. This is a geometrical confirmation of our interpretation based on the Raman spectra that the larger [n]CPP behave as pseudo-linear oligophenylenes.

Interestingly the γ angle increases by increasing the size of the [n]CPP. This angle in the [n]LPP is always 180°. This indicates that the curvature of the macrocycle is attained by forcing this angle from 180°. This would produce a lack of orbital overlap between the p_z orbital of adjacent carbon atoms.

Table S.1.2 Bond lengths and BLA values in Å based on the optimized geometries. [n]LPP denotes the linear oligophenylene. See insert below.

n	$r(CC)_{interring}$ [n]CPP: non-cylindrical (D_{nd})	$r_1(CC)_{ring}$ [n]CPP: non-cylindrical (D_{nd})	$r_2(CC)_{ring}$ [n]CPP: non-cylindrical (D_{nd})	BLA [n]CPP: non-cylindrical (D_{nd})	BLA [n]CPP: quasi-cylindrical	BLA [n]LPP: (D_2)
4	1.504	1.3935	1.412	0.0735	0.076	0.06309
6	1.490	1.393	1.410	0.0630	0.061	0.063
8	1.487	1.391	1.407	0.0626	0.0595	NA
10	1.48508	1.3917	1.4070	0.0632	0.059	NA
12	1.484	1.390	1.406	0.062	0.060	0.063

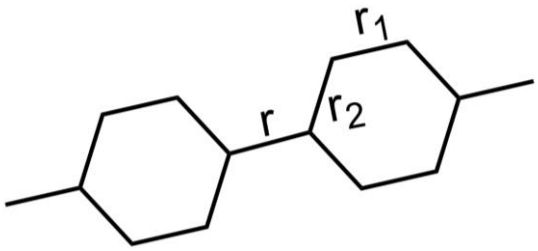

The inter-ring CC bonds (*r*, in Table 2) are anomalously large due to the above mentioned lack of orbital overlap between the p_z orbitals of adjacent benzenes due to the curvature (γ angle). This seems to indicate that inter-ring conjugation as mediated by this connecting bond is not much effective, or in other words, cyclic conjugation is of a rather different nature than linear π–conjugation. This opens the question on the elucidation of the mechanism of cyclic conjugation on these [n]CPPs which should be addressed in another future work. As for the benzene rings they disclose a quinonoidal shape with the r_1 CC bonds being stronger that their adjacent r_2 CC bonds. The quinonoidal character decreases as *n* of the [n]CPP increases. The BLA (bond length alternation patterns is anomalously large for the [n]CPP since the anomalous behavior of the inter-rings CC bonds imparted by the curvature. In agreement with the behavior of the angles and the Raman spectra, the BLAs for [12]CPP and [12]LPP converge to a common value. The geometrical values are not much dependent on the tilted angle between the rings (see the non-cylindrical and the quasi-cylindrical cases). Again this reveals the moderate or modest direct overlap between consecutive rings.

S2. Experimental and Theoretical [10]CPP Raman Spectra Accompanied by the Eigenvectors which Define the Main Raman Bands

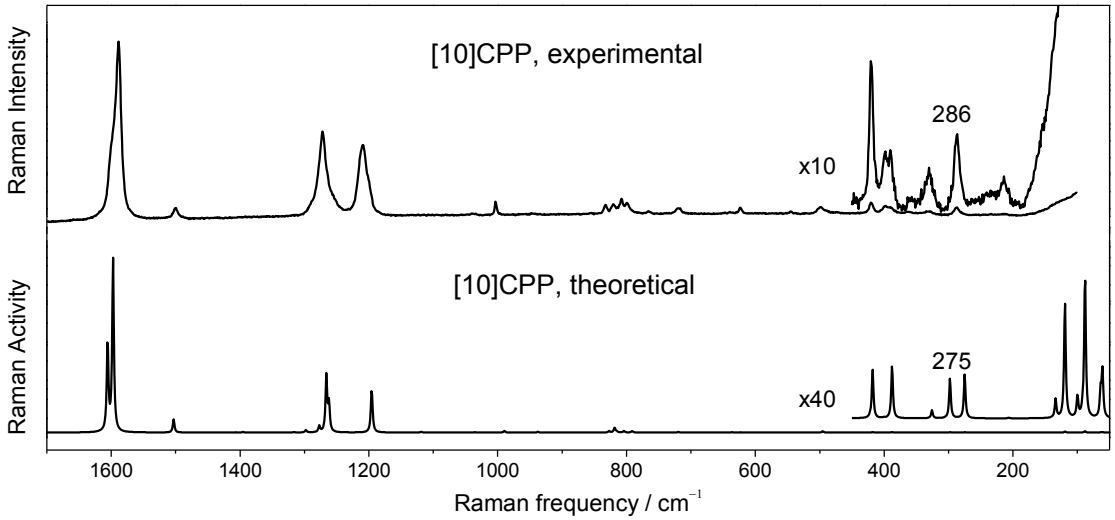

Figure S2.1. [10]CPP Raman spectra. Top: experimental spectrum measured with a 785 nm excitation wavelength in which the low frequency range has been zoomed in. Bottom: theoretical DFT/B3LYP/6-31G* spectrum. Pseudo-RBMs have been marked in both of them.

Table S2.1 Vibrational eigenvectors associated with the most relevant bands of the Raman spectrum of [10]CPP. Values obtained from calculations withB3LYP/6-31G* followed by uniform frequency scaling with a value equals to 0.97**.** In parentheses, experimental values are shown.

D_{5d} 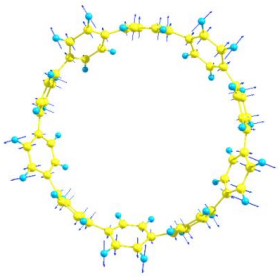	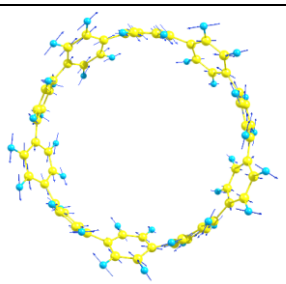
A_{1g}→ 137cm^{-1}	E_{2g}→ 274 (286) cm^{-1}

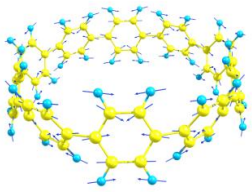	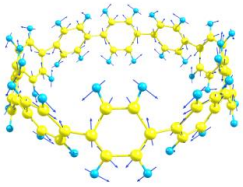	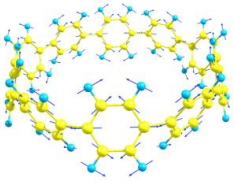
A_{1g}→1266 (1274) cm^{-1}	E_{1g}→1262(1269) cm^{-1}	A_{1g}→1196 (1209) cm^{-1}

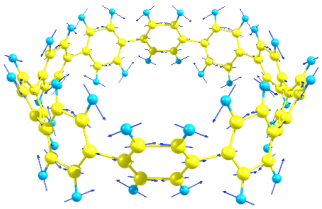	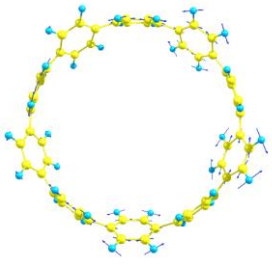
A_{1g}→1597 (1589) cm^{-1}	E_{2g}→1605 (1600) cm^{-1}

S3. Experimental and Theoretical [12]CPP Raman Spectra Accompanied by the Eigenvectors which Define the Main Raman Bands

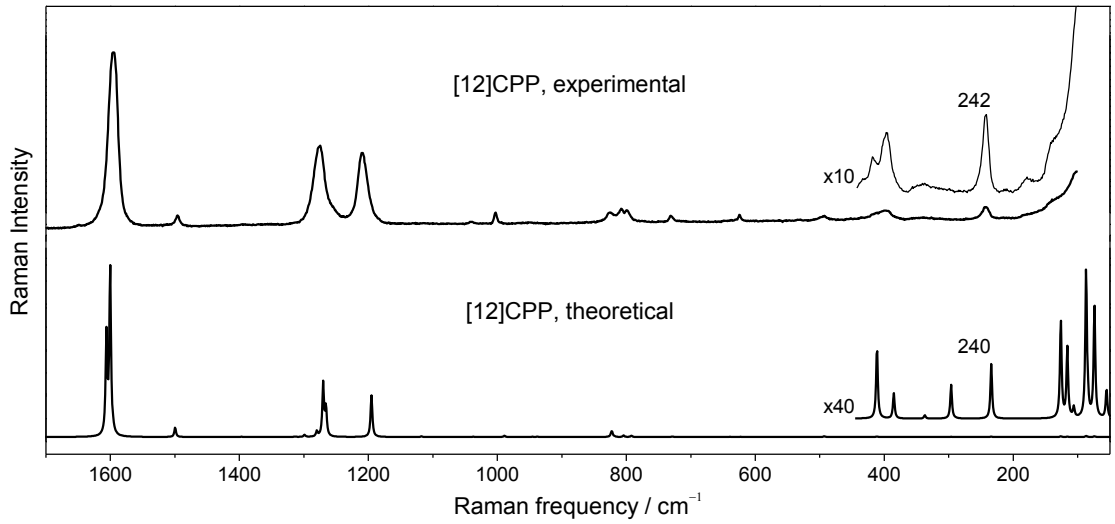

Figure S3.1 [12]CPP Raman spectra. Top: experimental spectrum measured with a 785 nm excitation wavelength in which the low frequency range has been zoomed in. Bottom: theoretical DFT/B3LYP/6-31G* spectrum. Pseudo-RBMs have been marked in both of them.

Table S3. Vibrational eigenvectors associated with the most relevant bands of the Raman spectrum of [12]CPP. Values obtained from calculations with B3LYP/6-31G* followed by uniform frequency scaling with a value equals to 0.97**.** In parentheses, experimental values are shown.

D_{6d} 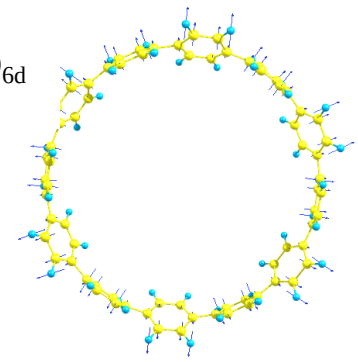	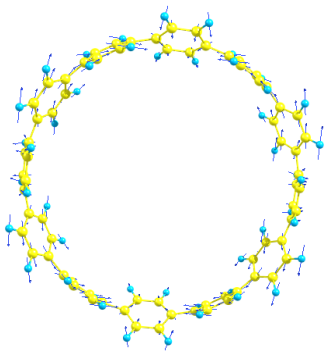
$A_1 \rightarrow 119\ cm^{-1}$	$E_2 \rightarrow 233\ (242)\ cm^{-1}$
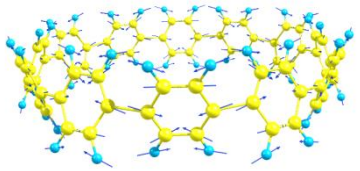	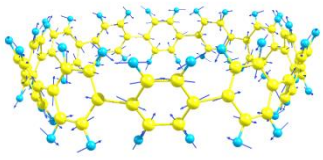 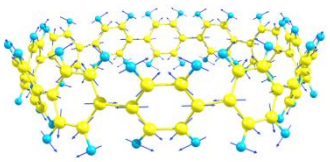
$A_1 \rightarrow 1270\ (1279)\ cm^{-1}$	$E_2 \rightarrow 1266\ (1273)\ cm^{-1}$ $A_1 \rightarrow 1195\ (1210)\ cm^{-1}$

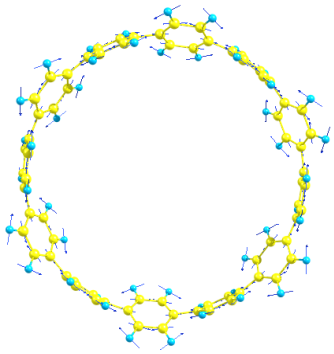	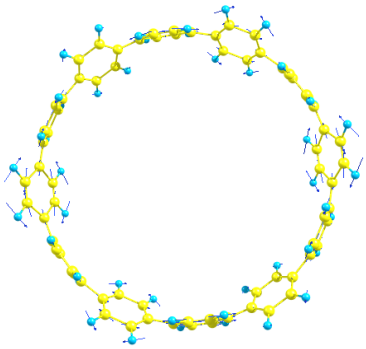
A_1→ 1600 (1593) cm^{-1}	E_2→1605 (1599) cm^{-1}

According to Figure 2 of the main text, Tables S2 and S3 show all the vibrational eigenvectors associated with the most relevant bands of the[10]- and [12]CPP Raman spectra, as well as the experimental values, in parentheses.

It is seen that although the so called RBMs are not well distinguished in the experimental spectra, the low frequency range is dominated by a mode which upshifts with the CPP decreasing size. These modes present an E_2 symmetry and are also circumferential, however they present one node while the RBMs do not present any node (totally symmetric), this is the reason why we will refer to these E_2 bands as circumferential modes (CMs) or as pseudo-RBMs in analogy to the SWCNTS.

The Raman spectral region around 1600 cm^{-1} in SWCNTs is dominated by the so-termed G modes.[11] These bands set their origin on the in plane C-C stretching band of graphene (G band) which splits in two when it rolls up to form the nanotube because of the generation of preferential vibrational directions, along the tube and across the tube diameter, generally G^+ and G^-. According to the vibrational displacement patterns, these G^- and G^+ modes correspond to either transversal (TO) or longitudinal (LO) modes, respectively in the semiconductor CNTs, meaning that the nuclear displacements can be either orthogonal (TO, A_{1g}) or parallel (LO, E_{1g}) relative to the nanotube axis direction. However in Armchair SWCNTs these G^- and G^+ modes correspond to the axial (LO, E_{1g}) and circumferential (TO, A_{1g}) modes respectively, which is only result of the Kohn anomalies due to their metallicity.[12, 13]

As mentioned in the main text, in the 1560-1600 cm^{-1} range the CPPs spectra is formed by two main bands too, one at lower Raman shift and higher intensity and the other one at higher Raman shift and lower intensity. As seen in Table S.2.1 and Table S.3.1, in terms of the nature of the eigenvectors, the higher frequency associated vibrational normal modes has $\mathbf{E_{2g}}$ symmetry (with several nodes in the vibrational wavefunction) while the lower frequency associated vibrational normal modes has $\mathbf{A_{1g}}$ symmetry (no nodes in their vibrational wavefunction). As a result, the $\mathbf{A_{1g}}$ modes are fully delocalized along the whole molecular structure (involve all benzene rings) while the $\mathbf{E_{2g}}$ modes are much more localized modes (residing on alternant rings). Therefore the $\mathbf{A_{1g}}$ mode bands are much more sensitive to the molecular size and in consequence to cyclic strain than the $\mathbf{E_{2g}}$ modes frequencies. Therefore, these vibrations resemble those found in benzene (mode 8a), in oligoparaphenylenes C-C stretching mode of the benzoid rings, [14,15] and the so-called G^+ bands in armchair SWCNTs.[16,17] Thus, we will refer to this bands as the G_1 and G_2, being the G_1 the one at lower frequency which would resemble as the G^+ of SWCNTs more accurately and, the G_2 the one at higher Raman shift.

S4. Raman Spectra in the Low Frequency Range Spectral for [6-12]CPP and Theoretical [6], [8], [10] & [12]CPP

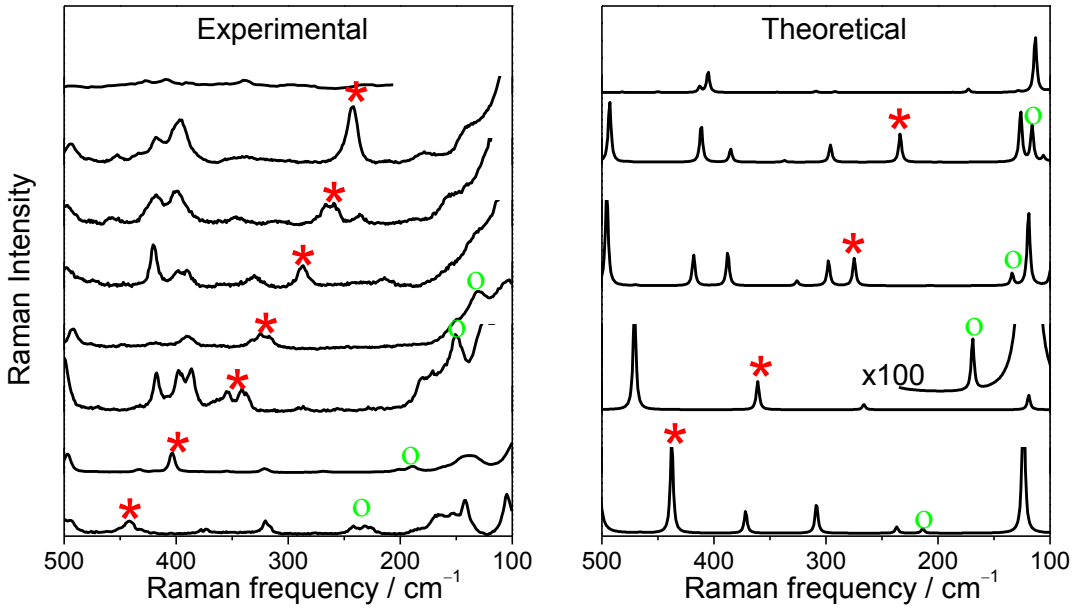

Figure S4.1. Raman spectra in the low frequency range spectral. Left: 785 nm experimental spectra of the compounds in solid state, from bottom to top, [6]CPP to [12]CPP; and the top one corresponds to the linear hexa-paraphenylene, [6]LPP. Right: theoretical DFT/B3LYP/6-31G* Raman spectra of [6], [8], [10], [12]CPP and [6]LPP (from bottom to top). Red stars correspond to the pseudo-RBMs and green circles to the RBMs.

Table S4.1 Vibrational eigenvectors associated with the most relevant low frequency bands of the Raman spectrum of [12]-, [10]-, [8]-, [6]CPP. Values obtained from calculations with B3LYP/6-31G* followed by uniform frequency scaling with a value equals to 0.97. In parentheses, experimental values are shown.

		RBM	Pseudo-RBM
[6]CPP	D_{3d}	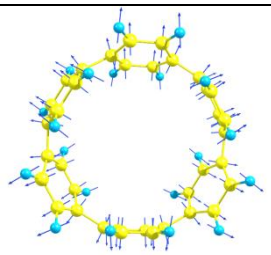	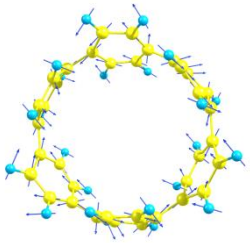
		A_{1g}→ 212 (231) cm^{-1}	E_g→ 438 (442) cm^{-1}
[8]CPP	D_{8h}	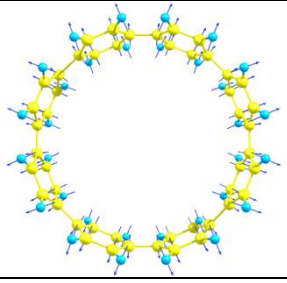	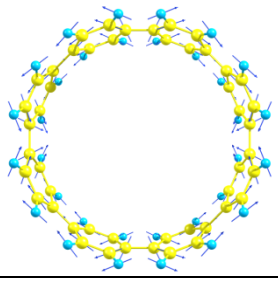
		A_{1g}→ 168 (165) cm^{-1}	E_{2g}→ 360 (356) cm^{-1}

[10]CPP	D_{5d}	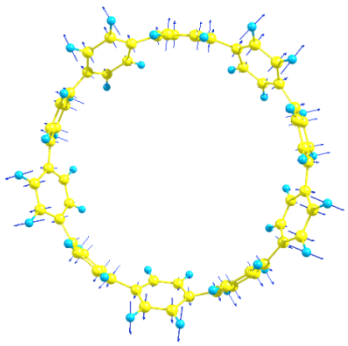	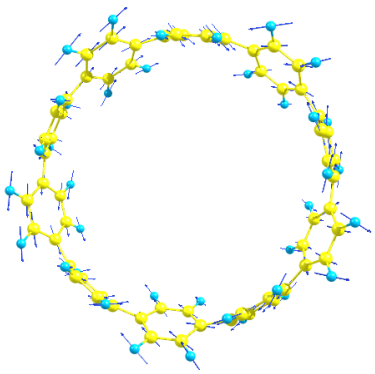
		A_{1g}→ 133 cm^{-1}	E_{2g}→ 274 (286) cm^{-1}
[12]CPP	D_{6d}	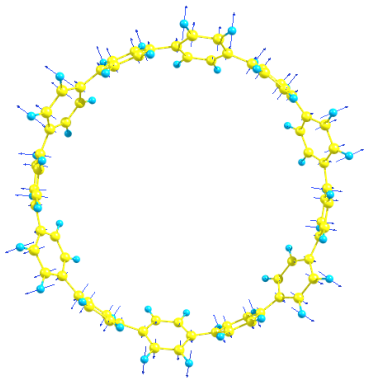	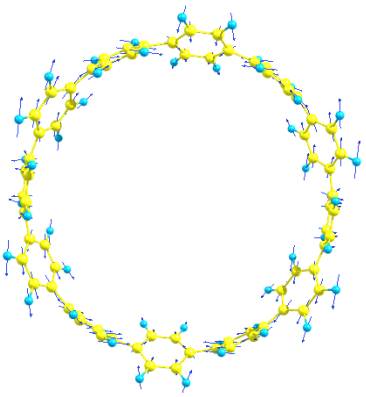
		A_1→115 cm^{-1}	E_2→233 (242) cm^{-1}

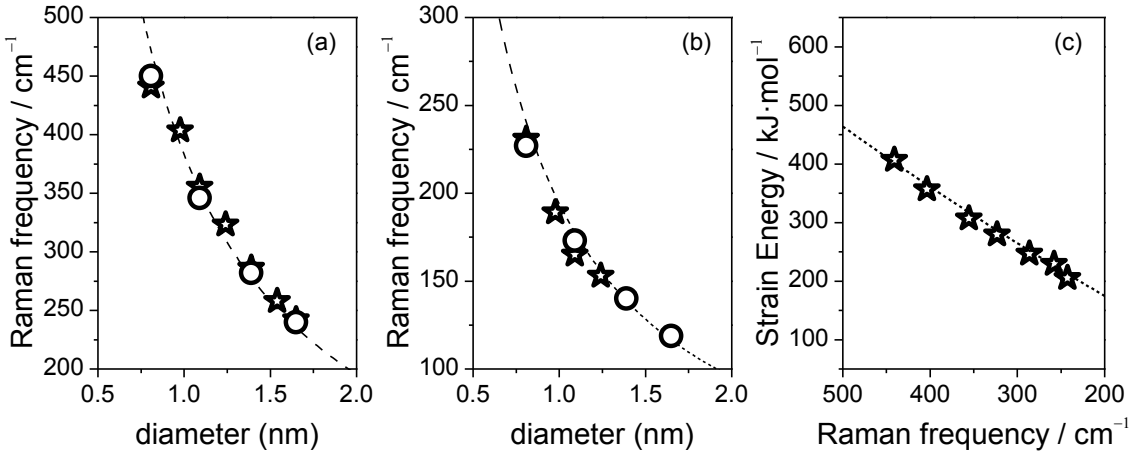

Figure S4.2 Raman frequency of the different [n]CPPs versus their corresponding diameters, (diameters are taken from ref. [4-10] of the main text) for: (a) pseudo-RBM, (b)RBM. (c) Variation of the strain energy of the [n]CPP versus the experimental pseudo-RBM frequencies (strain energy data taken from ref [18]). Symbols: experimental data (stars) and theoretical data (circles). Lines correspond to the functions described in the scheme 1 of the main text.

S5. Experimental and Theoretical Raman Spectra of Linear Hexa-paraphenylene, [6]LPP Accompanied by the Eigenvectors which Define the Main Raman Bands

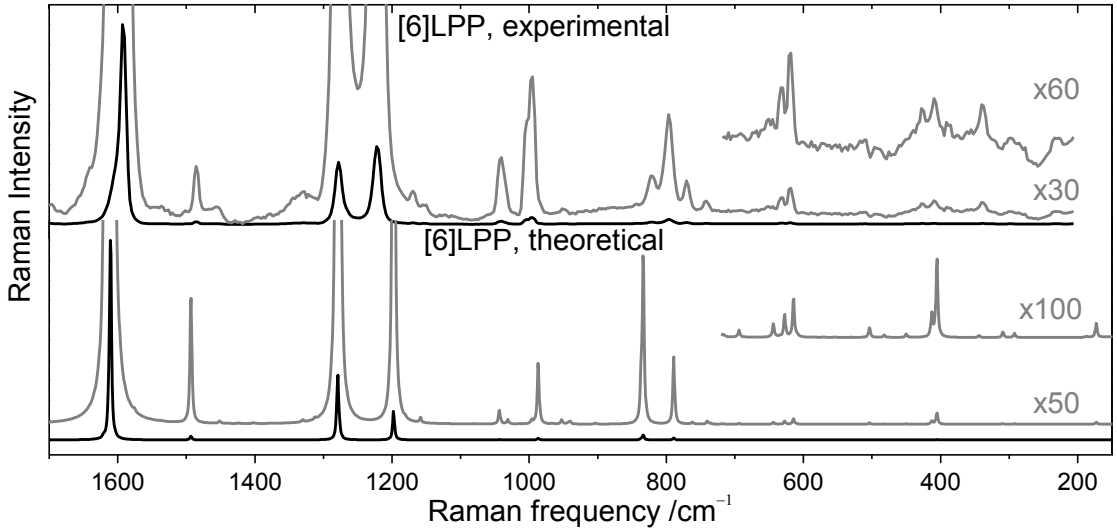

Figure S5.1 Raman spectra for linear hexa-paraphenylene, [6]LPP. Top: experimental spectrum measured with a 532 nm excitation wavelength. Bottom: theoretical DFT/B3LYP/6-31G* spectrum. In both of them, the low frequency range has been zoomed in to get a better insight of the absence of RBMs analogues.

Table S5.1 Vibrational eigenvectors associated with the most relevant bands of the Raman spectrum of [6]LPP. Values obtained from calculations with B3LYP/6-31G* followed by uniform frequency scaling with a value equals to 0.97**.** In parentheses, experimental values are shown.

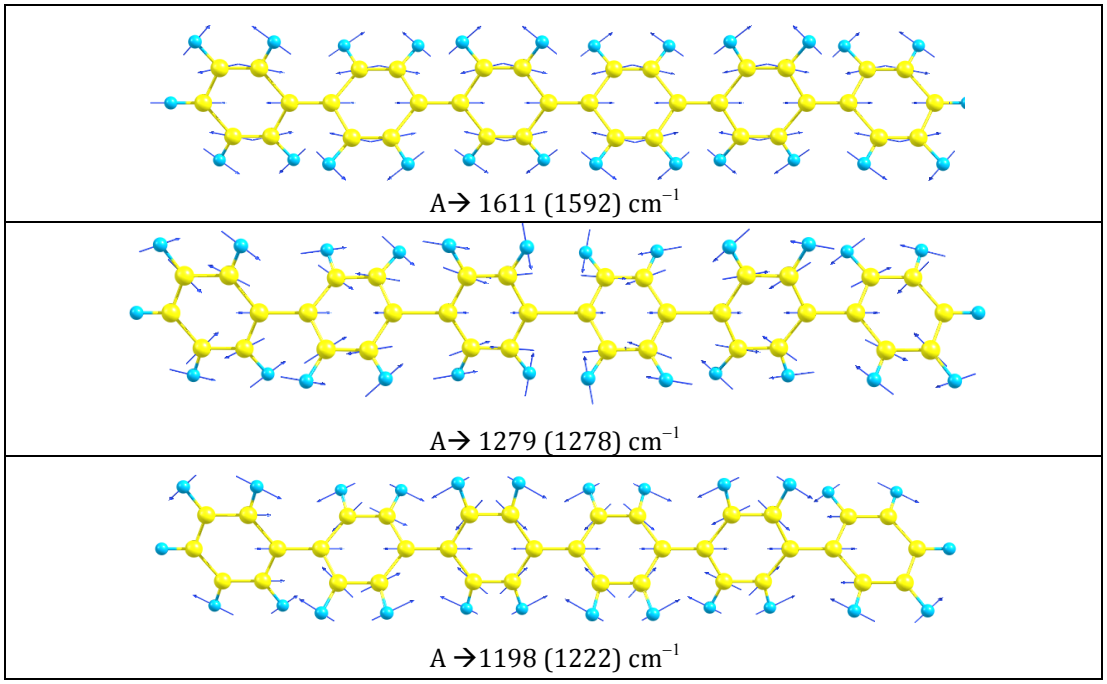

According to the main text here the Raman spectrum of a linear oligo-paraphenylene is presented ([6]LPP). Many of its features are analogues to the cyclic paraphenylene such as the bands around 1200 cm^{-1} and the one around 1600 cm^{-1}. However, the low frequency range is not dominated by any special characteristic. Moreover, the band at 1600 cm^{-1} does not present any splitting as the CPP do and it is because it is much closer to the 8a benzene mode than in the CPP's cases.

S6. Force Constants Analysis to Infer a Quantitative Degree of Quinonoidization for the [n]CPP Rings

Benzenes are totally planar molecules and oligo-paraphenylenes are linear molecules. This means that benzenes must loss somehow their planar character to be able to adopt the cycle-paraphenylenes' circumferential-like shape. Such loss of planarity is accompanied by partial "quinonoidization", which results in a decrease in the aromatic character of the ring and an increase of the cycle conjugation. Electron density increases localization on the C-C inter ring bonds and on the C_2-C_3 and C_5-C_6 bonds. This means that as the number of CPP rings decreases both the cycle curvature and the quinonoidal character increase.

The G^- mode in CNTs and the G_1 modes in CPPs are the result of the splitting of the graphitic G mode or the 8a benzene mode, because of the curvature induced in the system by forming either the CNTs or the CPPs, respectively [11]. This curvature creates preferential vibrational directions along the tangential direction of the circumference.

G_1 mode involves all the rings of the structure, owing to the "rupture" of the bond length alternation pattern along the consecutive sequence of ---C=C-C=C-C=C--- bonds. We suspect that this mode has a strong ring character and therefore its frequency would mainly account for such character (i.e., quinonoidal). In this sense, the frequency of this band is valid to establish the degree of quinonoidization of the benzene ring. Here, we suggest a model which, with our experimental data, allows us to quantify the quinonoidal character of a given CPP. Our aim is to provide with a simple approximation to quantify the quinonoidal character in these systems and therefore we know that a more accurate model can be made, but the simplicity of our procedure could be missing. Since the G^- mode is the result of the C-C vibration along the tube perimeter, we have carried out the vector decomposition of these vibrations and projected them on the central axis to obtain the resultant.

For our purpose here, we follow the next statements:

1. The Raman band that might account for the intra-ring quinonoidization. We propose the Raman band associated with the 8a mode of benzene to be the key quinonoidal band.
2. We consider two extreme situations for the rings, having either all benzoid or all quinonoid bonding. A quinonoidization "scale" based on the Raman band frequencies, where we must identify two limiting situations. We assume that these two situations are:
   - Benzene ring with a full aromatic structure (benzene itself). This would correspond to **0 % of quinonoidization**.
   - Benzene with a full quinonoidal structure. This would correspond to **100 % of quinonoidization.**

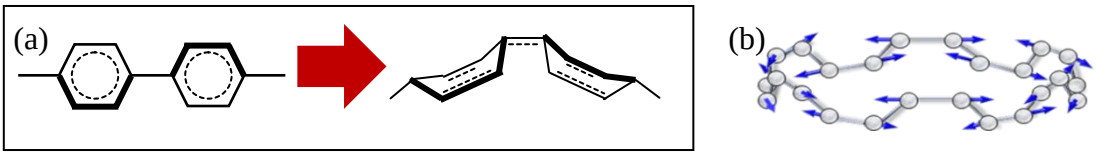

Figure S6.1. a) Scheme to represent the quinonoidization process by cycling of the paraphenylenes. b) Vibrational pattern of the TO mode of a CNT segment.

3. With these structures in mind we get their relevant ring force constant in internal coordinates from the literature and according to the topology of the vibration we define the value of the force constant. We used reference force constants from the literature:

- **BENZOID** references taken from J. L. Jules et al. [19]:
    a. C_6 C-C force constant → k_b = 7.86 (mdyne/Å)
    b. Taking as reference for a simple ethane, C-C stretching force constant → k_1 = 4.33 (mdyne/Å)
- **QUINONOID** references taken from Y. Yamakita et al. [20]:
    a. C=C, force constant → k_s = 7.875 (mdyne/Å)
    b. C-C, force constant → k_s = 5.156 (mdyne/Å)

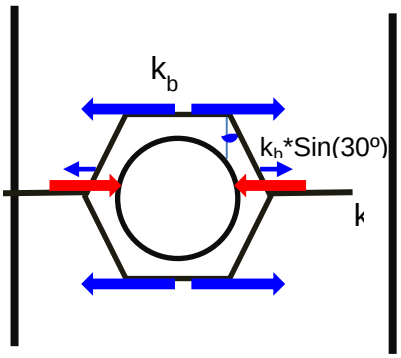

$$K_B = 2*k_b+4*0.5k_b-1*k_1 = 27.11 \text{ (mdyne/Å)}$$

Figure S6.2. Vibrational pattern of the G_1 mode of paraphenylene when is totally benzoid. Arrows indicate the Carbon displacements, where in blue are the considered as positive and in red the negative ones. We refer to vibrational amplitudes which are drawn in qualitative sizes so that we describe them as arbitrary relative displacements. K_B represents the value of the total force constant of the arranged vibration on the circumferential axis when considered as totally benzoid.

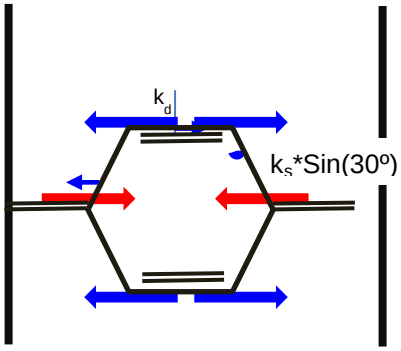

$$K_Q = 2*k_d+4*0.5*k_s-1*k_d = 18.19 \text{ (mdyne/Å)}$$

Figure S6.3. Vibrational pattern of the G_1 mode of paraphenylene considering it totally quinonoid. Arrows indicate the Carbon displacements, where in blue are the considered as positive and in red the negative ones. We refer to vibrational amplitudes which are drawn in qualitative sizes so that we describe them as arbitrary relative displacements. K_Q represents the value of the total force constant of the arranged vibration on the circumferential axis when considered as totally quinonoid.

4. With the force constant of the 8a mode in both extreme cases we calculate the value of the 8a mode frequency in the quinonoidal case (no Raman spectrum available). In this way we obtain the values of the 8a mode Raman frequency for the two extreme cases which sets up the two extreme value of our relative quinonoidal degree scale.

From the estimation of these force constants, K_B and K_Q, in these molecular systems and considering the following relationship:

$$\omega_i = \sqrt{\frac{K_i}{\mu_i}},$$

We can estimate the Raman shift for this mode, if the molecules were totally quinonoidal (ω_Q):

$$\frac{K_B}{K_Q} = \frac{26.99}{18.92} = 1.49 \qquad \frac{\omega_B}{\omega_Q} = \sqrt{1.49} \Rightarrow \omega_Q = \frac{1603\ \text{cm}^{-1}}{1.221} = 1313.23\ \text{cm}^{-1}$$

Where the same reduced mass was assumed and Raman shift of the 8a mode of benzene, 1603 cm^{-1}, was used [21,22].

Therefore, the two extreme references are:

- **100 % benzoid → 1603 cm^{-1}**
- **100 % quinonoid → 1313 cm^{-1}**

5. We use the experimental G_1 mode frequencies (derived from 8a mode of benzene) of the [n]CPP to assign a percentage of quinonoidization to every compound according to our frequency quinonoidization scale.

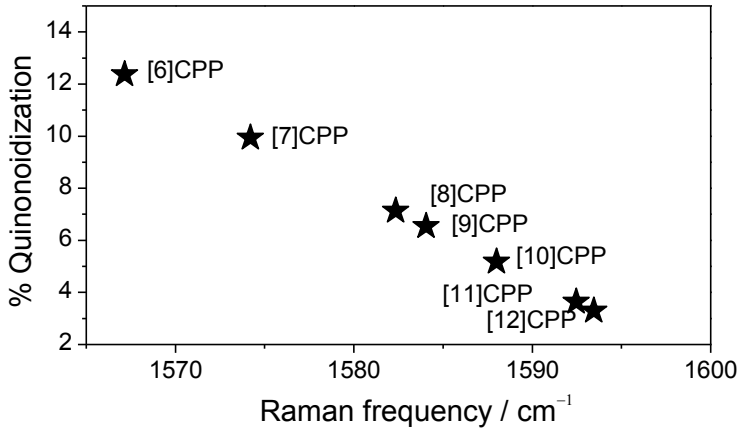

Figure S6.4. Variation of the [n]CPPs quinonoidal character relative to their G^- like mode frequencies.

We observe in Figure S6.4 that the quinonoidal character in CPPs is always below 15 %, so the rings essentially retain their aromatic character.

S7. Experimental Raman Spectra in the 1150-1350 cm^{-1} Range Spectral for [6-12]CPP, [6]LPP and Theoretical Spectra for [6]-, [8]-, [10]-& [12]CPP and [6]LPP Accompanied by the Eigenvectors which Define the Different Contributions

As mentioned in the main text, in linear paraphenylenes the intensity ratio between the 1280 and 1200 cm^{-1} bands, (A_g) C-C inter-ring stretching mode couples to a C-H bending mode, and breathing mode of the phenyl ring,[23] respectively, is intimately related with the torsional angle between neighboring benzenes or in other words with their conjugation along the molecule.[24] In Figure S7.1 we see that in CPPs these bands split into two contributions as result of the curvature induced to form cyclation. To be able to conduct a parallel analysis with the CPPs' sizes analogue to those performed in the literature with the linear paraphenylenes,[24] we have selected the same vibrational modes than used in such studies. We analyze intensity of E mode around 1260-1270 cm^{-1}, corresponding to ring breathing modes (dark blue contribution), divided by the intensity of the 1190-1220 cm^{-1} A mode that mainly emerges from in plane CH bending modes, (red contribution). These ratios are represented in figure S7.2 as function of the CPP size and in figure S7.3 as a function of the torsional angle of the even CPPs. It can be observed that the ratios show a gradual increase with the CPP size increase. It must be mentioned that although theoretical results are a great support on the assignment of these modes they are not too accurate in the intensity estimation. We make this analysis through the heights to make it comparable to the theoretical results. To be able to do this we have set as a common parameter the weights of the different contributions independently on the CPP size.

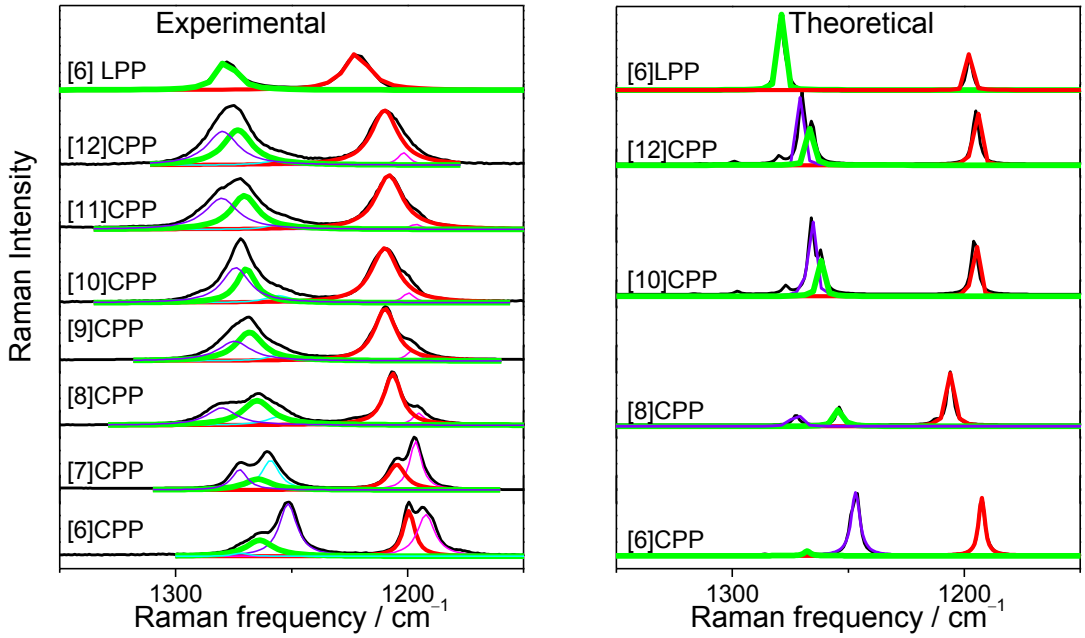

Figure S7.1. Raman spectra in the 1150-1350 cm^{-1} range. Left: 785 nm experimental spectra of the compounds in solid state, from bottom to top, [6]CPP to [12]CPP, and the top one corresponds to the linear hexa-paraphenylene, [6]LPP. Right: theoretical DFT/B3LYP/6-31G* spectra of [6]-, [8]-, [10]-, [12]CPP and [6]LPP. These spectra have been deconvoluted into their different contributions: red line corresponds to an A mode, C-H bending mode coupled to C-C interring stretching mode; purple line corresponds to an A symmetry mode, from a contribution of the symmetric phenyl breathing mode coupled to C-C interring stretching mode and symmetric C-H bending mode; green line corresponds to the E mode, antisymmetric phenyl breathing mode coupled to antisymmetric C-C interring stretching mod and to antisymmetric C-H bending mode. Blue and pink peaks are not accounted on the theoretical spectra, since these gather the contribution of one unique conformation for each molecule; however the real solid may be formed by more than one. Thus, blue and pink peaks may be due to the same kind of modes but from either other conformations, or from interactions between other neighboring molecules theoretically not accounted.

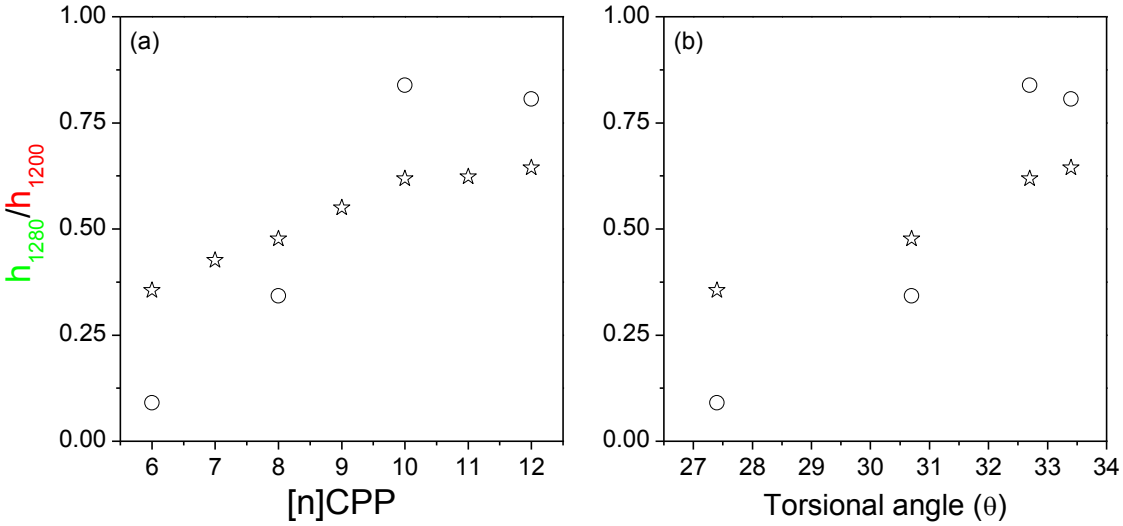

Figure S7.2. Height of the 1280 cm^{-1} band divided by the height of the 1200 cm^{-1} band versus (a) the [n]CPP; (b) the torsional angle of the even CPPs. Angles were taken from Y. Segawa et al. [25]. Stars correspond to experimental results, and circles to theoretical results.

Table S7.1. Experimental Raman shifts obtained for each contribution as function of the [n]CPPs number of benzene members. Colors correspond to the same assignation from the assignment of Figure S6.1.

[n]CPP	ω (cm^{-1})	ω (cm^{-1})	ω (cm^{-1})	ω (cm^{-1})	ω (cm^{-1})
6	1192	**1199**	1272	**1264**	1252
7	1197	**1205**	1259	**1264**	1272
8	1195	**1206**	1255	**1265**	1280
9	1198	**1210**	1256	**1268**	1275
10	1200	**1210**	1256	**1270**	1274
11	1196	**1208**	1254	**1270**	1280
12	1202	**1210**	1255	**1273**	1280

Table S7.2 Vibrational eigenvectors associated with the benzene breathing modes and C-C interring stretching modes coupled to C-H bending modes of the Raman spectra of [12]-, [10]-, [8]-, [6]CPP and [6]LPP. Values obtained from calculations with the B3LYP/6-31G* followed by uniform frequency scaling with a value equals to 0.97. In parentheses, experimental values are shown.

[6]CPP	D_{3d}	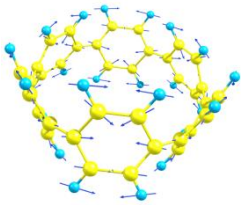	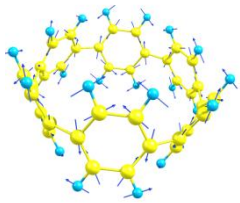	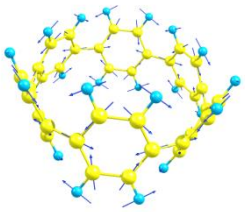
		A_{1g}→1246 (1252) cm^{-1}	E_g→1268 (1264) cm^{-1}	A_{1g}→1192 (1192) cm^{-1}
[8]CPP	D_{8h}	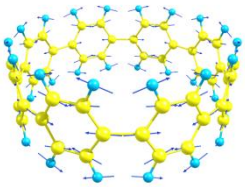	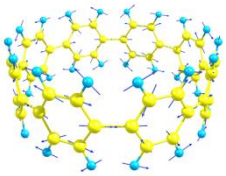	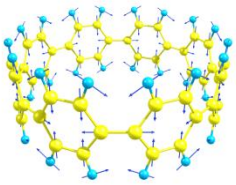
		A_{1g}→1272 (1280) cm^{-1}	E_{2g}→1254 (1268) cm^{-1}	A_{1g}→1206 (1206) cm^{-1}
[10]CPP	D_{5d}	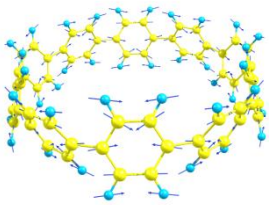	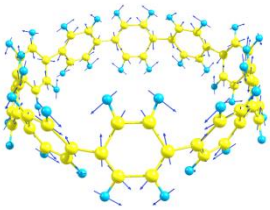	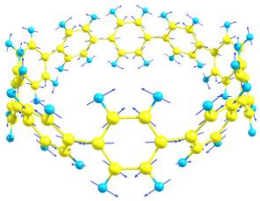
		A_{1g}→1266 (1274) cm^{-1}	E_{1g}→1262(1270) cm^{-1}	A_{1g}→1196 (1210) cm^{-1}
[12]CPP	D_{6d}	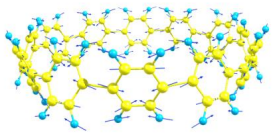	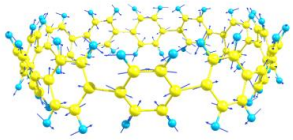	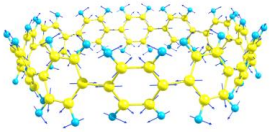
		A_1→1270 (1280) cm^{-1}	E_2→1266 (1273) cm^{-1}	A_1→1195 (1210) cm^{-1}
[6]LPP	D_2	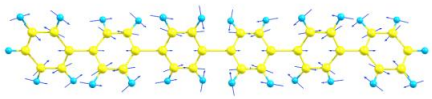	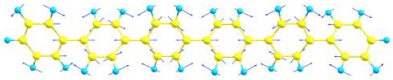	
		A→1279 (1278) cm^{-1}	A →1198 (1222) cm^{-1}	

S8. Analysis of the Effect of the 532 nm Laser Excitation on the Raman Experiments

All the experiments presented on this work have been carried out with a 785 nm laser excitation source to avoid any effect that the light absorption could cause on the molecules. We have detected and analyzed that, with 532 nm excitation wavelength, as plotted on figure S8.1, conformational changes are induced, so that these side effects of conformational modification by light absorption have been avoided by using lower excitation energy.

Figure S8.1 shows the time evolution of the Raman spectra of [8]CPP at 298 K by using 532 nm excitation wavelength. Changes in the spectra are clearly visible resulting in two new peaks at 1562 cm^{-1} and 1604 cm^{-1} (variable temperature alone does not produce any spectral change), see end of the point S8.

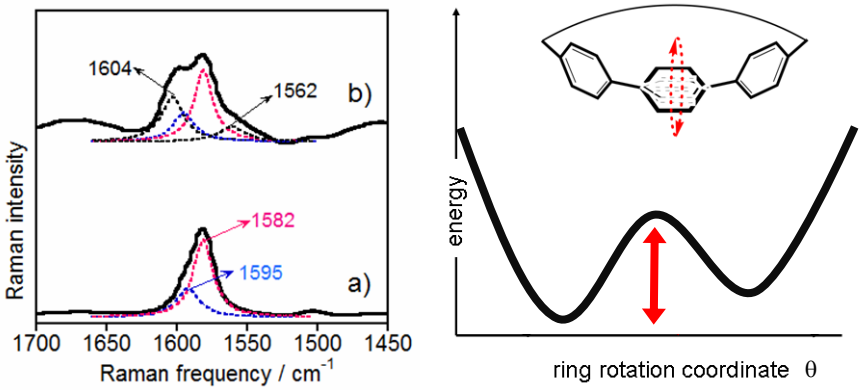

Figure S8.1. [8]CPP Raman spectra obtained with the 532 nm excitation line. a) Deconvoluted spectrum at initial time and at 298 K; b) Deconvoluted spectrum recorded after exposition time of approximately 300 min at 298 K. Right, the ring rotation is depicted and scheme of the energy barrier between two conformations is plotted.

Laser Excitation Response

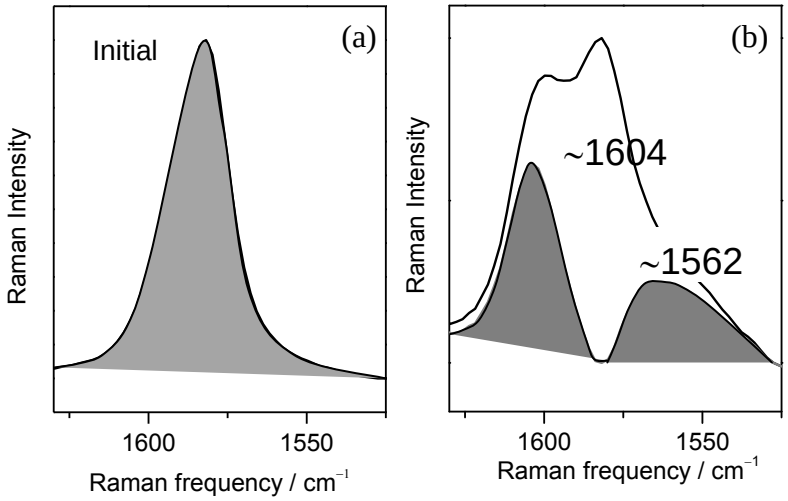

Figure S8.2. Raman spectra of [8]CPP with 532 nm excitation laser: a) at initial time and at 298 K; b) Spectrum recorded after exposition time around 300 min at 298 K, in grey the area of the resultant bands after subtracting the initial 1582 cm^{-1} band.

Time growth of the integrated areas of these new bands (relative to that at 1582 cm^{-1}) allows us to obtain the rate constant for each process which studied as a function of the temperature gives us the activation barriers associated with the conversion between the structures responsible for the two new Raman components.

To quantify the energy barrier implied in these changes we have carried out the same kind of time dependent laser excitation experiments at different temperatures. On this way through the representation of the increasing area of the different growing bands versus time we are able to obtain the rate constant of the transformation. As seen on the next figures, these growths seem to follow a first other kinetics. Therefore once the different rate constants have been obtained, applying an Arrhenius analysis, we are able to estimate the energy barriers involved in these changes.

These studies have only been conducted for [8]CPP and [12]CPP.

[8] CPP

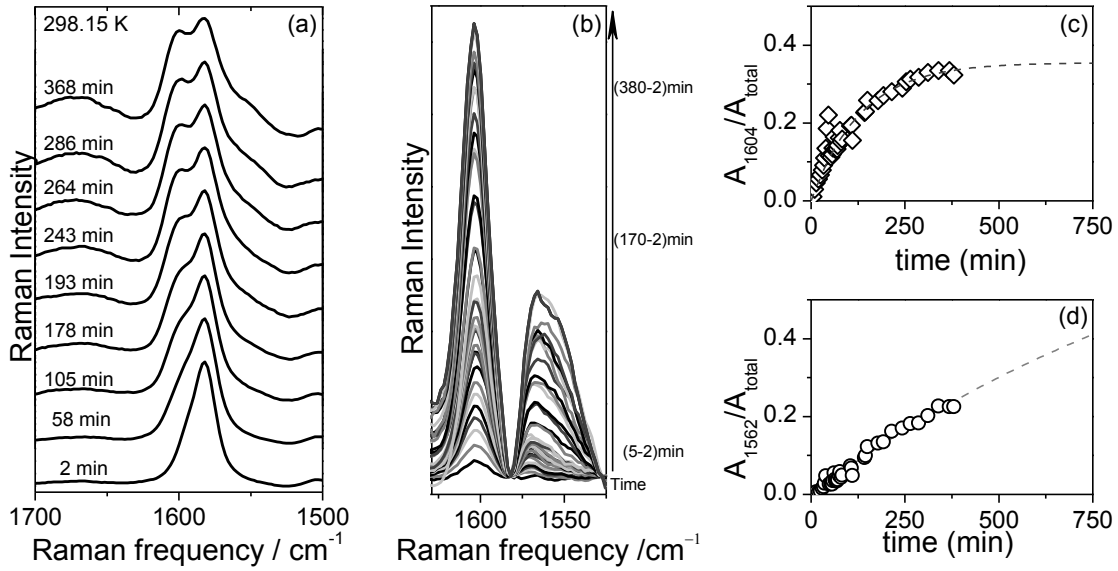

Figure S8.3. a) Raman spectra of [8]CPP at 532 nm excitation wavelength run at 298 K recorded at different excitation times. b) Spectra after subtracting the 1 min Raman spectrum to the different times. c) Area of the 1604 cm^{-1} contribution relative to the area of the total band versus time. d) Area of the 1562 cm^{-1} contribution relative to the area of the total band versus time.

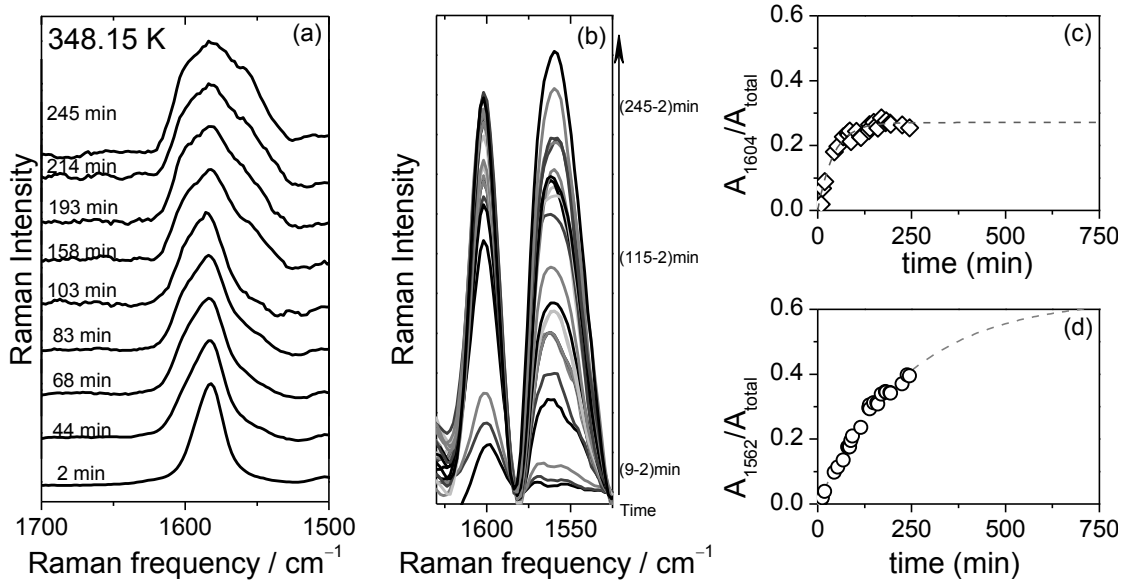

Figure S8.4. a) Raman spectra of [8]CPP at 532 nm excitation wavelength run at 348 K recorded at different excitation times. b) Spectra after subtracting the 1 min Raman spectrum to the different times. c) Area of the 1604 cm^{-1} contribution relative to the area of the total band versus time. d) Area of the 1562 cm^{-1} contribution relative to the area of the total band versus time.

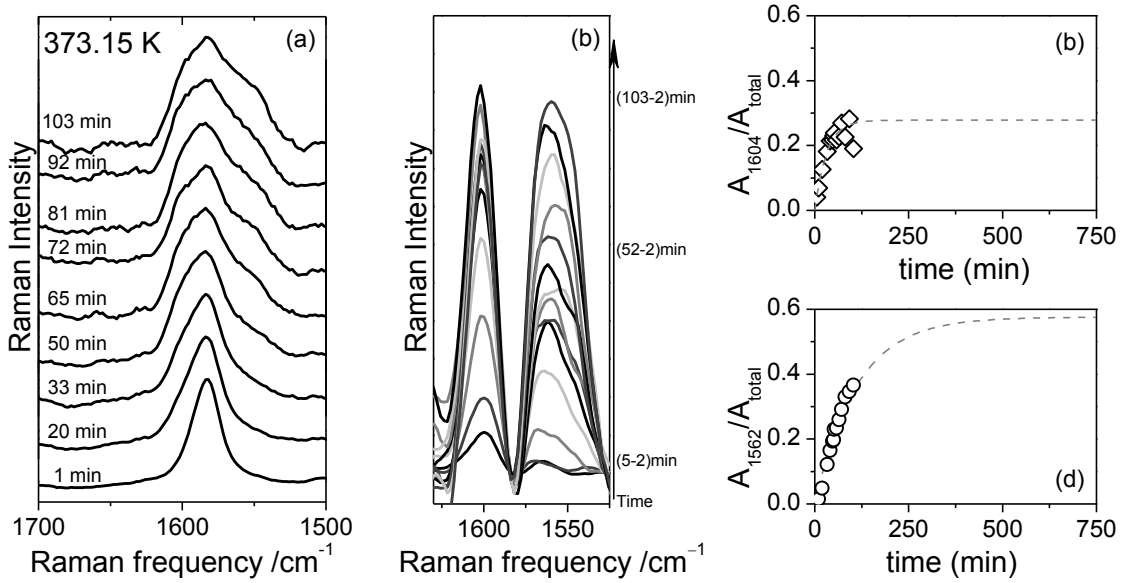

Figure S8.5. a) Raman spectra of [8]CPP at 532 nm excitation wavelength run at 373 K recorded at different excitation times. b) Spectra after subtracting the 1 min Raman spectrum to the different times. c) Area of the 1604 cm^{-1} contribution relative to the area of the total band versus time. d) Area of the 1562 cm^{-1} contribution relative to the area of the total band versus time.

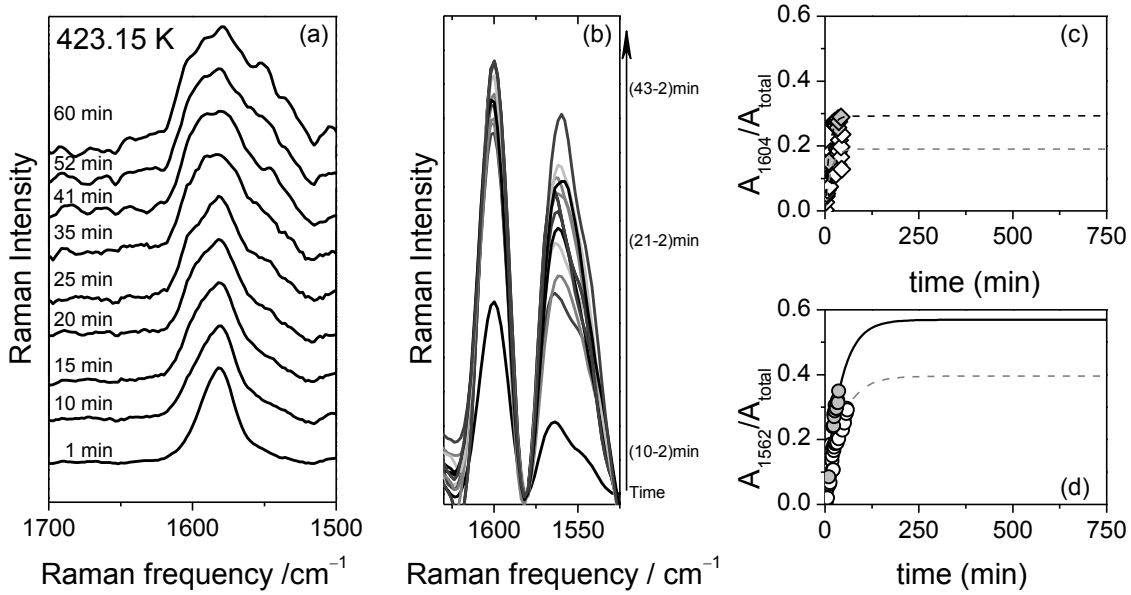

Figure S8.6. a) Raman spectra of [8]CPP at 532 nm excitation wavelength run at 423 K recorded at different excitation times. b) Spectra after subtracting the 1 min Raman spectrum to the different times. c) Area of the 1604 cm^{-1} contribution relative to the area of the total band versus time. d) Area of the 1562 cm^{-1} contribution relative to the area of the total band versus time.

With [8]CPP data and the growth of the 1562 cm^{-1} band, a value of E_{a1} = (28.4 ± 0.6) kJ/mol is determined, while for the 1604 cm^{-1}band it provides a value of E_{a2} = (19.9 ± 1.3) kJ/mol. These activation energies are different depending on the [n]CPP size, for instance, in [12]CPP the strongest 1594 cm^{-1}band only evolves into a band at 1602 cm^{-1} with a value of E_a = (22.0 ± 2.0) kJ/mol. These experimental activation energies are in excellent agreement with those energy barriers calculated for the full rotation of a given benzene regarding their vicinal rings around the inter-ring C-C bonds in [12]CPP [18]. As a result, the energy barriers for the conversion to a more aromatic species (i.e. 1600

cm^{-1} bands) is in consonance with the transformation into more distorted shapes and these barriers might be viewed as the maximal energy costs for full rotation (Figure S8.1). We speculate that the need of assistance by high energy radiation to develop the conformational effect can be explained by the formation after light absorption of an excited state closely related with the transient state for the rotation. The 1582 cm^{-1}→ 1562 cm^{-1} conversion suggesting a transformation into a more quinonoid structure is presently unclear.

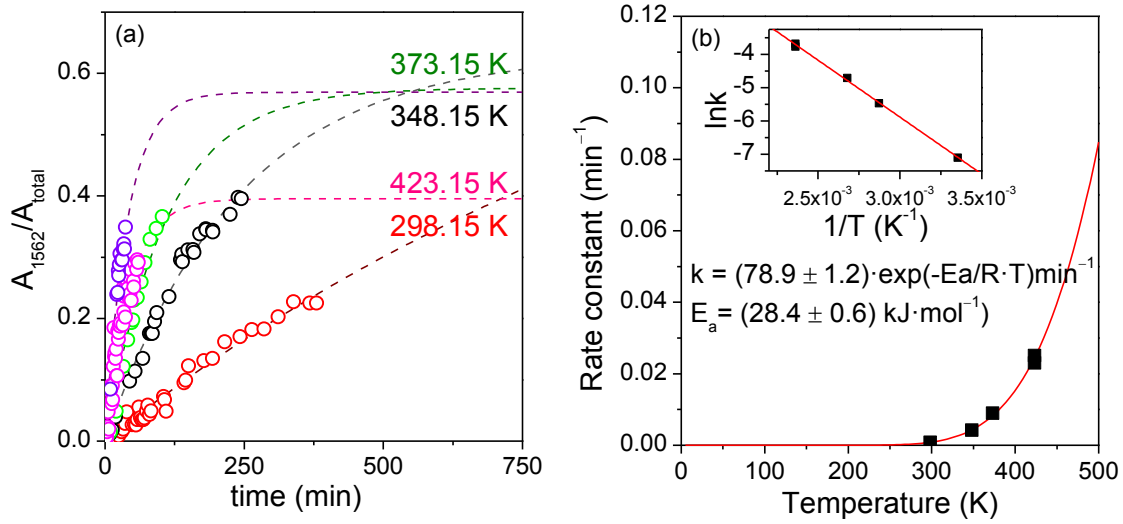

Figure S8.7. a) Time evolution of the [8]CPP area of the 1562 cm^{-1} contribution relative to the area of the total band for the different experimental temperatures. b) ln k (being k the experimental rate constants obtained from data in panel a) versus the inverse of temperature, the slope of this fit corresponds to the E_a/R.

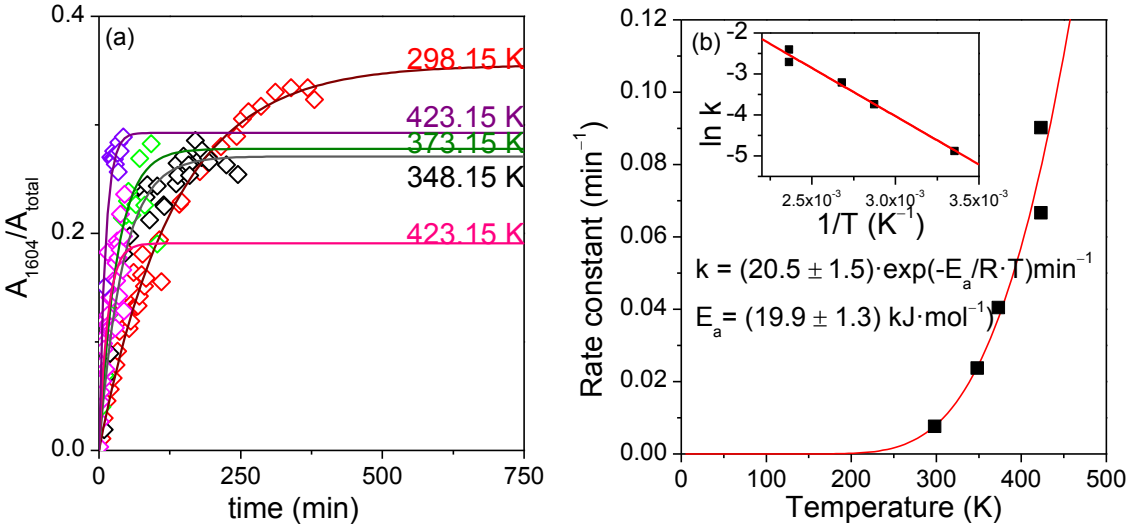

Figure S8.8. a) Time evolution of the [8]CPP area of the 1604 cm^{-1} contribution relative to the area of the total band for the different experimental temperatures. b) ln k (being k the experimental rate constants obtained from data in panel a) versus the inverse of temperature, the slope of this fit corresponds to the E_a/R.

[12]CPP

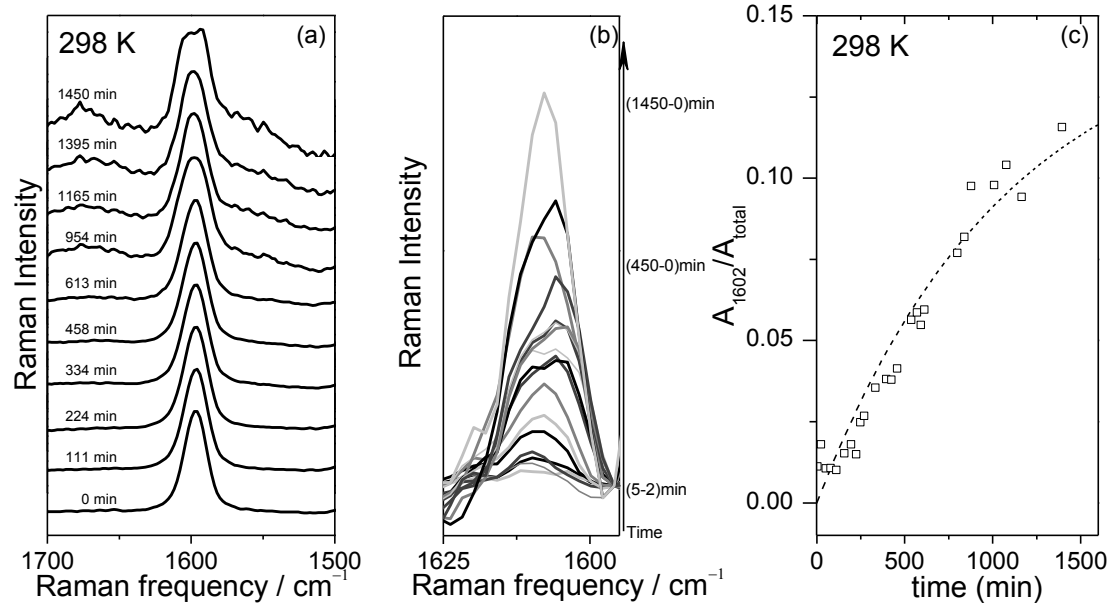

Figure S8.9. a) Raman spectra of [12]CPP at 532 nm excitation wavelength at 298 K recorded at different excitation times. b) Spectra after subtracting the zero time Raman spectrum to the different times. c) Area of the 1602 cm^{-1} contribution relative to the area of the total band versus time.

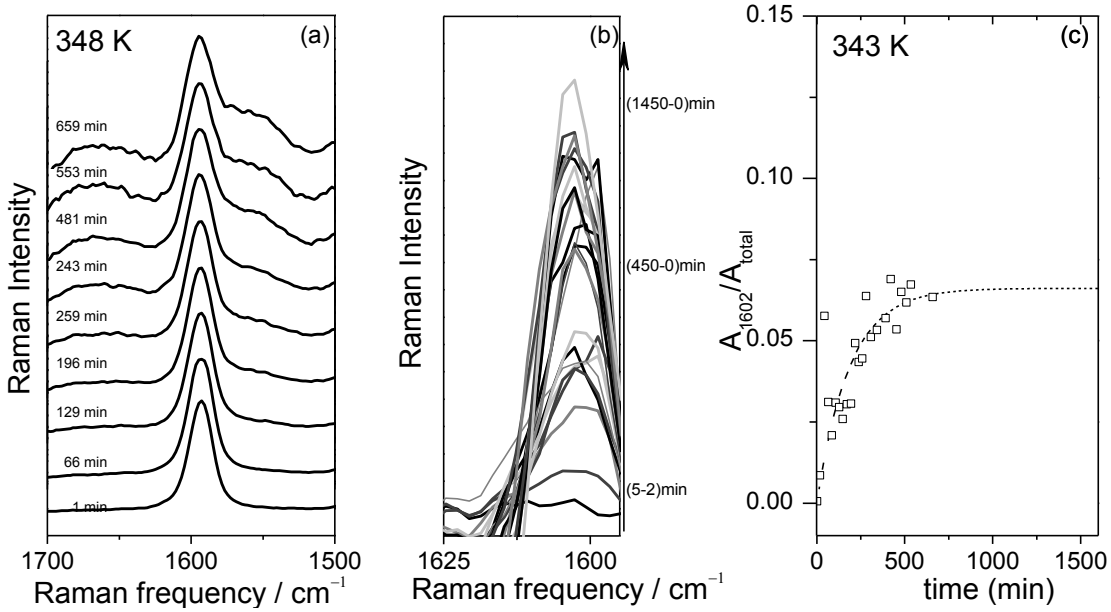

Figure S8.10. a) Raman spectra of [12]CPP at 532 nm excitation wavelength at 348 K recorded at different excitation times .b) Spectra after subtracting the 2 min Raman spectrum to the different times. c) Area of the 1602 cm^{-1} contribution relative to the area of the total band versus time.

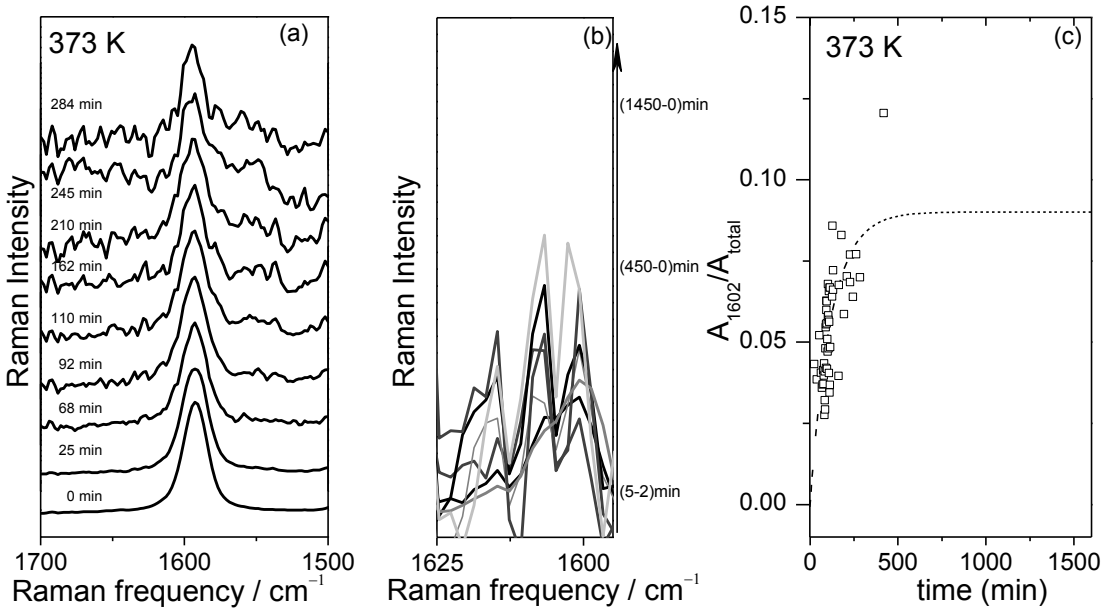

Figure S8.11. a) Raman spectra of [12]CPP at 532 nm excitation wavelength at 373 K recorded at different excitation times. b) Spectra after subtracting the 2 min Raman spectrum to the different times. c) Area of the 1602 cm^{-1} contribution relative to the area of the total band versus time.

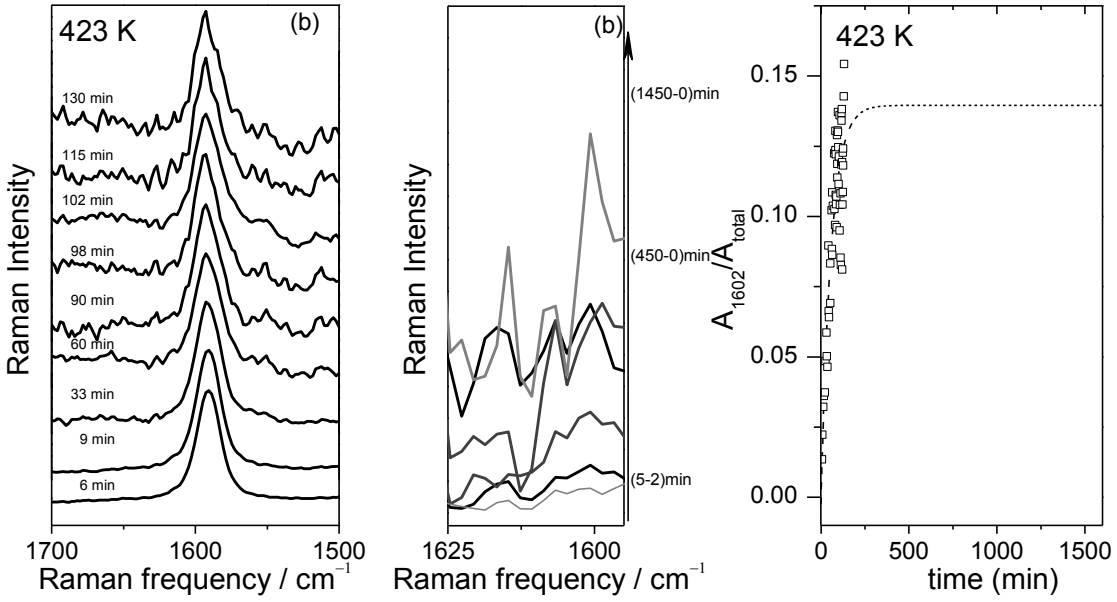

Figure S8.12. a) Raman spectra of [12]CPP at 532 nm excitation wavelength at 423 K recorded at different excitation times. b) Spectra after subtracting the 1 min time Raman spectrum to the different times. c) Area of the 1602 cm^{-1} contribution relative to the area of the total band versus time.

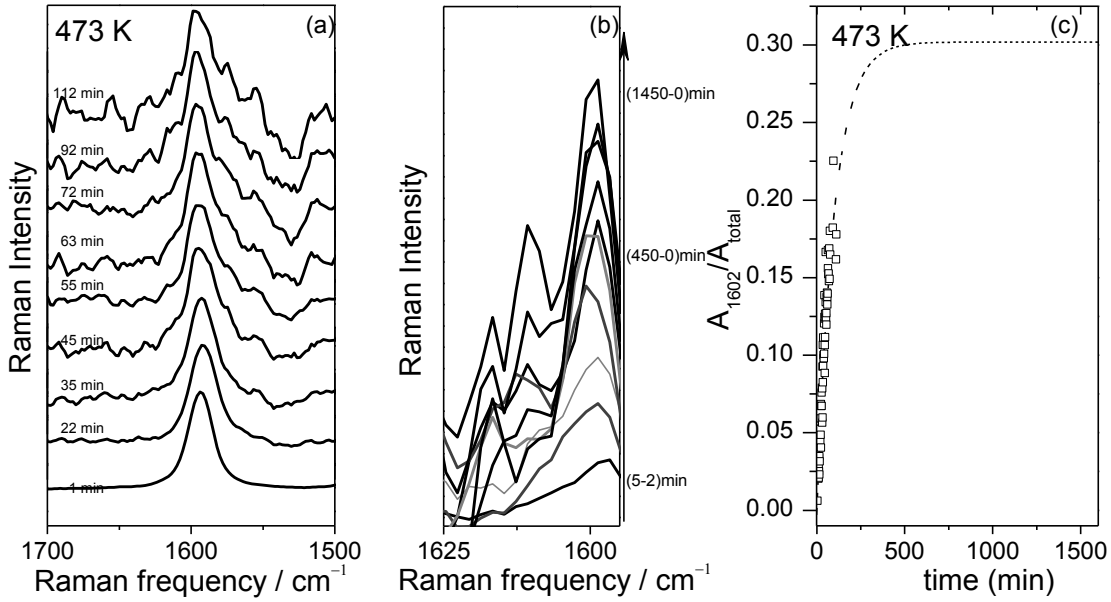

Figure S8.13. a) Raman spectra of [12]CPP at 532 nm excitation wavelength at 473 K recorded at different excitation times. b) Spectra after subtracting the 1 min time Raman spectrum to the different times. c) Area of the 1602 cm^{-1} contribution relative to the area of the total band versus time.

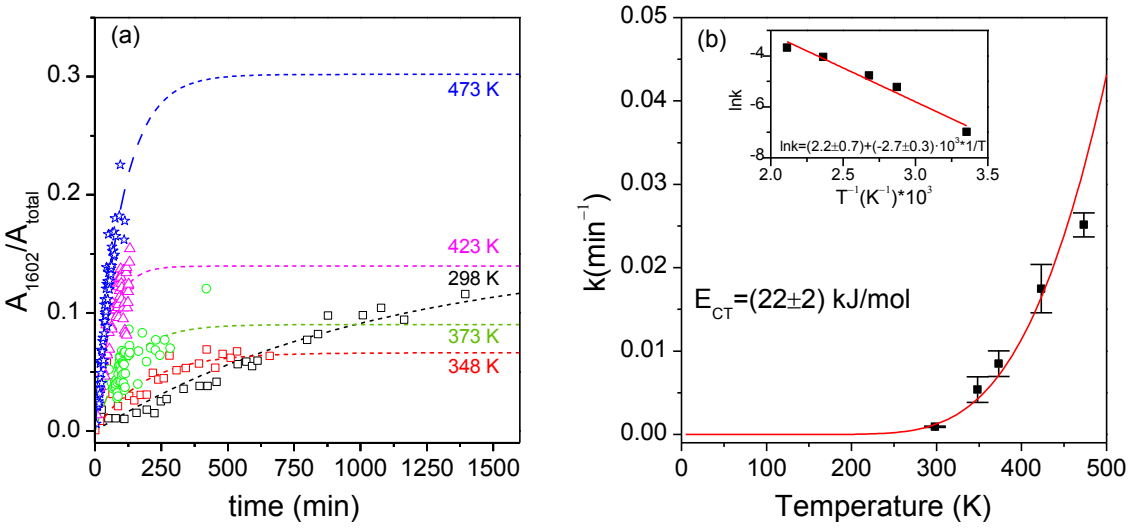

Figure S8.14. a) [12]CPP time evolution of the area of the 1602 cm^{-1} contribution, relative to the area of the total band for the different experimental temperatures. b) ln k (being k the experimental rate constants obtained from data in panel a) versus the inverse of temperature, the slope of this fit corresponds to the E_a/R.

Temperature response

It has been also studied the effect that temperature and laser excitation cause on the [n]CPPs samples. So, Raman spectra were measured heating the samples from room temperature up to 513 K, with a heating rate of 20 K/min, in steps between 25 and 50 K, depending on the run, with 20 minutes of stabilization between measurements. To avoid any possible laser induced modification, each measurement was taken over a different sample spot. In the figures below it is shown the effect of the heat within this temperature range for the [8] and [12] CPPs, not being observable any significant spectral modification, apart from broadening of certain bands. So, from these results we see that temperature by itself does not supply enough energy to induce the transformations which lead to the spectral changes, therefore that all the former analysis is justified.

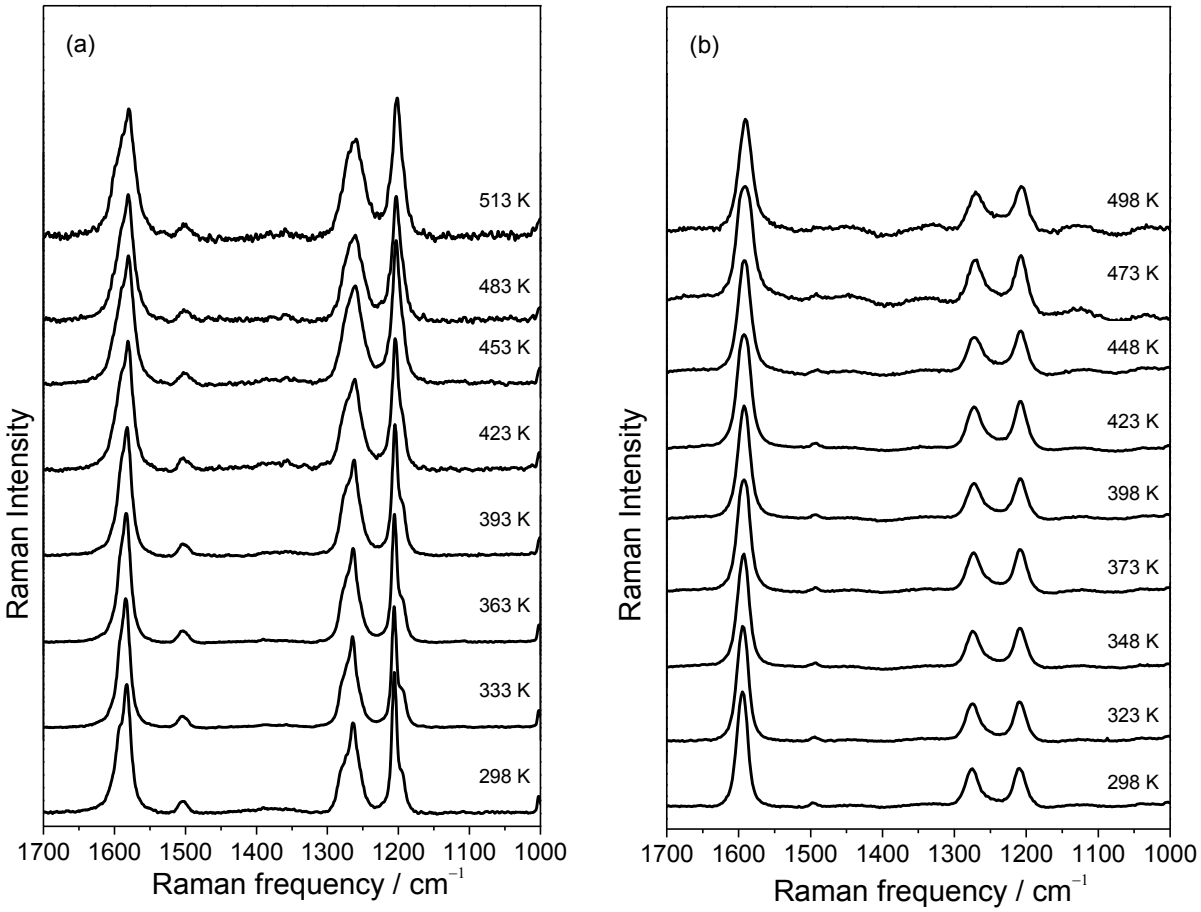

Figure S8.15. a) Raman spectra of [8]CPP and b) [12]CPP. Measurements carried out with 532 nm excitation wavelength at selected temperatures from 298 to 513 K.

S9.High Pressure Experiments for the [8]CPP and [10]CPP

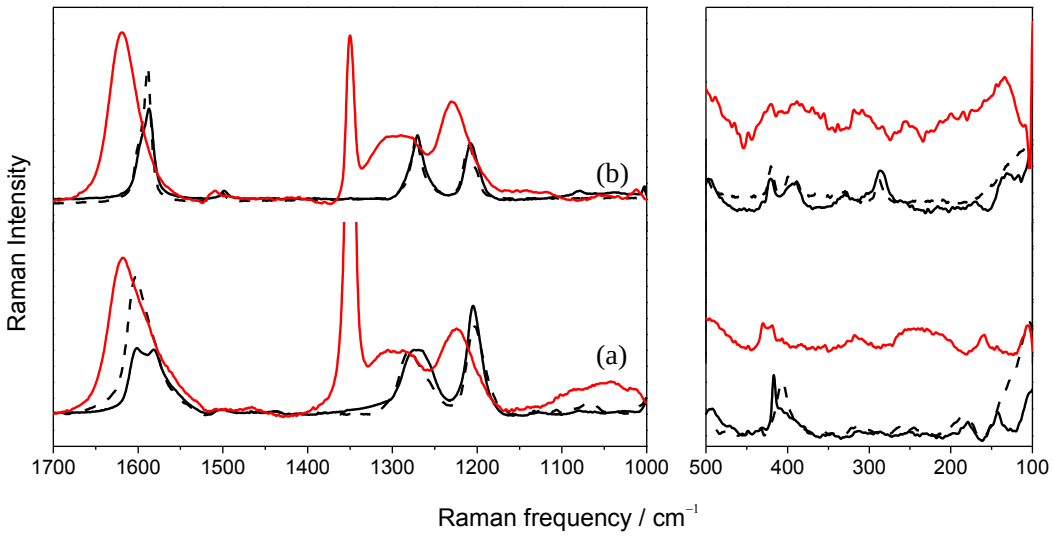

Figure S9.1 785 nm Raman spectra of: a) [8]CPP and b) [10]CPP, at room conditions (black lines), at a pressure around 6 GPa (red lines), and at room conditions after pressure release (dotted lines). Strong band at around 1350 cm^{-1} corresponds to diamond used as pressure sensor.

As it has been analyzed above, the Raman shift of the bands around 1600 cm^{-1} can be considered as reference to evaluate the benzoidal – quinonoidal character of the CPPs. On the Figure S9(a) the effect that pressure causes on [8]CPP can be observed. G_1 modes upshift and, consequently, it seems like pressure have increased the torsional angle between neighboring benzenes, transforming the CPP into a more benzoidal configuration. This effect may also be perceived by looking at the growth in the intensity ratios of the 1200 cm^{-1} bands. Similar behavior was observed in the laser induced conformational modification studied in S.8. It seems quite unlikely that pressure provokes similar conformational changes towards more benzoidal conformations. On regarding [10]CPP, pressure seems to cause different effect as shown in Figure S9(b), and there is not any significant change on the spectra once the pressure is released. CPPs become less reversible to pressure cycle as smaller they are being considered.

These analyses of the recovered samples have been carried out on different sample points to ensure whether the transformation of the samples is complete or not, being each point size limited by the laser spot-size, of about 3 μm. Therefore, within our accuracy the transformations of the samples can be considered homogeneous.

S10. Encapsulation of [6]CPP in [12]CPP

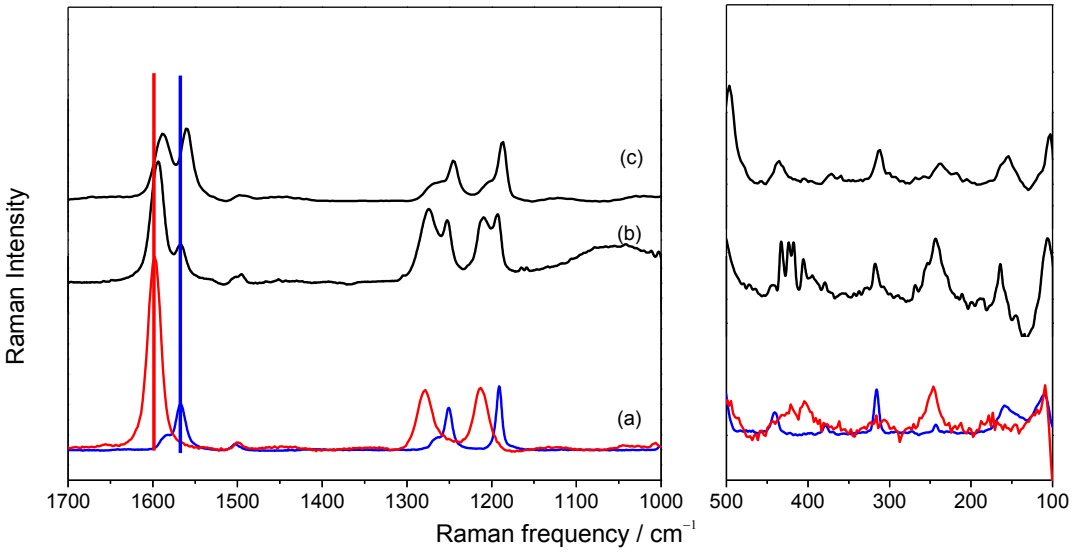

Figure S10.1 532 nm Raman spectra of: a) [6]CPP and[12]CPP in blue and red respectively; [6]CPP - [12]CPP solid state mixture, before high pressure was achieved; and c) after the pressure release ([6]CPP @ [12]CPP).

In figure S10, we can analyse the variations in the spectra of the [6]CPP - [12]CPP solid state mixture, before and after applying pressure. It is seen that although the initial sample presents the same features as if the individual spectra of [6]CPP and [12]CPP were joint together, the spectrum of the recovered sample presents significant changes. There is a downshift in the bands on the 1600 cm^{-1} region for both of the systems which may be caused by the Van der Waals interactions between the [12]- and [6]CPP. Moreover, regarding the intensity variations, it is seen how the 1200 cm^{-1} bands of the initial solid state mixture have the same intensity for both compounds, and the ones around 1600 cm^{-1} are different, the ones of [12]CPP are the ones with higher intensity. Once pressure has been released it is clearly seen how the intensity patterns have changed, now the contributions from the [6]CPP increase their intensity in any of the bands.

Additionally, it must be mentioned that while these pressures are reached on the [6]CPP this molecule adopts a sandwiched form. However, in this case, because it occupies the [12]CPP cavity, it does not suffer this kind of deformation. So it can be said that presence of the [12]CPP makes the [6]CPP to preserve its initial "circular" shape. Even when the pressures reached are higher than when it was squeezed alone, once encapsulated [6]CPP does not ovallize or flatten. In other words, this system constitutes a more robust supramolecular entity against mechanical modification, because a mechanical supporting effect of the inner molecule, and a pressure screening of the outer molecule. This kind of response is the observed in the case of double wall carbon nanotubes under pressure [26].

Because all the facts described, it can be said that due to the spatial facilities, pressure induces the formation of intermolecular interactions between [6]CPP - [12]CPP, giving rise to the here called ultra-short double wall carbon nanotubes.

S11. Encapsulation C_{60}@[9]CPP and C_{60}@[11]CPP

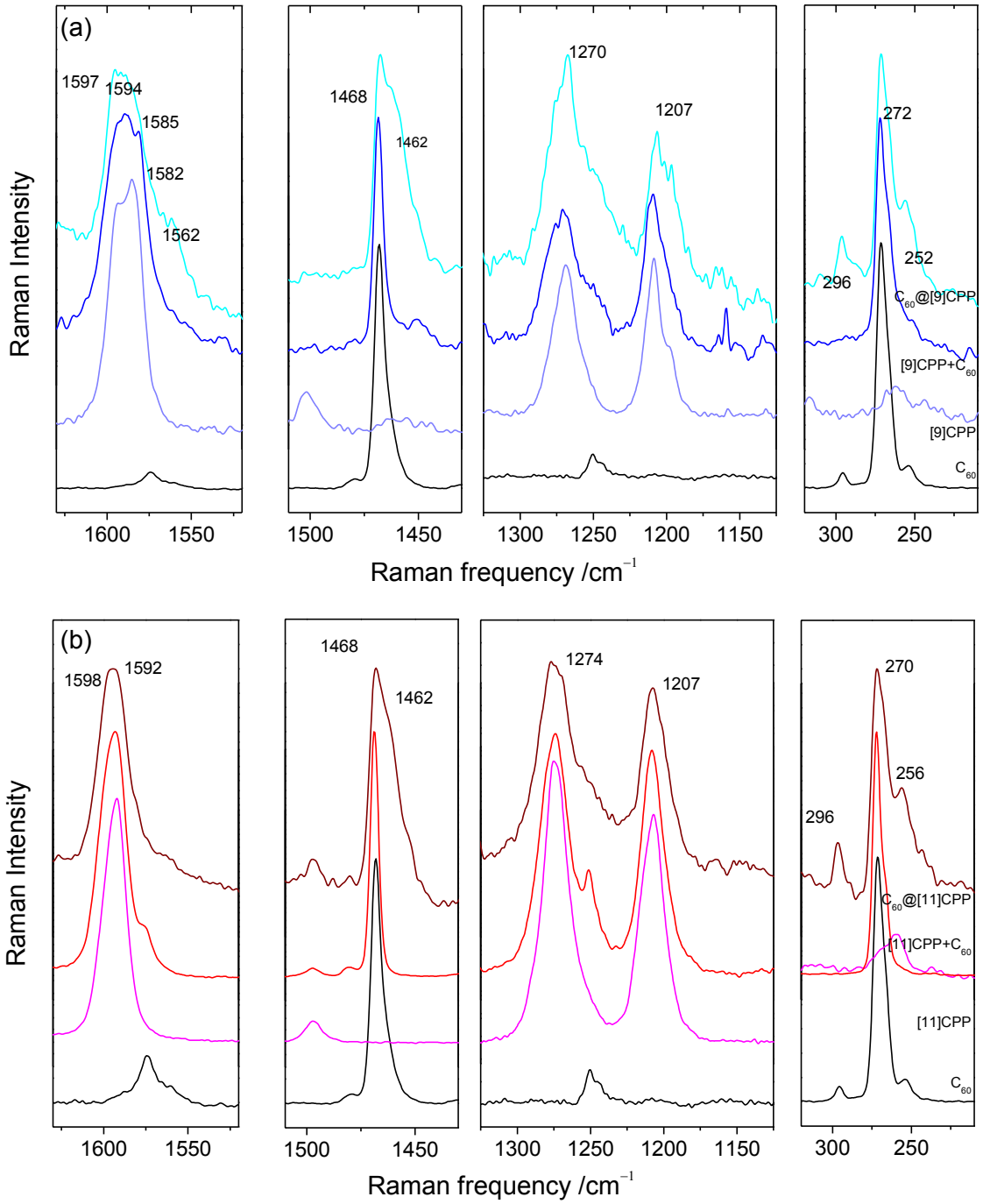

Figure S11.1 785 nm Raman spectra of a) (bottom to top) C_{60} in solid state, [9]CPP in solid state mixture of [9]CPP, C_{60} in solid state, and C_{60}@[9]CPP in solid state at room conditions after pressure release; b) (bottom to top) C_{60} in solid state, [11]CPP in solid state mixture of [11]CPP, C_{60} in solid state, and C_{60}@[11]CPP in solid state at room conditions after pressure release.

The same experiment than with [10]CPP was repeated with a mixture of [9]CPP - C_{60}. Required pressure to observe spectral changes was about 4 GPa. In this case the fullerene shows the same changes than in the [10]CPP case, so there must be some interaction between the [9]CPP and the C_{60}. However, the [9]CPP spectrum show different variations as a consequence of the experiment. The $I_{\beta(CH)}/I_{\nu(C-C)}$ increases, what means that the torsional angle has increased too. Moreover the C-C stretching band does not seem to downshift. This band is very broad and because of this we cannot perform a qualitative analysis. By gathering all this facts we can conclude that the C_{60}@[9]CPP has been formed but due to its diameter, 1.24 nm, it does not fit around the biggest C_{60} Van der Waals diameter, 1.38 nm, having to be placed not in its center but below the equatorial axis. This explains the rising on the torsional angle, necessary to hold on the fullerene, and agrees with the conservation of its benzoidal character.

Assuming that a $C_{60}^{\bullet-}$@[9]CPP$^{\bullet+}$ complex is also formed, the distinctive Raman band of the belt appears at 1561 cm^{-1}, displaced at lower frequencies than the [9]CPP$^{\bullet+}$ analogue, as a sign of the attainment of a larger quinonoidization in the phenylene core such as already occurred in the pristine molecules (i.e., larger quinonoidization in [9]CPP than in [10]CPP). It is noticeable that the pseudo-RBM in [9]CPP$^{\bullet+}$ appears almost at the same frequency than in [10]CPP$^{\bullet+}$ 296 and 254 cm^{-1} which might be the result of the template action of the $C_{60}^{\bullet-}$sphere.

The same experiment was performed with the [11]CPP-C_{60} mixture resulting that the bands from [11]CPP were almost not influenced by either the C_{60} molecules and the stress cycle. However the same frequencies downshifts take place for the C_{60}. This may mean that due to the [11]CPP bigger size, 1.52 nm, it is able to host the C_{60} without the need of any conformational change.

References Supporting Information

1 T. Iwamoto, Y. Watanabe, Y. Sakamoto, T. Suzuki, S. Yamago, *J. Am. Chem. Soc.* **133**, 8354 (2011).

2 J. Xia, R. Jasti, *Angew. Chem. Int. Ed*. **51**, 1 (2012).

3 V. G. Baonza, M. Taravillo, A. Arencibia, M. Cáceres, J. Núñez, *J. Raman Spectrosc.* **34**, 264-270 (2003).

4 E. del Corro, J. González, M. Taravillo, E. Flahaut, V. G. Baonza, *Nano Lett*. **8**, 2215 (2008).

5 A. D. Becke, *J. Chem. Phys.* **98**, 5648 (1993).

6 Gaussian 09, Revision A.02, M. J. Frisch, G. W. Trucks, H. B. Schlegel, G. E. Scuseria, M. A. Robb, J. R. Cheeseman, G. Scalmani, V. Barone, B. Mennucci, G. A. Petersson, H. Nakatsuji, M. Caricato, X. Li, H. P. Hratchian, A. F. Izmaylov, J. Bloino, G. Zheng, J. L. Sonnenberg, M. Hada, M. Ehara, K. Toyota, R. Fukuda, J. Hasegawa, M. Ishida, T. Nakajima, Y. Honda, O. Kitao, H. Nakai, T. Vreven, J. A. Montgomery, Jr., J. E. Peralta, F. Ogliaro, M. Bearpark, J. J. Heyd, E. Brothers, K. N. Kudin, V. N. Staroverov, R. Kobayashi, J. Normand, K. Raghavachari, A. Rendell, J. C. Burant, S. S. Iyengar, J. Tomasi, M. Cossi, N. Rega, J. M. Millam, M. Klene, J. E. Knox, J. B. Cross, V. Bakken, C. Adamo, J. Jaramillo, R. Gomperts, R. E. Stratmann, O. Yazyev, A. J. Austin, R. Cammi, C. Pomelli, J. W. Ochterski, R. L. Martin, K. Morokuma, V. G. Zakrzewski, G. A. Voth, P. Salvador, J. J. Dannenberg, S. Dapprich, A. D. Daniels, O. Farkas, J. B. Foresman, J. V. Ortiz, J. Cioslowski, and D. J. Fox, Gaussian, Inc., Wallingford CT, **2009.**

7 P. Pulay, G. Fogarasi, G. Pongor, J. E. Boggs, A. Vargha, *J. Am. Chem. Soc.* **105**, 7037 (1983).

8 http://www.chemcraftprog.com (browsed January 22nd, 2014)

9 http://gausssum.sourceforge.net/ (browsed January 22nd, 2014)

10 A. Almenningen, O. Bastiansen, L. Fernholt, B.N. Cyvin, S.J. Cyvin, S. Samdal, *J. Mol. Struct.* **128**, 59. (1985).

11 T.M.G. Mohiuddin, A. Lombardo, R. R. Nair, A. Bonetti, G. Savinini, R. Jalil, N. Bonini, D. M. Basko, C. Galiotis, N. Marzari, K. S. Novoselov, A. K. Geim, A. C. Ferrari, *Phys. Rev. B*, **79**, 205433 (2009).

12 J. S. Park, K. Sasaki, R. Saito, W. Izumida, M. Kalbac, H. Farhat, G. Dresselhaus, M. S. Dresselhaus, *Phys Rev. B* **80**, 081402 (2009).

13 H. Farhat, H. Son, Ge. G Samsonidze, S. Reich, M. S. Dresselhaus, J. Kong, *Phys Rev. Lett.* **99**, 145506 (2007).

14 A. Marucci, M. A. Pimenta, S. D. M. Brown, M. J. Matthews, M. S. Dresselhaus, M. Endo, *J. Mater. Res*. **14**, 3447 (1999).

15 G. Zannoni, G. Zerbi, *J. Chem. Phys.* **82**, 31 (1985).

16 A. Jorio, A. G. Souza Filho, G. Dresselhaus, M. S. Dresselhaus, A. K. Swan, M. S. Ünlü, B. B. Goldberg, M. A. Pimenta, J. H. Hafner, C. M. Lieber, R. Saito, *Phys. Rev. B* **65**, 155412 (2002).

17 E. H. Haroz, J. G. Duque, X. Tu, M. Zheng, A. R. Hight Walker, R. H. Hauge, S. K. Doorn, J. Kono, *Nanoscale* ***5***, 1411-1435 (2013).

18 Y. Segawa, H. Omachi, K. Itami, *Org. Lett.*, **12**, 2262 (2010).

19 J. L. Jules, J. R. Lombardi, *J. Molecular Structure (Theochem)* **255**, 664-665, (2003).

20 Y. Yamakita, M. Tamusi, *J. Phys. Chem.* **99**, 8524(1995).

21 E. B. Wilson, *Phys. Rev*. **45,** 706 (1934).

22 R. W. Wood, *Phys. Rev*. **36**, 1341 (1930).

23 G. Zannoni, G. Zerbi, *J. Chem. Phys*. **82**, 31 (1995).

24 G. Heimel, D. Somitsch, P. Knoll, J.L Brédas, E. Zojer, *J. Chem. Phys*. *122*, 114511 (2005).

25 Y. Segawa, A. Fukazawa, S. Matsuura, H. Omachi, S. Yamaguchi, S. Irie, K. Itami, *Or. Biomol. Chem.* **10**, 5979 (2012).

26 A. L. Aguiar, E. B. Barros, R. B. Capaz, A. G. Souza Filho, P. T. C. Freire, J. Mendes Filho, D. Machon, Ch. Caillier, Y. A. Kim, H. Muramatsu, M. Endo, A. San-Miguel, *J. Phys. Chem. C,* **115**, 5378 (2011).

Appendix 3

Faraday Discussions **173**, 157-171 (2014)

Supporting Information:

Chameleon-like Behaviour of Cyclo[n]paraphenylenes in Complexes with C_{70}. On their Impressive Electronic and Structural Adaptability as Probed by Raman Spectroscopy

M. Peña Alvarez, P. M. Burrezo, T. Iwamoto, L. Qiu,
M. Kertesz, M. Taravillo, V. G. Baonza,
J. T. López Navarrete, S. Yamago, J. Casado

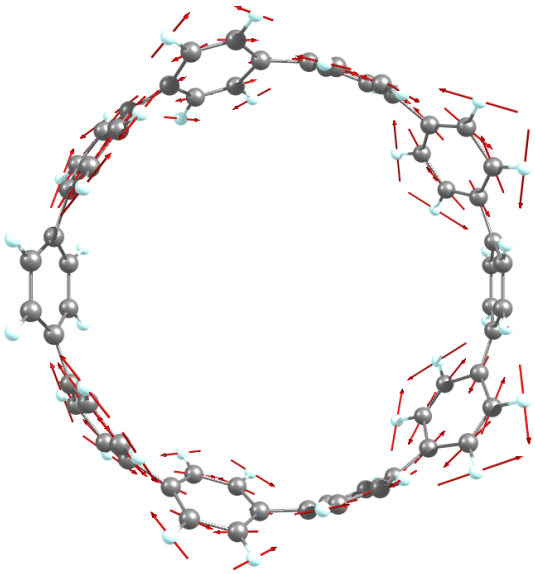

Fig. S1. Vibrational mode associated with the G_2 band of [10]CPP.

Cage Squashing Mode 1: 261 cm^{-1}

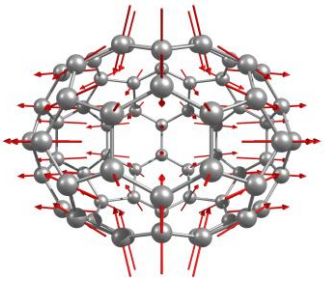

Cage Squashing Mode 2: 252 cm^{-1}

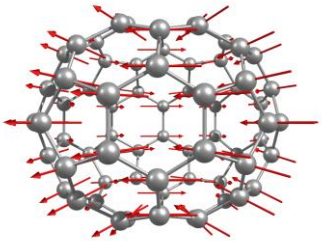

Cage Squashing Mode 2-1: 224 cm^{-1}

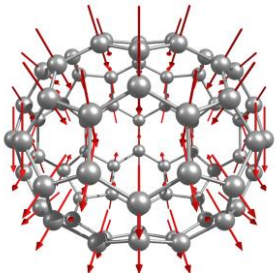

Fig. S2. Vibrational modes associated with the C_{70} low frequency modes, known as cage squashing modes.

Experimental Raman Spectra in the 1150-1350 cm^{-1} Range at Room Conditions

In linear paraphenylenes the intensity ratio between the 1280 and 1200 cm^{-1} bands, (A_g) C-C inter-ring stretching mode coupled to a C-H bending mode, and breathing mode of the phenyl ring,[1] respectively, it is intimately related with the torsional angle between neighboring benzenes or in other words with their conjugation along the molecule.[2] In Fig. S3 we analyze intensity of E mode around 1260-1270 cm^{-1}, corresponding to ring breathing modes (purple contribution), divided by the intensity of the 1190-1220 cm^{-1} A mode that mainly emerges from in plane CH bending modes, (light blue contribution).[3]

In the different complexes C_{70} complexes, here studied, the intensity ratio of the 1200 cm^{-1} bands behaves according to the observations already presented in the main text, for G bands of the CPPs.

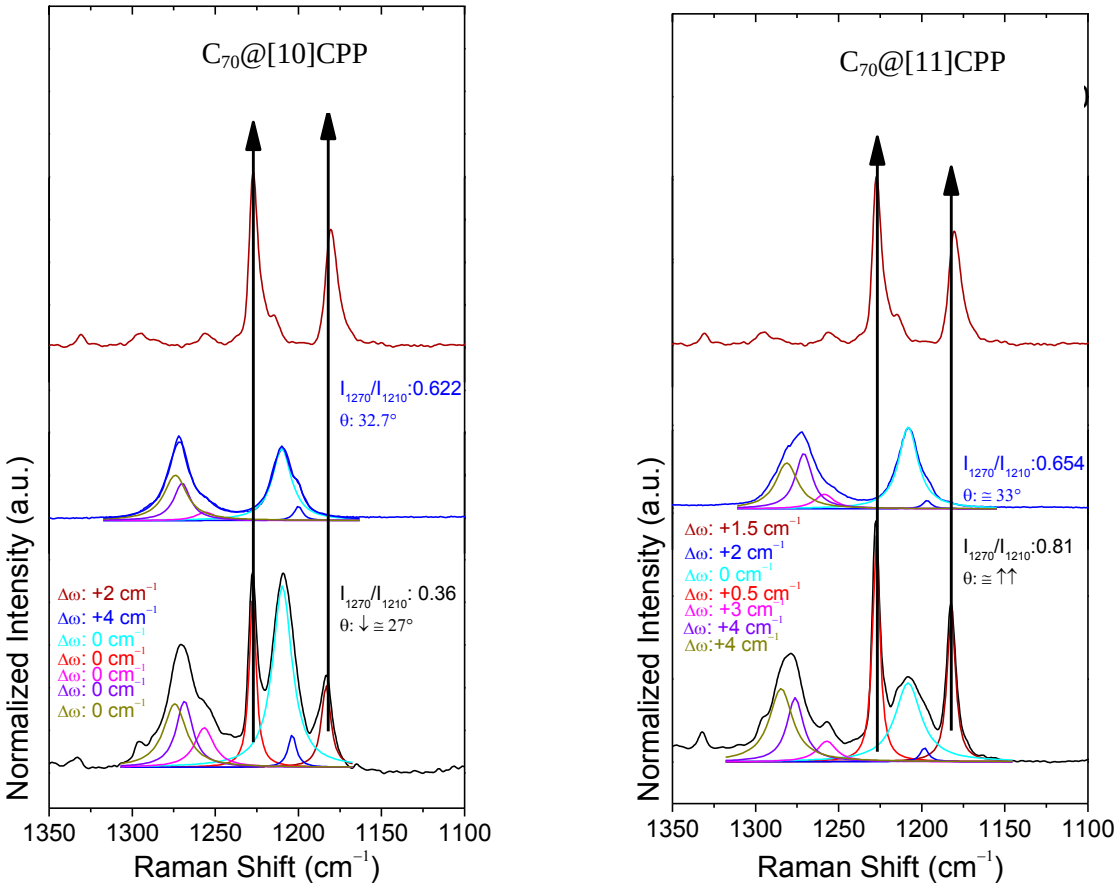

Fig. S3 785 nm experimental Raman spectra in the 1100-1350 cm^{-1} range. Left: C_{70}@[10]CPP; right: C_{70}@[11]CPP. From bottom to top: pristine complex (black), pristine [n]CPP (dark blue), pristine C_{70} (dark red), all registered in solid state and ambient conditions. These spectra have been deconvoluted into their different contributions: red lines correspond to C_{70} contributions (being the most intense ones at 1228 cm^{-1} and 1183 cm^{-1}, from the phenyl breathing mode and the C-C stretching mode, predominantly along the C_{70} short diameter direction, respectively). The remaining contributions are originated by different CPP vibrational modes: Light blue, around 1210 cm^{-1}, A mode, C-H bending mode coupled to C-C interring stretching mode; Purple peak, around 1270 cm^{-1}, corresponds to the E mode, antisymmetric phenyl breathing mode coupled to antisymmetric C-C interring stretching mode and to antisymmetric C-H bending mode. Olive green peak, around 1280 cm^{-1}, corresponds to an A symmetry mode, from a contribution of the symmetric phenyl breathing mode coupled to C-C interring stretching mode and symmetric C-H bending mode. Dark blue and pink peaks, around 1200 and 1255 cm^{-1} respectively, may be due to the same kind of modes but from either other conformations, or from interactions between other neighboring molecules theoretically not accounted.[3]

- In the [10]CPP complex, this ratio significantly diminishes as result of the closing torsional angle towards a more planar conformation. As seen in the main text, this conformation favors the interaction between the CPP and the fullerene in its standing orientation, around its small diameter.
- The contrary tendency is seen on the [11]CPP complex, with lying orientation, the intensity ratio, the torsional angle, increases as a result of the complexation.
- C_{70}@[9]CPP complex, as in the [10]CPP case, there is a significant decay in the intensity ratio, due to the planarization between neighboring benzenes. As explained in the main text, this is required to favor the interaction between the CPP and the fullerene in the standing orientation, although they do not precisely fit.
- C_{70}@[12]CPP complex, this ratio considerably increases, meaning that an interaction between the CPP and the C_{70} molecule exists, even if the CPP ratio is not the most favorable.

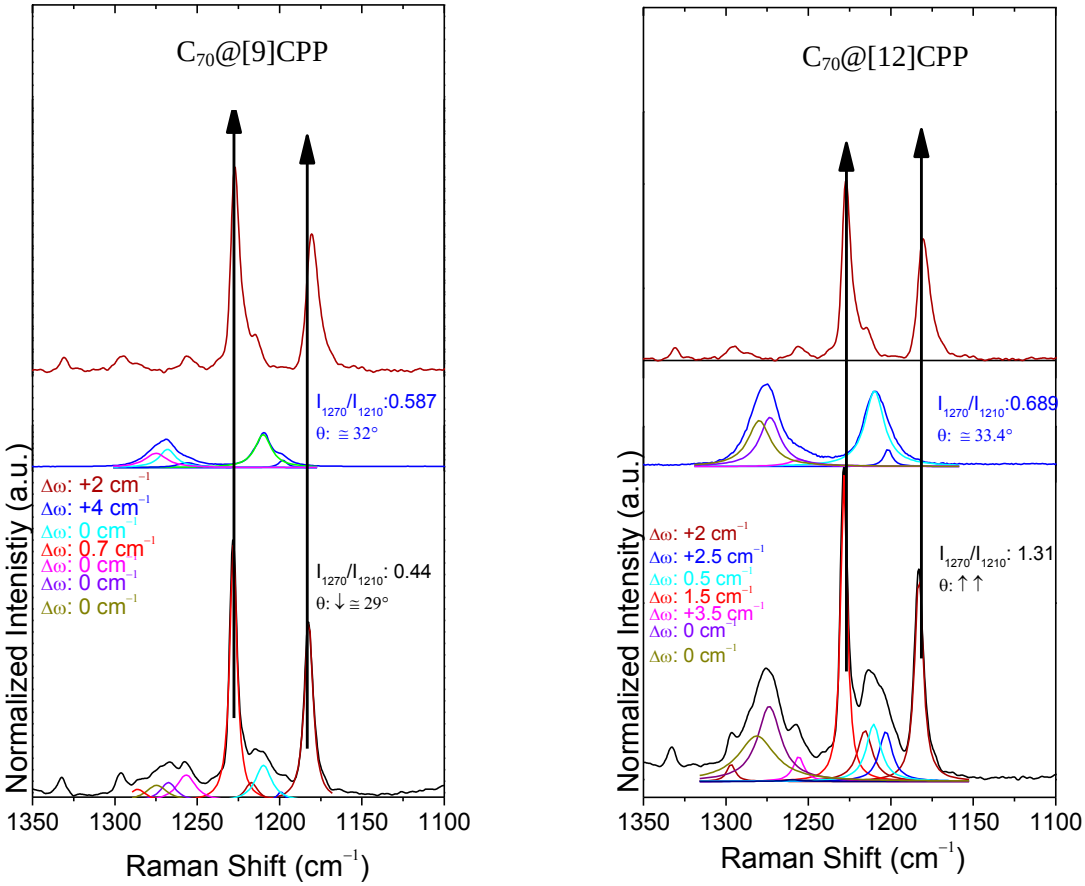

Fig. S4 785 nm experimental Raman spectra in the 1100-1350 cm^{-1} range. Left: C_{70}@[9]CPP; right: C_{70}@[12]CPP. From bottom to top: pristine complex (black), pristine [n]CPP (dark blue), pristine C_{70} (dark red), all registered in solid state and ambient conditions. These spectra have been deconvoluted into their different contributions: red lines correspond to C_{70} contributions (being the most intense ones at 1228 cm^{-1} and 1183 cm^{-1}, from the phenyl breathing mode and the C-C stretching mode, predominantly along the C_{70} short diameter direction, respectively). The remaining contributions are originated by different CPP vibrational modes: Light blue, around 1210 cm^{-1}, A mode, C-H bending mode coupled to C-C interring stretching mode; Purple peak, around 1270 cm^{-1}, corresponds to the E mode, antisymmetric phenyl breathing mode coupled to antisymmetric C-C interring stretching mode and to antisymmetric C-H bending mode. Olive green peak, around 1280 cm^{-1}, corresponds to an A symmetry mode, from a contribution of the symmetric phenyl breathing mode coupled to C-C interring stretching mode and symmetric C-H bending mode. Dark blue and pink peaks, around 1200 and 1255 cm^{-1} respectively, may be due to the same kind of modes but from either other conformations, or from interactions between other neighboring molecules theoretically not accounted.[3]

None important changes are observed on the Raman shifts of these bands, only the C_{70} C-C stretching mode (predominantly along the C_{70} short diameter) at about 1183 cm^{-1} seems to upshift, about 0.5 cm^{-1} more in the standing than in the lying orientation. Also the dark blue and pink peaks, around 1200 cm^{-1} band seems to be more affected by the CPP being placed in the C_{70} standing orientation than in its lying one.

Experimental Raman Spectra in the 1150-1350 cm^{-1} Range: High Temperature and High Pressure Treatments

Raman spectra of the complexes under extreme conditions of pressure and temperature are analyzed in the Fig. S5 and S6.

Pressure Effect

- In the [10]CPP complex, the 1200 cm^{-1} bands ratio significantly increases, hence increasing of the torsional angle. This is in agreement also with the more staggered conformation required for this CPP to accommodate the C_{70} molecule in its standing orientation, maximizing therefore the π-π interactions between both of the systems.
- Similar tendency is seen on the [11]CPP complex, the intensity ratio slightly increases to, as mentioned in the main text, improve the contacts between [11]CPP and C_{70}.
- C_{70}@[9]CPP complex, in the main text we suggest that pressure further helps the formation of the supramolecular complex through a more strained [9]CPP molecule while it slightly adapts to better fit C_{70}. This occurs by the flattening between neighboring benzenes as observed in the Fig. S6, with the intensity ratio of the 1268/1210 cm^{-1} bands.
- C_{70}@[12]CPP complex, the intensity ratio of the 1200 cm^{-1} bands decreases close to the value of the pristine complex.

None important changes are observed on the Raman shifts of these bands, but a downshift in the CPP bands, being the highest for the [9]CPP complex.

Temperature Effect

- In the [10]CPP complex, the 1200 cm^{-1} bands ratio practically remains the same than in the pristine complex, and the bands do not shift either.
- Similar tendency is seen in the [11]CPP complex, the intensity ratio slightly increases.

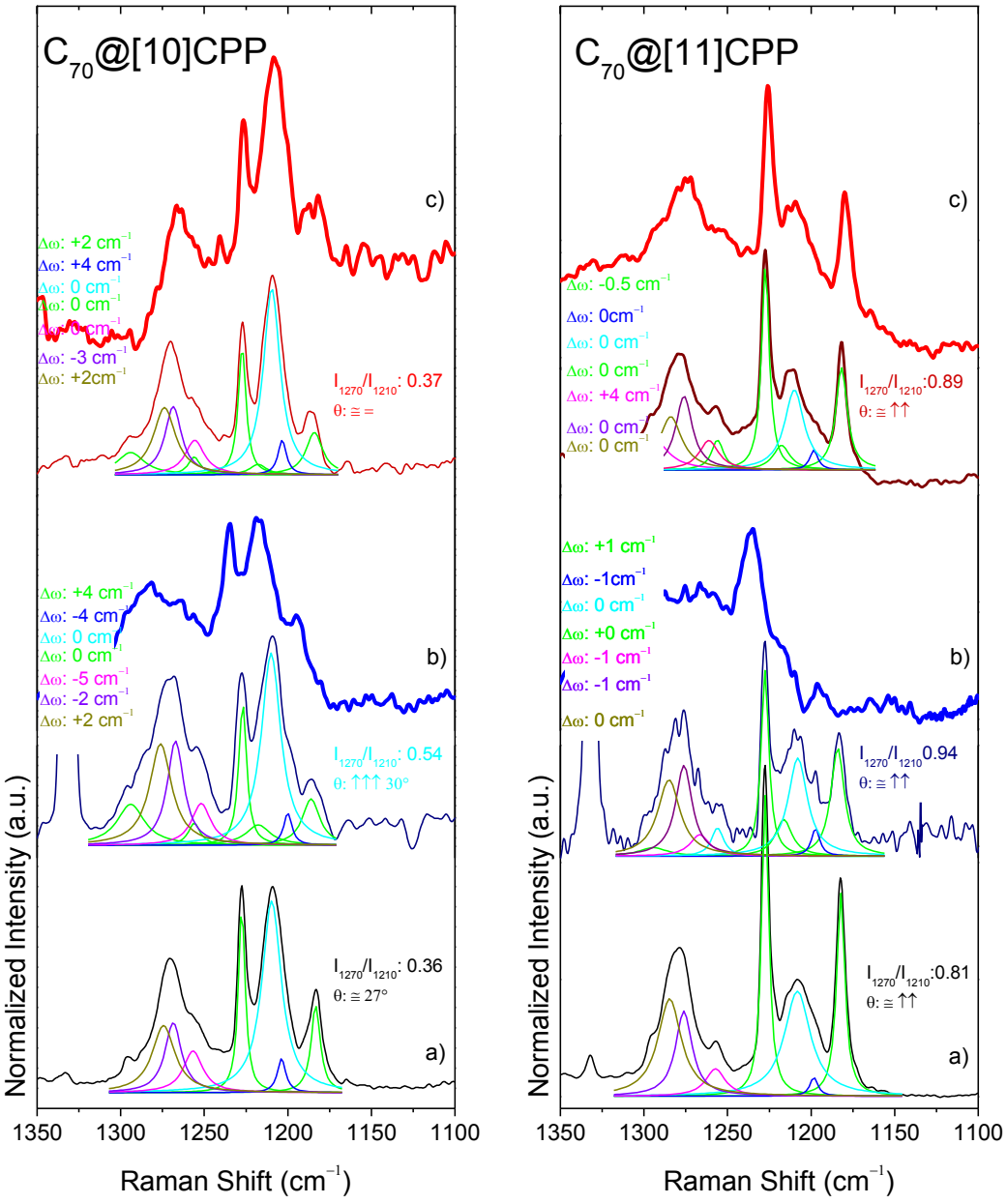

Fig. S5 785 nm experimental Raman spectra in the 1100-1350 cm^{-1} range. Left: C_{70}@[10]CPP; right: C_{70}@[11]CPP. From bottom to top: (a) pristine complex (black), at room temperature and pressure; (b) thick blue line corresponds to the spectrum at high pressure (≈ 2.0 GPa) and thin dark blue line corresponds to the recovered spectrum after pressure cycle; both spectra taken at 25 °C. (c) Thick red line corresponds to the spectrum at high temperature (140 °C) and thin dark red line corresponds to the recovered spectrum after thermal cycle. Both spectra are taken at room pressure. These spectra have been deconvoluted into their different contributions: red lines correspond to C_{70} contributions (being the most intense ones at 1228 cm^{-1} and 1183 cm^{-1}, from the phenyl breathing mode and the C-C stretching mode, predominantly along the C_{70} short diameter direction, respectively); The remaining contributions are originated by different CPP vibrational modes: Light blue, around 1210 cm^{-1}, A mode, C-H bending mode coupled to C-C interring stretching mode; Purple peak, around 1270 cm^{-1}, corresponds to the E mode, antisymmetric phenyl breathing mode coupled to antisymmetric C-C interring stretching mode and to antisymmetric C-H bending mode. Olive green peak, around 1280 cm^{-1}, corresponds to an A symmetry mode, from a contribution of the symmetric phenyl breathing mode coupled to C-C interring stretching mode and symmetric C-H bending mode. Dark blue and pink peaks, around 1200 and 1255 cm^{-1} respectively, may be due to the same kind of modes but from either other conformations, or from interactions between other neighboring molecules theoretically not accounted.[3]

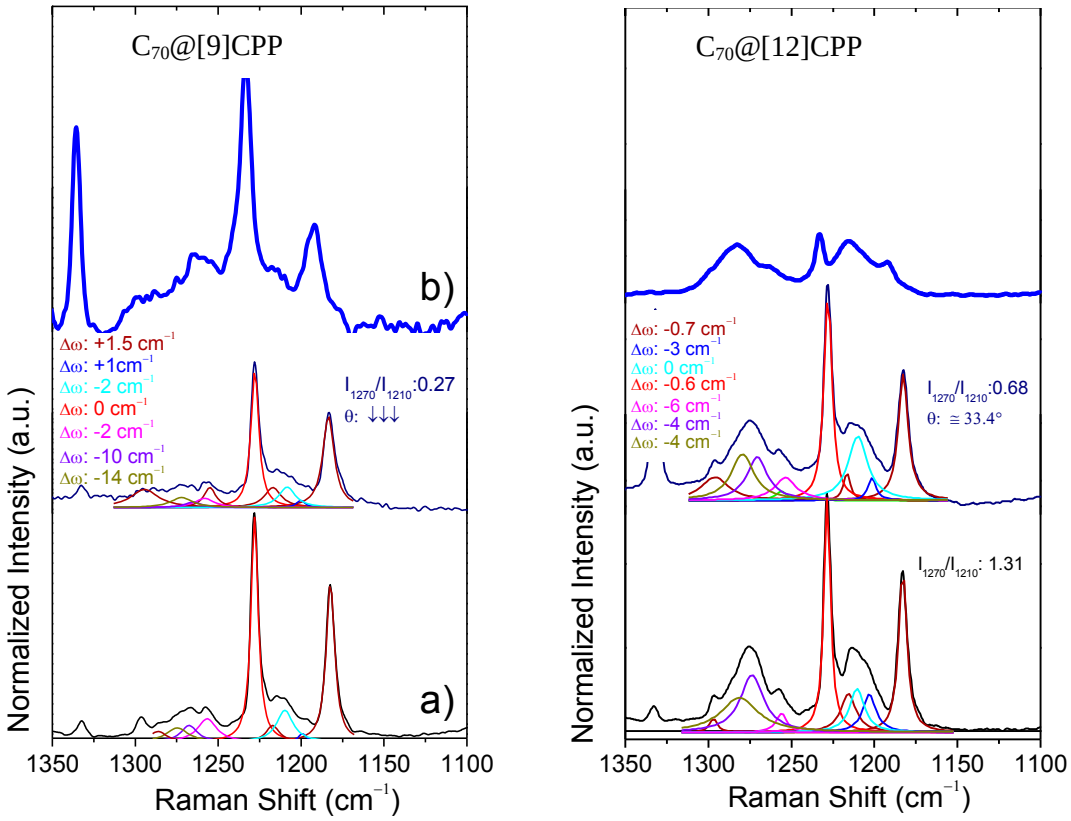

Fig. S6. 785 nm experimental Raman spectra in the 1100-1350 cm^{-1} range. Left: C_{70}@[9]CPP; right: C_{70}@[12]CPP. From bottom to top: (a) pristine complex (black), at room temperature and pressure; (b) thick blue line corresponds to the spectrum at high pressure (≈ 2.0 GPa) and thin dark blue line corresponds to the recovered spectrum after pressure cycle; both spectra taken at 25 °C. These spectra have been deconvoluted into their different contributions: red lines correspond to C_{70} contributions (being the most intense ones at 1228 cm^{-1} and 1183 cm^{-1}, from the phenyl breathing mode and the C-C stretching mode, predominantly along the C_{70} short diameter direction, respectively); The remaining contributions are originated by different CPP vibrational modes: Light blue, around 1210 cm^{-1}, A mode, C-H bending mode coupled to C-C interring stretching mode; Purple peak, around 1270 cm^{-1}, corresponds to the E mode, antisymmetric phenyl breathing mode coupled to antisymmetric C-C interring stretching mode and to antisymmetric C-H bending mode. Olive green peak, around 1280 cm^{-1}, corresponds to an A symmetry mode, from a contribution of the symmetric phenyl breathing mode coupled to C-C interring stretching mode and symmetric C-H bending mode. Dark blue and pink peaks, around 1200 and 1255 cm^{-1} respectively, may be due to the same kind of modes but from either other conformations, or from interactions between other neighboring molecules theoretically not accounted.[3]

Pressure Effect on the Fullerene Radial Breathing Mode

C_{70}@[10]CPP: as seen in the main text these G like modes linearly shift up to a critical pressure, 0.6 GPa, at which they stay constant with the increased pressure. As the pressure increases a second critical point at 1.6 GPa appears leading to a second linear region between their Raman shift and pressure. On the other hand, the tangential CC stretching mode of fullerene evolves with stress following two linear regimes before and after 1.6 GPa (see Fig. S7). These trends are explained by the stress induced orientational change of the C_{70} in the CPP cavity. It seems very likely that during the plateau the C_{70} is rotating towards a more standing conformation, and once that is reached, the stress induces the ovallization of the CPP around the C_{70}.

Accordingly, the C_{70} RBMs, which are directly affected by the C_{70} orientation in the ring cavity, follow stress evolution accordingly to the G modes of the CPP, presenting also a plateau between 0.6 and 1.6 GPa.

In the C_{70}@[11]CPP case, pressure induces again an overall upshift of the whole spectrum. The CPP G_1 band upshifts from 1597 cm^{-1} to 1603 cm^{-1} at 2 GPa, However, the whole spectra follow a different pressure trend than in the [10]CPP case. All the bands analysed depict two linear regimes separated by a critical pressure, 1.2 GPa. This change in the trend might be related with an extra flattening of the already flattened shape of [11]CPP in the standing complex, similar pressure responses have been observed in peapods.

Although is not so clear, the C_{70}@[9]CPP complex also have two different linear responses to stress which crosses at about 0.6 GPa (see Fig. S7). However, these seem to trend towards a similar behaviour to that presented by the [10]CPP. Unfortunately the fluorescence of this complex hinders any further observation.

Finally, as in the C_{70}@[11]CPP, the RBMs of the C_{70}@[12]CPP up-shifts with stress following two linear regimes (see Fig. S7), consequence of the probable stress induced deformation of the [12]CPP around the C_{70} and the crystalline reorganization.

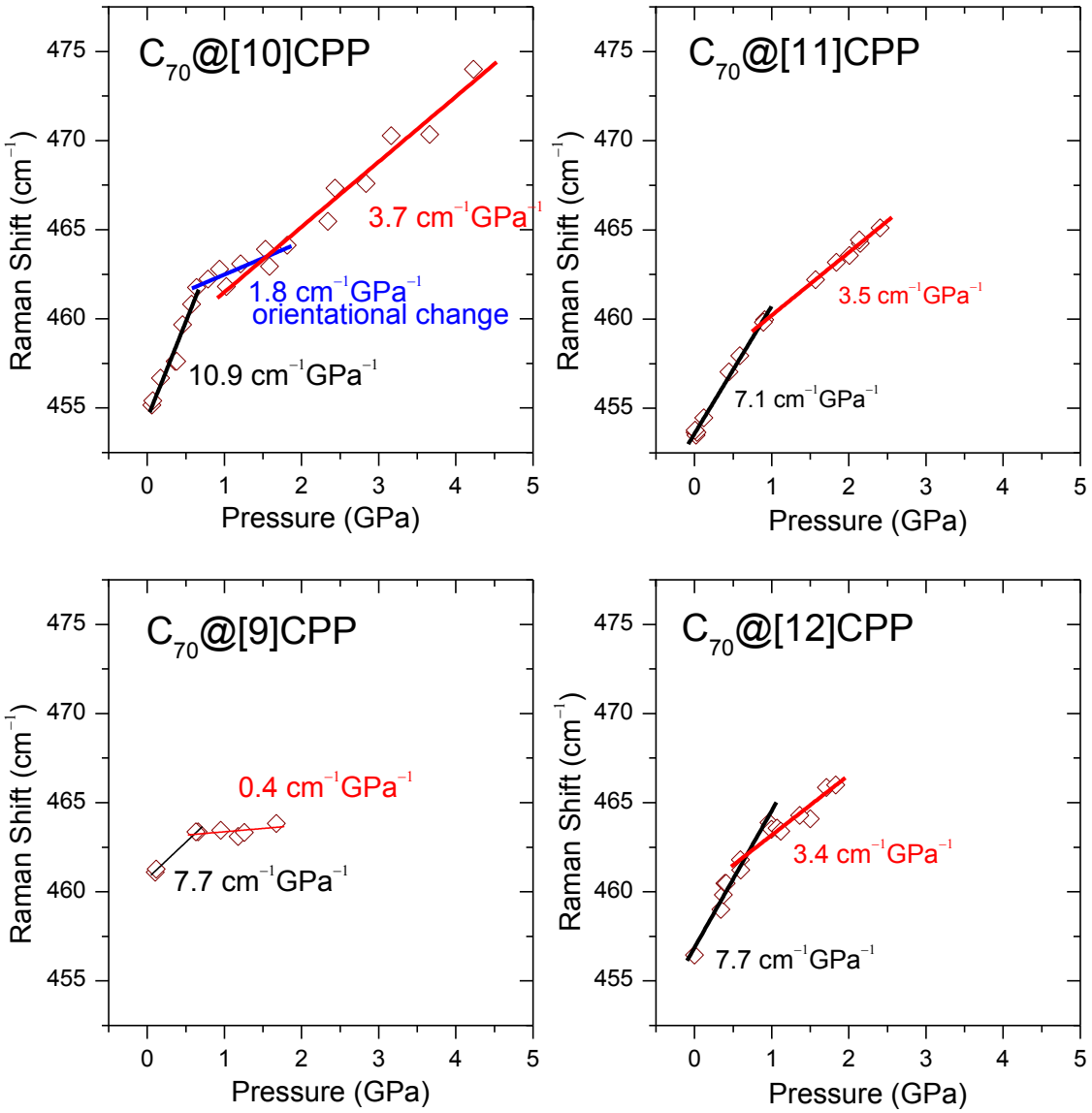

Fig. S7 Raman shift pressure evolution of the C_{70} Radial breathing mode: Raman bands of top: C_{70}@[10]CPP, left, and C_{70}@[11]CPP right; bottom: C_{70}@[9]CPP, left, and C_{70}@[12]CPP right. Pressure coefficients of each linear trend are expressed in $cm^{-1}GPa^{-1}$.

Variable Temperature Raman experiments

The C_{70} RBMs of the C_{70}@[10]CPP and C_{70}@[11]CPP behave differently with temperature, as seen in Fig. S8. While in the C_{70}@[11]CPP, they follow a reversible linear trend, in the C_{70}@[11]CPP case the trend is disturbed at low temperatures, between 300 and 340 K. This supports the results exposed in the main text, the change towards the lying orientation of the C_{70} in the complex.

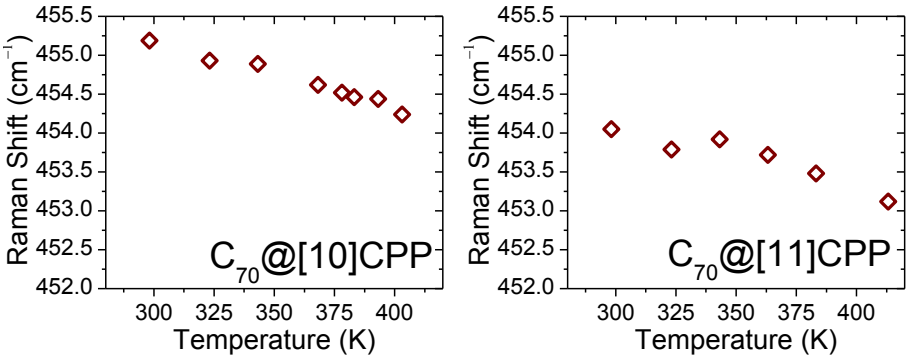

Fig. S8. Raman shift temperature evolution of the C_{70} Radial breathing mode of: C_{70}@[10]CPP, left, and C_{70}@[11]CPP, right.

References Supporting Information

1 G. Zannoni, G. Zerbi, Lattice dynamics and vibrational spectra of undoped and doped polyparaphenylene, *J. Chem. Phys*. **82**, 31 (1995).

2 G. Heimel, D. Somitsch, P. Knoll, J.L Brédas, E. Zojer, *J. Chem. Phys*. **122**, 114511 (2005).

3 M. Peña-Alvarez, P. M. Burrezo; M.Kertesz, T.Iwamoto, S.Yamago, J. Xia, R.Jasti, López J. T.Navarrete, M.Taravillo, V. G. Baonza and J. Casado, *Angew. Chem. Int. Ed*. **53**, 7033-7037 (2014).

Appendix 4

Supporting Information:

The Raman Fingerprint of Cyclic Conjugation: The case of the Stabilization of Cations and Dications in Cycloparaphenylenes

Experimental and theoretical details

Preparation of the oxidized species. [n]CPPs with *n* = 7, 8, 9, 10, 11 and 12 were synthesized by using a synthetic strategy through multinuclear arylplatinum complexes,[1] while [5]CPP and [6]CPP were synthesized through Suzuki–Miyaural cross-coupling/macrocyclization.[2,3] Triethyloxoniumhexa-chloroantimoniate ($Et_3O^+SbCl_6^-$) was used to generate the cations and dications in a free oxygen and water atmosphere at room temperature. All the reactions were done in solution of [n]CPP, 10^{-4} M, using dichloromethane as solvent, CH_2Cl_2, by stepwise addition of the salt $Et_3O^+SbCl_6^-$ (10^{-4} M). Chemical oxidations were monitored by in situ UV-Vis-NIR electronic absorption spectroscopy using a Cary 5000 UV-vis-NIR spectrometer.

Raman spectroscopy. Raman measurements at room temperature of the different [n]CPPs cations and dications were conducted under near-resonant or resonant conditions by selecting the excitation wavelengths that mostly fulfill one of the electronic absorption bands of the UV-Vis-NIR spectra. Available Raman excitation wavelengths are at 532, 633, 785 nm of an Invia Reflex Raman RENISHAW microscope. The 1064 nm excitation FT-Raman spectra were obtained with a Ram II spectrometer from Bruker. The experimental bands have been fitted with Lorentzian profiles with FWHM ranging between 12 and 15 cm^{-1}.

Summary of the excitation wavelengths used for the different Raman measurements carried out for neutral, cations and dications of the [n]CPPs.

n	**[n]CPP**	**[n]CPP$^{\bullet+}$**	**[n]CPP^{2+}**
5	785 nm	1064 nm	1064 nm
6	785 nm	1064 nm	1064 nm
7	785 nm	1064 nm	532 nm
8	785 nm	532 nm	1064 nm
9	785 nm	532 nm	1064 nm
10	785 nm	532 nm	1064 nm
11	785 nm	532 nm	1064 nm
12	785 nm	532 nm	1064 nm

Theoretical calculations. Quantum-chemical calculations were performed with Density Functional Theory (DFT) as implemented in the Gaussian 09 package.[4] All reported energy values and geometrical parameters refer to the geometry-optimized structures using the B3LYP/6-31G(d,p) method. All minima have been confirmed by vibrational calculations with all frequencies being real. The unrestricted UB3LYP/6-31(d,p) approach was used for neutrals, cations and dications. The ground state configuration for all neutral [n]CPPs and for dications with $n<9$ are closed shells. The geometries for the open-shell singlet dications were obtained from previous optimization of the triplet dications. For the open-shell singlet electronic ground state structures of the dications, we used the broken symmetry method with the keyword "guess = mix" at the (U)B3LYP level. Theoretical Raman spectra were represented with a FMHW of 3 cm^{-1}. Nucleus-Independent Chemical Shifts (NICS) calculations were done at the (U)B3LYP/6-3112+G(2df,p) level. All theoretical frequencies were scaled by a uniform factor of 0.96. All NICS values were computed at the (U)B3LYP/6-311+G(2df,p) level using the gauge including atomic orbitals (GIAO).

Chemical oxidation of [8]CPP

Figure S1 shows the UV-Vis-NIR spectra for [8]CPP, [8]CPP$^{\bullet+}$,[8]CPP^{2+}, and [8]CPP^{3+} (obtained as described in the previous section). Vertical excitations in Figure S2 were theoretically calculated with the TD-DFT theory using 40 states. In general, the agreement between experimental and theoretical data is very good.

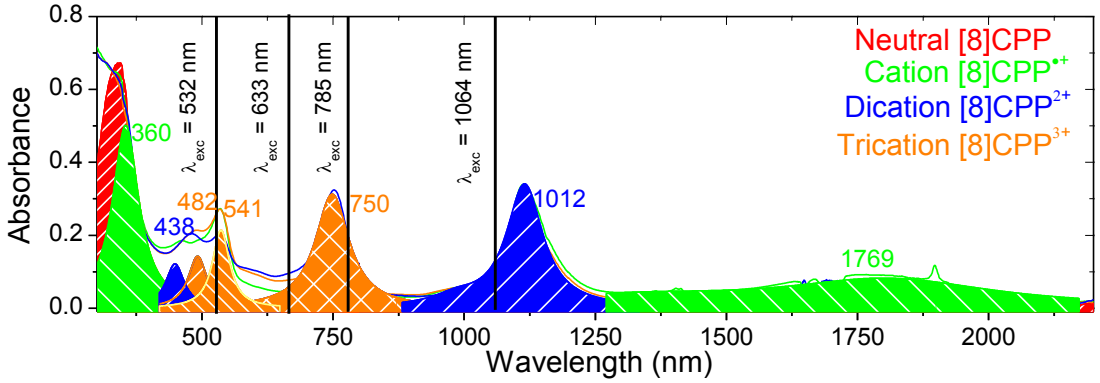

Figure S1. In situ UV-Vis-NIR electronic absorption spectra of [8]CPP obtained by chemical oxidation. Neutral [8]CPP is in red, radical cation [8]CPP$^{\bullet+}$ in green, dication [8]CPP^{2+} in blue and trication [8]CPP^{3+} in orange. The λ_{exc} values marked by vertical lines denote the laser excitation wavelengths used to obtain the resonant (or near-resonant) Raman spectrum for each species.

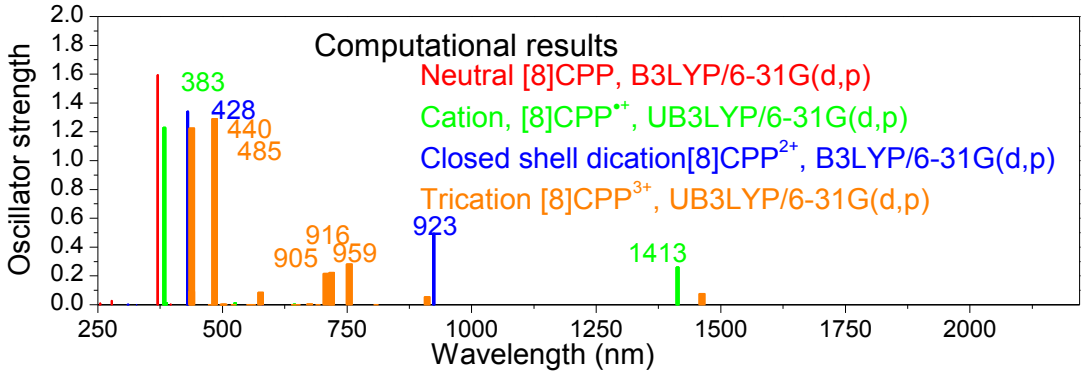

Figure S2. TD-(U)B3LYP/6-31G(d,p) vertical excitations for the different oxidation states of [8]CPP obtained at the optimized (U)B3LYP/6-31G(d,p) geometries using 40 excited states.

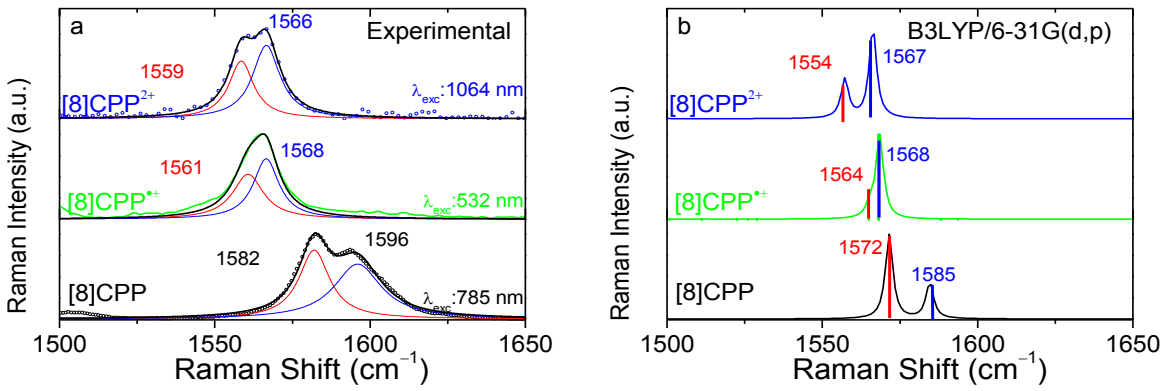

Figure S3. Raman spectra of neutral [8]CPP and its radical cation and dication in the 1500 - 1650 cm^{-1} spectral region. a) Experimental Raman spectra. b) (U)B3LYP/6-31G(d,p) computed scaled spectra at the optimized geometry of oxidized species. There are two major contributions in this region: the G_{A1g} low frequency feature is in red, and the G_{E2g}, high frequency feature is in blue.

UV-Vis-NIR characterization of oxidized [n]CPP

The cationic and dicationic species of [n]CPP from *n*=5 to 12 are characterized by UV-Vis-NIR absorption spectroscopy. In Figure S4 we show a comparison of these experimental spectra with the theoretical excitation energies predicted by TD-(U)B3LYP/6-31G(d,p) for all these species. Radical cations show two main bands, one broad band in the NIR region and another in the UV region. The NIR band is due to the mixture of the HOMO → SOMO and the HOMO-1 → SOMO transitions. These absorptions shift to longer wavelengths as *n* increases. This behavior is well predicted by theory. The smaller [n]CPP dications have two bands that appear between those of the radical cations. For dications larger than [9]CPP^{2+} the two bands of the dications start to progressively resemble those of the radical cations although the dicationic bands stay between those of the cationic species. Theoretical spectra also reproduce this behavior. For the dications, the band at longer wavelength in the NIR originates from the HOMO –LUMO transition. The second band is in the UV-Vis and it corresponds to the HOMO-1→LUMO+1 transition.

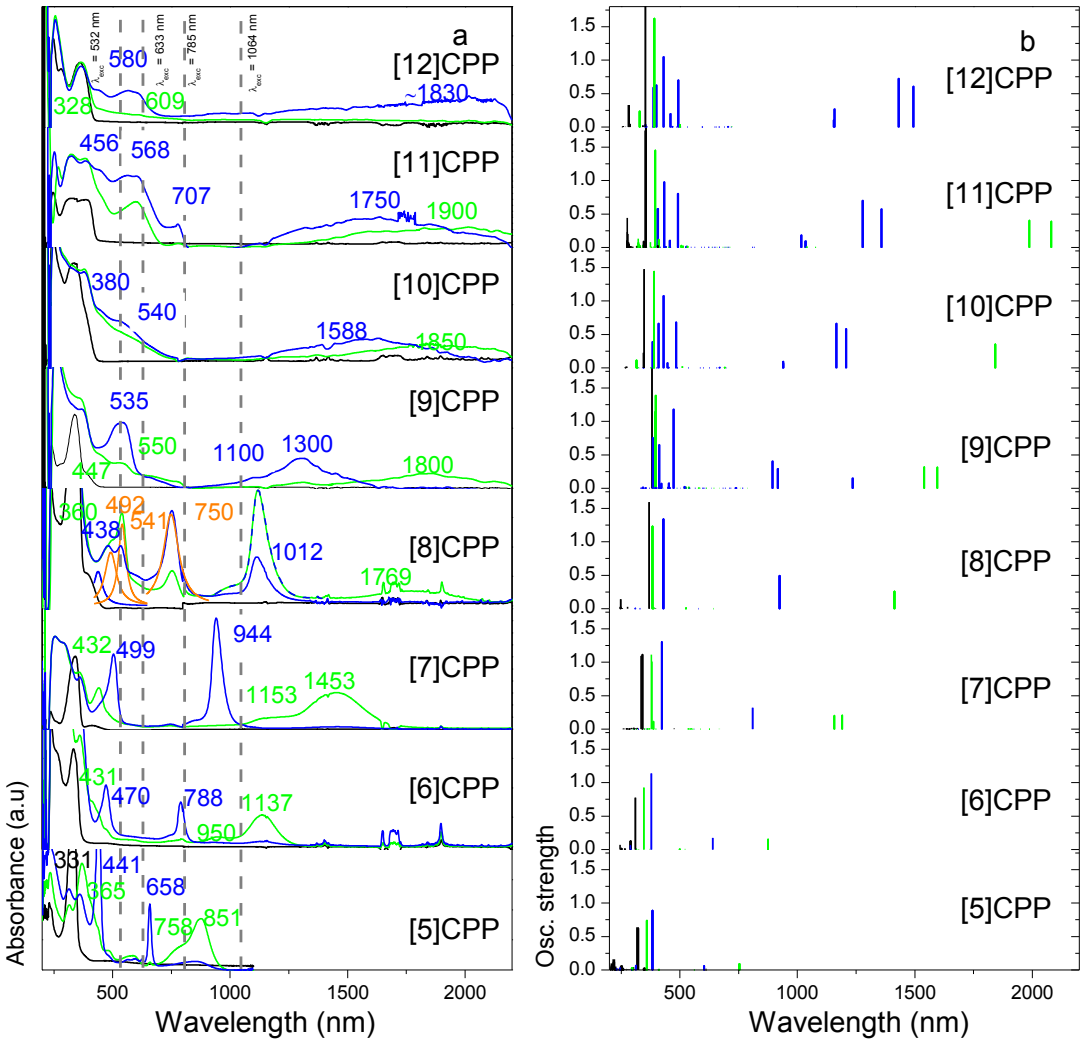

Figure S4. Electronic absorption spectra for neutral, cationic and dicationic species of [n]CPPs (from *n*=5 to *n*=12). (a) Experimental, and (b) computed vertical excitations at the TD-(U)B3LYP/6-31G(d,p) level. Red refers to the neutral, green to the radical cationic and blue to the dicationic species. The orange spectrum of [8]CPP corresponds to its radical trication, [8]CPP^{3+}.

Raman spectra of [n]CPP^{2+} dications

This section is devoted to the analysis of the Raman spectra of the dications of [n]CPPs. In Figure S5 we present the eigenvectors of the G modes for the representative cationic and dicationic species of [8]CPP. We compare the experimental and computed Raman spectra in the 1100-1700 cm^{-1} spectral region for the dications in Figure S6. The Raman shifts of the respective G bands are summarized in Figure S7.

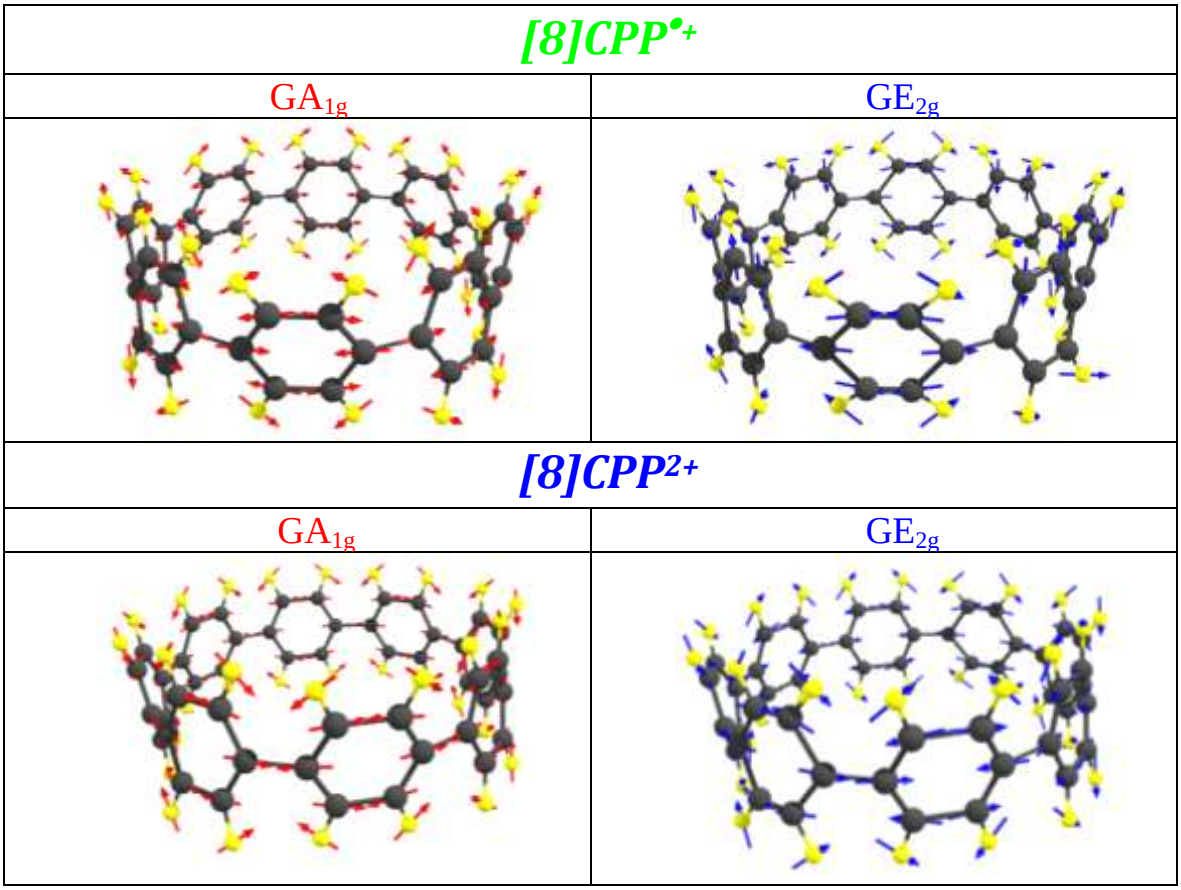

Figure S5. Vibrational eigenvectors from the theoretical (U)B3LYP/6-31G(d,p) Raman spectra of the G_{A1g} (the strongest) and G_{E2g} (weaker) bands of [8]CPP$^{\bullet+}$ (top) and [8]CPP^{2+} (bottom).

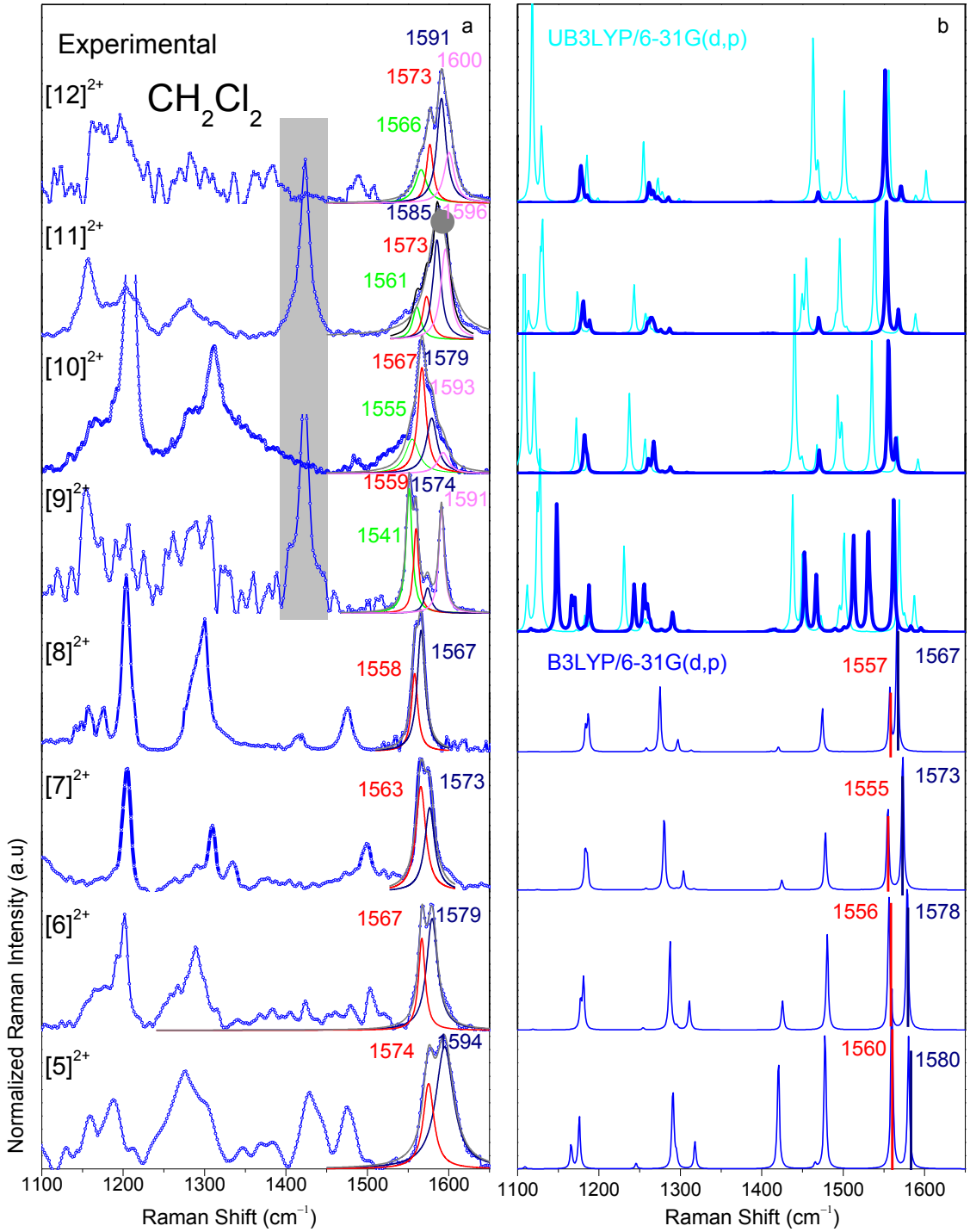

Figure S6. Raman spectra of the [n]CPP^{2+} dications in the 1400-1650 cm^{-1} region, normalized to the GA_{1g} band. a) Experimental spectra. Shadowed grey region corresponds to the most intense Raman band of the CH_2Cl_2 solvent which is detected in near-resonant spectra or when full resonance is not fulfilled. The GA_{1g} band is in red, the GE_{2g} one is in dark blue. Green and pink bands correspond to those which appear in the open shell singlets, and these are referred to as G_{OS1} and G_{OS2}, respectively. b) Computed spectra. Dark blue is obtained with B3LYP/6-31G(d,p) and the light blue (for n>9) refers to UB3LYP/6-31G(d,p).

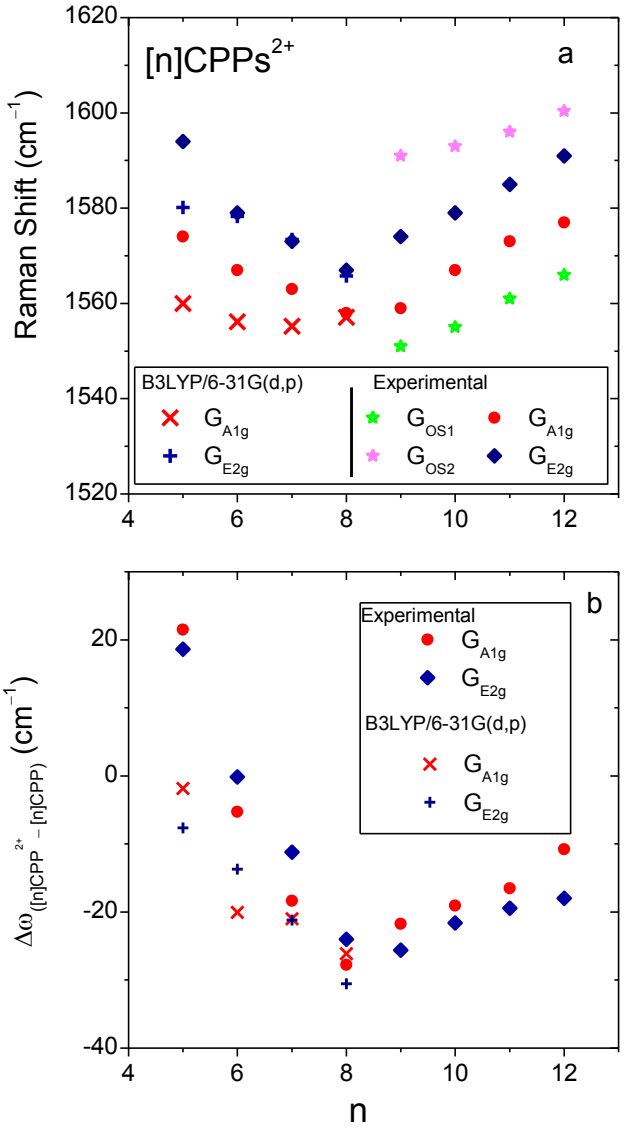

Figure S7. a) V-shape behavior of the Raman shift as a function of *n* of the G bands in the 1520 to 1600 cm^{-1} region for the [n]CPP^{2+} dications. b) Raman shifts of the G_{A1g} and G_{E2g} bands relative to their neutral analogues as a function of *n*. G_{OS1} and G_{OS2} designate side bands which are observed experimentally. These side bands only appear in the open-shell singlet computations and originate from the symmetry breaking discussed in the main text.

Molecular structure of [n]LPP^{2+} dications

Linear oligoparaphenylenes in their oxidized states, cations and dications are known to develop a well-defined quinonoid structure in the π conjugated path, more pronounced for the dications than the mono-cations. In this section we conduct an analysis of the geometries of the dicationic [n]LPPs with *n* = 3 to 6.

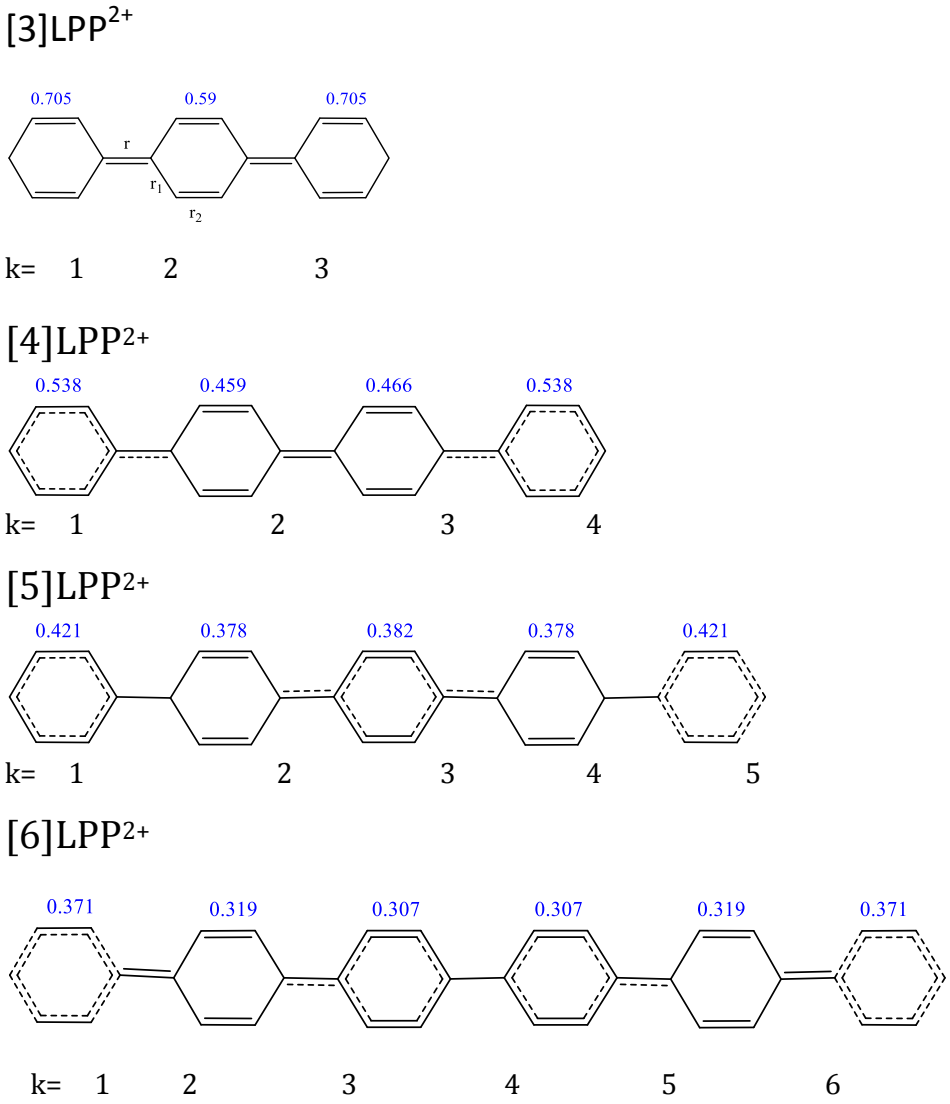

Figure S8. *Valence bond representation of the (U)*B3LYP6-31G(d,p) optimized structure of [3]LPP^{2+} (C_{2h}), [4]LPP^{2+} (C_2), [5]LPP^{2+} (C_{2h}), and [6]LPP^{2+} (D_2), together with the charge distribution on the rings.

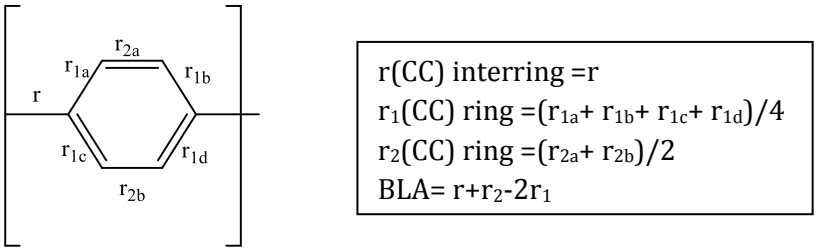

Figure S9. *Scheme of a phenyl unit with the definition of the C-C distances and BLA.*

Table S1. Computed parameters of [3]LPP^{2+} (C_{2h}), [4]LPP^{2+} (C_2), [5]LPP$^{\bullet+}$ (C_{2h}), [5]LPP^{2+} (C_{2h}), [6]LPP$^{\bullet+}$ (D_2) and [6]LPP^{2+} (D_2) using *(U)*B3LYP6-31G(d,p). *k* corresponds to the phenyl unit number.

	k	Charge (|e|)	r (Å)	r_1 (Å)	r_2 (Å)	BLA (Å)	θ torsion (°)
[3]LPP^{2+}	1	0.705		1.428	1.375	--	9.4
	2	0.590	1.423	1.448	1.361	-0.113	-9.4
	3	0.705	1.423	1.428	1.375	-0.058	--
[4]LPP^{2+}	1	0.538	--	1.420	1.380	--	15.6
	2	0.549	1.437	1.438	1.366	-0.073	-9.3
	3	0.466	1.426	1.438	1.366	-0.085	16.5
	4	0.538	1.437	1.420	1.380	-0.022	--
[5]LPP$^{\bullet+}$	1	0.192	--	1.403	1.385	--	28.0
	2	0.199	1.468	1.418	1.380	0.013	-21.9
	3	0.217	1.457	1.420	1.378	-0.005	21.9
	4	0.199	1.457	1.417	1.380	0.002	-28.0
	5	0.192	1.468	1.406	1.389	0.045	--
[5]LPP^{2+}	1	0.421	--	1.415	1.383	--	-19.3
	2	0.378	1.447	1.431	1.371	-0.045	11.6
	3	0.382	1.435	1.433	1.378	-0.053	-11.6
	4	0.378	1.435	1.431	1.371	-0.056	19.3
	5	0.421	1.447	1.415	1.383	0.000	
[6]LPP$^{\bullet+}$	1	0.155	--	1.401	1.394	--	37.0
	2	0.162	1.484	1.405	1.391	0.065	-35.9
	3	0.183	1.482	1.405	1.391	0.063	35.9
	4	0.183	1.482	1.405	1.391	0.062	-35.9
	5	0.162	1.482	1.405	1.391	0.063	37.0
	6	0.155	1.484	1.401	1.394	0.077	
[6]LPP^{2+}	1	0.371	--	1.404	1.383	--	19.8
	2	0.319	1.450	1.426	1.374	-0.027	-21.6
	3	0.307	1.456	1.418	1.381	0.001	27.3
	4	0.307	1.466	1.418	1.381	0.011	-21.6
	5	0.319	1.456	1.426	1.374	-0.021	19.8
	6	0.371	1.450	1.404	1.383	0.026	

Raman spectra of [5]- [6]LPP positively charged species

As seen in Figure S10 theoretical simulations for [5]LPP^{2+} and [6]LPP^{2+} predict them as open-shell singlet electronic ground states, as reported in the literature. [5,6] Figures S10a and S11a show the experimental NIR spectra of the neutral, cationic and dicationic forms of [5]LPP and [6]LPP. The IR bands redshift with increasing chain length. The Raman bands in the G band region are shown in Figure S10b and S11b. These Raman bands show a splitting that is associated with the open-shell character of the electronic ground state of both oxidized species.[7]

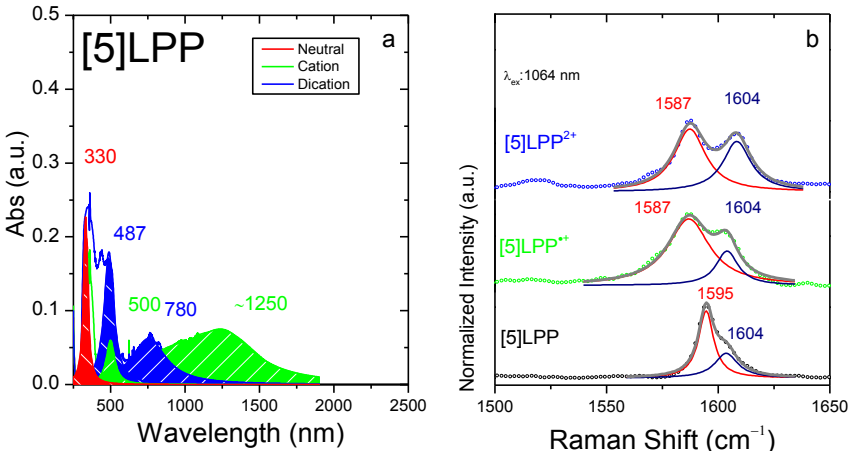

Figure S10. *a)* [5]LPP in situ UV-Vis-NIR electronic absorption spectra during oxidation. b) [5]LPP in situ Raman spectra during oxidation.

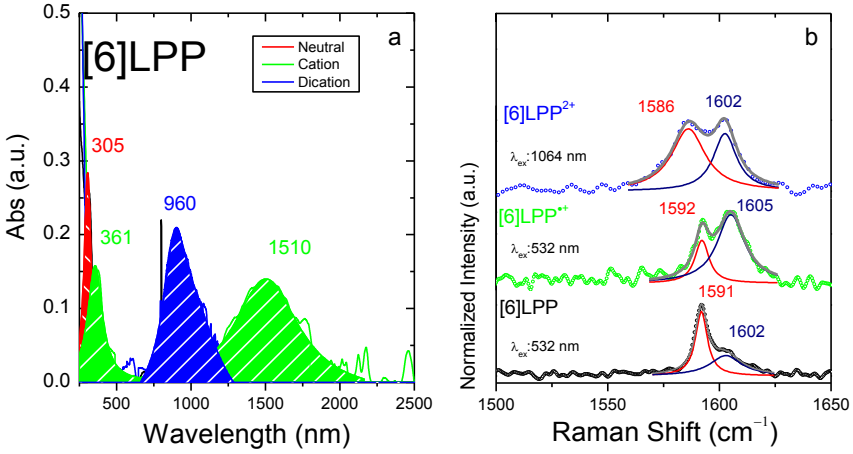

Figure S11. *a)* [6]LPP in situ UV-Vis-NIR electronic absorption spectra during oxidation. b) [6]LPP in situ Raman spectra during oxidation.

Strain energy of [n]CPP$^{\bullet+}$ and [n]CPP^{2+}: homodesmotic reactions

We have calculated the strain energy of the neutral, radical cations and dications of [n]CPPs by means of the homodesmotic reactions shown in Figures S12.[8,9] The data are summarized in Table S2. This method is the same as used earlier for neutral [n]CPPs by Bachrach et al.[10] and by Segawa et al.[11]

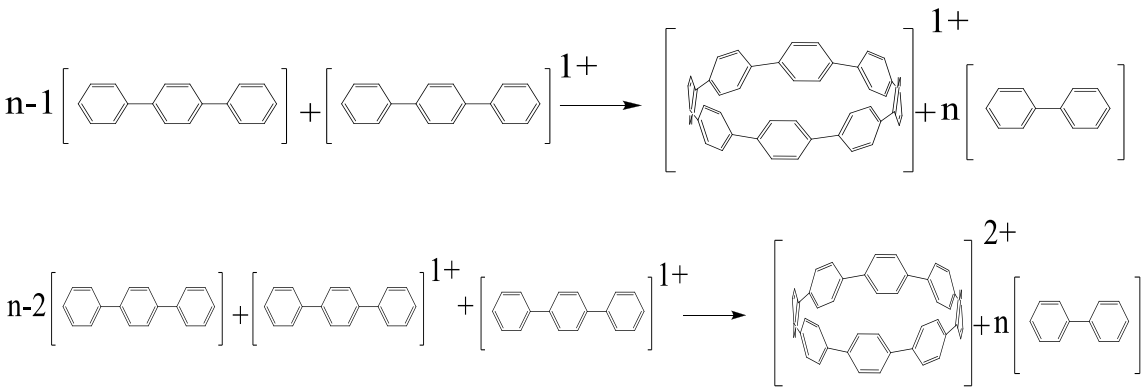

Figure S12. Homodesmotic reaction for the calculation of strain energies of [*n*]CPP$^{\bullet+}$ and of [*n*]CPP^{2+} dications both at the (U)B3LYP/6-31G(d,p) level.

Table S2. Point groups of symmetry and (U)B3LYP/6-31G(d,p) strain energies of neutral, cationic and dicationic species of [n]CPPs.

n	**[n]CPP**		**[n]CPP$^{\bullet+}$**		**[n]CPP^{2+}**	
	Point group[a]	Strain Energy (kcal/mol)	*Point group*[a]	Strain Energy (kcal/mol)	*Point group*[a]	Strain Energy (kcal/mol)
20	C_5~D_{10d}	29.9	C_1~D_{10d}	1.3	C_2	0.3
18	C_2~D_{9d}	33.2	C_1~D_{9d}	5.2	C_i	9.5
16	C_{4v}~D_{8d}	37.4	C_{4v}~D_{8d}	10.1	C_2	17.8
15	C_1~C_2	40.9	C_2	18.8	C_1~C_2	23.2
14	D_{7d}	44.8	C_1~C_2	17.6	C_1~C_2	29.1
13	C_1	47.2	C_1~C_2	20.5	C_1~C_2	34.6
12	D_{6d}	49.9	S_4~D_{6d}	23.9	C_{2v}	40.9
11	C_1	55.7	C_1	29.6	C_1	49.1
10	D_{5d}	57.9	C_i~C_{2h}	34.4	C_{2h}	57.5
9	C_1	70.5	C_1	43.1	C_1	68.5
8	D_{4d}	74.6	D_{4d}	49.3	C_{2v}~D_{4d}	79.8
7	C_1	86.6	C_1~D_{7h}	59.9	C_1~D_{7h}	94.2
6	D_{3d}	98.9	D_{3d}~D_{6h}	72.3	D_{3d}~D_{6h}	111.9
5	C_s	119.4	C_s~D_{5h}	89.9	C_s~D_{5h}	135.5
4	S_4~D_{2d}	146.9	S_4~D_{4h}	115.8	S_4~D_{4h}	169.3

[a] In the cases where two point groups are indicated, the actual point group corresponds to the first symbol, while the second point group symbol refers to an idealized structure.

Chemical structures and charge distributions on [n]CPP^{2+}

The singlet closed-shell to open-shell transition has a significant impact on the molecular geometries. Hence while the molecular structures for the smaller members of the series are completely uniform and therefore belong to the highest point group of symmetry, [9]CPP^{2+} and larger [n]CPP^{2+} dications have reduced symmetry. This symmetry reduction displays domains with different aromatic-quinonoid characters along the CC bond length alternation paths. Concomitantly with the aromatic-quinonoid differentiation, the positive charge distribution is also not uniform with larger amounts of local charges appearing for the rings with quinonoid character. For the [n]CPP^{2+} dications that have an open-shell singlet ground state configuration, there is a separation of the spin distribution in the macrocycle which is in agreement with diradical character of the dications. Combined with the change in the BLAs these deformed macrocycles develop structures that can be effectively described as two polarons with diradicaloid character or as diradical polaron pairs, DRPP.12 For $n < 9$, the systems converge toward closed shell ground states with zero spin densities. The main geometrical parameters of their optimized geometries are given in Table S3 for [5]- to [12]CPP^{2+}. In Table S4 we show the orbital topologies of the HOMO orbitals, the positive charge distribution and the electron density distribution for [5]- to [12]CPP^{2+}.

Table S3. Per ring charge distribution, spin density distribution main C-C bond lengths, resulting BLA values (see above) and torsional angles at the (U)B3LYP6-31G(d,p) level :for [5]CPP^{2+} with C_s~D_{5h} , [6]CPP^{2+} with D_{3d}~D_{6h}, [7]CPP^{2+} with C_1~D_{7h}, [8]CPP^{2+} with D_{4d}, [9]CPP^{2+} with C_1, [10]CPP^{2+} with C_{2h}, [11]CPP^{2+} with C_1 and [12]CPP^{2+} with C_{2v}. *k* corresponds to a consecutive numbering of the phenyl. See Figure 9 for C-C distances assignments.

	k	Charge per phenyl unit (|e|)	Spin density	r (Å)	r_1 (Å)	r_2 (Å)	BLA (Å)	θ torsion (°)
[5]CPP^{2+}	1-5	0.4	--	1.440	1.434	1.371	-0.058	0.0
[6]CPP^{2+}	1-6	0.33	--	1.445	1.430	1.374	0.040	0.0
[7]CPP^{2+}	1	0.288	--	1.451	1.416	1.384	-0.026	8.8
	2	0.287	--	1.451	1.417	1.383	-0.025	-9.0
	3	0.283	--	1.451	1.418	1.382	-0.024	8.7
	4	0.284	--	1.451	1.417	1.383	-0.025	-7.0
	5	0.284	--	1.451	1.416	1.384	-0.026	2.8
	6	0.283	--	1.451	1.416	1.384	-0.027	2.8
	7	0.287	--	1.451	1.416	1.384	-0.027	-7.0
[8]CPP^{2+}	1-8	0.25	--	1.456	1.423	1.378	-0.012	14.2
[9]CPP^{2+}	1	0.212	0.000	1.463	1.419	1.381	0.007	-19.6
	2	0.226	0.003	1.461	1.421	1.379	-0.002	9.1
	3	0.238	0.004	1.458	1.422	1.378	-0.009	9.3
	4	0.226	0.004	1.458	1.421	1.379	-0.004	-19.1
	5	0.212	0.001	1.461	1.419	1.380	0.004	19.4
	6	0.222	-0.001	1.463	1.419	1.381	0.006	-17.9
	7	0.226	-0.004	1.460	1.421	1.378	-0.004	17.6
	8	0.226	-0.004	1.458	1.421	1.380	-0.003	-17.7
	9	0.218	-0.003	1.460	1.419	1.380	0.002	19.4

	k	Charge per phenyl unit (|e|)	Spin density	r (Å)	r_1 (Å)	r_2 (Å)	BLA (Å)	θ torsion (°)
[10]CPP^{2+}	1	0.218	0.200	1.460	1.420	1.379	-0.002	-18.7
	2	0.206	0.160	1.460	1.419	1.380	0.003	21.7
	3	0.185	0.060	1.465	1.416	1.383	0.016	-23.2
	4	0.185	-0.060	1.468	1.416	1.383	0.019	21.3
	5	0.206	-0.160	1.465	1.419	1.380	0.008	-19.0
	6	0.218	-0.200	1.460	1.420	1.379	-0.002	18.7
	7	0.206	-0.160	1.465	1.419	1.380	0.008	-19.0
	8	0.185	-0.060	1.468	1.416	1.383	0.019	21.3
	9	0.185	0.060	1.465	1.416	1.383	0.016	-23.2
	10	0.206	0.160	1.460	1.419	1.380	0.003	21.7
[11]CPP^{2+}	1	0.158	-0.030	1.472	1.413	1.385	0.030	24.5
	2	0.177	-0.135	1.470	1.416	1.383	0.020	-22.0
	3	0.201	-0.201	1.463	1.419	1.380	0.006	19.3
	4	0.201	-0.201	1.460	1.419	1.380	0.003	-21.5
	5	0.177	-0.134	1.463	1.416	1.383	0.014	24.9
	6	0.157	-0.030	1.470	1.413	1.385	0.027	-25.1
	7	0.166	0.081	1.472	1.414	1.384	0.027	24.4
	8	0.194	0.178	1.466	1.418	1.381	0.010	-12.6
	9	0.208	0.217	1.461	1.420	1.379	-0.001	-12.3
	10	0.194	0.178	1.461	1.418	1.376	0.001	25.1
	11	0.166	0.080	1.466	1.414	1.384	0.022	-25.0
[12]CPP^{2+}	1	0.156	0.099	1.472	1.414	1.384	0.028	-26.6
	2	0.138	0.000	1.472	1.412	1.385	0.034	26.6
	3	0.156	-0.099	1.462	1.414	1.384	0.018	-24.1
	4	0.179	-0.175	1.462	1.417	1.382	0.010	21.2
	5	0.190	-0.200	1.462	1.418	1.380	0.006	-21.2
	6	0.179	-0.175	1.467	1.417	1.382	0.015	24.1
	7	0.156	-0.099	1.472	1.414	1.384	0.028	-26.6
	8	0.138	0.000	1.472	1.412	1.385	0.034	26.6
	9	0.156	0.099	1.462	1.414	1.384	0.018	-24.1
	10	0.179	0.175	1.462	1.417	1.382	0.010	21.2
	11	0.190	0.200	1.462	1.418	1.380	0.006	-21.2
	12	0.179	0.175	1.467	1.417	1.382	0.015	24.1

Table S4. For closed – shell singlet dications B3LYP6-31G(d,p) HOMO and HOMO-1 topologies (these are degenerated), and per ring positive charge distribution. For $n \geq 9$; open-shell singlet dications UB3LYP6-31G(d,p) HOMO topology, spin density distributions (red and blue indicate negative and positive values, respectively) and per ring positive charge distribution

Closed-shell singlet dications	HOMO pattern		Charge per phenyl unit (|e|)
[5]CPP^{2+} C_s~D_{5h}			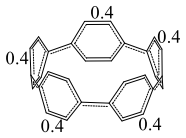
[6]CPP^{2+} D_{3d}~D_{6h}			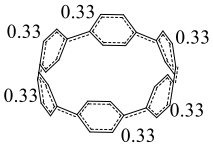
[7]CPP^{2+} C_1~D_{7h}	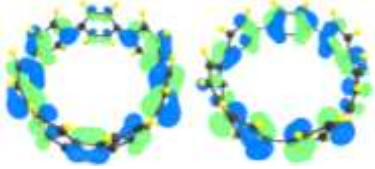		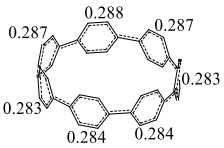
[8]CPP^{2+} C_{2v}~D_{4d}	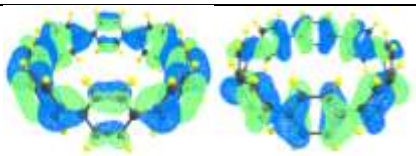		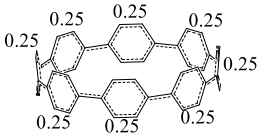
Open-shell singlet dications	**HOMO pattern**	**Per ring spin density distributions**	**Charge per phenyl unit (|e|)**
[9]CPP^{2+} C_1		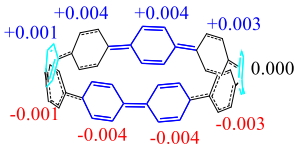	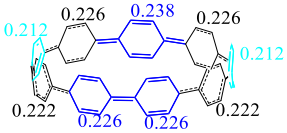
[10]CPP^{2+} C_{2h}~D_{5h}	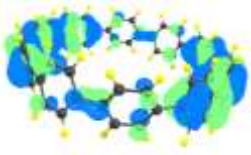	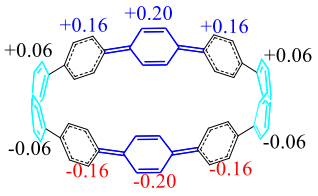	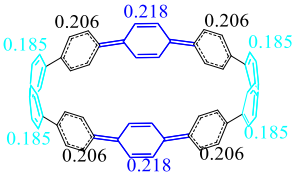
[11]CPP^{2+} C_1		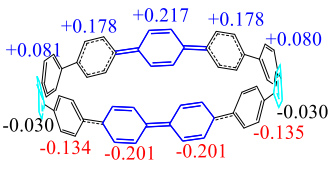	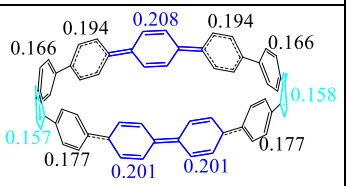
[12]CPP^{2+} C_{2v}		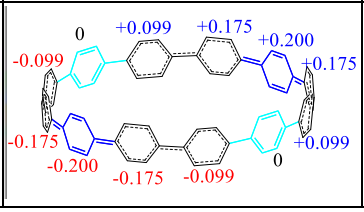	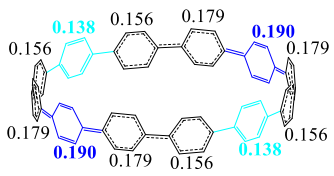

Diameter change from the neutral to the dicationic state

One of the consequences of the symmetry reduction (breaking) for n>8 in the [n]CPP^{2+} is the change from a nearly circular shape in the closed-shell molecules (n≤8) to a ellipsoid shape for n>8. For the latter, we differentiate two main axes, major and minor axis, such as drawn in Figure S13c. In this section we are going to study this distortion. In Figure S13a we display the [n]CPP^{2+} diameters of all species. Similar estimates were obtained by Segawa et al. for neutral [n]CPPs [13].

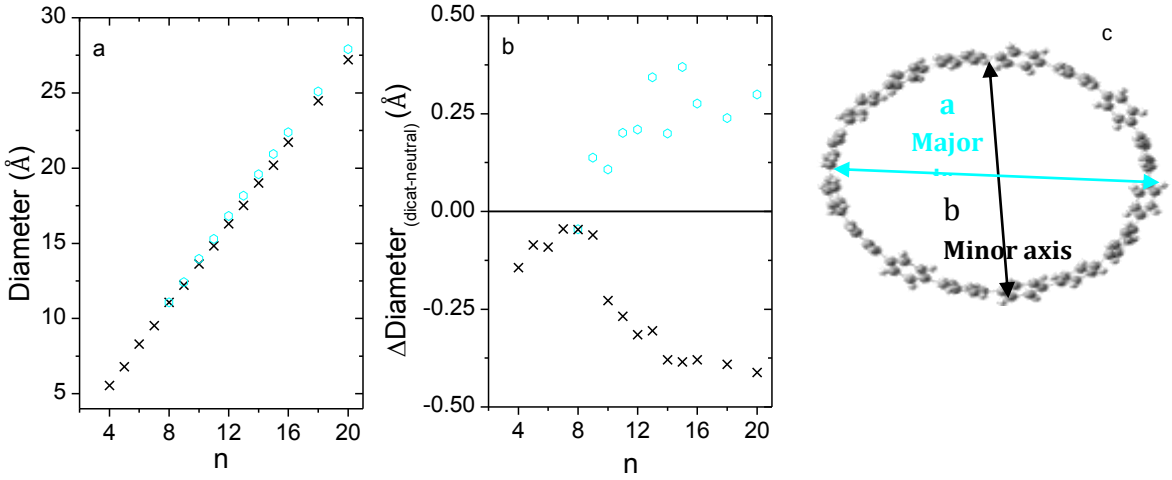

Figure S13. a) Major and minor axis lengths of the [n]CPP^{2+} dications obtained from (U)B3LYP/6-31G(d,p) calculations. Light blue circles (∘) correspond to the major axis (a in Figure S13c) and black crosses (x) correspond to the minor axis (b in Figure S13c). b) Differences in major and minor axis lengths of the dicationic species compared to the corresponding diameters of the neutral from B3LYP/6-31G(d,p) calculations. Light blue circles (∘) correspond to, ΔD_a=D(neutral)-a, and black crosses (x) correspond to ΔD_b=D(neutral)-b. Since neutrals have a circular shape they are defined with one diameter, D(neutral). c) Scheme indicating the ellipsoid structure in [12]CPP^{2+} where the b minor axis has been marked with a black arrow, and the a major axis with a light blue arrow.

Raman spectra of [n]CPP$^{\bullet+}$ radical cations

Figure S14 shows the Raman data of cationic [n]CPPs in the 1100-1700 cm^{-1} spectral region.

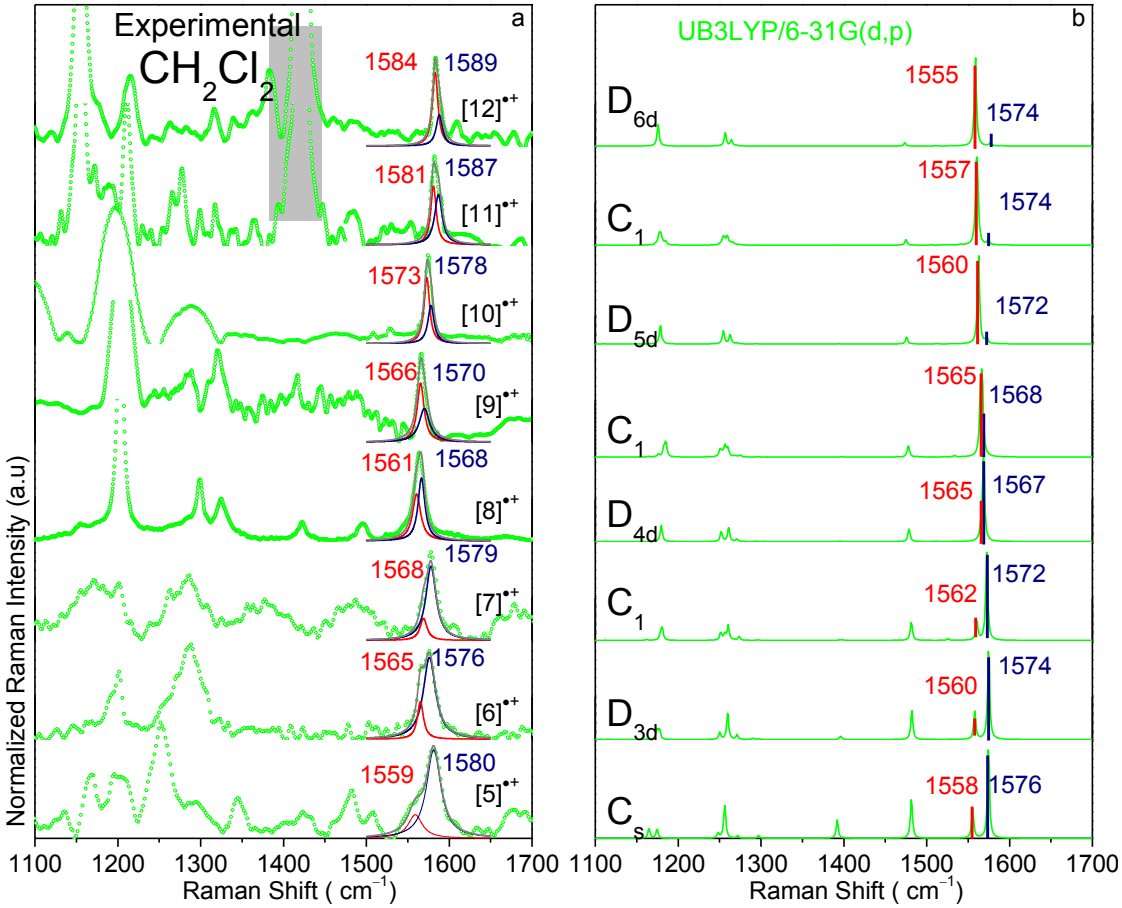

Figure S14. Raman spectra of the cationic species in the 1400-1650 cm^{-1} region, normalized to the GA_{1g} band. a) Experimental and b) computed spectra. Shadowed grey region corresponds to the most intense Raman band of the CH_2Cl_2 solvent which is detected in the near-resonant spectra or when full resonance is not fulfilled.

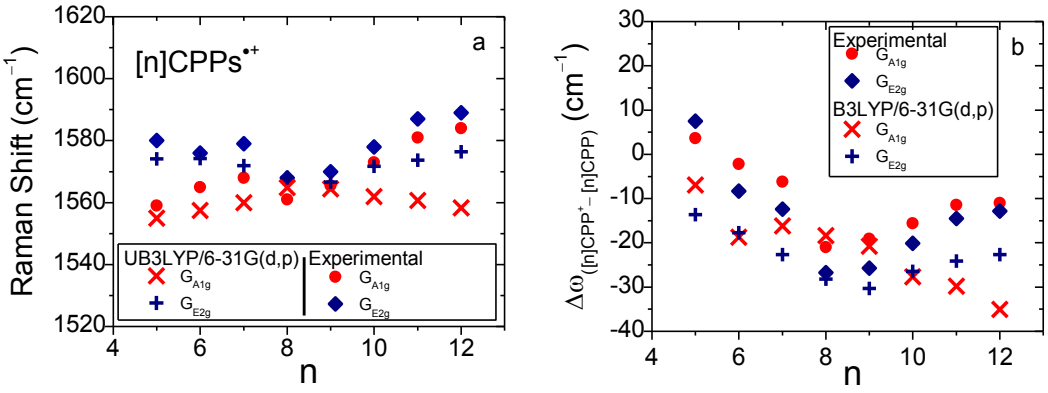

Figure S15. a) Raman shifts for each of the G-like bands as a function of *n*. b) Raman shift changes of the G_{A1g} and G_{E2g} bands relative to the values in the neutral analogues as a function of *n*.

Table S5. Per ring charge distribution, spin density distribution, main C-C bond lengths, resulting BLA values (see above) and torsional angles at the UB3LYP6-31G(d,p) level for: [5]CPP$^{\bullet+}$ (C_s~D_{5h}), [6]CPP$^{\bullet+}$ (D_{3d}~D_{6h}), [7]CPP$^{\bullet+}$ (C_1~D_{7h}), [8]CPP$^{\bullet+}$ (D_{4d}),, [9]CPP$^{\bullet+}$ (C_1), [10]CPP$^{\bullet+}$ (C_{2h}~D_{5h}), [11]CPP$^{\bullet+}$ $(C)_1$ and for [12]CPP$^{\bullet+}$ (S_4~D_{6d}). k corresponds to the consecutive numbering of phenyl units, see Figure 9 for C-C distances assignments.

	k	Charge per phenyl unit (|e|)	Spin density	r (Å)	r_1 (Å)	r_2 (Å)	BLA (Å)	θ torsion (°)
[5]CPP$^{\bullet+}$	1	0.200	0.201	1.467	1.422	1.381	0.004	3.6
	2	0.200	0.200	1.467	1.422	1.381	0.004	5.8
	3	0.200	0.199	1.467	1.422	1.381	0.004	5.7
	4	0.200	0.200	1.467	1.422	1.381	0.004	3.6
	5	0.200	0.201	1.467	1.422	1.381	0.004	0.0
[6]CPP$^{\bullet+}$	1-6	0.167	0.167	1.468	1.418	1.382	0.014	16.0
[7]CPP$^{\bullet+}$	1	0.142	0.138	1.471	1.416	1.384	0.022	-19.5
	2	0.147	0.141	1.469	1.417	1.383	0.018	8.8
	3	0.150	0.146	1.469	1.418	1.382	0.016	8.8
	4	0.146	0.148	1.469	1.417	1.383	0.018	-19.5
	5	0.143	0.146	1.469	1.416	1.384	0.021	21.1
	6	0.136	0.141	1.471	1.416	1.384	0.024	-20.0
	7	0.136	0.138	1.471	1.416	1.384	0.024	-7.0
[8]CPP$^{\bullet+}$	1-8	0.125	0.125	1.471	1.414	1.384	0.027	22.7
[9]CPP$^{\bullet+}$	1	0.111	0.110	1.472	1.413	1.385	0.031	26.4
	2	0.108	0.105	1.473	1.413	1.385	0.033	-26.6
	3	0.106	0.104	1.474	1.413	1.386	0.034	24.7
	4	0.106	0.104	1.474	1.413	1.386	0.034	-25.9
	5	0.108	0.106	1.471	1.413	1.385	0.031	24.4
	6	0.111	0.111	1.473	1.413	1.385	0.032	-25.5
	7	0.116	0.118	1.472	1.414	1.384	0.028	26.3
	8	0.118	0.125	1.473	1.415	1.384	0.027	-14.1
	9	0.116	0.119	1.473	1.419	1.384	0.019	-13.6
[10]CPP$^{\bullet+}$	1	0.099	0.099	1.474	1.412	1.386	0.035	-26.3
	2	0.099	0.099	1.474	1.412	1.386	0.035	26.3
	3	0.100	0.100	1.474	1.412	1.386	0.035	-26.3
	4	0.100	0.100	1.474	1.412	1.386	0.035	26.1
	5	0.100	0.100	1.474	1.412	1.386	0.035	-26.1
	6	0.099	0.099	1.474	1.412	1.386	0.035	26.3
	7	0.099	0.099	1.474	1.412	1.386	0.035	-26.3
	8	0.100	0.100	1.474	1.412	1.386	0.035	26.3
	9	0.100	0.100	1.474	1.412	1.386	0.035	26.1
	10	0.100	0.100	1.474	1.412	1.386	0.035	26.1
[11]CPP$^{\bullet+}$	1	0.088	0.087	1.475	1.411	1.386	0.039	27.5
	2	0.089	0.088	1.475	1.411	1.386	0.039	-26.1
	3	0.092	0.090	1.475	1.411	1.386	0.039	29.9
	4	0.096	0.097	1.474	1.412	1.386	0.035	-17.7
	5	0.097	0.103	1.475	1.413	1.385	0.035	-17.8
	6	0.096	0.097	1.475	1.412	1.386	0.036	30.4
	7	0.092	0.091	1.474	1.411	1.386	0.037	-26.1
	8	0.089	0.088	1.475	1.411	1.386	0.039	27.7
	9	0.088	0.087	1.475	1.411	1.386	0.039	-28.1
	10	0.087	0.086	1.475	1.411	1.386	0.040	26.8
	11	0.087	0.086	1.475	1.411	1.386	0.040	-28.1
[12]CPP$^{\bullet+}$	1-12	0.083	0.083	1.475	1.411	1.387	0.040	28.1/-28.2

Discussion of the C-C distances

The geometrical and structural deformation of the benzene units for [n]CPPs with n < 9 is significant. The respective computed data are presented in Figure S16.

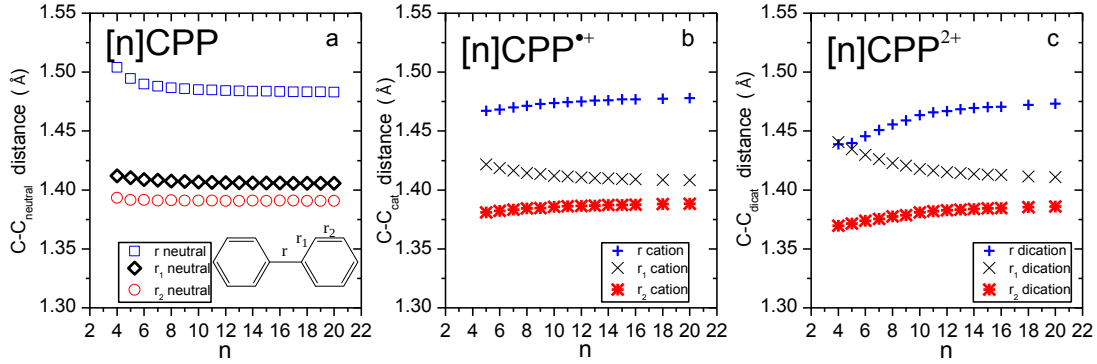

Figure S16. (U)B3LYP6-31G(d,p) average C-C distances (r, r_1, r_2) as a function of *n*. r, r_1 and r_2 are depicted as blue, black and red symbols, respectively. a) Neutral [n]CPP, b) $[n]CPP^{\bullet+}$ cations, and c) $[n]CPP^{2+}$ dications.

NICS values of neutral, cationic and dicationic [n]CPPs.

We used the Nucleus-Independent Chemical Shifts (NICSs) at the (U)B3LYP/6-311+G(2df,p) level to characterize the degree of aromaticity in a given structure. Negative values are typically associated with aromatic systems and positive values for non-aromatic systems.[14] The NICS value of benzene as a reference, $NICS_{benzene}(0)$, is -8 ppm at the ring center while $NICS_{benzene}(1)$ at 1 Å above the ring center is -10 ppm. In Figure S17, we summarize for each [n]CPP in neutral, cationic and dicationic state the obtained NICS at the center of each phenlyl unit and at the center of the [n]CPP cavity, NICS(0) and NICS(C) respectively. NICS(0) reach values as low as that of benzene with decreasing n and increasing charge. However, even though in neutral [n]CPPs the NICS(C) are always non-zero, these rapidly decrease with decreasing n towards –8 ppm for $[5]CPP^{\bullet+}$. For the dications NICS(C) becomes highly negative for n<9.

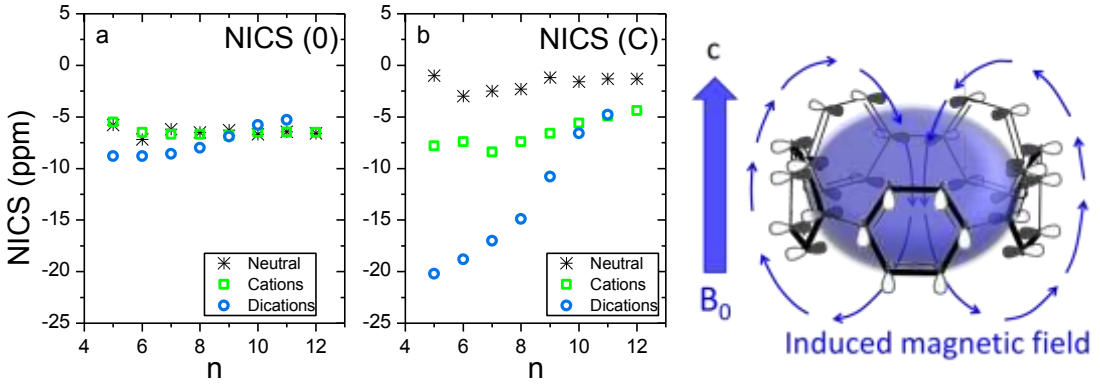

Figure S17. NICS values calculated at the (U)B3LYP/6-311+G(2df,p) theory level vs. *n* for three oxidation states of [n]CPPs. a) NICS(0) average values at the phenyl unit centers. b) NICS(C), at the center of the [n]CPP cavity. c) Scheme representing the induced magnetic field in $[5]CPP^{2+}$.

Energy calculation of the open shell singlet

Due to the well-known spin contamination problem in spin-unrestricted theory, we provide information on the $\langle S^2 \rangle$ values in Table S6 and the energetics using Yamaguchi's energy correction in Figure S18.

Table S6. Summary of the spin contamination, $\langle S^2 \rangle$ values for each structure.

	[n]CPPs				[n]LPP	
n	**Neutral $\langle S^2 \rangle$**	**Cation $\langle S^2 \rangle$**	**Dication Open Shell Singlet $\langle S^2 \rangle$**	**Dication Triplet $\langle S^2 \rangle$**	**Dication Open Shell Singlet $\langle S^2 \rangle$**	**Dication Triplet $\langle S^2 \rangle$**
2	--	--	--	--	0.000	2.017
3	--	--	--	--	0.000	2.017
4	--	--	--	--	0.383	2.024
5	0	0.755	0	2.023	0.505	2.021
6	0	0.755	0	2.023	0.845	2.021
7	0	0.754	0	2.021	0.913	2.020
8	0	0.754	0	2.020	0.948	2.019
9	0	0.753	0.276	2.019	0.966	2.017
10	0	0.753	0.524	2.017	0.976	2.015
11	0	0.753	0.681	2.000	0.980	2.014
12	0	0.752	0.742	2.014	0.983	2.013
13	0	0.752	0.802	2.013	0.985	2.011
14	0	0.752	0.833	2.012	0.986	2.013
15	0	0.752	0.851	2.010	0.986	2.009
16	0	0.752	0.858	2.009	0.986	2.009
18	0	0.751	0.877	2.007	0.986	2.007
20	0	0.751	0.891	2.006		2.006

We used the broken spin symmetry method to obtain open-shell singlet states. We estimate the exchange parameter, J, based on the formalisms derived by Noodleman15 using Yamaguchi modification.[16,17,18]

$$J = -\frac{E(Triplet) - E(\text{ Open Shell Singlet })}{\langle S^2 \rangle^{Triplet} - \langle S^2 \rangle^{\text{Open Shell Singlet}}}$$

$$E_{CorrectedOpenShellSinglet} = E(Triplet) + J * \langle S^2 \rangle^{Triplet}$$

E(Triplet) is the energy obtained from the dication optimization with triplet electronic configuration, E(Open Shell Singlet) to the energy obtained from the dication optimization broken spin (UB3LYP). The results are shown in Figure S18. As can be seen, the energy differences obtained with and without the correction are almost identical.

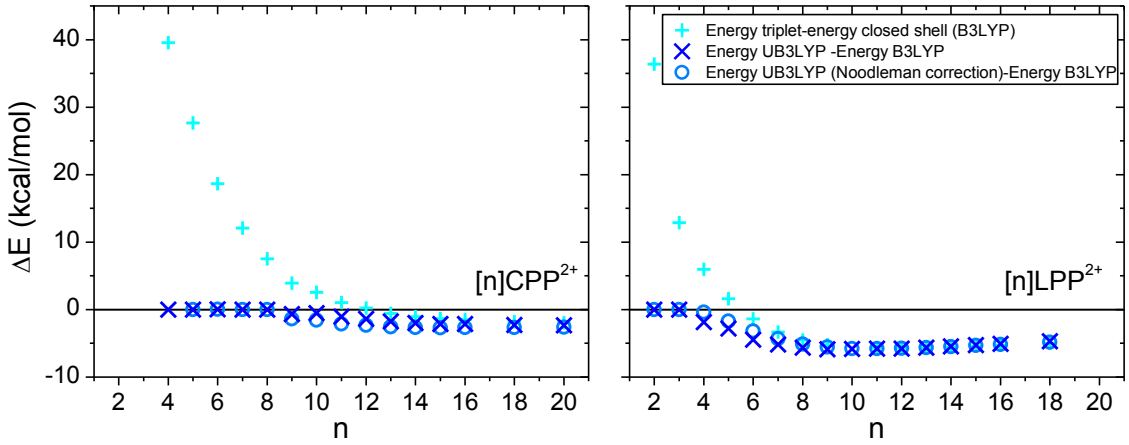

Figure S18. DFT/(U)B3LYP/6-31G(d,p) relative energies (ΔE) between the singlet closed-shell and open-shell); open-shell with the Noodleman correction and with the triplet of: a)[n]CPP^{2+} b) [n]LPP^{2+}. (**X**) correspond to ΔE= E(open-shell singlet dication) – E (closed-shell dication); light blue crosses (+) correspond to ΔE= E(triplet dication) – E (closed shell dication): circles (○) correspond to ΔE= E (corrected open-shell singlet dication) – E (closed-shell dication).

References

1 T. Iwamoto, Y. Watanabe, Y. Sakamoto, T. Suzuki, S. Yamago, *J. Am. Chem. Soc*. **133**, 8354–8361 (2011).

2 P. J. Evans, E. R. Darzi, R. Jasti, *Nature Chem*. **6**, 404–408 (2014).

3 J. Xia, R. Jasti, *Angew. Chem. Int. Ed*. **51**, 2474–2476 (2012).

4 Gaussian 09, Revision A.02, M. J. Frisch, G. W. Trucks, H. B. Schlegel, G. E. Scuseria, M. A. Robb, J. R. Cheeseman, G. Scalmani, V. Barone, B. Mennucci, G. A. Petersson, H. Nakatsuji, M. Caricato, X. Li, H. P. Hratchian, A. F. Izmaylov, J. Bloino, G. Zheng, J. L. Sonnenberg, M. Hada, M. Ehara, K. Toyota, R. Fukuda, J. Hasegawa, M. Ishida, T. Nakajima, Y. Honda, O. Kitao, H. Nakai, T. Vreven, J. A. Montgomery, Jr., J. E. Peralta, F. Ogliaro, M. Bearpark, J. J. Heyd, E. Brothers, K. N. Kudin, V. N. Staroverov, R. Kobayashi, J. Normand, K. Raghavachari, A. Rendell, J. C. Burant, S. S. Iyengar, J. Tomasi, M. Cossi, N. Rega, J. M. Millam, M. Klene, J. E. Knox, J. B. Cross, V. Bakken, C. Adamo, J. Jaramillo, R. Gomperts, R. E. Stratmann, O. Yazyev, A. J. Austin, R. Cammi, C. Pomelli, J. W. Ochterski, R. L. Martin, K. Morokuma, V. G. Zakrzewski, G. A. Voth, P. Salvador, J. J. Dannenberg, S. Dapprich, A. D. Daniels, O. Farkas, J. B. Foresman, J. V. Ortiz, J. Cioslowski, and D. J. Fox, Gaussian, Inc., Wallingford CT, (2009).

5 E. Zojer, J. Cornil, G. Leising, J. L. Brédas, *Phys. Rev. B* **59**, 7957–7967b(1999).

6] L. Cuff, C. Cui, M. Kertesz, *J. Am. Chem. Soc*. **116**, 9269–9274 (1994).

7 M. Peña-Alvarez, P. M. Burrezo, M. Kertesz, T. Iwamoto, S. Yamago, J. Xia, R. Jasti, J. T. López-Navarrete, M. Taravillo, V. G. Baonza, J. Casado, *Angew. Chem. Int. Ed.* **53**, 7033–7037 (2014).

8 P. George, M. Trachtman, C. W. Bock, A. M. Brett, *J. Chem. Soc., Perkin Trans. II* 1222–1227 (1976).

9 L. Radom, P. C. Hariharan, J. A. Pople, P. V. R. Schleyer, *J. Am. Chem. Soc.* **98**, 10–14 (1976).

10 S. M. Bachrach, D. Stück, *J. Org. Chem*. **75**, 6595–6604 (2010).

11 Y. Segawa, H. Omachi, K. Itami, *Org. Lett*. **12**, 2262–2265 (2010).

12 J. A. van Haare, E. E. Havinga, J. L. van Dongen, R. A. Janssen, J. Cornil, J. L. Brédas, *Chem. Eur. J.* **4**, 1509-1522(1998).

13 Y. Segawa, H. Omachi, K. Itami, *Org. Lett.* **12**, 2262-2265 (2010).

14 Z. Chen, C. S. Wannere, C. Corminboeuf, R. Putcha, P. V. R. Schleyer, *Chem. Rev.* **105**, 3842-3888 (2005).

15 J. Noodelman, *J. Chem. Phys.* **74**, 5734-5743 (1981).

16 K. Yamaguchi, H. Fkui, T. Fueno, *Chem. Lett*. 625-628 (1986).

17 T. Soda, K. Kitagawa, T. Onishi, Y. Takano, Y. Shigeta, H. Nagao, Y. Yoshioka, K. Yamaguchi, *Chem. Phys. Lett.* **319**, 223-230 (2000).

18 M. Podewitz, M. Reiher, Spin interactions in cluster chemistry. Advances in Inorganic Chemistry. Theoretical and Computational Inorganic Chemistry. Edited by R. van Eldik, J. Harvey, **62**, 177-230 (2010).